

# THIS WEEK

## EDITORIALS

**ERITREA** The lessons of a decaying national science system **p.8**

**WORLD VIEW** Arab women know their rights and when to go home **p.9**



**BIOSENSOR** Blue is the colour when protein is present **p.10**

## Murky manoeuvres

*Scientific reform promised to give Italy's scientists the respect and autonomy they deserve, and political posturing must not be allowed to tip the burgeoning system off balance.*

Three separate Italian court decisions, each in some way hinged on science, have shocked the international research community in recent months.

On 12 October, Italy's highest civil court ruled that compensation should be paid to a man who developed a tumour close to his brain that he claimed was caused by work-related use of mobile phones. On 22 October, a judge in L'Aquila sentenced six scientists and a government official to prison for manslaughter, saying that they failed to appropriately convey the risk of the 2009 earthquake, causing the deaths of 29 people who would otherwise have left their homes (see page 15).

The third decision, by a court in Brescia in July, ordered the temporary closure of Green Hill, a dog-breeding company in Montichiari that supplied animals for the toxicity tests officially required by bodies such as the European Medicines Agency and the US Food and Drug Administration, while mistreatment charges by animal-rights groups were investigated. The business had been regularly and rigorously checked by authorities over previous years, but has now effectively been destroyed because the judge placed the dogs in the care of the animal-rights groups, which distributed them to private homes.

Judges in Italy, as in democracies elsewhere, are supposed to make independent decisions based solely on the law. But the influence of a general societal mood is hard to avoid — and in Italy that society lacks understanding of, or respect for, science and its complexities.

Science is subject to a level of irrational suspicion in many countries, but in Italy there is a perception that science doesn't even matter — a state of affairs encouraged by decades of underfunding and political disdain. Italy invests just 1.26% of its gross domestic product in research and development (R&D), compared with Germany's 2.82% and a European Union (EU) average of 2%. In 2009, Italy employed only 226,000 full-time-equivalent R&D staff, whereas Germany had 535,000. The system has long suffered from the lack of a legally enforced meritocracy, allowing cronyism to taint academic appointment and promotion. Heads of research agencies have often been political appointees rather than competent experts.

Successive governments, well aware of the problems, introduced a series of reforms that tinkered with the system without fixing it, causing only further uncertainty. Then, three years ago, came a watershed: the reform-to-end-all-reforms intended to give more autonomy to research agencies, along with appropriate accountability. It sought to introduce an independent system to identify suitably qualified candidates as agency presidents (see <http://doi.org/fwskwv>), as well as a national research-evaluation agency whose assessments would be linked to funding. Designed by the centre-left government of Romano Prodi, it was finally passed into law in 2009 by the centre-right government of Silvio Berlusconi.

Enactment of such major reform has been a struggle, particularly for the newly appointed presidents of the 12 research agencies — which include the National Research Council, the National Institute of Nuclear Physics and the National Institute of Astrophysics — who

are currently finalizing their new statutes. But a spirit of confidence has emerged. The agency presidents have formed a loose, cooperative alliance. And even the historically timid national academy, Accademia Nazionale dei Lincei, has become outspoken — for example, loudly challenging the L'Aquila court decision.

But research minister Francesco Profumo seems set on tipping things off balance again. In a murky manoeuvre, he announced reform plans in a financial newspaper on 11 October that would, along with other major

***"In Italy there is a perception that science doesn't even matter."***

changes, merge all 12 agencies into a single national organization — before the end of the year. He argued, unconvincingly and without a technical plan, that such a system would help to save money and win EU research grants. In the style of the old guard, whose day was thought to be done, he did not consult the

general scientific community on the matter, not even agency presidents.

It is impossible to imagine such a thing happening in, say, Germany, a country whose successful scientific system Profumo says he would like to emulate. German politicians and their administrations are in appropriate awe of their research-agency presidents and of the scientific culture they represent. It is also hard to imagine courts there crudely running rough-shod over science.

Profumo's amateurish proposal, which he tried to insert into Prime Minister Mario Monti's crisis-related financial law for 2013–15, did not survive first-round parliamentary scrutiny, but Profumo seems set to try to push for some sort of high-speed change — his government is slated to dissolve in March.

Crucial for now is that scientific leaders are left in peace to complete the reform-to-end-all-reforms, and that science doesn't fall victim, once again, to opaque politics. Building respect for science takes time. ■

## Bad press

*Japan's media have played a large part in exacerbating the effects of a fraud.*

It is a shame that Shinya Yamanaka's recent Nobel prize had to be tainted by the shenanigans of Hisashi Moriguchi, the University of Tokyo project scientist who fabricated a story about having used Yamanaka's fêted technology on induced pluripotent stem (iPS) cells to treat patients who had heart failure.

The poor quality of journalism that led to the story being so widely reported was not an isolated incident in the coverage of science, in Japan or elsewhere. The *Yomiuri Shimbun's* presentation

of Moriguchi's 'accomplishments' was particularly disappointing. But other newspapers, including the *Nihon Keizai Shimbun*, have now admitted to having run unverified stories about Moriguchi over the past decade. Given the esoteric nature of the studies involved, reporting on science can be intimidating. So here are some practical steps to help a journalist challenge a specialist.

One can start by looking at publications. All scientists publish their results. If they don't it is a red flag. The publications give a scientist's affiliations, so if there is any doubt, it is easy to verify whether a scientist actually works where they say they do (a quick e-mail to Harvard University could have saved the *Yomiuri Shimbun* a lot of embarrassment). Publications also list the names of collaborators (making it easy to confirm with them that the scientist has done the experiments claimed), the names of the funders (making it easy to check whether resources were available) and declarations of conflicts of interest (revealing potential biases).

Most importantly, a journalist should talk to other researchers — those who do not collaborate with the scientist in question — about the study's significance and feasibility. Such researchers can usually be found by consulting references in the publication. If not — and an absence of proper references would be a warning sign — an Internet search will quickly bring up names. Although probably truer of North America and Europe than elsewhere, scientists are generally committed to keeping junk out of the literature. If it looks like junk, they'll tell you.

Of course, Moriguchi said that his latest results were not yet published. That should have triggered further questioning. Why would he present his results to the media first? Some scientists have a reason for doing so; Moriguchi did not. And it should have prompted a closer look at his work experience and past publications. Why do records of his career — which were available online — suggest that he had little or no experience in the field in which he was claiming to have made a revolutionary breakthrough? Why did he profess to work in a non-existent university Division of iPS Cell Research and Application?

And why was he taking an unconventional and unfamiliar

technology to the clinic? When he was questioned directly, as he was by *Nature*, things got worse. Why, for example, did he refuse to give the names of collaborators on the latest study? Poking the surface led to an outpouring of dubious statements.

People get away with fraud everywhere, but in Japan it seems that there are cultural factors that mean it goes unreported. Japanese scientists are less likely to be critical of their colleagues; there is less protection of whistleblowers who might not want to risk their careers; and journalists in Japan can be too polite, perhaps intimidated by the

**“Why would Moriguchi present his results to the media first?”**

illustrious image carried by *sensei* and afraid to ask awkward questions. Possibly because of a lack of confidence in their English or because of differences between time zones, they often do not contact scientists overseas.

The situation is exacerbated by a recent Japanese epidemic: iPS-cell mania. With the excitement over Yamanaka's pioneering results, media outlets are rushing to get new iPS-cell stories first, sometimes regardless of their quality. This tendency is fuelled by a paranoid attachment to iPS-cell technology. Many news stories describe an international race to translate iPS-cell research into medical advances, which Japan might lose. This fear seems to have inspired Moriguchi, who lamented in 2009 that Japan was in danger of falling behind in iPS-cell research (in a Correspondence in *Nature*: H. Moriguchi and C. Sato *Nature* 457, 257; 2009), and the *Yomiuri* reporters, who even envisaged a 'flexible' approval system in the United States that might allow Moriguchi to continue with his research.

This is all very silly. The beautiful thing about iPS-cell technology — and a major reason it won the Nobel prize — is that it can be used easily by scientists everywhere. If Japan wants to show its pride in Yamanaka's accomplishment, it should celebrate all achievements around the world. And if journalists want to understand just how important it is, they should put a new development in an international perspective. ■

## Fight the power

*Independence of academic institutions is crucial if nations are to rebuild.*

It is said that truth is the first casualty of war. But after wars have ended and nations are rebuilding, truth is a potent foe, too.

A free press and a strong academic establishment pose great threats to a despotic regime, and are often the first to feel pressure. In a News Feature on page 24, we document such tensions in Eritrea, where there are efforts to remove foreign influences from the nation's medical schools and to break up its academic institutions. Eritreans who have fled or been exiled lament the sorry state of these institutions, and fear that by severing ties to US universities, the government has squandered chances of extraordinary gains in public health. (Representatives of the Eritrean government did not respond to several requests for comments on these and other allegations.)

Many who helped to lead Eritrea to its independence in 1991 and establish the current regime were academics, students and physicians — the very type of people (and, in some cases, the actual people) that the country's leaders are now marginalizing. This irony should not be a surprise, given that thriving academic institutions in new regimes can serve as hotbeds of dissidence, unrest and further revolution.

For a country such as Eritrea to reach a stable equilibrium, this destructive cycle must be broken. And this is perhaps the best lesson that Eritrea can give to nations that must build new governments. It is expected that academics will be involved in the overthrow of unjust regimes, and that they will subsequently be called on to support

burgeoning governments. But these people must strive to remain independent from the start. The desire to trust and indulge former comrades may be strong, yet academics must reject all interference and resist any attempt by government to grab control of institutions.

To stand up to power in this way is difficult, but there is much at stake. Independent institutions will produce and support well-informed, independent citizens, who remain the most effective defence against corruption and the abuse of power. ■

### ANNOUNCEMENT

## Nature metrics

As of last week, *Nature* now provides a real-time online count of article-level metrics for its published research papers. Citation data, news mentions, blog posts and details of sharing through social networks, such as Facebook and Twitter, will be available for every research article published since last year.

Nature Publishing Group (NPG) hopes that the information will be of interest to readers, as well as feeding into the evolving debate about alternative ways to evaluate scientific output. The 2014 Research Excellence Framework exercise to assess UK research quality, for instance, will look at article citations and consider other measures for tracking research impact.

The information is available for 20 NPG journals published on [nature.com](http://nature.com), including the *Nature* research journals, *Nature Communications* and *Scientific Reports*. ■

A. AWAD



## How women scientists fare in the Arab world

**Rana Dajani** argues that true equality for women scientists requires recognition of their family roles as well.

I will never forget a rich Arab businessman I met in New York at the Clinton Global Initiative. He had an American lady in charge of his non-governmental organization. She was a great woman dedicated to her work, who would stay until midnight doing her job. He said that women in the Arab world will never succeed until they are ready to stay at work until midnight like the American woman. He complained that Arab women want to go home at five o'clock to look after their families. I was upset. I told him that it should be their choice how long they want to work; and if they have priorities such as family and want to leave at five, then this should be respected. It is men like him, and in some cases women, who undermine who we are.

The issues faced by women in science are beginning to receive more attention. On this page last week, Athene Donald highlighted one initiative to tackle gender bias (A. Donald *Nature* **490**, 447; 2012). I would like to offer a perspective from the Islamic world.

Despite the impression given by extremists, Islam gives women the right to education. More than four in ten women who go to university in Jordan go into science, engineering or medicine. Women outnumber men on courses in natural science, pharmacology and agriculture; numbers are equal in maths and computer science; and one in three engineering students in Jordan is a woman.

Some of the problems faced by women scientists in the Middle East are the same as those faced by women around the world. Our productivity, for instance, is measured on a male scale. The years we spend taking care of children are not calculated as part of the gross domestic product of a country. What is more important — to build physical things or to nurture a human being?

As an example of this male scale, L'Oréal and the United Nations Educational, Scientific and Cultural Organization are running a competition to award fellowships to Arab women scientists — but you have to be under 40 to enter. This is biased, and based on metrics from a male-dominated world, in which if a man doesn't make it by 40 he is a failure.

The feminist movement was a good thing, but it was too focused on equality with men and failed to enable us to respect ourselves as women and to be proud of who we are.

Another common challenge to all women scientists is lack of mentoring and networking. Most women scientists everywhere have two jobs — work and home — and most will not give up home for work. They will always be worried about the children, want to be with them, and feel that the father's presence won't compensate for their own absence. So they don't take time after work to have a coffee with their colleagues.

Yet this informal environment is where scientists learn what is going on; where they

lobby, network, mentor and get mentored. Women don't have the time. Networking is an extra effort. Men mentor each other and spend time together after work, fostering the men's club. Women rush home to take care of children, not because they have to but because they want to.

This is a major obstacle for women scientists in terms of opportunities, learning and support. That is why mentoring projects — something we lack in the Arab world — are important. But social media allow mentoring online, and some women scientists now plan to start an online mentoring scheme for women scientists in Jordan, in collaboration with the country's first woman university president, Rowaida Maaitah.

Women also have challenges specific to the Middle East. These may not be so obvious because they are subtle, and must be identified, studied and solved by Arab women themselves. For instance, the September

study about a bias among US scientists against women, mentioned by Donald last week (C. A. Moss-Racusin *et al. Proc. Natl Acad. Sci. USA* <http://doi.org/jkm>; 2012), would not necessarily translate to the Arab Muslim world, where the prevailing attitude among both men and women is that women work hard and are more dependable than men. One must not fall into the trap of transferring solutions from one culture to another.

I know of an American researcher who went to Bulgaria to help women fight for their rights. She went assuming that they would want to demand to work. But Bulgarian women who had lived under Communism wanted the exact opposite. They wanted the freedom to stay at home if they chose.

A much-misunderstood issue is the covering of the hair and sometimes the face by Muslim women. In the West, this is often considered a sign of oppression. Yet more than half the female students and academics in the Arab world choose to cover their hair for religious reasons, compared with fewer than 10% 20 years ago. These young women are educated, affluent and independent. I have a graduate student who covers her face who told me that she believed she would win a Nobel prize. This is not oppression.

I see the Arab spring as an opportunity for women to learn about their rights and to advocate for them — to distinguish between what is tradition and what is religion. This would weed out extremists who, through ignorance, distort the image of Islam. And it would weed out opportunists who want to misrepresent Muslim women. Throughout the Islamic civilization that flourished in the Middle Ages there were more than 8,000 women scholars. There are many more on the way today. ■

**Rana Dajani** is assistant professor of molecular biology at the Hashemite University in Zarqa, Jordan, and Fulbright visiting professor at Yale University.  
e-mail: [rdajani@hu.edu.jo](mailto:rdajani@hu.edu.jo)

ONE MUST NOT  
FALL INTO  
THE TRAP  
OF TRANSFERRING  
SOLUTIONS FROM  
ONE CULTURE  
TO ANOTHER.

➔ **NATURE.COM**  
Discuss this article  
online at:  
[go.nature.com/dbkllie](http://go.nature.com/dbkllie)

# RESEARCH HIGHLIGHTS

Selections from the  
scientific literature

## CANCER

### Predictor pairs images and genes

Automated image processing can be integrated with molecular profiling to provide a fuller portrait of cancer.

Pathologists routinely use visual examinations of cell types in tumour biopsies to direct patient care. However, it is hard to integrate these visual analyses with data from gene-expression studies.

Florian Markowetz and Yinyin Yuan at the University of Cambridge, UK, and their team came up with software that can analyse images of stained tissue sections to determine the identity and arrangement of cells in tumours. For some cell types, certain spatial patterns were associated with longer patient survival. However, an algorithm that combined image-based and gene-expression data predicted survival more accurately than algorithms that used either type of information alone.

*Sci. Transl. Med.* 4, 157ra143 (2012)

## MICROBIOLOGY

### Bacteria beaten by bacteria

Infections caused by a strain of *Clostridium difficile* responsible for recent epidemics might be treatable using a mix of gut bacteria.

A team led by Trevor Lawley of the Wellcome Trust Sanger Institute near Cambridge, UK, infected mice with the *C. difficile* strain and then treated them with an antibiotic commonly used in humans. Instead of killing the pathogen, the antibiotic displaced other gut bacteria and permitted a persistent *C. difficile* infection. Treating the infected mice with faeces from healthy

animals restored their intestinal flora and resolved their infections. A mixture of six different bacterial species isolated from the faeces had the same effect, promising a treatment more palatable to patients than faecal transplantation.

*PLoS Path.* 8, e1002995 (2012)

## CLIMATE-CHANGE ECOLOGY

### Plankton diversity loss looms

They are responsible for about half of all photosynthesis on Earth — and plankton could be drastically affected by climate change.

Mridul Thomas and his team

at Michigan State University in East Lansing considered 194 phytoplankton strains. Using the existing literature, the authors estimated the maximum growth rate, optimum temperature for growth and the temperature range over which growth can occur, for each of the strains. Many strains seem to be tightly adapted to the average temperature at their location. Tropical strains, in particular, tend to have optimal growth temperatures at or just below the mean temperature in their environment. The authors' models indicate that an average temperature rise of just 2°C in the tropics by 2100 could reduce the diversity of

phytoplankton in the region by a third — unless, that is, the plankton can evolve greater heat tolerance.

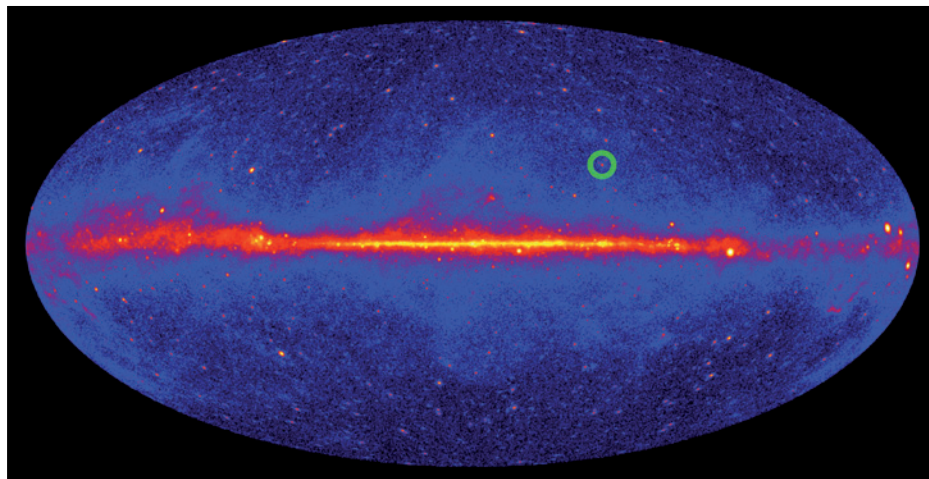
*Science* <http://dx.doi.org/10.1126/science.1224836> (2012)

## BIOSENSORS

### Naked-eye ELISA developed

Researchers have developed a sensitive bioassay that can be read with the naked eye.

The assay is based on a laboratory technique known as an ELISA (enzyme-linked immunosorbent assay), in which an enzyme generates a coloured compound whenever



## ASTRONOMY

### Picking out a predatory pulsar

Researchers have used raw computing power to hunt down a 'black widow' pulsar that is evaporating its companion star.

Pulsars are stellar remnants that emit lighthouse-like beams of radiation. They often emit gamma rays, but can usually be spotted only if they also emit easier-to-detect radio waves. However, Holger Pletsch of the Max Planck Institute for Gravitational Physics in Hannover, Germany, and his colleagues found

the current pulsar (pictured; circled) through a blind search of data from the Fermi Gamma-ray Space Telescope.

Using computers to analyse huge swathes of raw data, the team picked out the pulsar, which takes 93 minutes to orbit its companion star. This orbital period is the shortest of any binary pulsar of this type yet found.

*Science* <http://dx.doi.org/10.1126/science.1229054> (2012)

antibodies recognize a target molecule. However, detecting low levels of this compound requires expensive instruments that few labs in the developing world can afford, so Molly Stevens and Roberto de la Rica of Imperial College London devised an alternative.

In their method, the ELISA enzyme controls the aggregation of nanoparticles, giving rise to a blue colour if a target protein is present and a red colour if it is not. Although the bioassay cannot quantify protein levels, it can detect an HIV protein at concentrations as low as 1 attogram per millilitre.

*Nature Nanotechnol.* <http://dx.doi.org/10.1038/nnano.2012.186> (2012)

## MICROBIOLOGY

## Cheating yeast finish last

The 'tragedy of the commons' holds that cheaters have an advantage over cooperators because cheaters benefit from common goods without contributing to them. Studies in yeast suggest a new mechanism to avert such a tragedy.

Adam James Waite and Wenying Shou of the Fred Hutchinson Cancer Research Center in Seattle, Washington, started cultures that had equal amounts of three yeast strains: one that produced adenine and required lysine; another that produced lysine and required adenine; and a third, 'cheating' strain, which required lysine but did not supply any nutrients.

Contrary to expectations, 'cooperative' strains dominated in some cultures, and could occasionally drive cheaters to extinction. Genome sequencing revealed that the dominating strains had adapted to their new environment by

accumulating mutations that improved nutrient transport. When these mutations arose in cooperative strains and compensated for the cost of cooperation, the cheaters were outcompeted.

*Proc. Natl Acad. Sci. USA* <http://dx.doi.org/10.1073/pnas.1210190109> (2012)

## CLIMATE

## Tailored geoengineering

Climate-engineering techniques that cool Earth by reflecting sunlight back into space may be tailored to minimize negative effects on individual regions without compromising overall cooling.

Douglas MacMartin at the California Institute of Technology in Pasadena and his colleagues used a global climate model to explore the impact of techniques such as the injection of aerosols into the stratosphere. The team then modelled the effects of varying the interventions spatially and seasonally, and showed that the average global temperature could be reduced while still supporting goals such as the recovery of Arctic sea ice.

The model suggests that climate interventions could provide the world with more than a single 'global thermostat', the authors say. *Nature Clim. Change* <http://dx.doi.org/10.1038/nclimate1722> (2012)

## CONDENSED MATTER PHYSICS

## Building a space-time crystal

Just as a crystal consists of a regular array of particles repeated in space, so a space-time crystal should consist of a regular pattern of particles that also repeats cyclically over time. Now, Xiang Zhang at the University of California, Berkeley, and his team have published the first proposal for an experiment that could realize this abstract notion.

The authors' idea is to trap a ring of cold ions in a magnetic

## COMMUNITY CHOICE

The most viewed papers in science

## ANIMAL BEHAVIOUR

## Bears show knack for numbers

**HIGHLY READ**  
on [www.journals.elsevier.com/animal-behaviour](http://www.journals.elsevier.com/animal-behaviour) over the past 3 months

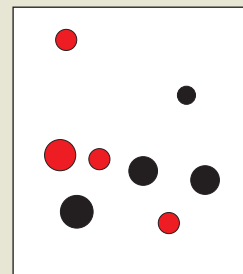
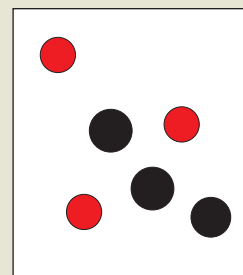
Bears may be able to estimate and compare numbers of items.

Jennifer Vonk of Oakland University in Rochester, Michigan, and Michael Beran of Georgia

State University in Atlanta trained three captive black bears (*Ursus americanus*) to distinguish between two groups of dots (pictured) displayed on a touch-screen computer. One bear was trained to touch the group containing the most dots, and the others to select the group with the fewest. By varying the size and positions of the dots, researchers tested whether the animals could recognize dot number independently of the total area covered by the dots. Although the bears showed a preference for dots occupying a larger area, they also showed some ability to judge the relative numbers of dots.

The bears' numerical skills may have evolved to help them in complex foraging environments, the authors suggest.

*Anim. Behav.* 84, 231–238 (2012)



J. VONK/ANIM. BEHAV./ELSEVIER

field so that they adopt a regular arrangement and then rotate in their lowest energy state, thereby creating temporal repetition. Such a device might be able to store quantum information, and could thus have applications in quantum computing, the researchers say. *Phys. Rev. Lett.* 109, 163001 (2012)

## PALAEOLOGY

## Palaeoflamingo nest found

A fossilized nest, found in Spain and containing five eggs, belonged to a previously unknown species of palaeoflamingo, the ancient ancestor of the modern, long-legged bird. The nest — made from twigs and leaves 15 million to 20 million years ago — was found alongside

bone fragments, encased in limestone in the Bardenas Reales de Navarra Natural Park.

Gerald Grellet-Tinner from the Field Museum in Chicago, Illinois, and his team report that the eggshells are characteristic of flamingos, whereas the nest and the number of eggs more closely resemble those of grebes, freshwater diving birds. Modern grebes and flamingos differ in their nest-building and feeding styles, but DNA studies have suggested that the two species are closely related. The present discovery supports that connection and points to a time when the two species shared survival strategies.

*PLoS ONE* 7, e46972 (2012)

**NATURE.COM**

For the latest research published by Nature visit:

[www.nature.com/latestresearch](http://www.nature.com/latestresearch)

# SEVEN DAYS

The news in brief

## POLICY

### Verdict shock wave

The six-year manslaughter sentences handed to six scientists and a government official for advice they gave preceding the 6 April 2009 earthquake in L'Aquila, Italy, have triggered concerns worldwide over the future of science advice. Anne Glover, chief scientific adviser to the European Commission, is among scientists warning that the verdict could mean researchers are less likely to agree to advise governments. See page 15 for more.

### Electronics boost

India unveiled an electronics policy that aims to build a domestic chip-manufacturing industry, creating 2 million jobs by 2020. Proposed initiatives include a fund to promote electronics research and development, and an institute focusing on semiconductor chip design. The government also plans to bolster postgraduate education to produce about 2,500 PhDs annually in electronics by 2020.

### Biofuels warning

Pushing up the proportion of alga-based biofuels used for transport to 5% of the total US requirement "would place unsustainable demands on energy, water, and nutrients", says a report from the US National Research Council. Consumption of water and fertilizer for the cultivation of algal biofuels can be prohibitive, and such concerns need to be addressed if these fuels are to fulfil their promise, adds the report, released on 24 October. See [go.nature.com/kyptgk](http://go.nature.com/kyptgk) for more.

### Nuclear restart

China will start approving new reactors again, ending a 19-month ban triggered by the

nuclear disaster in Fukushima, Japan, the Chinese government announced on 24 October. But enhanced safety standards and a temporary ban on inland reactors, which account for one-third of those planned, mean that nuclear reactors will supply 40 gigawatts of power by 2015, rather than 50 gigawatts as planned. China currently has 15 reactors supplying 12.5 gigawatts, or 1.8%, of its power.

### Fisheries trade-off

A proposal that would have placed the European Union's fisheries policies on a sounder scientific footing was watered down at a meeting of ministers on 23 October. Conservationists have criticized the decision to spend money from a new European

Maritime and Fisheries Fund on modernizing fishing fleets, arguing that such measures will not improve the sustainability of fish stocks and that more funds should be spent on data collection and monitoring fishing fleets. See [go.nature.com/t6j4qc](http://go.nature.com/t6j4qc) for more.

## BUSINESS

### Re-enter the Dragon

A commercial resupply capsule has returned safely from the International Space Station. The Dragon spacecraft, built by SpaceX of Hawthorne, California, splashed down some 400 kilometres off the California coast on 28 October. It was carrying around 750 kilograms of

return cargo, including scientific samples. This is the first of at least 12 commercial resupply missions that SpaceX will send to the station as part of a US\$1.6-billion contract.

### Solar exit

German engineering company Siemens announced that it would sell its solar business on 22 October. The Munich-based company also said that it was ending its participation in DESERTEC, a project seeking to produce power by tapping solar energy in the Sahara and other deserts. See page 16 for more.

### Nuclear rights

Hitachi has bought the rights to build nuclear power plants in the United Kingdom. The Japanese firm



KEYSTONEUSA-ZUMA/REX FEATURES

## Titanic storm batters US east coast

Hurricane Sandy, which was downgraded to a post-tropical cyclone as wind speeds dropped from about 145 kilometres per hour to around 105 kilometres per hour, made landfall near Atlantic City, New Jersey, at about 8 p.m. Eastern time on 29 October. The storm knocked out

power to millions and closed public transport in numerous cities, including New York, which was among the hardest hit. More than 15,000 flights have been cancelled, and estimates of the damage run to well over US\$10 billion. See [tinyurl.com/99wwz9w](http://tinyurl.com/99wwz9w) for more.

announced the purchase of the Horizon nuclear project from German owners E.ON and RWE for a reported £700 million (US\$1.1 billion). The deal clears the way for Hitachi to seek licensing approval for up to three 1,300-megawatt advanced boiling water reactors at each of two sites in Anglesey and Gloucestershire.

## PEOPLE

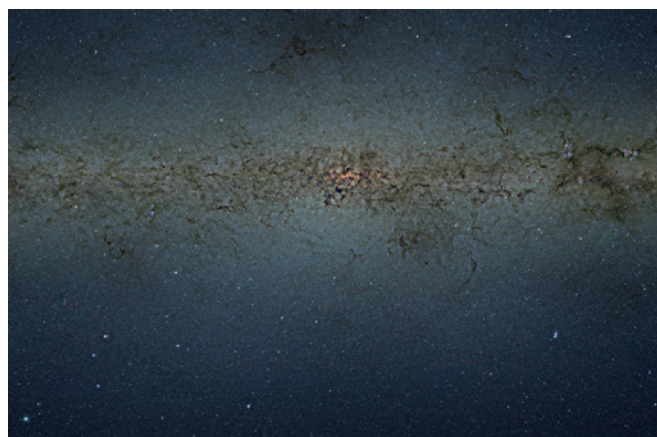
## Synchrotron chief

Three years after converting its 3-kilometre-long linear particle accelerator into an X-ray laser, the SLAC National Accelerator Laboratory in Menlo Park, California, named Chi-Chang Kao as its director, on 24 October. Kao, who develops applications of synchrotron radiation and was an associate laboratory director at SLAC, is the first scientist who is not a particle physicist to lead the facility. Having transformed itself from a particle-physics stronghold into an X-ray light source, SLAC now draws structural biologists, material scientists and other researchers.

## RESEARCH

## Starry, starry night

The European Southern Observatory (ESO) unveiled a 9-gigapixel image of the



centre of the Milky Way (**pictured**) on 24 October. If printed at the standard resolution of a book, the image, from the ESO's VISTA infrared survey telescope in Chile, would be 9 metres long and 7 metres high. Astronomers used the telescope data to create a catalogue of 84 million stars — the largest such catalogue compiled to date.

## Radiation study

The US National Academy of Sciences is undertaking a pilot study to look for cancer risks around six nuclear power plants and a nuclear fuel facility. The study was called for by the Nuclear Regulatory Commission in response to long-standing public concerns about radiation affecting the health of people living around the plants (see *Nature* 472,

15; 2011). Announced on 23 October, the academy study is expected to continue into at least 2014 and will cost around US\$2 million.

## Coastline review

An eight-year survey of coastal regions by China's State Oceanic Administration was completed on 26 October. Of 52 cities surveyed, 28 have serious water shortages, according to the assessment, which included 19,057 kilometres of continental coastline and 10,312 islands.

## Shanghai telescope

China unveiled a radio telescope at the base of Sheshan Mountain in Shanghai on 28 October. The telescope will be used with three others across China for very-long baseline interferometry, a technique

## COMING UP

## 2–3 NOVEMBER

A Cancer Research UK Cambridge Research Institute symposium will focus on unanswered questions in cancer sequencing. [tinyurl.com/9ns9c5n](http://tinyurl.com/9ns9c5n)

## 4–7 NOVEMBER

Updates from the Mars Curiosity rover will be discussed at the Geological Society of America meeting in Charlotte, North Carolina. [tinyurl.com/9ouo7kr](http://tinyurl.com/9ouo7kr)

## 5–7 NOVEMBER

The Fourth Canadian Science Policy Conference will discuss issues including how fundamental research can drive innovation. [www.cspc2012.ca](http://www.cspc2012.ca)

## 7–8 NOVEMBER

The European Food Safety Authority gathers scientists in Parma, Italy, to discuss challenges in risk assessment. [tinyurl.com/9zy5vgt](http://tinyurl.com/9zy5vgt)

that combines data from different telescopes to produce images of higher resolution than any of the telescopes can provide alone.

## EVENTS

## Canada quake

An earthquake off the west coast of Canada on 27 October triggered tsunami warnings for the Pacific. The magnitude-7.7 quake, centred close to the Queen Charlotte Islands, caused no major damage, however, and ultimately produced waves of only about a metre in Hilo, Hawaii. See [go.nature.com/2ug81s](http://go.nature.com/2ug81s) for more.

► **NATURE.COM**

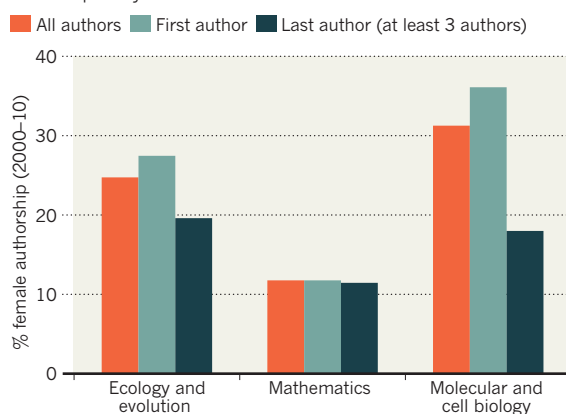
For daily news updates see: [www.nature.com/news](http://www.nature.com/news)

## TREND WATCH

An analysis of the gender of authors in research articles shows that women are not only under-represented as authors, but are also much less likely to be in the prestigious position of last author in all surveyed science fields except mathematics (see chart), in which authors tend to be listed alphabetically. The study, based on millions of articles in the academic journal archive JSTOR, was led by researchers at the University of Washington in Seattle and New York University (see [www.eigenfactor.org/gender](http://www.eigenfactor.org/gender)).

## GENDER BIAS IN RESEARCH

Women are under-represented as authors on research papers — but especially as last authors.

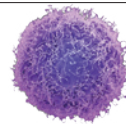


# NEWS IN FOCUS

**ANIMAL RESEARCH** An urgent housing search for the NIH's retired chimps **p.18**

**PHYSICS** Quantum theorists make light work of space-time rips **p.19**

**IMMUNOLOGY** Chinese vaccine tackles neglected form of hepatitis **p.21**



**GENOMICS** Single-cell sequencing reveals hidden diversity **p.27**

F. MONTEFORTE/AFP/GETTY



Official reassurances convinced many residents of L'Aquila that the earthquake risk was low, a factor that many blame for the 2009 quake's high death toll.

## SCIENTIFIC ADVICE

# L'Aquila verdict row grows

*Global backlash greets sentencing of Italian scientists who assessed earthquake risk.*

BY NICOLA NOSENGO IN ROME

To scientists in Italy, offering advice on risks looks to be a hazard in itself. In the aftermath of a judge's decision to sentence a group of seismic-risk experts to six years in prison, researchers in the country are demanding that legal safeguards be put in place for advisers, and that a clear division of responsibilities be made between scientific experts and government decision-makers.

On 22 October, a court in L'Aquila found six scientists and one government official guilty of playing down earthquake risks in the region just days before a devastating earthquake hit the city on 6 April 2009. Prosecutors had argued that

the group's assessment of a surge in seismic activity, and a subsequent press conference involving two members of the group, focused on simply reassuring the public rather than providing a careful evaluation of the potential hazards. Residents of L'Aquila say that they typically leave their homes when swarms of tremors shake the region, but the calming messages from the experts, the court heard, persuaded dozens of people to stay indoors. Many then perished as numerous buildings collapsed during the magnitude-6.3 quake (see *Nature* 477, 264–269; 2011).

The severity of the

sentences, however, surprised many — even the public prosecutor, Fabio Picuti, who had sought terms of four years — and condemnation quickly followed from the global scientific community (see *Nature* 490, 446; 2012).

Stefano Gresta, president of Italy's National Institute of Geophysics and Volcanology in Rome (where two of the convicted scientists worked) said at the time that the verdict “is likely to compromise the right/duty of scientists to take part in the public debate” because they will be “in fear of being convicted”. Statements of support for the scientists came from the American Geophysical Union, the Geological Society of America, the International Human Rights Network of Academies and ►

► **NATURE.COM**  
Read more about the background to this case:  
[go.nature.com/mkvy3o](http://go.nature.com/mkvy3o)

► Scholarly Societies and the science-promotion group Euroscience. The US National Academy of Sciences and the Royal Society, UK, issued a joint statement saying that the verdict “could lead to a situation in which scientists will be afraid to give expert opinion for fear of prosecution or reprisal”. And the chief scientific adviser to the European Commission, Anne Glover, told *Nature* that she is concerned about the fallout from the case. “It may become more difficult to motivate scientists to advise on inherently uncertain issues,” she says.

The verdict will set no legal precedent abroad. But there is a risk that L'Aquila could become an “informal precedent, in that it breaks down an aura of immunity surrounding science”, says Sheila Jasanoff, who specializes on the intersection of science and the law at Harvard Kennedy School in Cambridge, Massachusetts. “People and lawyers may be more willing to sue when they feel bad advice has been given.”

The day after the verdict, Luciano Maiani resigned as President of Italy's major risks commission, the expert panel that advises the national government on environmental hazards. Most of the convicted scientists had given their assessment of the seismic risk at L'Aquila as serving members of the committee. Maiani says that he was protesting not the verdict itself but the lack of legal protection for his committee.

Maiani, a physicist at the University of Rome, La Sapienza, and former director-general of CERN, Europe's particle-physics facility near Geneva in Switzerland, says that, since taking up his post at the beginning of

this year, he has been asking the government to commit legal assistance to the committee members, as well as financial insurance in case of civil proceedings, but his requests have been refused. “This way it is impossible to give truly independent advice,” he argues. “The obvious consequence is that scientists will tend to be more conservative in their advice, like some medical doctors who order too many tests and surgeries for fear of being sued. But this is not in society's best interest.”

The full reasoning behind the verdict is not yet public, leaving some Italian legal experts baffled as to why the judge issued such a heavy

**“Scientists are not elected, so it cannot be up to them to decide how to deal with an emergency.”**

sentence, making no distinction between scientists in an advisory role and government officials entitled to take decisions and speak to the public. “Normally, the official who asks for expert advice remains legally responsible for the actions he then takes, unless the advice was wilfully and seriously wrong,” says Stefano Rodotà, a legal specialist at La Sapienza and a former member of the Italian Parliament.

Glover says that the case underlines the importance of having clear rules on how scientific advice is given and used. “Before a scientist gives advice, it should be crystal clear to him or her what someone else is going to do with it”, she says, but, ultimately, elected officials should be held responsible for decisions

resulting from this process. “Scientists are not elected, so it cannot be up to them to decide how to deal with an emergency,” Glover says.

Many scientists contacted by *Nature* agree that better legal protection, along with transparent guidelines about the obligations of science advisers, are long overdue in Italy. “The case resulted from the fact that the legal role of scientific advisers is still not well defined in Italy,” says Mariachiara Tallacchini, who studies science-related legal issues at the Catholic University of Piacenza. “Countries such as the United Kingdom and the United States are more advanced in regulating science policy”.

John Beddington, the UK chief scientific adviser, agrees. “I do not think such an outcome would be possible in the United Kingdom, unless the advice was demonstrably grossly negligent or wilfully malicious,” he told *Nature*. “And in the case of civil proceedings, all advisers are indemnified by government.” Similar protection is granted to science advisers in the United States, where seismologists advising national and state governments would be immune from such prosecution.

In Italy, there may be no time for reform before the next crisis. On 26 October, a magnitude-5.0 earthquake hit the Pollino region in the south of the country, where shocks have been going on for months — a situation very similar to that seen in L'Aquila in 2009. Maiani, who has not yet left the major risks commission, says that he and the other committee members will continue to serve during the current emergency. ■ [SEE EDITORIAL P.7](#)

## ENERGY

# Sahara solar plan loses its shine

*Siemens' decision to pull out of DESERTEC reignites doubts.*

BY DEVIN POWELL

Dimming prospects for solar energy have caught up with a massive renewable-energy project planned for the Sahara Desert. By 2050, according to its backers, DESERTEC, a network of solar plants and other renewable sources scattered across North Africa and the Middle East, could generate more than 125 gigawatts of power that could be used locally or delivered to Europe through high-voltage direct-current cables beneath the Mediterranean Sea. But one of its major backers, Siemens, based in Munich, Germany, now says that it will leave Dii, the consortium trying to

advance DESERTEC, by the end of the year.

“We see our part in Dii as done,” says spokesman Torsten Wolf of Siemens, one of 13 founding partners of the consortium, which is also based in Munich.

Siemens also said that it will pull out of the solar-energy business altogether. Its decision was made in response to falling government subsidies for solar energy and a collapse in the price of solar equipment. But to DESERTEC's critics, Siemens' exit also adds to doubts about the plan, which is expected to cost hundreds of billions of dollars. “DESERTEC is an ambitious attempt to do everything at once,” says Jenny Chase, an analyst at Bloomberg New Energy

Finance in Zurich, Switzerland. “I think it's something that will be achieved organically, bit by bit, which will probably be cheaper, easier and achieve the same results.”

DESERTEC's origins lie with retired particle physicist Gerhard Knies, who, after the 1986 Chernobyl nuclear disaster, had the idea of harvesting the Sahara's plentiful sunshine for energy. With the help of Prince El Hassan Bin Talal of Jordan, Knies brought together research institutes in Germany and North Africa, including some in Morocco, Algeria and Egypt, to start looking into the idea.

“For generating electricity from renewable, carbon-free sources, the economics makes more sense if we go to the Middle East and North Africa,” says Ernst Rauch, Dii representative for the insurance company Munich Re, one of the consortium's shareholders.

Siemens provided funds and technical expertise for preliminary studies, and in June, Dii published the result: a report that maps out the most cost-effective distribution of renewable-energy sources in 2050, based on simulations run by the Fraunhofer Institute for Systems and Innovation Research in Karlsruhe, Germany (see ‘Power play’).

Paul van Son, Dii's chief executive, says that



Solar thermal power plants offer one option for supplying Europe with electricity through the DESERTEC project (artist's concept).

DESERTEC/BRIGHTSOURCE

he is not concerned about losing Siemens for the next phase of the work, a detailed look at specific projects. "It will not really affect us," he says, pointing out that Siemens is only one of dozens of shareholders and partners.

Siemens' exit from solar energy is an about-face for the company, which had been investing in solar thermal energy, long considered a key feature of DESERTEC, after acquiring the solar-thermal equipment designer Solel, based in Beit-Shemesh, Israel, in 2009. Plants built with this technology use mirrors

to concentrate sunlight on material that can absorb its heat. When released, the heat boils water, creating steam that can drive an electricity-generating turbine.

Solar thermal plants have become increasingly hard to sell in recent years, says Wolf, owing to the falling price of a competing technology, silicon solar panels. Between 2006 and 2012, the cost of these photovoltaic panels fell by around 65%, partly as a result of a glut of solar cells on the market. Waning government subsidies for solar

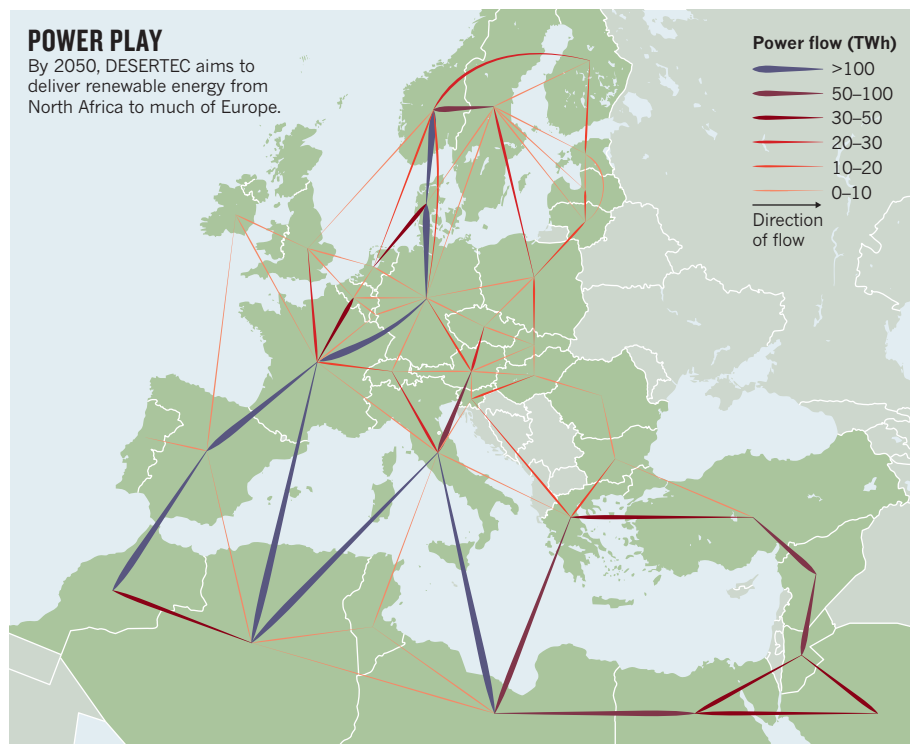
installations have made staying in the business even harder by lowering the demand for solar power, says Matthew Feinstein, an analyst at Lux Research in New York.

"It's been a bloodbath for the past year or so," says Feinstein. Last December saw the bankruptcy of Berlin-based Solon, Germany's first publicly traded solar company. Q.Cells, headquartered in Bitterfeld-Wolfen, one of the world's top solar-cell producers, followed in March. Siemens' exit from the business will deepen the gloom.

But Thimo Gropp, director of the non-profit DESERTEC Foundation that set up Dii, says the fall in costs that drove Siemens out of the business will ultimately benefit the project. "Other companies will fill this gap with their own products," he says. DESERTEC has endorsed one such project, a solar thermal plant planned for a site in Tunisia. Nur Energie, the London-based company behind the undertaking, hopes to supply Italy with power from the plant through an underwater cable.

And Siemens' relationship with DESERTEC may not be entirely over. The company says that it still supports the mission in principle, and may have something to offer down the road. Wind energy, for example, has taken on an increasingly important role in plans for DESERTEC, which hopes to tap into Africa's coastal winds. And Siemens now plans to focus on its wind portfolio.

The company has already received its first turbine orders from Africa. Morocco, which hopes to generate 6 gigawatts of power annually from renewable sources by 2020, bought 44 or them, to be installed at two wind farms. Although the projects have not been officially endorsed by DESERTEC, Wolf says that they fit the spirit of the endeavour perfectly. ■





Animals at Chimp Haven in Louisiana, where activists would like retired NIH research chimps to be sent.

## ANIMAL RESEARCH

# NIH faces chimp housing quandary

*Dozens of chimpanzees retired from research may have to continue to live in lab-like conditions.*

BY MEREDITH WADMAN

It is not easy to find living space for a great ape at short notice, let alone more than 100 of them. Yet that is precisely the problem that administrators at the US National Institutes of Health (NIH) are scrambling to solve, as the biomedical agency takes its most visible and decisive step away from invasive research on chimpanzees.

Scrutiny of the NIH's chimp research enterprise has been intensifying since the release last December of an Institute of Medicine report, which declared most of the invasive chimp studies to be scientifically unnecessary (see *Nature* 480, 424–425; 2011). The agency, based in Bethesda, Maryland, immediately put a moratorium on new grant applications for work involving chimps. In January 2013, a working group will recommend which of the grants already in progress should continue to be funded. The group will also advise on how many research-eligible chimps the agency should maintain

for current and future use, and where they should be housed.

On 21 September, NIH director Francis Collins declared the 110 agency-owned chimps at the New Iberia Research Center, which is part of the University of Louisiana at Lafayette, “permanently ineligible” for research. The move followed the centre’s decision a month earlier not to reapply for a key contract that has supported the NIH chimps housed there for decades. The existing NIH contract with the facility expires in August 2013, leaving the agency little time to avert a housing crisis for animals that can live for up to 60 years in captivity.

The problem presented by the New Iberia chimps is just the first manifestation of a bigger conundrum. The federal government owns or supports 670 chimpanzees, many of which were bred between 1986 and 1995, when it was hoped — incorrectly, as it turned out — that they would be a useful model

for HIV/AIDS. Although some have been used in virology studies and in the development of monoclonal antibodies, their use by federal researchers now looks set to dwindle.

Critics say that the housing problem should have been addressed long ago. “This is emblematic of the NIH’s failure to plan,” says Eric Kleiman, a research consultant for the Animal Welfare Institute in Washington DC. “The writing has been on the wall for how many years now?”

Collins announced the withdrawal of the 110 chimps from research in personal calls to British primatologist and chimp-welfare activist Jane Goodall, and Wayne Pacelle, director of the Humane Society of the United States in Washington DC. They were pleased with the news, but not with the NIH’s plans for housing many of the chimps. Collins said he would move 10–20 animals to fill available space at Chimp Haven in Keithville, Louisiana, the only federally supported chimpanzee sanctuary. The rest would go to the Texas Biomedical Research Institute in San Antonio, where each social group of four to six chimps would be housed in an indoor–outdoor enclosure about the size of a squash court, with extra space for elevated perches.

Chimp advocates say that Chimp Haven, a forested 80-hectare refuge that is currently home to 124 chimps, could accommodate the animals in more appropriate conditions than the research institute. “There is no comparison between a place like Chimp Haven and Texas Biomed,” says Kleiman. “Chimp Haven is chimpanzee-centred. Texas Biomed is a lab. It’s caging.”

“In a perfect world, we would absolutely like to move all of the chimps directly to Chimp Haven,” says Kathy Hudson, NIH deputy director for science, outreach and policy. “We are working collaboratively with Chimp Haven to try to figure out what are the options for being able to do that.” Managers at Chimp Haven say that they could house all 110 animals if they received US\$2.55 million to pay for shovel-ready construction projects that could be completed in four months.

But the NIH faces a ticking clock and a number of roadblocks. Perhaps the most daunting is the language of the 12-year-old federal law that established Chimp Haven. Although it obliges the government to provide ‘lifetime’ care for retired research chimpanzees, it also caps at \$30 million the money that the NIH’s parent agency, the Department of Health and Human Services, can spend in doing so. Chimp Haven, which began receiving government funds in 2002, is expected to hit the \$30 million cap during 2013.

Hudson says that the agency is looking at all alternatives, including finding space in other private sanctuaries and asking the New Iberia centre to keep some animals for the short term. If expanded to full capacity, Chimp Haven says that it could eventually house around 430 chimps. ■

A. FULTZ/CHIMP HAVEN

## PHYSICS

# Theorists bridge space-time rips

*Framework offers starting point to explaining how particles cope with fluctuations in gravity.*

BY EUGENIE SAMUEL REICH

Could an analysis based on relatively simple calculations point the way to reconciling the two most successful — and stubbornly distinct — branches of modern theoretical physics? Frank Wilczek and his collaborators hope so.

The task of aligning quantum mechanics, which deals with the behaviour of fundamental particles, with Einstein's general theory of relativity, which describes gravity in terms of curved space-time, has proved an enormous challenge. One of the difficulties is that neither is adequate to describe what happens to particles when the space-time they occupy undergoes drastic changes — such as those thought to occur at the birth of a black hole. But in a paper posted to the arXiv preprint server on 15 October (A. D. Shapere *et al.* <http://arxiv.org/abs/1210.3545>; 2012), three theoretical physicists present a straightforward way for quantum particles to move smoothly from one kind of 'topological space' to a very different one.

The analysis does not model gravity explicitly, and so is not an attempt to formulate a theory of 'quantum gravity' that brings general relativity and quantum mechanics under one umbrella. Instead, the authors, including Nobel laureate Frank Wilczek of the Massachusetts Institute of Technology (MIT) in Cambridge, suggest that their work might provide a simplified framework for understanding the effects of gravity on quantum particles, as well as describing other situations in which the spaces that quantum particles move in can radically alter, such as in condensed-matter-physics experiments. "I'm pretty excited," says Wilczek, "We have to see how far we can push it."

The idea is attracting attention not only because of the scope of its possible applications, but because it is based on undergraduate-level mathematics. "Their paper starts with the most elementary framework," says Brian Greene, a string theorist at Columbia

University in New York. "It's inspiring how far they can go with no fancy machinery."

Wilczek and his co-authors set up a hypothetical system with a single quantum particle moving along a wire that abruptly splits into two. The stripped-down scenario is effectively the one-dimensional version of an encounter



Frank Wilczek studies how fundamental particles respond to drastic changes in space-time.

with ripped space-time, which occurs when the topology of a space changes radically. The theorists concentrate on what happens at the endpoints of the wire — setting the 'boundary conditions' for the before and after states of the quantum wave associated with the particle. They then show that the wave can evolve continuously without facing any disruptions as the boundary conditions shift from one geometry to the other, incompatible one. "You can smoothly follow this process," says

Al Shapere at the University of Kentucky in Lexington, a co-author on the paper, adding that, like a magician's rings, the transformation is impossible to visualize, but does make mathematical sense.

The desire to escape the mathematical headaches caused by such transformations is one motivation for string theory, which allows smooth changes in the topology of space-time, says Greene. He suggests that the approach developed by Wilczek, Shapere and MIT undergraduate student Zhaoxi Xiong could be applied within string theory too.

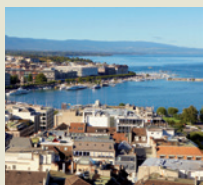
Although Wilczek originally believed that the result was new, a 1995 paper by Aiyalam Balachandran of Syracuse University in New York proposed a similar strategy for describing changes in topology in quantum mechanics (A. P. Balachandran *et al.* *Nucl. Phys. B* **446**, 299–314; 1995). Balachandran acknowledges that his work hasn't hit the mainstream and says that he hopes Wilczek's paper will prompt others to take a closer look. "Conventional approaches to this problem don't get very far," he says. "This opens up a new technique."

The framework might also provide inspiration for experimentalists working on condensed matter. Rob Myers, a string theorist at the Perimeter Institute for Theoretical Physics in Waterloo, Canada, says that he expects it to be relevant to an area called quantum quenches, in which quantum systems evolve in isolation from the environment and are then kicked out of equilibrium by an action of the experimentalist. Condensed-matter physicists have developed several quantum systems — including cold-atom traps and superconducting circuits — that can be used to test this idea.

Although the authors lay out their solution in only one dimension, Myers expects that the approach will readily generalize to describe real experiments in three dimensions. But he cautions that the paper represents only a first step. "To really see the impact of this work, that will take a while," he says. ■

  
**MORE  
ONLINE**

## TOP STORY



Ancient tsunami devastated Lake Geneva shoreline  
[go.nature.com/ptao2z](http://go.nature.com/ptao2z)

## MORE NEWS

- Testing magnesium's brain-boosting effects [go.nature.com/6sx71a](http://go.nature.com/6sx71a)
- ITER experiment struggles to put the pieces together [go.nature.com/sgnepd](http://go.nature.com/sgnepd)
- 'Penis worm' pokes holes in evolutionary dogma [go.nature.com/p3qkos](http://go.nature.com/p3qkos)

## PODCAST



Cancer risk for redheads, mapping the bird family tree and single-cell sequencing  
[go.nature.com/cykasc](http://go.nature.com/cykasc)



Poor sanitation at the Yusuf Batil refugee camp in South Sudan caused an outbreak of hepatitis E earlier this year.

## IMMUNOLOGY

# Hepatitis E vaccine debuts

*Success of Chinese biotech partnership raises hopes for prevention of overlooked diseases.*

BY SOO BIN PARK

Batches of the world's first vaccine against the hepatitis E virus began rolling out of a Chinese factory last week, promising to stem a disease that every year infects about 20 million people and claims 70,000 lives. The vaccine is being hailed as a victory for an unusual public-private partnership that could set a precedent in China's burgeoning biotechnology sector, and help to deliver other vaccines for diseases overlooked in the West.

The waterborne hepatitis E virus mostly occurs in developing countries that have poor sanitation, and it is particularly prevalent in east and south Asia. Although most cases cause only mild illness, it can lead to acute liver failure — the mortality rate reaches 4% in some regions and soars to 20% in women who are in the later stages of pregnancy. A severe outbreak of hepatitis E in the Xinjiang Uygur Autonomous Region in northwest China<sup>1</sup>, for example, caused almost 120,000 infections and more than 700 deaths between 1986 and 1988 (see 'Hidden epidemics'). There is no treatment, and improved sanitation has so far been the most effective way to stem the disease.

The new vaccine, which was approved by

China's State Food and Drug Administration (SFDA) in December 2011, could transform that picture. More than a decade ago, researchers at Xiamen University in Fujian province genetically modified a strain of the bacterium *Escherichia coli* to produce a protein that, when injected into humans, stimulates the body's immune system against hepatitis E. But pre-clinical and clinical development began in earnest only in 2000, when the Yangshengtang Group, a company with interests in food and health care, invested 15 million renminbi (US\$1.8 million in 2000) to set up a joint biotech laboratory in partnership with the university. The lab was given national status in 2006 by the Chinese Ministry of Science and Technology and relaunched as the National Institute of Diagnostics and Vaccine Development in Infectious Diseases (NIDVD).

The institute aims to unite academia and industry in commercializing new vaccines, particularly for emerging infectious diseases. Yangshengtang set up a subsidiary company called Innovax to take potential vaccines through clinical trials to manufacturing. The hepatitis E vaccine, Hecolin, is the company's first product to reach the market, but it also has a vaccine against human papilloma virus that

is currently in preclinical research. Approval for Hecolin came after a phase III clinical trial published in 2010 showed that it was highly effective in preventing infection among almost 100,000 healthy participants<sup>2</sup>.

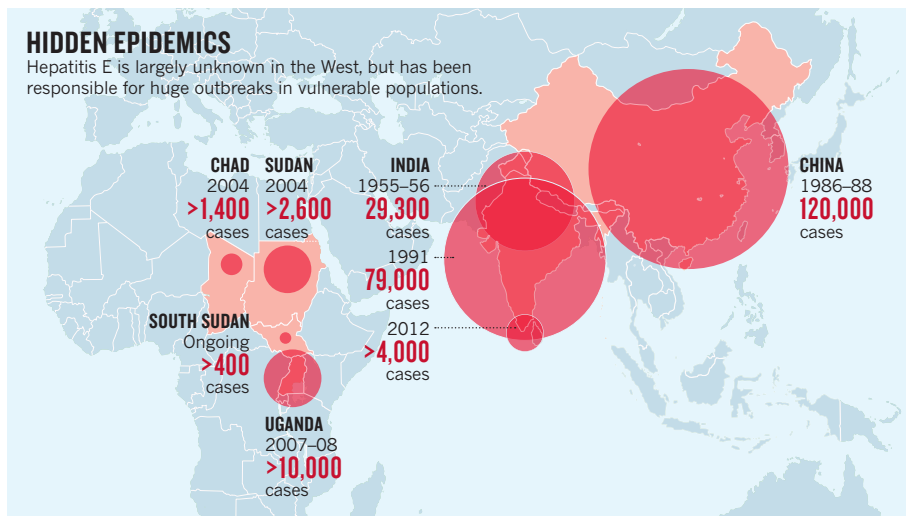
Hecolin cost about 500 million renminbi (US\$80 million) to develop, much of which came from the Chinese government through the university. The vaccine will be sold to distributors in China at a cost of 110 renminbi per dose, and the company expects it to reach sales of 62 million renminbi in 2013. That is hardly a blockbuster income, but, according to Jun Zhang, deputy director of the NIDVD, the public-private development model helps to ensure that vital vaccines are developed regardless of whether they prove to be profitable for manufacturers.

Zhang hopes that the success of Hecolin will attract further investment in such schemes, and says that the Chinese government has been encouraging. "Many people — including representatives of multinational pharmaceutical companies, venture capitalists, Chinese local government officials and Chinese entrepreneurs — think this is a worthy example of biotechnology investment," he says.

Zhang points out that UK drug-maker ►

## HIDDEN EPIDEMICS

Hepatitis E is largely unknown in the West, but has been responsible for huge outbreaks in vulnerable populations.



► GlaxoSmithKline had already developed a separate hepatitis E vaccine in collaboration with the US Army, which showed promise in phase II trials<sup>3</sup>. But with hepatitis E mostly occurring in developing countries, there was little commercial potential for the vaccine. “This is true not just of hepatitis E, but also many other plagues in the world,” says Zhang.

Medical products for conditions such as hepatitis E that predominantly affect the developing world “are not seen as big money

opportunities”, agrees Jeremy Farrar, director of the Oxford University Clinical Research Unit in Ho Chi Minh City, Vietnam. “New companies operating with different funding models offer a great opportunity, and one which could have a profound impact.”

Hecolin may have arrived just in time to tackle a rise in hepatitis E in Africa, where a 2007 outbreak<sup>4</sup> in Uganda infected more than 10,000 people and killed 160. By the end of September this year, more than 200 cases of jaundice

caused by hepatitis E had been reported in refugee camps in Kenya since August, and three refugee camps in South Sudan have seen 16 deaths and 400 cases of hepatitis E infection since July. “Cases are rising day by day, thus placing immense pressure on the available health services and resources. This is of grave humanitarian concern,” said South Sudan’s health ministry in a statement in September.

Xiamen University and Innovax are in talks with the World Health Organization (WHO) to register Hecolin with the organization’s Prequalification Programme, which makes medicines available to agencies such as the United Nations Children’s Fund and the Joint UN Programme on HIV/AIDS. “We have to be sure that these vaccines can be used anywhere,” says Farrar. “It would be a great shame if these products were not available outside China.”

“We have to accept that companies such as this one in China are going to be very important in the future,” he adds. “The rest of us have to catch up. We need to find a way, through the WHO, of ensuring the absolute transparency, safety and effectiveness of their vaccines.” ■

1. Zhuang, H., Cao, X. Y., Liu, C. B. & Wang, G. M. *Gastroenterol. Jpn.* **26**, 135–138 (1991).
2. Zhu, F.-C. et al. *Lancet* **376**, 895–902 (2010).
3. Shrestha, M. P. et al. *N. Engl. J. Med.* **356**, 895–903 (2007).
4. Teshale, E. H. et al. *Emerg. Infect. Dis.* **16**, 126–129 (2010).

SOURCES: J. M. HUGHES ET AL. *CLIN. INFECT. DIS.* **51**, 328–334 (2010); WHO/PROMED-MAIL

## FOOD SAFETY

# Bid to curb fried-food chemical goes cold

*Acrylamide levels still too high in Europe’s food, says report.*

BY KATHARINE SANDERSON

**T**he rich, roasted aroma of coffee or the golden-brown colour of crispy French fries are enough to set most mouths watering. But the high-temperature cooking that gives these foods their alluring taste, scent and texture also adds a sting: acrylamide, a probable human carcinogen.

Swedish scientists discovered in 2002 that a wide range of baked and fried goods contain worryingly high levels of acrylamide<sup>1</sup> — a simple organic molecule that is a neurotoxin and carcinogen in rats. The finding sparked an international effort to reduce concentrations of the chemical by changing ingredients and cooking methods.

Ten years on, a report<sup>2</sup> from the European Food Safety Authority (EFSA) in Parma, Italy, suggests that this effort has stalled, amid

patchy monitoring, uncertainty about acrylamide’s true health effects and the challenge of weeding out a molecule present in hundreds of products.

Soon after the Swedish discovery, two teams — one led by chemist Donald Mottram at the University of Reading, UK, the other by Richard Stadler at Nestlé in Lausanne, Switzerland — unpicked the chemistry behind the problem<sup>3,4</sup>. They found that sugars and amino acids such as asparagine found in potatoes and cereals were making acrylamide (C<sub>3</sub>H<sub>5</sub>NO) as a by-product of the Maillard reaction, the very process that generates the heady blend of colour, flavour and taste in cooked foods.

Subsequent epidemiological studies involving tens of thousands of people have looked for links between acrylamide and various forms of cancer in humans, including breast<sup>5</sup> and colorectal cancer<sup>6</sup>. For the most part, the results

have been negative. In 2007, however, a Dutch study<sup>7</sup> of almost 2,600 women found that, among those who had never smoked, women consuming about 40 micrograms of acrylamide per day doubled their risk of developing cancers of the womb or ovaries, compared with those taking in roughly 10 µg per day. And last month, a study<sup>8</sup> showed that women who ate acrylamide-rich food during pregnancy tended to give birth to smaller babies.

Despite the uncertainties over the dangers of acrylamide, Europe’s legislators and food producers vowed to take action. Since 2005, the industry group FoodDrinkEurope has maintained a ‘toolbox’ of tactics to help reduce acrylamide levels, such as changing potato varieties or storage conditions, and reducing cooking temperatures. According to Beate Kettlitz, the group’s director of food policy, 90% of large and medium-sized companies in Europe now select potato varieties with low levels of the sugars that can form acrylamide, and all control French-fry cooking times to limit browning.

In 2007, the European Commission instructed the EFSA to collate yearly data on acrylamide levels. Last week, the authority released the most recent figures<sup>2</sup> showing that acrylamide levels in finished food products hardly changed between 2007 and 2010. There have been isolated successes: in soft bread, for example, mean acrylamide levels dropped from 75 to 30 µg per kilogram. But for crispbreads,

the mean actually rose, from 232 to 249  $\mu\text{g kg}^{-1}$ . Overall, 6–17% of the food categories tested exceeded ‘indicative values of concern’<sup>9</sup> set out by the European Commission in 2011 (see ‘Would you like acrylamide with that?’).

Mottram, who has worked closely with the food industry to reduce acrylamide levels, says that he is disappointed the report does not reflect the huge strides taken by industry, not least in the period 2002–06.

The EFSA acknowledges that assessing whether the industry’s efforts are bearing fruit will take many years of more consistent sampling. For the current report, the agency relied on European Union (EU) member states to collect and submit acrylamide data. The response was inconsistent: only 16 of 25 countries provided data for every year of the survey, and submissions also waned over time. Despite submitting data every year, Belgium provided no figures at all on its beloved frites, for example.

Since 2010, the EU has required member countries to collect acrylamide data, and the EFSA report suggests that monitoring is improving as a result. Europe certainly takes acrylamide more seriously than other parts of the world. The US Food and Drug Administration has not routinely collected data on acrylamide in food since 2006, although it is currently calling on the food industry to submit more data, says agency spokesman Sebastian Cianci.

#### WOULD YOU LIKE ACRYLAMIDE WITH THAT?

Figures for 2007–10 suggest that fried and baked foods in Europe often contain worryingly high levels of the probable carcinogen acrylamide.

Food	Indicative value of concern ( $\mu\text{g kg}^{-1}$ )	% Samples exceeding indicative value
French fries	600	12
Potato crisps	1,000	17
Instant coffee	900	10
Soft bread	150	7
Crispbreads, biscuits	500	8

Source: ref. 2

Mottram is also developing new ways to tackle the problem. In August, he showed that acrylamide levels in French fries can be predicted from the cooking methods and the presence of key precursor chemicals in the partially cooked, frozen fries used by fast-food restaurants<sup>10</sup>. This model revealed that a change to the potato blanching process could make a big difference to the final acrylamide level. “The industry is not giving up on this,” he says.

Plant breeding and genetic modification could also help, by creating varieties with lower levels of acrylamide precursors. Nevertheless, the chemical will always be present in our food,

says Margareta Törnqvist from Stockholm University, who led the team that originally discovered the problem. “Acrylamide is natural; you can’t reduce it to zero,” she says. ■

1. Tareke, E., Rydberg, P., Karlsson, P., Eriksson, S. & Törnqvist, M. *J. Agric. Food Chem.* **50**, 4998–5006 (2002).
2. European Food Safety Authority EFSA *J.* **10**, 2938 (2012).
3. Mottram, D. S., Wedzicha, B. L. & Dodson, A. T. *Nature* **419**, 448–449 (2002).
4. Stadler, R. H. *et al. Nature* **419**, 449–450 (2002).
5. Wilson, K. M. *et al. Am. J. Epidemiol.* **169**, 954–961 (2009).
6. Larsson, S. C., Åkesson, A., Bergkvist, L. & Wolk, A. *Eur. J. Cancer* **45**, 513–516 (2009).
7. Hogervorst, J. G., Schouten, L. J., Konings, E. J., Goldbohm, R. A. & van den Brandt, P. A. *Cancer Epidemiol. Biomarkers Prev.* **16**, 2304–2313 (2007).
8. Pedersen, M. *et al. Environ. Health Perspect.* <http://dx.doi.org/10.1289/ehp.1205327> (2012).
9. Commission Recommendation of 10.1.2011 on Investigations into the Levels of Acrylamide in Food (European Commission, 2011); available at [go.nature.com/tkdm89](http://go.nature.com/tkdm89).
10. Parker, J. K. *et al. J. Agric. Food Chem.* **60**, 9321–9331 (2012).

#### CORRECTION

The story ‘Texas cancer fund seeks fresh start’ (*Nature* **490**, 459–460; 2012) gave the wrong location for Arizona State University with respect to Raymond DuBois’ new post. The campus is in Tempe, not Tucson.

**E**arly this year, Eritrea severed a scientific lifeline almost as old as the African nation itself. The Eritrean National Health Laboratory in Asmara cut long-standing ties with Washington University School of Medicine in St Louis, Missouri, potentially setting back many gains that the country had made in public health. “St Louis supplied everything: American doctors, expertise, chemicals, materials,” says Assefaw Ghebrekidan, an Eritrean ex-freedom fighter who now heads the public-health programme at Touro University in Mare Island, California. “And now it’s all over.”

Eritrea, an impoverished country of 3 million people on the Horn of Africa (see ‘A troubled corner’), is not known for its science. It ranks 177th out of 187 countries on the United Nations Human Development Index. It comes in last in terms of press freedom and is the eighth most militarized country in the world. The World Health Organization estimated that there were just 5 medical doctors per 100,000 people in the country in 2004.

But against this depressing backdrop, the country’s medical-research partnerships have been a source of promise and pride. Eritrea built its first medical school in 2003, aided by scientists from the Central University of Las Villas in Santa Clara, Cuba. After US universities helped to establish postgraduate training and research programmes in paediatrics, surgery, and obstetrics and gynaecology at the institution, Eritrean medical scientists published their first papers in international, peer-reviewed journals. Public health has benefited. In 1991, Eritrea was cursed with the highest maternal mortality rate in the world — 14 deaths per 1,000 births. In 2010, it was on track to meet the Millennium Development Goal of cutting that rate by 75% by 2015.

But progress in Eritrean science has now gone into reverse, say a number of scientists and doctors in exile. In response to mounting criticism from the United Nations and the United States over the country’s human-rights record, Eritrean President Isaias Afwerki is severing partnerships with all US universities, says Ghebrekidan. “Everything that Eritrea has worked so hard to achieve is at stake.”

Jon Abbink, an anthropologist at the Free University of Amsterdam, says that these actions will have widespread negative effects, “in the education system, in the constant ‘brain drain’ of educated people to greener and freer pastures, and in the inhibition of international scientific cooperation”. Eritrea, he says, is one of the few remaining countries in Africa that have failed to embrace scientific freedom. “It’s out of sync with global trends,” says Abbink.

Eritrea was once a colony of Italy, but the United Nations handed it over to Ethiopia after the Second World War. In 1961, Eritrea started to fight for its independence in a war that would last three decades: the United States



High-quality pharmaceuticals and intravenous fluids were prepared and surgeries performed in Eritrea’s ‘longest hospital in the world’ during the country’s fight for independence.

# ERITREA’S SHATTERED SCIENCE

BY SHANTA BARLEY

*An impoverished African nation was making promising strides in medicine — before the government clamped down on its foreign partnerships.*

supplied Ethiopia with guns and money, but the rebels, led by Afwerki and the Eritrean People’s Liberation Front (EPLF), persevered.

The liberation movement had remarkable credentials. “It was led by 29 doctors of medicine,” says Ghebrekidan, who was head of the EPLF’s medical services. “No other rebel movement has ever had so many intellectuals.” Even Afwerki had abandoned a degree in engineering to lead the fight.

Another academic, Melles Seyoum, was working as a pharmacist at an Ethiopian hospital when the war broke out. He coolly stole US\$140,000 worth of antibiotics, microscopes, surgical blades and stethoscopes and delivered them to Eritrean freedom fighters, wrote journalist Michela Wrong in her book *I Didn’t Do It For You* (HarperCollins, 2005). Seyoum became an integral member of the EPLF, teaching soldiers how to test blood and

ANGESOM TEKLEHAIMANOT BOKRU

prepare Petri dishes in a hospital 5 kilometres long and dug into the side of a rocky valley — a clinic known as ‘the longest hospital in the world’. After a visit in 1987, a British doctor wrote<sup>1</sup> about the impressive standards of care at the hospital: a 1-tonne machine manufactured antibiotics every day; a doctor performed facial reconstructions; and amputees played basketball.

## POWER STRUGGLE

In 1993, after the war ended and Eritrea gained independence, Afwerki was elected president by a national assembly largely composed of former members of his rebel army. He promised that within four years, Eritrea would have parliamentary and presidential elections, press laws and a new constitution. Seyoum enthusiastically backed Afwerki and was, in return, appointed director of the prestigious National Health Laboratory, which performed most of the country’s clinical testing and worked on developing treatments for disease.

But following a failed assassination attempt in 1996, the president postponed elections indefinitely and refused to implement the constitution that had been drafted. In 1998, he invaded Ethiopia, triggering a humiliating two-year war that caused the deaths of more than 60,000 Eritreans and a temporary loss of one-quarter of Eritrean territory. Afwerki’s popularity plummeted, and many of the academics who had helped to rebuild the country moved abroad.

On 3 October 2000, some of them decided to use their friendship with Afwerki to persuade him to hold elections or step down. From a conference hotel in Berlin, Ghebrekidan and 12 other scientists and professionals, many of whom had been involved in drafting the constitution, composed a letter to the president.

“Much of the world community, including our fellow Africans, perceive the Eritrean government and its leadership as aggressive and irresponsible,” wrote the group, urging Afwerki to implement the constitution, hold democratic elections and set free the growing number of people his regime had jailed. “We urge you most sincerely to seize this moment of crisis and turn it into an opportunity to reclaim your hard-earned reputation as a leader.” Four days later, after it had reached Afwerki, the letter was leaked to the press, igniting Eritrea’s first-ever public debate about leadership.

To its members’ surprise, the group — which became known as the G-13 — was invited to Eritrea for discussions with Afwerki. One member, Mohammed Kheir, later wrote that he was nervous that it might be a trap. But they accepted the invitation and flew to Eritrea. After waiting for several days, the president agreed to see them. Soldiers escorted the academics to his office, where Afwerki berated them for leaking the letter to the media — something that they denied — and cast them as traitors. The group was escorted back to the

airport. Since then, no members have returned to Eritrea; most now hold prestigious positions at US universities. “It is very fortunate that we escaped,” says Haile Debas, now head of the University of California Global Health Institute in San Francisco.

Although the plea failed to sway the president, it encouraged others to criticize him openly for the first time. In July 2001, Semere Kesete, leader of the student union at the University of Asmara — Eritrea’s only institute of higher learning — criticized the government for reducing academic freedom. He was arrested and thrown into solitary confinement, causing riots at the university. When the government demanded that the students do extra national service — on top of the 18 months required of all men and women — they didn’t turn up. In retaliation, the government bussed all of the students to the Danakil Depression in southern Eritrea, one of the hottest places on Earth, to build roads. Two students died from the heat.

## CRACKDOWN

A month later, Afwerki launched his biggest crackdown yet. He shut down all private media, threw 10 journalists in jail and imprisoned 11 politicians who had demanded elections — many of whom were old comrades in arms. He also began to dismantle the University of Asmara.

“What could be the justification for killing the only university we had capable of producing students that could be accepted by universities abroad?” asks an Eritrean scientist who lives out of the country and wishes to remain anonymous because of concerns about the safety of family members still in Eritrea. “The aim was simply to prevent the students from all being in one place, where they had the power to rise up,” says Debas. In place of the university, the government built a number of small colleges, arguing that these would be more accessible to students.

Even as Eritrea lost its only university, it continued to make progress in medicine. In 1997, the country had gained a proactive health minister, Saleh Meki, who helped to develop

crucial partnerships with US universities including George Washington University in Washington DC; Washington University in St Louis; Columbia University in New York City; Stony Brook University in New York; and the University of California, Berkeley. By bringing experts into Eritrea, these partnerships helped the country to pass scientific and public-health milestones. A polio-immunization campaign extended coverage to 95% of all one-year-olds and eradicated the disease. An anti-malaria drive from 2000 to 2004 reduced morbidity and case fatality by 84% and 40%, respectively.

In 2003, Haile Mezgebe, then a surgeon at George Washington University, was part of the group of medics who helped to set up the Orotta School of Medicine in Eritrea. Mezgebe moved to the country to run the collaboration; he was joined by Mary Polan, who travelled regularly from the department of obstetrics and gynaecology at Columbia University, and other US doctors and surgeons who worked to treat and train Eritreans. In 2009, Orotta graduated its first class of 39 doctors. “It was quite extraordinary,” says Jack Ladenson, a doctor based at Washington University. “Suddenly, in one day, there was a 30% increase in the number of doctors in Eritrea.”

## SUCCESS STORY

Meanwhile, clinical testing and research was taking off at the National Health Laboratory. In 1998, the only blood tests available in Eritrea had been done on a single machine. Scientists from Washington University installed new equipment at the lab and trained technicians to perform a range of chemical tests, including the haemoglobin A<sub>1c</sub> test for diabetes and a test for thyroid malfunction. They also launched a national diabetes-management programme and a long-term research project to gauge its progress; in 2007, the project leaders found<sup>2</sup> that the programme had significantly improved Eritrean diabetes management. Ladenson, Seyoum and others co-authored a paper<sup>3</sup> showing that the overall quality of chemical tests for disease at the national lab was on a par with that at Washington University. “A simple but sustainable national laboratory system has been established in the developing nation of Eritrea,” the paper said.

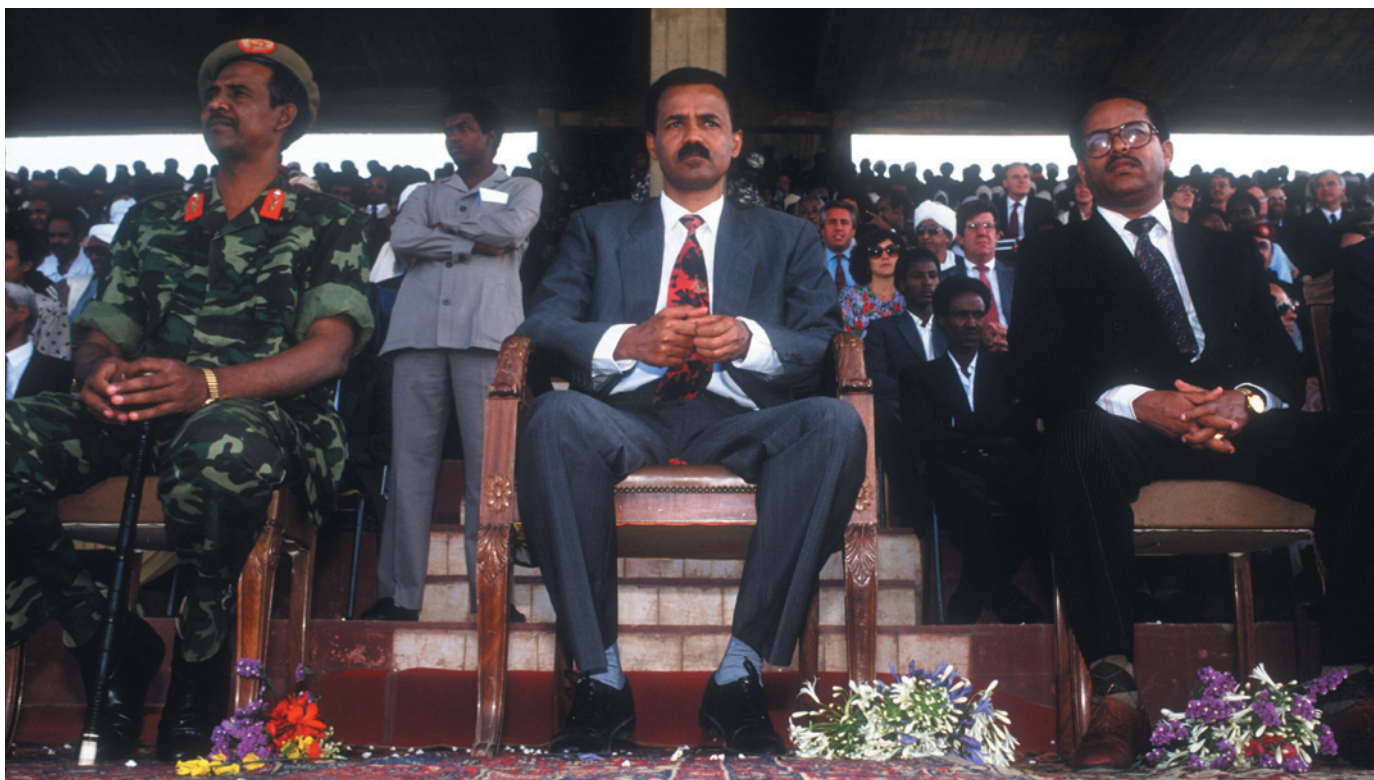
But outside the medical arena, the situation was less rosy. Richard Reid, a historian at the School of Oriental and African Studies in London, visited the Eritrea Institute of Technology in Mai Nefhi, one of the unaccredited colleges set up after the University of Asmara was shut down. He was told that students who cheated on exams or skipped classes were jailed on site. Military training was mandatory between 4 and 7 a.m., and students wryly referred to digging trenches as ‘digology’, adds Reid.

And any success in science and medicine was short lived. In 2008, without explanation, Meki was removed as health minister, along with the coordinator for US–Eritrean scientific

## A TROUBLED CORNER

Eritrea won independence from Ethiopia in 1993 after 30 years of war.





S. PETERSON/LIAISON/GETTY

Isaias Afwerki (centre) in 1992, a year before he became Eritrea's first president. He has recently halted the country's collaborations with US medical schools.

partnerships. The chair of the paediatrics department at Orotta was arrested because of his religious views. And in 2011, Afwerki ordered all scientists from George Washington University — including Mezgebe — to leave the country.

At the start of 2012, Afwerki cut off the partnership between the National Laboratory and Washington University in St Louis. Several sources, who wish to remain anonymous for fear of retaliation against friends and relatives, report that Seyoum, the lab's director, was "frozen", an Eritrean term for the practice of stripping government employees of their titles and duties while restricting them from travel and other jobs to silence them. *Nature* contacted officials in the Eritrean government and its US and UK embassies repeatedly by phone and e-mail for a response to these allegations, but had received none at the time of going to press.

The severing of ties may be a backlash against the United States and the United Nations over their criticism of Afwerki's human-rights record, says Ghebrekidan. In 2009, the United States imposed sanctions on Eritrea for supporting Islamist insurgents in Somalia. A highly publicized cable from US ambassador Ronald McMullen, later released by Wikileaks, said that "Eritrea's prisons are overflowing, and the country's unhinged dictator remains cruel and defiant". In July, the UN Human Rights Council established a special rapporteur to investigate reports of rights violations by Eritrean authorities, amid stories

## "THE GOVERNMENT HAS PERSECUTED NOT ONLY SCIENTISTS, BUT ALSO THE SCIENCE."

that Afwerki keeps his critics in solitary confinement in shipping containers.

Berhane Ghebrehwet, an Eritrean immunologist at Stony Brook University, says that Afwerki's distrust of foreign involvement and aid in Eritrea is understandable. The United States did, after all, support Ethiopia during the fight for independence. "You cannot cripple a man and then accuse him of having limped," he says. "All the president dreams of is to make Eritrea a prosperous and self-reliant nation at peace with itself, its neighbours and the rest of the world."

Others are less sympathetic. "Afwerki is getting more and more paranoid," says Ghebrekidan. "He thinks that the American doctors who come to save Eritrean lives are actually CIA agents."

Afwerki has effectively destroyed intellectual freedom in Eritrea, says Abbink. "No independent academic research in any field is possible." Fundamental research "or what is left of it" is now under pressure to pursue "practical" issues with immediate applications to development, he concludes.

Yet some scientists are still proud of the


progress Eritrea has made. Andemariam Gebremichael, dean of the Orotta School of Medicine, wrote in an e-mail that he aims to create "an environment where individuals develop their intellectual potential", adding that he hopes to produce another 150 doctors to bring the country up to international standards. It will be a significant challenge, writes Gebremichael. Only seven foreign teaching doctors — all Cuban — remain at the institution.

After a year in solitary confinement, student-union leader Kesete escaped with his guard to Ethiopia, and from there to the United States. "We walked for six days and nights, surviving on nothing more than biscuits," he says.

Kesete sees little prospect of change, and despairs of his country's future. "The government has persecuted not only scientists, but also the science itself," he says. He calls international collaborations a "waste of resources and energy", because Afwerki will not hesitate to eject foreign scientists, no matter how crucial they are to Eritrea's development. Rumours that the University of Asmara may reopen this year are preposterous, he adds. "It is safe to say that academia is dead." ■

**Shanta Barley** is a freelance writer in Perth, Australia. [SEE EDITORIAL P.8](#)

1. Powell, H. D. W. *Br. Med. J.* **295**, 1637–1639 (1987).
2. Windus, D. W. *et al. Clin. Chem.* **53**, 1954–1959 (2007).
3. Scott, M. G., Morin, S., Hock, K. G., Seyoum, M. & Ladenson, J. H. *Clin. Chem.* **53**, 1945–1953 (2007).



# THE SINGLE LIFE

*Sequencing DNA from individual cells is changing the way that researchers think of humans as a whole.*

BY BRIAN OWENS

**A**ll Nicholas Navin needed was one cell — the issue was how to get it. It was 2010, and the postdoctoral fellow at Cold Spring Harbor Laboratory in New York was exploring the genetic changes that drive breast cancer. Most of the cancer-genome studies before then had ground up bits of tumour tissue and sequenced the DNA en masse, giving a consensus picture of the cancer's genome. But Navin wanted to work out the sequence from individual cells to see how

they had mutated and diverged as the cancer grew.

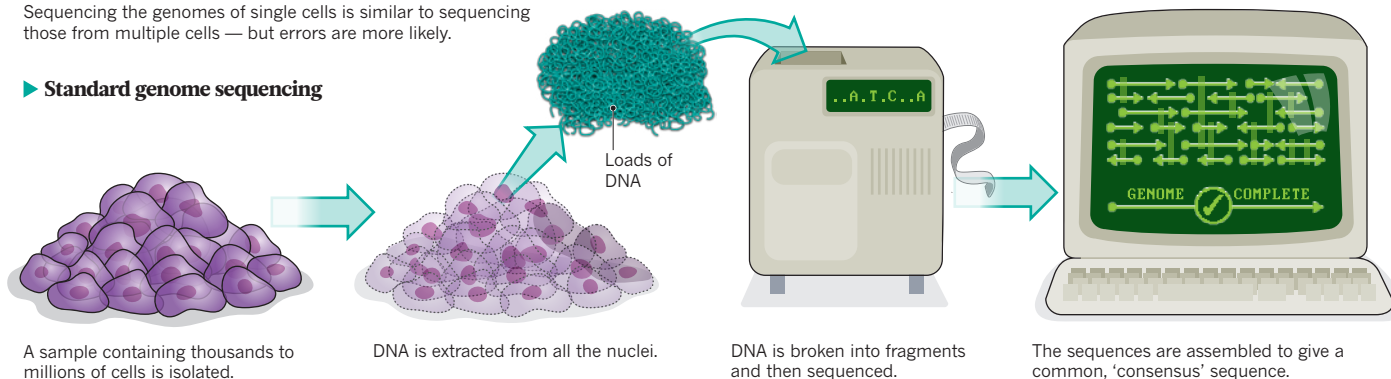
He ran into trouble almost immediately. "Cells like to stick together," he says. He tried the most advanced microdissection techniques, which use robots to peel cells apart or suck them into the tips of hair-thin glass pipettes. But he could never be sure that a second cell hadn't come along for the ride. Eventually, he settled on using chemicals to dissolve the cell's outer membrane and release the dense nucleus. Then he separated out the nucleus

VISUALS UNLIMITED/CORBIS

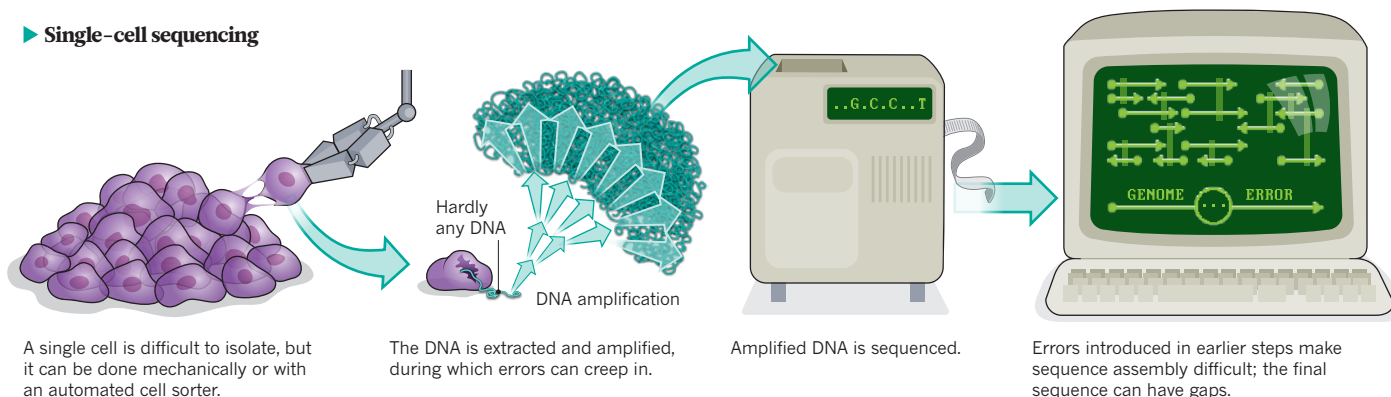
## ONE GENOME FROM MANY

Sequencing the genomes of single cells is similar to sequencing those from multiple cells — but errors are more likely.

### ► Standard genome sequencing



### ► Single-cell sequencing



using an automated cell sorter, and extracted its DNA. He repeated the process for around 100 cells, and the sequences he obtained revealed how the tumour had evolved from a few rogue cells into a complex mélange of genetically distinct ones<sup>1</sup>.

The ability to sequence 100 human cancer genomes was unthinkable a decade ago, and it is still a remarkable feat. Technology has moved apace, dramatically reducing costs and making genome sequencing fairly routine. But most human genomes, cancer or otherwise, are still sequenced from DNA extracted from multiple cells, which misses differences between cells that could be crucial in controlling gene expression, cell behaviour and drug response.

## “I THINK IT’S THE NEXT LEVEL OF COMPLEXITY.”

“People are becoming very interested in what is the variation from cell to cell,” says Navin, now at the University of Texas MD Anderson Cancer Center in Houston. Last month, the US National Institutes of Health (NIH) announced that it would be funding single-cell studies, including genome sequencing, to the tune of US\$90 million over 5 years.

But challenges abound. Amplifying the tiny amount of DNA in a single cell until there is enough to sequence without introducing too many errors is still difficult (see ‘One genome from many’). The bioinformatics required to stitch the data together and deal with artefacts can be fiendishly complicated. And, as Navin found, even isolating a cell can be tough. For this reason, several research groups have started with cells that are easily separated, such as sperm, or those that are likely

to have dramatic genomic differences, such as tumour cells.

But as the techniques are refined, scientists hope to work out ever more subtle differences between cells, such as the tiny genomic rearrangements that happen in many neurons and may serve a purpose in organizing information flow. One of the most startling facets of such research is not the differences between cells, but how tissues and organs manage to work coherently despite them. To get a handle on these issues, it makes sense to start at the smallest possible unit. “The cell is kind of the ultimate denomination of an organism,” Navin says.

### TUMOUR DIVERSITY

In his first effort with breast-cancer tumours<sup>1</sup>, Navin was able to sequence only about 10% of the DNA — not enough to see individual point mutations, but good enough to study larger segments that are commonly duplicated or deleted, called copy number variants.

The results suggested that the tumour was made up of three major populations of cells, which emerged from the root tumour population in leaps and spurts at different times during the tumour’s growth. “It suggested a model of evolution where, instead of having lots of gradual intermediates, we saw hundreds of chromosomal rearrangements that occurred probably in very short periods of evolutionary time,” he says.

Since moving to Texas, Navin has started a research group focused entirely on single-cell genomics. He has been improving his methods, and can now piece together up to 90% of a cell’s genome, he says, which allows him to study the mutations in individual cancer cells in much more detail.

The team has also looked at another type of breast cancer. Sequencing the tumour as a whole, the group found six mutations in cancer-associated genes. “It seemed like a very simple genome,” says Navin. But when his group sequenced four individual cells they identified “hundreds of additional mutations,

many of which were unique or 'private' to that individual cell". In addition to tumours, his group has studied a breast-cancer cell line that has been maintained in the laboratory. The cells in such lines might be expected to contain identical genomes, but in data that have not yet been published, the team found that about 1% of the mutations, involving 12,000–20,000 base pairs, differed from cell to cell and that these variations could not be detected when the cells were sequenced together. In both studies, many of the new-found mutations were in cancer genes, or in other regions expected to disrupt protein function.

"Nicholas's work was very nice," says Timour Baslan, a graduate student studying cancer genetics at Cold Spring Harbour Laboratory and a former colleague of Navin's in Michael Wigler's lab. "It was very informative, but it was extremely expensive" — \$1,000 or more per cell. Baslan and his colleagues are trying to bring down the cost. They add genetic barcodes — short, easily traceable strands of DNA — to a cell's DNA, which allows them to sequence cell genomes en masse then identify the sequences from individual cells. Use of the barcodes, in combination with improved bioinformatics approaches, brings the cost of a genome down to about \$60 per cell. At that price, more researchers can work with the number of cells necessary to dissect a tumour-cell population as it proliferates and evolves. "Now we're doing hundreds and we're thinking in the future we'll be able to do thousands," says Baslan.

Baslan's group is using the techniques to study which tumour cells are left behind after chemotherapy treatment and why those cells were resistant to the drugs. Such analysis could guide treatment, says Navin. "By sequencing a few single cells you can get an idea of the heterogeneity in a tumour before chemotherapy and that might affect your choice of which agent to use, or whether to subject the patient to chemotherapy at all," he says.

### EVERY SPERM IS SACRED

The tendency of sperm to swim alone makes the cells ideal for single-cell genomics. Adam Auton, a statistical geneticist at Albert Einstein College of Medicine in New York is using sperm to study recombination, the process that shuffles genes during the formation of germ cells and therefore influences which genes are inherited. "Recombination is one of the fundamental forces that shapes genetic diversity," he says. "In recent years we've learned that there is considerable variation in the recombination rate between different populations, between the sexes and even between individuals." But pinning down the rate in people once seemed impossible because it would have required finding individuals with hundreds of children and sequencing their genomes.

The ability to sequence single cells meant that researchers could take another approach. Working with a team at the Chinese sequencing powerhouse BGI, Auton sequenced nearly 200 sperm cells and was able to estimate the recombination rate for the man who had donated them. The work is not yet published, but Auton says that the group found an average of 24.5 recombination events per sperm cell, which is in line with estimates from indirect experiments<sup>2</sup>. Stephen Quake, a bio-engineer at Stanford University in California, has performed similar experiments in 100 sperm cells and identified several places in the genome in which recombination is more likely to occur. The location of these recombination 'hotspots' could help population biologists to map the position of genetic variants associated with disease.

Quake also sequenced half a dozen of those 100 sperm in greater depth, and was able to determine the rate at which new mutations arise: about 30 mutations per billion bases

per generation<sup>3</sup>, which is slightly higher than what others have found. "It's basically the population biology of a sperm sample," Quake says, and it will allow researchers to study meiosis and recombination in greater detail.

Perhaps the most intriguing potential use of single-cell sequencing lies in neuroscience. Alysson Muotri, a neuroscientist at the University of California, San Diego, would like to study how long interspersed nuclear elements (LINEs) — 'jumping' genes that can move around the genome — cause each neuron to differ from its neighbours. His group has compared the number of LINEs in human brain, heart and liver tissue, and found that brain tissue contains significantly more jumping genes than the others<sup>4</sup>. Each human neuron probably has between 80 and 300 unique insertions, he says, differences

## "EVERY TIME WE LOOK AT OUR DATA WE DISCOVER SOMETHING NEW."

that could affect a person's susceptibility to neurological disorders<sup>5</sup>, or provide the brain with a reservoir of diversity with which to respond to challenges. He says that it would be useful to sequence individual neurons and work out what effect this heterogeneity is having on brain function and even on personality. "I think it's the next level of complexity," he says. "We look at the brain and we think about the tissue, but actually it seems like lots of tissues in one, because the cells are so heterogeneous. It's almost like every cell was there for a purpose."

To make good on these plans, however, the techniques will need to improve further. Ramunas Stepanauskas, director of the Single Cell Genomics Center at the Bigelow Laboratory for Ocean Sciences in East Boothbay, Maine, says that the processes involved will continue to be integrated and miniaturized, until eventually they will form an off-the-shelf technology that involves just the press of a button — although he cautions that this is still many years off. In the meantime, his centre offers single-cell sequencing for labs that lack the necessary equipment and expertise to do it themselves. The US Department of Energy's Joint Genome Institute in Walnut Creek, California, offers a similar service.

With its new funding for single-cell studies, the NIH is attempting to spur innovation in the field. So is Life Technologies, a sequencing company based in Carlsbad, California, which is offering a \$1 million prize to the first researchers who can sequence the whole genome and all the RNA in a single human cancer cell using the company's technology. The deadline for the challenge is the end of this year, and the company says that there has been an enthusiastic response.

Baslan, for one, is intent on breaking down tissues into their components. "Every time we look at our data we discover something new," he says. "There's just so much analysis to be done that it's quite daunting." ■

**Brian Owens** is the assistant news editor for *Nature* in London.

1. Navin, N. *et al. Nature* **472**, 90–94 (2011).
2. McVean, G. A. T. *et al. Science* **304**, 581–584 (2004).
3. Wang, J., Fan, H. C., Behr, B. & Quake S. R. *Cell* **150**, 402–412 (2012).
4. Coufal, N. G. *et al. Nature* **460**, 1127–1131 (2009).
5. Muotri, A. R. *et al. Nature* **468**, 443–446 (2010).

# COMMENT

**POLITICS** US abortion lobby set to clash with prenatal diagnostics **p.33**



**DEVELOPMENT** Science must inform UN sustainability goals **p.35**

**NEUROSCIENCE** How does the mind extract meaning from language? **p.36**

**HISTORY** A masterful take on the age-old allure of alchemy **p.38**



## There's more to life than rats and flies

The tiny number of model organisms constrains research in ways that must be acknowledged and addressed, warns **Jessica Bolker**.

For most experimental biologists, life revolves around a handful of species: the mouse (*Mus musculus*), the nematode worm (*Caenorhabditis elegans*), the fruitfly (*Drosophila melanogaster*) and the thale cress (*Arabidopsis thaliana*). We assume that model organisms offer universal insights, and funding agencies largely support work on a shortlist of favoured species ([www.nih.gov/science/models](http://www.nih.gov/science/models)).

Scientists who submit grant proposals for a project using a standard model organism need not use up space to explain their choice. By contrast, choosing a less common

model that is uniquely suited to the research demands a lengthy justification to convince sceptical colleagues. Proposals for projects in unusual species are often returned with the suggestion that the applicant use a standard organism instead, because any worthwhile question should be accessible in a well-established model.

Investments in research with a handful of models have returned rich dividends in basic knowledge and medical progress. And many careers, labs and journals are built on the primacy of the fly, mouse and worm<sup>1</sup>.

But studying only a few organisms limits

science to the answers that those organisms can provide. The extraordinary resolving power of core models comes with the same trade-off as a high-magnification lens: a much reduced field of view. For instance, traditional models for developmental biology — such as the fly — were chosen because their phenotypic traits directly reflect their genotype, with minimal environmental input. These models are poorly suited to questions asked by scientists in emerging fields such as ecological developmental biology — ‘eco-devo’ — which focuses on external influences on developing phenotypes. ▶

ILLUSTRATION BY PHIL DISLEY

► Such limitations have serious consequences. Disparities between mice and humans may help to explain why the millions of dollars spent on basic research have yielded frustratingly few clinical advances<sup>1–4</sup>. Narrowing the research focus too far limits basic understanding, in ways that can lead directly to clinical failures. For example, an experimental treatment for multiple sclerosis that, in inbred mice, improved symptoms of induced disease produced unpredicted — and sometimes adverse — responses in human patients. The inbred mouse model failed to represent the genetic and immunological diversity of human cells, a shortcoming that was obvious in retrospect<sup>2</sup>.

It is time to think more critically about how we use models. This means articulating tacit assumptions, such as the adequacy of rodent models to fully represent specific human diseases. It means looking hard at how we select and use our favoured model species, and acknowledging both their strengths and their limitations. And it means mainstream funders and journals welcoming work in non-standard organisms.

### MODELS OF CONVENIENCE

How did a handful of species become central models? Sometimes it was more about convenience than strategic planning. *Drosophila* rose to prominence in the early 1900s in part because its short generation time was handy for student projects and its four pairs of large chromosomes were ideal for the study of eukaryotic genetics<sup>5</sup>. Yeast, mice, chickens and other domesticated species became lab favourites because they were already familiar and accessible. The existence of lab populations of frogs (*Xenopus laevis*) for use in pregnancy tests led to their recruitment as a model for developmental research.

As model-based science grew, these few species became increasingly dominant, despite the sometimes haphazard way that they had initially been chosen. We have now reached a point where, if researchers cannot tackle a problem using a familiar species, they may not study it at all<sup>1</sup>.

Take modern developmental biology. The field has centred on small, rapidly developing organisms with short generation times — most typically, *Drosophila* and *C. elegans*. Much of our current understanding of developmental principles is based on experiments in these species. However, evolutionary selection for rapid development has broad implications. It seems to favour stronger genetic control during development and less plasticity (or flexibility). Compared with related species, development in the models is

less responsive to external signals, whether adaptive or disruptive. Because plasticity and the role of the developmental environment are particularly hard to study in key models, these areas receive comparatively little attention<sup>6</sup>.

A similar narrowing has occurred in biomedical research. In the case of Parkinson's disease, potential treatments are often assessed by measuring motor function in a lesioned rat. But the rat model does not clearly represent other significant symptoms of Parkinson's that occur in human patients, such as cognitive decline. This may steer some researchers away from these aspects of the disease.

Similar biases rooted in the use of particular models may also contribute to the 'translational disconnect' with regard to neurodegenerative diseases such as Alzheimer's and amyotrophic lateral sclerosis<sup>3,4</sup>. The inability of highly inbred and often genetically modified rodent strains to fully represent the diversity of human patients and symptoms has called the power of such models into question, even within the research communities they serve<sup>1–4,7</sup>.

At the same time, the effects of apparently trivial environmental variations, such as the details of mouse handling, are often overlooked<sup>8</sup>. Aggression is the key behavioural phenotype in male mice lacking the enzyme neuronal nitric oxide synthase. This was not observed — and could not be seen — until animals were housed in groups rather than in standard individual cages<sup>9</sup>.

Few lab models explicitly account for the environment of organisms, despite increasing recognition that this may affect the outcome and replicability of experiments<sup>7</sup>.

In short, if we frame a research model or system too narrowly, leaving out key causal elements such as environmental influences, we cannot hope to construct a complete picture of the mechanisms that underlie crucial variations, for example in development and disease. To study environmental influences, we need to study species in which such factors matter. So the traits that define a successful model must shift as the questions for which we use them evolve.

### BEST FIT

Choosing a research model should be more than a matter of convenience or convention. Scientists need to ask more questions — about the goals of a specific experiment, how suitable a given model is to reaching those goals, and what environmental or other external factors might be relevant to how well the model works. For a given question, it is crucial to determine which aspects of human biology are essential (for example, our genetic diversity, unique characteristics of our immune system or particular disease symptoms) and assess how well they are represented in a candidate model (see 'Choosing the right candidate'). Where mismatches appear, we must limit our inferences from animal studies accordingly, and consider when and how to move to research in humans. For some kinds of biomedical

## MODEL PROBLEMS

### Choosing the right candidate

#### 1 Matching between the model and what it represents

**Example:** Does studying immunology in highly inbred mouse models shed useful light on the diversity of human immune function and disease<sup>1</sup>?

##### Key questions

- What do we need to know about a disease to develop treatments?
- What mechanisms link disease origin to symptoms?

##### Research objectives

- Discover aetiology of symptoms.
- Compare disease initiation and progression between models and humans.
- Assess whether therapeutic targets are well represented in specific models.
- Identify gaps between models and patients that may be significant with respect to basic knowledge and to treatment approaches.

#### 2 Need for additional models

**Example:** Where there are known obstacles to translating results from mice to humans, how do we develop alternative routes to find new treatments for human diseases<sup>3</sup>?

##### Key questions

- What aspects of human disease are poorly represented in current models?
- How might the utility of current models be expanded?
- What potential new models are available, or could be developed?

##### Research objectives

- Develop strategies to assess other aspects of human disease in current models.
- Identify new candidate models for specific questions.
- Develop criteria for selecting new models.

research, it may not matter that the damage or symptoms in the model developed by a different pathway to that which occurs in patients — orthopaedic injuries are one example. But in other areas, such as epidemiology, it matters a great deal.

Recognizing that standard models have limitations does not mean we should give them up. Rather, we should deliberately account for their limitations as part of study design — for example, by analysing the role of a gene in mouse strains with different genetic backgrounds. No single species, no matter how highly engineered, can ever serve as a universal model: every species has unique features that may be assets or faults, depending on the question being asked. For instance, the lack of developmental plasticity in *Drosophila* and of genetic variability in inbred rats limit what these models can tell us about ecological effects on development, but make them powerful tools for studying gene function during development.

We also need to broaden our range of models to include species such as Antarctic icefish, comb jellies, cichlids, dune mice and finches that are naturally endowed by evolution with features relevant to human diseases<sup>10</sup>. Studying the basis of unique adaptive traits in these animals may yield insight into human disorders such as osteoporosis, cataracts and cancer.

Immediately and practically, the US National Center for Advancing Translational Sciences in Bethesda, Maryland, should support the development of new systems for investigating problems that are not tractable in currently favoured models. It should also fund investigations into fundamental questions about model-based research (see 'Choosing the right candidate'). The resulting insights would help scientists to select the best models for advancing basic and applied research, and strengthen the bridges between them. ■

**Jessica Bolker** is an associate professor of zoology in the Department of Biological Sciences, University of New Hampshire, Durham 03824, New Hampshire, USA. e-mail: [jessica.bolker@unh.edu](mailto:jessica.bolker@unh.edu)

1. Davis, M. M. *Immunity* **29**, 835–838 (2008).
2. von Herrath, M. G. & Nepom, G. T. *J. Exp. Med.* **202**, 1159–1162 (2005).
3. Geerts, H. *CNS Drugs* **23**, 915–926 (2009).
4. Schnabel, J. *Nature* **454**, 682–685 (2008).
5. Kohler, R. E. *Lords of the Fly: Drosophila Genetics and the Experimental Life* (Univ. Chicago Press, 1994).
6. Bolker, J. A. *BioEssays* **17**, 451–455 (1995).
7. Beckers, J., Wurst, W. & Hrabé de Angelis, M. H. *Nature Rev. Genet.* **10**, 371–380 (2009).
8. Hurst, J. L. & West, R. S. *Nature Methods* **7**, 825–826 (2010).
9. Nelson, R. J. et al. *Nature* **378**, 383–386 (1995).
10. Maher, B. *Nature* **458**, 695–698 (2009).



Pro-choice and pro-life activists clash outside the US Supreme Court in Washington DC.

## Politics and fetal diagnostics collide

Without better regulation, non-invasive prenatal genetic tests will be targeted by US anti-abortion lobbyists, argues **Jaime S. King**.

In the United States, pro-life advocacy groups, notably Americans United for Life, based in Washington DC, have been making headway in their mission<sup>1</sup> to limit women's access to abortions "state by state, law by law and person by person". In 2011, 24 US states enacted 92 new provisions restricting abortion — nearly triple the previous record of 34 in 2005 (see 'Clamping down'). One of the strategies of pro-life advocates is to target the reasons for which a woman can have an abortion. Meanwhile, a major development in prenatal care, called non-invasive prenatal genetic testing (NIPT), promises to increase the genetic information available to women early during their pregnancy.

The US Food and Drug Administration (FDA) cannot control how people

use information from genetic tests. But by developing a clear regulatory framework for NIPT and improving public understanding of NIPT's benefits and limitations, the agency could help to allay fears that the tests will lead to a drastic increase in selective abortions.

NIPT has the potential to improve women's reproductive autonomy. But if it is not integrated cautiously into prenatal care, the technology could be targeted to support burgeoning strategies to restrict abortion.

In recent years, two blood tests combined with an ultrasound have been the most common method for determining a fetus's risk of having a congenital disease such as Down's syndrome. Results from this type ▶

► of test are available only at the beginning of the second trimester. A woman can then choose to schedule an amniocentesis, a more accurate but more invasive test. For this, a clinician inserts a needle into her abdomen to extract a sample of amniotic fluid, which contains the fetal cells needed for genetic testing. The procedure increases the risk of miscarriage by around 1%.

Instead, by analysing fragments of fetal DNA in a pregnant woman's blood, NIPT can reveal potential problems without physical risk. Offered when a fetus is just ten weeks old, NIPT gives a woman much more time to have genetic counselling and confirmatory tests, and to make a reasoned decision about whether to have an abortion while it is still legal for her to do so (in most US states, only before the fetus is 24 weeks old)<sup>2</sup>.

NIPT is now used to determine a fetus's blood type, sex and father, and to screen for chromosomal disorders such as Down's syndrome and trisomy 18. The technique is not yet offered commercially for single-gene conditions such as Tay-Sachs disease and cystic fibrosis, but it probably will be soon. Even the use of NIPT to reveal whole fetal genomes may not be far off. In June, researchers sequenced an entire fetal genome from a maternal blood sample<sup>3</sup>, and another group did the same a month later<sup>4</sup>.

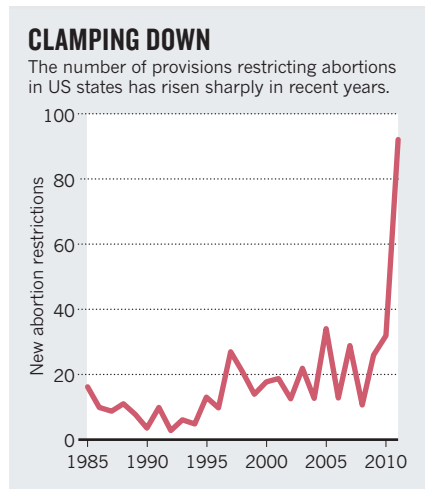
## RIGHTS AND REGULATIONS

In the United States, NIPT is emerging just as several states have begun to restrict women's access to abortions sought for certain reasons. In March, a Missouri state representative introduced the Abortion Ban For Sex Selection and Genetic Abnormalities Act of 2012. If this bill were to become law, it would prohibit doctors from carrying out abortions that they knew were being sought because of the fetus's sex or because the fetus had been "diagnosed with either a genetic abnormality or a potential for a genetic abnormality"<sup>5</sup>.

Abortions sought because of a fetus's sex are now banned in four states, and bans have been proposed in six others. In May, a bill that would ban all US providers from knowingly performing abortions sought because of the sex or race of the fetus nearly won the two-thirds majority needed, under 'fast-track' rules, to pass the US House of Representatives. Two weeks later, a similar bill, focused on 'sex selection' only, was presented to the US Senate. If it wins majorities there and in the House, it will be sent to the president, whose signature would make it national law.

As the use of NIPT becomes more widespread, pro-life advocates will almost

certainly see the technology as a reason to further constrain women's abortion rights. In June, the *National Catholic Register* wrote that pro-lifers view NIPT as "an enhanced 'search and destroy' diagnostic tool" that will drastically increase the number of abortions<sup>6</sup>. Even in Europe, where abortion



has historically been a less divisive issue, the technology has prompted anger from various groups. In June, two months before the life-sciences company LifeCodexx, based in Konstanz, Germany, made its PrenaTest for Down's syndrome commercially available, 30 Down's syndrome organizations from 16 countries formally objected to the sale of the test in the European Court of Human Rights.

Ideally, no fetus would ever be aborted because of its sex or skin colour. And it is hard to argue that allowing parents to check for hundreds or thousands of traits with one blood test will not facilitate abortions based on societal or individual prejudice. After all, in Asia, there are 160 million fewer girls and women than normal live-birth sex ratios would predict, partly because of the widespread use of ultrasound over the past two decades<sup>7</sup>.

But forcing women to have children they do not want will not end prejudice. Instead, it will create a slew of problems. Greater restrictions on abortion may result in more suffering for children<sup>8</sup>. Bills restricting terminations sought for particular reasons will drive a wedge between patients and providers. They will encourage women to withhold information or lie, and they will punish providers serving clients who tell them the truth. Moreover, by dictating which fetuses can legally be aborted, states are entering the dangerous territory of valuing some lives more than others.

US companies that sell NIPT products (such as the California-based firms Sequenom in San Diego, Verinata Health in Redwood City and Ariosa Diagnostics

in San Jose) are being cautious. They offer tests only through physicians and for a few conditions, and advertise them as 'screening tests' that may require follow-up procedures. Yet there is too much money to be made from a 'risk-free', relatively inexpensive pre-natal genetic test for this restrained approach to last. Worldwide, nearly 50 companies are now developing NIPT products.

## HANDLE WITH CARE

The FDA must step up its involvement to ensure that NIPT is integrated into prenatal care carefully — and, especially, to prevent it from being offered directly to consumers, as are other genetic tests.

The FDA still has not developed a comprehensive regulatory scheme for genetic tests, despite repeated calls to do so from government advisory groups (such as the US Secretary's Advisory Committee on Genetics, Health and Society) and non-profit organizations (such as the Genetics and Public Policy Center in Washington DC). This regulatory vacuum is especially problematic in the prenatal context, in which test results can affect parents' decisions to terminate or continue a pregnancy.

The FDA urgently needs to develop a regulatory framework that would allow parents to use prenatal genetic tests under the guidance of a physician and within some general boundaries. As a starting point, the FDA should specify the degree of accuracy and clinical utility required for companies to market a prenatal genetic test. It should also help physicians, pregnant women and the general public to understand the risks, benefits and limitations of such tests — by working with biotechnology companies offering NIPT products, professional societies such as the American Academy of Pediatrics and patient advocacy groups such as the National Down Syndrome Congress.

Abortion has always been a charged issue in the United States. Against this backdrop, NIPT must be handled with care. ■

**Jaime S. King** is at the University of California Hastings College of the Law, San Francisco, California 94102, USA. e-mail: kingja@uchastings.edu

1. Americans United for Life. *Defending Life 2012* (Americans United for Life, 2012).
2. Greely, H. T. *Nature* **469**, 289–291 (2011).
3. Kitzman, J. O. et al. *Sci. Transl. Med.* **4**, 137ra76 (2012).
4. Fan, H. C. et al. *Nature* **487**, 320–324 (2012).
5. Missouri House of Representatives, 96th General Assembly, 2nd sess. Missouri House Bill no. 1933 (2012).
6. McGovern, C. New Prenatal Testing Could Drastically Increase Abortion Rate. *National Catholic Register* (25 June 2012).
7. Hviistendahl, M. *Unnatural Selection: Choosing Boys over Girls and the Consequences of a World Full of Men* (PublicAffairs, 2011).
8. Sen, B., Wingate, M. S. & Kirby, R. *Soc. Sci. Med.* **75**, 156–164 (2012).

SOURCE: GUTTMACHER INST.

# Base sustainable development goals on science

**Gisbert Glaser** urges the United Nations' working group to do their research.

**A**t the Rio+20 United Nations conference in June 2012, the world's governments agreed to produce a set of sustainable development goals (SDGs). Unlike the Millennium Development Goals (MDGs), which are targeted at poor and emerging nations, the SDGs will have a global reach. They will apply to developed and developing countries alike, and will concern the Earth system as well as people.

This week, governments meeting in New York will discuss SDGs ahead of the launch of the UN working group tasked with defining their scope and path. I call on the representatives of member states to put good scientific data at the heart of the process.

Human pressure on the Earth system may move us beyond safe natural boundaries. As the climate changes, biodiversity is lost and ecosystems decline, we are on course to inter-linked environmental, economic and social crises that will make it difficult to provide the growing world population with food, water and energy. Only by setting human development on a sustainable trajectory will we safeguard Earth systems for future generations.

Science was short-changed at Rio+20, where green economy and institutional issues were at the fore. But decisions around complex issues such as water scarcity, ocean health, ecosystems and food security must be evidence-based. As a senior adviser to the International Council for Science (ICSU), headquartered in Paris, I feel it is crucial that the best available research underpins the development of goals, targets and indicators at global, regional and national levels. ICSU, having a special consultative status with the United Nations, has offered to provide scientific input to the working group, drawn from research communities worldwide.

Here I set out the steps that are needed to reach tractable goals that will drive sustainable development. These complement the Future Earth ten-year initiative for global sustainability research, which was launched at Rio+20 by the scientific community.

The SDG idea, put forward by Columbia and Guatemala in 2011, received widespread support at the Rio+20 conference. It builds on the MDG concept of setting voluntary, time-bounded targets. Some people are cynical about these, but I believe that the MDGs, even if not reached, have generated commitments and actions worldwide that would not otherwise have happened. For instance, the

MDG of halving between 1990 and 2015 the proportion of people whose income is less than US\$1 per day is on target.

## GLOBAL VISION

The Rio+20 outcome document<sup>1</sup> proposes that the SDGs must be “action-oriented, concise and easy to communicate, limited in number, aspirational, global in nature and universally applicable to all countries while taking into account different national realities, capacities and levels of development and respecting national policies and priorities”.

Meeting all of these requirements will be a challenge for the UN working group. A major difficulty is the interdisciplinary nature of sustainable development. It cuts across economic, environmental and social dimensions in ways that are not well understood. An understanding of climate change, for example, will be necessary to define measures across water, food and energy security. The working group will need to draw on the best available knowledge to analyse these linkages, possible synergies and trade-offs.

The working group's first action must be an extensive information-gathering exercise. This must include all work already undertaken on SDGs, targets and indicators. The group should set up consultations in countries across a range of development levels and seek wide input, from civil society, business, industry and the scientific community.

The long-term strategy of the SDGs must be decided. Should they become the successor to the MDGs after 2015, as some

countries have proposed? Or would this direct resources away from unmet MDGs? At Rio+20, all governments agreed that the SDGs should be “integrated into the United Nations development agenda beyond 2015”. I agree that is the way forward.

The goals should be built around cross-disciplinary themes such as food, water and energy security, rather than separate pillars of economy, environment and social development (see ‘Proposed themes’). Overarching goals, such as the eradication of poverty, might also be included<sup>2</sup> through a two-tier architecture: a handful of primary SDGs on top of a second layer of thematic ones.

The choice of primary goals is tied to the choice of measures of progress and human well-being. Economic indicators such as gross domestic product and the Human Development Index focus on the short term and fail to reflect the state of the environment and natural resources. Metrics must be based on ‘inclusive wealth’ — all forms of capital, from natural, social and human to financial and manufactured<sup>3</sup>. As shown by attempts to include ecosystem services and biodiversity within national metrics, this will not be easy.

Measuring progress on the SDGs will require agreed sets of indicators for use at national, regional and international levels and in developed and developing countries. Several have been proposed; none is currently in use everywhere<sup>4,5</sup>. Much more work is needed on science-based indicators.

As consumption accelerates and the world population rises, global sustainability must become a reality. Scientists must help the working group to devise a set of practical targets. Their adoption by the world's governments will be a test of political will. ■

**Gisbert Glaser** is a senior science-policy adviser to the International Council for Science in Paris, France.  
e-mail: [gisbert.glaser@icsu.org](mailto:gisbert.glaser@icsu.org)

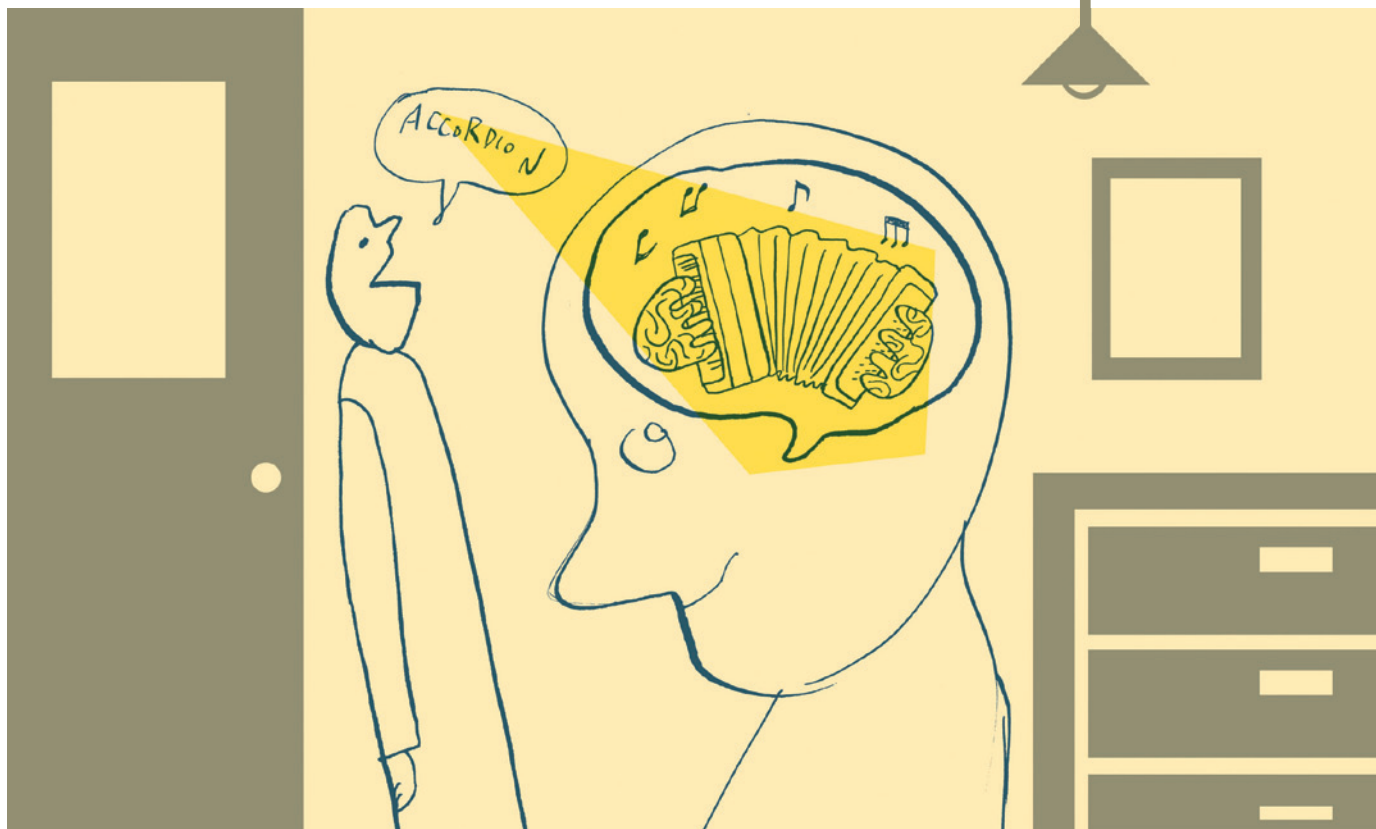
## SUSTAINABILITY

### Proposed themes

Goals suggested by Colombia, Peru and the United Arab Emirates at Rio+20.

- Food security
- Integrated water management
- Energy for sustainable development
- Sustainable and resilient cities
- Healthy and productive oceans
- Enhanced capacity of natural systems to support human welfare
- Improved efficiency and sustainability in resource use
- Enhanced employment and livelihood security

1. United Nations. *The Future We Want* (UN, 2012); available at <http://go.nature.com/ppewxp>.
2. Sachs, J. D. *Lancet* **379**, 2206–2211 (2012).
3. UN University International Human Dimensions Programme & UN Environment Programme (eds) *Inclusive Wealth Report 2012* (Cambridge Univ. Press, 2012).
4. UN Department of Economic and Social Affairs *Indicators of Sustainable Development: Guidelines and Methodologies. Third Edition* (UN, 2007).
5. Hak, T., Moldan, B. & Dahl, A. L. (eds) *Sustainability Indicators: A Scientific Assessment* SCOPE Series 67 (Island Press, 2007).



SATOSHI KAMBAYASHI

## NEUROSCIENCE

# Found in translation

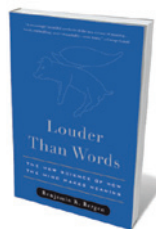
**Charles Fernyhough** enjoys a bold exploration of how the mind extracts meaning from what we read or hear.

**Y**ou are doing something quite remarkable. As you read these words, you are taking abstract symbols from the page or screen and extracting meaning from them. They are no longer mere squiggles of ink or pixels — or, in the case of spoken words, patterns of sound. You know what they refer to. Quite how the mind pulls off this nifty trick has troubled philosophers and cognitive scientists for as long as they have been thinking about language.

A prominent view within cognitive science is that linguistic terms are converted into signs or 'tokens' in a 'language of thought', sometimes known as *Mentalese*. These tokens correspond to the relevant entities in the world. When you read the word 'accordion', for example, a *Mentalese* token is activated, which allows you to have thoughts about a noisy musical instrument played by squeezing. In his impressive debut, *Louder Than Words*,

cognitive scientist Benjamin Bergen tries to persuade us of an alternative view: that we understand language through a process of embodied simulation. Bergen supports this view by reviewing around 200 scientific studies, by his count, from several teams that have been converging on this model during the past couple of decades.

According to Bergen's hypothesis, you understand the meaning of a word through the mental recreation of what it would be like to experience the thing being described. So when you hear the word 'accordion', the visual areas of your brain generate an image of an accordion. When you hear the verb 'squeeze',



**Louder Than Words: The New Science of How the Mind Makes Meaning**

BY BENJAMIN K. BERGEN  
Basic Books: 2012.  
312 pp. £18.99,  
\$27.99

your motor system rehearses the firing that would achieve a squeeze, without going so far as to send the corresponding commands to your muscles.

Much of Bergen's evidence for this account relies on different interference effects, such as the trusty "action-sentence compatibility effect". For example, subjects are asked to read a sentence describing an action (such as holding a marble with a closed fist) while simultaneously pressing a button in a way (such as with a flat palm) that is physically distinct from the described action. The mismatch between the described and performed actions slows language processing, suggesting that the comprehension of action-related language shares cognitive and neural resources with the real-life performance of those actions.

An obvious question is how Bergen's system deals with abstracts. Bergen reasons that much of our language about abstract concepts actually relies on concrete metaphors, meaning that both types of language can be underpinned by the same kinds of simulation. For

➔ **NATURE.COM**  
For more on  
linguistics, see:  
[go.nature.com/i5fbka](http://go.nature.com/i5fbka)

example, studies show that when you read the phrase 'grasp a concept', you comprehend it faster if you have just performed a grasping action with your hand. This theme of complex cognitive abilities being bootstrapped off evolutionarily more ancient systems makes good biological sense. Bergen's view of the language system as a repurposed machine, building on more primitive capacities for perception and action, is one of the attractions of his argument.

But for those familiar with the philosophy and cognitive science of language, there are plenty of unanswered questions in *Louder Than Words*. Explaining how language performs its many functions is notoriously difficult, and the question of how a mental event can ever be 'about' an element of the real world remains a tricky philosophical issue. One problem is that Mentalese isn't the only game in town. You can have an account of meaning based on neural representations of conceptual knowledge that doesn't posit a language of thought. As a result, *Louder Than Words* sometimes has the feel of an assault on a straw man.

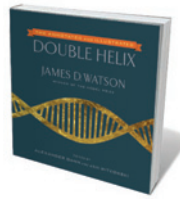
Bergen's treatment of language relies heavily on the 'conduit metaphor', by which one person's thoughts are packaged in words and sentences and unpacked by the listener or reader, rather than shaping and being shaped by a complex patterning of social exchanges. Bergen's theory lacks a developmental perspective: how do babies, for example, get started with word meanings? The model is also unclear on the role of consciousness. We are told that simulation can be unconscious, but elsewhere it is proposed to involve the "creation of mental experiences", presupposing that those experiences are conscious — because, by definition, if you experience something you must be conscious of it.

Bergen ends with a tricky question about the functional significance of mental simulation. Simulation happens when people process language, but does it actually achieve anything? His disarmingly honest conclusion, which dials back on a rather hyperbolic tone at the outset, is that simulation is ultimately neither necessary nor sufficient. He concedes that other forms of language understanding that don't involve embodied simulation are also important.

Bergen admits that his science is still in its infancy, and he sets out his account with enthusiasm, energy and some delightful touches of humour. If you want an engaging, well-informed tour of how cognitive science approaches the problem of meaning, you stand to learn a great deal from this book. ■

**Charles Fernyhough** is a reader in psychology at Durham University, UK, and the author of *Pieces of Light*, a book on autobiographical memory.  
e-mail: c.p.fernough@durham.ac.uk

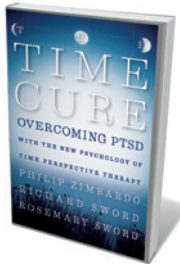
## Books in brief



### The Annotated and Illustrated Double Helix

James D. Watson, Alexander Gann and Jan Witkowski  
SIMON & SCHUSTER 368 pp. £19.99, \$30 (2012)

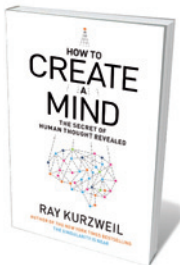
Few tales of modern science thrill as much as the race to discover DNA's double-helical structure. Fifty years after James Watson, Francis Crick and Maurice Wilkins won a Nobel prize for their sprint to the finish, Alexander Gann and Jan Witkowski have crafted a new edition of Watson's behind-the-scenes account, *The Double Helix* (1968). Annotated to clear up abiding mysteries; adorned with lab notes, sketches and photos; and beefed up with extras by Rosalind Franklin and other major players, this is a sampler of rare treats.



### The Time Cure: Overcoming PTSD with the New Psychology of Time Perspective Therapy

Philip Zimbardo, Richard Sword and Rosemary Sword  
JOSSEY-BASS 336 pp. £17.99 (2012)

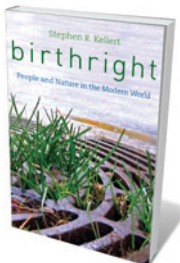
Psychologist Philip Zimbardo has long probed the nature of trauma — notably in his 1971 Stanford prison study — and how orientation towards the past or future affects mental well-being. Now, with therapists Richard and Rosemary Sword, he suggests these findings can guide treatment for people with post-traumatic stress disorder, who suffer harrowing flashbacks. A treatment plan (being tested by the US military), quantitative data and case studies are on offer.



### How to Create a Mind: The Secret of Human Thought Revealed

Ray Kurzweil  
VIKING BOOKS 352 pp. \$27.95 (2012)

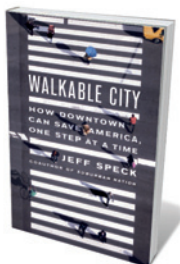
In *The Singularity Is Near* (Viking, 2005), Ray Kurzweil imagined a near future in which medical nanotechnology would allow us to decant copies of our brains into hyper-intelligent machines — and effectively live forever. Now the bestselling futurist and pioneering inventor explores a prime arena for today's big science: reverse engineering the brain. Using the brain's pattern-recognition capacity as a springboard, Kurzweil leaps from the physical brain and the processes of creativity to the debatable idea that, given the correct software, digital entities are effectively conscious.



### Birthright: People and Nature in the Modern World

Stephen R. Kellert  
YALE UNIVERSITY PRESS 264 pp. \$32.50 (2012)

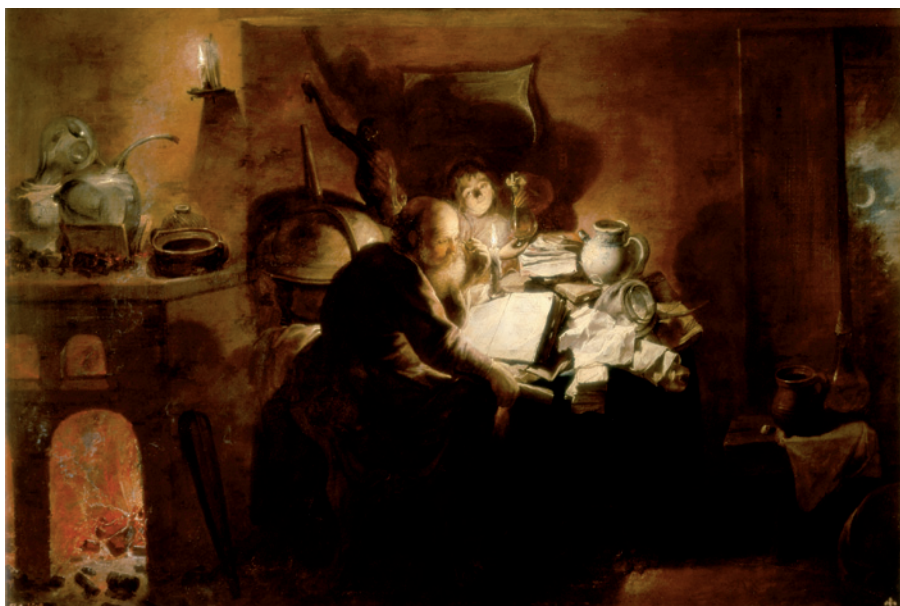
With his sometime-collaborator E. O. Wilson, social ecologist Stephen Kellert has asserted that biophilia — affinity for nature — is central to health, emotional well-being and much more. Here, Kellert challenges our "adversarial" approach to nature with an exploration of eight ways in which we derive meaning from it, from attraction to exploitation. He argues that, even in cities, natural complexity and dynamism are central to children's cognitive development, as they recognize, identify and evaluate rocks, clouds, trees and insects. This is a nuanced analysis punctuated with insightful personal narratives.



### Walkable City: How Downtown Can Save America, One Step at a Time

Jeff Speck  
FARRAR, STRAUS AND GIROUX 320 pp. \$27 (2012)

Vast intersections, pin-thin pavements, kilometres of concrete: many US city centres were built for cars, not feet. City planner Jeff Speck, working with scores of mayors, concluded that urban liveability demands walkability. He identifies the benefits of well-designed density, such as increased physical fitness, lower fuel use and higher productivity. His 'Ten Steps of Walkability', from well-shaped spaces to curbs on cars, are a blueprint for reclaiming downtown America.



*The Alchemist* (1640) by David Ryckaert III shows a practitioner at work.

## HISTORY

# Realms of gold

**Jennifer Rampling** relishes a masterful take on the age-old allure of alchemy.

Around 1680, Robert Boyle, author of *The Sceptical Chymist* (1660), described meeting a stranger who demonstrated an unusual experiment. Tipping some ruby-coloured powder onto the blade of a knife, he cast it into a crucible of molten lead. The lead congealed into “very yellow” metal, which Boyle’s tests proved — in his estimation — to be pure gold.

Boyle’s account, retold by Lawrence Principe, drives home a problem facing all scholars of alchemy: why, across the ages, have so many intelligent people been convinced by the promise of metallic transmutation? *The Secrets of Alchemy* comes closer than any other single work to explaining the grounds — rational and empirical, as well as religious and wishful — for alchemy’s longevity.

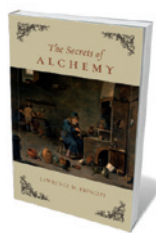
Principe’s delightful writing style brings to life a depth of learning matched by few in the field. This expertise, coupled with the author’s determination to strip his topic of anachronism, sets *The Secrets of Alchemy* apart from the usual introductory tome. After comments on alchemy’s lingering popular appeal (think Harry Potter and *Fullmetal Alchemist*), Principe engages with the misconceptions that have long dogged his subject, particularly its association with magic, mysticism and quackery. A key premise of the book is that these are often modern associations. To understand how alchemy ‘worked’ for its practitioners,

we must meet them on their own terms.

Principe traces the theory, practice and context of alchemy from its origins in Egypt in the first few centuries AD to its development and maturity in the medieval Islamic lands and Latin Europe. He then engages with Enlightenment critiques of transmutation, tracing their consequences up to today before returning to alchemy’s “Golden Age” in Renaissance Europe.

Some will recognize elements from Principe’s earlier work: the argument that ‘alchemy’ and ‘chemistry’ overlapped in the early modern world (and so should be referred to simply as ‘chymistry’); his concern that Enlightenment polemics and nineteenth-century fads have distorted alchemy’s modern reception; and his view that even the alchemists’ most outrageous allegories may disguise genuine chemical effects. In sum, he does not believe that alchemists made gold, but does show that they were serious in the attempt.

Like Boyle, Principe recognizes that sceptics will be convinced only by displays



**The Secrets of Alchemy**  
LAWRENCE M. PRINCIPLE  
University of Chicago Press: 2012.  
296 pp. \$25, £16

of incontrovertible expertise. The book is at its most fascinating when Principe reveals glimpses of his own skill. A chemist as well as a historian, he has recreated a range of alchemical experiments, revealing the practical foundations of seemingly opaque alchemical instructions. The first chapter opens with a recipe from one of the earliest surviving metallurgical treatises, the third-century Leiden Papyrus. The process can be easily replicated, producing a golden patina on a silver ingot. And if Principe’s photographic evidence does not convince, an endnote gives instructions on how to do it yourself.

Yet if alchemists engaged in ‘real’ chemistry, why did they disguise their methods in such baffling ways? In one sequence, Basil Valentine — a fictitious name assigned to a number of alchemical treatises — describes how a king is devoured by a wolf, but resurrected after the creature is cast into a fire. This exotic conceit evolved from an earlier tradition of alchemical secrecy. It also reflects a wider contemporary passion for emblematics — the encoding of meaning in playful images, mottoes and verses.

Such puzzles were designed to be solved. As Principe demonstrates, Valentine’s wolfish encounter is an allegory for the technique of purging gold using antimony ore, “the ravenous grey wolf”. This process culminates with the volatilization of gold. Difficult enough to achieve in modern labs, this was an astonishing technical feat for early practitioners, who were hampered by impure ingredients, non-standard apparatus and an absence of thermometry. Boyle also cracked Valentine’s puzzle, remarking that although difficult, “it eventually succeeded beautifully”.

So was Boyle a scientist, alchemist, apologist or interpreter? For that matter, how about Principe? As the book suggests, modern readers can profitably reflect on how they use such distinctions.

For, as Principe concludes, alchemy cannot simply be reduced to chemical procedures. Many practitioners subscribed to a widely held belief in the ‘connectedness’ of humans, God and nature. In this world view, analogy had demonstrative as well as illustrative power: similarity between small-scale and large-scale phenomena might offer clues to unseen laws of nature. Such correspondences strike us in alchemical writing, because they have disappeared from modern scientific discourse. *The Secrets of Alchemy* reminds that too-selective reading can mask the influence of such views on the past science we now accept as canonical. After Isaac Newton’s *Principia*, why not browse his theology — or alchemy? ■

**Jennifer Rampling** is a Wellcome Trust Postdoctoral Research Fellow in the Department of History of Science, University of Cambridge, UK.  
e-mail: jmr82@hermes.cam.ac.uk

## GEOGRAPHY

# Going all the way

Andrew Robinson follows the feet, wheels, ships and space stations that have circled the globe.

In the depths of the cold war, the new nuclear submarine *USS Triton* made the first underwater circumnavigation of the globe in just 84 days. During this covert mission, the crew collected oceanographic and gravitational data, discovered an undersea peak in the mid-Atlantic Ocean and studied the response of human beings to a closed and cramped environment — information deemed useful by the burgeoning US space programme.

The pioneering 1960 mission deliberately followed most of the route of the first-ever Earth circumnavigation, by Portuguese explorer Ferdinand Magellan and his crew in 1519–22. That expedition limped home after three years, *sans* leader, 86% of its men and four of its five ships. Conversely, the technologically sophisticated *Triton* suffered no fatalities, as its commander (and bestselling novelist) Edward Beach divulged in *Around the World Submerged* (Holt, 1962). But on one 3,200-kilometre detour, it delivered a crewman with a kidney stone to a small rescue party sworn to secrecy.

These two feats, along with dozens more, are expertly filleted in historian Joyce Chaplin's *Round About the Earth*. The book is a first of its kind: a history of circumnavigations covering sea and land, air and space, and almost all forms of transport, from feet and bicycles to Concorde and orbiting space stations. Chaplin makes telling use of details from primary sources. But, as she admits, none of the technologies — whether telegraph, aeroplanes, satellites or the Internet — has, despite grand initial claims, ever “saved the world” on its own.

Choice morsels abound, including the diary of a minor Venetian nobleman who survived Magellan's voyage; the journals of Captain James Cook and his plant-hunting co-traveller Joseph Banks, a future president of the Royal Society; and Charles Darwin's *Beagle* diaries and letters (1832–36). We also get *Following the Equator* (1897) by Mark Twain; the memoirs of solo sailors and fliers such as Joshua Slocum, Francis Chichester and Wiley Post; and stories of the Soviet cosmonauts and American astronauts. Even the celebrated travels of Phileas Fogg in Jules Verne's fictional *Around the World in Eighty Days* rate an extensive discussion.

Chaplin has clearly taken to heart the exchange she quotes from James Boswell's *The Life of Samuel Johnson*. Mulling over the idea of joining Cook's second circumnavigation (in 1772–75), Boswell tests it on the great lexicographer. “One is carried away with the general grand and indistinct notion of a VOYAGE ROUND THE WORLD,” says Boswell. “Yes, Sir,” Johnson replies, “but a man is to guard himself against taking a thing in general.”

Johnson was prescient, as Chaplin reminds us. For Cook was rewarded less for his geographical discoveries (or his application of the marine chronometer to the longitude problem) than for his essay on the prevention of scurvy, published in the Royal Society's *Philosophical Transactions* in 1776. The British government was deeply impressed that Cook had lost only 2.6% of his crew — and not one to scurvy, which had been the greatest killer of circumnavigating

in Hawaii in 1779, circumnavigators travelled in fear of the dangers. First among these was shipwreck, the result of poor navigational technology and stormy weather, but also starvation and disease at sea, and hostile encounters with indigenous people.

From Cook's death until the Second World War, dramatic improvements in medical treatment, transport and communications technology meant that circumnavigators had much less to fear. Perhaps most importantly, the umbrella of international imperialism endowed these explorers with planet-dominating confidence. HMS *Beagle* carried six guns when it set sail in 1831, whereas by 1872, HMS *Challenger* — a scientific expeditionary vessel exploring the deep oceans — carried a mere two. Moreover, these were intended for signalling rather than self-defence. In the mid-twentieth century, however, the old sense of danger returned, with the development of aeroplanes, rocket-propelled space capsules and the collapse of imperialism. What grew too, argues Chaplin, was doubt: the sense that Earth “is again beginning to bite back, now that the environmental costs of planetary domination have begun to haunt us”.

On the whole, the book's tripartite structure works well in the first two sections, but is less convincing in the third, which strangely neglects the issue of global climatic change.

Although science and technology make their presence felt throughout the book, the emphasis is on history, politics, cultures and the personalities of the travellers — the “geodrama” of circumnavigation, as the author calls it. After all, even the scientifically distinguished James Lind (the eighteenth-century physician widely credited with introducing citrus fruits on voyages to protect against scurvy, through the first-ever clinical trial) was convinced that accommodating a sailor's yearning for land was efficacious. Lind reported without a hint of scepticism that scurbutic seamen began to revive when they were taken ashore, stripped and buried up to their necks in the earth. ■

**Andrew Robinson** is the author of *The Story of Measurement and The Shape of the World: The Mapping and Discovery of the Earth*.  
e-mail: andrew.robinson33@virgin.net



**Round About the Earth: Circumnavigation from Magellan to Orbit**

JOYCE E. CHAPLIN  
Simon & Schuster:  
2012. 560 pp. \$35



**Cartographer Battista Agnese's 1545 map traces Ferdinand Magellan's expedition.**

sailors since the time of Magellan.

Chaplin imposes order on her disparate material and draws meaning from it by sticking to the historical chronology of circumnavigation and dividing the half-millennium since Magellan into three major sections: “Fear”, “Confidence” and “Doubt”. From Magellan's violent death in the Philippines in 1521 to the notorious demise of Cook

# Correspondence

## Handful of papers dominates citation

An 'impact disparity' is emerging in science — only a few papers earn the largest share of citations. This is comparable to the income disparity in the United States, known as the 1% phenomenon, where 1% of the population earns a disproportionate 17.4% of total income (see [go.nature.com/yajthu](http://go.nature.com/yajthu)).

The number of citations acquired by a paper is a proxy of its impact. We found that of all papers published in five leading journals in 1990, the most highly cited 1% in each collected around 17% of citations in 2010 (see 'The 1% effect'; data from Thomson Reuters Science Citation Index).

Changes over time in the citation share of the top 1% are evidence of endogenous shifts in underlying processes. These trends are particularly pronounced for citations of older papers. For example, the top 1% of 1990 papers collected only about 5% of citations in 1991.

This shift of attention over time towards the top 1% may reflect the fact that, although the number of research papers has exploded, the time scientists devote to reading them has not. Researchers increasingly rely on crowd sourcing to discover relevant work, a process that favours the leading papers at the expense of the remaining 99%.

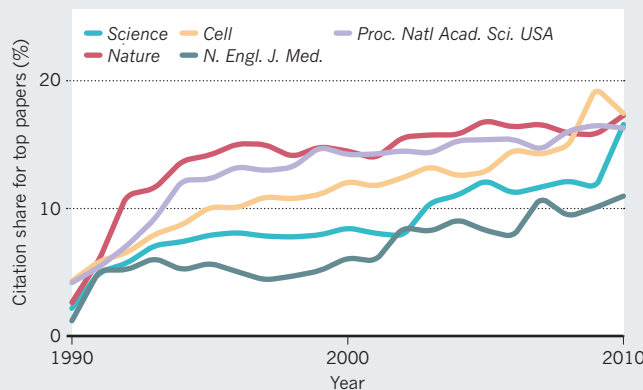
**Albert-László Barabási,**  
**Chaoming Song, Dashun Wang**  
*Northeastern University, Boston, Massachusetts, USA.*  
[barabasi@gmail.com](mailto:barabasi@gmail.com)

## Call to register new species in ZooBank

We wish to clarify a few points in your discussion of the decision by the International Commission on Zoological Nomenclature (ICZN) to allow naming of new species in electronic-only publications (*Nature* **489**, 178; 2012).

### THE 1% EFFECT

The top 1% of the most highly cited papers published in 1990 have accrued a disproportionate share of citations over the past 20 years.



The amendment is already in force, retroactive to 1 January 2012 (see, for example, *Bull. Zool. Nomenclature* **69**, 161–169; 2012; available at [go.nature.com/atytlr](http://go.nature.com/atytlr)). It remains to be seen which electronic publication will first satisfy the requirements of the amendment. The ICZN official registry, ZooBank, did not support all the requirements until the beginning of September, when the commissioners' votes became official.

New animal species will not need to be registered in ZooBank. It is the electronic works themselves that must be registered to count as published for nomenclatural purposes. In the amendment, registration of new names is a recommendation, not a requirement. We encourage zoologists to comply with this recommendation, which will aid in automated indexing, linking and data extraction.

The amendment allows the ICZN to issue declarations clarifying whether new methods of production, distribution, formatting or archiving can be used to publish works that comply with the requirements of the *International Code of Zoological Nomenclature*. This, coupled with the error-checking capabilities in ZooBank, will enable the code to evolve rapidly

and help authors to fulfil the new requirements.

**Gary Rosenberg** *Drexel University, Philadelphia, Pennsylvania, USA.*

[rosenberg@ansp.org](mailto:rosenberg@ansp.org)

**Frank-T. Krell** *Denver Museum of Nature & Science, Denver, Colorado, USA.*

**Richard Pyle** *Bernice P. Bishop Museum, Honolulu, Hawaii, USA.*

## Problems enforcing Ecuador ecology law

Ecuador has more species per unit area than any other country, a unique ecology that is now uniquely protected under its constitution. But upholding these highly commendable conservation policies is a challenge.

For example, a landmark legal precedent was set in a lawsuit brought in early 2011 against the local government for damages to the Vilcabamba River caused by a road-construction project. The defendant was ordered to pay for recuperation of the river. One year on, there has still been no substantial remediation (see [go.nature.com/6m4aea](http://go.nature.com/6m4aea)).

In light of this situation, we are concerned that the imminent strip mining in southern Ecuador of gold and copper ore worth US\$200 billion could

put a serious strain on the country's legal system and its environmental policies.

**Kelly Swing** *Tiputini Biodiversity Station, University San Francisco de Quito, Quito, Ecuador.*  
[kswing@usfq.edu.ec](mailto:kswing@usfq.edu.ec)

**Luis Sempértegui** *Superior Court (retired), Loja Province, Ecuador.*

## Open collaboration is key to new drugs

As chair of the board of the Structural Genomics Consortium (SGC), I would like to acknowledge the commitment of the hundreds of scientists from industry and academia who collaborate with the SGC to make freely available synthetic probes that are potentially important to public health. You feature one such molecule, JQ1, now being investigated for blocking unwanted gene expression, in your discussion of epigenetics targets in cancer (*Nature* **488**, 148–150; 2012).

JQ1 resulted from collaboration between SGC researchers and Jay Bradner's group at the Dana-Farber Cancer Institute in Massachusetts, building on the work of scientists at Mitsubishi Tanabe Pharma in Japan and with guidance from scientists at GlaxoSmithKline in the United Kingdom. As you point out, the huge impact of the study is due in large part to the collaborators' willingness to distribute JQ1 without restriction.

Other such examples resulting from open collaborations between industry and academia include inhibitors of the molecules JMJD3 (L. Kruidenier *et al.* *Nature* **488**, 404–408; 2012), BRD4 (P. Filippakopoulos *et al.* *Nature* **468**, 1067–1073; 2010) and G9- $\alpha$ -methyltransferase (M. Vedadi *et al.* *Nature Chem. Biol.* **7**, 566–574; 2011).

**Markus Gruetter** *University of Zurich, Switzerland.*  
[gruetter@bioc.uzh.ch](mailto:gruetter@bioc.uzh.ch)

# MIDNIGHT IN THE CATHEDRAL OF TIME

*Dream sequence.*

BY PRESTON GRASSMANN

Walking through the crowded streets in Canvas Town, I pass a booth that claims to sell the god-ware of angelic systems; codes that open gateways to palaces of corporate data. I pass the aisles of snake-oil salesmen, hawking the latest nanotech cures for assorted ailments, from back pain to cancer. Through the aisles, the gold and silver relics of archaic religions are nestled among the silicon and plastic wafers of data-chips.

The man I'm searching for sits in the corner of the tent and looks up slowly. His eyes catch a glint of light from mechanically modified plasma-eels that swim in a tank at the entrance of his shop. As I enter, he smiles and hunches slowly forward, a conspirator waiting to whisper a secret. Towers fall and cathedrals break apart across his chest, streets narrow across his ribs to make room for buildings; his skin altering in the movement.

"You finally made it back," he says, his lips turning a mountain ravine into a cave of broken stalactites. He watches me with grey-green eyes.

"What made you think I would?" I ask, watching as two eels collide in a surge of blue light, plasma flickering around their bodies. A few people stand at the entrance, placing their hands on the surface of the tank to watch the storm surge around their fingers.

"Lucid dreamers always return."

I begin to see the illustrations spreading outwards from his body, an artist's outline that turns into solid shapes. The mountain across his cheekbones begins to melt, spreading down his chest, colours pouring across his skin like watercolours.

The DJ stays where he is, unmoving, as if waiting for me to act.

"One reading is all it takes for some," he says, reaching out for the data-chip. I place it in his open palm. "Before they become..."

"Dream junkies?"

He nods slowly.

A crowd begins to gather outside the shop.

He replays the images of dreams from previous customers.

Another image forms across his chest;

bright green palms swaying among a village of burning homes, spires of smoke rising across his shoulders like wings.

The data-chips were dreams rendered into code. There were only a few technicians who understood how such data could be used, and even fewer who could render them into



coherent forms. This man had chosen to turn it into an art. As he read the data-card, the images would be distilled and remixed, projected on his skin in high resolution.

"Shall we keep this private?" he asks, the pictures on his skin shifting too quickly to be seen.

"Yes."

He rises for a moment to move the audience away and pulls a low Japanese panel-screen across the entrance.

"There are more details here than before," he says, as the shadows across his chest begin to resolve, her face becoming clearer, chiaroscuro lines opening into the shadowed hollows of her eyes, the twist of a red mouth, the familiar angles of her cheeks. She stands

at the entrance. "It's midnight..." she says, the voice of the DJ altering to let hers come through.

She is wraith-thin and dressed in a silk robe and she retreats back into the cathedral, moving as if part of some clockwork mechanism. Through a sequence of images, I watch myself enter, searching for her through the aisles. Everything inside is turning with rusted clockwork parts and the corroded mandalas of half-broken gears. In the pews, worshippers hold the remains of broken clocks. The springs and cogs are spread across their open palms like hymnals.

"Horo-shippers," the DJ says softly, smiling. "Clever."

And then I find her, staring up at the altar. She doesn't turn away as I approach. Even as I put my hand on her shoulder, she remains still. All at once, everything stops. The DJ is motionless, his smile fading as the images of the gears stop turning and the parts fall out of the worshippers' hands and clatter on the floor. And then there is only stillness inside and I run to the altar and beat my fists against its walls, striking out against the mechanism. "Not yet," I say, my own voice echoing around me. "Come back."

That's when the face of the man begins to shift and flow, and she is there, the slope of her cheeks, the curve of her mouth, the soft line of her eyebrows, eyes rendered in the space of eyelids; the same bright, piercing blue-green that I remember so well. And then her body forms, shaping itself across the terrain of his arms, his chest, flowing down the length of his body, until the DJ's skin is only a faint outline around hers. For a moment I can still see the gears, as if she has become the cathedral, the movements of time, her heart the mechanism that makes the gears turn, but they soon fade until it is only her body reaching out for mine.

"Come," she says, and though I know this can't be part of my recorded dream, that it's only an offering, I will hold her for as long as I can. ■

**Preston Grassmann** is co-author of *The Floating World*, a collaboration with K. J. Bishop. He currently lives in Japan, surrounded by a growing collection of drawings, paintings and unreliable maps of the Tokyo underground.

## TECHNOLOGY FEATURE

# READING THE SECOND GENOMIC CODE

*Transient changes to the genome make its code more complex to interpret but they still put a gleam in the eye of drug and technology developers.*

ALENGO/ISTOCKPHOTO



BY VIVIAN MARX

**D**NA is famous as the instruction manual of life — the multi-billion-base-pair data tape that directs how a fertilized egg turns into the specific cells, tissues and organs of, say, a sharp-eyed soccer pro who is musically inclined but who also battles depression.

But DNA works with many partners, including ‘epigenetic’ factors, which influence gene expression in ways that don’t involve changes to the underlying sequence (see ‘Polygamous DNA’). An important example is methylation, in which methyl groups are tacked on to various locations along the double helix to control the activity of particular genes. Methylation

also affects histones, the spool-like proteins around which DNA is tightly wound inside the nucleus: the chemical modifications help to control when this protein–DNA complex, called chromatin, opens up so that the genetic instructions can be read.

Figuring out when and how such epigenetic changes get made — or damaged — has become a crucial part of scientists’ efforts to understand both the normal development of cells and their progression into cancer and other diseases. It can be painstaking work. Sometimes, says Andrew Feinberg, an epigeneticist at Johns Hopkins University in Baltimore, Maryland, the available techniques often pick up only “little biochemical shadows” of events going on at a particular location, while

the complete set of players and their mechanisms remain mysterious. And even when you can identify an epigenetic molecule, says Tony Kouzarides, a molecular biologist at the University of Cambridge, UK, “you have to work out why it is there, and what it is doing there”.

Nonetheless, epigeneticists have made remarkable progress over the past two decades. Their tool kit now includes advanced sequencing techniques, targeted antibodies and even laser cell sorting — and it should soon encompass ultrasensitive nanofluidic and nanopore sequencing methods. The community is also turning to advanced bioinformatics to cope with the sheer volume of data — especially the wealth of epigenetic information from the Encyclopedia of DNA ►

► Elements (ENCODE) project, which this year released more than 1,600 genome-wide data sets covering more than 100 cell types<sup>1</sup>.

Technology development is now kicking into high gear as epigenetics researchers push to decipher the genome's many partners, and to deepen understanding of health and disease.

## BEYOND A PRECIPITATING HEADACHE

The standard method used to study epigenetic histone modifications is called chromatin immunoprecipitation (ChIP), coupled with sequencing<sup>2</sup>. The basic idea is to shear DNA while it is still wrapped around the histones, use antibodies to capture specific protein–DNA complexes from the fragments, and then study which DNA sequences are attached to which proteins. The approach helps to unpick how the interactions are tuning genes — activating some, silencing others.

The technique has its drawbacks, however. Sriharsa Pradhan, an RNA biologist at New England BioLabs in Ipswich, Massachusetts, says that he is often unable to reproduce work from published epigenetics studies. “Most of the failures happen if the antibody is not good,” Pradhan says. It might pick up too many DNA–protein complexes — “every Tom, Dick and Harry” in a sample — and so does not offer the resolution that scientists seek.

Kouzarides agrees that the quality of the antibody matters greatly for ChIP and many other lab procedures. That's what led him to co-found Abcam, an antibody supplier with headquarters now in Cambridge, UK. The goal is exceptionally high quality, says Kouzarides, who is on Abcam's board of directors — but it is a constant struggle. “You are at the mercy of the rabbits,” he says, referring to the animals used to generate the antibodies. “Some generate good antibodies, some generate bad antibodies” — and there is no predicting which is which.

Monoclonal antibodies could offer more reliability, says Kouzarides, because they avoid the problem of batch-to-batch variability. But for reasons that still aren't clear, he says, some of them do not work well for ChIP. For now, the field has to use animals to generate the antibody mixes useful for ChIP. “You have to put up with the unreliable nature of antibodies because it's the only way to do such experiments at the moment,” he says.

Another drawback with standard ChIP is its bias, says Alan Tackett of the University of Arkansas for Medical Sciences in Little Rock. Although the technique lets scientists localize

a specific protein acting on a genomic site, “you have to know what protein or histone modification you are targeting”. And scientists need to have on hand an antibody that matches the protein of interest. So ChIP is not easily multiplexed to profile multiple areas of the genome at the same time.

In response to this shortfall, Tackett and his Arkansas colleagues, along with scientists at the Johns Hopkins School of Medicine, have developed chromatin affinity purification with mass spectrometry (ChAP-MS)<sup>3</sup>. The approach involves cutting out a 1,000-base-pair region of a chromosome, purifying it and determining all the epigenetic changes that are present. The team has used the approach in yeast to detect different chromatin states, silenced genes and other regions in which genes are still active. And Tackett says that around ten other labs have begun exploring it, too.

He is now readying the technique for use in human cell lines and tissues. “We are working on the mammalian version and anticipate having that complete within the year,” he says. One challenge for ChAP-MS is that the analysis requires  $10^7$  to  $10^{10}$  cells, so Tackett and his colleagues are trying to lower that number. And Tackett is confident about the technology's promise. “We see this ultimately taking the place of ChIP in epigenetics labs,” he says, with mass spectrometry being available through proteomics core facilities on campuses, he says.

Other scientists are proposing different alternatives to ChIP, which “is not a very efficient process”, says Paul Soloway at Cornell University in Ithaca, New York. In addition to the challenges involved in sample processing, ChIP usually queries just one epigenetic mark at a time in a population of cells. That means that the results of multiple ChIP-seq experiments have to be aligned to determine if some cells have one mark and others have another, or if, perhaps, all cells have both.

Soloway wants to offer scientists greater resolution for ChIP analysis. He also wants the approach to be scalable, delivering detail and screening for multiple epigenetic marks in a single experiment. His answer is a nanofluidic device based on a silica wafer that is in the prototype stage and which comes in two formats<sup>4</sup>. One of them quantifies the molecules with at least one epigenetic mark. The other, a

branched nanofluidic device, sorts and quantifies the molecules. Using fluorescent labels and optics-based sorting, the molecules are shunted to one chamber or another for later analysis, such as DNA sequencing. “Because silica is clear and non-fluorescent, we can make measurements of individual molecules using highly sensitive optics,” he says.

Ultimately, Soloway would like to be able to go through whole genomes in a rapid, multiplexed way. He says that standard ChIP is still ahead of his technique because it can generate materials in the amounts needed for sequencing, whereas he still needs to get from single molecules to the pico- and nanograms needed.

Soloway believes that his technology will find a home in drug development, helping researchers to quickly and quantitatively characterize how drug candidates affect epigenetic marks. Clinical applications could include helping to monitor how patients fare when treated with epigenomic drugs, and identify how epigenetic marks vary during the course of a disease such as cancer, he says. In January, together with the Cornell engineers Harold Craighead and Stephen Levy who worked on the technology, he founded Odyssey Molecular in Ithaca, to commercialize the device.

## FINDING OTHER MARKS

DNA methylation has important roles in cells, including the regulation of genes during development and disease. One of several methods used to find these sections of the genome is methylated-DNA immunoprecipitation, which uses an antibody that locates 5-methylcytosine, a methylated form of the DNA base cytosine.

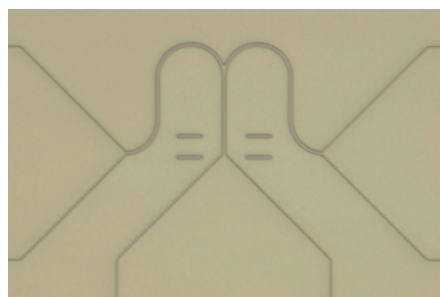
A different approach targets methylated parts of the genome in ‘CpG islands’, which are characterized by a specific chemical bond between the DNA bases cytosine and guanine. In an analysis of methylation levels for 240,000 of the several million CpG islands in the ENCODE data, John Stamatiouannopoulos at the University of Washington in Seattle and his colleagues found a strong association between methylation and accessibility for genes to be read<sup>5</sup>. As Wendy Bickmore from the Medical Research Council Human Genetics Unit at the University of Edinburgh, UK, notes, the results support the idea that DNA methylation is blocked where the transcription factors that read DNA bind. This mechanism, she says, is relevant to the interpretation of disease-associated sites that show altered DNA methylation<sup>6</sup>.

One widely used technique to determine DNA methylation patterns across a genome is bisulphite sequencing. The addition of bisulphite to DNA converts cytosine to uracil, but skips methylated cytosines, thereby allowing the methylation status of DNA segments to be determined through high-throughput sequencing. Many companies offer bisulphite conversion kits. “It's cheap enough now and there are statistical tools for understanding it, so there's no reason to use another method,” says



**“Whatever you see in one moment will change in the next.”**

Tony Kouzarides



**A nanofluidic device can sort through DNA molecules to find those with epigenetic marks.**

Feinberg.

Yet detecting methylation is time-consuming, so scientists in academia and industry have been exploring ways to improve the approach. Some teams, including one at Osaka University in Japan and one at the University of Oxford, UK, are exploring the use of nanopores, tiny gates through which to run a DNA strand. And Pacific Biosciences, a sequencing firm in Menlo Park, California, is using tags to prepare single strands of DNA for high-throughput sequencing.

At Washington University in St Louis, meanwhile, Rob Mitra is leading an effort to be more precise in capturing methylation data, because this information can, for example, be an early sign of tumour development. Mitra and his team, including graduate student Maximiliaan Schillebeeckx, have developed a technique that uses lasers to separate out the cells of interest. He calls the technique laser capture microdissection–reduced representation bisulphite sequencing. Among the advantages, says Mitra, is that the technique covers “the majority of the CpG islands and it’s relatively inexpensive”.

Reduced representation bisulphite sequencing is similar to whole-genome bisulphite sequencing, but sequences only the parts of the genome that include CpG-dense regions. The technique uses enzymes to cut up purified genomic DNA into fragments that contain CpG islands. The fragments are then processed, and those of a certain size are subjected to bisulphite conversion, amplified and then sequenced.

The approach is geared to work on small amounts of DNA — perhaps even less than a nanogram — and in formalin-fixed, paraffin-embedded tissue, which is “typically not in as good shape as good fresh frozen DNA”, Mitra says. This type of tissue fixation is typically used in biobank samples.

His technique could be a tool for researchers who work with specific cell types or with complex tissues, such as neurological samples, in which it is hard to isolate the cell type of interest, he says. The method also avoids the need for multiple labour-intensive purifications. And, he says, “at each point in space, you get a genome-wide profile of methylation, so now you can start to correlate methylation profiles spatially”, Mitra says. A researcher can see, for example, if similar regions of complex tissue are methylated similarly. By coupling genome-wide methylation analysis with laser capture to isolate targeted cell populations, the tool can help researchers to address questions in these challenging tissues, he says.

## EXPANDED REACH

Along with the flood of data that ENCODE brought to epigenetics came data standards, quality metrics, software tools and ways to convey how experiments are done, allowing comparisons between labs. This development has heightened awareness about the “good technologies” needed to study how the genetic

code is put into action, says Adam Petterson, a senior scientist at Zymo Research in Irvine, California, which is one of many companies offering epigenetics services to academics as well as drug-discovery companies.

Such awareness is going to become ever more important as epigenetics grows to encompass not just multiple cell types, but multiple species. The modENCODE project ([www.modencode.org](http://www.modencode.org)) is mapping regulatory patterns in two frequently used model organisms, the fruitfly *Drosophila melanogaster* and the nematode worm *Caenorhabditis elegans*, and the Mouse ENCODE consortium is focusing on epigenomic mapping of the mouse. “A huge way to understand function is by comparative epigenomics,” says Feinberg, who would like to see efforts across many more species.

These developments will inevitably require increased reliance on massive computation, says Kouzarides, who sees bioinformatics as a rate-limiting step in epigenetics. Researchers need ways to integrate and do global analyses



**“Now you can start to correlate methylation profiles spatially.”**

Rob Mitra

of the emerging maps of epigenomic marks and their effects, as well as ways to do high-resolution analyses, preferably at the single-cell level (see page 27). Without such computational tools, Kouzarides says, “it’s almost impossible to appreciate the complexity of the information”. For scientists who would rather not dig into the data themselves, Michael Snyder and his team at Stanford University in California have developed Regulome-DB ([regulome.stanford.edu](http://regulome.stanford.edu)), an automated tool to explore non-coding regions of the human genome. Manolis Kellis at the Massachusetts Institute of Technology in Cambridge and his group have set up Haplo-Reg ([www.broadinstitute.org/mammals/haploreg](http://www.broadinstitute.org/mammals/haploreg)), a tool that helps to link non-coding variant patterns to possible clinical conditions.

## TRANSIENT DRUGS

The potential for clinical applications is an important motivator for epigenetics research. The transient nature of epigenetic changes gives drug developers and biomedical researchers reasons to dream about how their efforts might reverse changes that contribute to disease. “Those sorts of things that are more malleable are likely the things that we can target,” Feinberg says.

Four drugs that act on epigenetic pathways have been approved by the US Food and Drug Administration (FDA), and the next wave of

candidates is being readied in biotech and pharmaceutical companies. Kouzarides, for example, is looking at chromatin modifications and develops drug candidates that could right the wrongs in cancers in which, for example, epigenetic influences lead to the misregulation of cell pathways<sup>7</sup>.

Targeting an aggressive form of leukaemia for which treatments are lacking, Kouzarides and his team have explored how to inhibit bromodomain and extraterminal (BET) proteins and remove them from chromatin. BET proteins belong to a class of epigenetic reader that targets histones, recruits multi-protein complexes to the spot where they attach and instructs cellular processes involved in reading genetic information.

The journey from the lab to the clinic is not usually quick, Kouzarides says. In this case, however, a candidate under development for inflammation was found to be applicable for the leukaemia. Now, the small-molecule inhibitor of the BET protein is in clinical development at GlaxoSmithKline, headquartered in London.

Kouzarides believes that chromatin-modification pathways are promising drug targets because they involve proteins interacting with other proteins. In the past, drugs have tended to target enzymes, and it has not been considered feasible to target protein–protein interactions with small molecules. But his work<sup>8</sup>, along with that of others, has shown that it is possible to develop specific small molecules against the BET proteins that recognize a small epigenetic modification present on chromatin.

Constellation Pharmaceuticals in Cambridge, Massachusetts, is also exploring the BET family, as well as other enzymes that modify chromatin<sup>9</sup>. These therapies are going to be part of the second-generation epigenetic drugs that target specific modifications with a role in disease, explains Keith Dionne, the company’s president and chief executive. The past, more coarse scientific understanding of chromatin has shifted to an appreciation of the “subtle distinctions” between chromatin states, explains James Audia, the company’s chief scientific officer.

Earlier this year, Constellation and Genentech began collaborating on the development of inhibitors of BET proteins and another class of epigenetic modifier, the EZH2 chromatin-writers. These proteins seem to be part of a complex that represses gene expression; mutated versions have been linked to some cancers.

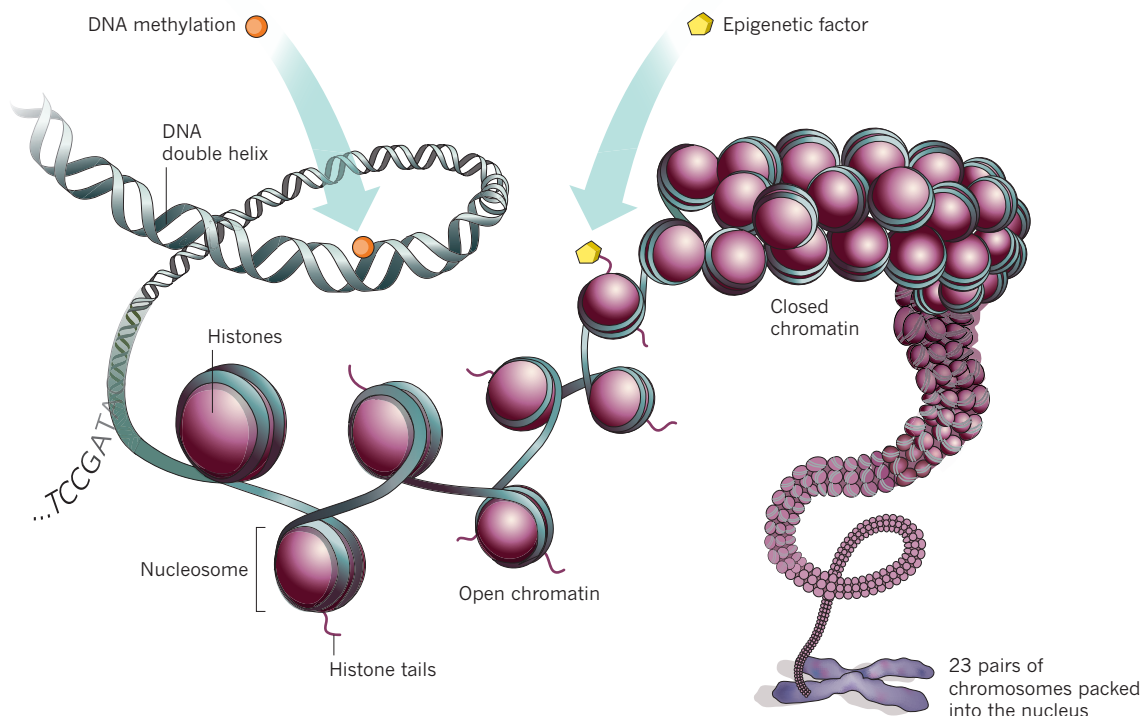
As Patrick Trojer, director of biology at Constellation Pharmaceuticals explains, cancers use chromatin modification to gain an advantage, for example to inactivate a pathway that creates room for unhindered tumour growth. As part of the company’s drug-discovery programme, he and his colleagues develop techniques to study the details of chromatin changes. The understanding of chromatin biology is one of the company’s strong suits, he says.

To support this application-based research, Trojer and his colleagues use a number of

B. BOSTON

## POLYGAMOUS DNA

DNA works with many partners. DNA methylation, for example, influences the way that genes are expressed without changing the underlying DNA sequence, and other epigenetic factors bind to histones to control when chromatin complexes open up and allow their DNA to be read.



epigenetic techniques. ChIP-seq is a lab standard in which antibodies are “the key” to the technique, he says. But the company has also made histone mass spectrometry a priority, because it allows the scientists to query the chromatin changes without using antibodies and to query a number of modifications at once. The company set up an in-house high-throughput facility to screen for potential compounds.

Although other companies tend to outsource these tasks, the company wants to integrate findings about chromatin biology into drug discovery with an in-house suite of tools that includes mass spectrometry and biophysical analyses, Dionne explains.

Another Cambridge-based epigenetics company, Epizyme, focuses on a family of proteins called histone methyltransferases. These epigenetic modifiers act on histones, by catalysing the transfer of methyl groups onto specific positions in the protein. The company has partnerships with the pharmaceutical companies Glaxo-SmithKline; Celgene Corporation in Summit, New Jersey; and Eisai in Woodcliff Lake, New Jersey, as well as the Leukemia and Lymphoma Society in White Plains, New York, and the Multiple Myeloma Research Foundation in Norwalk, Connecticut. So far, 96 histone methyltransferases have been identified in humans, says Robert Copeland, Epizyme’s chief scientific officer. “We believe there are at least 20 of those enzymes that are high-value targets for human cancers.”

The company’s goal is to find a molecule that

blocks an enzyme active in an epigenetic pathway but not its nearest neighbours, he says. It is a selectivity that has been difficult to come by in the development of biotherapeutic drugs.

Copeland believes that epigenetics drugs fit into a trend of defining a cancer not by its anatomical location but by its molecular profile, which includes epigenetic signatures. Like many companies in this field, he and his colleagues mine the publicly available databases, noting that many genetic alterations in epigenetic pathways are found in human cancers.

Kouzarides believes that many cancer cells will be very vulnerable to epigenetic drugs because they rely on only one or two epigenetic pathways, whereas normal cells draw on several pathways for their functions. At the same time, he believes that epigenetics researchers and technology developers will still want to develop and refine experimental methods, for example to explore the three-dimensional structure of epigenomic events, to see how chromatin is changing throughout the genome. “It’s very difficult to look at chromatin itself,” he says. “Technology still has to evolve to look at *in vivo* chromatin effects.” The available epigenetic data are “extensive, but still a very small snapshot” of epigenetic changes, he says. They represent a situation at a specific time in a specific cell.

Epigenetics might find its way into preventive medicine, too. Scanning the epigenome could be a way to detect disease well before symptoms arise. The blood pricked from the heels of newborn babies is one way to begin. In many countries, the blood spots are placed on Guthrie

cards and stored indefinitely by hospitals and health-care systems. Scientists at Queen Mary, University of London are exploring how DNA methylation patterns change between newborns and in cells from the same children when they are three years old. Differences in epigenetic marks could be clues to health.

If the sequencing companies are betting right, then genome sequencing could become commonplace for many patients, perhaps even part of an annual physical examination. An epigenetic read-out, updated at regular intervals, might be an important companion file to that genome sequence.

But this type of progress depends on deeper understanding of epigenetic mechanisms and technology that has yet to evolve, Kouzarides says. Because epigenetic events change constantly in the cell, “whatever you see in one moment will change in the next”, he says. ■

**Vivien Marx** is technology editor at *Nature* and *Nature Methods*.

1. The ENCODE Project Consortium *Nature* **489**, 57–74 (2012).
2. Park, P. J. *Nature Rev. Genet.* **10**, 669–680 (2009).
3. Byrum, S. D., Raman, A., Taverna, S. D. & Tackett, A. J. *Cell Rep.* **2**, 198–205 (2012).
4. Cipriani, B. R. et al. *Proc. Natl Acad. Sci. USA* **109**, 8477–8482 (2012).
5. Thurman, R. E. et al. *Nature* **489**, 75–82 (2012).
6. Ecker, J. R. et al. *Nature* **489**, 52–55 (2012).
7. Dawson, M. A. & Kouzarides, T. *Cell* **150**, 12–27 (2012).
8. Dawson, M. A. et al. *Nature* **478**, 529–533 (2011).
9. Mertz, J. A. et al. *Proc. Natl Acad. Sci. USA* **108**, 16669–16674 (2011).

## Self-assembly gets new direction

By controlling the placement of 'sticky' patches on particles, assemblies can be made that mimic atomic bonding in molecules. This greatly expands the range of structures that can be assembled from small components. [SEE ARTICLE P.51](#)

MATTHEW R. JONES & CHAD A. MIRKIN

Imagine trying to assemble a bookcase from parts covered in glue that stick to each other equally well wherever they touch, regardless of their relative orientations. You would quickly find the task to be extremely challenging, because the components would keep joining together in haphazard configurations, rather than fitting neatly into their intended positions. Indeed, even relatively simple structures, let alone your bookcase, are impossible to create when the interactions between individual parts lack two key properties: specificity and directionality.

Scientists working with colloids — micro- and nanoscale particles suspended in a liquid — as components of self-assembling systems have found themselves in an analogous predicament. In general, the particles are spherical and uniformly sticky across their surfaces, and they interact through nonspecific forces. The lack of specificity has been addressed by attaching single-stranded DNA molecules to particles, so that they interact only with other particles bearing complementary DNA<sup>1</sup>. But imparting directional bonding interactions to colloidal particles has remained more of a challenge. On page 51 of this issue, Wang *et al.*<sup>2</sup> take the concept of DNA-mediated interactions a step further with their report of micrometre-sized particles that have symmetrically arranged, 'sticky' patches of DNA on their surfaces. The patches force the particles to interact only along certain vectors, mimicking the connectivity of atoms in molecules. This work is a major advance on earlier attempts to generate directional interactions between particles<sup>3–12</sup>, and greatly increases the sophistication of structures that can be built 'bottom up' from smaller components.

Directional interactions between atoms — a concept called valency — are common and form the basis for the rich structural complexity of many naturally occurring materials, from organic molecules to atomic lattices. In atoms, coordination environments (the arrangements of atoms, molecules or ions bound to a central atom) typically adopt highly symmetrical geometries, such as linear, triangular, tetrahedral or octahedral. Electron orbitals are responsible for the directionality of this bonding, which

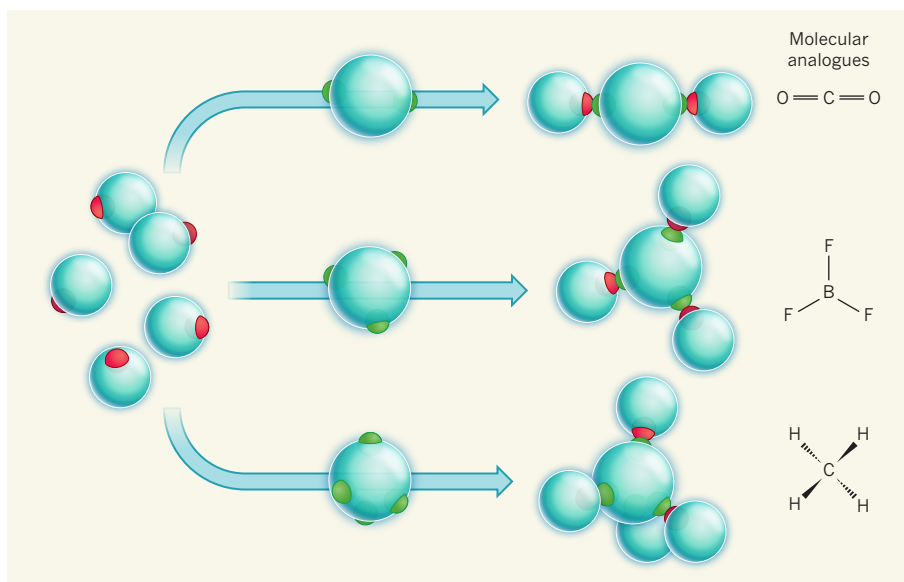


**Figure 1 | Self-assembly of patchy particles.** Wang *et al.*<sup>2</sup> report the synthesis of micrometre-sized particles that have surface patches (red and green regions) positioned to mimic the arrangements of bonds around atoms. The authors attached single-stranded DNA (not shown) to these patches, so that the resulting particles bind only to neighbouring particles whose patches bear the complementary DNA sequence; in the examples shown, red patches bind to green patches. When matching particles are mixed together, they self-assemble into clusters that resemble the atomic arrangements of molecules, such as linear carbon dioxide (CO<sub>2</sub>), triangular boron trifluoride (BF<sub>3</sub>) and tetrahedral methane (CH<sub>4</sub>). In the molecular structure of methane, solid wedges indicate bonds projecting above the plane of the page, whereas broken wedges represent bonds projecting below that plane.

chemists regularly study and manipulate. It has long been the goal of many colloid scientists to synthesize 'artificial atoms' that interact with these same symmetries, in principle enabling man-made components to assemble predictably and with the same diversity as atoms<sup>4,5</sup>.

Previous attempts at particle-based valency have struggled to localize sticky patches at symmetric sites and have been limited primarily to two-sided particles<sup>6–9</sup>. Others have used different particle shapes, such as rods, triangular prisms and octahedra, as a means to break the conventional spherical symmetry of the particle, inducing interactions that loosely mimic valency<sup>10–12</sup>. Wang *et al.* have vastly expanded the morphological diversity of such structures by creating particles with up to seven symmetrically positioned patches that precisely mimic atomic orbital arrangements.

To make these colloidal cousins to atoms, Wang *et al.* started with *n* polymer spheres

packed into clusters with geometries that can be tailored to resemble various polyhedra<sup>13</sup>, such as triangles (*n* = 3), tetrahedra (*n* = 4), and octahedra (*n* = 6). By swelling the clusters in a controlled way from the centre outwards — by treating them with styrene — then polymerizing the styrene, the authors made particles that had 'islands' of the original spheres protruding from the newly formed surface (see Fig. 1b, c of the paper<sup>2</sup>). These small, exposed regions resemble patches, and maintain the geometry of the original cluster. The authors then attached single-stranded DNA molecules to the patches, which resulted in sticky regions that mediate inter-particle binding through hybridization with complementary DNA strands attached to patches on neighbouring particles. The locations of the patches provide directionality, whereas the sequence-dependent binding of DNA imparts specificity.

With their artificial 'atoms' in hand, Wang

*et al.* went on to synthesize artificial ‘molecules’ by combining mixtures of particles that have matched valencies and complementary DNA strands (Fig. 1). For example, when they mixed small monovalent ‘B’ particles (which have one patch) with a larger, tetravalent ‘A’ particle (which has four patches), they obtained an AB<sub>4</sub> cluster in which a central A particle was surrounded by four satellite B particles in a tetrahedral arrangement. Similarly, combinations of other appropriately matched particles yielded linear (AB<sub>2</sub>) or triangular (AB<sub>3</sub>) morphologies and even copolymer arrangements — long chains of alternating A and B particles. By increasing the patch size on divalent particles so that more than one monovalent particle can bind to a single patch, the authors produced even more-complex molecular motifs, such as systems that mimic the different arrangements of atoms around a double bond.

Despite their strong analogy to atoms, these patchy particles are quite large (500 to 900 nanometres in diameter), a feature that powerfully modifies the dynamics of their interactions compared with atoms. Wang and co-workers took advantage of this size difference to monitor the formation kinetics of their artificial molecules in real time using optical microscopy (for videos in the Supplementary Information to the paper, see [go.nature.com/fagxzu](http://go.nature.com/fagxzu)). Such detailed kinetic studies based on direct observation are currently impossible with atoms, and so these particles might one day function as a model system to shed light on certain aspects of the dynamic and packing behaviour of matter at the smallest length scales.

In some respects, Wang and colleagues’ particles are even more amenable to tailoring than naturally occurring atoms and molecules. For example, particles of different size can be combined in a multitude of configurations; the length and sequence of the DNA molecules on a given patch can modulate the spacing and connectivity between particles; and the symmetry and number of patches on a particle can be tuned to access geometries not found in any natural system. The authors’ work therefore greatly expands the toolbox for assembling systems of colloidal particles. It will be surprising if some of the newly accessible configurations do not yield mechanistic insight into atomic systems, or give rise to materials that have previously unknown properties.

A major challenge for the future will be to expand Wang and co-workers’ methods to generate even more sophisticated structures, for example by controlling the geometry of patches in a way that does not follow the highly symmetrical arrangements governed by simple polyhedra. Ring-like patches, linear patches and patches confined to an equatorial plane have all been shown theoretically to exhibit fascinatingly complex, self-assembled arrangements<sup>14</sup>.

In addition, the property of chirality — the characteristic of objects that have

non-superimposable mirror-image forms — may be introduced into these structures if each patch on a single particle contains a different type of DNA strand that binds to a distinct kind of particle. A tetrahedral particle could therefore capture four separate, differently sized particles, creating a cluster with a chiral centre. Control over chirality at the micro- and nanoscale is rapidly becoming a goal of great scientific interest because exotic phenomena not found in nature are thought to arise from such structural motifs<sup>15</sup>. Finally, extension of the principles developed by Wang *et al.* to particles of alternative compositions (such as those made from noble metals, semiconductors or oxides) will allow optical, electronic and catalytic materials to be coupled in previously impossible architectures that have potentially new emergent properties.

Wang and colleagues’ work demonstrates the power of valency when applied to man-made materials, and challenges the scientific community to find methods to generalize this principle to particles at smaller and smaller length scales. With such tools in hand, scientists and engineers may one day be able to construct materials from the bottom up with a precision that makes assembling a bookcase look like child’s play. ■

## ECOLOGY

# Bumblebees and pesticides

**A study showing the effects of two pesticides on bumblebees highlights the need for risk assessments to consider multiple species and the complex chain of factors that determines insect exposure to chemicals. [SEE LETTER P105](#)**

JULIET L. OSBORNE

**B**ee and pollination science is blooming. Research efforts around the world are seeking to explain bee colony losses, which could threaten both wild and agricultural plant systems owing to the crucial role of bees in pollination. The impact of pesticides on bees is one factor that has caught the attention of scientists and the public alike: more than 100 papers and reports have been published on this topic so far this year, including research<sup>1–3</sup>, scientific reviews<sup>4–6</sup> and reports on regulatory risk-assessment procedures<sup>7–9</sup>. On page 105 of this issue<sup>10</sup>, Gill *et al.* strike at the heart of this debate, providing a thorough data set that examines bumblebee responses to two pesticides\*.

Gill and colleagues investigated the effects of two insecticides (imidacloprid and  $\lambda$ -cyhalothrin) on the development and growth of bumblebee colonies, and on

**Matthew R. Jones and Chad A. Mirkin** are in the Departments of Materials Science and Engineering and of Chemistry, Northwestern University, Evanston, Illinois 60208, USA. e-mail: [chadnano@northwestern.edu](mailto:chadnano@northwestern.edu)

1. Mirkin, C. A., Letsinger, R. L., Mucic, R. C. & Storhoff, J. J. *Nature* **382**, 607–609 (1996).
2. Wang, Y. *et al.* *Nature* **491**, 51–55 (2012).
3. Alivisatos, A. P. *et al.* *Nature* **382**, 609–611 (1996).
4. Glotzer, S. C. & Solomon, M. J. *Nature Mater.* **6**, 557–562 (2007).
5. Macfarlane, R. J. *et al.* *Science* **334**, 204–208 (2011).
6. Xu, X., Rosi, N. L., Wang, Y., Huo, F. & Mirkin, C. A. *J. Am. Chem. Soc.* **128**, 9286–9287 (2006).
7. Huo, F., Lytton-Jean, A. K. R. & Mirkin, C. A. *Adv. Mater.* **18**, 2304–2306 (2006).
8. DeVries, G. A. *et al.* *Science* **315**, 358–361 (2007).
9. Walther, A. & Müller, A. H. E. *Soft Matter* **4**, 663–668 (2008).
10. Jones, M. R. *et al.* *Nature Mater.* **9**, 913–917 (2010).
11. Jones, M. R., Macfarlane, R. J., Prigodich, A. E., Patel, P. C. & Mirkin, C. A. *J. Am. Chem. Soc.* **133**, 18865–18869 (2011).
12. Li, M., Schnablegger, H. & Mann, S. *Nature* **402**, 393–395 (1999).
13. Manoharan, V. N., Elsesser, M. T. & Pine, D. J. *Science* **301**, 483–487 (2003).
14. Zhang, Z. & Glotzer, S. C. *Nano Lett.* **4**, 1407–1413 (2004).
15. Soukoulis, C. M. & Wegener, M. *Nature Photon.* **5**, 523–530 (2011).

the foraging activity of individual bees, by tagging them with microchips. The researchers placed feeders of sugar syrup that had been spiked with imidacloprid, and/or filter paper treated with  $\lambda$ -cyhalothrin, in the path of bumblebees leaving their nest boxes. Significantly, the bees were not restricted to visiting the treated material — they could bypass the filter paper and the feeder, and they were able to forage in the surrounding landscape for pollen and nectar.

The authors report that fewer adult worker bees emerged from pupae in the colonies exposed to imidacloprid, which resonates with a previous study<sup>2</sup> that found reduced production of queen bees in imidacloprid-treated colonies. Gill and colleagues also found that bees from such colonies exhibited increased foraging activity, and that a higher proportion of foragers did not return to the colony.

\*This article and the paper under discussion<sup>10</sup> were published online on 21 October 2012.

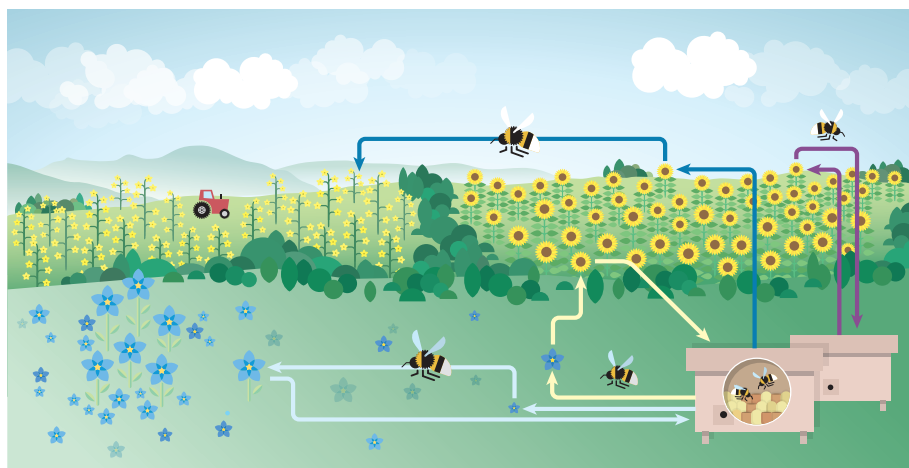


**Figure 1 | A complex exposure landscape.** In a typical agricultural setting, different crops may be sprayed with different pesticides at different times and doses. Bees will obtain food both from these crops and from wild plants, which makes it difficult to estimate their overall exposure to chemicals. Furthermore, bees returning to the colony after foraging may pass on the pesticides as they feed larvae. In an attempt to partially mimic this exposure complexity, Gill *et al.*<sup>10</sup> placed pesticide-laden feeders and filter paper (not shown) at the entrance to boxed colonies of bumblebees, which could also access flowers on crops and wild plants in the wider landscape. The researchers measured the effect of these added pesticides at both the individual-bee and colony level.

In colonies exposed to  $\lambda$ -cyhalothrin, they observed higher mortality of worker bees in the nest. Finally, they report that colonies exposed to both pesticides showed additive effects predictable from the individual treatment results.

This paper is important for three reasons. First, whereas most studies on bees and pesticides, and most risk-assessment models, focus on honeybees, Gill *et al.* studied bumblebees, which have a different biology and ecology and may be more vulnerable to pesticides<sup>2</sup>. Honeybees are smaller than bumblebees, so individual insects may be more susceptible to acute effects of chemicals, but their colonies contain tens of thousands of workers, and colony-level effects may be buffered by this sheer size. By contrast, a bumblebee colony has only a few dozen workers, so it is likely to be less resilient to the loss of individuals. The smaller colony size also makes it more difficult to monitor the survival of wild bumblebee colonies. European regulatory authorities are urgently considering how to incorporate data on bumblebees into pesticide risk assessments<sup>3,6</sup>, and Gill and colleagues' findings provide useful input to this discussion.

Second, and unusually, the authors measured effects of pesticides on both individual bees and the whole colony. This dual evaluation stems from the concept that, if a bee acquires an acute lethal dose in the field, it will not return to the colony; however, if it ingests a sublethal dose, it might bring the material back to the colony, feed it to the brood and potentially affect the development and survival of nest-mates (an effect that would have greater impact in small colonies). Gill and colleagues' study is a helpful step towards considering this complex combination of

sublethal dosage, acute and chronic mortality, and overall colony impacts, but these processes need further attention.

Examining the effects of a combination of chemicals is the third strength of this study, particularly because current regulatory requirements do not take into account the fact that insects will be exposed to multiple products<sup>5-7</sup>. Gill *et al.* chose chemical doses to approximate those to which a bee might be exposed in the field, although there will almost certainly be debate about whether these doses (and methods of exposure) were realistic. The chosen concentrations match label guidelines for application, but these may not reflect what farmers actually use in best or common practice.

And herein lies the catch. There are simply not sufficient field data available on the variable spatial and temporal distribution of pesticides on or in plant material, nor on bee foraging choices, to make useful comparisons between field and experimental exposure<sup>6</sup>. Insects probably experience a complex 'pesticide-exposure landscape' comprising multiple chemicals from several manufacturers, in one or multiple locations, applied at different doses and different times by several farmers<sup>5</sup> (Fig. 1). Regardless of whether the doses used by Gill and colleagues closely match field doses, their study should stimulate further exploration of the exposure landscape for bees and other non-target organisms.

The UK government and other regulatory agencies around the world are currently considering updating guidelines for pesticide registration and use. To what extent should single studies such as this one influence these decisions? Although Gill and colleagues' experimental design does not fit the normal three-tiered approach to risk assessment

(which incorporates laboratory, semi-field and field experiments<sup>7,8</sup>), it does expose areas where the current assessment system provides insufficient evidence. Indeed, the authors' recommendations — the need for evaluations of effects on bumblebees, at individual and colony levels, and of the effects of combinations of chemicals — closely match recent recommendations from European agencies<sup>7,8</sup>. However, the requirement for standardization and repeatability of protocols inevitably makes for slow implementation of such recommendations. So the question remains: should policy-makers make decisions on the strength of current evidence, or should they wait for more?

Furthermore, this debate is complicated by the impact of multiple other factors on bees. For example, we have as yet no convincing demonstration of the relative effects of pesticides on bee colonies compared to the effects of parasites, pathogens and foraging resources. It is not experimentally feasible to study all possible combinations of factors in all landscapes, but modelling colony dynamics, foraging patterns and external influences is a practical and time-efficient way to make progress. Such models should be built using robust data sets and possess enough detail on life-cycle dynamics to be considered realistic<sup>11</sup>. The part played by mass-flowering crops, such as oilseed rape and sunflowers, also needs to be evaluated more clearly. These crops may have both positive and negative impacts on bees: they can enhance bee colony growth and pollinator-species diversity in otherwise flower-poor environments, but they are typically treated with pesticides. So the net effect on pollinator populations of growing thousands of hectares of these crops has yet to be established.

And finally, the balance between protecting crops from pest damage and protecting pollinators needs further consideration. What alternative pest-management strategies would farmers adopt, for example, if a particular class of agrochemical were removed from their toolkit? The debate on pesticide use would be enhanced by a sound framework in which to represent the relevant socioeconomic and environmental trade-offs.

In summary, this single study does not provide a full explanation for bee declines, nor a definitive answer to questions about how to change pesticide regulations. But its convincing and detailed data set highlights the appropriateness of including bumblebees in agrochemical risk assessments and, more broadly, the need for a better understanding of pesticide-exposure landscapes. ■

**Juliet L. Osborne** is at the Environment and Sustainability Institute, University of Exeter, Penryn, Cornwall TR10 9EZ, UK.  
e-mail: j.l.osborne@exeter.ac.uk

1. Henry, M. *et al. Science* **336**, 348–350 (2012).

2. Whitehorn, P. R., O'Connor, S., Wackers, F. L. & Goulson, D. *Science* **336**, 351–352 (2012).
3. Department for Environment, Food and Rural Affairs *Neonicotinoid Insecticides and Bees: The State of the Science and the Regulatory Response* (DEFRA, 2012).
4. Blacquière, T., Smagghe, G., van Gestel, C. A. M. & Mommaerts, V. *Ecotoxicology* **21**, 973–992 (2012).
5. Thompson, H. M. *Interaction Between Pesticides and Other Factors in Effects on Bees* EFSA Supporting Publs 2012:EN-340 (2012).
6. European Food Safety Authority *EFSA J.* **10**, 2752 (2012).
7. EFSA Panel on Plant Protection Products and Their Residues *EFSA J.* **10**, 2668 (2012).
8. Fischer, D. & Moriarty, T. *Pesticide Risk Assessment for Pollinators: Summary of a SETAC Pellston Workshop* Pensacola, Florida (Soc. Environ. Toxicol. Chem., 2011).
9. Oliver, R. *Am. Bee J.* **152**, 805–810 (2012).
10. Gill, R. J., Ramos-Rodriguez, O. & Raine, N. E. *Nature* **491**, 105–108 (2012).
11. Henry, M. *et al. Science* **337**, 1453 (2012).

The author declares competing financial interests. See [go.nature.com/c2a5kj](http://go.nature.com/c2a5kj) for details.

## ASTEROIDS

# Dark and stormy weather

Can some of the ageing effects on asteroid surfaces be caused by an interplanetary rain of carbon-rich Solar System debris? Observations from the Dawn space mission suggest that the answer is yes. [SEE LETTERS P.79 & P.83](#)

BETH ELLEN CLARK

One might expect the asteroids of our Solar System to show their age in similar ways. After all, asteroids are simply rocks that orbit the Sun through interplanetary space, and they are all subject to the same ageing processes: solar wind, micrometeorite bombardment and the occasional major impact. But asteroids do not all age in the same way, claim McCord *et al.*<sup>1</sup> and Pieters *et al.*<sup>2</sup> in this issue. Their analyses of observations of asteroid Vesta, obtained by the Dawn space mission, indicate that the asteroid's surface is not coloured with age in the same way as other bodies that, like Vesta, lack an atmosphere. Rather, Vesta shows its age by incorporating carbon-rich material from impactors (Fig. 1).

Perhaps it is not too surprising that carbonaceous material of external origin (exogenic material) is found on Vesta, one of the largest bodies in the main asteroid belt that lies between the orbits of Mars and Jupiter. Extraterrestrial spherules and micrometeorites found in Earth's stratosphere, which is just above the lowest portion of the atmosphere, have long been known to be compositionally related to carbonaceous chondrite meteorites<sup>3</sup>. (Chondrite meteorites contain spherules of igneous material thought to have originated in the primitive solar nebula, from which the Sun and planets formed.) However, it is surprising that the material is abundant enough to change the remotely sensed optical properties of the Vestan surface.

McCord *et al.* present compelling evidence based on Vesta's colour and brightness, as well as modelling of the putative population of impactors, to support their hypothesis that

Vesta's surface is contaminated with carbonaceous material that is rich in volatile elements. Pieters *et al.* describe an analysis of the spectral differences between fresh and mature Vestan surface patches, and suggest that maturation is linked with contamination — the older the Vestan surface patch, the greater the abundance of carbonaceous exogenic material incorporated. Thus, it seems that, on Vesta, dark, carbon-rich impactor material falls to the surface and darkens the location of the impact. Due to subsequent impacts, the dark material then spreads out over time and mixes with uncontaminated surface areas.

But where does this material come from, and does it coat other asteroids in the main belt?



**Figure 1 | Asteroid Vesta.** Analyses by McCord *et al.*<sup>1</sup> and Pieters *et al.*<sup>2</sup> indicate that the dark surface areas of asteroid Vesta, seen here in an image obtained by the Dawn space mission, are a result of the deposition of carbon-rich material from low-velocity impactors.



## 50 Years Ago

The temptation to establish new scientific journals appears to be irresistible. The first number of *Radio Chimica Acta* has a foreword by a great German radiochemist, Otto Hahn, in which he poses the rhetorical question as to whether a journal, specially devoted to radiochemistry, can discharge an important function differing from that already performed by existing chemical and physical journals ... He concludes that a place is needed where the results now published in a variety of journals can be brought together ... To have an additional journal for papers of this kind recalls the words of the sonnet “So all is dressing old words new, spending again what is already spent”. In short, interested workers must pay again to read those papers which they should reasonably be able to expect to find in the journals to which they already subscribe.

From *Nature* 3 November 1962

## 100 Years Ago

*Modern Problems.* By Sir Oliver Lodge — From the scientific point of view, one of the most interesting chapters is that on the smoke nuisance, in which the author deals with the problems of combustion, and advocates the use of gas fires and the suppression of crude combustion of coal in towns. As to river and sea mists, and fogs of non-avoidable kind, Sir Oliver suggests electrification of the atmosphere on a large scale ... No one can tell for certain what would happen by this atmospheric electrification, but it is possible and even probable that the results might be of incalculable benefit ... When we think of the tremendous harmfulness of fog ... it seems obvious that the prospect of a cure of this evil would justify a large national grant for expenditure on trials in a large way.

From *Nature* 31 October 1912

The material almost certainly comes from dark asteroids in the main belt, because asteroids can be ground down to micrometeorite particles by mutual collisions over billions of years. The idea that similar exogenic material coats other large asteroids has yet to be tested. However, perplexing spectral signatures of hydrated minerals, consistent with volatile-rich carbonaceous materials, have been found on objects that would otherwise be interpreted as metallic<sup>4,5</sup> or inconsistent with the presence of stable volatile compounds<sup>6</sup>. In fact, almost a decade ago, astronomers using ground-based telescopes detected evidence of hydrated minerals on Vesta itself<sup>7</sup>. At the time, those measurements were considered suspect, but they now seem to be vindicated by the Dawn results.

Are the carbonaceous materials found on Vesta the result of low-velocity impactors? The fate of a rocky impactor depends in part on its velocity relative to the speed of sound in the rock. Carbonaceous materials have relatively high porosities<sup>8</sup>. Therefore, sound waves travel through them slowly and impact-associated shock-wave pressures may be quite low, favouring the survival of large fractions of such impactors. Without high shock-wave pressures, much less material might be vaporized and lost to space<sup>9</sup>. McCord *et al.* present estimates of impactor fluxes and of the amount of impactor material that Vesta has accumulated (see Supplementary Information to the paper<sup>1</sup>). On the basis of these estimates, they conclude that sufficient material has been deposited on the Vestan surface to cover it with a blanket up to about 1–2 metres deep.

The delivery of exogenic material is not generally what comes to mind when considering

space weathering. The term is used to refer to processes that change the optical properties of the remotely sensed surface of an airless body. Studies of lunar soils and rocks brought back by the Apollo-mission astronauts have provided important information about space weathering on the Moon. Furthermore, direct evidence of space weathering on asteroids was supplied by the NEAR mission to the near-Earth asteroid 433 Eros<sup>10</sup> and by the Hayabusa mission to asteroid 25143 Itokawa<sup>11</sup>.

Before the Dawn-mission findings, the consensus was that some lunar-like space weathering occurs on asteroids<sup>12–14</sup>, and that its strength depends on the composition of the target material — that is, the material from which the asteroid is made. In the leading model of asteroidal space weathering, condensates bearing sub-microscopic iron are deposited on grain surfaces after the target material has been vaporized by solar-wind sputtering and micrometeorite bombardment. Space weathering is known to cause surface darkening and spectral changes, and so these processes and their effects must be considered when interpreting the spectral properties of airless bodies. According to Pieters and colleagues, two other processes should now be considered when trying to explain the Dawn observations of Vesta: the mobility of regolith (powdery rubble that covers a planetary body) and fine-scale mixing of surface material. Therefore, the results prompt two questions. Why does Vesta not exhibit lunar-like space weathering? And was our model wrong, or do the weathering processes compete with each other?

The goal of the Dawn mission is to characterize the conditions and processes that were active during the Solar System's earliest epoch

by investigating Vesta and Ceres, two of the largest asteroids that are still intact. Dawn has completed its tour of Vesta and will arrive at Ceres in February 2015 to send back data on that asteroid's low-brightness surface. It will be interesting to see whether these observations allow us to distinguish Ceres' bulk material from the 'rain' of carbonaceous material that may be contaminating its surface. ■

**Beth Ellen Clark** is in the *Physics Department, Ithaca College, Ithaca, New York 14850, USA, and with NASA's OSIRIS-REx asteroid sample return mission at the University of Arizona.*  
e-mail: bclark@ithaca.edu

1. McCord, T. B. *et al.* *Nature* **491**, 83–86 (2012).
2. Pieters, C. M. *et al.* *Nature* **491**, 79–82 (2012).
3. Brownlee, D. E., Bates, B. & Schramm, L. *Meteorit. Planet. Sci.* **32**, 157–175 (1997).
4. Ockert-Bell, M. E. *et al.* *Icarus* **210**, 674–692 (2010).
5. Rivkin, A. S., Howell, E. S., Lebofsky, L. A., Clark, B. E. & Britt, D. T. *Icarus* **145**, 351–368 (2000).
6. Rivkin, A. S., Davies, J. K., Clark, B. E., Trilling, D. E. & Brown, R. H. *Lunar Planet. Sci. Conf.* **XXXII**, 1723 (2001).
7. Hasegawa, S. *et al.* *Geophys. Res. Lett.* **30**, 2123 (2003).
8. Britt, D. T. & Consolmagno, G. J. *Icarus* **146**, 213–219 (2000).
9. Rivkin, A. S. & Bottke, W. *Lunar Planet. Sci. Conf.* **XXVII**, 1077–1078 (1996).
10. Clark, B. E., Hapke, B., Pieters, C. & Britt, D. in *Asteroids III* (eds Bottke, W. F. Jr, Cellino, A., Paolicchi, P. & Binzel, R. P.) 585–599 (Univ. Arizona Press, 2002).
11. Noguchi, T. *et al.* *Science* **333**, 1121–1125 (2011).
12. Hapke, B. J. *Geophys. Res.* **106**, 10039–10073 (2001).
13. Pieters, C. M. *et al.* *Meteorit. Planet. Sci.* **35**, 1101–1107 (2000).
14. Sasaki, S., Nakamura, K., Hamabe, Y., Kurahashi, E. & Hiroi, T. *Nature* **410**, 555–557 (2001).

## NEUROSCIENCE

## Sleep to oblivion

These days, it is hard to imagine having a surgical procedure without anaesthetics. Yet some 170 years after their first use in medicine, the way in which these drugs exert their hypnotic effects remains a mystery. Writing in *Current Biology*, Moore *et al.* shed light on the question (J. T. Moore *et al.* *Curr. Biol.* <http://dx.doi.org/10.1016/j.cub.2012.08.042>; 2012).

Many biological molecules are sensitive to anaesthetics, among them membrane ion-channel proteins. To make matters more complex, there are dozens of anaesthetic agents, and yet they don't seem to share a single molecular target. An emerging theory is that these drugs inhibit the neural circuitry associated with wakefulness. Moore and colleagues asked whether they also affect sleep-promoting neurons.

The authors focused on the anaesthetic agent isoflurane and its effects on the

ventrolateral preoptic nucleus (VLPO) — a key component of the arousal (wakefulness) neurocircuitry. Neurons of the VLPO are active during sleep and, in response to inhibitory neuromodulators such as GABA, they inhibit signalling by downstream arousal-promoting neurons. Moore *et al.* find that concentrations of isoflurane that induce sedation or anaesthetic hypnosis also activate VLPO neurons, just like sleep does. Moreover, damaging these neurons reduces the hypnotic effects of isoflurane.

Of the two neuronal subpopulations that form the VLPO, only one is thought to be involved in promoting sleep. By studying slices of mouse hypothalamus — the brain region in which VLPO neurons are found — Moore and colleagues show that isoflurane specifically activates the sleep-promoting subpopulation. Exactly how it does so is unknown, but the researchers' data indicate



ISTOCKPHOTO/THINKSTOCK

that a reduction in the conductance of potassium ions is involved.

The authors do not rule out a role for other sleep-promoting neuronal circuits in mediating the effects of anaesthetics. But their take-home message is that, to understand how anaesthetics act, studying sleep induction is probably just as useful as investigating the inhibition of wakefulness.

**Sadaf Shadan**

## OPTICS

# Nanotube holograms

**Carbon nanotubes interact strongly with light — a property that makes them ideal components of holographic devices. The realization of such a device opens up fresh opportunities for holography.**

STÉPHANE LAROUCHE & DAVID R. SMITH

Many of us grew up watching *Star Wars* and dreaming of a day when we would receive three-dimensional images as messages, like Princess Leia's urgent plea to Obi-Wan Kenobi. Although such applications are still science fiction, static three-dimensional images formed using holographic devices are real and have many practical uses, including chemical sensing, data storage and imaging. But the potential of dynamic holograms and other advanced forms continues to stimulate research into techniques and materials that might bring us closer to realizing the holograms of science fiction. Writing in *Advanced Materials*, Butt *et al.*<sup>1</sup> report one such development: the fabrication of a high-resolution hologram using an array of carbon nanotubes. This achievement might pave the way for holographic devices that respond to light polarization and for reconfigurable holograms.

Single-walled carbon nanotubes are hollow cylinders formed from graphene sheets — single layers of carbon atoms arranged in a hexagonal network. They can be as small as one nanometre in diameter, with lengths ranging from a few nanometres to many centimetres. Multi-walled nanotubes, such as those made by Butt *et al.*, can also be constructed, and consist of many concentric graphene cylinders.

Ever since Sumio Iijima's headline-grabbing report<sup>2</sup> of carbon nanotubes in 1991, these tiny objects have been studied for their electrical, optical and mechanical properties. For example, depending on how the graphene sheets are wrapped, nanotubes can act as electrical conductors, semiconductors or insulators. Butt and colleagues' nanotubes behave as conductors, and therefore interact strongly with light — a characteristic that was of most interest to the authors.

Large quantities of carbon nanotubes can be produced by a technique known as arc discharge, but this yields a mixture of nanotubes, along with other carbon products, as a powder. Arc discharge is therefore ill-suited for fabricating devices (such as Butt and colleagues' holographic device) that require nanotubes of controlled dimensions located at specific positions. The authors therefore used a different synthetic approach<sup>3,4</sup> that allows much better control of the size and position of the nanotubes formed — a technique that had previously been used by some of the same authors

to produce other optical devices<sup>5</sup>.

First, the researchers deposited a 15-nanometre-thick layer of nickel on a silicon substrate. They then patterned the nickel using a lithographic process to create an array of dots each about 100 nm in diameter. Finally, they grew carbon nanotubes at the positions of the dots by treating the substrate with a gaseous mixture of acetylene ( $C_2H_2$ ) and ammonia ( $NH_3$ ) in the presence of plasma (a partially ionized gas). Under these conditions, carbon atoms from the acetylene diffuse through the nickel to form nanotubes that grow under the dots, which end up sitting on the top of the nanotubes. Meanwhile, the ammonia etches away any other carbon products that form on the rest of the substrate, leaving it pristine. This approach provided good spatial control of the resulting nanotube array: the nanotubes had an average diameter of 140 nm with a standard deviation of 13 nm, and the distance between most of them was within 25 nm of the desired spacing of 400 nm.

It is a common misconception that all holograms are three-dimensional images. On the contrary, most holograms in use are two-dimensional, or consist of a few discrete, two-dimensional layers that give some depth to an image but are not fully three-dimensional. Devices that produce two-dimensional holograms can be thought of as light-beam converters — for example, they can create a projectable image from a uniform plane wave (in which the wavefronts are parallel planes, each separated from the next by a distance of one optical wavelength). Butt and colleagues' holographic device is two-dimensional, and produces an image of the word 'CAMBRIDGE' (Fig. 1). When the device is illuminated, the incident light induces polarization — currents that oscillate in the conducting nanotubes. The polarization from each nanotube in turn generates radiation in all directions, in a process called scattering. Each nanotube can thus be thought of as a nanoscale optical antenna.

The radiation scattered from each nanotube in the device interferes constructively or destructively with the radiation scattered from all the other nanotubes depending on the direction of observation, creating bright and dark pixels in its image plane. The process of designing a hologram for the nanotube device therefore involves determining the distribution of scattering elements that is needed to produce a desired image. At distances sufficiently

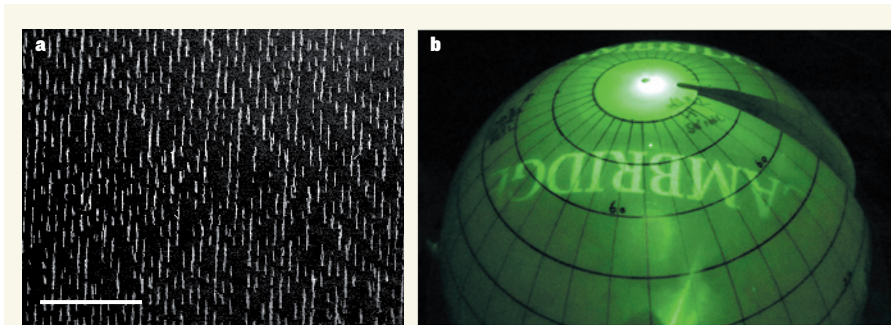


**Figure 1 | Image from a nanotube array.** **a**, This micrograph depicts part of Butt and colleagues' holographic device<sup>1</sup>, which consists of a grid of carbon nanotubes. When illuminated, the presence or absence of nanotubes at each position of the grid generates a complex interference pattern that determines which pixels in the image formed by the device are light or dark; in this case, about half of the grid points contain a nanotube. Scale bar, 5 micrometres. **b**, The device generates an image of the word 'CAMBRIDGE', shown here projected on a hemispherical screen of radius 15 centimetres. (Images from ref. 1.)

far away from the holographic device, in what is called the Fraunhofer regime, the light transmission of the device and its image are simply related by a mathematical operation: the Fourier transform. This means that the arrangement of nanotubes required to produce a given image can be calculated mathematically.

To independently control the intensity of a given number of pixels in an image, one needs at least the same number of elements in the holographic device. In the case of Butt and colleagues' work, the image consisted of  $300 \times 300$  black or white pixels. Their device therefore consists of  $300 \times 300$  positions at which a nanotube is either present or not.

Butt *et al.* mention two reasons why carbon nanotubes are interesting components for creating holographic devices. First, the nanotubes are small and so can be patterned on a tiny grid. This is helpful because smaller grids provide holograms that have larger fields of view; a problem with currently available holographic displays is that their fields of view are somewhat restricted. Second, nanotubes interact so strongly with light that they can be used to create holograms even though their physical cross-section is small.

However, it should be noted that the nickel dots used as a template for the nanotube array would themselves produce a very similar image to that produced by the nanotubes. The role of the nanotubes is to enhance the holographic device's interaction with light and to introduce new properties into the device. For example, Butt *et al.* point out that the interaction between a nanotube and light is strongly influenced by the orientation of the long axis of the nanotube to the direction of polarization of the light. This might allow the creation of polarization-dependent holograms. One could even imagine applications in which the orientation of nanotubes is altered to activate a hologram.

The use of nanotube holograms for commercial applications will require cheaper and

faster ways of producing them — Butt and colleagues' approach for creating nickel dots is well suited to research, but does not scale to mass production. However, the authors' work certainly opens up intriguing possibilities.

#### ORIGINS OF LIFE

## The cooperative gene

**The origin of life on Earth remains one of the great unsolved mysteries. A new study suggests that cooperation among molecules could have contributed to the transition from inanimate chemistry to biology. [SEE ARTICLE P.72](#)**

JAMES ATTWATER & PHILIPP HOLLIGER

Cooperation operates at all scales of life, from whole organisms, such as wolves hunting in packs, to individual cells acting in a coordinated fashion during development or organ function. On page 72 of this issue, Vaidya *et al.*<sup>1</sup> describe networks of RNA molecules that assemble one another, suggesting that cooperation may be as old as life itself\*.

The molecular architecture of modern-day organisms is based around a division of labour: the nucleic acids DNA and RNA are used mainly for the storage and processing of genetic information, with proteins fulfilling metabolic and structural roles. However, there is compelling evidence for a primordial biology that lacked DNA and proteins and instead relied on RNA for both heredity and metabolism<sup>2</sup>. A cornerstone of this 'RNA world' is self-replication by RNA molecules that also mutate and hence evolve towards ever more efficient self-replication.

But how did such a self-replicating RNA — the original 'selfish gene' — arise from the chemical ingredients present on the early

\*This article and the paper under discussion<sup>1</sup> were published online on 17 October 2012.

Carbon-nanotube holographic devices made from semiconducting nanotubes would be particularly interesting, because they might enable holograms to be turned on or off electrically. Indeed, if every nanotube could be switched on and off individually, it might be possible to create reconfigurable holograms, bringing Princess Leia's message one step closer to reality. ■

**Stéphane Larouche and David R. Smith** are at the Center for Metamaterials and Integrated Plasmonics, Department of Electrical and Computer Engineering, Pratt School of Engineering, Duke University, Durham, North Carolina 27708, USA.

e-mail: [stephane.larouche@duke.edu](mailto:stephane.larouche@duke.edu)

1. Butt, H. *et al.* *Adv. Mater.* <http://dx.doi.org/10.1002/adma.201202593> (2012).
2. Iijima, S. *Nature* **354**, 56–58 (1991).
3. Teo, K. B. K. *et al.* *Appl. Phys. Lett.* **79**, 1534–1536 (2001).
4. Chhowalla, M. *et al.* *J. Appl. Phys.* **90**, 5308–5317 (2001).
5. Butt, H., Dai, Q., Rajesekharan, R., Wilkinson, T. D. & Amarantunga, G. A. J. *ACS Nano* **5**, 9138–9143 (2011).

Earth? Recent advances in prebiotic chemistry<sup>2</sup> (the study of the chemical reactions that might have led to the formation of the molecules typical of today's organisms) offer glimpses of how RNA's building blocks could have accumulated and polymerized into short chains<sup>2</sup>. Indeed, even some very short RNAs can perform chemical reactions<sup>3</sup> (and are therefore called RNA enzymes, or ribozymes). But it seems likely that the more complex functionalities required for self-replication would necessitate the assembly of longer, structurally more complex ribozymes, which known prebiotic reactions do not produce.

Vaidya and colleagues' remarkable work points to a possible strategy to begin bridging this gap, based on a principle of self-organization first proposed more than 30 years ago<sup>4</sup>. In this scenario, self-replicating RNA entities go beyond simply making copies of themselves and act on other replicators through a cyclic network of reinforcing loops called hypercycles (Fig. 1). The authors' laboratory had previously described a ribozyme — from an *Azoarcus* bacterium — that had the ability to assemble itself when fragmented<sup>5</sup>. Now Vaidya *et al.* show that variants of such RNA fragments can assemble and act on one another

to form cooperative self-assembly cycles very much like the proposed hypercycles, in which ribozyme 1 aids assembly of ribozyme 2; 2 aids 3; and 3 aids 1 (Fig. 1).

The authors' key finding is that, through such cooperative cycles, participating RNAs gain an advantage and can outcompete selfish replication cycles, in which a particular fragment assembles itself. Cooperation also allowed full-length ribozyme assembly from sets of four different RNA fragments. Thus, cooperation between small RNA molecules can aid the emergence of longer, more complex RNAs.

The authors describe a certain three-member cooperative cycle in great detail, but the data in one of their experiments hint at the potential for much larger cycles and networks of cooperating RNAs. This observation in particular suggests many lines of investigation that could advance our understanding of molecular cooperation and its significance to the RNA world. Questions for future enquiry include how such networks develop over time, and whether network complexity scales with efficiency — that is, whether larger or more interconnected networks always replicate more efficiently than simpler alternatives.

How might such networks have arisen (and persisted) in the pools of random RNA chains generated on the early Earth? In the present study, all members of the pool are derived from a set of 'prefabricated' fragments of the *Azoarcus* ribozyme. It will be important to determine how cooperative RNA networks perform in the presence of many unrelated and potentially interfering RNAs, and how much sequence variation within the *Azoarcus* fragments can be tolerated before self-assembly is abolished. The present work is encouraging in this respect, as it shows that limited sequence diversity in the three-member system yielded better assembly than defined fragments, demonstrating that some sequence variation can be harnessed for gains in efficiency.

Comparison with an earlier two-component system, in which two ribozymes catalysed each other's synthesis from a mixture of four fragments<sup>6</sup>, is illustrative. This system displayed exponential self-replication and, when seeded with fragments of defined sequence variation, yielded a diverse pool of recombinant molecules, some of which were more efficient replicators than the initial ones. Thus, such molecular systems can harness the powerful evolutionary potential of recombination to reassemble themselves into more active replicators. Vaidya and colleagues' use of a ribozyme system that had a larger degree of freedom in the choice of assembly partners has now enabled networks to develop beyond this two-component system.

However, the need for defined RNA components is likely to constrain the evolutionary potential of such systems, because recombinants are unable to break away from the

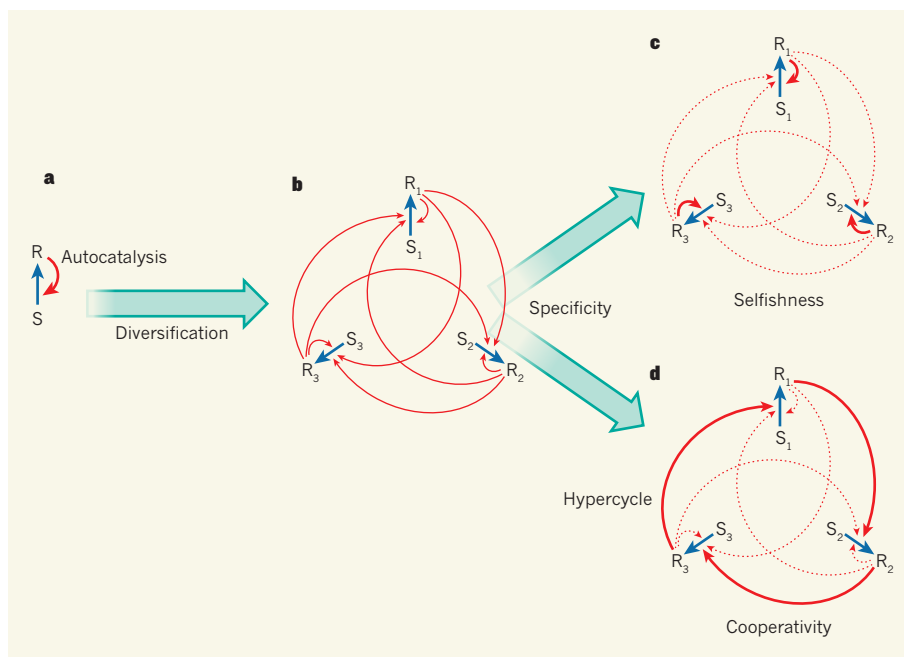


**Figure 1 | The emergence of hypercycles.** **a**, A primordial replicator molecule (R) enhances its own assembly from substrate molecules (S) in a simple autocatalytic cycle. **b**, Imperfect replication generates a set of related replicators, each promoting the synthesis of all the others. **c**, **d**, The introduction of biases in replicator specificity gives structure to the network and can lead to selfish subsystems (**c**) or to a cooperative 'hypercycle' (**d**), akin to the system described by Vaidya and colleagues<sup>1</sup>. Such hypercycles remain globally autocatalytic, but are more resistant to the accumulation of mutations, enabling replicators to specialize and to acquire new functions. Thick and dashed red arrows indicate increased and decreased efficacy, respectively, at enhancing replicator assembly.

prescribed component structure. A more general capacity for self-replication and evolution would require a different type of system that has the ability to copy genetic information — akin to present-day biology, in which RNA or DNA sequences are replicated by polymerase enzymes 'letter by letter' from monomer units. Although RNA-polymerizing ribozymes have been described<sup>7</sup>, their activity falls short of self-replication, despite recent improvements<sup>8</sup>.

The excursions into 'molecular ecology' described by Vaidya *et al.* suggest that cooperative networks might be designed to harness the best of both types of system, if synthesis of short RNAs by polymerizing ribozymes could be coupled to a ribozyme system capable of self-assembly<sup>9</sup>. Such networks might outperform replicators that go it alone, and exploit recombination to resist the gradual accumulation of harmful mutations<sup>10</sup> and the concomitant deterioration of the encoded genetic information. Finally, complete covalent assembly might not be essential for higher-order functions such as molecular kin recognition and polymerizing activities. Indeed, non-covalent assembly of multiple RNA chains into functional complexes has precedents in modern-day biology, notably the ribosome, a large complex of multiple RNA and protein chains, which catalyses protein synthesis and may date back to the RNA world.

The precise molecular events that led to

the origin of life on Earth are likely to be lost in time, but science can construct molecular 'doppelgängers' of the ancestral molecules and explore the plausibility of different ways in which the transition from prebiotic to biotic matter might have occurred. Vaidya and colleagues make a persuasive case for the benefits of cooperation even at this nascent stage of life. The first genes may not have been so selfish, after all. ■

**James Attwater and Philipp Holliger** are at the MRC Laboratory of Molecular Biology, Cambridge CB2 0QH, UK.  
e-mail: ph1@mrc-lmb.cam.ac.uk

- Vaidya, N. *et al.* *Nature* **491**, 72–77 (2012).
- Atkins, J. F., Gesteland, R. F. & Cech, T. R. (eds) *RNA Worlds: From Life's Origins to Diversity in Gene Regulation* (Cold Spring Harb. Lab. Press, 2011).
- Turk, R. M., Chumachenko, N. V. & Yarus, M. *Proc. Natl Acad. Sci. USA* **107**, 4585–4589 (2010).
- Eigen, M. & Schuster, P. *Naturwissenschaften* **65**, 341–369 (1978).
- Hayden, E. J. & Lehman, N. *Chem. Biol.* **13**, 909–918 (2006).
- Lincoln, T. A. & Joyce, G. F. *Science* **323**, 1229–1232 (2009).
- Johnston, W. K., Unrau, P. J., Lawrence, M. S., Glasner, M. E. & Bartel, D. P. *Science* **292**, 1319–1325 (2001).
- Wochner, A., Attwater, J., Coulson, A. & Holliger, P. *Science* **332**, 209–212 (2011).
- Meyer, A. J., Ellefson, J. W. & Ellington, A. D. *Acc. Chem. Res.* <http://dx.doi.org/10.1021/ar200325v> (2012).
- Muller, H. J. *Genetics* **48**, 903 (1963).

# Colloids with valence and specific directional bonding

Yufeng Wang<sup>1</sup>, Yu Wang<sup>1</sup>, Dana R. Breed<sup>2</sup>, Vinodhan N. Manoharan<sup>3,4</sup>, Lang Feng<sup>5</sup>, Andrew D. Hollingsworth<sup>5</sup>, Marcus Weck<sup>1</sup> & David J. Pine<sup>5</sup>

**The ability to design and assemble three-dimensional structures from colloidal particles is limited by the absence of specific directional bonds. As a result, complex or low-coordination structures, common in atomic and molecular systems, are rare in the colloidal domain. Here we demonstrate a general method for creating the colloidal analogues of atoms with valence: colloidal particles with chemically distinct surface patches that imitate hybridized atomic orbitals, including  $sp$ ,  $sp^2$ ,  $sp^3$ ,  $sp^3d$ ,  $sp^3d^2$  and  $sp^3d^3$ . Functionalized with DNA with single-stranded sticky ends, patches on different particles can form highly directional bonds through programmable, specific and reversible DNA hybridization. These features allow the particles to self-assemble into ‘colloidal molecules’ with triangular, tetrahedral and other bonding symmetries, and should also give access to a rich variety of new microstructured colloidal materials.**

The past decade has seen an explosion in the kinds of colloidal particles that can be synthesized<sup>1,2</sup>, with many new shapes, such as cubes<sup>3</sup>, clusters of spheres<sup>4–6</sup> and dimpled particles<sup>7,8</sup> reported. Because the self-assembly of these particles is largely controlled by their geometry, only a few relatively simple crystals have been made: face-centred and body-centred cubic crystals and variants<sup>9</sup>. Colloidal alloys increase the diversity of structures<sup>10–12</sup>, but many structures remain difficult or impossible to make. For example, the diamond lattice, predicted more than 20 years ago to have a full three-dimensional photonic band-gap<sup>13</sup>, still cannot be made by colloidal self-assembly because it requires fourfold coordination. Without directional bonds, such low-coordination states are unstable.

Unlike colloids, atoms and molecules control their assembly and packing through valence. In molecules such as methane ( $\text{CH}_4$ ), the valence orbitals of the carbon atom adopt  $sp^3$  hybridization and form four equivalent C–H bonds in a tetrahedral arrangement. In the colloidal domain, the kinds of structures that could be made would vastly increase if particles with controlled symmetries and highly directional interactions were available. What is needed are colloids with valence<sup>14</sup>.

One approach is to decorate the surface of colloidal particles with ‘sticky patches’ made of synthetic organic or biological molecules (for example) and assigned to specific locations<sup>15–19</sup>. Bonding between particles occurs through patch–patch interactions, so that in principle the location and functionality of the patches can endow particles with bonding directionality and valence. This approach is conceptually simple, yet challenging to realize. For example, so-called Janus particles with asymmetrically functionalized surfaces can be made, but normally have only a single patch<sup>20–22</sup>. Triblock Janus particles have also been fabricated by glancing-angle deposition and assembled into a kagome lattice, the two-dimensional analogue of a diamond crystal<sup>23</sup>. However, only two patches are made using this method, and low quantities of particles are obtained. Other strategies have used faceted particles<sup>24</sup>, particles with protrusions<sup>25</sup> or coordinated patches<sup>26–28</sup>, but three-dimensional directional bonding and assembly have yet to be demonstrated<sup>29</sup>.

Here we demonstrate the synthesis and assembly of colloidal particles with directional interactions that mimic those of atoms with

either monovalent  $s$  or  $p$  orbitals, or multivalent  $sp$ ,  $sp^2$ ,  $sp^3$ ,  $sp^3d$ ,  $sp^3d^2$  or  $sp^3d^3$  hybridized orbitals. We do so by making particles with various numbers of patches,  $n = 1–7$  and higher, that adopt spherical, linear, triangular, tetrahedral, trigonal bipyramidal, octahedral or pentagonal dipyramidal symmetries. The patches are then site-specifically coated with oligonucleotides, enabling a reversible and controllable attraction between patches on different particles. Using these colloidal ‘atoms’, we demonstrate that a vast collection of colloidal molecules and macromolecules are readily accessible through self-assembly schemes that are analogous to chemical reactions.

## Synthesis

The fabrication of patchy particles, summarized in Fig. 1a, starts with cross-linked amidinated polystyrene microspheres, 540 nm or 850 nm in diameter<sup>30</sup>. Small clusters of these microspheres are assembled using an emulsion-evaporation method<sup>5</sup> that produces so-called ‘minimal-moment’ clusters with reproducible symmetries and configurations: spheres, dumbbells, triangles, tetrahedra, triangular dipyramids, octahedra and pentagonal dipyramids, for clusters of  $n = 1–7$  particles (Fig. 1b).

Patchy particles are formed from the clusters using a two-stage swelling process followed by polymerization<sup>31</sup>. First, a low-molecular-mass, water-insoluble organic compound (1-chlorodecane) is introduced into the colloidal clusters that are suspended in water with surfactant (sodium dodecyl sulphate, SDS). Adding a small amount of acetone to the suspension aids in the transport of the 1-chlorodecane into the colloidal clusters. We also introduce an oil-soluble initiator, benzoyl peroxide (BPO), and 1,2-dichloroethane, which dissolves BPO and is miscible with 1-chlorodecane. Subsequent stripping of the acetone and 1,2-dichloroethane from the solution traps both the 1-chlorodecane and the BPO in the polymer particles. The clusters are then swollen by the styrene monomer. The 1-chlorodecane introduced earlier acts as an osmotic swelling agent that increases the amount of monomer that can be absorbed by the clusters<sup>32</sup>. Because each cluster of a given number of particles contains the same amount of swelling agent, chemical equilibrium assures that

<sup>1</sup>Molecular Design Institute and Department of Chemistry, New York University, New York, New York 10003, USA. <sup>2</sup>The Dow Chemical Company, 2301 North Brazosport Boulevard, Freeport, Texas 77541, USA. <sup>3</sup>School of Engineering and Applied Sciences, Harvard University, Cambridge, Massachusetts 02138, USA. <sup>4</sup>Department of Physics, Harvard University, Cambridge, Massachusetts 02138, USA.

<sup>5</sup>Center for Soft Matter Research and Department of Physics, New York University, New York, New York 10003, USA.

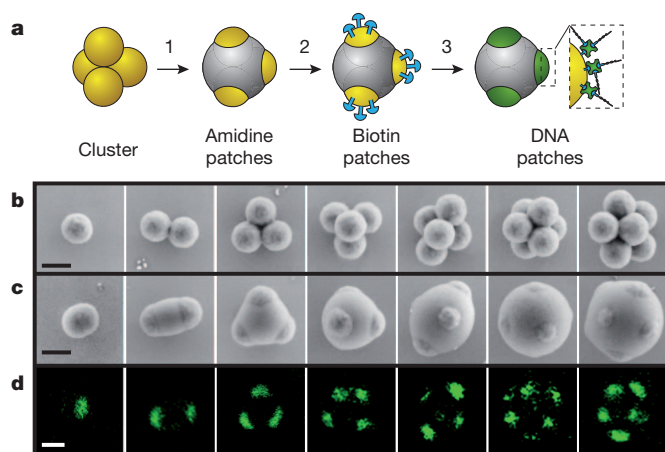


**Figure 1 | DNA patchy particle fabrication.** **a**, Preparation of colloidal particles with DNA-functionalized patches having well-defined symmetries. A four-patch particle is shown as an example. 1, A cluster of four amidinated polystyrene microspheres, prepared by the method of ref. 5, is swollen with styrene such that the extremities of the cluster—a tetrahedron in this case—protrude from the styrene droplet. The styrene is then polymerized and the protrusions from the original cluster become patches. 2, Biotin is site-specifically functionalized on the patches. 3, Biotinylated DNA oligomers are introduced and bind to the particle patches via a biotin–streptavidin–biotin linkage. **b**, Electron micrographs of amidinated colloidal clusters, showing the particle configurations for clusters of  $n = 1$ –7 microspheres. **c**, Electron micrographs of amidinated patchy particles after encapsulation. The patches inherit the symmetries of their parent clusters. **d**, Confocal fluorescent images of corresponding patchy particles, verifying that only the patches are functionalized with DNA. The fluorescence comes from the dye-labelled streptavidin that links DNA with the patches. Scale bars, 500 nm.

clusters of the same size all swell by the same amount, with the total amount of swelling controlled by the quantity of added monomer.

After swelling, we polymerize the styrene by thermally degrading the BPO previously introduced into each cluster. Swelling is controlled so that the extremities of the original clusters are not encapsulated, but are left as patches. Clusters of the same order  $n$  are encapsulated to the same extent, leading to uniform patch configurations, as seen in Fig. 1c, which shows scanning electron microscope (SEM) images of particles with 1 to 7 patches (see Supplementary Fig. 1a for higher-order patches). Using BPO as the initiator ensures that there are no functional groups introduced, so the surface created by swelling the clusters—the ‘anti-patch’ surface—is chemically inert and different from the patches: only the patches have the functional amidine groups.

Patch size is controlled during the swelling process by adjusting the amount of monomer that is introduced: the more monomer that is added, the smaller the patches are. Figure 2 shows that considerable variation in patch size can be achieved in this way. Small patches favour greater directionality, and larger patches permit multiple links per patch, as we discuss below.

A key design feature of our method is the use of clusters as intermediates. Their diversity in particle number and symmetry is translated directly to the number and symmetry of the particle patches. In contrast to the planar symmetry of Janus particles<sup>23,33</sup>, the symmetries of these patchy particles are fully three-dimensional.

Our method converts essentially all the starting colloidal particles into particles with one or more patches. Each sample produced contains large scalable quantities of particles having different valence (numbers of patches), the relative distribution of which can be changed by adjusting the emulsification conditions used when making the clusters<sup>34</sup>. Using a higher shear rate, for example, makes smaller emulsion droplets, which skews the distribution towards lower-valence particles. We fractionate the particles through density gradient centrifugation, obtaining up to 12 clear bands corresponding to particles

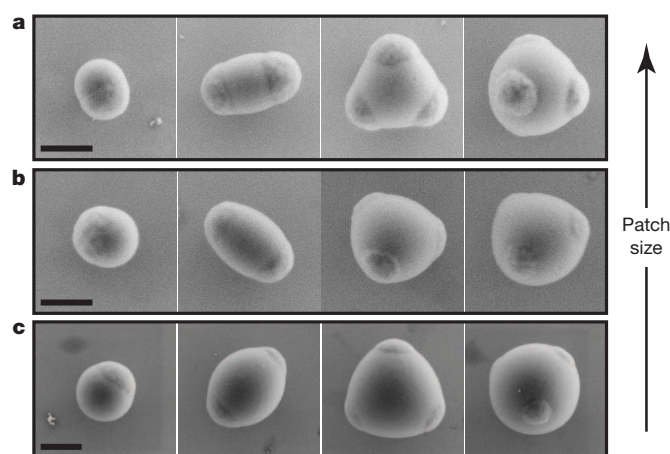


**Figure 2 | Control of patch size.** Electron micrographs of patchy particles, showing that the sizes of patches can be adjusted by changing encapsulation conditions. **a**, Particles with relatively large patches are fabricated when clusters are swollen with 1.0 ml of styrene monomer. Primary spheres are 540 nm in diameter. **b**, Under identical conditions, smaller patches are obtained when more monomer (1.2 ml) is added. **c**, Smaller patches, relative to particle size, are obtained using primary microspheres 850 nm in diameter. Using larger particles facilitates observation under an optical microscope. Divalent, trivalent and tetravalent particles from this batch were used in colloidal molecule formation, and the monovalent particles were used in kinetics study, as discussed below. Arrow indicates increasing patch size. Scale bars, 500 nm.

with different valence (see Supplementary Fig. 1b, c). Table 1 summarizes the fraction of particles obtained in each band for two different shearing conditions. For the lower-shear preparation, each of the four upper bands, which correspond to particles with 1 to 4 patches, contains  $10^8$  to  $10^9$  identical particles. For the higher-shear preparation, greater quantities are produced in the upper bands and lower quantities are produced in the lower bands. In most cases, we use conditions (see Methods) that produce the most 2-, 3- and 4-patch particles, which are the ones most useful for making analogues of common molecules. If pure samples containing patchy particles of identical valence are desired, then it is the fractionation step that ultimately limits the quantity available. Typically, we collect the same valence from up to 40 separations run in parallel, accumulating  $10^9$  to  $10^{11}$  particles.

The amidine groups on the colloid surface are crucial to the patchy particle fabrication process. First, the positive charge created from the dissociation of amidine hydrogen chloride salt ( $-(C(NH)NH_3Cl)$ ), along with the SDS surfactant, stabilizes the microspheres as well as the clusters by electrostatic repulsion. Second, when the clusters are swollen and encapsulated, the positive charges make the patches of the cluster more hydrophilic than the monomer–water interface, which is stabilized only by SDS. This difference in interfacial energies leads to finite contact angles and well-defined patches. Most importantly, the amidine groups can be easily functionalized in aqueous solution.

We functionalize the amidinated patches with biotin, and then use a biotin–streptavidin–biotin linkage to attach DNA with

**Table 1 | Quantities of particles in the different bands**

Number of patches	1	2	3	4	5	6	7
High shear	61%	15%	4%	1%	0.2%*	0.02%*	0.001%*
Low shear	7%	16%	25%	15%	8%	5%	3%

Density gradient centrifugation is used to fractionate the patchy particles. The fraction of identical particles obtained from a single centrifuge tube is shown. Fractions of 10%–20% correspond to  $10^8$ – $10^9$  particles in a single fractionation.

\* For these higher-valence particles, the fractions were estimated from their number ratio relative to lower-valence particles observed under a microscope (see Methods).

single-stranded 'sticky' ends. The first step uses sulpho-NHS-biotin (biotinamidohexanoic acid 3-sulpho-*N*-hydroxysuccinimide ester sodium salt, a water-soluble biotin derivative) and is carried out in phosphate-buffered saline (PBS) (pH = 7.42), where the *N*-hydroxysuccinimide ester (NHS) can react with amidine groups and covalently link the biotin to the patches.

The DNA oligomer is prepared separately. It has three parts. At the 5' end, it has a biotin as an anchoring molecule. In the middle, there is a 49-base-pair double helix that acts as a spacer. Finally, at the 3' terminus, a single strand of 11 complementary or 8 palindrome base pairs forms the sticky end (for sequences, see Methods). Mixing DNA with streptavidin in a 1:1 ratio yields a streptavidin–DNA complex, which is then added to the biotin-functionalized patchy particles to produce DNA-functionalized patchy particles. The streptavidin contains a fluorescent tag for visualization by confocal microscopy. Figure 1d shows that only the patches of the particle are fluorescent, indicating that the streptavidin–DNA complex successfully coats the particle patches and that the amidine–NHS chemistry used for biotin functionalization works as designed.

The binding between patches on different particles is realized by hybridizing DNA oligomers on different patches. The oligomers, about 18 nm in length, provide short-range attractions and thus enforce the directionality defined by the particle patches. DNA is widely used for linking nanoparticles because it can be synthesized with control over the length and sequences of the base pairs, which, in turn, controls the specificity and the strength of interaction<sup>35–38</sup>. Hybridization of the complementary strands is fully reversible with temperature so that particle assembly can be controlled by varying temperature.

The oligomers we use to functionalize purified patchy particles are complementary DNA strands designated R (red) or G (green) and designed to bind selectively only to each other, or a palindrome P strand that only binds to other P strands. To differentiate the particles under the confocal microscope, red fluorescent (Alexa 647) streptavidin is used with R particles, and green fluorescent (Alexa 488) streptavidin is used with G particles (see Supplementary Fig. 2).

### Assembly of colloidal molecules

With our collection of R, G and P patchy particles, we can build colloidal assemblies that mimic not only the geometry, but also the chemistry of molecules. Figure 3a (left panel) shows the formation of AB-type colloidal molecules from two 1-patch particles with complementary sticky ends. The system produces colloidal dumbbells without the random aggregation observed using spherical particles uniformly coated with DNA, and consistently with there being only one patch per particle. The confocal fluorescent image in Fig. 3a (middle panel) shows only complementary R–G particle pairs and no R–R or G–G pairs, confirming that DNA hybridization drives particle assembly. The resulting dumbbells are the colloidal analogues of AB-type molecules such as hydrogen chloride (Fig. 3a, right panel). Here, in contrast to hydrogen and chlorine, the sizes of the two atoms are the same, although they need not be. Patchy particles of different sizes can be fabricated and DNA bonds of various strengths can be used, so colloidal molecules of different size ratio and bond strength can be obtained.

Figure 3b shows linear AB<sub>2</sub>-type colloidal molecules, the colloidal analogues of molecules like carbon dioxide (CO<sub>2</sub>) or beryllium chloride (BeCl<sub>2</sub>), that are obtained when green divalent (2-patch) particles are mixed with red monovalent particles. Triangle-like AB<sub>3</sub> (Fig. 3c) and tetrahedron-like AB<sub>4</sub> (Fig. 3d) colloidal molecules are similarly obtained by mixing trivalent (3-patch) particles and tetravalent (4-patch) particles, respectively, with monovalent particles (see Supplementary Video 1 for all colloidal molecules).

Bonding specificity is critical for the formation of all of the AB<sub>*n*</sub> structures. It promotes the formation of AB bonds while prohibiting the formation of AA and BB bonds, ensuring that the divalent,

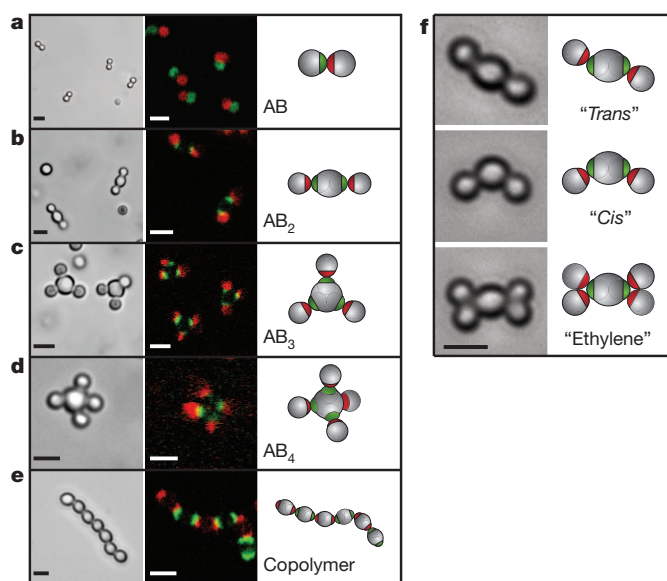


**Figure 3 | Specific directional bonding between colloidal atoms observed with optical microscopes.** **a–e**, Bright-field (left panels), confocal fluorescent (middle panels), and schematic images (right panels), show colloidal molecules self-assembled from patchy particles. **a**, Complementary green and red monovalent particles form dumbbell-shaped AB-type molecules. Supra-colloidal molecules AB<sub>2</sub>, AB<sub>3</sub> and AB<sub>4</sub> are formed by mixing red monovalent with green divalent (**b**), trivalent (**c**) and tetravalent (**d**) particles. **e**, If complementary divalent particles are mixed, linear alternating polymer chains spontaneously assemble. **f**, When particles with bigger patches are used, *cis*–*trans*-like isomers can form. Introducing more monovalent particles leads to ethylene-like colloidal molecules. Images are bright-field (left panels) and schematic (right panels). Scale bars, 2 μm.

trivalent and tetravalent particles can act as the central atoms and the bonding interactions mimic that of atomic orbitals in geometry and valence. Complementary monovalent particles then serve as ligands that form bonds with the central atom. The confocal images in Fig. 3 (middle panels) show the directionality and specificity of the interactions between the central atoms and their monovalent particle ligands.

Other structures that can be made include colloidal analogues of alternating copolymers, formed using complementary divalent particles. Figure 3e shows that only green and red divalent particles bind to each other.

If particles have patches big enough to accommodate more than one complementary particle, molecular isomers and branched polymers are obtained. Figure 3f shows two isomers of a nonlinear AB<sub>2</sub>-type assembly that mimic the *cis*- and *trans*-conformations of molecules with a double bond. Such isomers may behave quite differently from one another in diffusion, rotation and reactivity. Additional monovalent particles can bind to the isomers and form ethylene-like structures (Fig. 3f, bottom panels). In the assembly of colloidal polymers from divalent particles, particles with bigger patches lead to branched chains and cross-linked networks (see Supplementary Fig. 3a). These results highlight the importance of controlling the patch size and in particular the ability to make patches sufficiently small that steric hindrance prevents more than one particle from attaching (see Supplementary Fig. 4 for SEM pictures of patchy particles used in colloidal molecules and geometry analysis for hindrance).

Self-complementary palindrome strands can also be used for self-assembly of mono- and divalent particles. Monovalent particles with palindrome sticky DNA yield A<sub>2</sub>-type colloidal molecules, analogous to H<sub>2</sub> or Cl<sub>2</sub>, whereas divalent particles yield homopolymers. One can also envision higher-order palindrome particles that might assemble into extended open structures like a diamond lattice<sup>39</sup>.

## Colloidal reactions

The self-assembly of patchy particles into a target structure can be viewed as a ‘colloidal reaction’ or more generally as “supracolloidal chemistry”<sup>40</sup>. As in conventional chemical reactions, colloidal particles with a particular morphology and binding capacity are used as reagents and mixed together stoichiometrically. For example, four equivalents of monovalent and one equivalent of complementary tetravalent particles assemble into  $AB_4$  colloidal molecules. The yield is about 50% after a few days; that is, half of the tetravalent particles have four monovalent particles attached, with the remainder consisting of incomplete structures like  $AB_3$ ,  $AB_2$  and  $AB$ . Using an excess of the monovalent particles increases the yield of the final  $AB_4$  product, just as for conventional chemical reactions. A fivefold excess of monovalent particles, for example, increases the yield of  $AB_4$  to 80% (see Supplementary Fig. 3b). It should also be possible to increase the yield by increasing the strength of the DNA-mediated patch binding, which can be done by increasing the length of the DNA sticky ends or by increasing the density of the DNA attached to the patches<sup>41</sup>.

An obvious and important difference between the molecular and colloidal domains is the size of the constituents. The much larger colloids exhibit much slower dynamics and reaction kinetics, and thus can be observed *in situ* under an optical microscope. As shown in Fig. 4a, the formation of an  $AB_4$  molecule proceeds by the central tetravalent particle picking up monovalent particles, one at a time, over a period of about 30 min (see Supplementary Video 2). In the case of divalent particle chain formation, the ‘polymerization’ also follows a step-growth mechanism. Figure 4b illustrates how a polymer chain can be extended by adding divalent particles one by one at the end (see Supplementary Video 3). Alternatively, two polymer chains can fuse into a longer chain.

We can understand the stepwise growth mechanism by examining the kinetics of formation of the  $AB_3$  molecules (see Supplementary Fig. 5 and Supplementary Video 4). We first heat a trivalent and monovalent particle mixture, with monovalent particles in large excess, to 55 °C, well above the melting temperature  $T_m$  (50 °C) of the DNA, thus causing the particles to dissociate. The system is then quenched to room temperature, well below  $T_m$ , so that the reaction

kinetics is controlled by diffusion and by the size of the sticky patches. The collision frequency between monovalent and trivalent particles can be estimated from the well-known Smoluchowski equation<sup>42</sup>:

$$J \approx 4\pi(b_m + b_t)(D_m + D_t)C_m$$

where  $b_m = 0.49 \mu\text{m}$  is the radius of the monovalent particle,  $b_t = 0.91 \mu\text{m}$  is the radius of the trivalent particle, and  $C_m$  is the number concentration of the monovalent particles, estimated to be one particle per  $50 \mu\text{m}^3$  from direct observation. The diffusion coefficients are about  $D_m = 0.50 \mu\text{m}^2 \text{s}^{-1}$  and  $D_t = 0.28 \mu\text{m}^2 \text{s}^{-1}$  for the monovalent and trivalent particles, respectively. These values give a collision frequency between trivalent and monovalent particles of  $0.27 \text{s}^{-1}$  or a time between collisions of 3.6 s. Not every collision results in a bond, however, owing to the anisotropic nature of patchy particles. Only collisions between patches with complementary DNA can result in adhesion, with a rate proportional to the patch size. Thus, smaller patches form bonds more slowly than larger patches.

We define  $A$  as the fractional surface area of a particle occupied by patches (see Supplementary Figs 4 and 5), with values estimated from SEM measurements of  $A_m = 0.23$  for the monovalent particle and  $A_t = 0.077$  for all three patches of the trivalent particle (see Supplementary Table 1). The estimated reaction time for the first monovalent particle to adhere to a trivalent particle is  $1/JA_mA_t$  or about 3.4 min. The area  $A$  for the trivalent–monovalent particle assembly immediately falls to 0.040 because one of the three patches is covered, and because the attached monovalent particle increases the total surface area of the complex. With two monovalent particles attached,  $A$  falls to 0.016. Thus the times for the second and third monovalent particles to attach are estimated to be 6.5 min and 16 min, respectively, which is consistent with the times observed experimentally and with the observed stepwise assembly of patchy particles (see also Supplementary Video 2).

## Discussion

We expect that our colloids with valence can assemble not only into the molecular analogues shown here, but also into bulk colloidal phases of fundamental and practical interest. Tetrahedrally coordinated glasses, diamond crystals and empty liquids<sup>43</sup> have all proved difficult or impossible to make with existing colloids but should be accessible using our method. However, making scalable quantities of purified divalent and higher-valence colloidal atoms remains a challenge, owing to the limitations of fractionation by density gradient centrifugation. This difficulty might be overcome by large-scale separations<sup>44</sup>, or by developing methods that produce clusters with controlled morphology so that no separation is needed. Indeed, the swelling and functionalization methods we use to make our colloidal particles could readily be adapted for use with clusters made using other recently developed techniques<sup>22,25,45</sup>.

The ability to design colloidal particles with a variety of well-controlled three-dimensional bonding symmetries opens a wide spectrum of new structures for colloidal self-assembly, beyond colloidal assemblies whose structures are defined primarily by repulsive interactions and colloidal shape. Furthermore, the specificity of DNA interactions between patches means that colloids with different properties, such as size, colour, chemical functionality or electrical conductivity could be linked in well-defined sequences and orientations to make new functional materials. Such materials might include photonic crystals with programmed distributions of defects or three-dimensional electrically wired networks. We note that although valence and interaction strength in atomic systems are coupled by underlying quantum mechanical rules, they can be independently varied in our system. This raises the intriguing prospect of our patchy particles not merely mimicking atoms, but functioning as “designer

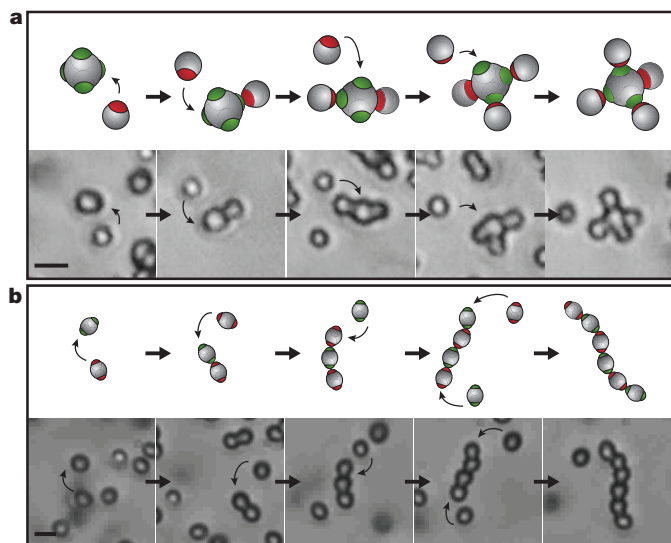


**Figure 4 | Step-wise sequential kinetics of supracolloidal reactions.**

Schematic images (top panels) and snapshots from videos (bottom panels) show step-by-step reactions between colloidal atoms. Bent arrows point from the colloidal atom to the site where it is going to attach. Straight arrows indicate the time sequence. **a**, Monovalent particles attach to tetravalent particle, one by one, forming an  $AB_4$ -type colloidal molecule. **b**, Complementary divalent particles polymerize into a linear chain structure. Scale bar,  $2 \mu\text{m}$ . Videos of these processes are available in the Supplementary Information.

atoms<sup>46</sup> that can undergo reactions, unconstrained by the rules that govern bonding at the atomic scale, to yield structures with no analogues in the atomic or molecular realm<sup>43,47</sup>.

## METHODS SUMMARY

Cross-linked amidinated polystyrene microspheres were synthesized using a surfactant-free emulsion polymerization method. The amidinated clusters were prepared as described by ref. 5. Shearing conditions were optimized to control cluster distribution. A two-stage swelling and polymerization method was used to encapsulate the clusters, thereby fabricating mixtures of patchy particles that were separated by density gradient centrifugation. After purification, the separated particles were dispersed in 10 mM PBS (pH 7.42, 100 mM NaCl) containing 0.1% (w/w) Triton X-100 and reacted with sulpo-NHS-biotin to convert the functionalities on the patches from amides to biotins. 5'-Biotin-DNA was mixed with fluorescent streptavidin in a 1:1 ratio and the resulting complex was used to attach DNA to the biotinylated patches. Finally, the DNA-containing particles were washed with and dispersed in an aqueous PBS containing 1% (w/w) Pluronic F127. This suspension was used for all self-assembly experiments. For the self-assembly studies, the mixture of interest was sealed in a hydrophobic capillary tube and imaged using optical microscopy. Particles dried on a silicon wafer were imaged by field-emission SEM. The fluorescent images were obtained using a Leica SP5 confocal fluorescence microscope. Laser lines at 488 nm and 633 nm were used to excite the green and red fluorescence.

**Full Methods** and any associated references are available in the online version of the paper.

Received 12 June; accepted 4 September 2012.

1. Glotzer, S. C. & Solomon, M. J. Anisotropy of building blocks and their assembly into complex structures. *Nature Mater.* **6**, 557–562 (2007).
2. Sacanna, S. & Pine, D. J. Shape-anisotropic colloids: building blocks for complex assemblies. *Curr. Opin. Colloid Interf. Sci.* **16**, 96–105 (2011).
3. Rossi, L. *et al.* Cubic crystals from cubic colloids. *Soft Matter* **7**, 4139–4142 (2011).
4. Meng, G., Arkus, N., Brenner, M. P. & Manoharan, V. N. The free-energy landscape of clusters of attractive hard spheres. *Science* **327**, 560–563 (2010).
5. Manoharan, V. N., Elsesser, M. T. & Pine, D. J. Dense packing and symmetry in small clusters of microspheres. *Science* **301**, 483–487 (2003).
6. Kraft, D. J. *et al.* Self-assembly of colloids with liquid protrusions. *J. Am. Chem. Soc.* **131**, 1182–1186 (2009).
7. Sacanna, S., Irvine, W. T. M., Chaikin, P. M. & Pine, D. J. Lock and key colloids. *Nature* **464**, 575–578 (2010).
8. Zoldesi, C. I., van Walree, C. A. & Imhof, A. Deformable hollow hybrid silica/siloxane colloids by emulsion templating. *Langmuir* **22**, 4343–4352 (2006).
9. Li, F., Josephson, D. P. & Stein, A. Colloidal assembly: the road from particles to colloidal molecules and crystals. *Angew. Chem. Int. Edn* **50**, 360–388 (2011).
10. Leunissen, M. E. *et al.* Ionic colloidal crystals of oppositely charged particles. *Nature* **437**, 235–240 (2005).
11. Macfarlane, R. J. *et al.* Nanoparticle superlattice engineering with DNA. *Science* **334**, 204–208 (2011).
12. Velikov, K. P., Christova, C. G., Dullens, R. P. A. & van Blaaderen, A. Layer-by-layer growth of binary colloidal crystals. *Science* **296**, 106–109 (2002).
13. Ho, K. M., Chan, C. T. & Soukoulis, C. M. Existence of a photonic gap in periodic dielectric structures. *Phys. Rev. Lett.* **65**, 3152–3155 (1990).
14. Nelson, D. R. Toward a tetravalent chemistry of colloids. *Nano Lett.* **2**, 1125–1129 (2002).
15. Glotzer, S. C. Some assembly required. *Science* **306**, 419–420 (2004).
16. Manoharan, V. N. *Building Materials with Colloidal Spheres*. PhD thesis, Univ. California, Santa Barbara (2004).
17. Breed, D. R. *Engineered Colloids: Patchy Particles with Reversible, Directional Interactions*. PhD thesis, Univ. California, Santa Barbara (2007).
18. Bianchi, E., Blaak, R. & Likos, C. N. Patchy colloids: state of the art and perspectives. *Phys. Chem. Chem. Phys.* **13**, 6397–6410 (2011).
19. Zhang, Z. & Glotzer, S. C. Self-assembly of patchy particles. *Nano Lett.* **4**, 1407–1413 (2004).
20. Xu, X., Rosi, N. L., Wang, Y., Huo, F. & Mirkin, C. A. Asymmetric functionalization of gold nanoparticles with oligonucleotides. *J. Am. Chem. Soc.* **128**, 9286–9287 (2006).
21. Huo, F., Lytton-Jean, A. K. R. & Mirkin, C. A. Asymmetric functionalization of nanoparticles based on thermally addressable DNA interconnects. *Adv. Mater.* **18**, 2304–2306 (2006).
22. Hong, L., Cacciuto, A., Luijten, E. & Granick, S. Clusters of amphiphilic colloidal spheres. *Langmuir* **24**, 621–625 (2008).
23. Chen, Q., Bae, S. C. & Granick, S. Directed self-assembly of a colloidal kagome lattice. *Nature* **469**, 381–384 (2011).
24. Jones, M. R., Macfarlane, R. J., Prigodich, A. E., Patel, P. C. & Mirkin, C. A. Nanoparticle shape anisotropy dictates the collective behavior of surface-bound ligands. *J. Am. Chem. Soc.* **133**, 18865–18869 (2011).
25. Kraft, D. J., Groenewold, J. & Kegel, W. K. Colloidal molecules with well-controlled bond angles. *Soft Matter* **5**, 3823–3826 (2009).
26. Cho, Y.-S. *et al.* Particles with coordinated patches or windows from oil-in-water emulsions. *Chem. Mater.* **19**, 3183–3193 (2007).
27. Zhang, G., Wang, D. & Möhwald, H. Patterning microsphere surfaces by templating colloidal crystals. *Nano Lett.* **5**, 143–146 (2005).
28. Pawar, A. B. & Kretzschmar, I. Multifunctional patchy particles by glancing angle deposition. *Langmuir* **25**, 9057–9063 (2009).
29. Pawar, A. B. & Kretzschmar, I. Fabrication, assembly, and application of patchy particles. *Macromol. Rapid Commun.* **31**, 150–168 (2010).
30. Ottewill, R. & Shaw, J. Studies on the preparation and characterization of monodisperse polystyrene lattices. *Colloid Polym. Sci.* **215**, 161–166 (1967).
31. Ugelstad, J., Kaggerud, K. H., Hansen, F. K. & Berge, A. Absorption of low molecular weight compounds in aqueous dispersions of polymer-oligomer particles. 2: A two step swelling process of polymer particles giving an enormous increase in absorption capacity. *Makromol. Chem.* **180**, 737–744 (1979).
32. Ugelstad, J. *et al.* Thermodynamics of swelling. Preparation and application of some composite, monosized polymer particles. *Makromol. Chem.* **10**, 215–234 (1985).
33. Walther, A. & Müller, A. H. E. Janus particles. *Soft Matter* **4**, 663–668 (2008).
34. Zerrouki, D. *et al.* Preparation of doublet, triangular, and tetrahedral colloidal clusters by controlled emulsification. *Langmuir* **22**, 57–62 (2006).
35. Mirkin, C. A., Letsinger, R. L., Mucic, R. C. & Storhoff, J. J. A DNA-based method for rationally assembling nanoparticles into macroscopic materials. *Nature* **382**, 607–609 (1996).
36. Alivisatos, A. P. *et al.* Organization of 'nanocrystal molecules' using DNA. *Nature* **382**, 609–611 (1996).
37. Leunissen, M. E. *et al.* Switchable self-protected attractions in DNA-functionalized colloids. *Nature Mater.* **8**, 590–595 (2009).
38. Nykypanchuk, D., Maye, M. M., van der Lelie, D. & Gang, O. DNA-guided crystallization of colloidal nanoparticles. *Nature* **451**, 549–552 (2008).
39. Zhang, Z., Keys, A. S., Chen, T. & Glotzer, S. C. Self-assembly of patchy particles into diamond structures through molecular mimicry. *Langmuir* **21**, 11547–11551 (2005).
40. Chen, Q. *et al.* Supracolloidal reaction kinetics of Janus spheres. *Science* **331**, 199–202 (2011).
41. Dreyfus, R. *et al.* Aggregation-disaggregation transition of DNA-coated colloids: Experiments and theory. *Phys. Rev. E* **81**, 041404 (2010).
42. van Kampen, N. G. *Stochastic Processes in Physics and Chemistry* 3rd edn, 292–297 (Elsevier, 2007).
43. Romano, F., Sanz, E. & Sciortino, F. Crystallization of tetrahedral patchy particles in silica. *J. Chem. Phys.* **134**, 174502–174508 (2011).
44. Johnson, P. M., van Kats, C. M. & van Blaaderen, A. Synthesis of colloidal silica dumbbells. *Langmuir* **21**, 11510–11517 (2005).
45. Perro, A. *et al.* A chemical synthetic route towards "colloidal molecules". *Angew. Chem. Int. Edn* **48**, 361–365 (2009).
46. Frenkel, D. Playing tricks with designer "atoms". *Science* **296**, 65–66 (2002).
47. Miller, M. A. & Wales, D. J. Novel structural motifs in clusters of dipolar spheres: knots, links, and coils. *J. Phys. Chem. B* **109**, 23109–23112 (2005).

**Supplementary Information** is available in the online version of the paper.

**Acknowledgements** We thank M. T. Elsesser, D. Kraft, and G.-R. Yi for discussions. This work was supported partially by the MRSEC Program of the National Science Foundation under award number DMR-0820341. Additional financial support was provided by the National Science Foundation (ChE-0911460). We acknowledge support from the MRI programme of the National Science Foundation under award number DMR-0923251 for the purchase of a Zeiss field emission scanning electron microscope.

**Author Contributions** V.N.M. and D.J.P. thought of patchy particles and how to make them. D.R.B. developed the functionalization of patches. Yufeng Wang and Yu Wang optimized the control of patch size and DNA functionalization, performed the experiments, and collected and analysed the data. A.D.H. helped with particle synthesis. L.F. designed the DNA sequences and modelled the kinetics. M.W. and D.J.P. supervised the project. D.J.P., Yufeng Wang and Yu Wang wrote the paper with revisions from all of the authors.

**Author Information** Reprints and permissions information is available at [www.nature.com/reprints](http://www.nature.com/reprints). The authors declare no competing financial interests. Readers are welcome to comment on the online version of the paper. Correspondence and requests for materials should be addressed to D.J.P. ([pine@nyu.edu](mailto:pine@nyu.edu)) or M.W. ([marcus.weck@nyu.edu](mailto:marcus.weck@nyu.edu)).

## METHODS

**Microspheres and cluster formation.** Amidinated poly(styrene) microspheres were synthesized using the standard surfactant-free emulsion polymerization method described in the literature<sup>30</sup> (monomer: styrene; initiator: 2,2'-azobis(isobutyramidine) dihydrochloride; cross-linker: 3 mol.% divinyl benzene). The amidinated microsphere clusters were prepared as described by ref. 5. In a variation on the original report, we used SDS as surfactant and changed the shear rate to control cluster distribution. The following two shear experiments were carried out as described in the main document and corresponding to patchy particle distributions in Supplementary Fig. 1: condition a (low shear): 90 s at 8,000 r.p.m., using a T25 IKA emulsifier. 60 s at 9,500 r.p.m. and then 60 s at 13,500 r.p.m.; condition b (high shear): 90 s at 8,000 r.p.m., 90 s at 9,500 r.p.m. and then 120 s at 13,500 r.p.m. The final clusters were washed with an aqueous solution of 0.1% SDS followed by repeated centrifugation and redispersion. Finally, we adjust the cluster concentration to 1% (w/w) and modified the pH to 2.93 using HCl.

**Patchy particle fabrication.** A two-stage swelling and polymerization method was employed to encapsulate the clusters to fabricate patchy particles. Typically, 10 ml of the cluster suspension was charged into a 50 ml two-necked flask along with a magnetic stir bar. The flask was submerged in an oil bath and the temperature was set to 35°C. One millilitre of acetone was added and the suspension was stirred at 300 r.p.m. In a separated glass vial, 50 mg of benzoyl peroxide were dissolved in 0.63 ml of 1,2-dichloroethane. Then, 0.88 ml of 1-chlorodecane was added to the vial followed by the addition of 5 ml of an aqueous solution of 0.1% SDS. The resulting mixture was then vortexed to create an emulsion, from which 200 µl were added to the cluster suspension. The resulting mixture was stirred for 12 h at 35°C. Then, the acetone was removed via evaporation under reduced pressure (30 mm Hg). The flask was equipped with a condenser containing an oil bubbler at the top. Using a needle, nitrogen was bubbled through the suspension for 30 min. Then, 1 ml of styrene (with inhibitor removed) was added and allowed to swell the clusters. After 2 h, the temperature was raised to 65°C to initiate polymerization. The polymerization was allowed to take place for 14 h. Then, the reaction was cooled to room temperature, which terminates the polymerization, yielding the desired patchy particles as a mixture.

**Density gradient centrifugation.** The patchy particle mixture was separated by density gradient centrifugation. A 5–20% w/w linear gradient of glycerol in water solution was made by a 'two-jar'-type gradient maker. Typically, 300 µl of the patchy particle mixture was loaded on top of 12 ml of the gradient solution followed by centrifugation for 24 min at 1,800g at 20°C. Individual bands were extracted carefully using a syringe with pipetting needles. The individual fractions were washed first with an aqueous solution containing 0.1% w/w Triton X-100 (three times) followed by an aqueous solution containing 10 mM PBS (pH 7.42, 100 mM NaCl) and 0.1% w/w Triton X-100 (three times).

To obtain the quantity of particles in each band we used the mass of polystyrene and the size of the particles. For this, the particles were washed with deionized water, dried under vacuum, and weighed. For higher-valence particles, the

quantity was estimated by measuring the number ratio relative to lower-valence particles under a microscope.

**Biotin functionalization.** One milligram of sulfo-NHS-biotin was charged into a dram vial containing a stir bar. Half a millilitre of patchy particles of interest was added to the vial and the suspension was allowed to stir for 12 h. Biotin was used in large excess. Unreacted biotin was removed by washing the functionalized particles six times with an aqueous solution containing 10 mM PBS (pH 7.42, 100 mM NaCl) and 0.1% w/w Triton X-100.

**DNA conjugation.** The single-stranded oligonucleotides used in this study were purchased from Integrated DNA Technologies USA. The sequences are shown below with the single-stranded sticky ends underlined (BioTEG designates a biotin-tetra-ethyleneglycol):

Green (G): 5'-/5BioTEG/ATCGCTACCCCTTCGCACAGTCAATCCAGAGAGCCCTGCCTTTCATTACGACCTACTTCTAC-3'.

Red (R): 5'-/5BioTEG/ATCGCTACCCCTTCGCACAGTCAATCCAGAGAGCCCTGCCTTTCATTACGAGTAGAAGTAGG-3'.

Palindrome (P): 5'-/5BioTEG/ATCGCTACCCCTTCGCACAGTCAATCCAGAGAGCCCTGCCTTTCATTACGATACGCGTA-3'.

Complementary strand for the backbone (CS): 5'-CGTAATGAAAGGCAGGGCTCTCTGGATTGACTGTGCGAAGGGTAGCGAT-3'.

The 5'-biotin-DNA was prepared by mixing G, R or P with CS in a 1:1.5 ratio, heating it to 95°C, and then cooling it slowly over a two-hour period to 25°C.

The 5'-biotin-DNA was mixed with streptavidin (Life Technology, 2 mg ml<sup>-1</sup>, labelled with green or red fluorescence) in 1:1 molar ratio in a centrifuge tube and agitated for 1 h. The resulting DNA-streptavidin complex was then attached to the biotin patchy particles. Typically, we added a 100 µl suspension of biotin patchy particles to 10 µl of the DNA-streptavidin complex and agitated the mixture for 3 h at 25°C. The resulting particles were washed with and dispersed in an aqueous solution of PBS containing 1% w/w Pluronic F127 as surfactant. This dispersion can be stored at 4°C and directly used for the self-assembly studies.

**Self-assembly.** For the self-assembly studies, the patchy particles of interest were combined and the mixture transferred to a flat capillary tube (2 mm × 100 µm × 1 cm). The capillary tube was pretreated with plasma and exposed to hexamethyldisilazane vapour to make it hydrophobic. After addition of the sample, the capillary tube was sealed by ultra-violet-curing glue or wax. The capillary tube temperature was controlled by using a Linkam microscope hot stage.

**Microscopy.** Particles (clusters or patchy particles) in the dried state were imaged using a Merlin (Carl Zeiss) field-emission SEM. The samples were prepared by placing a drop of a dilute aqueous particle suspension on a silicon wafer followed by evaporation of the water under vacuum. Fluorescent images were taken using a Leica SP5 confocal fluorescence microscope. Laser lines 488 nm and 633 nm were used to excite green and red fluorescence. Some of the microscope images were digitally post-processed to improve brightness and contrast.

# An integrated map of genetic variation from 1,092 human genomes

The 1000 Genomes Project Consortium\*

By characterizing the geographic and functional spectrum of human genetic variation, the 1000 Genomes Project aims to build a resource to help to understand the genetic contribution to disease. Here we describe the genomes of 1,092 individuals from 14 populations, constructed using a combination of low-coverage whole-genome and exome sequencing. By developing methods to integrate information across several algorithms and diverse data sources, we provide a validated haplotype map of 38 million single nucleotide polymorphisms, 1.4 million short insertions and deletions, and more than 14,000 larger deletions. We show that individuals from different populations carry different profiles of rare and common variants, and that low-frequency variants show substantial geographic differentiation, which is further increased by the action of purifying selection. We show that evolutionary conservation and coding consequence are key determinants of the strength of purifying selection, that rare-variant load varies substantially across biological pathways, and that each individual contains hundreds of rare non-coding variants at conserved sites, such as motif-disrupting changes in transcription-factor-binding sites. This resource, which captures up to 98% of accessible single nucleotide polymorphisms at a frequency of 1% in related populations, enables analysis of common and low-frequency variants in individuals from diverse, including admixed, populations.

Recent efforts to map human genetic variation by sequencing exomes<sup>1</sup> and whole genomes<sup>2–4</sup> have characterized the vast majority of common single nucleotide polymorphisms (SNPs) and many structural variants across the genome. However, although more than 95% of common (>5% frequency) variants were discovered in the pilot phase of the 1000 Genomes Project, lower-frequency variants, particularly those outside the coding exome, remain poorly characterized. Low-frequency variants are enriched for potentially functional mutations, for example, protein-changing variants, under weak purifying selection<sup>1,5,6</sup>. Furthermore, because low-frequency variants tend to be recent in origin, they exhibit increased levels of population differentiation<sup>6–8</sup>. Characterizing such variants, for both point mutations and structural changes, across a range of populations is thus likely to identify many variants of functional importance and is crucial for interpreting

individual genome sequences, to help separate shared variants from those private to families, for example.

We now report on the genomes of 1,092 individuals sampled from 14 populations drawn from Europe, East Asia, sub-Saharan Africa and the Americas (Supplementary Figs 1 and 2), analysed through a combination of low-coverage (2–6×) whole-genome sequence data, targeted deep (50–100×) exome sequence data and dense SNP genotype data (Table 1 and Supplementary Tables 1–3). This design was shown by the pilot phase<sup>2</sup> to be powerful and cost-effective in discovering and genotyping all but the rarest SNP and short insertion and deletion (indel) variants. Here, the approach was augmented with statistical methods for selecting higher quality variant calls from candidates obtained using multiple algorithms, and to integrate SNP, indel and larger structural variants within a single framework (see

**Table 1 | Summary of 1000 Genomes Project phase I data**

	Autosomes	Chromosome X	GENCODE regions*
Samples	1,092	1,092	1,092
Total raw bases (Gb)	19,049	804	327
Mean mapped depth (×)	5.1	3.9	80.3
SNPs			
No. sites overall	36.7 M	1.3 M	498 K
Novelty rate†	58%	77%	50%
No. synonymous/non-synonymous/nonsense	NA	4.7/6.5/0.097 K	199/293/6.3 K
Average no. SNPs per sample	3.60 M	105 K	24.0 K
Indels			
No. sites overall	1.38 M	59 K	1,867
Novelty rate†	62%	73%	54%
No. inframe/frameshift	NA	19/14	719/1,066
Average no. indels per sample	344 K	13 K	440
Genotyped large deletions			
No. sites overall	13.8 K	432	847
Novelty rate†	54%	54%	50%
Average no. variants per sample	717	26	39

NA, not applicable.

\*Autosomal genes only.

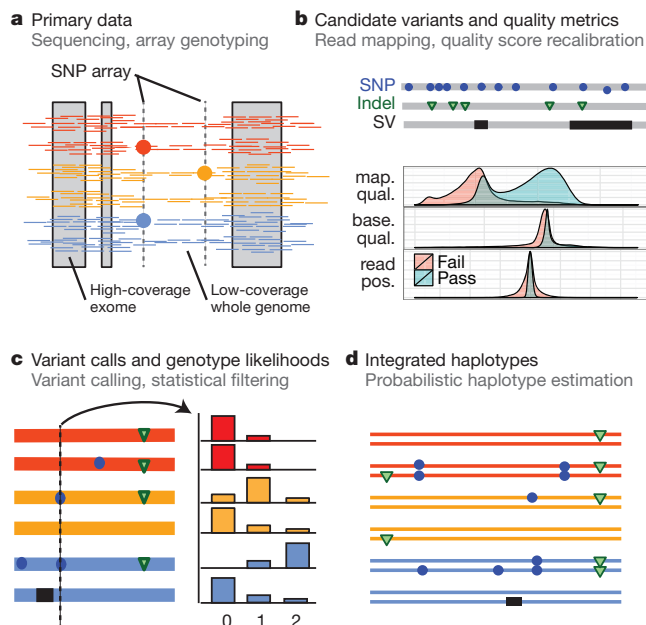
†Compared with dbSNP release 135 (Oct 2011), excluding contribution from phase I 1000 Genomes Project (or equivalent data for large deletions).

\*Lists of participants and their affiliations appear at the end of the paper.

## BOX 1

## Constructing an integrated map of variation

The 1,092 haplotype-resolved genomes released as phase I by the 1000 Genomes Project are the result of integrating diverse data from multiple technologies generated by several centres between 2008 and 2010. The Box 1 Figure describes the process leading from primary data production to integrated haplotypes.



**a**, Unrelated individuals (see Supplementary Table 10 for exceptions) were sampled in groups of up to 100 from related populations (Wright's  $F_{ST}$  typically  $<1\%$ ) within broader geographical or ancestry-based groups<sup>2</sup>. Primary data generated for each sample consist of low-coverage (average  $5\times$ ) whole-genome and high-coverage (average  $80\times$  across a consensus target of 24 Mb spanning more than 15,000 genes) exome sequence data, and high density SNP array information. **b**, Following read-alignment, multiple algorithms were used to identify candidate variants. For each variant, quality metrics were obtained, including information about the uniqueness of the surrounding sequence (for example, mapping quality (map. qual.)), the quality of evidence supporting the variant (for example, base quality (base. qual.) and the position of variant bases within reads (read pos.)), and the distribution of variant calls in the population (for example, inbreeding coefficient). Machine-learning approaches using this multidimensional information were trained on sets of high-quality known variants (for example, the high-density SNP array data), allowing variant sites to be ranked in confidence and subsequently thresholded to ensure low FDR. **c**, Genotype likelihoods were used to summarize the evidence for each genotype at bi-allelic sites (0, 1 or 2 copies of the variant) in each sample at every site. **d**, As the evidence for a single genotype is typically weak in the low-coverage data, and can be highly variable in the exome data, statistical methods were used to leverage information from patterns of linkage disequilibrium, allowing haplotypes (and genotypes) to be inferred.

Box 1 and Supplementary Fig. 1). Because of the challenges of identifying large and complex structural variants and shorter indels in regions of low complexity, we focused on conservative but high-quality subsets: biallelic indels and large deletions.

Overall, we discovered and genotyped 38 million SNPs, 1.4 million bi-allelic indels and 14,000 large deletions (Table 1). Several technologies were used to validate a frequency-matched set of sites to

assess and control the false discovery rate (FDR) for all variant types. Where results were clear, 3 out of 185 exome sites (1.6%), 5 out of 281 low-coverage sites (1.8%) and 72 out of 3,415 large deletions (2.1%) could not be validated (Supplementary Information and Supplementary Tables 4–9). The initial indel call set was found to have a high FDR (27 out of 76), which led to the application of further filters, leaving an implied FDR of 5.4% (Supplementary Table 6 and Supplementary Information). Moreover, for 2.1% of low-coverage SNP and 18% of indel sites, we found inconsistent or ambiguous results, indicating that substantial challenges remain in characterizing variation in low-complexity genomic regions. We previously described the 'accessible genome': the fraction of the reference genome in which short-read data can lead to reliable variant discovery. Through longer read lengths, the fraction accessible has increased from 85% in the pilot phase to 94% (available as a genome annotation; see Supplementary Information), and 1.7 million low-quality SNPs from the pilot phase have been eliminated.

By comparison to external SNP and high-depth sequencing data, we estimate the power to detect SNPs present at a frequency of 1% in the study samples is 99.3% across the genome and 99.8% in the consensus exome target (Fig. 1a). Moreover, the power to detect SNPs at 0.1% frequency in the study is more than 90% in the exome and nearly 70% across the genome. The accuracy of individual genotype calls at heterozygous sites is more than 99% for common SNPs and 95% for SNPs at a frequency of 0.5% (Fig. 1b). By integrating linkage disequilibrium information, genotypes from low-coverage data are as accurate as those from high-depth exome data for SNPs with frequencies  $>1\%$ . For very rare SNPs ( $\leq 0.1\%$ , therefore present in one or two copies), there is no gain in genotype accuracy from incorporating linkage disequilibrium information and accuracy is lower. Variation among samples in genotype accuracy is primarily driven by sequencing depth (Supplementary Fig. 3) and technical issues such as sequencing platform and version (detectable by principal component analysis; Supplementary Fig. 4), rather than by population-level characteristics. The accuracy of inferred haplotypes at common SNPs was estimated by comparison to SNP data collected on mother–father–offspring trios for a subset of the samples. This indicates that a phasing (switch) error is made, on average, every 300–400 kilobases (kb) (Supplementary Fig. 5).

A key goal of the 1000 Genomes Project was to identify more than 95% of SNPs at 1% frequency in a broad set of populations. Our current resource includes  $\sim 50\%$ , 98% and 99.7% of the SNPs with frequencies of  $\sim 0.1\%$ , 1.0% and 5.0%, respectively, in  $\sim 2,500$  UK-sampled genomes (the Wellcome Trust-funded UK10K project), thus

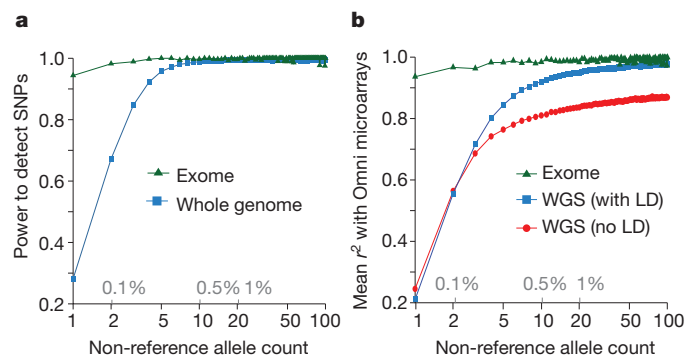


**Figure 1 | Power and accuracy.** **a**, Power to detect SNPs as a function of variant count (and proportion) across the entire set of samples, estimated by comparison to independent SNP array data in the exome (green) and whole genome (blue). **b**, Genotype accuracy compared with the same SNP array data as a function of variant frequency, summarized by the  $r^2$  between true and inferred genotype (coded as 0, 1 and 2) within the exome (green), whole genome after haplotype integration (blue), and whole genome without haplotype integration (red). LD, linkage disequilibrium; WGS, whole-genome sequencing.

meeting this goal. However, coverage may be lower for populations not closely related to those studied. For example, our resource includes only 23.7%, 76.9% and 99.3% of the SNPs with frequencies of  $\sim 0.1\%$ ,  $1.0\%$  and  $5.0\%$ , respectively, in  $\sim 2,000$  genomes sequenced in a study of the isolated population of Sardinia (the SardiNIA study).

### Genetic variation within and between populations

The integrated data set provides a detailed view of variation across several populations (illustrated in Fig. 2a). Most common variants (94% of variants with frequency  $\geq 5\%$  in Fig. 2a) were known before the current phase of the project and had their haplotype structure mapped through earlier projects<sup>2,9</sup>. By contrast, only 62% of variants in the range  $0.5\text{--}5\%$  and 13% of variants with frequencies of  $\leq 0.5\%$  had been described previously. For analysis, populations are grouped by the predominant component of ancestry: Europe (CEU (see Fig. 2a for definitions of this and other populations), TSI, GBR, FIN and IBS), Africa (YRI, LWK and ASW), East Asia (CHB, JPT and CHS) and the Americas (MXL, CLM and PUR). Variants present at 10% and above across the entire sample are almost all found in all of the populations studied. By contrast, 17% of low-frequency variants in the range  $0.5\text{--}5\%$  were observed in a single ancestry group, and 53% of rare variants at  $0.5\%$  were observed in a single population (Fig. 2b). Within ancestry groups, common variants are weakly differentiated (most within-group estimates of Wright's fixation index ( $F_{ST}$ ) are  $<1\%$ ; Supplementary Table 11), although below  $0.5\%$  frequency variants are up to twice as likely to be found within the same population compared with random samples from the ancestry group (Supplementary Fig. 6a). The degree of rare-variant differentiation varies between populations. For example, within Europe, the IBS and FIN populations carry excesses of rare variants (Supplementary Fig. 6b), which can arise through events such as recent bottlenecks<sup>10</sup>, 'clan' breeding structures<sup>11</sup> and admixture with diverged populations<sup>12</sup>.

Some common variants show strong differentiation between populations within ancestry-based groups (Supplementary Table 12), many of which are likely to have been driven by local adaptation either directly or through hitchhiking. For example, the strongest differentiation between African populations is within an NRSF (neuron-restrictive silencer factor) transcription-factor peak (PANC1 cell line)<sup>13</sup>, upstream of *ST8SIA1* (difference in derived allele frequency LWK – YRI of 0.475 at rs7960970), whose product is involved in ganglioside generation<sup>14</sup>. Overall, we find a range of 17–343 SNPs (fewest = CEU – GBR, most = FIN – TSI) showing a difference in frequency of at least 0.25 between pairs of populations within an ancestry group.

The derived allele frequency distribution shows substantial divergence between populations below a frequency of 40% (Fig. 2c), such that individuals from populations with substantial African ancestry (YRI, LWK and ASW) carry up to three times as many low-frequency variants ( $0.5\text{--}5\%$  frequency) as those of European or East Asian origin, reflecting ancestral bottlenecks in non-African populations<sup>15</sup>. However, individuals from all populations show an enrichment of rare variants ( $<0.5\%$  frequency), reflecting recent explosive increases in population size and the effects of geographic differentiation<sup>6,16</sup>. Compared with the expectations from a model of constant population size, individuals from all populations show a substantial excess of high-frequency-derived variants ( $>80\%$  frequency).

Because rare variants are typically recent, their patterns of sharing can reveal aspects of population history. Variants present twice across the entire sample (referred to as  $f_2$  variants), typically the most recent of informative mutations, are found within the same population in 53% of cases (Fig. 3a). However, between-population sharing identifies recent historical connections. For example, if one of the individuals carrying an  $f_2$  variant is from the Spanish population (IBS) and the other is not (referred to as IBS–X), the other individual is more likely to come from the Americas populations (48%, correcting for sample size) than from elsewhere in Europe (41%). Within the East Asian populations, CHS and CHB show stronger  $f_2$  sharing to each other

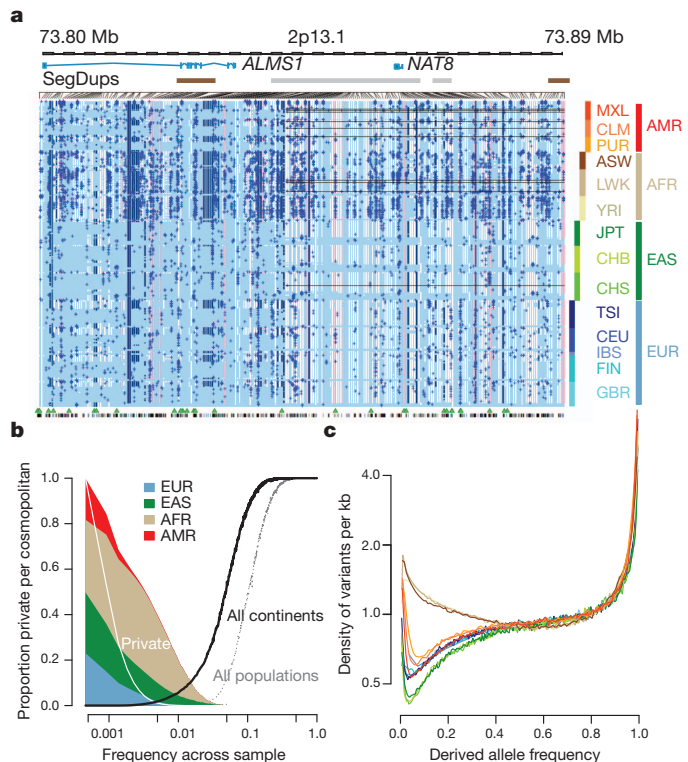


**Figure 2 | The distribution of rare and common variants.** **a**, Summary of inferred haplotypes across a 100-kb region of chromosome 2 spanning the genes *ALMS1* and *NAT8*, variation in which has been associated with kidney disease<sup>45</sup>. Each row represents an estimated haplotype, with the population of origin indicated on the right. Reference alleles are indicated by the light blue background. Variants (non-reference alleles) above  $0.5\%$  frequency are indicated by pink (typed on the high-density SNP array), white (previously known) and dark blue (not previously known). Low frequency variants ( $<0.5\%$ ) are indicated by blue crosses. Indels are indicated by green triangles and novel variants by dashes below. A large, low-frequency deletion (black line) spanning *NAT8* is present in some populations. Multiple structural haplotypes mediated by segmental duplications are present at this locus, including copy number gains, which were not genotyped for this study. Within each population, haplotypes are ordered by total variant count across the region. Population abbreviations: ASW, people with African ancestry in Southwest United States; CEU, Utah residents with ancestry from Northern and Western Europe; CHB, Han Chinese in Beijing, China; CHS, Han Chinese South, China; CLM, Colombians in Medellin, Colombia; FIN, Finnish in Finland; GBR, British from England and Scotland, UK; IBS, Iberian populations in Spain; LWK, Luhya in Webuye, Kenya; JPT, Japanese in Tokyo, Japan; MXL, people with Mexican ancestry in Los Angeles, California; PUR, Puerto Ricans in Puerto Rico; TSI, Toscani in Italy; YRI, Yoruba in Ibadan, Nigeria. Ancestry-based groups: AFR, African; AMR, Americas; EAS, East Asian; EUR, European. **b**, The fraction of variants identified across the project that are found in only one population (white line), are restricted to a single ancestry-based group (defined as in **a**, solid colour), are found in all groups (solid black line) and all populations (dotted black line). **c**, The density of the expected number of variants per kilobase carried by a genome drawn from each population, as a function of variant frequency (see Supplementary Information). Colours as in **a**. Under a model of constant population size, the expected density is constant across the frequency spectrum.

(58% and 53% of CHS–X and CHB–X variants, respectively) than either does to JPT, but JPT is closer to CHB than to CHS (44% versus 35% of JPT–X variants). Within African-ancestry populations, the ASW are closer to the YRI (42% of ASW–X  $f_2$  variants) than the LWK (28%), in line with historical information<sup>17</sup> and genetic evidence based on common SNPs<sup>18</sup>. Some sharing patterns are surprising; for example, 2.5% of the  $f_2$  FIN–X variants are shared with YRI or LWK populations.

Independent evidence about variant age comes from the length of the shared haplotypes on which they are found. We find, as expected,

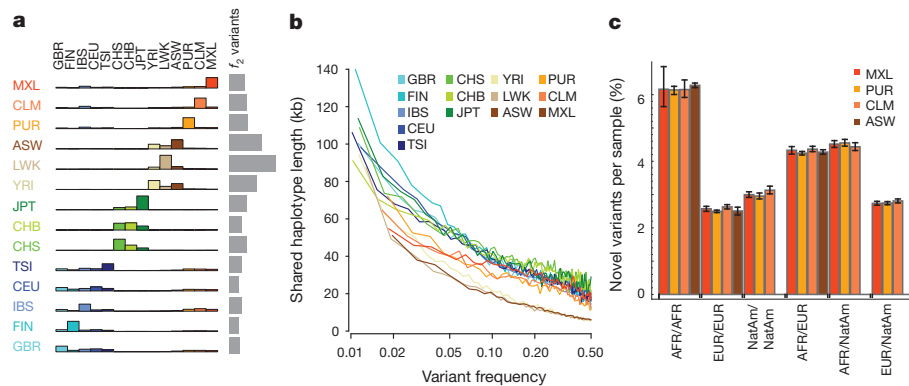


**Figure 3 | Allele sharing within and between populations.** **a**, Sharing of  $f_2$  variants, those found exactly twice across the entire sample, within and between populations. Each row represents the distribution across populations for the origin of samples sharing an  $f_2$  variant with the target population (indicated by the left-hand side). The grey bars represent the average number of  $f_2$  variants carried by a randomly chosen genome in each population. **b**, Median length of haplotype identity (excluding cryptically related samples and singleton variants, and allowing for up to two genotype errors) between two

chromosomes that share variants of a given frequency in each population. Estimates are from 200 randomly sampled regions of 1 Mb each and up to 15 pairs of individuals for each variant. **c**, The average proportion of variants that are new (compared with the pilot phase of the project) among those found in regions inferred to have different ancestries within ASW, PUR, CLM and MXL populations. Error bars represent 95% bootstrap confidence intervals. NatAm, Native American.

a negative correlation between variant frequency and the median length of shared haplotypes, such that chromosomes carrying variants at 1% frequency share haplotypes of 100–150 kb (typically 0.08–0.13 cM; Fig. 3b and Supplementary Fig. 7a), although the distribution is highly skewed and 2–5% of haplotypes around the rarest SNPs extend over 1 megabase (Mb) (Supplementary Fig. 7b, c). Haplotype phasing and genotype calling errors will limit the ability to detect long shared haplotypes, and the observed lengths are a factor of 2–3 times shorter than predicted by models that allow for recent explosive growth<sup>6</sup> (Supplementary Fig. 7a). Nevertheless, the haplotype length for variants shared within and between populations is informative about relative allele age. Within populations and between populations in which there is recent shared ancestry (for example, through admixture and within continents),  $f_2$  variants typically lie on long shared haplotypes (median within ancestry group 103 kb; Supplementary Fig. 8). By contrast, between populations with no recent shared ancestry,  $f_2$  variants are present on very short haplotypes, for example, an average of 11 kb for FIN – YRI  $f_2$  variants (median between ancestry groups excluding admixture is 15 kb), and are therefore likely to reflect recurrent mutations and chance ancient coalescent events.

To analyse populations with substantial historical admixture, statistical methods were applied to each individual to infer regions of the genome with different ancestries. Populations and individuals vary substantially in admixture proportions. For example, the MXL population contains the greatest proportion of Native American ancestry (47% on average compared with 24% in CLM and 13% in PUR), but the proportion varies from 3% to 92% between individuals (Supplementary Fig. 9a). Rates of variant discovery, the ratio of non-synonymous to synonymous variation and the proportion of variants that are new vary systematically between regions with different ancestries. Regions of Native American ancestry show less variation, but a higher fraction of the variants discovered are novel (3.0% of variants per sample; Fig. 3c) compared with regions of European ancestry (2.6%). Regions of African ancestry show the highest rates of novelty (6.2%) and heterozygosity (Supplementary Fig. 9b, c).

### The functional spectrum of human variation

The phase I data enable us to compare, for different genomic features and variant types, the effects of purifying selection on evolutionary conservation<sup>19</sup>, the allele frequency distribution and the level of differentiation between populations. At the most highly conserved coding sites, 85% of non-synonymous variants and more than 90% of stop-gain and splice-disrupting variants are below 0.5% in frequency,

compared with 65% of synonymous variants (Fig. 4a). In general, the rare variant excess tracks the level of evolutionary conservation for variants of most functional consequence, but varies systematically between types (for example, for a given level of conservation enhancer variants have a higher rare variant excess than variants in transcription-factor motifs). However, stop-gain variants and, to a lesser extent, splice-site disrupting changes, show increased rare-variant excess whatever the conservation of the base in which they occur, as such mutations can be highly deleterious whatever the level of sequence conservation. Interestingly, the least conserved splice-disrupting variants show similar rare-variant loads to synonymous and non-coding regions, suggesting that these alternative transcripts are under very weak selective constraint. Sites at which variants are observed are typically less conserved than average (for example, sites with non-synonymous variants are, on average, as conserved as third codon positions; Supplementary Fig. 10).

A simple way of estimating the segregating load arising from rare, deleterious mutations across a set of genes comes from comparing the

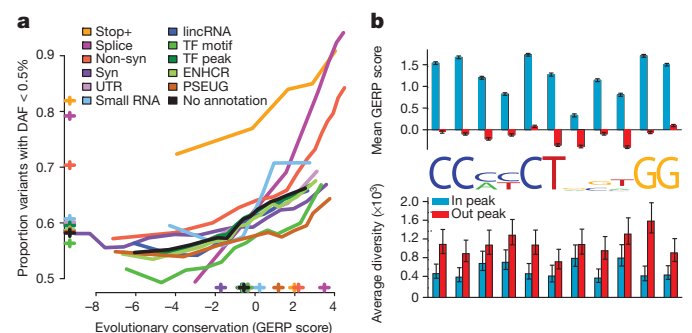


**Figure 4 | Purifying selection within and between populations.** **a**, The relationship between evolutionary conservation (measured by GERP score<sup>19</sup>) and rare variant proportion (fraction of all variants with derived allele frequency (DAF) < 0.5%) for variants occurring in different functional elements and with different coding consequences. Crosses indicate the average GERP score at variant sites (x axis) and the proportion of rare variants (y axis) in each category. ENHCR, enhancer; lincRNA, large intergenic non-coding RNA; non-syn, non-synonymous; PSEUG, pseudogene; syn, synonymous; TF, transcription factor. **b**, Levels of evolutionary conservation (mean GERP score, top) and genetic diversity (per-nucleotide pairwise differences, bottom) for sequences matching the CTCF-binding motif within CTCF-binding peaks, as identified experimentally by ChIP-seq in the ENCODE project<sup>13</sup> (blue) and in a matched set of motifs outside peaks (red). The logo plot shows the distribution of identified motifs within peaks. Error bars represent  $\pm 2$  s.e.m.

ratios of non-synonymous to synonymous variants in different frequency ranges. The non-synonymous to synonymous ratio among rare (<0.5%) variants is typically in the range 1–2, and among common variants in the range 0.5–1.5, suggesting that 25–50% of rare non-synonymous variants are deleterious. However, the segregating rare load among gene groups in KEGG pathways<sup>20</sup> varies substantially (Supplementary Fig. 11a and Supplementary Table 13). Certain groups (for example, those involving extracellular matrix (ECM)–receptor interactions, DNA replication and the pentose phosphate pathway) show a substantial excess of rare coding mutations, which is only weakly correlated with the average degree of evolutionary conservation. Pathways and processes showing an excess of rare functional variants vary between continents (Supplementary Fig. 11b). Moreover, the excess of rare non-synonymous variants is typically higher in populations of European and East Asian ancestry (for example, the ECM–receptor interaction pathway load is strongest in European populations). Other groups of genes (such as those associated with allograft rejection) have a high non-synonymous to synonymous ratio in common variants, potentially indicating the effects of positive selection.

Genome-wide data provide important insights into the rates of functional polymorphism in the non-coding genome. For example, we consider motifs matching the consensus for the transcriptional repressor CTCF, which has a well-characterized and highly conserved binding motif<sup>21</sup>. Within CTCF-binding peaks experimentally defined by chromatin-immunoprecipitation sequencing (ChIP-seq), the average levels of conservation within the motif are comparable to third codon positions, whereas there is no conservation outside peaks (Fig. 4b). Within peaks, levels of genetic diversity are typically reduced 25–75%, depending on the position in the motif (Fig. 4b). Unexpectedly, the reduction in diversity at some degenerate positions, for example, at position 8 in the motif, is as great as that at non-degenerate positions, suggesting that motif degeneracy may not have a simple relationship with functional importance. Variants within peaks show a weak but consistent excess of rare variation (proportion with frequency <0.5% is 61% within peaks compared with 58% outside peaks; Supplementary Fig. 12), supporting the hypothesis that regulatory sequences contain substantial amounts of weakly deleterious variation.

Purifying selection can also affect population differentiation if its strength and efficacy vary among populations. Although the magnitude of the effect is weak, non-synonymous variants consistently show

greater levels of population differentiation than synonymous variants, for variants of frequencies of less than 10% (Supplementary Fig. 13).

## Uses of 1000 Genomes Project data in medical genetics

Data from the 1000 Genomes Project are widely used to screen variants discovered in exome data from individuals with genetic disorders<sup>22</sup> and in cancer genome projects<sup>23</sup>. The enhanced catalogue presented here improves the power of such screening. Moreover, it provides a ‘null expectation’ for the number of rare, low-frequency and common variants with different functional consequences typically found in randomly sampled individuals from different populations.

Estimates of the overall numbers of variants with different sequence consequences are comparable to previous values<sup>1,20–22</sup> (Supplementary Table 14). However, only a fraction of these are likely to be functionally relevant. A more accurate picture of the number of functional variants is given by the number of variants segregating at conserved positions (here defined as sites with a genomic evolutionary rate profiling (GERP)<sup>19</sup> conservation score of >2), or where the function (for example, stop-gain variants) is strong and independent of conservation (Table 2). We find that individuals typically carry more than 2,500 non-synonymous variants at conserved positions, 20–40 variants identified as damaging<sup>24</sup> at conserved sites and about 150 loss-of-function (LOF) variants (stop-gains, frameshift indels in coding sequence and disruptions to essential splice sites). However, most of these are common (>5%) or low-frequency (0.5–5%), such that the numbers of rare (<0.5%) variants in these categories (which might be considered as pathological candidates) are much lower; 130–400 non-synonymous variants per individual, 10–20 LOF variants, 2–5 damaging mutations, and 1–2 variants identified previously from cancer genome sequencing<sup>25</sup>. By comparison with synonymous variants, we can estimate the excess of rare variants; those mutations that are sufficiently deleterious that they will never reach high frequency. We estimate that individuals carry an excess of 76–190 rare deleterious non-synonymous variants and up to 20 LOF and disease-associated variants. Interestingly, the overall excess of low-frequency variants is similar to that of rare variants (Table 2). Because many variants contributing to disease risk are likely to be segregating at low frequency, we recommend that variant frequency be considered when using the resource to identify pathological candidates.

The combination of variation data with information about regulatory function<sup>13</sup> can potentially improve the power to detect pathological

**Table 2 | Per-individual variant load at conserved sites**

Variant type	Number of derived variant sites per individual			Excess rare deleterious	Excess low-frequency deleterious
	Derived allele frequency across sample				
	<0.5%	0.5–5%	>5%		
All sites	30–150 K	120–680 K	3.6–3.9 M	ND	ND
Synonymous*	29–120	82–420	1.3–1.4 K	ND	ND
Non-synonymous*	130–400	240–910	2.3–2.7 K	76–190†	77–130†
Stop-gain*	3.9–10	5.3–19	24–28	3.4–7.5†	3.8–11†
Stop-loss	1.0–1.2	1.0–1.9	2.1–2.8	0.81–1.1†	0.80–1.0†
HGMD-DM*	2.5–5.1	4.8–17	11–18	1.6–4.7†	3.8–12†
COSMIC*	1.3–2.0	1.8–5.1	5.2–10	0.93–1.6†	1.3–2.0†
Indel frameshift	1.0–1.3	11–24	60–66	ND§	3.2–11†
Indel non-frameshift	2.1–2.3	9.5–24	67–71	ND§	0–0.73†
Splice site donor	1.7–3.6	2.4–7.2	2.6–5.2	1.6–3.3†	3.1–6.2†
Splice site acceptor	1.5–2.9	1.5–4.0	2.1–4.6	1.4–2.6†	1.2–3.3†
UTR*	120–430	300–1,400	3.5–4.0 K	0–350‡	0–1.2 K‡
Non-coding RNA*	3.9–17	14–70	180–200	0.62–2.6‡	3.4–13‡
Motif gain in TF peak*	4.7–14	23–59	170–180	0–2.6‡	3.8–15‡
Motif loss in TF peak*	18–69	71–300	580–650	7.7–22‡	37–110‡
Other conserved*	2.0–9.9 K	7.1–39 K	120–130 K	ND	ND
Total conserved	2.3–11 K	7.7–42 K	130–150 K	150–510	250–1.3 K

Only sites in which ancestral state can be assigned with high confidence are reported. The ranges reported are across populations. COSMIC, Catalogue of Somatic Mutations in Cancer; HGMD-DM, Human Gene Mutation Database (HGMD) disease-causing mutations; TF, transcription factor; ND, not determined.

\* Sites with GERP >2

† Using synonymous sites as a baseline.

‡ Using ‘other conserved’ as a baseline.

§ Rare indels were filtered in phase I.

non-coding variants. We find that individuals typically contain several thousand variants (and several hundred rare variants) in conserved (GERP conservation score  $>2$ ) untranslated regions (UTR), non-coding RNAs and transcription-factor-binding motifs (Table 2). Within experimentally defined transcription-factor-binding sites, individuals carry 700–900 conserved motif losses (for the transcription factors analysed, see Supplementary Information), of which 18–69 are rare ( $<0.5\%$ ) and show strong evidence for being selected against. Motif gains are rarer ( $\sim 200$  per individual at conserved sites), but they also show evidence for an excess of rare variants compared with conserved sites with no functional annotation (Table 2). Many of these changes are likely to have weak, slightly deleterious effects on gene regulation and function.

A second major use of the 1000 Genomes Project data in medical genetics is imputing genotypes in existing genome-wide association studies (GWAS)<sup>26</sup>. For common variants, the accuracy of using the phase I data to impute genotypes at sites not on the original GWAS SNP array is typically 90–95% in non-African and approximately 90% in African-ancestry genomes (Fig. 5a and Supplementary Fig. 14a), which is comparable to the accuracy achieved with high-quality benchmark haplotypes (Supplementary Fig. 14b). Imputation accuracy is similar for intergenic SNPs, exome SNPs, indels and large deletions (Supplementary Fig. 14c), despite the different amounts of information about such variants and accuracy of genotypes. For low-frequency variants (1–5%), imputed genotypes have between 60% and 90% accuracy in all populations, including those with admixed ancestry (also comparable to the accuracy from trio-phased haplotypes; Supplementary Fig. 14b).

Imputation has two primary uses: fine-mapping existing association signals and detecting new associations. GWAS have had only a few examples of successful fine-mapping to single causal variants<sup>27,28</sup>, often because of extensive haplotype structure within regions of association<sup>29,30</sup>. We find that, in Europeans, each previously reported GWAS signal<sup>31</sup> is, on average, in linkage disequilibrium ( $r^2 \geq 0.5$ ) with 56 variants: 51.5 SNPs and 4.5 indels. In 19% of cases at least one of these variants changes the coding sequence of a nearby gene (compared with 12% in control variants matched for frequency, distance to nearest gene and ascertainment in GWAS arrays) and in 65% of cases

at least one of these is at a site with GERP  $>2$  (68% in matched controls). The size of the associated region is typically  $<200$  kb in length (Fig. 5b). Our observations suggest that trans-ethnic fine-mapping experiments are likely to be especially valuable: among the 56 variants that are in strong linkage disequilibrium with a typical GWAS signal, approximately 15 show strong disequilibrium across our four continental groupings (Supplementary Table 15). Our current resource increases the number of variants in linkage disequilibrium with each GWAS signal by 25% compared with the pilot phase of the project and by greater than twofold compared with the HapMap resource.

## Discussion

The success of exome sequencing in Mendelian disease genetics<sup>32</sup> and the discovery of rare and low-frequency disease-associated variants in genes associated with complex diseases<sup>27,33,34</sup> strongly support the hypothesis that, in addition to factors such as epistasis<sup>35,36</sup> and gene-environment interactions<sup>37</sup>, many other genetic risk factors of substantial effect size remain to be discovered through studies of rare variation. The data generated by the 1000 Genomes Project not only aid the interpretation of all genetic-association studies, but also provide lessons on how best to design and analyse sequencing-based studies of disease.

The use and cost-effectiveness of collecting several data types (low-coverage whole-genome sequence, targeted exome data, SNP genotype data) for finding variants and reconstructing haplotypes are demonstrated here. Exome capture provides private and rare variants that are missed by low-coverage data (approximately 60% of the singleton variants in the sample were detected only from exome data compared with 5% detected only from low-coverage data; Supplementary Fig. 15). However, whole-genome data enable characterization of functional non-coding variation and accurate haplotype estimation, which are essential for the analysis of *cis*-effects around genes, such as those arising from variation in upstream regulatory regions<sup>38</sup>. There are also benefits from integrating SNP array data, for example, to improve genotype estimation<sup>39</sup> and to aid haplotype estimation where array data have been collected on additional family members. In principle, any sources of genotype information (for example, from array CGH) could be integrated using the statistical methods developed here.

Major methodological advances in phase I, including improved methods for detecting and genotyping variants<sup>40</sup>, statistical and machine-learning methods for evaluating the quality of candidate variant calls, modelling of genotype likelihoods and performing statistical haplotype integration<sup>41</sup>, have generated a high-quality resource. However, regions of low sequence complexity, satellite regions, large repeats and many large-scale structural variants, including copy-number polymorphisms, segmental duplications and inversions (which constitute most of the ‘inaccessible genome’), continue to present a major challenge for short-read technologies. Some issues are likely to be improved by methodological developments such as better modelling of read-level errors, integrating *de novo* assembly<sup>42,43</sup> and combining multiple sources of information to aid genotyping of structurally diverse regions<sup>40,44</sup>. Importantly, even subtle differences in data type, data processing or algorithms may lead to systematic differences in false-positive and false-negative error modes between samples. Such differences complicate efforts to compare genotypes between sequencing studies. Moreover, analyses that naively combine variant calls and genotypes across heterogeneous data sets are vulnerable to artefact. Analyses across multiple data sets must therefore either process them in standard ways or use meta-analysis approaches that combine association statistics (but not raw data) across studies.

Finally, the analysis of low-frequency variation demonstrates both the pervasive effects of purifying selection at functionally relevant sites in the genome and how this can interact with population history to lead to substantial local differentiation, even when standard metrics of structure such as  $F_{ST}$  are very small. The effect arises primarily

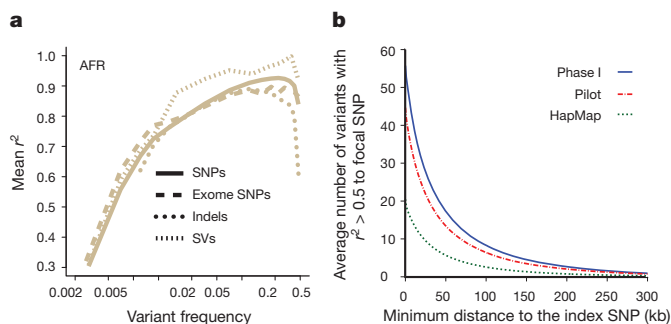


**Figure 5 | Implications of phase I 1000 Genomes Project data for GWAS.** **a**, Accuracy of imputation of genome-wide SNPs, exome SNPs and indels (using sites on the Illumina 1 M array) into ten individuals of African ancestry (three LWK, four Maaai from Kinyawa, Kenya (MKK), two YRI), sequenced to high coverage by an independent technology<sup>3</sup>. Only indels in regions of high sequence complexity with frequency  $>1\%$  are analysed. Deletion imputation accuracy estimated by comparison to array data<sup>46</sup> (note that this is for a different set of individuals, although with a similar ancestry, but included on the same plot for clarity). Accuracy measured by squared Pearson correlation coefficient between imputed and true dosage across all sites in a frequency range estimated from the 1000 Genomes data. Lines represent whole-genome SNPs (solid), exome SNPs (long dashes), short indels (dotted) and large deletions (short dashes). SV, structural variants. **b**, The average number of variants in linkage disequilibrium ( $r^2 > 0.5$  among EUR) to focal SNPs identified in GWAS<sup>47</sup> as a function of distance from the index SNP. Lines indicate the number of HapMap (green), pilot (red) and phase I (blue) variants.

because rare variants tend to be recent and thus geographically restricted<sup>6–8</sup>. The implication is that the interpretation of rare variants in individuals with a particular disease should be within the context of the local (either geographic or ancestry-based) genetic background. Moreover, it argues for the value of continuing to sequence individuals from diverse populations to characterize the spectrum of human genetic variation and support disease studies across diverse groups. A further 1,500 individuals from 12 new populations, including at least 15 high-depth trios, will form the final phase of this project.

## METHODS SUMMARY

All details concerning sample collection, data generation, processing and analysis can be found in the Supplementary Information. Supplementary Fig. 1 summarizes the process and indicates where relevant details can be found.

Received 4 July; accepted 1 October 2012.

- Tennessen, J. A. *et al.* Evolution and functional impact of rare coding variation from deep sequencing of human exomes. *Science* **337**, 64–69 (2012).
- The 1000 Genomes Project Consortium. A map of human genome variation from population-scale sequencing. *Nature* **467**, 1061–1073 (2010).
- Drmanac, R. *et al.* Human genome sequencing using unchained base reads on self-assembling DNA nanoarrays. *Science* **327**, 78–81 (2010).
- Mills, R. E. *et al.* Mapping copy number variation by population-scale genome sequencing. *Nature* **470**, 59–65 (2011).
- Marth, G. T. *et al.* The functional spectrum of low-frequency coding variation. *Genome Biol.* **12**, R84 (2011).
- Nelson, M. R. *et al.* An abundance of rare functional variants in 202 drug target genes sequenced in 14,002 people. *Science* **337**, 100–104 (2012).
- Mathieson, I. & McVean, G. Differential confounding of rare and common variants in spatially structured populations. *Nature Genet.* **44**, 243–246 (2012).
- Gravel, S. *et al.* Demographic history and rare allele sharing among human populations. *Proc. Natl Acad. Sci. USA* **108**, 11983–11988 (2011).
- The International HapMap Consortium. A second generation human haplotype map of over 3.1 million SNPs. *Nature* **449**, 851–861 (2007).
- Salmela, E. *et al.* Genome-wide analysis of single nucleotide polymorphisms uncovers population structure in Northern Europe. *PLoS ONE* **3**, e3519 (2008).
- Lupski, J. R., Belmont, J. W., Boerwinkle, E. & Gibbs, R. A. Clan genomics and the complex architecture of human disease. *Cell* **147**, 32–43 (2011).
- Lawson, D. J., Hellenthal, G., Myers, S. & Falush, D. Inference of population structure using dense haplotype data. *PLoS Genet.* **8**, e1002453 (2012).
- ENCODE Project Consortium. A user's guide to the encyclopedia of DNA elements (ENCODE). *PLoS Biol.* **9**, e1001046 (2011).
- Sasaki, K. *et al.* Expression cloning of a novel Gal $\beta$ (1–3/1–4)GlcNAc  $\alpha$ 2,3-sialyltransferase using lectin resistance selection. *J. Biol. Chem.* **268**, 22782–22787 (1993).
- Marth, G. *et al.* Sequence variations in the public human genome data reflect a bottlenecked population history. *Proc. Natl Acad. Sci. USA* **100**, 376–381 (2003).
- Keinan, A. & Clark, A. G. Recent explosive human population growth has resulted in an excess of rare genetic variants. *Science* **336**, 740–743 (2012).
- Hall, G. M. *Slavery and African Ethnicities in the Americas: Restoring the Links* (Univ. North Carolina Press, 2005).
- Bryc, K. *et al.* Genome-wide patterns of population structure and admixture in West Africans and African Americans. *Proc. Natl Acad. Sci. USA* **107**, 786–791 (2010).
- Davydov, E. V. *et al.* Identifying a high fraction of the human genome to be under selective constraint using GERP++. *PLoS Comput. Biol.* **6**, e1001025 (2010).
- Kanehisa, M., Goto, S., Sato, Y., Furumichi, M. & Tanabe, M. KEGG for integration and interpretation of large-scale molecular data sets. *Nucleic Acids Res.* **40**, D109–D114 (2012).
- Kim, T. H. *et al.* Analysis of the vertebrate insulator protein CTCF-binding sites in the human genome. *Cell* **128**, 1231–1245 (2007).
- Bamshad, M. J. *et al.* Exome sequencing as a tool for Mendelian disease gene discovery. *Nature Rev. Genet.* **12**, 745–755 (2011).
- Cancer Genome Atlas Research Network. Integrated genomic analyses of ovarian carcinoma. *Nature* **474**, 609–615 (2011).
- Stenson, P. D. *et al.* The Human Gene Mutation Database: 2008 update. *Genome Med.* **1**, 13 (2009).
- Forbes, S. A. *et al.* COSMIC: mining complete cancer genomes in the Catalogue of Somatic Mutations in Cancer. *Nucleic Acids Res.* **39**, D945–D950 (2011).
- Howie, B., Marchini, J. & Stephens, M. Genotype imputation with thousands of genomes. *G3 (Bethesda)* **1**, 457–470 (2011).
- Sanna, S. *et al.* Fine mapping of five loci associated with low-density lipoprotein cholesterol detects variants that double the explained heritability. *PLoS Genet.* **7**, e1002198 (2011).
- Gregory, A. P., Dendrou, C. A., Bell, J., McVean, G. & Fugger, L. TNF receptor 1 genetic risk mirrors outcome of anti-TNF therapy in multiple sclerosis. *Nature* **488**, 508–511 (2012).
- Hassanein, M. T. *et al.* Fine mapping of the association with obesity at the *FTO* locus in African-derived populations. *Hum. Mol. Genet.* **19**, 2907–2916 (2010).
- Maller, J., The Wellcome Trust Case Control Consortium. Fine mapping of 14 loci identified through genome-wide association analyses. *Nature Genet.* (in the press).
- Hindorf, L. A. *et al.* Potential etiologic and functional implications of genome-wide association loci for human diseases and traits. *Proc. Natl Acad. Sci. USA* **106**, 9362–9367 (2009).
- Bamshad, M. J. *et al.* The Centers for Mendelian Genomics: A new large-scale initiative to identify the genes underlying rare Mendelian conditions. *Am. J. Med. Genet. A.* (2012).
- Momozawa, Y. *et al.* Resequencing of positional candidates identifies low frequency *IL23R* coding variants protecting against inflammatory bowel disease. *Nature Genet.* **43**, 43–47 (2011).
- Raychaudhuri, S. *et al.* A rare penetrant mutation in *CFH* confers high risk of age-related macular degeneration. *Nature Genet.* **43**, 1232–1236 (2011).
- Strange, A. *et al.* A genome-wide association study identifies new psoriasis susceptibility loci and an interaction between *HLA-C* and *ERAP1*. *Nature Genet.* **42**, 985–990 (2010).
- Zuk, O., Hechter, E., Sunyaev, S. R. & Lander, E. S. The mystery of missing heritability: Genetic interactions create phantom heritability. *Proc. Natl Acad. Sci. USA* **109**, 1193–1198 (2012).
- Thomas, D. Gene-environment-wide association studies: emerging approaches. *Nature Rev. Genet.* **11**, 259–272 (2010).
- Degner, J. F. *et al.* DNase I sensitivity QTLs are a major determinant of human expression variation. *Nature* **482**, 390–394 (2012).
- Flannick, J. *et al.* Efficiency and power as a function of sequence coverage, SNP array density, and imputation. *PLOS Comput. Biol.* **8**, e1002604 (2012).
- Handsaker, R. E., Korn, J. M., Nemesh, J. & McCarroll, S. A. Discovery and genotyping of genome structural polymorphism by sequencing on a population scale. *Nature Genet.* **43**, 269–276 (2011).
- Li, Y., Sidore, C., Kang, H. M., Boehnke, M. & Abecasis, G. R. Low-coverage sequencing: implications for design of complex trait association studies. *Genome Res.* **21**, 940–951 (2011).
- Iqbal, Z., Caccamo, M., Turner, I., Flicek, P. & McVean, G. *De novo* assembly and genotyping of variants using colored de Bruijn graphs. *Nature Genet.* **44**, 226–232 (2012).
- Simpson, J. T. & Durbin, R. Efficient construction of an assembly string graph using the FM-index. *Bioinformatics* **26**, i367–i373 (2010).
- Sudmant, P. H. *et al.* Diversity of human copy number variation and multicopy genes. *Science* **330**, 641–646 (2010).
- Chambers, J. C. *et al.* Genetic loci influencing kidney function and chronic kidney disease. *Nature Genet.* **42**, 373–375 (2010).
- Conrad, D. F. *et al.* Origins and functional impact of copy number variation in the human genome. *Nature* **464**, 704–712 (2010).
- Hindorf, L. A. *et al.* A Catalog of Published Genome-Wide Association Studies. Available at <http://www.genome.gov/gwastudies> (accessed, September 2012).

Supplementary Information is available in the online version of the paper.

**Acknowledgements** We thank many people who contributed to this project: A. Naranjo, M. V. Parra and C. Duque for help with the collection of the Colombian samples; N. Kälin and F. Laplace for discussions; A. Schlattl and T. Zichner for assistance in managing data sets; E. Appelbaum, H. Arbery, E. Birney, S. Bumpstead, J. Camarata, J. Carey, G. Cochrane, M. DaSilva, S. Dökel, E. Drury, C. Duque, K. Gyaltsen, P. Jokinen, B. Lenz, S. Lewis, D. Lu, A. Naranjo, S. Ott, I. Padialeau, M. V. Parra, N. Patterson, A. Price, L. Sadzewicz, S. Schirner, N. Sengamalai, J. Sullivan, F. Ta, Y. Vaydylevich, O. Venn, K. Watkins and A. Yurovsky for assistance, discussion and advice. We thank the people who generously contributed their samples, from these populations: Yoruba in Ibadan, Nigeria; the Han Chinese in Beijing, China; the Japanese in Tokyo, Japan; the Utah CEPH community; the Luhya in Webuye, Kenya; people with African ancestry in the Southwest United States; the Tuscans in Italy; people with Mexican ancestry in Los Angeles, California; the Southern Han Chinese in China; the British in England and Scotland; the Finnish in Finland; the Iberian Populations in Spain; the Colombians in Medellín, Colombia; and the Puerto Ricans in Puerto Rico. This research was supported in part by Wellcome Trust grants WT098051 to R.M.D., M.E.H. and C.T.S.; WT090532/Z/09/Z, WT085475/Z/08/Z and WT095552/Z/11/Z to P.D.; WT086084/Z/08/Z and WT090532/Z/09/Z to G.A.M.; WT089250/Z/09/Z to I.M.; WT085532AIA to P.F.; Medical Research Council grant G0900747(91070) to G.A.M.; British Heart Foundation grant RG/09/12/28096 to C.A.A.; the National Basic Research Program of China (973 program no. 2011CB809201, 2011CB809202 and 2011CB809203); the Chinese 863 program (2012AA02A201); the National Natural Science Foundation of China (30890032, 31161130357); the Shenzhen Key Laboratory of Transomics Biotechnologies (CXB201108250096A); the Shenzhen Municipal Government of China (grants ZYC200903240080A and ZYC201105170397A); Guangdong Innovative Research Team Program (no. 2009010016); BMBF grant 01GS08201 to L.H.; BMBF grant 0315428A to R.H.; the Max Planck Society; Swiss National Science Foundation 31003A\_130342 to E.T.D.; Swiss National Science Foundation NCCR 'Frontiers in Genetics' grant to E.T.D.; Louis Jeantet Foundation grant to E.T.D.; Biotechnology and Biological Sciences Research Council (BBSRC) grant BB/I021213/1 to A.R.-L.; German Research Foundation (Emmy Noether Fellowship KO 4037/1-1) to J.O.K.; Netherlands Organization for Scientific Research VENI grant 639.021.125 to K.Y.; Beatrice Pinos Program grants 2006BP-A 10144 and 2009BP-B 00274 to M.V.; Israeli Science Foundation grant 04514831 to E.H.; Genome Québec and the Ministry of Economic Development, Innovation and Trade grant PSR-SIIRI-195 to P.A.W.; National Institutes of Health (NIH) grants U01HG5214, RC2HG5581 and R01MH84698 to G.R.A.; R01HG4719 and R01HG3698 to G.T.M.; RC2HG5552 and U01HG6513 to G.R.A. and G.T.M.; R01HG4960 and R01HG5701 to B.L.B.; U01HG5715 to C.D.B. and A.G.C.; T32GM8283 to D.C.I.; U01HG5208 to M.J.D.; U01HG6569 to M.A.D.; R01HG2898 and R01CA166661 to S.E.D.; U01HG5209, U01HG5725 and P41HG4221 to C.L.E.; P01HG4120 to E.E.E.; U01HG5728 to Yu.F.; U54HG3273 and U01HG5211 to R.A.G.;

R01HL95045 to S.B.G.; U41HG4568 to S.J.K.; P41HG2371 to W.J.K.; ES015794, AI077439, HL088133 and HL078885 to E.G.B.; RC2HL102925 to S.B.G. and D.M.A.; R01GM59290 to L.B.J. and M.A.B.; U54HG3067 to E.S.L. and S.B.G.; T15LM7033 to B.K.M.; T32HL94284 to J.L.R.-F.; DP2OD6514 and BAA-NIAID-DAIT-NIHAI2009061 to P.C.S.; T32GM7748 to X.S.; U54HG3079 to R.K.W.; UL1RR024131 to R.D.H.; HHSN268201100040C to the Coriell Institute for Medical Research; a Sandler Foundation award and an American Asthma Foundation award to E.G.B.; an IBM Open Collaborative Research Program award to Y.B.; an A.G. Leventis Foundation scholarship to D.K.X.; a Wolfson Royal Society Merit Award to P.Do.; a Howard Hughes Medical Institute International Fellowship award to P.H.S.; a grant from T. and V. Stanley to S.C.Y.; and a Mary Beryl Patch Turnbull Scholar Program award to K.C.B. E.H. is a faculty fellow of the Edmond J. Safra Bioinformatics program at Tel-Aviv University. E.E.E. and D.H. are investigators of the Howard Hughes Medical Institute. M.V.G. is a long-term fellow of EMBO.

**Author Contributions** Details of author contributions can be found in the author list.

**Author Information** All primary data, alignments, individual call sets, consensus call sets, integrated haplotypes with genotype likelihoods and supporting data including details of validation are available from the project website (<http://www.1000genomes.org>). Variant and haplotypes for specific genomic regions and specific samples can be viewed and downloaded through the project browser (<http://browser.1000genomes.org/>). Common project variants with no known medical impact have been compiled by dbSNP for filtering ([http://www.ncbi.nlm.nih.gov/variation/docs/human\\_variation\\_vcf/](http://www.ncbi.nlm.nih.gov/variation/docs/human_variation_vcf/)). The authors declare competing financial interests: details are available in the online version of the paper. Reprints and permissions information is available at [www.nature.com/reprints](http://www.nature.com/reprints). Readers are welcome to comment on the online version of the paper. Correspondence and requests for materials should be addressed to G.A.M. (mcvean@well.ox.ac.uk). This work is licensed under a Creative Commons Attribution-NonCommercial-ShareAlike 3.0 Unported licence. To view a copy of this licence, visit <http://creativecommons.org/licenses/by-nc-sa/3.0/>

**The 1000 Genomes Consortium** (Participants are arranged by project role, then by institution alphabetically, and finally alphabetically within institutions except for Principal Investigators and Project Leaders, as indicated.)

**Corresponding author** Gil A. McVean<sup>1,2</sup>

**Steering committee** David M. Altshuler<sup>3,4,5</sup> (Co-Chair), Richard M. Durbin<sup>6</sup> (Co-Chair), Gonçalo R. Abecasis<sup>7</sup>, David R. Bentley<sup>8</sup>, Aravinda Chakravarti<sup>9</sup>, Andrew G. Clark<sup>10</sup>, Peter Donnelly<sup>1,2</sup>, Evan E. Eichler<sup>1,1</sup>, Paul Flicek<sup>1,2</sup>, Stacey B. Gabriel<sup>3</sup>, Richard A. Gibbs<sup>13</sup>, Eric D. Green<sup>14</sup>, Matthew E. Hurles<sup>5</sup>, Bartha M. Knoppers<sup>15</sup>, Jan O. Korbel<sup>16</sup>, Eric S. Lander<sup>3</sup>, Charles Lee<sup>17</sup>, Hans Lehrach<sup>18,19</sup>, Elaine R. Mardis<sup>20</sup>, Gabor T. Marth<sup>21</sup>, Gil A. McVean<sup>1,2</sup>, Deborah A. Nickerson<sup>22</sup>, Jeanette P. Schmidt<sup>23</sup>, Stephen T. Sherry<sup>24</sup>, Jun Wang<sup>25,26,27</sup>, Richard K. Wilson<sup>20</sup>

**Production group: Baylor College of Medicine** Richard A. Gibbs<sup>13</sup> (Principal Investigator), Huyen Dinh<sup>13</sup>, Christie Kovar<sup>13</sup>, Sandra Lee<sup>13</sup>, Lora Lewis<sup>13</sup>, Donna Muzny<sup>13</sup>, Jeff Reid<sup>13</sup>, Min Wang<sup>13</sup>; **BGI-Shenzhen** Jun Wang<sup>25,26,27</sup> (Principal Investigator), Xiaodong Fang<sup>25</sup>, Xiaosen Guo<sup>25</sup>, Min Jian<sup>25</sup>, Hui Jiang<sup>25</sup>, Xin Jin<sup>25</sup>, Guoqing Li<sup>25</sup>, Jingxiang Li<sup>25</sup>, Yingrui Li<sup>25</sup>, Zhuo Li<sup>25</sup>, Xiao Liu<sup>25</sup>, Yao Lu<sup>25</sup>, Xuedi Ma<sup>25</sup>, Zhe Su<sup>25</sup>, Shuaishuai Tai<sup>25</sup>, Meifang Tang<sup>25</sup>, Bo Wang<sup>25</sup>, Guangbiao Wang<sup>25</sup>, Honglong Wu<sup>25</sup>, Renhua Wu<sup>25</sup>, Ye Yin<sup>25</sup>, Wenwei Zhang<sup>25</sup>, Jiao Zhao<sup>25</sup>, Meiru Zhao<sup>25</sup>, Xiaole Zheng<sup>25</sup>, Yan Zhou<sup>25</sup>; **Broad Institute of MIT and Harvard** Eric S. Lander<sup>3</sup> (Principal Investigator), David M. Altshuler<sup>3,4,5</sup>, Stacey B. Gabriel<sup>3</sup> (Co-Chair), Namrata Gupta<sup>3</sup>; **European Bioinformatics Institute** Paul Flicek<sup>12</sup> (Principal Investigator), Laura Clarke<sup>12</sup>, Rasko Leinonen<sup>12</sup>, Richard E. Smith<sup>12</sup>, Xiangqun Zheng-Bradley<sup>12</sup>; **illumina** David R. Bentley<sup>8</sup> (Principal Investigator), Russell Grocock<sup>8</sup>, Sean Humphray<sup>8</sup>, Terena James<sup>8</sup>, Zoya Kingsbury<sup>8</sup>; **Max Planck Institute for Molecular Genetics** Hans Lehrach<sup>18,19</sup> (Principal Investigator), Ralf Sudbrak<sup>18</sup> (Project Leader), Marcus W. Albrecht<sup>28</sup>, Vyacheslav S. Amstislavskiy<sup>18</sup>, Tatiana A. Borodina<sup>28</sup>, Matthias Lienhard<sup>18</sup>, Florian Mertes<sup>18</sup>, Marc Sultan<sup>18</sup>, Bernd Timmermann<sup>18</sup>, Marie-Laure Yaspo<sup>18</sup>; **US National Institutes of Health** Stephen T. Sherry<sup>24</sup> (Principal Investigator); **University of Oxford** Gil A. McVean<sup>1,2</sup> (Principal Investigator); **Washington University in St Louis** Elaine R. Mardis<sup>20</sup> (Co-Principal Investigator) (Co-Chair), Richard K. Wilson<sup>20</sup> (Co-Principal Investigator), Lucinda Fulton<sup>20</sup>, Robert Fulton<sup>20</sup>, George M. Weinstock<sup>20</sup>; **Wellcome Trust Sanger Institute** Richard M. Durbin<sup>6</sup> (Principal Investigator), Senduran Balasubramanian<sup>6</sup>, John Burton<sup>6</sup>, Petr Danecek<sup>6</sup>, Thomas M. Keane<sup>6</sup>, Anja Kolb-Kocokinski<sup>6</sup>, Shane McCarthy<sup>6</sup>, James Stalker<sup>6</sup>, Michael Quail<sup>6</sup>

**Analysis group: Affymetrix** Jeanette P. Schmidt<sup>23</sup> (Principal Investigator), Christopher J. Davies<sup>23</sup>, Jeremy Gollub<sup>23</sup>, Teresa Webster<sup>23</sup>, Brant Wong<sup>23</sup>, Yiping Zhan<sup>23</sup>; **Albert Einstein College of Medicine** Adam Auton<sup>29</sup> (Principal Investigator); **Baylor College of Medicine** Richard A. Gibbs<sup>13</sup> (Principal Investigator), Fuli Yu<sup>13</sup> (Project Leader), Matthew Bainbridge<sup>13</sup>, Danny Challis<sup>13</sup>, Uday S. Evani<sup>13</sup>, James Lu<sup>13</sup>, Donna Muzny<sup>13</sup>, Uma Nagaswamy<sup>13</sup>, Jeff Reid<sup>13</sup>, Aniko Sabo<sup>13</sup>, Yi Wang<sup>13</sup>, Jin Yu<sup>13</sup>; **BGI-Shenzhen** Jun Wang<sup>25,26,27</sup> (Principal Investigator), Lachlan J. M. Coin<sup>25</sup>, Lin Fang<sup>25</sup>, Xiaosen Guo<sup>25</sup>, Xin Jin<sup>25</sup>, Guoqing Li<sup>25</sup>, Qibin Li<sup>25</sup>, Yingrui Li<sup>25</sup>, Zhenyu Li<sup>25</sup>, Haoxiang Lin<sup>25</sup>, Binghang Liu<sup>25</sup>, Ruibang Luo<sup>25</sup>, Nan Qin<sup>25</sup>, Haojing Shao<sup>25</sup>, Bingqiang Wang<sup>25</sup>, Yinfeng Xie<sup>25</sup>, Chen Ye<sup>25</sup>, Chang Yu<sup>25</sup>, Fan Zhang<sup>25</sup>, Hancheng Zheng<sup>25</sup>, Hongmei Zhu<sup>25</sup>; **Boston College** Gabor T. Marth<sup>21</sup> (Principal Investigator), Erik P. Garrison<sup>21</sup>, Deniz Kural<sup>21</sup>, Wan-Ping Lee<sup>21</sup>, Wen Fung Leong<sup>21</sup>, Alistair N. Ward<sup>21</sup>, Jiantao Wu<sup>21</sup>, Mengyao

Zhang<sup>21</sup>; **Brigham and Women's Hospital** Charles Lee<sup>17</sup> (Principal Investigator), Lauren Griffin<sup>17</sup>, Chih-Heng Hsieh<sup>17</sup>, Ryan E. Mills<sup>17,30</sup>, Xinghua Shi<sup>17</sup>, Marcin von Grotthuss<sup>17</sup>, Chengsheng Zhang<sup>17</sup>; **Broad Institute of MIT and Harvard** Mark J. Daly<sup>3</sup> (Principal Investigator), Mark A. DePristo<sup>3</sup> (Project Leader), David M. Altshuler<sup>3,4,5</sup>, Eric Banks<sup>3</sup>, Gaurav Bhatia<sup>3</sup>, Mauricio O. Carneiro<sup>3</sup>, Guillermo del Angel<sup>3</sup>, Stacey B. Gabriel<sup>3</sup>, Giulio Genovese<sup>3</sup>, Namrata Gupta<sup>3</sup>, Robert E. Handsaker<sup>3,5</sup>, Chris Hartl<sup>3</sup>, Eric S. Lander<sup>3</sup>, Steven A. McCarroll<sup>3</sup>, James C. Nemesh<sup>3</sup>, Ryan E. Poplin<sup>3</sup>, Stephen F. Schaffner<sup>3</sup>, Khalid Shakir<sup>3</sup>; **Cold Spring Harbor Laboratory** Seungtae C. Yoon<sup>31</sup> (Principal Investigator), Jayon Lihm<sup>31</sup>, Vladimir Makarov<sup>32</sup>; **Dankook University** Hanjun Jin<sup>33</sup> (Principal Investigator), Wook Kim<sup>34</sup>, Ki Cheol Kim<sup>34</sup>; **European Molecular Biology Laboratory** Jan O. Korbel<sup>16</sup> (Principal Investigator), Tobias Rausch<sup>16</sup>; **European Bioinformatics Institute** Paul Flicek<sup>12</sup> (Principal Investigator), Kathryn Beal<sup>12</sup>, Laura Clarke<sup>12</sup>, Fiona Cunningham<sup>12</sup>, Javier Herrero<sup>12</sup>, William M. McLaren<sup>12</sup>, Graham R. S. Ritchie<sup>12</sup>, Richard E. Smith<sup>12</sup>, Xiangqun Zheng-Bradley<sup>12</sup>; **Cornell University** Andrew G. Clark<sup>10</sup> (Principal Investigator), Srikanth Gottipati<sup>35</sup>, Alon Keinan<sup>10</sup>, Juan L. Rodriguez-Flores<sup>10</sup>; **Harvard University** Pardis C. Sabett<sup>3,36</sup> (Principal Investigator), Sharon R. Grossman<sup>3,36</sup>, Shervin Tabrizi<sup>3,36</sup>, Ridhi Tariyal<sup>3,36</sup>; **Human Gene Mutation Database** David N. Cooper<sup>37</sup> (Principal Investigator), Edward V. Ball<sup>37</sup>, Peter D. Stenson<sup>37</sup>; **illumina** David R. Bentley<sup>8</sup> (Principal Investigator), Bret Barnes<sup>38</sup>, Markus Bauer<sup>8</sup>, R. Keira Cheetham<sup>8</sup>, Tony Cox<sup>8</sup>, Michael Eberle<sup>8</sup>, Sean Humphray<sup>8</sup>, Scott Kahn<sup>38</sup>, Lisa Murray<sup>8</sup>, John Peden<sup>8</sup>, Richard Shaw<sup>8</sup>; **Leiden University Medical Center** Kai Ye<sup>39</sup> (Principal Investigator); **Louisiana State University** Mark A. Batzer<sup>40</sup> (Principal Investigator), Miriam K. Konkel<sup>40</sup>, Jerilyn A. Walker<sup>40</sup>; **Massachusetts General Hospital** Daniel G. MacArthur<sup>41</sup> (Principal Investigator), Monkol Lek<sup>41</sup>; **Max Planck Institute for Molecular Genetics** Ralf Sudbrak<sup>18</sup> (Project Leader), Vyacheslav S. Amstislavskiy<sup>18</sup>, Ralf Herwig<sup>18</sup>; **Pennsylvania State University** Mark D. Shriver<sup>42</sup> (Principal Investigator); **Stanford University** Carlos D. Bustamante<sup>43</sup> (Principal Investigator), Jake K. Byrnes<sup>44</sup>, Francisco M. De La Vega<sup>10</sup>, Simon Gravel<sup>43</sup>, Eimear E. Kenny<sup>43</sup>, Jeffrey M. Kidd<sup>43</sup>, Phil Lacroute<sup>43</sup>, Brian K. Maples<sup>43</sup>, Andres Moreno-Estrada<sup>43</sup>, Fouad Zakharia<sup>43</sup>; **Tel-Aviv University** Eran Halperin<sup>45,46,47</sup> (Principal Investigator), Yael Baran<sup>45</sup>; **Translational Genomics Research Institute** David W. Craig<sup>48</sup> (Principal Investigator), Alexis Christoforides<sup>48</sup>, Nils Homer<sup>49</sup>, Tyler Izatt<sup>48</sup>, Ahmet A. Kurdoglu<sup>48</sup>, Shripad A. Sinar<sup>48</sup>, Kevin Squire<sup>50</sup>; **US National Institutes of Health** Stephen T. Sherry<sup>24</sup> (Principal Investigator), Chunlin Xiao<sup>24</sup>; **University of California, San Diego** Jonathan Sebat<sup>51,52</sup> (Principal Investigator), Vineet Bafna<sup>53</sup>, Kenny Ye<sup>54</sup>; **University of California, San Francisco** Esteban G. Burchard<sup>55</sup> (Principal Investigator), Ryan D. Hernandez<sup>55</sup> (Principal Investigator), Christopher R. Gignoux<sup>55</sup>; **University of California, Santa Cruz** David Haussler<sup>56,57</sup> (Principal Investigator), Sol J. Katzman<sup>56</sup>, W. James Kent<sup>56</sup>; **University of Chicago** Bryan Howie<sup>58</sup>; **University College London** Andres Ruiz-Linares<sup>59</sup> (Principal Investigator); **University of Geneva** Emmanouil T. Dermitzakis<sup>60,61,62</sup> (Principal Investigator), Tuuli Lappalainen<sup>60,61,62</sup>; **University of Maryland School of Medicine** Scott E. Devine<sup>63</sup> (Principal Investigator), Xinyue Liu<sup>63</sup>, Ankit Maroo<sup>63</sup>, Luke J. Tallon<sup>63</sup>; **University of Medicine and Dentistry of New Jersey** Jeffrey A. Rosenfeld<sup>64,65</sup> (Principal Investigator), Leslie P. Michelson<sup>64</sup>; **University of Michigan** Gonçalo R. Abecasis<sup>7</sup> (Principal Investigator) (Co-Chair), Hyun Min Kang<sup>7</sup> (Project Leader), Paul Anderson<sup>7</sup>, Andrea Angius<sup>66</sup>, Abigail Bigham<sup>67</sup>, Tom Blackwell<sup>1</sup>, Fabio Busonero<sup>7,66,68</sup>, Francesco Cucca<sup>66,68</sup>, Christian Fuchsberger<sup>7</sup>, Chris Jones<sup>69</sup>, Goo Jun<sup>7</sup>, Yun Li<sup>70</sup>, Robert Lyons<sup>71</sup>, Andrea Maschio<sup>7,66,68</sup>, Eleonora Porcu<sup>7,66,68</sup>, Fred Reinier<sup>69</sup>, Serena Sanna<sup>66</sup>, David Schlesinger<sup>72</sup>, Carlo Sidore<sup>7,66,68</sup>, Adrian Tan<sup>7</sup>, Mary Kate Trost<sup>7</sup>; **University of Montréal** Philip Awadalla<sup>73</sup> (Principal Investigator), Alan Hodgkinson<sup>73</sup>; **University of Oxford** Gerton Lunter<sup>1</sup> (Principal Investigator), Gil A. McVean<sup>1,2</sup> (Principal Investigator) (Co-Chair), Jonathan L. Marchini<sup>1,2</sup> (Principal Investigator), Simon Myers<sup>1,2</sup> (Principal Investigator), Claire Churchhouse<sup>2</sup>, Olivier Delaneau<sup>2</sup>, Anjali Gupta-Hinch<sup>1</sup>, Zamin Iqbal<sup>1</sup>, Iain Mathieson<sup>1</sup>, Andy Rimmer<sup>1</sup>, Dionysia K. Xifara<sup>1</sup>; **University of Puerto Rico** Taras K. Oleksyk<sup>74</sup> (Principal Investigator); **University of Texas Health Sciences Center at Houston** Yunxin Fu<sup>75</sup> (Principal Investigator), Xiaoming Liu<sup>75</sup>, Momiao Xiong<sup>75</sup>; **University of Utah** Lynn Jorde<sup>76</sup> (Principal Investigator), David Witherspoon<sup>76</sup>, Jinchuan Xing<sup>77</sup>; **University of Washington** Evan E. Eichler<sup>11</sup> (Principal Investigator), Brian L. Browning<sup>78</sup> (Principal Investigator), Can Alkan<sup>22,79</sup>, Iman Hajirasouliha<sup>80</sup>, Fereydoon Hormozdizadeh<sup>22</sup>, Arthur Ko<sup>22</sup>, Peter H. Sudmant<sup>22</sup>; **Washington University in St Louis** Elaine R. Mardis<sup>20</sup> (Co-Principal Investigator), Ken Chen<sup>81</sup>, Asif Chinwalla<sup>20</sup>, Li Ding<sup>20</sup>, David Dooling<sup>20</sup>, Daniel C. Koboldt<sup>20</sup>, Michael D. McLellan<sup>20</sup>, John W. Wallis<sup>20</sup>, Michael C. Wendt<sup>20</sup>, Qunyan Zhang<sup>20</sup>; **Wellcome Trust Sanger Institute** Richard M. Durbin<sup>6</sup> (Principal Investigator), Matthew E. Hurles<sup>6</sup> (Principal Investigator), Chris Tyler-Smith<sup>6</sup> (Principal Investigator), Cornelis A. Albers<sup>82</sup>, Qasim Ayub<sup>6</sup>, Senduran Balasubramanian<sup>6</sup>, Yuan Chen<sup>6</sup>, Alison J. Coffey<sup>6</sup>, Vincenza Colonna<sup>6,83</sup>, Petr Danecek<sup>6</sup>, Ni Huang<sup>6</sup>, Luke Jostins<sup>6</sup>, Thomas M. Keane<sup>6</sup>, Heng Li<sup>3,6</sup>, Shane McCarthy<sup>6</sup>, Aylwyn Scally<sup>6</sup>, James Stalker<sup>6</sup>, Klaudia Walter<sup>6</sup>, Yali Xue<sup>6</sup>, Yujun Zhang<sup>6</sup>; **Yale University** Mark B. Gerstein<sup>84,85,86</sup> (Principal Investigator), Alexei Abyzov<sup>84,86</sup>, Suganthi Balasubramanian<sup>86</sup>, Jieming Chen<sup>84</sup>, Declan Clarke<sup>87</sup>, Yao Fu<sup>84</sup>, Lukas Habegger<sup>84</sup>, Arif O. Harmanci<sup>84</sup>, Mike Jin<sup>86</sup>, Ekta Khurana<sup>86</sup>, Xinmeng Jasmine Mu<sup>84</sup>, Cristina Sisu<sup>84</sup>

**Structural variation group: BGI-Shenzhen** Yingrui Li<sup>25</sup>, Ruibang Luo<sup>25</sup>, Hongmei Zhu<sup>25</sup>; **Brigham and Women's Hospital** Charles Lee<sup>17</sup> (Principal Investigator) (Co-Chair), Lauren Griffin<sup>17</sup>, Chih-Heng Hsieh<sup>17</sup>, Ryan E. Mills<sup>17,30</sup>, Xinghua Shi<sup>17</sup>, Marcin von Grotthuss<sup>17</sup>, Chengsheng Zhang<sup>17</sup>; **Boston College** Gabor T. Marth<sup>21</sup> (Principal Investigator), Erik P. Garrison<sup>21</sup>, Deniz Kural<sup>21</sup>, Wan-Ping Lee<sup>21</sup>, Alistair N. Ward<sup>21</sup>, Jiantao Wu<sup>21</sup>, Mengyao Zhang<sup>21</sup>; **Broad Institute of MIT and Harvard** Steven A. McCarroll<sup>3</sup> (Project Leader), David M. Altshuler<sup>3,4,5</sup>, Eric Banks<sup>3</sup>, Guillermo del Angel<sup>3</sup>, Giulio Genovese<sup>3</sup>, Robert E. Handsaker<sup>3,5</sup>, Chris Hartl<sup>3</sup>, James C. Nemesh<sup>3</sup>, Khalid Shakir<sup>3</sup>; **Cold Spring Harbor Laboratory** Seungtae C. Yoon<sup>31</sup> (Principal Investigator), Jayon Lihm<sup>31</sup>, Vladimir Makarov<sup>32</sup>; **Cornell University** Jeremiah Degenhardt<sup>10</sup>; **European Bioinformatics Institute** Paul Flicek<sup>12</sup> (Principal Investigator), Laura Clarke<sup>12</sup>, Richard E. Smith<sup>12</sup>, Xiangqun Zheng-Bradley<sup>12</sup>;

**European Molecular Biology Laboratory** Jan O. Korbel<sup>16</sup> (Principal Investigator) (Co-Chair), Tobias Rausch<sup>16</sup>, Adrian M. Stütz<sup>16</sup>, **illumina** David R. Bentley<sup>2</sup> (Principal Investigator), Bret Barnes<sup>38</sup>, R. Keira Cheetham<sup>8</sup>, Michael Eberle<sup>8</sup>, Sean Humphray<sup>8</sup>, Scott Kahn<sup>38</sup>, Lisa Murray<sup>8</sup>, Richard Shaw<sup>8</sup>; **Leiden University Medical Center** Kai Ye<sup>39</sup> (Principal Investigator); **Louisiana State University** Mark A. Batzer<sup>40</sup> (Principal Investigator), Miriam K. Konkel<sup>40</sup>, Jerilyn A. Walker<sup>40</sup>; **Stanford University** Phil Lacroute<sup>43</sup>; **Translational Genomics Research Institute** David W. Craig<sup>48</sup> (Principal Investigator), Nils Homer<sup>49</sup>; **US National Institutes of Health** Deanna Church<sup>24</sup>, Chunlin Xiao<sup>24</sup>; **University of California, San Diego** Jonathan Sebat<sup>51,52</sup> (Principal Investigator), Vineet Bafna<sup>53</sup>, Jacob J. Michaelson<sup>58</sup>, Kenny Ye<sup>54</sup>; **University of Maryland School of Medicine** Scott E. Devine<sup>63</sup> (Principal Investigator), Xinyue Liu<sup>63</sup>, Ankit Maroo<sup>63</sup>, Luke J. Tallon<sup>63</sup>; **University of Oxford** Gerton Lunter<sup>1</sup> (Principal Investigator), Gil A. McVean<sup>1,2</sup> (Principal Investigator), Zamin Iqbal<sup>1</sup>; **University of Utah** David Witherspoon<sup>76</sup>, Jinchuan Xing<sup>77</sup>; **University of Washington** Evan E. Eichler<sup>11</sup> (Principal Investigator) (Co-Chair), Can Alkan<sup>22,79</sup>, Iman Hajirasouliha<sup>80</sup>, Fereydoon Hormozdian<sup>22</sup>, Arthur Ko<sup>22</sup>, Peter H. Sudmant<sup>22</sup>; **Washington University in St Louis** Ken Chen<sup>81</sup>, Asif Chinwalla<sup>20</sup>, Li Ding<sup>20</sup>, Michael D. McLellan<sup>20</sup>, John W. Wallis<sup>20</sup>; **Wellcome Trust Sanger Institute** Matthew E. Hurles<sup>6</sup> (Principal Investigator) (Co-Chair), Ben Blackburne<sup>6</sup>, Heng Li<sup>3,6</sup>, Sarah J. Lindsay<sup>6</sup>, Zemin Ning<sup>6</sup>, Aylwyn Scally<sup>6</sup>, Klaudia Walter<sup>6</sup>, Yujun Zhang<sup>6</sup>; **Yale University** Mark B. Gerstein<sup>84,85,86</sup> (Principal Investigator), Alexej Abyzov<sup>84,86</sup>, Jieming Chen<sup>84</sup>, Declan Clarke<sup>87</sup>, Ekta Khurana<sup>86</sup>, Xinmeng Jasmine Mu<sup>84</sup>, Cristina Sisu<sup>84</sup>

**Exome group: Baylor College of Medicine** Richard A. Gibbs<sup>13</sup> (Principal Investigator) (Co-Chair), Fuli Yu<sup>13</sup> (Project Leader), Matthew Bainbridge<sup>13</sup>, Danny Challis<sup>13</sup>, Uday S. Evani<sup>13</sup>, Christie Kovar<sup>13</sup>, Lora Lewis<sup>13</sup>, James Lu<sup>13</sup>, Donna Muzny<sup>13</sup>, Uma Nagaswamy<sup>13</sup>, Jeff Reid<sup>13</sup>, Aniko Sabo<sup>13</sup>, Jin Yu<sup>13</sup>; **BGI-Shenzhen** Xiaosen Guo<sup>25</sup>, Yingrui Li<sup>25</sup>, Renhua Wu<sup>25</sup>; **Boston College** Gabor T. Marth<sup>21</sup> (Principal Investigator) (Co-Chair), Erik P. Garrison<sup>21</sup>, Wen Fung Leong<sup>21</sup>, Alistair N. Ward<sup>21</sup>; **Broad Institute of MIT and Harvard** Guillermo del Angel<sup>3</sup>, Mark A. DePristo<sup>3</sup>, Stacey B. Gabriel<sup>3</sup>, Namrata Gupta<sup>3</sup>, Chris Hart<sup>3</sup>, Ryan E. Poplin<sup>3</sup>; **Cornell University** Andrew G. Clark<sup>10</sup> (Principal Investigator), Juan L. Rodriguez-Flores<sup>10</sup>; **European Bioinformatics Institute** Paul Flicek<sup>12</sup> (Principal Investigator), Laura Clarke<sup>12</sup>, Richard E. Smith<sup>12</sup>, Xiangqun Zheng-Bradley<sup>12</sup>; **Massachusetts General Hospital** Daniel G. MacArthur<sup>41</sup> (Principal Investigator); **Stanford University** Carlos D. Bustamante<sup>43</sup> (Principal Investigator), Simon Gravel<sup>43</sup>; **Translational Genomics Research Institute** David W. Craig<sup>48</sup> (Principal Investigator), Alexis Christoforides<sup>48</sup>, Nils Homer<sup>49</sup>, Tyler Izatt<sup>48</sup>; **US National Institutes of Health** Stephen T. Sherry<sup>24</sup> (Principal Investigator), Chunlin Xiao<sup>24</sup>; **University of Geneva** Emmanouil T. Dermitzakis<sup>60,61,62</sup> (Principal Investigator); **University of Michigan** Gonçalo R. Abecasis<sup>7</sup> (Principal Investigator), Hyun Min Kang<sup>7</sup>; **University of Oxford** Gil A. McVean<sup>1,2</sup> (Principal Investigator); **Washington University in St Louis** Elaine R. Mardis<sup>20</sup> (Principal Investigator), David Dooling<sup>20</sup>, Lucinda Fulton<sup>20</sup>, Robert Fulton<sup>20</sup>, Daniel C. Koboldt<sup>20</sup>; **Wellcome Trust Sanger Institute** Richard M. Durbin<sup>6</sup> (Principal Investigator), Senduran Balasubramaniam<sup>6</sup>, Thomas M. Keane<sup>6</sup>, Shane McCarthy<sup>6</sup>, James Stalker<sup>6</sup>; **Yale University** Mark B. Gerstein<sup>84,85,86</sup> (Principal Investigator), Suganthi Balasubramanian<sup>86</sup>, Lukas Habegger<sup>84</sup>

**Functional interpretation group: Boston College** Erik P. Garrison<sup>21</sup>; **Baylor College of Medicine** Richard A. Gibbs<sup>13</sup> (Principal Investigator), Matthew Bainbridge<sup>13</sup>, Donna Muzny<sup>13</sup>, Fuli Yu<sup>13</sup>, Jin Yu<sup>13</sup>; **Broad Institute of MIT and Harvard** Guillermo del Angel<sup>3</sup>, Robert E. Handsaker<sup>3,5</sup>; **Cold Spring Harbor Laboratory** Vladimir Makarov<sup>32</sup>; **Cornell University** Juan L. Rodriguez-Flores<sup>10</sup>; **Dankook University** Hanjun Jin<sup>33</sup> (Principal Investigator), Wook Kim<sup>34</sup>, Ki Cheol Kim<sup>34</sup>; **European Bioinformatics Institute** Paul Flicek<sup>12</sup> (Principal Investigator), Kathryn Beal<sup>12</sup>, Laura Clarke<sup>12</sup>, Fiona Cunningham<sup>12</sup>, Javier Herrero<sup>12</sup>, William M. McLaren<sup>12</sup>, Graham R. S. Ritchie<sup>12</sup>, Xiangqun Zheng-Bradley<sup>12</sup>; **Harvard University** Shervin Tabrizi<sup>3,36</sup>; **Massachusetts General Hospital** Daniel G. MacArthur<sup>41</sup> (Principal Investigator), Monkol Lek<sup>41</sup>; **Stanford University** Carlos D. Bustamante<sup>43</sup> (Principal Investigator), Francisco M. De La Vega<sup>10</sup>; **Translational Genomics Research Institute** David W. Craig<sup>48</sup> (Principal Investigator), Ahmet A. Kurdoglu<sup>48</sup>; **University of Geneva** Tuuli Lappalainen<sup>60,61,62</sup>; **University of Medicine and Dentistry of New Jersey** Jeffrey A. Rosenfeld<sup>64,65</sup> (Principal Investigator), Leslie P. Michelson<sup>64,65</sup>; **University of Montréal** Philip Awadalla<sup>73</sup> (Principal Investigator), Alan Hodgkinson<sup>73</sup>; **University of Oxford** Gil A. McVean<sup>1,2</sup> (Principal Investigator); **Washington University in St Louis** Ken Chen<sup>81</sup>; **Wellcome Trust Sanger Institute** Chris Tyler-Smith<sup>6</sup> (Principal Investigator) (Co-Chair), Yuan Chen<sup>6</sup>, Vincenza Colonna<sup>6,83</sup>, Adam Frankish<sup>6</sup>, Jennifer Harrow<sup>6</sup>, Yali Xue<sup>6</sup>; **Yale University** Mark B. Gerstein<sup>84,85,86</sup> (Principal Investigator) (Co-Chair), Alexej Abyzov<sup>84,86</sup>, Suganthi Balasubramanian<sup>86</sup>, Jieming Chen<sup>84</sup>, Declan Clarke<sup>87</sup>, Yao Fu<sup>84</sup>, Arif O. Harmanci<sup>84</sup>, Mike Jin<sup>86</sup>, Ekta Khurana<sup>86</sup>, Xinmeng Jasmine Mu<sup>84</sup>, Cristina Sisu<sup>84</sup>

**Data coordination centre group: Baylor College of Medicine** Richard A. Gibbs<sup>13</sup> (Principal Investigator), Gerald Fowler<sup>13</sup>, Walker Hale<sup>13</sup>, Divya Kalra<sup>13</sup>, Christie Kovar<sup>13</sup>, Donna Muzny<sup>13</sup>, Jeff Reid<sup>13</sup>; **BGI-Shenzhen** Xun Wang<sup>25,26,27</sup> (Principal Investigator), Xiaosen Guo<sup>25</sup>, Guoqing Li<sup>25</sup>, Yingrui Li<sup>25</sup>, Xiaole Zheng<sup>25</sup>; **Broad Institute of MIT and Harvard** David M. Altshuler<sup>3,4,5</sup>; **European Bioinformatics Institute** Paul Flicek<sup>12</sup> (Principal Investigator) (Co-Chair), Laura Clarke<sup>12</sup> (Project Leader), Jonathan Barker<sup>12</sup>, Gavin Kelman<sup>12</sup>, Eugene Kulesha<sup>12</sup>, Rasko Leinonen<sup>12</sup>, William M. McLaren<sup>12</sup>, Rajesh Radhakrishnan<sup>12</sup>, Asier Roa<sup>12</sup>, Dmitriy Smirnov<sup>12</sup>, Richard E. Smith<sup>12</sup>, Ian Streeter<sup>12</sup>, Iliana Toneva<sup>12</sup>, Brendan Vaughan<sup>12</sup>, Xiangqun Zheng-Bradley<sup>12</sup>; **illumina** David R. Bentley<sup>2</sup> (Principal Investigator), Tony Cox<sup>8</sup>, Sean Humphray<sup>8</sup>, Scott Kahn<sup>38</sup>; **Max Planck Institute for Molecular Genetics** Ralf Sudbrak<sup>18</sup> (Project Leader), Marcus W. Albrecht<sup>29</sup>, Matthias Lienhard<sup>18</sup>; **Translational Genomics Research Institute** David W. Craig<sup>48</sup> (Principal Investigator), Tyler Izatt<sup>48</sup>, Ahmet A. Kurdoglu<sup>48</sup>; **US National Institutes of Health** Stephen T. Sherry<sup>24</sup> (Principal Investigator) (Co-Chair), Victor Ananiev<sup>24</sup>, Zinaida Belait<sup>24</sup>, Dimitriy Beloslyudtsev<sup>24</sup>, Nathan Bouk<sup>24</sup>, Chao Chen<sup>24</sup>, Deanna Church<sup>24</sup>, Robert Cohen<sup>24</sup>, Charles Cook<sup>24</sup>, John Garner<sup>24</sup>, Timothy

Hefferon<sup>24</sup>, Mikhail Kimelman<sup>24</sup>, Chunlei Liu<sup>24</sup>, John Lopez<sup>24</sup>, Peter Meric<sup>24</sup>, Chris O'Sullivan<sup>89</sup>, Yuri Ostapchuk<sup>24</sup>, Lon Phan<sup>24</sup>, Sergiy Ponomarev<sup>24</sup>, Valerie Schneider<sup>24</sup>, Eugene Shekhtman<sup>24</sup>, Karl Sirotkin<sup>24</sup>, Douglas Slotta<sup>24</sup>, Chunlin Xiao<sup>24</sup>, Hua Zhang<sup>24</sup>; **University of California, Santa Cruz** David Haussler<sup>56,57</sup> (Principal Investigator); **University of Michigan** Gonçalo R. Abecasis<sup>7</sup> (Principal Investigator); **University of Oxford** Gil A. McVean<sup>1,2</sup> (Principal Investigator); **University of Washington** Can Alkan<sup>22,79</sup>, Arthur Ko<sup>22</sup>; **Washington University in St Louis** David Dooling<sup>20</sup>; **Wellcome Trust Sanger Institute** Richard M. Durbin<sup>6</sup> (Principal Investigator), Senduran Balasubramaniam<sup>6</sup>, Thomas M. Keane<sup>6</sup>, Shane McCarthy<sup>6</sup>, James Stalker<sup>6</sup>

**Samples and ELSI group** Aravinda Chakravarti<sup>9</sup> (Co-Chair), Bartha M. Knoppers<sup>15</sup> (Co-Chair), Gonçalo R. Abecasis<sup>7</sup>, Kathleen C. Barnes<sup>90</sup>, Christine Beiswanger<sup>91</sup>, Esteban G. Burchard<sup>55</sup>, Carlos D. Bustamante<sup>43</sup>, Hongyu Cai<sup>25</sup>, Hongzhi Cao<sup>25</sup>, Richard M. Durbin<sup>6</sup>, Neda Gharani<sup>91</sup>, Richard A. Gibbs<sup>13</sup>, Christopher R. Gignoux<sup>55</sup>, Simon Gravel<sup>43</sup>, Brenna Henn<sup>43</sup>, Danielle Jones<sup>35</sup>, Lynn Jorde<sup>6</sup>, Jane S. Kaye<sup>92</sup>, Alon Keinan<sup>10</sup>, Alastair Kent<sup>93</sup>, Angeliki Kerasidou<sup>1</sup>, Yingrui Li<sup>25</sup>, Rasika Mathias<sup>94</sup>, Gil A. McVean<sup>1,2</sup>, Andres Moreno-Estrada<sup>43</sup>, Pilar N. Ossorio<sup>95,96</sup>, Michael Parker<sup>97</sup>, David Reich<sup>3</sup>, Charles N. Rotimi<sup>98</sup>, Charmaine D. Royal<sup>99</sup>, Karla Sandoval<sup>43</sup>, Yeyang Su<sup>25</sup>, Ralf Sudbrak<sup>18</sup>, Zhongming Tian<sup>25</sup>, Bernd Timmermann<sup>18</sup>, Sarah Tishkoff<sup>100</sup>, Lorraine H. Toji<sup>91</sup>, Chris Tyler-Smith<sup>6</sup>, Marc Via<sup>101</sup>, Yuhong Wang<sup>25</sup>, Huanming Yang<sup>25</sup>, Ling Yang<sup>25</sup>, Jiayong Zhu<sup>25</sup>

**Sample collection: British from England and Scotland (GBR)** Walter Bodmer<sup>102</sup>; **Colombians in Medellín, Colombia (CLM)** Gabriel Bedoya<sup>103</sup>, Andres Ruiz-Linares<sup>59</sup>; **Han Chinese South (CHS)** Cai Zhi Ming<sup>25</sup>, Gao Yang<sup>104</sup>, Chu Jia You<sup>105</sup>; **Finnish in Finland (FIN)** Leena Peltonen<sup>†</sup>; **Iberian populations in Spain (IBS)** Andres Garcia-Montero<sup>106</sup>, Alberto Orfao<sup>107</sup>; **Puerto Ricans in Puerto Rico (PUR)** Julie Dutil<sup>108</sup>, Juan C. Martinez-Cruzado<sup>74</sup>, Taras K. Oleksyk<sup>74</sup>

**Scientific management** Lisa D. Brooks<sup>109</sup>, Adam L. Felsenfeld<sup>109</sup>, Jean E. McEwen<sup>109</sup>, Nicholas C. Clemm<sup>109</sup>, Audrey Duncanson<sup>110</sup>, Michael Dunn<sup>110</sup>, Eric D. Green<sup>14</sup>, Mark S. Guyer<sup>109</sup>, Jane L. Peterson<sup>109</sup>

**Writing group** Gonçalo R. Abecasis<sup>7</sup>, Adam Auton<sup>29</sup>, Lisa D. Brooks<sup>109</sup>, Mark A. DePristo<sup>3</sup>, Richard M. Durbin<sup>6</sup>, Robert E. Handsaker<sup>3,5</sup>, Hyun Min Kang<sup>7</sup>, Gabor T. Marth<sup>21</sup>, Gil A. McVean<sup>1,2</sup>

<sup>1</sup>Wellcome Trust Centre for Human Genetics, Oxford University, Oxford OX3 7BN, UK. <sup>2</sup>Department of Statistics, Oxford University, Oxford OX1 3TG, UK. <sup>3</sup>The Broad Institute of MIT and Harvard, 7 Cambridge Center, Cambridge, Massachusetts 02142, USA. <sup>4</sup>Center for Human Genetic Research, Massachusetts General Hospital, Boston, Massachusetts 02114, USA. <sup>5</sup>Department of Genetics, Harvard Medical School, Cambridge, Massachusetts 02142, USA. <sup>6</sup>Wellcome Trust Sanger Institute, Wellcome Trust Genome Campus, Cambridge CB10 1SA, UK. <sup>7</sup>Center for Statistical Genetics, Biostatistics, University of Michigan, Ann Arbor, Michigan 48109, USA. <sup>8</sup>illumina United Kingdom, Chesterford Research Park, Little Chesterford, Near Saffron Walden, Essex CB10 1XL, UK. <sup>9</sup>McKusick-Nathans Institute of Genetic Medicine, Johns Hopkins University School of Medicine, Baltimore, Maryland 21205, USA. <sup>10</sup>Center for Comparative and Population Genomics, Cornell University, Ithaca, New York 14850, USA. <sup>11</sup>Department of Genome Sciences, University of Washington School of Medicine and Howard Hughes Medical Institute, Seattle, Washington 98195, USA. <sup>12</sup>European Bioinformatics Institute, Wellcome Trust Genome Campus, Cambridge CB10 1SD, UK. <sup>13</sup>Baylor College of Medicine, Human Genome Sequencing Center, Houston, Texas 77030, USA. <sup>14</sup>US National Institutes of Health, National Human Genome Research Institute, 31 Center Drive, Bethesda, Maryland 20892, USA. <sup>15</sup>Centre of Genomics and Policy, McGill University, Montréal, Québec H3A 1A4, Canada. <sup>16</sup>European Molecular Biology Laboratory, Genome Biology Research Unit, Meyerhofstraße 1, 69117 Heidelberg, Germany. <sup>17</sup>Department of Pathology, Brigham and Women's Hospital and Harvard Medical School, Boston, Massachusetts 02115, USA. <sup>18</sup>Max Planck Institute for Molecular Genetics, Ihnestraße 63-73, 14195 Berlin, Germany. <sup>19</sup>Dahlem Centre for Genome Research and Medical Systems Biology, D-14195 Berlin-Dahlem, Germany. <sup>20</sup>The Genome Center, Washington University School of Medicine, St Louis, Missouri 63108, USA. <sup>21</sup>Department of Biology, Boston College, Chestnut Hill, Massachusetts 02467, USA. <sup>22</sup>Department of Genome Sciences, University of Washington School of Medicine, Seattle, Washington 98195, USA. <sup>23</sup>Affymetrix, Inc., Santa Clara, California 95051, USA. <sup>24</sup>US National Institutes of Health, National Center for Biotechnology Information, 45 Center Drive, Bethesda, Maryland 20892, USA. <sup>25</sup>BGI-Shenzhen, Shenzhen 518083, China. <sup>26</sup>The Novo Nordisk Foundation Center for Basic Metabolic Research, University of Copenhagen, DK-2200 Copenhagen, Denmark. <sup>27</sup>Department of Biology, University of Copenhagen, DK-2100 Copenhagen, Denmark. <sup>28</sup>Alacris Theranostics GmbH, D-14195 Berlin-Dahlem, Germany. <sup>29</sup>Department of Genetics, Albert Einstein College of Medicine, Bronx, New York 10461, USA. <sup>30</sup>Department of Computational Medicine and Bioinformatics, University of Michigan, Ann Arbor, Michigan 48109, USA. <sup>31</sup>Cold Spring Harbor Laboratory, Cold Spring Harbor, New York 11724, USA. <sup>32</sup>Seaver Autism Center and Department of Psychiatry, Mount Sinai School of Medicine, New York, New York 10029, USA. <sup>33</sup>Department of Nanobiomedical Science, Dankook University, Cheonan 330-714, South Korea. <sup>34</sup>Department of Biological Sciences, Dankook University, Cheonan 330-714, South Korea. <sup>35</sup>Department of Biological Statistics and Computational Biology, Cornell University, Ithaca, New York 14853, USA. <sup>36</sup>Center for Systems Biology and Department Organismic and Evolutionary Biology, Harvard University, Cambridge, Massachusetts 02138, USA. <sup>37</sup>Institute of Medical Genetics, School of Medicine, Cardiff University, Heath Park, Cardiff CF14 4XN, UK. <sup>38</sup>illumina, Inc., San Diego, California 92122, USA. <sup>39</sup>Molecular Epidemiology Section, Department of Medical Statistics and Bioinformatics, Leiden University Medical Center 2333 ZA, The Netherlands. <sup>40</sup>Department of Biological Sciences, Louisiana State University, Baton

Rouge, Louisiana 70803, USA. <sup>41</sup>Analytic and Translational Genetics Unit, Massachusetts General Hospital, Boston, Massachusetts 02114, USA. <sup>42</sup>Department of Anthropology, Penn State University, University Park, Pennsylvania 16802, USA. <sup>43</sup>Department of Genetics, Stanford University, Stanford, California 94305, USA. <sup>44</sup>Ancestry.com, San Francisco, California 94107, USA. <sup>45</sup>Blavatnik School of Computer Science, Tel-Aviv University, 69978 Tel Aviv, Israel. <sup>46</sup>Department of Microbiology, Tel-Aviv University, 69978 Tel Aviv, Israel. <sup>47</sup>International Computer Science Institute, Berkeley, California 94704, USA. <sup>48</sup>The Translational Genomics Research Institute, Phoenix, Arizona 85004, USA. <sup>49</sup>Life Technologies, Beverly, Massachusetts 01915, USA. <sup>50</sup>Department of Human Genetics, David Geffen School of Medicine, University of California, Los Angeles, California 90024, USA. <sup>51</sup>Department of Psychiatry, University of California, San Diego, La Jolla, California 92093, USA. <sup>52</sup>Department of Cellular and Molecular Medicine, University of California, San Diego, La Jolla, California 92093, USA. <sup>53</sup>Department of Computer Science, University of California, San Diego, La Jolla, California 92093, USA. <sup>54</sup>Department of Epidemiology and Population Health, Albert Einstein College of Medicine, Bronx, New York 10461, USA. <sup>55</sup>Department of Bioengineering and Therapeutic Sciences and Medicine, University of California, San Francisco, California 94158, USA. <sup>56</sup>Center for Biomolecular Science and Engineering, University of California, Santa Cruz, California 95064, USA. <sup>57</sup>Howard Hughes Medical Institute, Santa Cruz, California 95064, USA. <sup>58</sup>Department of Human Genetics, University of Chicago, Chicago, Illinois 60637, USA. <sup>59</sup>Department of Genetics, Evolution and Environment, University College London, London WC1E 6BT, UK. <sup>60</sup>Department of Genetic Medicine and Development, University of Geneva Medical School, 1211 Geneva, Switzerland. <sup>61</sup>Institute for Genetics and Genomics in Geneva (iGE3), University of Geneva, 1211 Geneva, Switzerland. <sup>62</sup>Swiss Institute of Bioinformatics, 1211 Geneva, Switzerland. <sup>63</sup>Institute for Genome Sciences, University of Maryland School of Medicine, Baltimore, Maryland 21201, USA. <sup>64</sup>IST/High Performance and Research Computing, University of Medicine and Dentistry of New Jersey, Newark, New Jersey 07107, USA. <sup>65</sup>Department of Invertebrate Zoology, American Museum of Natural History, New York, New York 10024, USA. <sup>66</sup>Istituto di Ricerca Genetica e Biomedica, CNR, Monserrato, 09042 Cagliari, Italy. <sup>67</sup>Department of Anthropology, University of Michigan, Ann Arbor, Michigan 48109, USA. <sup>68</sup>Dipartimento di Scienze Biomediche, Università delgi Studi di Sassari, 07100 Sassari, Italy. <sup>69</sup>Center for Advanced Studies, Research, and Development in Sardinia (CRS4), AGCT Program, Parco Scientifico e tecnologico della Sardegna, 09010 Pula, Italy. <sup>70</sup>Department of Genetics, University of North Carolina at Chapel Hill, Chapel Hill, North Carolina 27599, USA. <sup>71</sup>University of Michigan Sequencing Core, University of Michigan, Ann Arbor, Michigan 48109, USA. <sup>72</sup>National Institute on Aging, Laboratory of Genetics, Baltimore, Maryland 21224, USA. <sup>73</sup>Department of Pediatrics, University of Montréal, Ste. Justine Hospital Research Centre, Montréal, Québec H3T 1C5, Canada. <sup>74</sup>Department of Biology, University of Puerto Rico, Mayagüez, Puerto Rico 00680, USA. <sup>75</sup>The University of Texas Health Science Center at Houston, Houston, Texas 77030, USA. <sup>76</sup>Eccles Institute of Human Genetics, University of Utah School of Medicine, Salt Lake City, Utah 84112, USA. <sup>77</sup>Department of Genetics, Rutgers University, The State University of New Jersey, Piscataway, New Jersey 08854, USA. <sup>78</sup>Department of Medicine, Division of Medical Genetics, University of Washington, Seattle, Washington 98195, USA. <sup>79</sup>Department of Computer Engineering, Bilkent University, TR-06800 Bilkent, Ankara, Turkey. <sup>80</sup>Department of Computer Science, Simon Fraser University, Burnaby, British Columbia V5A 1S6, Canada. <sup>81</sup>Department of Bioinformatics and Computational Biology, The University of Texas MD Anderson Cancer Center, Houston, Texas 77230, USA. <sup>82</sup>Department of Haematology, University of Cambridge and National Health Service Blood and Transplant, Cambridge CB2 1TN, UK. <sup>83</sup>Institute of Genetics and Biophysics, National Research Council (CNR), 80125 Naples, Italy. <sup>84</sup>Program in Computational Biology and Bioinformatics, Yale University, New Haven, Connecticut 06520, USA. <sup>85</sup>Department of Computer Science, Yale University, New Haven, Connecticut 06520, USA. <sup>86</sup>Department of Molecular Biophysics and Biochemistry, Yale University, New Haven, Connecticut 06520, USA. <sup>87</sup>Department of Chemistry, Yale University, New Haven, Connecticut 06520, USA. <sup>88</sup>Beyster Center for Genomics of Psychiatric Diseases, University of California, San Diego, La Jolla, California 92093, USA. <sup>89</sup>US National Institutes of Health, National Human Genome Research Institute, 50 South Drive, Bethesda, Maryland 20892, USA. <sup>90</sup>Division of Allergy and Clinical Immunology, School of Medicine, Johns Hopkins University, Baltimore, Maryland 21205, USA. <sup>91</sup>Coriell Institute for Medical Research, Camden, New Jersey 08103, USA. <sup>92</sup>Centre for Health, Law and Emerging Technologies, University of Oxford, Oxford OX3 7LF, UK. <sup>93</sup>Genetic Alliance, London N1 3QP, UK. <sup>94</sup>Johns Hopkins University School of Medicine, Baltimore, Maryland 21205, USA. <sup>95</sup>Department of Medical History and Bioethics, Morgridge Institute for Research, University of Wisconsin-Madison, Madison, Wisconsin 53706, USA. <sup>96</sup>University of Wisconsin Law School, Madison, Wisconsin 53706, USA. <sup>97</sup>The Ethox Centre, Department of Public Health, University of Oxford, Old Road Campus, Oxford OX3 7LF, UK. <sup>98</sup>US National Institutes of Health, Center for Research on Genomics and Global Health, National Human Genome Research Institute, 12 South Drive, Bethesda, Maryland 20892, USA. <sup>99</sup>Institute for Genome Sciences and Policy, Duke University, Durham, North Carolina 27708, USA. <sup>100</sup>Department of Genetics, University of Pennsylvania School of Medicine, Philadelphia, Pennsylvania 19104, USA. <sup>101</sup>Department of Animal Biology, Unit of Anthropology, University of Barcelona, 08028 Barcelona, Spain. <sup>102</sup>Cancer and Immunogenetics Laboratory, University of Oxford, John Radcliffe Hospital, Oxford OX3 9DS, UK. <sup>103</sup>Laboratory of Molecular Genetics, Institute of Biology, University of Antioquia, Medellín, Colombia. <sup>104</sup>Peking University Shenzhen Hospital, Shenzhen 518036, China. <sup>105</sup>Institute of Medical Biology, Chinese Academy of Medical Sciences and Peking Union Medical College, Kunming 650118, China. <sup>106</sup>Instituto de Biología Molecular y Celular del Cancer, Centro de Investigación del Cancer/IBMCC (CSIC-USAL), Institute of Biomedical Research of Salamanca (IBSAL) & Banco Nacional de ADN Carlos III, University of Salamanca, 37007 Salamanca, Spain. <sup>107</sup>Instituto de Biología Molecular y Celular del Cancer, Centro de Investigación del Cancer/IBMCC (CSIC-USAL), Institute of Biomedical Research of Salamanca (IBSAL) & Cytometry Service and Department of Medicine, 37007 University of Salamanca, Salamanca, Spain. <sup>108</sup>Ponce School of Medicine and Health Sciences, Ponce, Puerto Rico 00716, USA. <sup>109</sup>US National Institutes of Health, National Human Genome Research Institute, 5635 Fishers Lane, Bethesda, Maryland 20892, USA. <sup>110</sup>Wellcome Trust, Gibbs Building, 215 Euston Road, London NW1 2BE, UK.

‡Deceased.

# Generation of functional thyroid from embryonic stem cells

Francesco Antonica<sup>1</sup>, Dominika Figini Kasprzyk<sup>1</sup>, Robert Opitz<sup>1</sup>, Michelina Iacovino<sup>2</sup>, Xiao-Hui Liao<sup>3</sup>, Alexandra Mihaela Dumitrescu<sup>3</sup>, Samuel Refetoff<sup>3,4</sup>, Kathelijne Peremans<sup>5</sup>, Mario Manto<sup>6</sup>, Michael Kyba<sup>2</sup> & Sabine Costagliola<sup>1</sup>

**The primary function of the thyroid gland is to metabolize iodide by synthesizing thyroid hormones, which are critical regulators of growth, development and metabolism in almost all tissues. So far, research on thyroid morphogenesis has been missing an efficient stem-cell model system that allows for the *in vitro* recapitulation of the molecular and morphogenic events regulating thyroid follicular-cell differentiation and subsequent assembly into functional thyroid follicles. Here we report that a transient overexpression of the transcription factors NKX2-1 and PAX8 is sufficient to direct mouse embryonic stem-cell differentiation into thyroid follicular cells that organize into three-dimensional follicular structures when treated with thyrotropin. These *in vitro*-derived follicles showed appreciable iodide organification activity. Importantly, when grafted *in vivo* into athyroid mice, these follicles rescued thyroid hormone plasma levels and promoted subsequent symptomatic recovery. Thus, mouse embryonic stem cells can be induced to differentiate into thyroid follicular cells *in vitro* and generate functional thyroid tissue.**

The mammalian thyroid consists of two endocrine cell types, the thyroid follicular cells (TFCs) that produce the thyroid hormones T3 and T4 and the C-cells that produce calcitonin<sup>1</sup>. In the adult thyroid gland, TFCs are organized into follicular structures<sup>2</sup>, in which a monolayer of polarized TFCs enclose a luminal compartment filled with a colloidal mass containing thyroid hormone precursors bound to thyroglobulin<sup>3</sup>. A follicular organization of TFCs is considered to be the prerequisite for efficient thyroid hormone biosynthesis<sup>4</sup>. It has been demonstrated that NKX2-1 (ref. 5) and PAX8 (ref. 6) function are vital for TFC survival, differentiation<sup>2</sup> and function during thyroid organogenesis and in mature thyroid tissue<sup>1</sup>. During thyroid organogenesis, the onset of NKX2-1 (ref. 7) and PAX8 (ref. 8) co-expression in a small group of ventral foregut endodermal cells represents the first molecular marker of cell specification towards a TFC fate. Although NKX2-1 (ref. 7) and PAX8 (ref. 8) are expressed individually in a variety of tissues and cell types, their co-expression is restricted to cells committed to differentiate into TFCs. Induced overexpression of defined transcription factors has been shown to have a directing effect on the differentiation of embryonic stem cells (ESCs) into specific cell types<sup>9–11</sup>. Despite the success of this experimental approach for cell differentiation or reprogramming, protocols promoting coordinated self-assembly of differentiated cells into distinct morphological units with functional properties reminiscent of organs and tissues *in vivo*<sup>12–14</sup> are still very sparse. In this study, we explore whether overexpression of the transcription factors NKX2-1 and PAX8 could promote differentiation of murine ESCs into TFCs and subsequent self-formation of thyroid follicles.

## *In vitro* thyroid cell differentiation

Because the factors and signalling pathways inducing concurrent expression of NKX2-1 and PAX8 have not yet been resolved<sup>2</sup>, we generated recombinant ESC lines (Fig. 1a and Supplementary Fig. 1a, c, e) in which expression of these transcription factors can be temporally induced on the addition of doxycycline (Dox;  $1 \mu\text{g ml}^{-1}$ ) to the

medium<sup>15</sup> (Supplementary Fig. 1b, d, f). These genetic manipulations did not affect the pluripotent state of the ESCs (Supplementary Fig. 1g). In our experimental set-up, Dox induction of NKX2-1 and PAX8 was initiated after a 4-day ESC culture in hanging drops to allow for differentiation into embryoid bodies (Fig. 1b). We first used a recombinant ESC line in which Dox treatment induces NKX2-1 and PAX8 overexpression (Supplementary Fig. 1a, b). After 3 days of Dox treatment (on days 4, 5 and 6), co-expression of NKX2-1 and PAX8 was detectable by immunofluorescence in almost all Dox-treated cells on day 7 but never in cells incubated in the absence of Dox (Supplementary Fig. 2a). To determine whether the combined activity of NKX2-1 and PAX8 promotes TFC differentiation, we first examined the expression of various TFC markers by quantitative reverse transcriptase PCR (qRT-PCR). Notably, messenger RNA expression of functional markers, including the thyroid-stimulating hormone (TSH) receptor (*Tshr*), the sodium/iodide symporter NIS (*Slc5a5*) and thyroglobulin (*Tg*), was strongly upregulated within 3 days of Dox treatment (Supplementary Fig. 2b). The expression of *Foxe1*, another key transcription factor for thyroid development<sup>16</sup>, was also upregulated (Supplementary Fig. 2b), and NKX2-1<sup>+</sup> FOXE1<sup>+</sup> cells were prominent throughout cell cultures (Supplementary Fig. 2c). Interestingly, our qRT-PCR analyses also demonstrated a robust increase in endogenous *Nkx2-1* and *Pax8* mRNA levels (Supplementary Fig. 2d), indicating an auto-induction of these transcription factors. Together, these data demonstrate that forced co-expression of NKX2-1 and PAX8 readily acts on cell fate, driving the differentiation towards a TFC lineage. However, assembly of Dox-treated cells into three-dimensional aggregates reminiscent of follicle-like epithelial structures was rarely observed under these conditions. This was true for cell cultures using a variety of distinct Dox treatment protocols, suggesting that additional factors might be required to promote follicular morphogenesis. We therefore revised the treatment protocol on the basis of two critical observations. First, we limited the Dox treatment to a 3-day period from day 4 to day 6 (Fig. 1b), as this seemed to be sufficient to induce the auto-induction of

<sup>1</sup>Institute of Interdisciplinary Research in Molecular Human Biology (IRIBHM), Université Libre de Bruxelles, 808 route de Lennik, 1070 Brussels, Belgium. <sup>2</sup>Lillehei Heart Institute and Department of Pediatrics, University of Minnesota, Minneapolis, 55455 Minnesota, USA. <sup>3</sup>Department of Medicine, The University of Chicago, Chicago, 60637 Illinois, USA. <sup>4</sup>Departments of Pediatrics & Genetics, The University of Chicago, Chicago, 60637 Illinois, USA. <sup>5</sup>Department of Veterinary Medical Imaging & Small Animal Orthopaedics, Faculty of Veterinary Medicine, Ghent University, B-9820 Merelbeke, Belgium. <sup>6</sup>FNRS, ERASME, Université Libre de Bruxelles, 808 Route de Lennik, 1070 Brussels, Belgium.

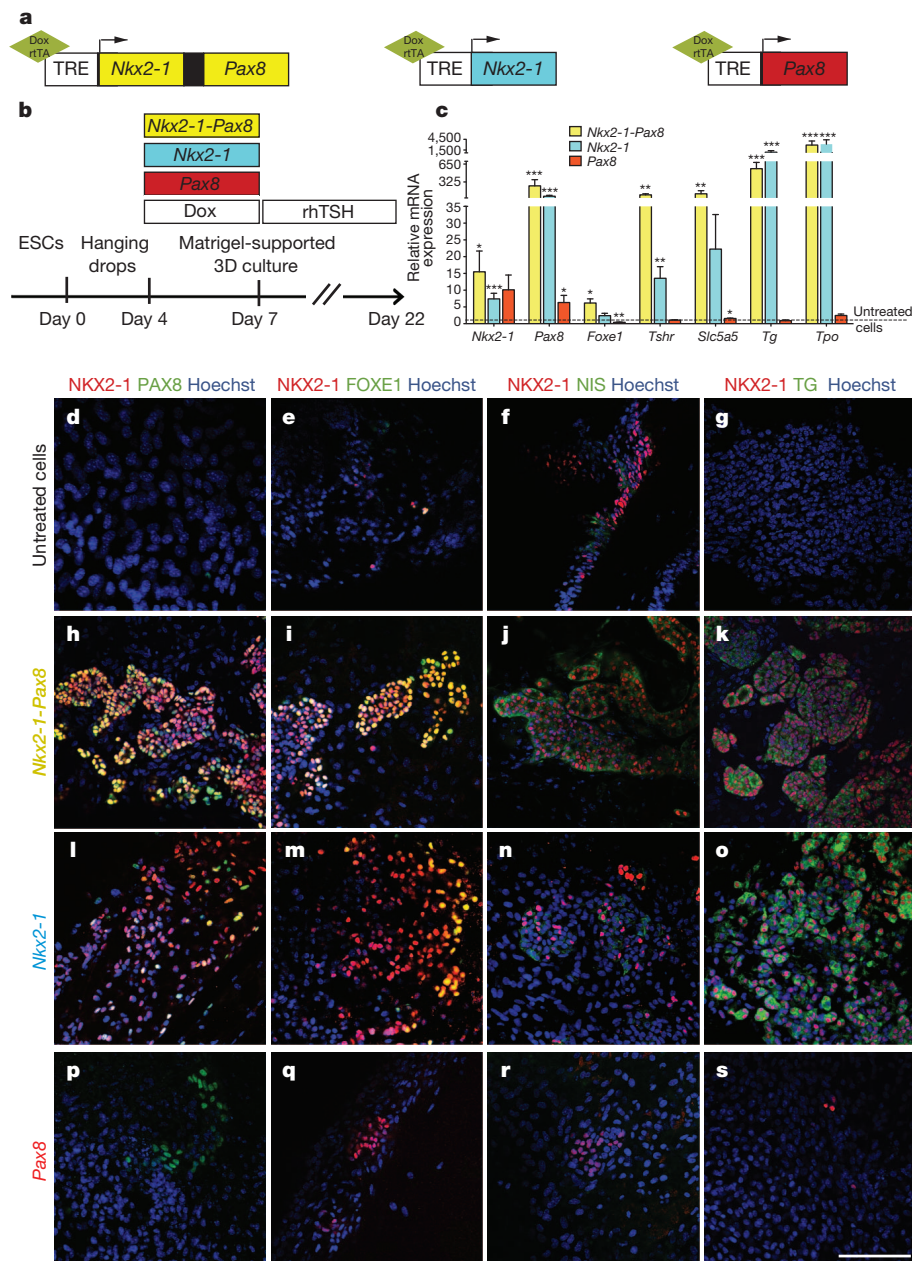


**Figure 1 | Ectopic expression of *Nkx2-1* and *Pax8* promotes the differentiation of ESCs into thyroid follicles.** **a**, Schematic representation of tetracycline-inducible murine ESC lines. **b**, Schematic diagram of the thyroid follicle differentiation protocol from ESCs. **c**, Expression of endogenous *Nkx2-1* and *Pax8*, *Foxe1*, *Tshr*, *Slc5a5*, *Tg* and *Tpo* at day 22 in cells differentiated after Dox-mediated induction of *Nkx2-1-Pax8* (yellow columns), *Nkx2-1* (cyan columns) and *Pax8* (red columns). Relative expression of each transcript is

presented as fold change compared to untreated cells at day 22 as mean  $\pm$  s.e.m. ( $n = 6$ ). Unpaired *t*-test was used for statistical analysis. \* $P < 0.05$ , \*\* $P < 0.01$ , \*\*\* $P < 0.001$ . **d–s**, Immunostaining at day 22 of untreated cells (**d–g**) and after Dox-mediated induction of *Nkx2-1-Pax8* (**h–k**), *Nkx2-1* (**l–o**) and *Pax8* (**p–s**) for NKX2-1 and PAX8 (**d, h, l, p**), NKX2-1 and FOXE1 (**e, i, m, q**), NKX2-1 and NIS (**f, j, n, r**) and NKX2-1 and TG (**g, k, o, s**). Scale bars, 100  $\mu$ m. rtTA, reverse tetracycline transactivator; TRE, tetracycline-responsive element.

endogenous *Nkx2-1* and *Pax8* mRNA expression. Second, we treated cells from day 7 onwards with recombinant human TSH (rhTSH; 1 mU ml<sup>-1</sup>) (Fig. 1b), as the robust upregulation of *Tshr* mRNA indicated that the cells had acquired an ability to respond to rhTSH. When using this sequential Dox–rhTSH treatment schedule, qRT–PCR analyses of day-22 cell cultures indeed showed a sustained elevation of endogenous *Nkx2-1* and *Pax8* mRNA expression (Fig. 1c and Supplementary Fig. 3a, b). Moreover, these cell cultures also showed a high expression of functional TFC markers such as *Tshr*, *Slc5a5*, *Tg* and *Tpo* (which codes for thyroid peroxidase) (Fig. 1c and Supplementary Fig. 3a, b). Immunofluorescence analyses at day 22 demonstrated that the sequential Dox–rhTSH treatment clearly promoted the differentiation of NKX2-1<sup>+</sup> cells co-expressing PAX8

(Fig. 1h and Supplementary Fig. 3g, k), FOXE1 (Fig. 1i and Supplementary Fig. 3h, l), NIS (Fig. 1j; Supplementary Fig. 3i, m) and TG (Fig. 1k and Supplementary Fig. 3j, n). No such co-expression was seen in the absence of Dox-induced transgene expression (Fig. 1d–g and Supplementary Fig. 3c–f). The efficiency of TFC differentiation, quantified as the percentage of NKX2-1<sup>+</sup> PAX8<sup>+</sup> cells, reached 60.5  $\pm$  8.1% in the sequential Dox–rhTSH treatment protocol (mean  $\pm$  s.e.m.,  $n = 3$ ; see Methods). Most importantly, and in contrast to a 3-day Dox treatment without subsequent TSH treatment, the sequential Dox–rhTSH treatment greatly stimulated the assembly of TFC-like cells into distinct three-dimensional structures reminiscent of thyroid follicles (Supplementary Fig. 3k–n; compare with Supplementary Fig. 3g–j).

## In vitro formation of functional follicles

A follicular organization of TFCs is considered the prerequisite for thyroid hormone biosynthesis, which occurs under physiological conditions extracellularly at the TFC–colloid interface. Iodide organification requires a complex biosynthetic machinery including NIS-mediated iodide uptake<sup>17</sup> at the basal pole<sup>18</sup>, TG synthesis and targeting to the apical pole, H<sub>2</sub>O<sub>2</sub> generation at the TFC–colloid interface by dual oxidase and TPO-mediated iodination of TG<sup>4</sup> (Fig. 2a). Immunofluorescence analyses of the follicular aggregates demonstrated polarization characteristics consistent with thyroid follicles in intact animals (Fig. 2b). The NKX2-1<sup>+</sup> cells surrounding a luminal space showed basolateral localization of NIS (Fig. 2c) and E-cadherin (Fig. 2d), as well as apical localization of zona occludens 1 (ZO-1; also known as TJP1) (Fig. 2e). Conversely, TG immunofluorescence was observed both intracellularly and in the luminal compartment (Fig. 2f). It should be noted that neither endothelial cells nor C-cells were observed after 22 days of cell culture, as judged by the absence of detectable PECAM-1 and calcitonin staining, respectively. Together, these data demonstrate the efficiency of the sequential Dox–rhTSH treatment to generate cells with a molecular signature highly similar to

TFCs and to promote the assembly of these TFC-like cells into three-dimensional follicular structures strongly resembling thyroid follicles. We next studied whether Dox induction of either NKX2-1 or PAX8 alone was sufficient to promote TFC differentiation and follicle morphogenesis. Dox induction of NKX2-1 alone for 3 days was sufficient to upregulate the expression of various TFC markers as assessed by qRT–PCR (Supplementary Fig. 4a, b) and by immunostaining for PAX8 (Supplementary Fig. 4c) and FOXE1 (Supplementary Fig. 4d). However, with the exception of *Pax8* mRNA expression, the effects of NKX2-1 overexpression were weaker relative to Dox induction of NKX2-1 and PAX8 (Supplementary Fig. 2b) and no upregulation was evident for endogenous *Nkx2-1* mRNA (Supplementary Fig. 4a). When using the sequential Dox–rhTSH protocol, NKX2-1 induction was clearly sufficient to promote differentiation towards a TFC-like cell fate (Fig. 1c, l–o) but failed to efficiently promote formation of follicle-like cell aggregates (compare Fig. 1k with Fig. 1o). Given the vital role of TSH treatment for folliculogenesis, as observed in the NKX2-1- and PAX8-overexpression model, the comparatively low level of *Tshr* upregulation induced by overexpression of NKX2-1 might represent one plausible factor explaining the lack of follicle morphogenesis in the

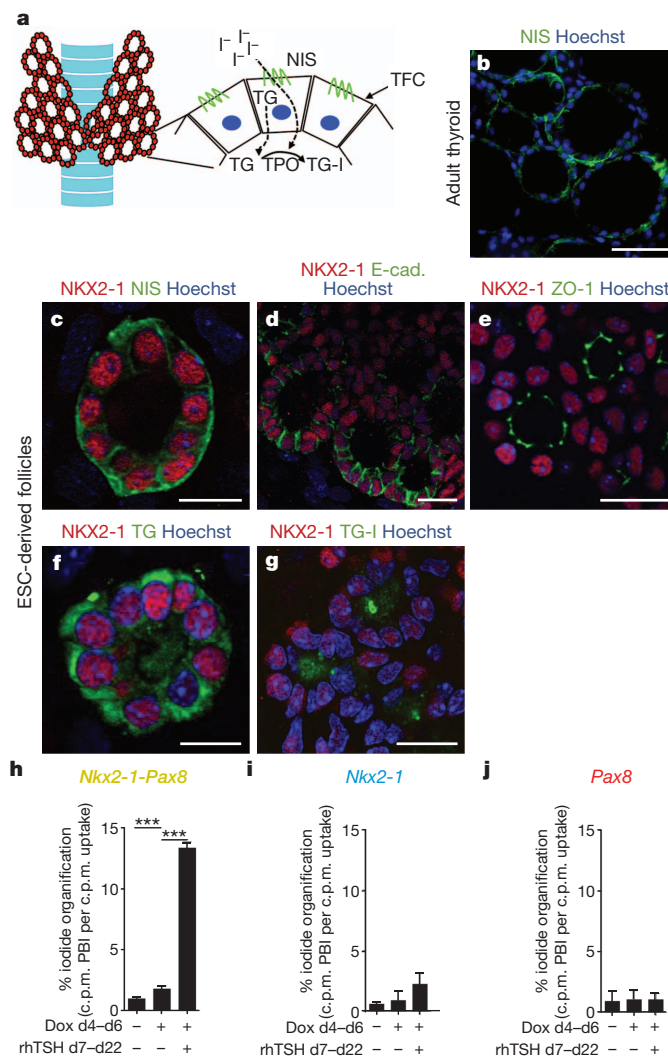


**Figure 2 | ESC-derived thyroid cells show full morphological and functional maturation.** **a**, Schematic diagram of the thyroid gland organized in follicles. **b**, Immunostaining of NIS in adult thyroid tissue. **c–f**, Immunofluorescence at day 22 of thyroid follicles derived from ESCs on ectopic expression of *Nkx2-1* and *Pax8* for NKX2-1 and NIS (**c**), NKX2-1 and E-cadherin (E-cad.) (**d**), NKX2-1 and ZO-1 (**e**) and NKX2-1 and TG (**f**). **g**, Immunodetection of TG-I in the luminal compartment of NKX2-1-positive follicles. **h–j**,

Iodide-organification assay in cells differentiated after Dox induction of *Nkx2-1-Pax8* (**h**), *Nkx2-1* (**i**) and *Pax8* (**j**). Histograms show the organification percentage of iodine-125 at day 22 in cells differentiated without Dox and rhTSH (left column), in the presence of Dox only (centre column) and on Dox and rhTSH treatment (right column). Data are mean  $\pm$  s.e.m. ( $n = 3$ ). Tukey's multiple comparison test was used for statistical analysis. \*\*\* $P < 0.001$ . Scale bars, 200  $\mu$ m (**b**) and 20  $\mu$ m (**c–g**). PBI, protein-bound <sup>125</sup>I.

NKX2-1-overexpression model (see Fig. 1c and Supplementary Fig. 4a, b). In notable contrast to NKX2-1 overexpression, Dox induction of PAX8 had only marginal effects on TFC marker expression, both at the mRNA (Supplementary Fig. 5a, b) and protein-expression level (Supplementary Fig. 5c, d). Treatment with rhTSH after Dox induction of PAX8 did not promote TFC differentiation as judged from the day-22 analyses of TCF marker gene expression (Fig. 1c) and immunofluorescence staining (Fig. 1p–s). Together, these data indicate that transient NKX2-1 overexpression is sufficient to drive cell differentiation towards the TFC lineage. Conversely, PAX8 did not promote TFC differentiation when overexpressed alone but strongly enhanced TFC differentiation when overexpressed together with NKX2-1. Most importantly, overexpression of both NKX2-1 and PAX8 was a critical requirement for the rhTSH-dependent self-assembly of TFC into follicle-like structures. The high similarity between *in vitro*-generated follicle-like structures and true thyroid follicles, both at the molecular and morphological level, prompted us to examine whether these follicular structures were functional for the two hallmarks of thyroid tissue: iodide trapping and thyroid hormone synthesis. We therefore assessed day-22 cell cultures derived from the sequential Dox–rhTSH protocol for their capacity to organify iodide. The first evidence for active iodide organification was obtained by immunofluorescence detection of iodinated TG (TG-I) within the luminal compartment of follicular aggregates (Fig. 2g) using an antibody that selectively recognizes iodinated TG epitopes<sup>19</sup>. Positive TG-I staining was limited to cell cultures obtained after Dox induction of NKX2-1 and PAX8 and subsequent rhTSH treatment. We next used a ‘classical’ iodide-organification assay that measured the relative incorporation of radioiodine into TCA-precipitable proteins after 2 h of incubation in a <sup>125</sup>I-supplemented medium. Measurements of radioiodine incorporation corroborated the TG-I staining results as a strong and significant increase of iodide organification was exclusively seen in cell cultures on Dox induction of NKX2-1 and PAX8 and subsequent rhTSH treatment (Fig. 2h–j and Supplementary Fig. 6). The capacity of such cell cultures for robust iodide organification is in line with their TFC-like molecular signature and their three-dimensional follicular organization. In turn, the lack of similar functional properties of cell cultures derived after the induction of either NKX2-1 (Fig. 2i) or PAX8 alone (Fig. 2j) would be consistent with a failure of TFC differentiation (Dox induction of PAX8 alone) or a reduced competence in forming follicular aggregates on rhTSH treatment (Dox induction of NKX2-1 alone). Together, our data demonstrate that the differentiation protocol relying on overexpression of NKX2-1 and PAX8 allows for deriving *in vitro* follicular organoid structures that recapitulate molecular, morphological and functional properties of bona fide thyroid follicles. In addition, this protocol highlights the vital role of TSH in completing the process of follicular maturation.

### **In vivo functionality of derived follicles**

To assess the potential *in vivo* functionality of the ESC-derived thyroid follicles, we grafted follicular organoids under the kidney capsules of female mice previously made hypothyroid by intraperitoneal <sup>131</sup>I injection (Fig. 3a). Histological evaluation of the kidney region 1 month after transplantation demonstrated successful integration of grafted organoids in the host niche (Fig. 3b, c). At the grafting site (Fig. 3b), numerous follicles containing a monolayered epithelium were present at the cortical area of the host organ (Fig. 3c and Supplementary Fig. 7a). *In situ* chromosome Y painting on paraffin sections of the grafting region provided clear evidence that the follicular structures originated from male ESC-derived organoids, on a background of female kidney tissue of the hosts (Supplementary Fig. 8a, b). Immunostaining demonstrated that the follicular epithelium was made up of cells positive for NKX2-1 (Fig. 3d), PAX8 (Fig. 3e) and FOXE1 (Fig. 3f), a molecular signature highly similar to the thyrocytes of orthotopic thyroid tissue. Further immunohistochemical analyses corroborated the development of functional thyroid follicles at the grafting sites,

including cytosolic TG expression and TG deposition in the luminal compartment (Fig. 3g), polarized NIS (Fig. 3h) and E-cadherin (Supplementary Fig. 7b) expression at the basolateral membrane as well as detection of the thyroid hormone T4 in the colloid (Fig. 3i and Supplementary Fig. 7a). Importantly, immunostaining for the pan-endothelial marker PECAM-1 showed that thyroid follicles were surrounded by a dense network of small blood vessels, demonstrating the formation of classical angio-follicular units (Supplementary Fig. 7c, d). Lastly, we could not detect any calcitonin staining in the grafted tissue, whereas calcitonin staining was clearly detectable in the orthotopic thyroid tissue of adult mice (data not shown). Thus, consistent with the proposed origin and migration path of C-cells<sup>20</sup>, the ectopic thyroid tissue grafts are free of C-cells, indicating that our differentiation protocol does not promote C-cell development.

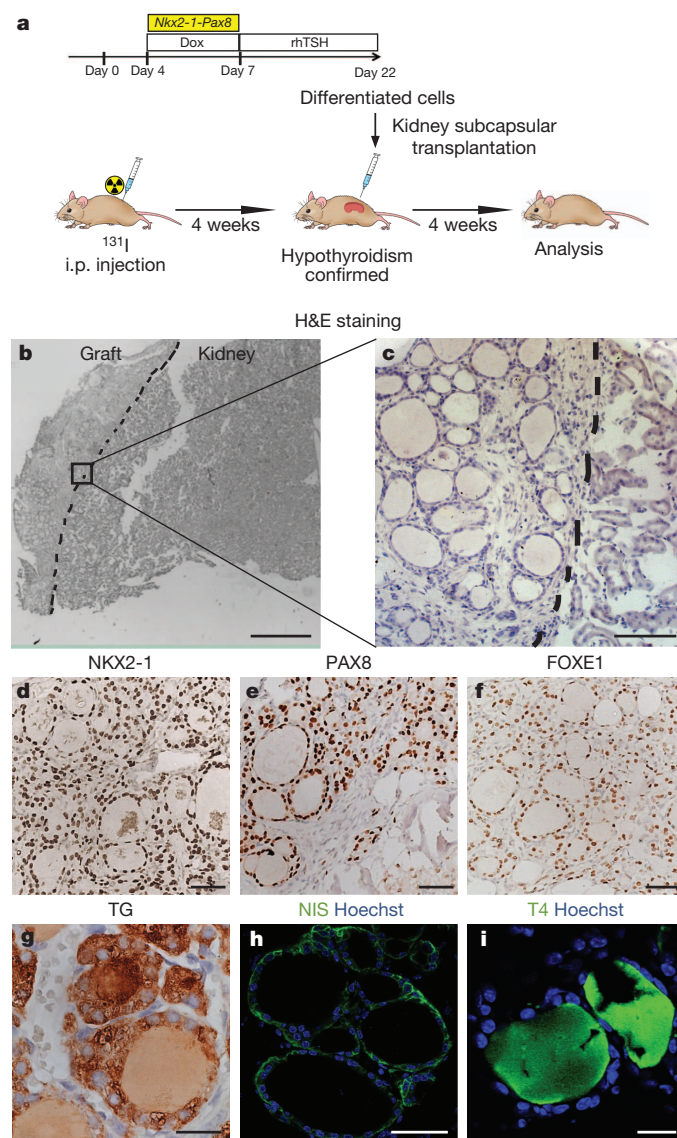


**Figure 3 | Grafting of ESC-derived thyroid follicles in mice.** **a**, Schematic diagram of protocol for ESC-derived thyroid follicle transplantation in the renal capsule of mice with radio-iodine-ablated thyroid (hypothyroid mice). **b–i**, Histological analysis of kidney sections 4 weeks after grafting. Hematoxylin and eosin staining on optimal cutting temperature embedded grafted kidney showed the localization of the transplanted tissue in the cortical area of the host organ (left side) (**b**) and single cuboidal epithelium organization of transplanted tissue (**c**), the immunohistochemistry of NKX2-1 (**d**), PAX8 (**e**), FOXE1 (**f**), TG (**g**), and the immunofluorescence of NIS (**h**) and T4 (**i**) in the grafted tissue. i.p., intraperitoneal. Scale bars, 300  $\mu$ m (**b**), 100  $\mu$ m (**c**), 50  $\mu$ m (**d**, **e**, **f**, **h**) and 20  $\mu$ m (**g**, **i**).

## Functional rescue in hypothyroid mice

We next evaluated the ability of the ESC-derived tissue grafts to restore thyroid homeostasis in mice with radioiodine-ablated thyroid tissue. Plasma T4 levels measured in female mice at 1 month after  $^{131}\text{I}$  injection showed a severe hypothyroid status at the time when ESC-derived organoids were transplanted (Fig. 4a and Supplementary Fig. 9a). Four weeks after grafting (8 weeks after  $^{131}\text{I}$  injection), mice grafted with cells that were differentiated on overexpression of NKX2-1 and PAX8 and subsequent rhTSH treatment showed a substantial increase in plasma T4 levels (Fig. 4b and Supplementary Fig. 9b), with a complete rescue of thyroid homeostasis being evident in eight out of nine animals. Notably, mice transplanted with cells that were differentiated without Dox and rhTSH treatment remained hypothyroid

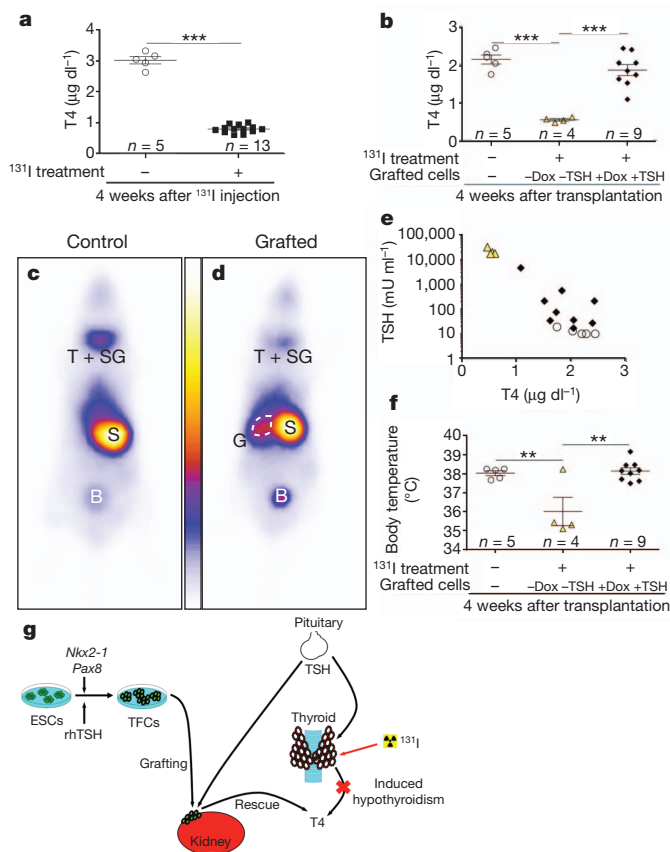


**Figure 4 | Rescue of experimentally induced hypothyroidism by transplantation of ESC-derived thyroid follicles.** **a**, Total plasma T4 levels 4 weeks after injection in untreated mice (open circles) and iodine-131-treated mice (black squares). **b**, Total plasma T4 levels 4 weeks after the transplantation of differentiated cells in iodine-131-treated mice. **c**, **d**, Whole-body images of mice 30 min after the injection of 99mTc-pertechnetate. Four weeks after grafting, a body scan was performed on untreated control mice (**c**) or iodine-131-treated mice grafted with ESC-derived follicles (**d**). B, bladder; G, grafted ESC-derived follicles; S, stomach; T + SG, thyroid and salivary glands. **e**, Relationship between plasma TSH and T4 levels 4 weeks after grafting. **f**, Body-temperature measurements 4 weeks after grafting. In **b**, **e**, **f**, open circles show iodine-131-untreated and ungrafted mice; yellow triangles show mice treated with iodine-131 and grafted with cells differentiated without Dox and rhTSH (-Dox -TSH) and black diamonds show mice treated with iodine-131 and grafted with cells differentiated with Dox and rhTSH (+Dox +TSH). The values are shown as a dot plot (**a**, **b**, **f**) or scatter plot (**e**) and data are mean  $\pm$  s.e.m. Unpaired *t*-test (**a**) and Tukey's Multiple Comparison Test (**b**, **f**) were used for statistical analysis. \*\* $P < 0.01$ , \*\*\* $P < 0.001$ . **g**, Summary diagram showing that *Nkx2-1* and *Pax8* co-expression in combination with rhTSH treatment leads to the differentiation of ESCs into fully functional thyroid follicles that promote *in vivo* hormonal and symptomatic recovery of the hypothyroid state.

(Fig. 4b), as was the case for mice that received no grafts at all (Supplementary Fig. 9b). To demonstrate that the grafted thyroid tissue was responsible for the restoration of plasma T4 levels, we performed whole-body scintigraphy of mice after intramuscular injection of 99mTc-pertechnetate, a  $\gamma$  emitter transported by the sodium/iodide symporter (Fig. 4c, d). As shown in Fig. 4c, strong 99mTc-pertechnetate uptake was observed in control mice in the neck region (where the thyroid and salivary glands reside), the stomach and the bladder. In athyroid mice grafted with ESC-derived thyroid follicles, 99mTc-pertechnetate uptake was markedly decreased in the neck region, owing to the absence of the thyroid gland (Fig. 4d). The remaining weak signal in the neck region was due to NIS activity in the salivary gland. Importantly, a very strong signal was detectable at the grafting site close to the kidney. These data provide strong evidence that the grafted tissue was responsible for the restoration of plasma T4 levels. Along with the restoration of normal T4 plasma levels, mice grafted with ESC-derived thyroid follicles also show a progressive decrease in plasma TSH levels (Fig. 4e and Supplementary Fig. 9c). Moreover, acute TSH administration<sup>21</sup> to athyroid grafted mice was effective in producing an increase in circulating levels of T4, suggesting TSH responsiveness of the grafted tissue (Supplementary Fig. 10). To examine whether our grafting approach also resulted in a symptomatic recovery, we analysed body temperature in mice from the different treatment groups. Decreased body temperature was found to be a robust and sensitive response to lowered plasma thyroid hormone concentrations. Importantly, mice grafted with ESC-derived thyroid follicles showed a full normalization of body temperature at 4 weeks after transplantation, providing a compelling example for symptomatic recovery along with the normalization of plasma hormone concentrations (Fig. 4f and Supplementary Fig. 11). These *in vivo* data clearly demonstrate that ESC-derived thyroid follicles have potent functional capacity to compensate for the lack of orthotopic thyroid tissue, allowing for the full rescue of experimentally induced hypothyroidism (Fig. 4g).

## Conclusion and perspectives

We have developed a protocol that allows for the generation of functional thyroid follicles from ESCs on the basis of transient overexpression of two transcription factors followed by rhTSH treatment. Recently, elegant studies have demonstrated self-formation of two ectoderm-derived complex organs, adenohypophysis<sup>13</sup> and optic cup<sup>12</sup>, using three-dimensional ESC culture systems, as well as the capacity of colon stem cells to recapitulate *in vitro* the self-organization of an endoderm-derived tissue, the crypt-villus structures<sup>22,23</sup>. Although a few previous studies have reported on the detection of thyrocyte-like cells in ESC cultures<sup>24–27</sup>, the present study is the first to demonstrate self-formation of thyroid follicles from ESC-derived TFCs and their capacity for iodide organization *in vitro*. Importantly, when transplanted into mice, the ESC-derived cells generated functional thyroid tissue able to rescue thyroid hormone deficits in athyroid animals. The latter finding of our study in particular opens a new avenue for application of stem-cell technologies in the treatment of hypothyroidism, an area that has so far received relatively little attention in regenerative medicine. In this context, one should bear in mind that congenital hypothyroidism, resulting from either dysfunctional (15%) or dysplastic (85%) thyroid tissue, is the most common congenital endocrine disease in humans, affecting one in 2,000 newborns<sup>28</sup>.

## METHODS SUMMARY

Recombinant murine ESC (A2Lox *Nkx2-1-Pax8*, A2Lox *Nkx2-1* and A2Lox *Pax8*) lines, generated as previously described in ref. 15, were differentiated in embryoid bodies by the hanging drop method<sup>29</sup>. Embryoid bodies were embedded in growth-factor-reduced Matrigel and re-plated into 12-well plates. The subsequent exposure to Dox and rhTSH was performed as described in Fig. 1b. During *in vitro* differentiation, cells were subjected to extensive phenotypic characterization using qRT-PCR, immunohistochemistry, immunofluorescence and iodide-organification assays. *In vivo* studies were performed in hypothyroidism-induced mouse models generated as previously described in ref. 30. In cell-transplantation studies,

22-day-long cultures were digested with a dispase–collagenase mixture, and the purified cellular population enriched with ESC-derived thyroid follicles were transplanted under the renal capsule. Histological examination of the kidneys, T4 and TSH plasma levels and body-temperature measurements were performed 4 weeks after transplantation.

**Full Methods** and any associated references are available in the online version of the paper.

**Received 13 March; accepted 17 August 2012.**

**Published online 10 October 2012.**

- De Felice, M. Thyroid development and its disorders: genetics and molecular mechanisms. *Endocr. Rev.* **25**, 722–746 (2004).
- De Felice, M. & Di Lauro, R. Minireview: intrinsic and extrinsic factors in thyroid gland development: an update. *Endocrinology* **152**, 2948–2956 (2011).
- Mauchamp, J., Mirrione, A., Alquier, C. & Andre, F. Follicle-like structure and polarized monolayer: role of the extracellular matrix on thyroid cell organization in primary culture. *Biol. Cell* **90**, 369–380 (1998).
- Nunez, J. & Pommier, J. Formation of thyroid hormones. *Vitam. Horm.* **39**, 175–229 (1982).
- Kimura, S. *et al.* The T/ebp null mouse: thyroid-specific enhancer-binding protein is essential for the organogenesis of the thyroid, lung, ventral forebrain, and pituitary. *Genes Dev.* **10**, 60–69 (1996).
- Mansouri, A., Chowdhury, K. & Gruss, P. Follicular cells of the thyroid gland require Pax8 gene function. *Nature Genet.* **19**, 87–90 (1998).
- Lazzaro, D., Price, M., de Felice, M. & Di Lauro, R. The transcription factor TTF-1 is expressed at the onset of thyroid and lung morphogenesis and in restricted regions of the foetal brain. *Development* **113**, 1093–1104 (1991).
- Plachov, D. *et al.* Pax8, a murine paired box gene expressed in the developing excretory system and thyroid gland. *Development* **110**, 643–651 (1990).
- Kyba, M., Perlingeiro, R. C. & Daley, G. Q. HoxB4 confers definitive lymphoid-myeloid engraftment potential on embryonic stem cell and yolk sac hematopoietic progenitors. *Cell* **109**, 29–37 (2002).
- Ahfeldt, T. *et al.* Programming human pluripotent stem cells into white and brown adipocytes. *Nature Cell Biol.* **14**, 209–219 (2012).
- Kamiya, D. *et al.* Intrinsic transition of embryonic stem-cell differentiation into neural progenitors. *Nature* **470**, 503–509 (2011).
- Eiraku, M. *et al.* Self-organizing optic-cup morphogenesis in three-dimensional culture. *Nature* **472**, 51–56 (2011).
- Suga, H. *et al.* Self-formation of functional adenohypophysis in three-dimensional culture. *Nature* **480**, 57–62 (2011).
- Eiraku, M. & Sasai, Y. Mouse embryonic stem cell culture for generation of three-dimensional retinal and cortical tissues. *Nature Protocols* **7**, 69–79 (2012).
- Iacovino, M. *et al.* Inducible cassette exchange: a rapid and efficient system enabling conditional gene expression in embryonic stem and primary cells. *Stem Cells* **29**, 1580–1588 (2011).
- De Felice, M. *et al.* A mouse model for hereditary thyroid dysgenesis and cleft palate. *Nature Genet.* **19**, 395–398 (1998).
- Dai, G., Levy, O. & Carrasco, N. Cloning and characterization of the thyroid iodide transporter. *Nature* **379**, 458–460 (1996).
- Carrasco, N. Iodide transport in the thyroid gland. *Biochim. Biophys. Acta* **1154**, 65–82 (1993).
- Hartog, M. T. D., Boer, M. D., Veenboer, G. J. M. & Vijlder, J. J. M. D. Generation and characterization of monoclonal antibodies directed against noniodinated and iodinated thyroglobulin, among which are antibodies against hormonogenic sites. *Endocrinology* **127**, 3160–3165 (1990).
- Fontaine, J. Multistep migration of calcitonin cell precursors during ontogeny of the mouse pharynx. *Gen. Comp. Endocrinol.* **37**, 81–92 (1979).
- Moeller, L. C. *et al.* Hypothyroidism in thyroid transcription factor 1 haploinsufficiency is caused by reduced expression of the thyroid-stimulating hormone receptor. *Mol. Endocrinol.* **17**, 2295–2302 (2003).
- Sato, T. *et al.* Single Lgr5 stem cells build crypt-villus structures *in vitro* without a mesenchymal niche. *Nature* **459**, 262–265 (2009).
- Yui, S. *et al.* Functional engraftment of colon epithelium expanded *in vitro* from a single adult Lgr5<sup>+</sup> stem cell. *Nature Med.* **18**, 618–623 (2012).
- Lin, R. Y., Kubo, A., Keller, G. M. & Davies, T. F. Committing embryonic stem cells to differentiate into thyrocyte-like cells *in vitro*. *Endocrinology* **144**, 2644–2649 (2003).
- Arufe, M. C. *et al.* Directed differentiation of mouse embryonic stem cells into thyroid follicular cells. *Endocrinology* **147**, 3007–3015 (2006).
- Jiang, N. *et al.* Differentiation of E14 mouse embryonic stem cells into thyrocytes *in vitro*. *Thyroid* **20**, 77–84 (2010).
- Longmire, T. A. *et al.* Efficient derivation of purified lung and thyroid progenitors from embryonic stem cells. *Cell Stem Cell* **10**, 398–411 (2012).
- Grüters, A. & Krude, H. Detection and treatment of congenital hypothyroidism. *Nature Rev. Endocrinol.* **8**, 104–113 (2012).
- Bondue, A. *et al.* Mesp1 acts as a master regulator of multipotent cardiovascular progenitor specification. *Cell Stem Cell* **3**, 69–84 (2008).
- Abel, E. D. *et al.* Divergent roles for thyroid hormone receptor  $\beta$  isoforms in the endocrine axis and auditory system. *J. Clin. Invest.* **104**, 291–300 (1999).

**Supplementary Information** is available in the online version of the paper.

**Acknowledgements** We thank G. Vassart, C. Blanpain and P. Vanderhaeghen for discussions and comments and V. Janssens for technical help. X.-H.L., A.M.D. and S.R. are supported in part by grants DK15070 and DK91016 from the National Institutes of Health. This work was supported by the Belgian Fonds de la Recherche Scientifique Medicale (FRSM[2]3\_4\_557\_08 and [3]3\_4598\_12), Action de Recherche Concertée de la Communauté Française de Belgique (ARC N°AUWB-08/13-ULB10), Fonds d'Encouragement à la Recherche and grants from the Belgian National Fund for Scientific Research (FNRS). F.A. and D.F.K. are FNRS and Fund for Research in the Industry and the Agriculture (FRIA) research fellows, R.O. is an FNRS Postdoctoral Researcher and S.C. is an FNRS Senior Research Associate.

**Author Contributions** F.A. and S.C. developed the project, designed the experiments and analysed the data. F.A. performed most of the *in vitro* experiments and *in vivo* studies. D.F.K. provided technical help for the *in vitro* differentiation and functional characterization of the cells. M.I. and M.K. provided A2Lox-Cre embryonic stem cells. X.-H.L. analysed blood TSH levels. A.M.D. read the manuscript and made experimental suggestions. S.R. provided suggestions and advice on the experimental procedures. K.P. performed the whole-body scan. M.M. performed body-temperature measurements. F.A., R.O. and S.C. wrote the manuscript. All authors read and approved the final manuscript.

**Author Information** Reprints and permissions information is available at [www.nature.com/reprints](http://www.nature.com/reprints). The authors declare no competing financial interests. Readers are welcome to comment on the online version of the paper. Correspondence and requests for materials should be addressed to S.C. ([scostag@ulb.ac.be](mailto:scostag@ulb.ac.be)).

## METHODS

**ESC culture for maintenance and differentiation.** A2Lox.Cre mouse ESCs<sup>15</sup> were routinely propagated on  $\gamma$ -ray-irradiated murine embryonic fibroblasts in DMEM (Invitrogen) supplemented with 15% embryonic-stem-certified fetal bovine serum (Invitrogen), 0.1 mM non-essential amino acids (Invitrogen), 1 mM sodium pyruvate (Invitrogen), 0.1 mM 2-mercaptoethanol (Sigma), 50 U ml<sup>-1</sup> penicillin and 50  $\mu$ g ml<sup>-1</sup> streptomycin (Invitrogen) and 1,000 U ml<sup>-1</sup> leukaemia inhibitory factor (ESGRO). Embryoid bodies were differentiated as described previously in ref. 29. In brief, embryoid bodies, generated by culturing ESCs in hanging drops (1,000 cells per drop) for up to 4 days, were collected and embedded in growth-factor-restricted Matrigel (BD Biosciences); 50  $\mu$ l Matrigel drops (containing roughly 6 embryoid bodies per drop) were re-plated on 15-mm diameter glass coverslips into 12-well plates. Embryoid bodies were differentiated and cultured using a differentiation medium previously described in ref. 29 but supplemented with 1  $\mu$ g ml<sup>-1</sup> Dox (Sigma) and 1 mU ml<sup>-1</sup> rhTSH (Genzyme) where indicated.

**Cell preparation for *in vivo* transplantation.** Cells at day 22 of differentiation (grown in 12-well plates) were washed twice with Hanks's balanced salt solution (HBSS, containing calcium and magnesium; Invitrogen) and incubated with a digestion medium (1 ml per well) containing 10 U ml<sup>-1</sup> dispase II (Roche) and 125 U ml<sup>-1</sup> collagenase type IA (Sigma) in HBSS for 30 min at 37 °C. Cells were gently dissociated, re-suspended manually with a P1000 Gilson and collected in a 15-ml Falcon tube (12 wells per tube that represent roughly 72 embryoid bodies). Cells were rinsed twice with differentiation medium following centrifugation at 200g for 3 min. Low-speed centrifugation allowed the separation of aggregates (pellet mainly composed of thyroid follicles) and single cells (supernatant). Finally, each pellet was re-suspended in 65  $\mu$ l of differentiation medium and a volume of 8  $\mu$ l was used for transplantation.

**Generation of tetracycline-inducible ESC lines.** The tetracycline-inducible *Nkx2-1*, *Pax8* and *Nkx2-1-Pax8* ESC lines were generated as previously described in ref. 10. In brief, the coding sequences of either *Nkx2-1* or *Pax8*, separated by an IRES sequence (for the A2Lox *Nkx2-1-Pax8* ESC line), or only *Nkx2-1* (for the A2Lox *Nkx2-1* ESC line) or *Pax8* (for the A2Lox *Pax8* ESC line) were cloned into a p2Lox targeting vector in order to create the following vectors: p2Lox-*Nkx2-1-Pax8*, p2Lox-*Nkx2-1* and p2Lox-*Pax8*. 5,000,000 ESCs were electroporated with the different p2Lox vectors, allowing the unidirectional recombination of the transgene in the hypoxanthine phosphoribosyltransferase locus. Positive clones were isolated using 300  $\mu$ g ml<sup>-1</sup> neomycin (Invitrogen) selection. Clones were screened by immunofluorescence against NKX2-1 and PAX8 after 24 h in the presence or absence of 1  $\mu$ g ml<sup>-1</sup> Dox to verify transgene expression.

**RNA extraction and qRT-PCR.** For total RNA preparation, cells were lysed in RNeasy Lysis buffer (Qiagen) + 1% 2-mercaptoethanol, and RNA was isolated using RNeasy RNA preparation microkit (Qiagen) according to the manufacturer's instructions. Reverse transcription was done using Superscript II kit (Invitrogen). qPCR was performed in duplicate using Power SYBR green mix and a 7500 Real-Time PCR System (Applied Biosystem). Results are presented as linearized values normalized to the housekeeping gene *Tbp* and the indicated reference value ( $2^{-\Delta\Delta C_t}$ ). The gene-expression profile was confirmed in two different clones. Primers used were as follows: *TBP*, forward 5'-TGTAACGCA GCTTCAAAATATTGTAT-3', reverse 5'-AAATCAACGCGAGTTGTCGTG-3'; *Nkx2-1* (endogenous isoform), forward 5'-GGCGCCATGTCTTGTCT-3', reverse 5'-GGGCTCAAGCGCATCTCA-3'; *Pax8* (endogenous isoform), forward 5'-CAGCCTGCTGAGTTCTCCAT-3', reverse 5'-CTGTCTCAGGCCAAGTC CTC-3'; *Foxe1*, forward 5'-GGCGGCATCTACAAGTTTCAT-3', reverse 5'-GGATCTTGAGGAAGCAGTCG-3'; *Tshr*, forward 5'-GTCTGCCAATATT TCCAGGATCTA-3', reverse 5'-GCTCTGTCAAGGCATCAGGGT-3'; *Slc5a5*, forward 5'-AGCTGCCAACACTTCCAGAG-3', reverse 5'-GATGAGAGCAC CACAAAGCA-3'; *Tg*, forward 5'-GTCCAATGCCAAATGATGGTC-3', reverse 5'-GAGAGCATCGGTGCTGTAAAT-3'; *Tpo*, forward 5'-ACAGTACAGTTCT CCACGGATG-3', reverse 5'-ATCTCTATTGTTCACGCCCC-3'.

**Immunofluorescence and immunohistochemistry.** For immunofluorescence experiments, cells were fixed in 4% paraformaldehyde (Sigma) for 30 min and washed three times in PBS. Cells were blocked in a solution of PBS containing 3% bovine serum albumin (BSA; Sigma), 5% horse serum (Invitrogen) and 0.3% Triton X-100 (Sigma) for 30 min at room temperature (between 20 and 23.5 °C). The primary and secondary antibodies were diluted in a solution of PBS containing 3% BSA, 1% horse serum and 0.1% Triton X-100. Primary antibodies were incubated overnight at 4 °C followed by incubation with secondary antibodies for 2 h at room temperature. Nuclei were stained with Hoechst 33342 (Invitrogen). Coverslips were mounted with Glycergel (Dako). For histological examination, grafted animals, previously anaesthetized, were perfused with 4% paraformaldehyde and the explanted kidneys were fixed overnight in 4% paraformaldehyde. Tissues were processed for paraffin or Tissue-Tek O.C.T. Compound (Sakura) inclusion. Immunohistochemistry on paraffin-embedded tissue sections was

performed as described previously in ref. 31. Optimal cutting temperature embedded tissue sections were incubated in blocking buffer containing 5% horse serum, 1% BSA and 0.2% Triton X-100 in PBS for 1 h at room temperature. For PECAM-1 immunostaining only, a prior antigen retrieval was performed by incubating tissue sections in 0.1% trypsin solution for 30 min at 37 °C. Primary antibodies were diluted in blocking solution and incubated overnight at 4 °C (at room temperature for anti-PECAM-1). Sections were rinsed three times in PBS and incubated with secondary antibodies diluted in blocking solution at 1:400 for 1 h at room temperature. Nuclei were stained with Hoechst 33342 (Invitrogen) and slides were mounted with Glycergel (Dako).

**Antibodies.** The following primary antibodies were used: mouse anti-NKX2-1 (clone 8G7G3/1 Invitrogen, 1:3,000), rabbit anti-NKX2-1 (PA 0100 Biopat, 1:3,000), rabbit anti-PAX8 (PA 0300 Biopat, 1:3,000), rabbit anti-FOXE1 (PA 0200 Biopat, 1:600), rabbit anti-TG (A0251 Dako, 1:3,000), rabbit anti-NIS (a gift from N. Carrasco, 1:1,000), mouse anti-E-cadherin (610181 BD, 1:3,000; 1:200 for immunohistochemistry on cryosections), mouse anti-ZO-1 (339100 Invitrogen, 1:750), rabbit anti-T4 (MP Biochemicals, 1:3,000), mouse anti-TG-I (a gift from C. Ris-Stalpers, 1:2,000), rat anti-PECAM-1 (557355 BD, 1:100), rabbit anti-calcitonin (A0576 Dako, 1:8,000), mouse anti-SSEA-1 (MAB4301 Millipore, 1:500), rabbit anti-Oct4 (ab19857 Abcam, 1:500) and rabbit anti-Nanog (ab21603 Abcam, 1:200). Secondary antibodies were donkey anti-mouse, anti-rabbit and anti-rat IgG conjugated with DyLight-488, Cy3 and DyLight-647 (Jackson ImmunoResearch), goat anti-chicken IgG conjugated with Alexa-488 (Invitrogen) and donkey biotinylated anti-rabbit IgG (Jackson ImmunoResearch).

**FISH analysis.** Fluorescence *in situ* hybridization (FISH) analysis on paraffin-embedded tissue sections was modified from a previous description<sup>32</sup>. In brief, sections, previously de-paraffinized in toluene (three times, 5 min for each) and rehydrated through graded alcohols to water, were incubated in 1 M sodium thiocyanate (Sigma) for 10 min at 80 °C, washed in PBS and then digested in 0.4% pepsin (Sigma, P7012) in 0.1 M HCl for 10 min at 37 °C. Digestion was quenched in 0.2% glycine (Sigma) in 2X PBS, and sections were then rinsed twice in 1X PBS, post-fixed in 4% paraformaldehyde, washed three times in 1X PBS and finally dehydrated through graded alcohols and air dried. The probe mixture was prepared according to manufacturer's instructions. In brief, 3  $\mu$ l of mouse iDetect biotin-labelled chromosome Y paint probe (Star-FISH, Cambio; IDMB1055) were diluted in 7  $\mu$ l of supplied hybridization buffer. The probe mixture was added to the sections, covered with a glass coverslip (22  $\times$  22 mm), sealed with rubber cement, and probes/sections were denatured for 10 min at 60 °C and then incubated overnight at 37 °C in a humid chamber. The next day, detection of Y chromosome was performed using biotin-labelled chromosome detection protocol detect with Texas Red (Star-FISH, Cambio; 1082-KT-50) according to the manufacturer's instructions.

**Iodide organization assay.** Cells at day 22 of differentiation were washed with HBSS and incubated with 1 ml of an organization medium containing 1,000,000 c.p.m. per ml <sup>125</sup>I (PerkinElmer) and 100 nM sodium iodide (Sigma) in HBSS for 2 h at 37 °C. After addition of 1 ml 4 mM methimazole (MMI, Sigma), a TPO inhibitor, cells were washed with ice-cold HBSS and detached by a solution containing 0.1% trypsin (Invitrogen) and 1 mM EDTA (Invitrogen) in PBS for 15 min. Cells were collected in polyester tubes and radioactivity was measured with a  $\gamma$ -counter, indicating the cell iodide uptake. Subsequently, proteins were precipitated twice by addition of 1 mg  $\gamma$ -globulins (Sigma) and 2 ml 20% TCA followed by centrifugation at 2,000 r.p.m. for 10 min and the radioactivity of protein-bound [<sup>125</sup>I] (PBI) was measured using a  $\gamma$ -counter. Iodide organization was calculated as an iodide uptake/PBI ratio and the values expressed as a percentage. Background protein-bound radioactivity was measured in cells incubated with organization medium supplemented with 2 mM methimazole. Results were confirmed in three different clones for each ESC line.

**Generation of the induced-hypothyroidism mouse model and transplantation of ESC-derived thyroid follicles.** All animal experiments and care were in compliance with institutional guidelines and local ethical committees. 129P2/OlaHsd mice (5-week-old females) were provided by the Harlan Laboratory. The hypothyroidism mouse model was generated as described previously in ref. 30. In brief, experimental hypothyroidism was induced by administering 150  $\mu$ Ci of <sup>131</sup>I by intraperitoneal injection to mice, which had been placed on a low-iodine diet (custom iodine-deficient food, SAFE) for 8 days. Four weeks after the administration of <sup>131</sup>I, plasma levels of T4 were analysed to confirm the hypothyroid status. One week later (fifth week), the hypothyroid mice were weighed and anaesthetized with 3 ml kg<sup>-1</sup> of an anaesthetic solution composed of 20 mg ml<sup>-1</sup> of ketamine (Ketalar; Pfizer) and 2 mg ml<sup>-1</sup> xylazine (Rompun; Bayer) and then injected with a volume of 8  $\mu$ l Dox/rhTSH-treated or -untreated day-22 cells into the unilateral kidney under the capsule using a 30G needle syringe (Hamilton Bonaduz AG) (the kidney was exposed by skin/muscle/peritoneum incision through the dorsolateral approach). Four weeks later (ninth week), the grafted

mice were subjected to body-temperature measurement, blood sampling for plasma T4 and TSH measurements, whole-body imaging and sacrifice for histological examination of the kidneys.

**Body-temperature measurement.** Rectal temperature was measured in conscious mice using a highly sensitive dedicated sensor (Iso-Temp-2) connected to an Apollo-1000 unit (World Precision Instruments). Animals were restrained and kept motionless to obtain a stable rectal temperature.

**Plasma T4 and TSH-level measurements.** Total T4 levels were assayed by a <sup>125</sup>I radioimmunoassay (Coat-A-Count Canine T4, Siemens) according to the manufacturer's instructions. TSH was measured in 50 µl of serum as described previously in ref. 33. Labelled TSH was provided from the Institute of Isotopes Co.

**TSH-stimulation test.** The TSH-stimulation test was modified from a previous description<sup>21</sup>. In brief, a single injection of 10 mU of bovine TSH (Sigma) was given intraperitoneally to animals pretreated for 4 days with 3 µg T3 (Sigma) per day. Blood sampling was performed before and 3 h after bovine TSH injection for the measurement of T4.

**Whole-body planar imaging.** Pertechnetate was used in this study because it is a good indicator for demonstrating the presence of NIS. Approximately 30 min after intramuscular injection of 37 MBq (1 mCi) <sup>99m</sup>Tc-pertechnetate in the thigh region, the scans were performed on a dual-head gamma camera (Toshiba, GCA 7200 A) equipped with a low-energy high-resolution collimator. For this procedure mice were anaesthetized with isoflurane (IsoFlo; 2% end-tidal

concentration) and kept with oxygen using a re-breathing system and a mask. One static image (acquisition time 10 min, matrix 128 × 128, zoom 3) was made in ventral recumbency.

**Statistical analysis.** Statistical significance was tested as follows: two-group comparison by unpaired *t*-test and multiple-group comparison by the one-way analysis of variance test with a post-hoc Tukey's comparison test. For quantification of NKX2-1 and PAX8 double-positive cell numbers, at least 2,000 cells were counted in ten different fields from three biologically independent experiments.

**Imaging.** Fluorescence imaging was performed on a Zeiss LSM510 META confocal microscope, a Zeiss Axio Observer Z1 microscope with AxioCamMR3 camera and a Leica DMI6000 with DFC365FX camera. Images were processed with ImageJ. Bright-field imaging was performed on a Zeiss Axioplan2 microscope with the AxioCamHR camera. Images were processed with Axiovision release 4.8 software. Photoshop CS5 (Adobe) was used to adjust brightness, contrast and picture size.

31. Rodriguez, W. *et al.* Deletion of the RNaseIII enzyme dicer in thyroid follicular cells causes hypothyroidism with signs of neoplastic alterations. *PLoS ONE* **7**, e29929 (2012).
32. Poulsom, R. *et al.* Bone marrow contributes to renal parenchymal turnover and regeneration. *J. Pathol.* **195**, 229–235 (2001).
33. Pohlenz, J. *et al.* Improved radioimmunoassay for measurement of mouse thyrotropin in serum: strain differences in thyrotropin concentration and thyrotroph sensitivity to thyroid hormone. *Thyroid* **9**, 1265–1271 (1999).

# Spontaneous network formation among cooperative RNA replicators

Nilesh Vaidya<sup>1</sup>, Michael L. Manapat<sup>2</sup>, Irene A. Chen<sup>3†</sup>, Ramon Xulvi-Brunet<sup>3</sup>, Eric J. Hayden<sup>4</sup> & Niles Lehman<sup>1</sup>

**The origins of life on Earth required the establishment of self-replicating chemical systems capable of maintaining and evolving biological information. In an RNA world, single self-replicating RNAs would have faced the extreme challenge of possessing a mutation rate low enough both to sustain their own information and to compete successfully against molecular parasites with limited evolvability. Thus theoretical analyses suggest that networks of interacting molecules were more likely to develop and sustain life-like behaviour. Here we show that mixtures of RNA fragments that self-assemble into self-replicating ribozymes spontaneously form cooperative catalytic cycles and networks. We find that a specific three-membered network has highly cooperative growth dynamics. When such cooperative networks are competed directly against selfish autocatalytic cycles, the former grow faster, indicating an intrinsic ability of RNA populations to evolve greater complexity through cooperation. We can observe the evolvability of networks through *in vitro* selection. Our experiments highlight the advantages of cooperative behaviour even at the molecular stages of nascent life.**

The 'RNA world' is a plausible stage in the development of life because RNA simultaneously possesses evolvability and catalytic function<sup>1</sup>. An RNA organism that could evolve in such a fashion is likely to have been one of the Earth's first life forms. A search is underway<sup>2,3</sup> for an RNA autoreplicase that relies on its individual genotype to compete for survival and reproduction by Darwinian-type evolution in a fitness landscape. Yet the transition from a prebiotic chemistry to this stage of life is not understood. Several authors have proposed that the most primitive life thrived less on discrete genotypes and instead on collections of molecular types more subject to systems chemistry than to straightforward selection dynamics<sup>4–9</sup>. In particular, it was suggested that webs of functionally linked, genetically related replicators were required in the earliest phases of life's appearance to prevent informational decay (the so-called error catastrophe)<sup>4,10–12</sup>.

An empirical demonstration of RNA replicator networks could illuminate critical features of this early stage of life. Ribozymes are good candidates for this because they can evolve outside of an organismal context, construct other RNAs, exhibit self-sustained reproduction, and explore sequence space in efficient ways<sup>13–15</sup>. However, their ability to form catalytic networks capable of expanding as predicted from theory has not yet been shown, despite the observation that collections of nucleic acids have the potential to manifest complexity<sup>6,16</sup>. Simulations show that molecular networks should arise, evolve and provide a population with resistance against parasitic sequences<sup>8</sup>. These results are robust within structured environments such as cells or on grids, but are less so in a solution phase. Recent experimental work *in vitro* has been very successful at demonstrating simple ecologies<sup>17–19</sup>, reciprocity between two species<sup>6,16,20</sup>, and sustained exponential growth via cross catalysis<sup>15</sup>. Empirical efforts to date have been limited by an inability to expand past reciprocal interactions between two species to prebiotically relevant systems that have the capacity to increase their complexity by expanding to three, and then more, members<sup>18,21</sup>. Specifically, the use of systems in which the recognition domain in the catalyst and the target domain in the substrate are co-located in each replicator has prevented networks of more than two members from forming. If this molecular feature could

be circumvented, larger networks could be realized within RNA populations in the test tube and help demonstrate a potential escape from the error catastrophe problem that tends to plague selfish systems.

## The *Azoarcus* ribozyme system

The ~200-nucleotide (nt) *Azoarcus* group I intron ribozyme<sup>22</sup> can be broken into fragments that can covalently self-assemble by catalysing recombination reactions in an autocatalytic fashion<sup>23,24</sup> (Supplementary Fig. 1). By allowing variation in the sequence recognition mechanism by which this assembly occurs, which is provided by the 3-nt internal guide sequence (IGS) at the 5' end of the ribozyme, many such autonomously self-assembling ribozymes become possible. We sought to determine if these ribozymes could display cooperative behaviour if their IGS sequences target the assembly of other ribozymes, but not themselves.

To create a cooperative network, we fragmented the *Azoarcus* ribozyme into two pieces in three different ways with the intent of observing how they could spontaneously reassemble via intermolecular cooperation (Fig. 1a, b). We manipulated the IGS (canonically GUG) and its target triplet to generate both matched and mismatched partners. We mixed various IGS and target pairs in two-piece constructs to test the ability of mismatched pairs to promote self-assembly (Supplementary Fig. 2). From these data, we chose three mismatched pairs that exhibit relatively little autocatalysis: GUG/CGU, GAG/CAU, and GCG/CUU. These crippled pairs are denoted I<sub>1</sub>, I<sub>2</sub> and I<sub>3</sub>, respectively, meaning that they are informational subsystems, albeit weakly autocatalytic.

We chose the triplet pairs so that when the three subsystems are mixed together, they should constitute a cyclical cooperative network in which the output of one subsystem can catalyse the replication of the next one in the cycle (Fig. 1b). This occurs because the IGS of one subsystem is matched to the target in the next subsystem, and the physical separation of the IGS and its target allows for cycles of more than two members. When the six RNAs (W, **h**•X•Y•Z, W•X, **h**•Y•Z, W•X•Y and **h**•Z; • indicates covalent bonding) are allowed to fold together and be co-incubated in equimolar ratios, we expect the subsystems first to

<sup>1</sup>Department of Chemistry, Portland State University, PO Box 751, Portland, Oregon 97207, USA. <sup>2</sup>School of Engineering and Applied Sciences and Program for Evolutionary Dynamics, Harvard University, Cambridge, Massachusetts 02138, USA. <sup>3</sup>FAS Center for Systems Biology, Harvard University, Cambridge, Massachusetts 02138, USA. <sup>4</sup>Department of Bioengineering, Stanford University, Stanford, California 94305, USA. <sup>†</sup>Present address: Department of Chemistry and Biochemistry, University of California, Santa Barbara, California 93106, USA.

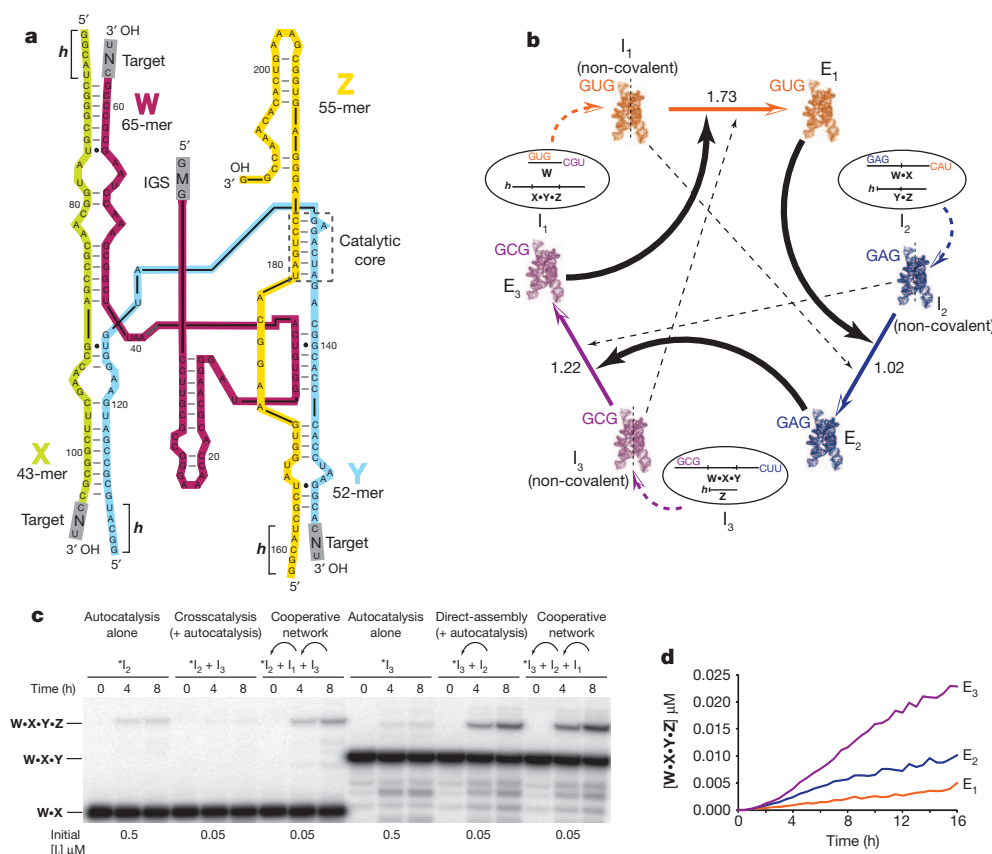


**Figure 1 | Cooperative covalent assembly of recombinase ribozymes.**

**a**, Design of recombinase ribozymes capable of spontaneous cooperative covalent assembly from fragments. The *Azoarcus* ribozyme<sup>25</sup> can be broken at three loop regions to obtain four oligomers capable of self-assembling into a full-length molecule<sup>26,27</sup>. The grey box in **W** (magenta) is the internal guide sequence (IGS), whereas those at the 3' ends of the **W**, **X** (lime) and **Y** (blue) fragments are recombination targets (tags) recognized by the IGS, which guides the catalysis of a covalent closure (•) of the loops. **b**, A cooperative system comprised of three subsystems, each created from partitioning the molecule into two pieces at different junctions:  $I_1$  (**W** + **h•X•Y•Z**),  $I_2$

(**W•X** + **h•Y•Z**) and  $I_3$  (**W•X•Y** + **h•Z**). Numbers over arrows estimate the cooperative advantage for each step (see text). **c**, Electrophoretic observation of assemblies of  $E_2$  and  $E_3$ . The 5' fragments of  $I_2$  or  $I_3$  were independently 5'-radiolabelled with <sup>32</sup>P (that is,  $*I_2$  or  $*I_3$ ). The reactions were performed by incubating 0.5 μM (for autocatalysis) or 0.05 μM (for direct assembly, cross catalysis and cooperation) of each fragment for 8 h. Where appropriate, the arrows identify the subsystems being assembled by the previous subsystems in the network, where the IGS and recombination tags match. **d**, Yields of individual  $E_i$  ribozymes over time, measured every 30 min for 16 h when all six  $I_i$  RNA fragments are co-incubated at 0.05 μM.

form non-covalent versions of ribozymes, and then catalyse the formation of covalent versions of the next ribozyme in the cycle.

To test whether cooperation between enzymes occurred, we took several approaches. First, for the cycle to exhibit positive feedback<sup>4</sup>, there should be a distinct advantage to being a covalently contiguous ribozyme ( $E_i$ ), as opposed to remaining fragmented ( $I_i$ ). Once covalent ribozymes are formed, they should further promote synthesis of their target ribozymes, at faster rates than the non-covalent versions would. When we tested each in isolation, we found that the  $E_i$  ribozymes recombined their respective target substrates into products 1.3–6.3-fold more than the  $I_i$  versions when assayed separately (Supplementary Fig. 3). Second, by examining each subsystem in isolation or in pairs, we could compare the relative strengths of autocatalysis ( $E_i$  synthesizing  $E_i$ ), cross-catalysis ( $E_{i+1}$  synthesizing  $E_i$ ), and what should be the most efficient, direct catalysis ( $E_i$  synthesizing  $E_{i+1}$ ). When we incubated just the two RNAs from any one subsystem, such as  $I_2$ , alone, there is minimal synthesis of the corresponding ribozyme  $E_2$ ; after a few hours roughly 0.1% of **W•X** is converted into **W•X•Y•Z**. This low background level of autocatalytic synthesis reflects residual catalytic activity available to a mismatched IGS and IGS target, for example GAG with CAU<sup>25</sup>, showing that each  $I_i$  subsystem has severely limited information-replication potential in isolation. Likewise, when the four RNAs of two subsystems were co-incubated, the cross-catalytic synthesis of the ribozyme corresponding to the preceding subsystem in the cycle is similarly poor, again hindered by an IGS–IGS–target mismatch (Fig. 1c). After only 1 h of

incubation, the yield of  $E_3$  from 0.5 μM  $I_3$  is  $0.10 \pm 0.02\%$  (autocatalysis), and the yield of  $E_3$  from 0.5 μM  $I_3$  and 0.5 μM  $E_1$  is  $0.7 \pm 0.06\%$  (cross-catalysis), but the yield of  $E_3$  from 0.5 μM  $I_3$  and 0.5 μM  $I_2$  is  $13 \pm 0.5\%$  (direct catalysis) (data not shown; errors given as s.e.m.). These differences are all statistically significant as measured by *t*-tests several planned comparisons ( $P < 0.001$ ). From these data we determined that direct catalysis is significantly more efficient than catalysis resulting from mismatched IGS sequences and their targets.

When all six RNAs of all three subsystems are co-incubated, cooperation causes the synthesis of **W•X•Y•Z** to rapidly escalate, as expected. The composite yield of full-length RNA after 16 h when  $I_1$ ,  $I_2$  and  $I_3$  are mixed is 125-fold higher than the sum of the yields of the three subsystems in isolation (Supplementary Fig. 4). This enhancement can be readily visualized after shorter periods of time (Fig. 1c). Each subsystem grows at a different rate (Fig. 1d). The synthesis of  $E_3$  by  $E_2$  is more rapid than that of the other two ribozymes, presumably because the non-covalent version of the enzyme ( $I_2$ ) is nearly as efficient as the covalent version ( $E_2$ ); it could also be because certain IGS–IGS target pairs are more efficient<sup>25</sup>. Importantly, we can detect two-step (relayed) cooperativity by comparing the yields with and without the intervening enzyme. In the case of  $E_1$  for example, after 4 h the increase in yield of  $E_1$  upon addition of  $I_2$  to  $I_1$  with  $I_3$  present is 2.5%, whereas the increase in yield of adding  $I_2$  to  $I_1$  without  $I_3$  present is only 0.02%, showing the operation of  $E_2$  through  $E_3$  onto  $E_1$  (Supplementary Table 1); this is supported by doping experiments (Supplementary Fig. 5).

To observe the advantage of cooperation in another way, we constructed a control system in which the  $I_i$  molecules could act as catalysts, but could not be covalently assembled themselves because their target sequences were not a match for any catalyst in the system (Supplementary Fig. 5). Cooperation would be manifest when enzymes synthesize other enzymes, and there is some benefit to being covalent. Thus we measured the yields of  $W \cdot X \cdot Y \cdot Z$  molecules at 8 h in this control system and in our normal system (that is, Fig. 1b). The yields in the control system were consistently worse, and we calculated the ratio ( $E_i$  catalysis +  $I_i$  catalysis) to ( $I_i$  catalysis only) as the advantage of being covalent in each leg of the cycle. These ratios, indicated above the coloured arrows in Fig. 1b, are 1.73, 1.02 and 1.22 for  $i = 1, 2$  and 3, respectively. Assuming these values are multiplicative, the cooperative benefit is about 2.2 for the entire cycle.

An impediment to truly hyperbolic growth for such a system<sup>4</sup> is the occasional formation of non-productive complexes (for example,  $W \cdot Y \cdot Z$ ) through partially complementary base pairing (Fig. 1a). We can detect such complexes (Supplementary Fig. 6), but when they are minimized by pre-folding each RNA separately, the yield after 2 h increases by 25–50% (Supplementary Fig. 7). As shown by heat-cool regimes, reverse reactions that have the net effect of breaking down covalent ribozymes into fragments may also have a small role in preventing hyperbolic growth (Supplementary Fig. 8).

## Cooperation versus selfishness

Next we tested whether a three-membered cooperative system has the potential to have higher fitness than purely autocatalytic systems when placed in direct competition (Fig. 2). To construct 'selfish' autocatalytic subsystems ( $S_i$ ), we reverted the IGS–IGS target pairs within each subsystem so that they would match. To create  $S_1$  we used  $GUG \cdot W_{CAU}$  and  $h \cdot X \cdot Y \cdot Z$ , to create  $S_2$  we used  $GAG \cdot W \cdot X_{CUU}$  and  $h \cdot Y \cdot Z$ , and to create  $S_3$  we used  $GCG \cdot W \cdot X \cdot Y_{CGU}$  and  $h \cdot Z$ . Each of these subsystems replicates well in isolation. Upon mixing of RNAs, we tracked selfish and cooperative ribozymes by the composition (matched or mismatched, respectively) of the  $W$ -containing fragments because these contain the IGS and hence the most crucial genetic element (Fig. 2a). When we compared the total yield of  $S_1 + S_2 + S_3$  to that of  $I_1 + I_2 + I_3$ , the former out-performed the latter at all time points (that is, selfishness wins in isolation). One reason for this result is that there would be less time delay in initiating covalent synthesis in the all-selfish system. However, when we placed

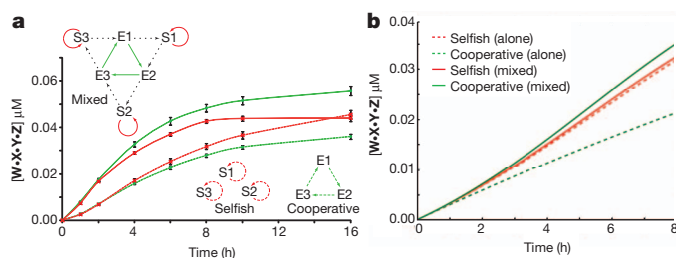


**Figure 2 | Cooperative chemistry out-competes selfish chemistry when directly competed.** **a**, Empirical results using cooperative ( $I_1, I_2$  and  $I_3$ , that is, Fig. 1b) and selfish subsystems ( $S_1, S_2$  and  $S_3$ , where IGS and IGS targets were changed to be matching in each subsystem). Yields of total  $W \cdot X \cdot Y \cdot Z$  RNA tracked the concentrations of cooperative (mismatched) or selfish (matched)  $W$ -containing RNAs (0.05  $\mu M$  initial concentrations) over time either when the cooperative (green) and selfish (red) sets of subsystems were incubated separately (dashed lines) or together in the same reaction mixture (solid lines; upper left inset). Data points are averages of three independent trials. Error bars show the standard error of the mean (s.e.m.), and the yields of the cooperative trials in the mixed experiment are significantly greater than those of the selfish trials at the 10- and 16-h time points ( $P < 0.05$  by  $t$ -tests using Sidak's correction for multiple *a posteriori* comparisons). **b**, Simulation of growth dynamics using a toy model of the network of cooperation and selfish interactions (see Supplementary Information). Cooperative enzymes fare better in competition than do selfish enzymes, as demonstrated empirically in panel a.

all six subsystems (12 RNAs:  $I_1 + I_2 + I_3 + S_1 + S_2 + S_3$ ) in the same reaction, the relative yields at later times are reversed, and the growth of the enzymes resulting from the cooperative network now exceeds those from the selfish subsystems (that is, cooperation wins in competition). These results are independent of the exact RNA fragments we chose, as the same result can be seen in other systems with different IGS and IGS targets (see Supplementary Fig. 9). The yield reversal upon mixing happens because the selfish enzymes now participate in—and effectively expand—the cooperative network (Supplementary Fig. 10). This would be a mechanism for a network connectivity increase when the subsystems involved are competing for at least one shared resource, in this case the catalytic core ( $Y \cdot Z$ ), because all  $W$ -containing fragments can use the same 3' fragments. Whereas selfish enzymes can also benefit from the network, the asymmetry in the proficiencies of the various IGS–IGS-target pairings creates potential for an asymmetry in the relative benefits of the various enzymes in the mixed environment. This feature would have been common in primordial genetic systems, allowing us to posit that cooperation could have been predisposed even in homogeneously mixed environments.

## Modelling

Empirical systems such as the one described above are subject to the particularities of chemical and methodological idiosyncrasies, so we sought to generalize these results by constructing mathematical models that show that under a certain set of parameters, the laboratory results should indeed be possible. First we constructed an ordinary differential equation (ODE) model for the three-membered network shown in Fig. 1b. We tracked the yield of each of the three  $E_i$  ribozymes separately—using three identical replicates from the same initial reaction mixture—by taking aliquots every 30 min for 16 h (Fig. 1d). We used standard optimization techniques to find the rate constants of all the possible reactions in Fig. 1b that produced trajectories in the ODE system closest to the observed data (Supplementary Information). We used these estimated rate constants to construct a second ODE model that would mimic the cooperative growth of the three subsystems. In general, the non-covalent versions of the ribozymes form relatively tight complexes, with  $K_d$  values in the low nanomolar range. When we built cooperative behaviour into the model by relying on differential equations of type  $dE_i/dt = k_{ij}[I_j][E_i]$ , the experimental data were fit very well in all three subsystems (Supplementary Fig. 11). When we removed direct catalysis from the model and inserted only autocatalysis instead, the quality of the fit decayed substantially such that the root mean squared error was 2.4-fold greater (Supplementary Fig. 12), confirming these results. These data support the contention that replication of the subsystems is indeed cooperative.

Next we constructed a toy model comparing the cooperative and selfish behaviours seen in Fig. 2a using the dynamical relationships that can exist among all enzymes (Fig. 2b). The 'selfish' enzymes perform some altruistic catalysis when alternative substrates become available. The empirical data display more striking yield differences than the model, perhaps because the time delays in bringing the results of the selfish catalytic events back to the selfish subsystems are exacerbated by physical processes such as diffusion. Again this result is general, at least within this network topology, and does not depend on the particular IGS–IGS-target pairings chosen. In essence, although the selfish replicators can parasitize the cooperators, the cooperative network benefits more by incorporating the selfish RNAs. Interestingly, the opposite is generally true in evolutionary dynamics: groups of cooperative individuals grow more quickly than groups of selfish individuals, but a group consisting of both types will eventually be dominated by the selfish<sup>26</sup>. One limitation to the experiment shown in Fig. 2a is that there is only a single iteration of selection. The RNAs used to seed the experiment limit its evolutionary potential; Supplementary Fig. 13 depicts joint genotype frequency changes over time. Experiments in a serial transfer format are needed to show the selection of one strategy over the other (see below), but we

can use both our data and modelling to predict that cooperation would have been advantageous in simpler chemical systems that preceded organismal biology.

## Randomization experiment

The system described in Fig. 1 is only one of a very large number of possibilities. To test the notion that cooperative networks of RNA could form spontaneously, we randomized the middle nucleotide of both the IGS (M) and its target triplet (N) in fragments of the ribozyme, generating both matched and mismatched partners within a population. We created three pools of randomized fragments containing the IGS on the 5' end of the ribozyme:  $\text{GMG}\mathbf{W}\text{CNU}$ ,  $\text{GMG}\mathbf{W}\mathbf{X}\text{CNU}$  and  $\text{GMG}\mathbf{W}\mathbf{X}\mathbf{Y}\text{CNU}$ , plus three fragments containing the catalytic core and the 3' end of the ribozyme:  $\mathbf{X}\mathbf{Y}\mathbf{Z}$ ,  $\mathbf{Y}\mathbf{Z}$  and  $\mathbf{Z}$  (Fig. 3a). Fourfold variation in M and in N, combined with threefold variation in the junction (j) where recombination occurs (before X, Y or Z) leads to 48 genotypic possibilities (Fig. 3a). These assembled ribozymes can be distinguished by three variables: (1) the middle nucleotide of the IGS (M), (2) the location of the junction (x, y or z) and (3) the middle nucleotide of the target (N). We therefore denote each ribozyme with the three-letter code  $\text{MjN}$ , where  $j = x, y$  or  $z$ . Each of these ribozymes can be covalently assembled by any other ribozyme, itself covalently contiguous or not, provided that M in the catalyst is complementary to N in the substrate.

When we incubated equimolar amounts of these six RNA sets, all 48 possible full-length  $\mathbf{W}\mathbf{X}\mathbf{Y}\mathbf{Z}$  *Azoarcus* ribozymes arose. The relative frequencies of the 48 possible full-length ribozymes recovered at each time point over an 8 h time course (Supplementary Table 2) show that, in accordance with the above and published data<sup>25</sup>, recombination at the Y–Z junction is favoured, but no single genotype ever

exceeded 13% of the total. Growth in the randomization experiment showed markedly greater yields (2–12-fold) than in our engineered three-membered system (Fig. 3b), indicating that far more productive interactions among RNA species are occurring in the former.

From approximately three million  $\mathbf{W}\mathbf{X}\mathbf{Y}\mathbf{Z}$  genotypes sampled at each time point, distinct trends portray indirect evidence of a rapid succession from smaller to increasingly larger networks of cooperators (Fig. 3c, d). Genotypes that could easily propagate by selfish autocatalytic replication peak at or before the first time point at 30 min (Fig. 3c, dotted line with crosses). These are  $S_j$  genotypes (for example, those in Fig. 2) where M and N are complementary. A prime example is  $\text{CyG}$ , which could increase in number from the association of  $\text{GCG}\mathbf{W}\mathbf{X}\text{CGU}$  and  $\mathbf{Y}\mathbf{Z}$  molecules, and this genotype rose in frequency from 4.8% to 7.2% between 30 min and 2 h. Out of the 48 possible product genotypes, twelve (25%) are of this type.

After peaking early, the frequencies of autocatalysts dropped below random expectation and then slowly climbed. Because of extremely large sample sizes, these deviations are highly significant (two-tailed G-tests of independence;  $P \ll 0.001$ ). However, this later frequency increase may not be a consequence of autocatalysis per se, but of the incorporation of autocatalysts into higher-ordered networks, akin to the mechanism by which cooperative networks assimilate selfish replicators (Fig. 2 and Supplementary Fig. 10). Analyses of the frequencies of the product genotypes cannot reveal the identities of the catalysts that made them, and thus do not provide direct evidence of replicator cycles. Nevertheless, we examined whether networks of two or more distinct members could be increasing over time. Some pairs of genotypes can cooperate with each other to form two-membered cycles (for example,  $\text{AxG} + \text{GzU}$ ), whereas others cannot (for

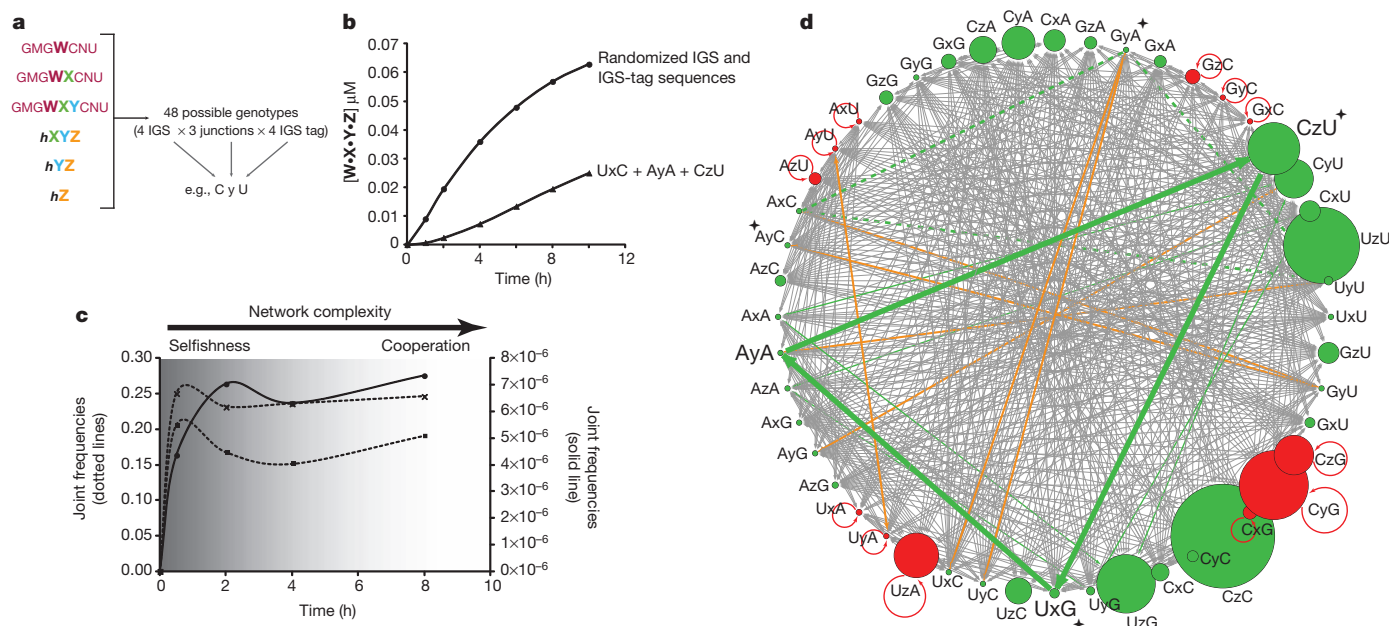


**Figure 3 | The randomization experiment.** **a**, Experimental design. The middle nucleotides of the IGS and the tags were randomized to create diverse RNA pools. A reaction of 300 pmol each (0.5  $\mu\text{M}$ ) of  $\text{GMG}\mathbf{W}\text{CNU}$ ,  $\text{GMG}\mathbf{W}\mathbf{X}\text{CNU}$ ,  $\text{GMG}\mathbf{W}\mathbf{X}\mathbf{Y}\text{CNU}$ ,  $\mathbf{X}\mathbf{Y}\mathbf{Z}$ ,  $\mathbf{Y}\mathbf{Z}$  and  $\mathbf{Z}$  was sampled at 0.5, 2, 4 and 8 h, and millions of recombined full-length  $\mathbf{W}\mathbf{X}\mathbf{Y}\mathbf{Z}$  ribozymes were genotyped by nucleotide sequence analysis (Supplementary Table 2). **b**, Comparison of growth curves from fixed and randomized RNAs. Yields over time were compared for the simple three-membered cycle (filled triangles,  $\text{UxG} + \text{AyA} + \text{CzU}$ ; the sum of the three curves in Fig. 1d) to that in the randomized format (filled circles, panel **a**) when both were performed at the same RNA pool concentrations (0.05  $\mu\text{M}$ ). **c**, Proposed succession from simple to complex networks using genotype frequency data from experiment in panel **a**. Simple autocatalytic cycles where M and N are complementary were directly tracked by the sum of such  $\mathbf{W}\mathbf{X}\mathbf{Y}\mathbf{Z}$  molecules (dashed line with crosses; for example,  $\text{AzU}$ ). Reciprocal two-membered cycles were tracked by the sum ( $\times 10$ ,

for ease of presentation) of the joint frequencies of all genotypes that can potentially participate in such cycles (dashed line with squares; for example,  $\text{AxG} + \text{UxU}$ ). The rise of three-membered cycles can be seen from the sum ( $\times 10,000$  for ease of presentation) of joint frequencies of three sets of genotypes: Fig. 1b and its two permutations by junction (solid line;  $\text{UxG} + \text{AyA} + \text{CzU}$ ;  $\text{UyG} + \text{AzA} + \text{CxU}$ ;  $\text{UzG} + \text{AxG} + \text{CyU}$ ). See Supplementary Information for calculation of the joint frequencies. **d**, The potential network of RNA genotypes. Each node is one of the 48 possible  $\text{MjN}$  genotypes; size scales with relative frequency in the 8 h pool. Nodes are autocatalysts (red) or those that must replicate cooperatively (green). Grey arrows show all possible direct catalytic events; orange arrows show reciprocal two-membered cycles in which the frequencies of both members at least double between 30 min and 2 h; green arrows show key three-membered networks: thick green is the system studied in depth (Fig. 1b), thin green are permutations by junction, dotted green is  $\text{AxG} + \text{GyA} + \text{UyU}$ . Starred genotypes can participate in a four-membered network.

example,  $AxC + UzG$ ). We noticed that the global joint frequencies of the members comprising all possible two-membered cycles peaked at 30 min, declined and recovered, although delayed with respect to the autocatalysts (Fig. 3c). Support for the succession from autocatalysts to these two-membered cycles is found in the frequencies of two possible partners for the autocatalysts GjC, which are CxG and CzG (autocatalysts themselves); the sum of these rose monotonically between 2–8 h (3.7% to 6.1%).

At roughly 2 h, a succession to three-membered cycles may have occurred. Although there are hundreds of such possible assemblages, the joint frequencies of the members of diverse ones requiring synthesis at all three junctions (such as  $UxG + AyA + CzU$ ) jump at the 2 h mark (Fig. 3c, solid line). Many others peak then as well; the joint frequency of the  $AxC + GyA + UyU$  trio increases nearly 20-fold after the 30 min point. At 4 h and later the possibility of succession to even higher-ordered networks that subsume all simpler ones obfuscates individual trends. Visualization of all possible connections among genotypes underscores these conclusions (Fig. 3d). By 8 h the network is dominated by genotypes that can only be replicated via cooperation (green circles). In fact, the variance in the genotype frequencies drops monotonically over the course of the experiment, indicating that all genotypes increasingly participate in the network over time.

### Serial transfer of the randomized population

The experiments depicted in Fig. 3 portray the dynamic changes that occur on a kinetic time scale as a batch of RNAs approaches equilibrium. In an actual prebiotic scenario, however, this effect would be iterated and perhaps magnified over several generations, as opposed to being an asymptotic value that results from mixing several RNAs in a single reaction vessel. To bring a stronger evolutionary flavour, we repeated the randomization experiment but in a serial transfer format. Starting with another aliquot of the exact same set of RNAs (that is, products from the same *in vitro* transcription), we carried a population through eight serial transfers, taking 10% of the population each hour into a fresh tube of fragments. In this manner the  $W \cdot X \cdot Y \cdot Z$  molecules that spontaneously assemble are continually being fed with new fragments, such that selection will favour those molecules and networks that grow faster and persist over iterations. Given that the assembly that occurs each round can be strongly influenced by the actions of naive RNAs from the 90% fresh material, we opted to assay genotypic change by sampling only the most high-frequency genotypes: those present in an abundance greater than random chance ( $1/48$ ). By manually sequencing the same number of genotypes (75) from transfers number 1 and 8 and enumerating those genotypes present more frequently than random expectation ( $2/75 > 1/48$ ), we were able to observe the amalgamation of an RNA network over time (Fig. 4). At the 1 h time point, no closed network was possible and autocatalysts were relatively frequent (33%), but by 8 h a reflexively autocatalytic set was present in which every reaction is catalysed by at least one molecule involved in any of the reactions of the set<sup>27</sup>. This set included nine genotypes and fewer autocatalysts (25%), although the latter drop is not quite statistically significant (one-tailed *G*-test of independence;  $P = 0.14$ ). Such expansion of the network to add additional genotypes is a more general case than the direct competition that we described in Fig. 2. As another indicator of the effect of serial transfer, the outcome of this experiment differed markedly from the batch assembly experiment (Fig. 3). After 8 h in the batch experiment the genotypes were dominated by pyrimidine-containing IGSs and targets ( $YzY$ ; Fig. 3d). By contrast, the serial transfer experiment, although also reiterating the bias for the  $Y-Z$  junction, distinctly favoured IGS and target sequences containing purines ( $RzR$ ; Fig. 4).

### Fragmentation into four pieces

Lastly, we tested whether increased fragmentation of the RNA could provide additional complexity, and enhance the pre-biological relevance. We did this by breaking the molecule up into four pieces instead of two, creating four-piece versions of  $I_1$ ,  $I_2$  and  $I_3$  analogously

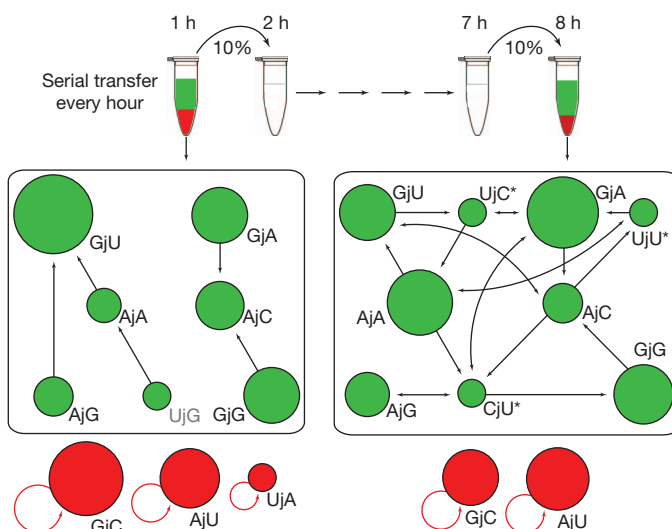


**Figure 4 | The serial transfer experiment.** The same RNA used to seed the randomization experiment (Fig. 3) was also subjected to a serial transfer protocol. For the first iteration, 50 pmol each of  $GMG \cdot W_{CNU}$ ,  $GMG \cdot W \cdot X_{CNU}$ ,  $GMG \cdot W \cdot X \cdot Y_{CNU}$ ,  $X \cdot Y \cdot Z$ ,  $Y \cdot Z$  and  $Z$  were incubated in a 100  $\mu$ l volume. After 1-h time points, 10% of the reaction mixture was transferred to a new tube containing 90% fresh RNA with a total volume of 100  $\mu$ l. The population was sampled via 5' RACE and RT-PCR to capture variation in all positions of any  $W \cdot X \cdot Y \cdot Z$  molecules present in the population. The 1 and 8 h populations were cloned, and genotype frequencies were obtained by manual sequence analysis of 75 clones each (Supplementary Table 3). Any genotype present twice or more was included on this diagram (see text); size of the circles scales to relative frequencies within their respective populations. All possible catalytic interactions are shown with arrows among non-autocatalytic genotypes (green), with autocatalytic genotypes (red) not participating in the network. Grey genotype in the 1st iteration disappears. Genotypes with asterisks appear by the 8th iteration.

to Fig. 1a, b. When we mixed the resulting 12 RNAs together, we observed two interesting phenomena (Fig. 5). First, the growth curve was distinctly sigmoidal, indicating that when more fragments are involved, the cooperativity of the system becomes even more apparent. In the four-piece fragmentation,  $W \cdot X \cdot Y \cdot Z$  ribozymes can be made via many pathways, including those in which more than one enzyme cooperates to construct the product: for example, an  $E_1$  ribozyme could recombine the  $W-X$  junction, an  $E_2$  ribozyme could recombine the  $X-Y$  junction, and an  $E_3$  ribozyme could recombine the  $Y-Z$  junction. Second, analysis of the sequences of the product  $W \cdot X \cdot Y \cdot Z$  ribozymes showed that such cooperation was common (Supplementary Fig. 14). In fact 85% of all ribozymes required help from enzymes from at least two subsystems (Fig. 5).

### Discussion

Our results illustrate a scenario in which simple autocatalytic cycles form easily but are later supplanted by more complex cooperative networks that take advantage of the autocatalysts. Our system describes the short-term kinetic phenomena that provide the foundation for evolutionary behaviour<sup>10</sup> in the presence of sequence variation throughout the ribozymes analogous to those described as “prelife”<sup>9</sup>. Features of the system described here that would make it relevant to early evolution are that it is comprised solely of RNA (although other polymers could display cooperative behaviour<sup>17,18</sup>) and that the 3-nt IGS or IGS targets are essentially the tag sequences<sup>28</sup> that have been suggested as a means to form molecular coalitions that can partition genetic information in a homogeneous milieu. Closure of autocatalytic sets would have been facilitated by the cooperative aggregation of oligomers with related tags<sup>21</sup>. Subsequent expansion of cooperative networks as shown here is possible by invasion of the network by a new set with a distinct tag sequence, for example, moving from the

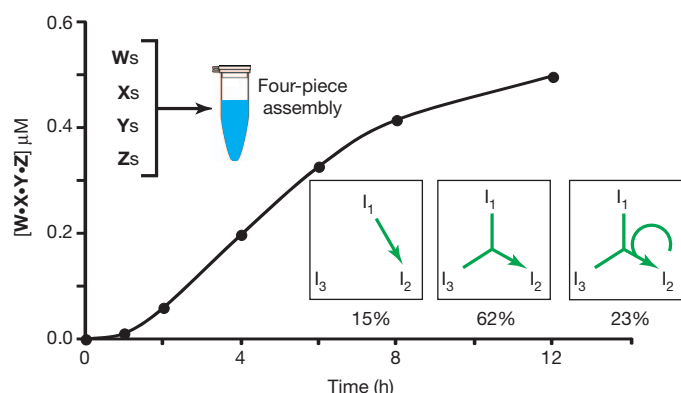


**Figure 5 | Growth curve of a four-piece system.** A more highly fragmented system based on that shown in Fig. 1b was created by breaking the ribozyme into four fragments for each  $I_i$  subsystem. The resulting 12 RNAs were co-incubated at  $0.5 \mu\text{M}$  each, and samples were removed over time for both yield analysis (plot) and nucleotide sequence analysis (frequencies). The  $W \cdot X \cdot Y \cdot Z$  RNAs can be assembled from a minimum of one, two or three IGS-bearing enzymes (examples shown with diagrams); the high frequencies of the latter two classes demonstrates the system's cooperativity.

three-membered cycle to a four-membered cycle such as by inclusion of a new IGS-IGS-target pair (Fig. 3d, starred genotypes), and then well beyond four members (Fig. 4). Longer-term evolutionary optimization would have required spatial heterogeneity<sup>29</sup> or compartmentalization<sup>8,30</sup> to provide lasting immunity against parasitic species or short autocatalytic cycles. Over time, a transition back to purely selfish replicators based on polymerization chemistry could proceed<sup>7</sup>.

In our system, we show how RNA networks have the potential to arise spontaneously and to buffer informational decay. A key to the latter is the use of recombination for replication. Although allowing for some genotypic variability, it does not lead to the accumulation of deleterious mutations as does template-directed polymerization<sup>31</sup>. Highly interdependent networks of genetically related replicators as a means to circumvent the error catastrophe in nascent life have been proposed<sup>11</sup>. The three-membered cycle shown here resembles a hypercycle as envisioned previously<sup>4,21,32</sup>, but without hyperbolic growth. We prefer to focus on the observation that the cycle can be derived from simpler cycles and has the potential to expand to more complex ones as evidence that RNA molecular coalitions can show spontaneous order-producing dynamics, which already has theoretical support<sup>27</sup>. Molecular ecological succession is a plausible model for a bridge between selfish replicators and cooperative systems.

## METHODS SUMMARY

**Experimental.** Ribozyme assays or covalent self-assembly from oligomers were performed as described previously<sup>24,25</sup>. Briefly, RNA oligomers were incubated together in 100 mM  $\text{MgCl}_2$  and 30 mM EPPS buffer (pH 7.5) for 5 min–16 h at  $48^\circ\text{C}$  at a final concentration of  $0.01$ – $2.0 \mu\text{M}$  each. Visualization and quantification was possible via phosphorimaging when W-containing fragments were 5'-end-labelled with  $\gamma\text{-}^{32}\text{P}$ ATP before use. For genotyping,  $\sim 200$ -nt RNA was excised from a gel and subject to PCR with reverse transcription (RT-PCR) using W- and Z-specific primers. High-throughput sequence analysis on the Illumina platform was possible after 5' RACE to capture the sequence variability in the IGS of assembled ribozymes. For manual sequence analysis, the PCR products were cloned into *Escherichia coli* and individual colonies were picked for colony PCR reactions. Resulting amplicons were either subjected to nucleotide-sequence analysis or restriction fragment length polymorphism (RFLP) analysis.

**Modelling.** The cooperative system was modelled as a set of six differential equations describing the concentrations over time of the six principal species (see Supplementary Information). These equations are derived from the detectable catalysis reactions (encompassing six direct-catalysis reactions and three cross-catalysis reactions). The experimental time series data from the full three-component system and from the two-component subsystems yielding detectable product were fit simultaneously to the model by standard optimization techniques.

Received 11 March 2011; accepted 6 September 2012.

Published online 17 October; corrected online 31 October 2012.

- Joyce, G. F. RNA evolution and the origins of life. *Nature* **338**, 217–224 (1989).
- Zaher, H. S. & Unrau, P. J. Selection of an improved RNA polymerase ribozyme with superior extension and fidelity. *RNA* **13**, 1017–1026 (2007).
- Wochner, A., Attwater, J., Coulson, A. & Holliger, P. Ribozyme-catalyzed transcription of an active ribozyme. *Science* **332**, 209–212 (2011).
- Eigen, M. & Schuster, P. The hypercycle. A principle of natural self-organization. Part A: emergence of the hypercycle. *Naturwissenschaften* **64**, 541–565 (1977).
- Kauffman, S. A. *The Origins of Order: Self-Organization and Selection in Evolution* (Oxford Univ. Press, 1993).
- Sievers, D. & von Kiedrowski, G. Self-replication of complementary nucleotide-based oligomers. *Nature* **369**, 221–224 (1994).
- Levy, M. & Ellington, A. D. The descent of polymerization. *Nature Struct. Biol.* **8**, 580–582 (2001).
- Szathmáry, E. The origin of replicators and reproducers. *Phil. Trans. Royal Soc. B* **361**, 1761–1776 (2006).
- Nowak, M. A. & Ohtsuki, H. Preevolutionary dynamics and the origin of evolution. *Proc. Natl Acad. Sci. USA* **105**, 14924–14927 (2008).
- Eigen, M. Selforganization of matter and the evolution of biological macromolecules. *Naturwissenschaften* **58**, 465–523 (1971).
- Maynard Smith, J. Hypercycles and the origin of life. *Nature* **280**, 445–446 (1979).
- Kun, Á., Santos, M. & Szathmáry, E. Real ribozymes suggest a relaxed error threshold. *Nature Genet.* **37**, 1008–1011 (2005).
- Doudna, J. A. & Szostak, J. W. RNA-catalysed synthesis of complementary-strand RNA. *Nature* **339**, 519–522 (1989).
- Joyce, G. F. Forty years of *in vitro* evolution. *Angew. Chem. Int. Ed.* **46**, 6420–6436 (2007).
- Lincoln, T. A. & Joyce, G. F. Self-sustained replication of an RNA enzyme. *Science* **323**, 1229–1232 (2009).
- Levy, M. & Ellington, A. D. Exponential growth by cross-catalytic cleavage of deoxyribozymes. *Proc. Natl Acad. Sci. USA* **100**, 6416–6421 (2003).
- Lee, D. H., Severin, K., Yokobayashi, Y. & Ghadiri, M. R. Emergence of symbiosis in peptide self-replication through a hypercyclic network. *Nature* **390**, 591–594 (1997).
- Lee, D. H., Severin, K. & Ghadiri, M. R. Autocatalytic networks: the transition from molecular self-replication to molecular ecosystems. *Curr. Opin. Chem. Biol.* **1**, 491–496 (1997).
- Voytek, S. B. & Joyce, G. F. Niche partitioning in the coevolution of 2 distinct RNA enzymes. *Proc. Natl Acad. Sci. USA* **106**, 7780–7785 (2009).
- Kim, D.-E. & Joyce, G. F. Cross-catalytic replication of an RNA ligase ribozyme. *Chem. Biol.* **11**, 1505–1512 (2004).
- Eigen, M. & Schuster, P. The hypercycle. A principle of natural self-organization. Part C: the realistic hypercycle. *Naturwissenschaften* **65**, 341–369 (1978).
- Reinhold-Hurek, B. & Shub, D. A. Self-splicing introns in tRNA genes of widely divergent bacteria. *Nature* **357**, 173–176 (1992).
- Hayden, E. J. & Lehman, N. Self-assembly of a group I intron from inactive oligonucleotide fragments. *Chem. Biol.* **13**, 909–918 (2006).
- Hayden, E. J., von Kiedrowski, G. & Lehman, N. Systems chemistry on ribozyme self-construction: evidence for anabolic autocatalysis in a recombination network. *Angew. Chem. Int. Ed.* **47**, 8424–8428 (2008).
- Draper, W. E., Hayden, E. J. & Lehman, N. Mechanisms of covalent self-assembly of the Azoarcus ribozyme from four fragment oligonucleotides. *Nucleic Acids Res.* **36**, 520–531 (2008).
- Nowak, M. A. *Evolutionary Dynamics: Exploring the Equations of Life* (Harvard Univ. Press, 2006).
- Hordijk, W. & Steel, M. Detecting autocatalytic, self-containing sets in chemical reaction systems. *J. Theor. Biol.* **227**, 451–461 (2004).
- Weiner, A. M. & Maizels, N. 3' terminal tRNA-like structures tag genomic RNA molecules for replication: implications for the origin of protein synthesis. *Proc. Natl Acad. Sci. USA* **84**, 7383–7387 (1987).
- Boerlijst, M. C. & Hogeweg, P. Spiral wave structures in prebiotic evolution: hypercycles stable against parasites. *Physica D* **48**, 17–28 (1991).
- Szathmáry, E. & Demeter, L. Group selection of early replicators and the origin of life. *J. Theor. Biol.* **128**, 463–486 (1987).
- Lynch, M., Burger, R., Butcher, D. & Gabriel, W. The mutational meltdown in asexual populations. *J. Hered.* **84**, 339–344 (1993).
- Eigen, M. & Schuster, P. The hypercycle. A principle of natural self-organization. Part B: the abstract hypercycle. *Naturwissenschaften* **65**, 7–41 (1978).

Supplementary Information is available in the online version of the paper.

**Acknowledgements** We would like to thank A. Burton, R. Ghadiri, P. Higgs, B. Larson, K. Chacón and A. López García de Lomana for help during preparation of this manuscript. This work was supported by NASA grant NNX10AR15G to N.L., the Center for Life in Extreme Environments at Portland State University, and a fellowship from the Human Frontier Science Program Organization to R.X.-B.

**Author Contributions** N.L. and N.V. conceived the basic idea and conducted the experiments; E.J.H. and I.A.C. contributed to the evaluation of the results; I.A.C., M.L.M. and R.X.-B. constructed the mathematical models; N.L. wrote the manuscript.

**Author Information** Reprints and permissions information is available at [www.nature.com/reprints](http://www.nature.com/reprints). The authors declare no competing financial interests. Readers are welcome to comment on the online version of the paper. Correspondence and requests for materials should be addressed to N.L. (niles@pdx.edu).

# Distinctive space weathering on Vesta from regolith mixing processes

C. M. Pieters<sup>1</sup>, E. Ammannito<sup>2</sup>, D. T. Blewett<sup>3</sup>, B. W. Denevi<sup>3</sup>, M. C. De Sanctis<sup>2</sup>, M. J. Gaffey<sup>4</sup>, L. Le Corre<sup>5</sup>, J.-Y. Li<sup>6</sup>, S. Marchi<sup>7</sup>, T. B. McCord<sup>8</sup>, L. A. McFadden<sup>9</sup>, D. W. Mittlefehldt<sup>10</sup>, A. Nathues<sup>5</sup>, E. Palmer<sup>11</sup>, V. Reddy<sup>5</sup>, C. A. Raymond<sup>12</sup> & C. T. Russell<sup>13</sup>

The surface of the asteroid Vesta has prominent near-infrared absorption bands characteristic of a range of pyroxenes, confirming a direct link to the basaltic howardite–eucrite–diogenite class of meteorites<sup>1,2,3</sup>. Processes active in the space environment produce ‘space weathering’ products that substantially weaken or mask such diagnostic absorption on airless bodies observed elsewhere<sup>4,5</sup>, and it has long been a mystery why Vesta’s absorption bands are so strong. Analyses of soil samples from both the Moon<sup>6</sup> and the asteroid Itokawa<sup>7</sup> determined that nanophase metallic particles (commonly nanophase iron) accumulate on the rims of regolith grains with time, accounting for an observed optical degradation. These nanophase particles, believed to be related to solar wind and micrometeoroid bombardment processes, leave unique spectroscopic signatures that can be measured remotely<sup>8–10</sup> but require sufficient spatial resolution to discern the geologic context and history of the surface, which has not been achieved for Vesta until now. Here we report that Vesta shows its own form of space weathering, which is quite different from that of other airless bodies visited. No evidence is detected on Vesta for accumulation of lunar-like nanophase iron on regolith particles, even though distinct material exposed at several fresh craters becomes gradually masked and fades into the background as the craters age. Instead, spectroscopic data reveal that on Vesta a locally homogenized upper regolith is generated with time through small-scale mixing of diverse surface components.

When well-developed (weathered, or ‘mature’) soils of the Moon are compared with freshly exposed material<sup>4,11</sup>, they are found to be darker, to have weaker absorption bands and to exhibit a red-sloped continuum to a wavelength of 2.6  $\mu\text{m}$  (reflectance increasing towards longer wavelength). Through decades of research, it has been recognized in the laboratory<sup>6,10</sup>, experimentally<sup>8</sup> and with physical modelling<sup>10</sup> that the nanometre-scale particles of metallic iron (called nanophase iron, or npFe<sup>0</sup>) that accumulates on the surface of soil grains produces all three of the observed optical properties of lunar soils. These properties have been used to evaluate space weathering on other airless bodies, but the results have been contentious, largely as a result of incomplete information or necessary simplifying assumptions. Because Vesta is bright and is found to have strong absorption bands in telescopic data, comparable to those of howardite–eucrite–diogenite (HED) meteorites<sup>3,12,13</sup>, it was originally argued that space weathering does not occur to any significant extent on asteroids<sup>14</sup>. However, one of the largest groups of asteroids (S-type) was found to have a mineralogy (low-calcium pyroxene and olivine) comparable to that of the most common class of meteorites (ordinary chondrites), but the asteroids also have a red-sloped continuum and much weaker diagnostic absorption bands than their possible meteorite counterparts. This required either that an asteroid–meteorite link be made between some S-type asteroids and ordinary chondrites by space weathering processes on the asteroid or, if no space

weathering occurs, that alternative compositional interpretations be found to account for the measured optical properties<sup>15,16</sup>.

This debate over space weathering produced two types of compositional interpretation of S-type asteroids, which implied dramatically different models of thermal evolution for the inner Solar System (one requiring melting and differentiation; the other allowing a preponderance of unprocessed chondritic materials). The resulting impasse began to be resolved when two S-type asteroids were visited by spacecraft. Data from the NEAR-Shoemaker spacecraft provided strong evidence that the S-type asteroid Eros was indeed chondritic<sup>17</sup> and space weathered<sup>18</sup>. Decisive new information came from the recent return of many grains of samples from the surface of the near-Earth S-type asteroid Itokawa by the Hayabusa mission. The samples conclusively showed not only that Itokawa is of LL chondritic composition<sup>19</sup> as predicted from remote sensing<sup>20</sup>, but also that half of the grains studied contained thin rims of nanophase iron- and sulphur-rich particles<sup>7</sup>, accounting for the previously observed, weak, lunar-like space weathering optical effects<sup>21</sup>. Chondrite meteorites are commonly rich in FeS; thus, the sulphur component of the Itokawa nanophase particles is particularly noteworthy because the lunar nanophase particles are dominated largely by Fe<sup>0</sup> alone.

Vesta is found to be both different from and similar to these other airless bodies and provides key information on processes active in the asteroid belt. Data from the Dawn mission used here are from an imaging spectrometer, the Visible and Infrared Spectrometer<sup>1</sup> (VIR), and a multispectral camera with bands across the shorter wavelengths, the Framing Camera<sup>2</sup>. The VIR data were acquired during the survey phase of the mission from an altitude of  $\sim 2,700$  km and at a resolution of 690 m per pixel, and the Framing Camera data were acquired during the high-altitude mapping orbit (HAMO) phase from an altitude of  $\sim 680$  km and at a resolution of 64 m per pixel.

As on the Moon, material freshly excavated by craters on Vesta is found to be quite distinct from surrounding soils, and fresh craters of all sizes commonly have a local disturbed area or system of rays radiating from the crater across nearby terrain. Canuleia, a typical fresh crater  $\sim 11$  km in diameter, shows this diversity (Fig. 1). Several manifestations of bright and dark materials are observed on a variety of scales on Vesta<sup>22,23</sup>, and small, morphologically fresh craters ( $< 1$  km in diameter) can be surrounded by either bright or dark ray material (Fig. 2). Vesta is also seen to have an extensive impact-generated regolith and widespread mass wasting<sup>24</sup> such as can be observed for the two large craters in Fig. 2. Exposures of distinct bright and dark materials hundreds of metres in extent are seen along the walls of several craters even though the craters no longer have prominent rays. Because craters with softened and slightly more subdued morphology than the freshest craters do not have bright (or dark) ray systems, processes must exist on Vesta that alter surface soil and effectively erase such features over time.

<sup>1</sup>Department of Geological Sciences, Brown University, Providence, Rhode Island 02912, USA. <sup>2</sup>Istituto di Astrofisica e Planetologia Spaziali, INAF, ARTOV, 00133 Rome, Italy. <sup>3</sup>Johns Hopkins University Applied Physics Laboratory, Laurel, Maryland 20723, USA. <sup>4</sup>Department of Space Studies, University of North Dakota, North Dakota 58202, USA. <sup>5</sup>Max-Planck Institute for Solar System Research, 37191 Katlenburg-Lindau, Germany. <sup>6</sup>Department of Astronomy, University of Maryland, College Park, Maryland 20742, USA. <sup>7</sup>NASA Lunar Science Institute, Boulder, Colorado 80302, USA. <sup>8</sup>Bear Fight Institute, 22 Fiddler's Road, Box 667, Winthrop, Washington 98862, USA. <sup>9</sup>NASA Goddard Space Flight Center, Greenbelt, Maryland 20771, USA. <sup>10</sup>NASA Johnson Space Center, Houston, Texas 77058, USA. <sup>11</sup>Planetary Science Institute, 1700 East Fort Lowell Road, Suite 106, Tucson, Arizona 85719, USA. <sup>12</sup>Jet Propulsion Laboratory, Caltech, Pasadena, California 91109, USA. <sup>13</sup>University of California, Los Angeles, California 90095, USA.

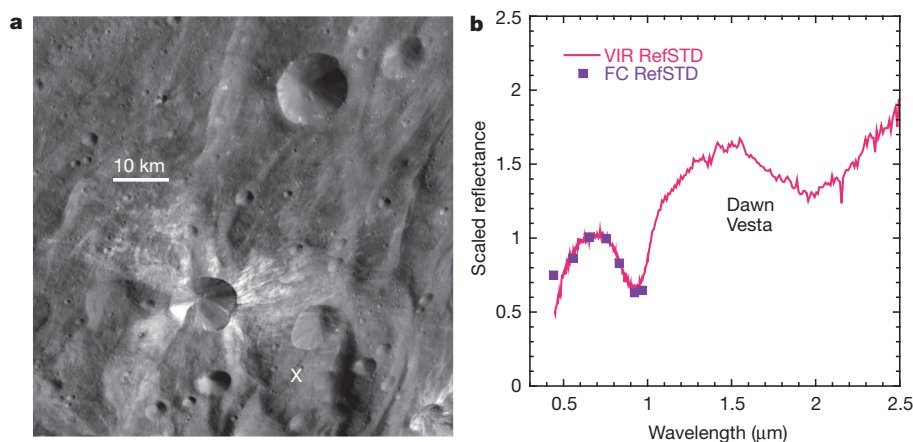


**Figure 1 | The optical properties across a typical area on Vesta as measured by Dawn.** **a**, Canuleia, a fresh crater (11.6 km in diameter, at 34° S, 295° E in the Dawn coordinate system<sup>31</sup>), has prominent bright rays. Most but not all rays are brighter than the surroundings. A crater of similar size with more subdued features (older) and no ray system is seen to the northeast. The white 'X' indicates a background reference region of soil used as a standard for comparison (RefSTD). Dawn Framing Camera HAMO image: FC21B0010859\_11293124257F1A. **b**, Visible/near-infrared spectra of soil background reference region indicated in **a**, as acquired by the Dawn Framing

Camera (FC) and the VIR. The Framing Camera obtained colour data for seven spectral bands<sup>2</sup> (0.44–0.98 μm) including half of a ferrous absorption, due to pyroxene, near 1 μm. As an imaging spectrometer, the VIR acquired images at lower spatial resolution but at high spectral resolution containing 864 spectral channels<sup>1</sup> (0.25–5.1 μm), which allow full assessment of the two ferrous absorptions of pyroxene near 1 and 2 μm. A colour composite of this area at higher spatial resolution, derived from lower-altitude Framing Camera data, can be found in Supplementary Fig. 1.

Spectra acquired by the VIR and Framing Camera are compared for the same large (~10-km) region of background soil unaffected by rays from Canuleia (Fig. 1) and are found to be largely in agreement. This background material is representative of average Vesta soil, and its spectrum has the prominent diagnostic absorption features of pyroxene that are characteristic of Vesta's basaltic composition<sup>1–3</sup>. The location of five areas of soil recently affected by the impacts that created Canuleia and Sossia craters are shown in Fig. 3. Spectra for these fresh (unweathered) areas have similar pyroxene features (Fig. 4). The bright and dark ray patterns are readily seen in photometrically corrected data (Supplementary Fig. 3). VIR spectra of these fresh areas and background soil are compared with analogous high-resolution spectra acquired by

the Moon Mineralogy Mapper<sup>25</sup> for a fresh crater in basaltic lunar terrain (Fig. 4).

At the present spatial resolution of the Dawn data, all Vesta spectra are dominated by prominent absorptions due to different types of pyroxene<sup>1</sup>. On a local scale, where compositional variations are relatively small, it can be seen that brighter areas typically have stronger pyroxene absorption bands, and there is an overall correlation of brightness with the strength of the absorption bands<sup>22</sup>. Only one area (no. 2; see Fig. 3) has spectral variations suggestive of the presence of a minor component of different mineral constituents (best seen in Fig. 4e, f). The spectra for the lunar fresh crater and background (mature) soils in Fig. 4 illustrate the three optical properties of space weathering linked to npFe<sup>0</sup> seen on the Moon: soils are darker, have weaker absorption bands and exhibit a red-sloped near-infrared continuum (0.7–1.5 μm). Although a correlation between brightness and band strength is seen for both Vesta and the Moon, there is an important difference between the two bodies in terms of the relationship between freshly exposed and background material: areas on Vesta do not exhibit the notable change in continuum slope across the near-infrared that is observed for background soils of the Moon.

The observed lack of a consistent and systematic change in the near-infrared continuum slope on Vesta indicates that grain coating of opaque, nanophase iron particles comparable to that produced during space weathering of the Moon and smaller asteroids seems not to be present in any substantial amount on Vesta. This conclusion is consistent with detailed analyses of lunar and HED regolith breccias that observed a sparsity of lunar-like nanophase iron rims in HED meteorites<sup>26</sup>. Furthermore, the relative spectra in Fig. 4e, f indicate that across the visible part of the spectrum (0.5–0.7 μm) these freshly exposed dark areas (for example no. 5) are relatively 'bluer' than background soil, and that freshly exposed bright areas (for example nos 1 and 3) are relatively 'redder' than background soil. This is opposite to the predicted effect of the presence of npFe<sup>0</sup> grain coatings<sup>4,5,10</sup>, but is more consistent with the presence of a finely dispersed, micrometre-size opaque phase that darkens and lowers the spectral contrast of a mafic-rich host<sup>27</sup>.

Because it is now recognized that the cratered surface of Vesta has not been resurfaced recently and that the giant Rheasilvia basin at the asteroid's south pole is no younger than ~1 Gyr (refs 28, 29), Vesta's



**Figure 2 | Diverse material exposed at fresh craters in a well-developed regolith on Vesta.** Examples of bright and dark rays surrounding small (<1-km), fresh craters (large white and black arrows) are observed along with discrete bright and dark material within the steep walls of older craters without rays (small arrows). Slump material dominates one wall of each of the two larger craters, illustrating the mobility of the regolith. The crater on the left is Helena (~20 km in diameter, at 41° S, 123° E in the Dawn coordinate system<sup>31</sup>). A photometrically corrected image containing this region can be found in Supplementary Fig. 2.

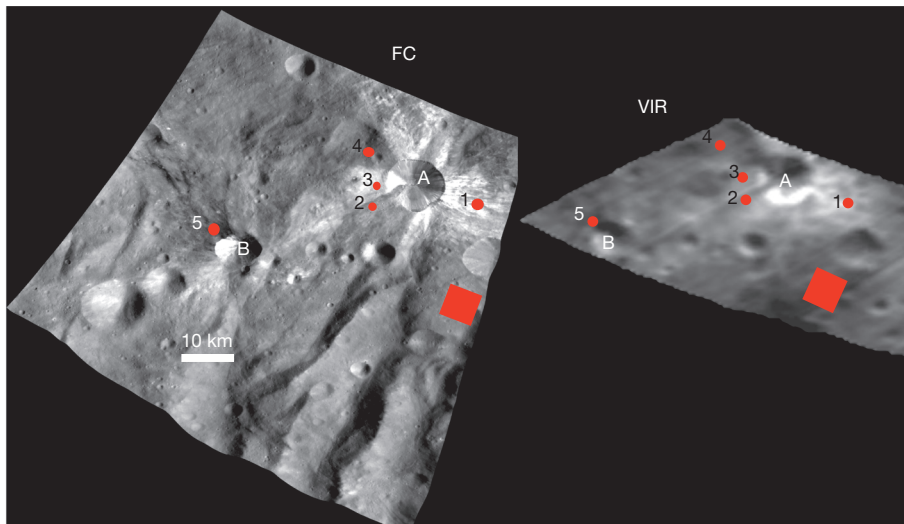


**Figure 3 | The Canuleia region mapped at different spatial resolutions by Dawn's two optical instruments.** Framing Camera and VIR images acquired during the Dawn HAMO and survey phases, respectively, contain the two morphologically fresh craters Canuleia (A) and Sossia (B). Spectra for five areas (indicated with small red circles, numbered from brightest to darkest in VIR data) were extracted as examples to highlight the diversity seen for freshly exposed material along bright (nos 1 and 3) and dark (no. 5) rays of fresh craters. The large red square is the area used as a background reference standard for both VIR and Framing Camera data on this region. A photometrically corrected image containing Canuleia and Sossia can be found in Supplementary Fig. 3 and clarifies the scale and extent of bright and dark variations across the region.

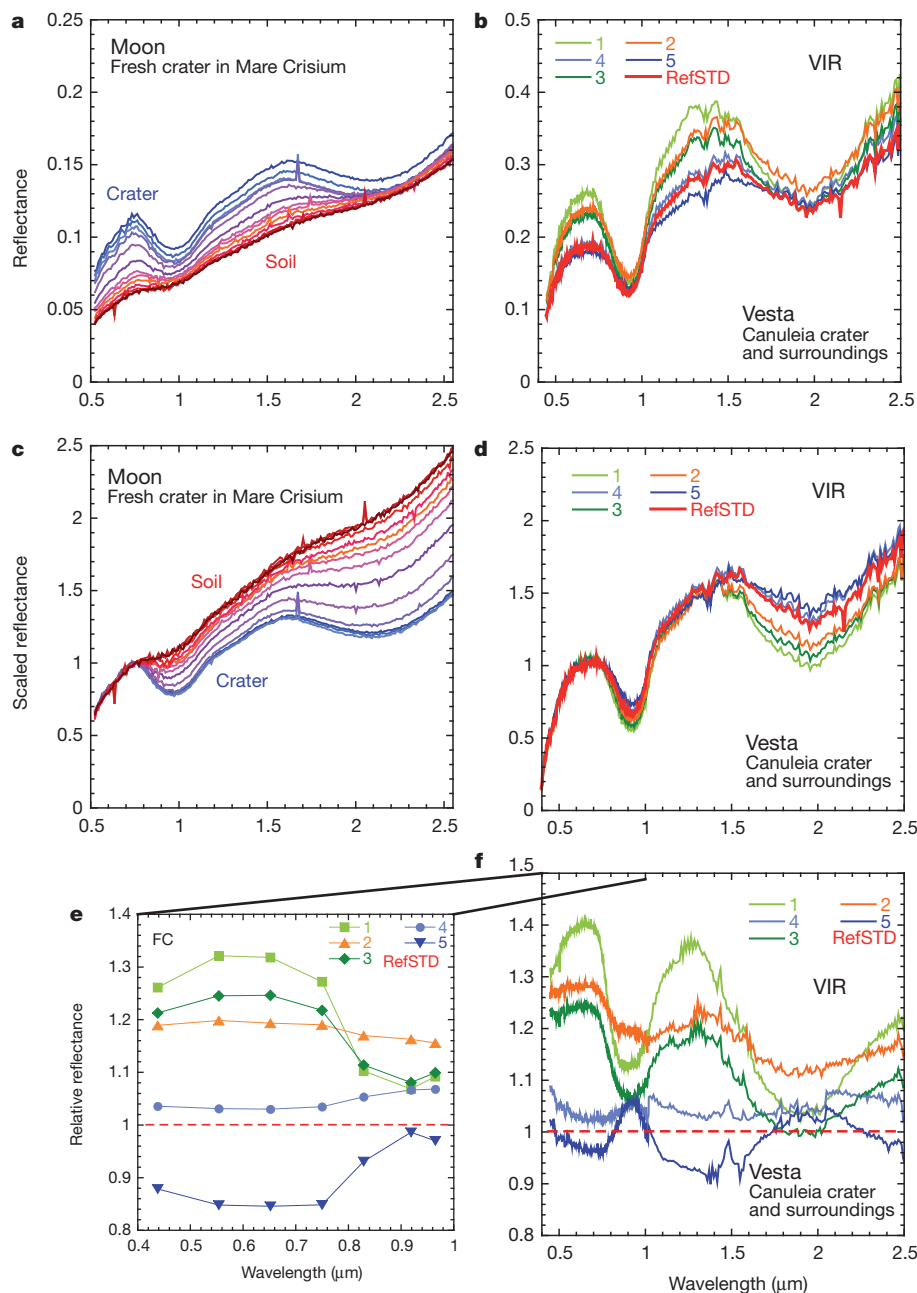


**Figure 4 | Spectroscopic comparisons of Vesta soils with similar materials on the Moon.** Spectra of the five areas of freshly exposed material and background regolith at Canuleia and Sossia identified in Fig. 3 are compared with spectra of comparable material on the Moon (presented as a traverse from an unnamed fresh crater towards background soils). **a, b**, Reflectance spectra illustrating brightness variations between crater materials and background soil (red spectra). **c, d**, Reflectance spectra scaled to 1 at  $0.75 \mu\text{m}$  to allow comparison of spectral features. Lunar soils have a steeper continuum from  $0.75$  to  $1.50 \mu\text{m}$  compared with the fresh crater, whereas there is no continuum change for Vesta. **e, f**, Reflectance spectra of Canuleia and Sossia areas in **b** divided by the background reflectance (red spectrum). These relative reflectance spectra maintain measured brightness differences, but capture subtle spectral variations and illustrate the excellent agreement between instruments despite the different illumination conditions of the measurements. See Supplementary Information for Framing Camera spectral traverses from Canuleia across background soils in a form similar to **e** (Supplementary Fig. 4); high-spatial-resolution images of the fresh lunar crater that provides the spectra in **a** and **c** (Supplementary Fig. 5); and spectra of howardite meteorites, prepared similarly to **b** and **f** (Supplementary Fig. 6).

surface is dominated by at least 1 Gyr of regolith evolution. Although distinctive material freshly exposed on the surface of Vesta by recent craters is indeed shown to blend into surrounding background regolith with time, space weathering on Vesta is quite different from that on other airless bodies. Regolith evolution on Vesta involves large- and small-scale impact events that produce particulate material and redistribute components. Compared with impact velocities of  $\sim 15 \text{ km s}^{-1}$  for bodies colliding at a distance from the Sun of one astronomical unit (where the Earth and Moon reside), the low average velocity<sup>30</sup> of  $\sim 5 \text{ km s}^{-1}$  expected for Vesta's location in the main asteroid belt suggest that mechanical brecciation dominates over melting and vaporization. Vesta's regolith does not accumulate detectable nanophase opaque particles on rims of grains. Instead, physical regolith processes on Vesta are sufficiently robust to alter optical properties by producing a locally well-mixed surficial regolith derived from observed host lithologies that include diverse bright and dark components<sup>22,23</sup>. The surficial regolith is mixed locally by smaller impacts that continually stir the regolith, and the process is enhanced by high regolith mobility driven by Vesta's relatively steep topography<sup>24</sup> and local gravity gradients. The new information about the surface of Vesta forces our concept of space weathering to go beyond one focused solely on solar wind and micrometeoroid interactions. We must include regolith mobility and fine-scale mixing as part of the complex assortment of global processes acting on an airless planetary surface over time.

Received 17 June; accepted 20 August 2012.

- De Sanctis, M. C. *et al.* Spectroscopic characterization of mineralogy and its diversity across Vesta. *Science* **336**, 697–700 (2012).
- Reddy, V. *et al.* Color and albedo heterogeneity of Vesta from Dawn. *Science* **336**, 700–704 (2012).
- McCord, T. B., Adams, J. B. & Johnson, T. V. Asteroid Vesta: spectral reflectivity and compositional implications. *Science* **168**, 1445–1447 (1970).
- Pieters, C. M. *et al.* Space weathering on airless bodies: resolving a mystery with lunar samples. *Meteorit. Planet. Sci.* **35**, 1101–1107 (2000).
- Hapke, B. Space weathering from Mercury to the asteroid belt. *J. Geophys. Res.* **106**, 10039–10073 (2001).
- Keller, L. P. & McKay, D. S. The nature and origin of rims on lunar soil grains. *Geochim. Cosmochim. Acta* **61**, 2331–2341 (1997).
- Noguchi, T. *et al.* Incipient space weathering observed on the surface of Itokawa dust particles. *Science* **333**, 1121–1125 (2011).
- Sasaki, S., Nakamura, K., Hamabe, Y., Kurahashi, E. & Hiroi, H. Production of iron nanoparticles by laser irradiation in a simulation of lunar-like space weathering. *Nature* **410**, 555–557 (2001).
- Marchi, S., Brunetto, R., Magrin, S., Lazzarin, M. & Gandolfi, D. Space weathering of near-Earth and main belt silicate-rich asteroids: observations and ion irradiation experiments. *Astron. Astrophys.* **443**, 769–775 (2005).
- Noble, S. K., Pieters, C. M. & Keller, L. P. An experimental approach to understanding the optical effects of space weathering. *Icarus* **192**, 629–642 (2007).
- Adams, J. B. & McCord, T. B. Alteration of lunar optical properties: age and composition effects. *Science* **171**, 567–571 (1971).
- Hiroi, T., Pieters, C. & Takeda, H. Grain size of the surface regolith of asteroid 4 Vesta estimated from its reflectance spectrum in comparison with HED meteorites. *Meteoritics* **29**, 394–396 (1994).
- Pieters, C. M. *et al.* in *Asteroids, Comets, and Meteors* 273–288 (Cambridge Univ. Press, 2006).
- Matson, D. L., Johnson, T. V. & Veeder, G. J. Soil maturity and planetary regoliths: the Moon, Mercury, and the asteroids. *Proc. Lunar Sci. Conf.* **8**, 625–627 (1977).
- Clark, B. E., Hapke, B., Pieters, C. & Britt, D. in *Asteroids III* (eds Bottke, W. F., Cellino, A., Paolicchi, P. & Binzel, R. P.) 585–599 (Univ. Arizona Press, 2002).
- Chapman, C. R. Space weathering of asteroid surfaces. *Annu. Rev. Earth Planet. Sci.* **32**, 539–567 (2004).
- Trombka, J. *et al.* The elemental composition of asteroid 433 Eros: results of the NEAR-Shoemaker X-ray spectrometer. *Science* **289**, 2101–2105 (2000).
- Clark, B. E. *et al.* Space weathering on Eros: constraints from albedo and spectral measurements of Psyche crater. *Meteorit. Planet. Sci.* **36**, 1617–1637 (2001).
- Nakamura, T. *et al.* Itokawa dust particles: a direct link between S-type asteroids and ordinary chondrites. *Science* **333**, 1113–1116 (2011).
- Binzel, R. P. *et al.* MUSES-C target asteroid (25143) 1998 SF36: a reddened ordinary chondrite. *Meteorit. Planet. Sci.* **36**, 1167–1172 (2001).
- Hiroi, T. *et al.* Developing space weathering on the asteroid 25143 Itokawa. *Nature* **443**, 56–58 (2006).
- McCord, T. *et al.* Dark material on Vesta from the infall of carbonaceous volatile-rich material. *Nature* <http://dx.doi.org/10.1038/nature11561> (this issue).
- Li, J.-Y. *et al.* Investigating the origin of bright materials on Vesta: synthesis, conclusions, and implications. *Proc. Lunar Planet. Sci. Conf.* **43**, abstr. 2381 (2012).
- Jaumann, R. *et al.* Vesta's shape and morphology. *Science* **336**, 687–690 (2012).
- Pieters, C. M. *et al.* The Moon Mineralogy Mapper (M<sup>3</sup>) on Chandrayaan-1. *Curr. Sci.* **96**, 500–505 (2009).
- Noble, S. K., Keller, L. P., & Pieters, C. M. Evidence of space weathering in regolith breccias II: asteroidal regolith breccias. *Meteorit. Planet. Sci.* **45**, 2007–2015 (2010).
- Britt, D. & Pieters, C. M. Darkening in black and gas-rich ordinary chondrite meteorites: the spectral effects of opaque morphology and distribution. *Geochim. Cosmochim. Acta* **58**, 3905–3919 (1994).
- Marchi, S. *et al.* The violent collisional history of asteroid 4 Vesta. *Science* **336**, 690–694 (2012).
- Schenk, P. *et al.* The geologically recent giant impact basin at Vesta's south pole. *Science* **336**, 694–697 (2012).
- Bottke, W. F. & Nolan, M. C. Greenberg, R. & Kolloord, R. A. Velocity distributions among colliding asteroids. *Icarus* **107**, 255–268 (1994).
- Russell, C. T. *et al.* Dawn at Vesta: testing the protoplanetary paradigm. *Science* **336**, 684–686 (2012).

Supplementary Information is available in the online version of the paper.

**Acknowledgements** We acknowledge the Dawn Instrument, Flight and Operations teams for the successful development, cruise, orbital insertion and operations of the Dawn spacecraft at Vesta. US team members are supported by the NASA Discovery Program through contract NNM05AA86C to the University of California, Los Angeles and by the NASA Dawn participating scientist programme.

**Author Contributions** C.M.P., D.T.B., M.C.D.S., S.M., L.A.M., D.W.M., V.R. and C.T.R. contributed to writing and improving the manuscript. E.A., L.L.C. and A.N. provided calibrated Dawn data. E.P. provided data searches. All authors contributed to discussion of the results.

**Author Information** Reprints and permissions information is available at [www.nature.com/reprints](http://www.nature.com/reprints). The authors declare no competing financial interests. Readers are welcome to comment on the online version of the paper. Correspondence and requests for materials should be addressed to C.M.P. ([carle\\_pieters@brown.edu](mailto:carle_pieters@brown.edu)).

# Dark material on Vesta from the infall of carbonaceous volatile-rich material

T. B. McCord<sup>1</sup>, J.-Y. Li<sup>2</sup>, J.-P. Combe<sup>1</sup>, H. Y. McSween<sup>3</sup>, R. Jaumann<sup>4</sup>, V. Reddy<sup>5,6</sup>, F. Tosi<sup>7</sup>, D. A. Williams<sup>8</sup>, D. T. Blewett<sup>9</sup>, D. Turrini<sup>7</sup>, E. Palomba<sup>7</sup>, C. M. Pieters<sup>10</sup>, M. C. De Sanctis<sup>7</sup>, E. Ammannito<sup>7</sup>, M. T. Capria<sup>7</sup>, L. Le Corre<sup>5</sup>, A. Longobardo<sup>7</sup>, A. Nathues<sup>5</sup>, D. W. Mittlefehldt<sup>11</sup>, S. E. Schröder<sup>5</sup>, H. Hiesinger<sup>12</sup>, A. W. Beck<sup>13</sup>, F. Capaccioni<sup>7</sup>, U. Carsenty<sup>4</sup>, H. U. Keller<sup>14</sup>, B. W. Denevi<sup>9</sup>, J. M. Sunshine<sup>15</sup>, C. A. Raymond<sup>16</sup> & C. T. Russell<sup>17</sup>

Localized dark and bright materials, often with extremely different albedos, were recently found on Vesta's surface<sup>1,2</sup>. The range of albedos is among the largest observed on Solar System rocky bodies. These dark materials, often associated with craters, appear in ejecta and crater walls, and their pyroxene absorption strengths are correlated with material brightness. It was tentatively suggested that the dark material on Vesta could be either exogenic, from carbon-rich, low-velocity impactors, or endogenic, from freshly exposed mafic material or impact melt, created or exposed by impacts. Here we report Vesta spectra and images and use them to derive and interpret the properties of the 'pure' dark and bright materials. We argue that the dark material is mainly from infall of hydrated carbonaceous material (like that found in a major class of meteorites and some comet surfaces<sup>3–5</sup>), whereas the bright material is the uncontaminated indigenous Vesta basaltic soil. Dark material from low-albedo impactors is diffused over time through the Vestan regolith by impact mixing, creating broader, diffuse darker regions and finally Vesta's

background surface material. This is consistent with howardite-eucrite-diogenite meteorites coming from Vesta.

Vesta has a mean diameter<sup>6</sup> of 525 km and is the second-most massive object in the main asteroid belt of our Solar System, smaller than Ceres and similar to Pallas. These three bodies form a separate class of intact objects in the asteroid belt that have experienced planetary processes<sup>7</sup>, such as thermal evolution<sup>8</sup> powered by short-lived radio-nuclides incorporated at the time of accretion. This process in general results in mineralogical alteration due to heating, and differentiation, with denser materials sinking towards the centre. In contrast, most other main-belt asteroids seem to be pieces of collisionally disrupted objects. Although subdued albedo differences on global<sup>9</sup> and broadly regional<sup>10</sup> scales were known to exist from telescopic observations, localized and intense dark and bright occurrences were not anticipated (see Supplementary Information).

We used photometrically uniform near-global albedo spectral image mosaics constructed from the Dawn<sup>11</sup> Framing Camera and

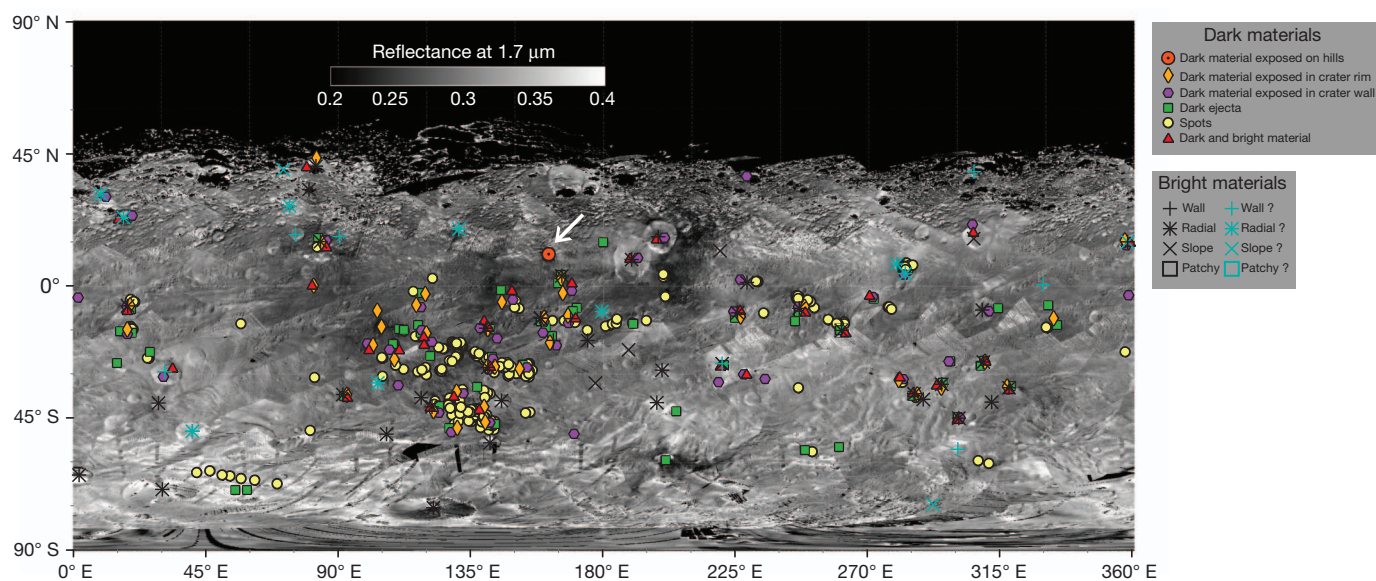


**Figure 1 | Locations of dark and bright material.** Mapped occurrences of local dark- and bright-material locations (points) are shown here plotted on a 1.7-μm albedo map derived from VIR images. The albedo mosaic also exhibits broad low-albedo regions, especially between about 70° and 220° longitude, near which the localized dark-material points tend to cluster, suggesting a

causal relationship. Bright- and dark-material local examples tend not to be uniformly distributed or correlated with each other. For this base map, the entire VIR infrared data set from late Approach, Survey and High-Altitude Mapping orbits was converted into reflectance and mosaicked.

<sup>1</sup>Bear Fight Institute, 22 Fiddler's Road, Box 667, Winthrop, Washington 98862, USA. <sup>2</sup>Planetary Science Institute, Tucson, Arizona 85719, USA. <sup>3</sup>University of Tennessee, Knoxville, Tennessee 37996, USA. <sup>4</sup>DLR, Institute of Planetary Research, Berlin, 80302, Germany. <sup>5</sup>Max Planck Institute for Solar System Research, Max-Planck-Strasse 2, 37191 Katlenburg, Germany. <sup>6</sup>University of North Dakota, Grand Forks, North Dakota 58202, USA. <sup>7</sup>Istituto Nazionale di Astrofisica (INAF), Via Fosso del Cavaliere 100, Rome 00133, Italy. <sup>8</sup>ASU, Tempe, Arizona 85287, USA. <sup>9</sup>Johns Hopkins University Applied Physics Laboratory, Laurel, Maryland 20723, USA. <sup>10</sup>Brown University, Providence, Rhode Island 02912, USA. <sup>11</sup>Astromaterials Research Office, NASA Johnson Space Center, Houston, Texas 77058, USA. <sup>12</sup>Institut für Planetologie, Westfälische Wilhelms-Universität Münster, Schlossplatz 2, 48149 Münster, Germany. <sup>13</sup>Department of Mineral Sciences, Smithsonian National Museum of Natural History, Washington DC 20024, USA. <sup>14</sup>Institut für Geophysik und extraterrestrische Physik, Mendelssohnstrasse 3, 38106 Braunschweig, Germany. <sup>15</sup>Department of Astronomy, University of Maryland, College Park, Maryland 20742, USA. <sup>16</sup>California Institute of Technology, Jet Propulsion Laboratory, Pasadena, California 91109, USA. <sup>17</sup>University of California, Los Angeles, California 90095, USA.

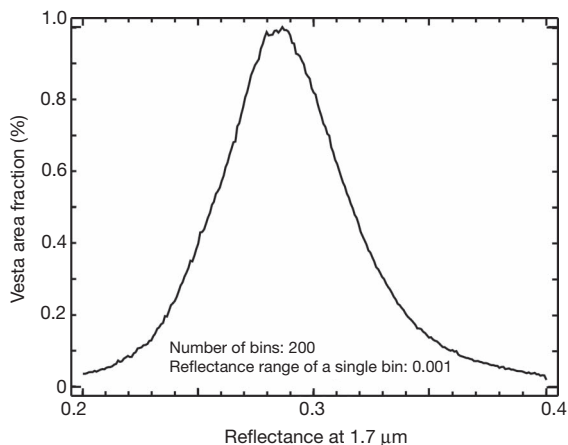


**Figure 2 | Frequency distribution of albedos.** The global distribution of albedos at 1.7  $\mu\text{m}$ , derived from the infrared global base map (Fig. 1) at a spatial resolution of about 1 km. The curve represents surface area fraction (not number of pixels). At higher resolutions this distribution would develop smaller peaks at each extreme of brightness, representing individual dark- and bright-material locations. At this resolution, the broad global distribution represents mixing between dark and bright materials.

the visible and infrared mapping spectrometer (VIR) to demonstrate that dark and bright materials are distributed non-uniformly and are uncorrelated (as seen in Fig. 1), suggesting different origins. Unlike bright material, some dark material also occurs over larger areas with more diffuse boundaries.

Investigation of the 1.7- $\mu\text{m}$  albedo frequency distribution at the spatial scale of 1 km per pixel surprisingly showed it to be unimodal, lacking any special albedo classes (Fig. 2). The bright material appears to be distinct from dark material on a local scale<sup>1,2</sup>, but globally at this resolution these albedo classes form a continuum distribution with a peak at the global average albedo. This suggests a mixing of dark and bright materials to produce the range of Vesta surface materials.

We compared VIR infrared spectra for dark and bright material (Fig. 3). The pyroxene signature clearly dominates Vesta's spectra globally<sup>8</sup> and in detail<sup>2,12</sup>, a product of Vesta's igneous past<sup>8</sup>. Dark

material has weaker apparent absorptions<sup>2</sup>. We then applied a Multiple-Endmember Linear Spectral Unmixing Model<sup>13</sup> to derive the spectrum of each of Vesta's surface materials within each VIR pixel, using the fewest possible spectral endmembers. We found that the VIR spectra could be modelled using the weighted sum of only two spectral endmembers, called 'bright' and 'dark' materials in Fig. 3. The modelled dark-material endmember spectrum shows no absorption bands, with a reddish slope that flattens towards longer wavelengths. The modelled bright-material endmember spectrum shows the classic, strong pyroxene 2- $\mu\text{m}$  band and the expected pyroxene continuum shape<sup>8,12</sup>. Our conclusion is that, for the most part, Vesta's surface material can be thought of as having two spectral components—the dark and bright endmember spectra—in different proportions. This is consistent with the mixing-process hypothesis and suggests that the dark spectral component is the agent diluting the pyroxene spectral signature. The identity of the bright endmember is probably the intrinsic Vesta basaltic soil, rich in unaltered, crystalline pyroxenes. This relationship between bright and dark materials is further supported by the strong correlation of the 1- $\mu\text{m}$  pyroxene absorption band strength with albedo from analysis of the Framing Camera colour data<sup>2</sup> and shown here (Fig. 4). We note that the dark-material spectrum is very similar to that of carbonaceous chondrite material, such as is found in a major class of meteorites (the carbonaceous chondrites).

Regions of Vesta where the residuals from the spectral mixing analysis are largest (but still small) have some of the strongest pyroxene signatures. These represent the best opportunity to study intrinsic Vesta material, for example, at some apparent impact structures that may be sampling ejecta from the Rheasilvia basin near the south pole.

Suggestions for the origin of discrete areas of dark material include indigenous sources (such as opaque-rich lava flows and impact melts) as well as contamination from exogenous material (delivered from foreign, impacting bodies). A search of Dawn VIR spectra for OH spectral features near 3  $\mu\text{m}$  was made<sup>14,15</sup>, prompted by the discovery of OH and H<sub>2</sub>O in the lunar surface. A 2.8- $\mu\text{m}$  absorption was found<sup>16</sup> and its analysis indicates<sup>17</sup> that the dark material appears to be relatively enriched in OH (Fig. 5). Carbonaceous chondrite meteorite material often contains 10–20% OH-bearing hydrated minerals, whereas none of the other suggested dark-material sources contain

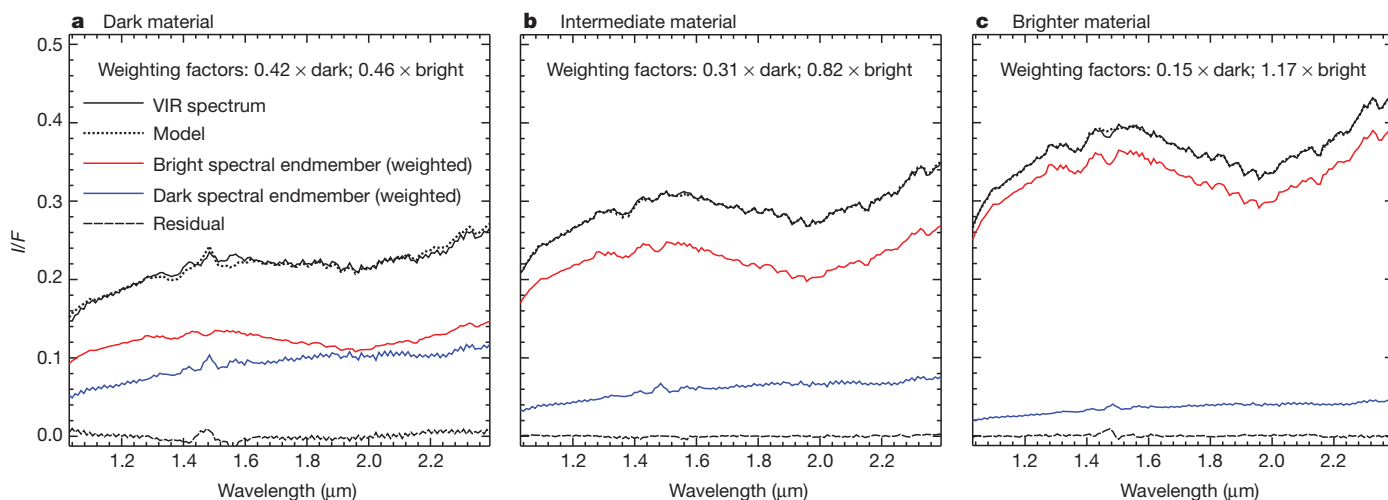


**Figure 3 | Reflectance spectra of dark and bright materials.**  $I/F = \pi R/(d^2 F)$ , where  $R$  is the spectral radiance of the target's surface in units of  $\text{W m}^{-2} \text{sr}^{-1} \mu\text{m}^{-1}$ ,  $F$  is the spectral irradiance or solar flux in units of  $\text{W m}^{-2} \mu\text{m}^{-1}$  and  $d$  is the distance between the Sun and the target. Reflectance spectra for a representative VIR scene (366894613) illustrate Vesta spectra modelling results for three different types of units near the region indicated by the white arrow in Fig. 1. **a**, The VIR dark-material unit spectrum (solid black line) is modelled using the two weighted endmember spectra (red and blue spectra). The model result is the dotted black line overlying the VIR spectrum;

the resulting residual is shown as a dashed black line. The residual shows no distinctive features and overall is near the noise level of the VIR data, suggesting successful modelling. (The feature near 1.44  $\mu\text{m}$  is a calibration artefact.)

**b, c**, Similar examples for intermediate and brighter materials nearby. The weighting factors are given on the plots and the mixture spectrum is calculated as the weighted sum of dark + bright. This analysis was performed at several other areas with similar results, before we successfully modelled the entire mosaic shown in Fig. 1.

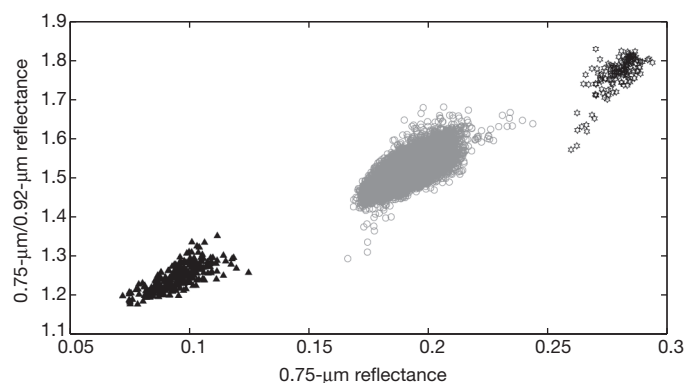


**Figure 4 | Correlation of pyroxene absorption with material reflectance.** The strength of the '1- $\mu\text{m}$ ' pyroxene absorption, measured by the ratio of reflectance at 0.75  $\mu\text{m}$  to that at 0.92  $\mu\text{m}$ , is strongly correlated with the reflectance in the continuum (0.75  $\mu\text{m}$ ), shown here for three example regions. Data are from the framing camera<sup>2</sup>. Greater ratio values correspond to stronger absorption bands. Dark (black filled circles) and bright (black open circles) areas cluster near the extremes of the plot, while background material (grey open circles) appears near the middle of this apparent mixing line. Dark material pixels are from Cornelia crater (9.3° S, 225.5° E), background material is from an area located between 5° S–17° N, 320° E–356° E and the bright material is from Tuccia crater (40° S, 197° E) in the Claudia coordinate system used by Dawn. If the entire surface of Vesta were treated here, rather than only example areas, the three clusters of points would merge into a continuum from least to greatest reflectance.

OH. Further, the Gamma Ray and Neutron Detector investigation reports<sup>18</sup> excess H (without identifying the molecular form) for certain regions that correspond with the broader darker areas shown in Fig. 1.

The most common group of differentiated meteorites, the howardite-eucrite-diogenites (HEDs), display reflectance spectra strongly suggesting that they originated from Vesta<sup>8</sup>. Three types of dark materials occur in the HEDs<sup>19</sup>: clasts of carbonaceous chondrite material in howardites, impact melts and shock-blackened materials in HED breccias, and fine-grained eucrites with quenched textures. These dark components occur in a few samples up to 60 per cent by volume but more typically compose a few per cent by volume of the rocks<sup>20,21</sup>. Although several types of dark material exist in the HEDs, only the

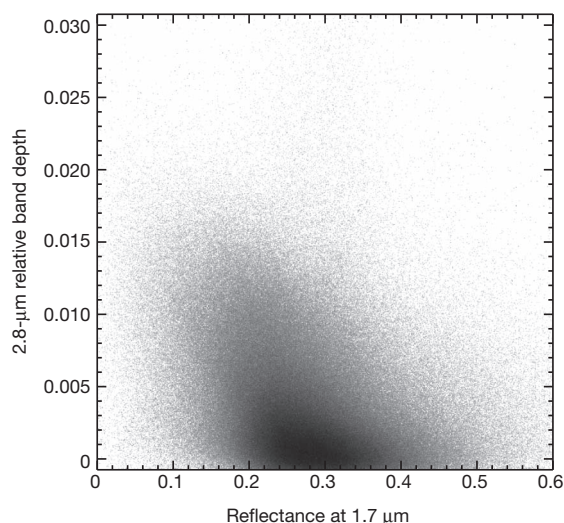


**Figure 5 | Correlation of OH spectral absorption with material reflectance.** Two-dimensional scatter plot from global observations of Vesta by VIR show a diffuse anti-correlation of the OH-related 2.8- $\mu\text{m}$ -absorption band depth<sup>9,15</sup> and Vesta's reflectance at 1.7  $\mu\text{m}$  (Fig. 1). The OH signature is correlated with the dark material in Vesta's surface.

carbonaceous material is consistent with the properties of the dark constituent of Vesta's surface.

It is plausible that enough dark material to match what we observe could be delivered on Vesta by low albedo (probably carbonaceous) asteroids over time. In addition to Vesta's small size and surface gravity, its location in the asteroid belt implies that most impacts occur at lower velocities, favouring the preservation of a larger fraction of the impacting material (see Supplementary Information). Analytical estimates we performed (see Supplementary Information) indicate that about 300 low-albedo asteroids with diameters between 1 km and 10 km could have impacted Vesta during the last 3.5 billion years, that is, once the asteroid belt assumed its present structure<sup>22</sup>. These impactors would deliver to the Vestan surface about  $(3\text{--}4) \times 10^{18}$  g of low-albedo, probably carbonaceous material. This mass would be enough to wrap Vesta in a thick dark blanket 1–2 m thick. Impact gardening would occur, creating a dark crustal mixed zone to a depth of one to several kilometres. Further, it is well documented that the addition of small amounts of fine-grained opaque material to a semi-transparent material (such as Vesta's pyroxene-rich surface) reduces the reflectance of the mixture in a highly effective, nonlinear manner<sup>23</sup>.

Thus, we see on Vesta a dramatic example of a common process that must affect many Solar System objects: that of contamination and alteration of indigenous surfaces owing to impact and retention and mixing of the impactor material. This process also provides a mechanism by which to transport hydrated and organic-rich materials to Vesta and other bodies. This hypothesis is consistent with evidence observed in the HED meteorites<sup>19</sup> and strengthens the connection between the HEDs and Vesta<sup>8,19</sup>.

Received 16 June; accepted 29 August 2012.

1. Jaumann, R. *et al.* Vesta's shape and morphology. *Science* **336**, 687–690 (2012).
2. Reddy, V. *et al.* Color and albedo heterogeneity of Vesta from Dawn. *Science* **336**, 700–704 (2012).
3. Sandford, S. A. *et al.* Organics captured from comet 81P/Wild 2 by the Stardust Spacecraft. *Science* **314**, 1720–1724 (2006).
4. Sunshine, J. M. *et al.* Exposed water ice deposits on the surface of comet 9P/Tempel 1. *Science* **311**, 1453–1455 (2006).
5. Gibb, E. L. *et al.* The organic composition of C/2001 A2 (LINEAR). II. Search for heterogeneity within a comet nucleus. *Icarus* **188**, 224–232 (2007).
6. Russell, C. T. *et al.* Dawn at Vesta: testing the protoplanetary paradigm. *Science* **336**, 684–686 (2012).
7. McCord, T. B., McFadden, L. A., Russell, C. T., Sotin, C. & Thomas, P. C. Ceres, Vesta, and Pallas: protoplanets, not asteroids. *Trans. AGU* **87**, 105–109 (2006).
8. McCord, T. B., Adams, J. B. & Johnson, T. V. Asteroid Vesta: spectral reflectivity and compositional implications. *Science* **168**, 1445–1447 (1970).
9. Degewij, J., Tedesco, E. F. & Zellner, B. H. Albedo and color contrasts on asteroid surfaces. *Icarus* **40**, 364–374 (1979).
10. Zellner, B. H. *et al.* Hubble Space Telescope images of asteroid 4 Vesta in 1994. *Icarus* **128**, 83–87 (1997).
11. Russell, C. T. & Raymond, C. A. The Dawn mission to Vesta and Ceres. *Space Sci. Rev.* **163**, 3–23 (2011).
12. De Sanctis, M. C. *et al.* Spectroscopic characterization of mineralogy and its diversity across Vesta. *Science* **336**, 697–700 (2012).
13. Combe, J.-Ph. *et al.* Analysis of OMEGA/Mars Express data hyperspectral data using a Multiple-Endmember Linear Spectral Unmixing Model (MELSUM): methodology and first results. *Planet. Space Sci.* **56**, 951–975 (2008).
14. Combe, J.-Ph. *et al.* Water and other volatiles on Vesta after the lunar case. *Lunar Planet. Sci. Conf.* **431**, 2463 (2012).
15. De Sanctis, M. C. *et al.* Detection of widespread hydrated materials on Vesta by VIR imaging spectrometer on board the Dawn mission. *Astrophys. J. Lett.* **758**, L36 (2012).
16. Pieters, C. M. *et al.* Character and spatial distribution of OH/H<sub>2</sub>O on the surface of the Moon seen by M<sup>3</sup> on Chandrayaan-1. *Science* **326**, 568–572 (2009).
17. McCord, T. B. *et al.* Sources and physical processes responsible for OH/H<sub>2</sub>O in the lunar soil as revealed by the Moon Mineralogy Mapper (M<sup>3</sup>). *J. Geophys. Res.* **116**, E00G05 (2011).
18. Prettyman, T. H. *et al.* Elemental mapping by Dawn reveals exogenic H in Vesta's regolith. *Science* doi:10.1126/science.1225354.
19. McSweeney, H. Y., Mittlefehldt, D. W., Beck, A. W., Mayne, R. G. & McCoy, T. J. HED meteorites and their relationship to the geology of Vesta and the Dawn mission. *Space Sci. Rev.* **163**, 141–174 (2011).
20. Zolensky, M. E., Weisberg, M. K., Buchanan, P. C. & Mittlefehldt, D. W. Mineralogy of carbonaceous chondrite clasts in HED achondrites and the Moon. *Meteorit. Planet. Sci.* **31**, 518–537 (1996).
21. Beck, A. W., Welten, K. C., McSweeney, H. Y., Viviano, C. E. & Caffee, M. W. Petrologic and textural diversity among the PCA 02 howardite group, one of the largest pieces of the Vestan surface. *Meteorit. Planet. Sci.* **47**, 947–969 (2012).

22. Coradini, A., Turrini, D., Federico, C. & Magni, G. Vesta and Ceres: crossing the history of the Solar System. *Space Sci. Rev.* **163**, 25–40 (2011).
23. Clark, R. N. Spectral properties of mixtures of montmorillonite and dark grains—implications for remote sensing minerals containing chemically and physically adsorbed water. *J. Geophys. Res.* **88**, 10635–10641 (1983).

**Supplementary Information** is available in the online version of the paper.

**Acknowledgements** This research was supported by the NASA Dawn Project under contract from UCLA, by the NASA Dawn at Vesta Participating Scientist program, the Italian Space Agency, the Max Planck Institute for Solar System Research, and the Germany Aerospace Agency (DLR). We acknowledge the support of the Dawn Science, Instrument and Operations Teams.

**Author Contributions** T.B.McC. designed the study, directed the research and wrote the manuscript; J.-P.C., J.-Y.L. and H.Y.McS. were the major contributors helping to design the study, direct the research and write the manuscript. D.T., T.B.McC. and J.-P.C. wrote the Supplementary Information. J.-P.C. performed the spectral unmixing of the VIR mapping spectrometer data and the correlation of OH with albedo. J.-P.C. and F.T. produced global maps from the VIR mapping spectrometer data. V.R. performed the correlation of albedo with band strength. L.L.C. and R.J. produced global mapping of Vesta with Framing Camera images. H.Y.McS., V.R. and D.W.M. contributed to the laboratory analysis of Vestan meteorites. J.-P.C., E.P., E.A., M.C.D.S. and A.L. contributed to the location of dark materials and to the spectral analysis of hydroxyl-rich areas from the VIR mapping spectrometer data. R.J. provided the location of dark materials from Framing Camera images. D.T. provided estimates of amounts of dark material coming from carbonaceous chondrite meteorites. J.-P.C., J.-Y.L., F.C., E.P. and A.L. contributed to the photometric correction for the VIR mapping spectrometer. J.-Y.L., S.E.S. and L.L.C.

contributed to the photometric correction of Framing Camera images. F.T. and J.-P.C. investigated the need for thermal emission correction of the VIR mapping spectrometer. D.A.W. contributed much of the geologic context of dark material, developed example site descriptions, and wrote or edited geological context materials. D.T.B. participated in developing the dark-material interpretation and edited the manuscript. C.M.P. participated in providing context for the mixing effects on the resulting surface material and integrating space-weathering concepts. M.C.D.S. is the Principal Investigator of the VIR mapping spectrometer and helped to provide the VIR data. A.N. is the Principal Investigator of the Framing Camera and helped to provide the Framing Camera data. M.T.C. and F.C. analysed the thermal properties of the surface of Vesta. D.W.M. located bright materials from Framing Camera images. E.A., F.C., F.T., A.L., M.C.D.S. and J.-P.C. contributed to the calibration of the VIR mapping spectrometer. A.N., S.E.S. and V.R. contributed to the calibration of the Framing Camera. E.A. contributed to the sequencing of data acquisition for the VIR mapping spectrometer. S.E.S. contributed to the sequencing of data acquisition for the Framing Camera. H.H. contributed to the design and development of the Framing Camera. A.W.B., U.C., H.U.K., B.W.D. & J.M.S. participated in the working group studying the bright material. C.A.R. is the deputy Principal Investigator of the Dawn mission. C.T.R. is the Principal Investigator of the Dawn mission. All authors discussed the results and commented on the manuscript.

**Author Information** Data from the Dawn mission are publicly available through the NASA Planetary Data System. Reprints and permissions information is available at [www.nature.com/reprints](http://www.nature.com/reprints). The authors declare no competing financial interests. Readers are welcome to comment on the online version of the paper. Correspondence and requests for materials should be addressed to T.B.M. (tmccord@bearfightinstitute.com) or J.-P.C. (jean-philippe\_combe@bearfightinstitute.com).

# Observation of spatially ordered structures in a two-dimensional Rydberg gas

Peter Schauß<sup>1</sup>, Marc Cheneau<sup>1</sup>, Manuel Endres<sup>1</sup>, Takeshi Fukuhara<sup>1</sup>, Sebastian Hild<sup>1</sup>, Ahmed Omran<sup>1</sup>, Thomas Pohl<sup>2</sup>, Christian Gross<sup>1</sup>, Stefan Kuhr<sup>1,3</sup> & Immanuel Bloch<sup>1,4</sup>

The ability to control and tune interactions in ultracold atomic gases has paved the way for the realization of new phases of matter. So far, experiments have achieved a high degree of control over short-range interactions, but the realization of long-range interactions has become a central focus of research because it would open up a new realm of many-body physics. Rydberg atoms are highly suited to this goal because the van der Waals forces between them are many orders of magnitude larger than those between ground-state atoms<sup>1</sup>. Consequently, mere laser excitation of ultracold gases can cause strongly correlated many-body states to emerge directly when atoms are transferred to Rydberg states. A key example is a quantum crystal composed of coherent superpositions of different, spatially ordered configurations of collective excitations<sup>2–5</sup>. Here we use high-resolution, *in situ* Rydberg atom imaging to measure directly strong correlations in a laser-excited, two-dimensional atomic Mott insulator<sup>6</sup>. The observations reveal the emergence of spatially ordered excitation patterns with random orientation, but well-defined geometry, in the high-density components of the prepared many-body state. Together with a time-resolved analysis, this supports the description of the system in terms of a correlated quantum state of collective excitations delocalized throughout the gas. Our experiment demonstrates the potential of Rydberg gases to realize exotic phases of matter, thereby laying the basis for quantum simulations of quantum magnets with long-range interactions.

The strongly enhanced interaction between Rydberg atoms makes them unique building blocks for a variety of applications, ranging from quantum optics and quantum information processing<sup>1,7,8</sup> to engineering of exotic quantum many-body phases<sup>9–11</sup>. For the last purpose, two main ideas have been explored theoretically. First, the weak admixing of a Rydberg state to the atomic ground state using off-resonant laser coupling has been suggested as a way to benefit from the long-range interactions without persistent population of the Rydberg state<sup>9,10,12</sup>. Second, direct laser excitation leads to the formation of a gas of Rydberg excitations, also called a Rydberg gas. This strongly correlated system<sup>13</sup> can exhibit highly non-classical states characterized by the coherent superposition of ordered structures in the spatial distribution of the Rydberg excitations<sup>2–5,14–16</sup>. Here the excitation dynamics proceeds on a timescale of a few microseconds, on which the atoms can be considered frozen in space, representing strongly interacting effective spins. At the heart of the formation of such correlated states lies the dipole blockade effect<sup>1,7,8</sup> that prevents simultaneous Rydberg excitation of two close-by atoms<sup>17–21</sup>. Recent experiments using two trapped atoms have shown how this blockade effect can be used to implement fast two-qubit quantum gates<sup>22,23</sup>. In larger ultracold atomic ensembles, the coherence of the collective excitation has been demonstrated<sup>24–26</sup> and evidence for strong correlations could be found by observing universal scaling laws for the number of excited Rydberg atoms<sup>27,28</sup>. However, direct measurements of spatial ordering have remained an outstanding challenge. Important steps in this direction were recently explored using a field-ion-microscope<sup>20</sup>, allowing the measurement of the blockade radius in a

three-dimensional Rydberg gas. Recent theoretical work, on the other hand, has proposed detection schemes with potential resolution below the blockade radius, based on conditional Raman transfer<sup>29</sup> or electromagnetically induced transparency<sup>30</sup>.

Here we demonstrate an alternative approach that permits direct imaging of Rydberg excitation patterns, and precise measurements of correlation functions. This allows us to probe the underlying constituents of the excited many-body state, revealing the spatial ordering of the high-density components. Two key advances form the basis of our observations. First, a two-dimensional atomic Mott insulator provides a dense and well-ordered initial system that maximizes coherence times during the excitation dynamics. Second, we developed an all-optical technique to image individual Rydberg atoms *in situ* with high spatial and temporal resolution.

The physical system considered here is a two-dimensional gas of rubidium atoms trapped in a rotationally invariant harmonic confinement potential and pinned in a square optical lattice. The gas was prepared deep in the Mott-insulating phase, ensuring uniform filling with one atom per site within a disk of radius  $R \approx \sqrt{N_{\text{at}} a_{\text{lat}}^2 / \pi}$ , where  $N_{\text{at}}$  is the total number of atoms and  $a_{\text{lat}}$  the lattice spacing. The atoms were initially in their electronic ground state,  $|g\rangle$ , and then resonantly coupled to a Rydberg state,  $|e\rangle$ . In the interaction picture, the internal dynamics of the atoms is governed by the many-body Hamiltonian:

$$\hat{H} = \frac{\hbar\Omega}{2} \sum_i \left( \hat{\sigma}_{eg}^{(i)} + \hat{\sigma}_{ge}^{(i)} \right) + \sum_{i \neq j} \frac{V_{ij}}{2} \hat{\sigma}_{ee}^{(i)} \hat{\sigma}_{ee}^{(j)} \quad (1)$$

Here, the vectors  $i = (i_x, i_y)$  label the lattice sites in the plane. The first term in this Hamiltonian describes the coherent coupling of the ground and excited states with Rabi frequency  $\Omega$ , where  $\hat{\sigma}_{ge}^{(i)} = |e_i\rangle\langle g_i|$  and  $\hat{\sigma}_{eg}^{(i)} = |g_i\rangle\langle e_i|$  are the local transition operators. The second term is the van der Waals interaction potential between two atoms in the Rydberg state. In our case it is repulsive and takes the asymptotic form  $V_{ij} = -C_6/r_{ij}^6$ , with the van der Waals coefficient  $C_6 < 0$  and  $r_{ij} = a_{\text{lat}}|i - j|$  the distance between the two atoms at sites  $i$  and  $j$ . The projection operator  $\hat{\sigma}_{ee}^{(i)} = |e_i\rangle\langle e_i|$  measures the population of the Rydberg state at site  $i$ . This model is valid as long as the mechanical motion of the atoms and all decoherence effects can be neglected (Supplementary Information).

The dynamics of this strongly correlated system can be understood intuitively from its energy spectrum in the absence of optical driving. It is instructive to group the large number of many-body states,  $2^{N_{\text{at}}}$ , according to the number of Rydberg excitations,  $N_e$ , contained in each state (Fig. 1a). All singly excited states ( $N_e = 1$ ) with different positions of the Rydberg atom have identical energies and form a  $N_{\text{at}}$ -fold degenerate manifold. For multiply excited states ( $N_e > 1$ ), this degeneracy is lifted by the strong van der Waals interaction, giving rise to a broad energy band (Fig. 1a). Starting from the ground state, the creation of

<sup>1</sup>Max-Planck-Institut für Quantenoptik, 85748 Garching, Germany. <sup>2</sup>Max-Planck-Institut für Physik komplexer Systeme, 01187 Dresden, Germany. <sup>3</sup>University of Strathclyde, Department of Physics, SUPA, Glasgow G4 0NG, UK. <sup>4</sup>Ludwig-Maximilians-Universität, Fakultät für Physik, 80799 München, Germany.

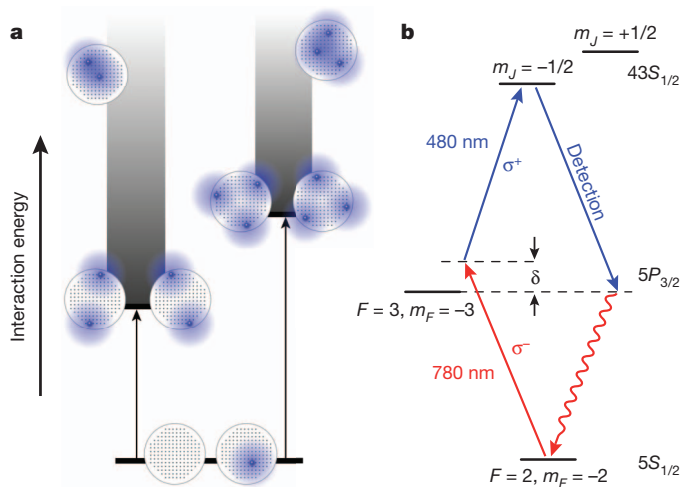


**Figure 1 | Schematics of the many-body excitation.** **a**, Energy spectrum in the absence of optical driving. States with more than one excitation form a broad energy band (shown as a grey shading for  $N_e = 2$  on the left and  $N_e = 3$  on the right) above the degenerate manifold comprising the ground state and all singly excited states. For each excitation number  $N_e > 1$ , the states with lowest energy correspond to spatially ordered configurations, which maximize the distance between the Rydberg excitations. The minimal interaction energy (black arrows) is determined by the finite system size and increases with  $N_e$ . Possible spatial configurations of the excitations (blue dots) in the initial Mott-insulating state (black dots) are shown schematically as circular insets next to their respective interaction energy. The blockade radius is depicted by the blue shaded disk around the excitation. **b**, Simplified level scheme of  $^{87}\text{Rb}$ , showing the transitions used for the Rydberg excitation and detection. See text for details.

the first excitation is resonant, while the sequential coupling to many-body states with larger number of excitations is rapidly detuned by the interactions. In fact, the rapid variation of the van der Waals potential with distance prevents the excitation of all those states where Rydberg atoms are separated by less than the blockade radius,  $R_b$ , defined by  $\hbar\Omega = -C_6/R_b^6$ . The existence of this exclusion radius is expected to have a striking consequence: whereas the total many-body state exhibits finite-range correlations on a scale of  $R_b$  (ref. 13), its high-density components with a Rydberg density close to  $1/R_b^3$  should display a crystalline structure, meaning that the position of the Rydberg atoms is correlated over a distance comparable to the system size.

The excitation dynamics of all configurations should occur in an entirely coherent fashion, resulting in highly non-classical many-body states. The approximate rotational symmetry of our system leads to symmetric superpositions of all microscopic configurations with different orientation but identical relative positions of the Rydberg atoms. Also, as the coupling addresses all states within an energy range  $\sim \hbar\Omega$ , it produces a coherent superposition of many-body states with different numbers of excitations and slightly different separation between the Rydberg atoms (Fig. 1a). This collective nature of the excited many-body states dramatically changes the timescale on which their dynamics occurs. The coupling strength to the state with a single excitation is enhanced by a factor  $\sqrt{N_{\text{at}}} \gg 1$  (ref. 8) and the coupling to states with  $N_e > 1$  is similarly enhanced, with  $N_{\text{at}}$  replaced by the number of energetically accessible configurations in each  $N_e$ -manifold<sup>3</sup>.

Our experiments began with the preparation of a two-dimensional degenerate gas of 150–390  $^{87}\text{Rb}$  atoms confined to a single antinode of a vertical ( $z$ -axis) optical lattice<sup>31</sup>. The gas was brought deep into the Mott-insulating phase by adiabatically turning on a square optical lattice with period  $a_{\text{lat}} = 532$  nm in the  $x$ - $y$  plane. Within the system radius,  $R = 3.5$   $\mu\text{m}$  to 5  $\mu\text{m}$ , the probability of a lattice site being occupied by a single atom was typically 80%. The atoms were then initialized in the hyperfine ground state  $|g\rangle \equiv |5S_{1/2}, F=2, m_F=-2\rangle$

and coupled to the Rydberg state  $|e\rangle \equiv |43S_{1/2}, m_J = -1/2\rangle$ , using the standard notation for the fine and hyperfine structure (Fig. 1b). The coupling was achieved through a two-photon process via the intermediate state  $|5P_{3/2}, F=3, m_F=-3\rangle$  using lasers of wavelengths 780 nm and 480 nm and  $\sigma^-$  and  $\sigma^+$  polarization, respectively (Fig. 1b and Methods). The resulting two-photon Rabi frequency was  $\Omega/(2\pi) = 170(20)$  kHz (the number in parentheses denotes the uncertainty of the last digit), yielding a blockade radius of  $R_b = 4.9(1)$   $\mu\text{m}$ . Following the initial preparation, we suddenly switched on the excitation lasers and let the system evolve for a variable duration  $t$ . After the excitation pulse, we detected the Rydberg excitations by first removing all atoms in the ground state with a resonant laser pulse, then de-exciting the Rydberg atoms to the ground state via stimulated emission towards the intermediate state (Fig. 1b and Methods) and finally recording their position using high-resolution fluorescence imaging<sup>31</sup>. The accuracy of the measurement was limited by the probability, 75(10)%, of detecting a Rydberg atom and by a background signal due to on average 0.2(1) non-removed ground state atoms per picture (Supplementary Information). The spatial resolution of our detection technique is limited to about one lattice site by the residual motion of the atoms in the Rydberg state before de-excitation (Supplementary Information). Repeating the experiment many times allowed for sampling the different spatial configurations of Rydberg atoms constituting the many-body state and to measure their respective statistical weight.

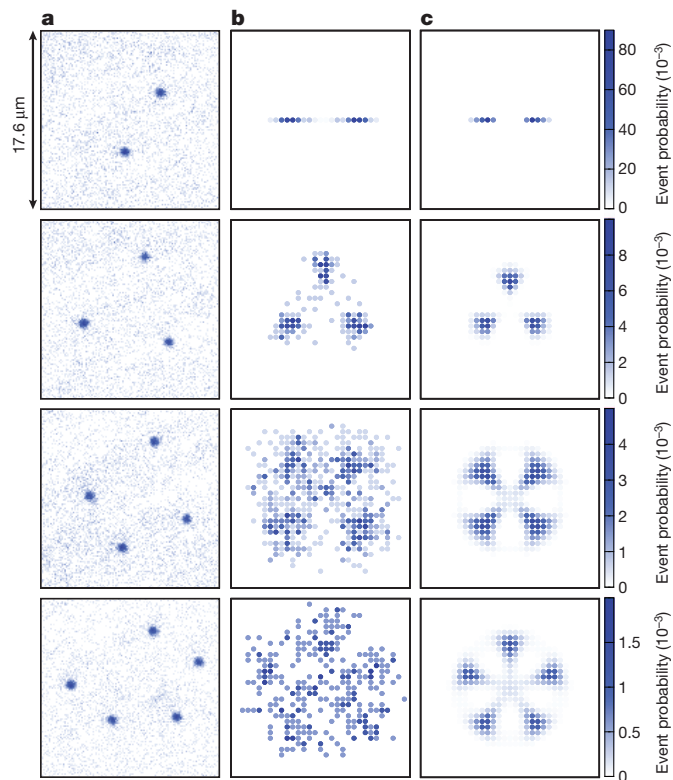


**Figure 2 | Spatially ordered components of the many-body states.** Spatial distribution of excitations for the observed microscopic configurations sorted according to their number of excitations,  $N_e = 2$ –5 (top to bottom). **a**, Examples of false-colour fluorescence images in which de-excited Rydberg atoms are directly visible as dark-blue spots. **b**, Histograms of the spatial distribution of Rydberg atoms obtained after centring and aligning the individual microscopic configurations to a reference axis (Methods). The initial atom distribution had a diameter of 7.2(8)  $\mu\text{m}$  and 10.8(8)  $\mu\text{m}$  for  $N_e = 2$ –3 and  $N_e = 4$ –5, respectively. **c**, Theoretical prediction from numerical simulations of the excitation dynamics governed by the many-body Hamiltonian of equation (1) for the same conditions as in the experiment (Supplementary Information). Colour scale at right of each row applies only to the sub-panels of **b** and **c** in that row.

In Fig. 2a we show typical images of microscopic configurations with  $N_e = 2-5$ . In order to analyse the structure of the many-body state, we group the individual images according to their number of excitations and determine the spatial distributions of the excitations,  $\rho_e(i) = \langle \hat{\sigma}_{ee}^{(i)} \rangle$ , where  $\langle \cdot \rangle$  denotes the average from repeated measurements. These distributions display a typical ring-shaped profile (Supplementary Fig. 1), which results from the blockade effect and from the rotational symmetry of the system. Spatially ordered structures become visible once each microscopic configuration has been centred and aligned to a fixed reference axis (Fig. 2b and Methods).

For our smallest sample ( $R \approx 3.5 \mu\text{m}$ ), we observe strong correlations between  $N_e = 2$  excitations that are separated by a distance of  $\sim 6 \mu\text{m}$ , due to the interaction blockade. In the same data set, configurations with  $N_e = 3$  show an arrangement on an equilateral triangle, revealing both strong radial and azimuthal ordering. These correlations persist for larger numbers of Rydberg excitations, which we can prepare in larger samples ( $R \approx 5 \mu\text{m}$ ). They form quadratic and pentagonal configurations for  $N_e = 4$  and  $N_e = 5$ , respectively. However, since their interaction energy is larger, these states are populated only with low probability, leading to a reduced signal-to-noise ratio. Our experimental data are in good agreement with numerical simulations of the many-body dynamics according to the Hamiltonian of equation (1), for the same atom numbers, temperature and laser parameters as in the experiment (Fig. 2c and Supplementary Information). These simulations are based on a truncation of the underlying Hilbert space, exploiting the dipole blockade, and neglect any dissipative effects (ref. 3 and Supplementary Information). The spatial distributions of excitations provided by the simulation reproduce all the features observed in the experiment. The only apparent discrepancy is the overall slightly larger size of the measured structures, which can be attributed to the spatial resolution of our detection method, as discussed below.

For a more quantitative analysis of spatial correlations, we also measured the pair correlation function (Fig. 3a)

$$g^{(2)}(r) = \frac{\sum_{i \neq j} \delta_{r, r_{ij}} \langle \hat{\sigma}_{ee}^{(i)} \hat{\sigma}_{ee}^{(j)} \rangle}{\sum_{i \neq j} \delta_{r, r_{ij}} \langle \hat{\sigma}_{ee}^{(i)} \rangle \langle \hat{\sigma}_{ee}^{(j)} \rangle} \quad (2)$$

which characterizes the occurrence of two excitations separated by a distance  $r$ . Here  $\delta_{r, r_{ij}}$  is the Kronecker symbol that restricts the sum to

sites  $(i, j)$  for which  $r_{ij} = r$ . In contrast to the spatial distributions presented above, the average is now taken over all values of  $N_e$ . The pair correlation function  $g^{(2)}(r)$  shows a strong suppression at distances smaller than  $r = 4.8(2) \mu\text{m}$ , which coincides with the expected blockade radius  $R_b = 4.9(1) \mu\text{m}$ . Moreover, we find a clear peak at  $r = 5.6(2) \mu\text{m}$  and evidence for weak oscillations extending to the boundaries of our system. This indicates that the overall many-body state only exhibits finite-range correlations. Our theoretical calculation of  $g^{(2)}(r)$  (grey line in Fig. 3a) exhibits similar features, but shows more pronounced oscillations and vanishes perfectly within the blockade radius. These discrepancies can be attributed to several imperfections of the detection technique. The sharp peak at short distances  $r \lesssim 1 \mu\text{m}$  results from hopping of single atoms to adjacent sites during fluorescence imaging with a small probability of approximately 1%, which is falsely detected as two neighbouring excitations. The non-zero value of  $g^{(2)}(r)$  for distances  $r \lesssim 3 \mu\text{m}$  arises from the imperfect removal of the ground-state atoms. Finally, the shift and slight broadening of the peak in the correlation function is attributed to the residual motion of the Rydberg atoms before imaging (Supplementary Information). When we take account of these independently characterized effects in the theoretical calculations (green line in Fig. 3a), we recover excellent agreement with the measurements.

Because our system size is comparable to the blockade radius, the excitations in states with  $N_e > 1$  are localized along the circumference of the system. We characterize the resulting angular order by introducing an azimuthal correlation function that reflects the probability of finding two excitations with a relative angle  $\Delta\phi$  measured with respect to the centre of mass of the distribution of excitations:

$$\tilde{g}^{(2)}(\Delta\phi) = \frac{\int d\phi \langle \hat{n}(\phi) \hat{n}(\phi + \Delta\phi) \rangle}{2\pi \langle \hat{n}(\phi) \rangle \langle \hat{n}(\phi + \Delta\phi) \rangle} \quad (3)$$

Here  $\hat{n}(\phi) = \sum_i \delta_{\phi, \phi_i} \hat{\sigma}_{ee}^{(i)}$  is the azimuthal distribution of excitations, with  $(r_i, \phi_i)$  the polar coordinates of site  $i$ . As can be seen in Fig. 3b, the spatially ordered structure is clearly visible as correlations at relative angles  $\Delta\phi = v \times 360^\circ / N_e$ , with  $v = 1, 2, \dots, N_e$ , even for the largest excitation numbers.

We finally analyse the many-body excitation dynamics of the system. In Fig. 4a we show the time evolution of the average number of Rydberg excitations,  $\bar{N}_e = \sum_i \langle \hat{\sigma}_{ee}^{(i)} \rangle$ , which quickly saturates to a

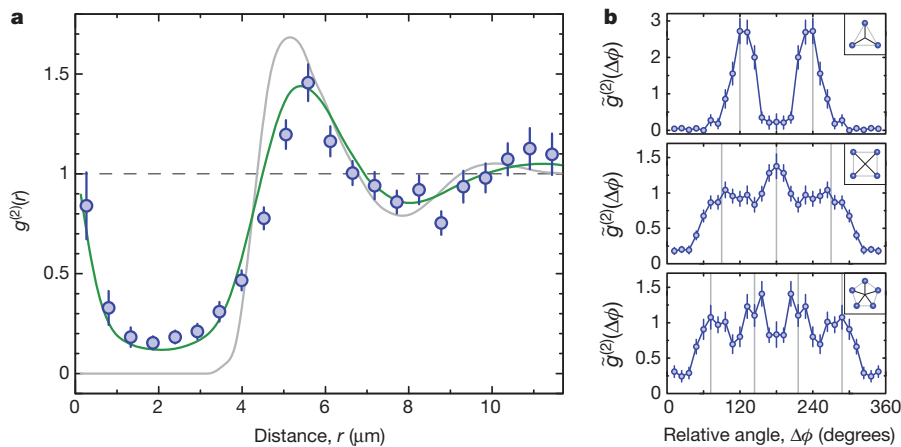


**Figure 3 | Correlation functions of Rydberg excitations.** **a**, Pair correlation function. The blockade effect results in a strong suppression of the probability of finding two excitations separated by a distance less than the blockade radius  $R_b = 4.9(1) \mu\text{m}$ . Moreover, we observe a peak at  $r \approx 5.6 \mu\text{m}$  and a weak oscillation at larger distances. The initial atom distribution had a diameter of  $10.8(8) \mu\text{m}$ . The experimental data (blue circles) are compared to the theoretical prediction both taking into account the independently characterized imperfections of our detection method (green line) and disregarding these imperfections (grey line). The dashed line marks the value of  $g^{(2)}$  in the absence

of correlations. Error bars, s.e.m. of  $g^{(2)}(r)$ . **b**, Azimuthal correlation function. The spatially ordered structure of the high-density components is best visible in the angular correlations around the centre of mass of the distribution of excitations, characterized by the correlation function  $\tilde{g}^{(2)}(\Delta\phi)$  defined in equation (3). By construction, this function is symmetric around  $180^\circ$ . Correlations are observed at the angles expected for the respective configurations shown in the insets. The peaks close to  $180^\circ$  are more pronounced because the centre of mass of a configuration is likely to lie close to the intersections of the diagonals, owing to the blockade effect. Error bars, s.e.m.

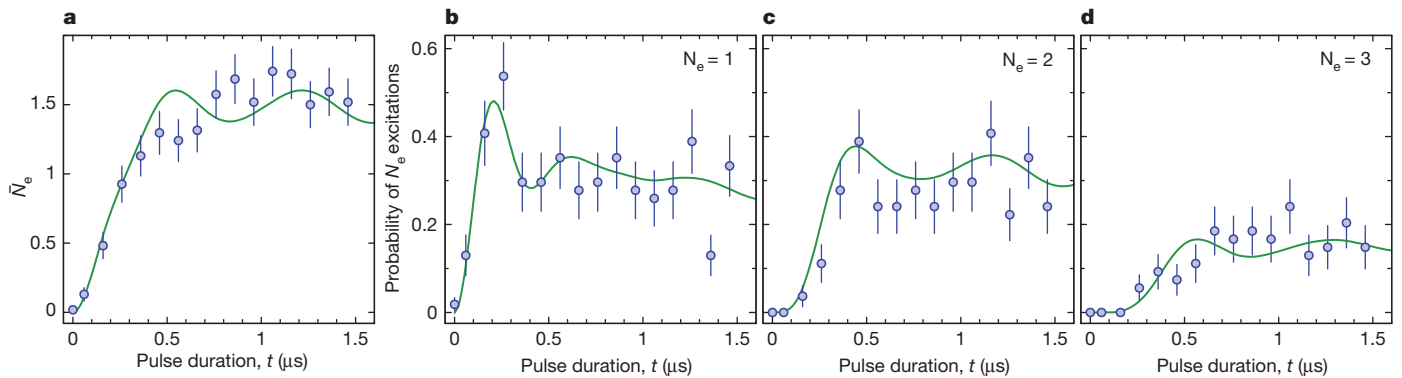


**Figure 4 | Time evolution of the number of Rydberg excitations.** **a**, Average number of detected Rydberg atoms as a function of the excitation pulse duration. Error bars, s.e.m. **b–d**, Time evolution of the probability of observing  $N_e = 1$  (**b**),  $N_e = 2$  (**c**) and  $N_e = 3$  (**d**) Rydberg excitations. The experimental

small value  $\bar{N}_e \approx 1.5$ , much smaller than the total number of atoms in the system,  $N_{\text{at}} = 150(30)$ . The saturation is reached in  $\sim 500$  ns, a factor of ten faster than the Rabi period  $2\pi/\Omega$ , owing to the collective enhancement of the optical coupling strength. The probability of observing  $N_e$  Rydberg excitations shows a similar saturation profile for each excitation number  $N_e$  (Fig. 4b–d), but on a timescale that increases with  $N_e$ , from about 200 ns for  $N_e = 1$  to about 600 ns for  $N_e = 3$ . This can be attributed to the variation of the collective enhancement factor associated with the number of energetically accessible microscopic configurations for a given  $N_e$ . The theoretical excitation dynamics corresponding to the Hamiltonian, equation (1), shows remarkable agreement with the experimental data when the finite detection efficiency is included. This provides evidence that the dynamics observed in the experiment is coherent, as expected on these timescales, which are much shorter than the lifetime of the Rydberg state of  $25(5) \mu\text{s}$  in the lattice and the timescale of other decoherence effects (Supplementary Information). The absence of high-contrast Rabi oscillations in the time evolution of the average number of Rydberg excitations is caused by the strong dephasing between many-body states with different interaction energies arising from the different spatial distribution of excitations. However, remnant signatures of Rabi oscillations can still be observed. In particular, the population of the singly excited states shows a peak around  $t = 200(50)$  ns (Fig. 4b), which matches the  $\pi$ -pulse time of the enhanced Rabi frequency  $\pi/(\sqrt{N_{\text{at}}}\Omega) = 240(40)$  ns. Further evidence for the coherence of the dynamics can be found in the spatially resolved analysis of the excitation dynamics (Supplementary Information).

We have characterized the strongly correlated excitation dynamics of a resonantly driven Rydberg gas using optical detection with unprecedented spatial resolution, and observed ordered Rydberg excitation patterns in the high-density components of the many-body states produced. One future challenge lies in the deterministic preparation of ground-state Rydberg crystals with a well-defined number of excitations via adiabatic sweeps of the laser parameters<sup>3,4,14</sup>. Together with the demonstrated imaging technique, this would enable precise studies of quantum phase transitions in long-range interacting quantum systems on the microscopic level<sup>2–4,15</sup>. Also, by combining the dipole blockade effect with the single-atom addressing already demonstrated in our experimental set-up, it should be possible to engineer mesoscopic quantum gates<sup>32</sup>; such a system could serve as an experimental ‘toolbox’ for digital quantum simulations of a broad class of spin models, including such fundamental systems as Kitaev’s toric code<sup>33</sup>.

## METHODS SUMMARY

**Rydberg excitation and detection scheme.** The two excitation laser beams were counterpropagating along the  $z$  axis, with an intermediate-state detuning  $\delta/(2\pi) = 742(2)$  MHz (Fig. 1b). During the sequence, a magnetic offset field of  $B \approx 30$  G along the  $z$  axis defined the quantization axis. The excitation pulse was

performed by switching the laser at 780 nm while the laser at 480 nm was on. The temporal resolution of our measurement was thus set by the rise time of the 780 nm light, which was  $\sim 40$  ns. Immediately after the excitation pulse, we used near-resonant circularly polarized laser beams to drive the transitions  $|5S_{1/2}, F=1\rangle \rightarrow |5P_{3/2}, F=2\rangle$  and  $|5S_{1/2}, F=2\rangle \rightarrow |5P_{3/2}, F=3\rangle$  and remove all ground-state atoms, with a fidelity of 99.9% in  $10 \mu\text{s}$ . Subsequently, the Rydberg atoms were stimulated down to the ground state by resonantly driving the  $|43S_{1/2}, m_J = -1/2\rangle \rightarrow |5P_{3/2}, F=3, m_F = -3\rangle$  transition for  $2 \mu\text{s}$ .

**Computation of the histograms.** The histograms shown in Fig. 2b are based on the digitized atom distribution reconstructed from the raw images<sup>31</sup>. They reflect the Rydberg atom distribution in a region of interest covering a disk of radius  $R_{\text{max}} = 1.5 \times R$ . Each individual image was aligned in the following way. First, we set the origin of the coordinate system to the centre of mass of the atom distribution. Then, for each atom we determined the angle between its position vector and a reference axis, and rotated the image about the origin by the mean value of these angles (repeating this operation would leave the configuration unchanged). The histograms contain data taken at different evolution times up to  $4 \mu\text{s}$ , as we found no significant temporal dependence of the excitation patterns. The theoretical calculations used the same parameters as in the experiment (including temperature and atom number distribution of the initial state) and followed the same procedure to determine the Rydberg atom densities. Both the experimental and theoretical histograms were normalized such that the value at each bin represents the probability of observing a microscopic configuration with a Rydberg atom located at this position.

Received 11 July; accepted 13 September 2012.

- Saffman, M., Walker, T. & Mølmer, K. Quantum information with Rydberg atoms. *Rev. Mod. Phys.* **82**, 2313–2363 (2010).
- Weimer, H., Löw, R., Pfau, T. & Büchler, H. P. Quantum critical behavior in strongly interacting Rydberg gases. *Phys. Rev. Lett.* **101**, 250601 (2008).
- Pohl, T., Demler, E. & Lukin, M. D. Dynamical crystallization in the dipole blockade of ultracold atoms. *Phys. Rev. Lett.* **104**, 043002 (2010).
- Schachenmayer, J., Lesanovsky, I., Micheli, A. & Daley, A. J. Dynamical crystal creation with polar molecules or Rydberg atoms in optical lattices. *N. J. Phys.* **12**, 103044 (2010).
- Gärtner, M., Heeg, K. P., Gasenzer, T. & Evers, J. Dynamical formation of floating Rydberg excitation crystals. Preprint at <http://arXiv.org/abs/1203.2884v2> (2012).
- Bloch, I., Dalibard, J. & Zwerger, W. Many-body physics with ultracold gases. *Rev. Mod. Phys.* **80**, 885–964 (2008).
- Jaksch, D., Cirac, J. I., Zoller, P., Côté, R. & Lukin, M. D. Fast quantum gates for neutral atoms. *Phys. Rev. Lett.* **85**, 2208–2211 (2000).
- Lukin, M. *et al.* Dipole blockade and quantum information processing in mesoscopic atomic ensembles. *Phys. Rev. Lett.* **87**, 037901 (2001).
- Pupillo, G., Micheli, A., Boninsegni, M., Lesanovsky, I. & Zoller, P. Strongly correlated gases of Rydberg-dressed atoms: quantum and classical dynamics. *Phys. Rev. Lett.* **104**, 223002 (2010).
- Henkel, N., Nath, R. & Pohl, T. Three-dimensional roton excitations and supersolid formation in Rydberg-excited Bose-Einstein condensates. *Phys. Rev. Lett.* **104**, 195302 (2010).
- Cinti, F. *et al.* Supersolid droplet crystal in a dipole-blockaded gas. *Phys. Rev. Lett.* **105**, 135301 (2010).
- Honer, J., Weimer, H., Pfau, T. & Büchler, H. Collective many-body interaction in Rydberg dressed atoms. *Phys. Rev. Lett.* **105**, 160404 (2010).
- Robicheaux, F. & Hernández, J. Many-body wave function in a dipole blockade configuration. *Phys. Rev. A* **72**, 063403 (2005).

14. van Bijnen, R. M. W., Smit, S., van Leeuwen, K. H., Vredenbregt, E. J. D. & Kokkelmans, S. J. J. M. F. Adiabatic formation of Rydberg crystals with chirped laser pulses. *J. Phys. B* **44**, 184008 (2011).
15. Lesanovsky, I. Many-body spin interactions and the ground state of a dense Rydberg lattice gas. *Phys. Rev. Lett.* **106**, 025301 (2011).
16. Höning, M., Muth, D., Petrosyan, D. & Fleischhauer, M. Steady-state crystallization of Rydberg excitations in an optically driven lattice gas. Preprint at <http://arXiv.org/abs/1208.2911> (2012).
17. Tong, D. *et al.* Local blockade of Rydberg excitation in an ultracold gas. *Phys. Rev. Lett.* **93**, 063001 (2004).
18. Urban, E. *et al.* Observation of Rydberg blockade between two atoms. *Nature Phys.* **5**, 110–114 (2009).
19. Gaëtan, A. *et al.* Observation of collective excitation of two individual atoms in the Rydberg blockade regime. *Nature Phys.* **5**, 115–118 (2009).
20. Schwarzkopf, A., Sapiro, R. & Raithel, G. Imaging spatial correlations of Rydberg excitations in cold atom clouds. *Phys. Rev. Lett.* **107**, 103001 (2011).
21. Dudin, Y. O. & Kuzmich, A. Strongly interacting Rydberg excitations of a cold atomic gas. *Science* **336**, 887–889 (2012).
22. Wilk, T. *et al.* Entanglement of two individual neutral atoms using Rydberg blockade. *Phys. Rev. Lett.* **104**, 010502 (2010).
23. Isenhower, L. *et al.* Demonstration of a neutral atom controlled-NOT quantum gate. *Phys. Rev. Lett.* **104**, 010503 (2010).
24. Raitzsch, U. *et al.* Echo experiments in a strongly interacting Rydberg gas. *Phys. Rev. Lett.* **100**, 013002 (2008).
25. Reetz-Lamour, M., Amthor, T., Deiglmayr, J. & Weidemüller, M. Rabi oscillations and excitation trapping in the coherent excitation of a mesoscopic frozen Rydberg gas. *Phys. Rev. Lett.* **100**, 253001 (2008).
26. Dudin, Y. O., Li, L., Bariani, F. & Kuzmich, A. Observation of coherent many-body Rabi oscillations. *Nature Phys.* <http://dx.doi.org/10.1038/nphys2413> (published online, 9 September 2012).
27. Löw, R. *et al.* Universal scaling in a strongly interacting Rydberg gas. *Phys. Rev. A* **80**, 033422 (2009).
28. Viteau, M. *et al.* Rydberg excitations in Bose-Einstein condensates in quasi-one-dimensional potentials and optical lattices. *Phys. Rev. Lett.* **107**, 060402 (2011).
29. Olmos, B., Li, W., Hofferberth, S. & Lesanovsky, I. Amplifying single impurities immersed in a gas of ultracold atoms. *Phys. Rev. A* **84**, 041607(R) (2011).
30. Günter, G. *et al.* Interaction enhanced imaging of individual Rydberg atoms in dense gases. *Phys. Rev. Lett.* **108**, 013002 (2012).
31. Endres, M. *et al.* Observation of correlated particle-hole pairs and string order in low-dimensional Mott insulators. *Science* **334**, 200–203 (2011).
32. Müller, M., Lesanovsky, I., Weimer, H., Büchler, H. P. & Zoller, P. Mesoscopic Rydberg gate based on electromagnetically induced transparency. *Phys. Rev. Lett.* **102**, 170502 (2009).
33. Weimer, H., Müller, M., Lesanovsky, I., Zoller, P. & Büchler, H. P. A Rydberg quantum simulator. *Nature Phys.* **6**, 382–388 (2010).

**Supplementary Information** is available in the online version of the paper.

**Acknowledgements** We thank R. Löw for discussions. We acknowledge funding by MPG, DFG, EU (NAMEQUAM, AQUATE, Marie Curie Fellowship to M.C.) and JSPS (Postdoctoral Fellowship for Research Abroad to T.F.).

**Author Contributions** All authors contributed extensively to the work presented in this paper.

**Author Information** Reprints and permissions information is available at [www.nature.com/reprints](http://www.nature.com/reprints). The authors declare no competing financial interests. Readers are welcome to comment on the online version of the paper. Correspondence and requests for materials should be addressed to P.S. ([peter.schauss@mpq.mpg.de](mailto:peter.schauss@mpq.mpg.de)).

# Fluvial response to abrupt global warming at the Palaeocene/Eocene boundary

Brady Z. Foreman<sup>1</sup>, Paul L. Heller<sup>1</sup> & Mark T. Clementz<sup>1</sup>

Climate strongly affects the production of sediment from mountain catchments as well as its transport and deposition within adjacent sedimentary basins<sup>1–3</sup>. However, identifying climatic influences on basin stratigraphy is complicated by nonlinearities, feedback loops, lag times, buffering and convergence among processes within the sediment routing system<sup>3,4</sup>. The Palaeocene/Eocene thermal maximum (PETM) arguably represents the most abrupt and dramatic instance of global warming in the Cenozoic era and has been proposed to be a geologic analogue for anthropogenic climate change<sup>5</sup>. Here we evaluate the fluvial response in western Colorado to the PETM. Concomitant with the carbon isotope excursion marking the PETM we document a basin-wide shift to thick, multistoried, sheets of sandstone characterized by variable channel dimensions, dominance of upper flow regime sedimentary structures, and prevalent crevasse splay deposits. This progradation of coarse-grained lithofacies matches model predictions for rapid increases in sediment flux and discharge<sup>1,3</sup>, instigated by regional vegetation overturn<sup>5,6</sup> and enhanced monsoon precipitation<sup>7,8</sup>. Yet the change in fluvial deposition persisted long after the approximately 200,000-year-long PETM<sup>9</sup> with its increased carbon dioxide levels in the atmosphere, emphasizing the strong role the protracted transmission of catchment responses to distant depositional systems has in constructing large-scale basin stratigraphy. Our results, combined with evidence for increased dissolved loads<sup>10</sup> and terrestrial clay export<sup>5,11,12</sup> to world oceans, indicate that the transient hyper-greenhouse climate of the PETM may represent a major geomorphic ‘system-clearing event’<sup>13</sup>, involving a global mobilization of dissolved and solid sediment loads on Earth’s surface.

During the PETM, an extreme global warming event that occurred about 56 million years ago<sup>5</sup>, mean annual temperatures increased by 5°–8° C, precipitation and vegetation patterns dramatically altered worldwide, and both atmospheric and oceanic circulation was perturbed<sup>5,6,8</sup>. The warming was associated with a massive exogenic pulse of isotopically light carbon into Earth’s oceans and atmosphere, recorded as a major negative carbon isotope excursion in a suite of organic and carbonate substrates hosted in marine and terrestrial strata<sup>5</sup>. Although more than 4,000 petagrams of carbon (PgC) were released in less than 10,000 years (10 kyr), a high atmospheric partial pressure of CO<sub>2</sub> ( $p_{\text{CO}_2}$  exceeding 1,200 p.p.m.; ref. 5) persisted for an additional 190 kyr or so before being sequestered<sup>5,9</sup>.

Here we characterize shifts in the nature of fluvial deposition spanning the PETM within the intermontane Piceance Creek basin of western Colorado, USA (Fig. 1), which formed during the Laramide orogeny<sup>14</sup>. Palaeocene and early Eocene deposition<sup>15–17</sup> is represented by the Wasatch formation, and is separated from base to top into the Atwell Gulch, Molina and Shire members<sup>16</sup>. Our new  $\delta^{13}\text{C}$  record using dispersed organic carbon documents an approximately 3.0‰ excursion from background values of about –23.0‰ (Vienna Pee Dee Belemnite standard, VPDB) (Fig. 2; Supplementary Data), constrained between pollen and mammalian fossil localities characteristic of the latest Palaeocene and earliest Eocene epochs<sup>15–17</sup> (Supplementary

Discussion; Supplementary Fig. 1). The beginning of the isotope excursion occurs within an approximately 10-m-thick sequence of crevasse splay deposits; the lowest values occur with the first laterally continuous sand-body, demarcating the onset of the deposition of the Molina member. The excursion persists for an additional 30 m or so of the Molina member (Fig. 2; Supplementary Fig. 1; Supplementary Data). The Molina member can be continuously traced in outcrop for about 40 km both east–west and north–south in the study area around DeBeque, Colorado<sup>18</sup>. Equivalent sand-rich PETM intervals crop out about 90 km north and about 50 km east of DeBeque, and are recognizable in well data in intervening areas<sup>16,18</sup>.

The Atwell Gulch member is a mud-dominated succession of purple, orange and red palaeosols (Supplementary Figs 2 and 3). Fluvial sand-bodies are thin and laterally restricted (Fig. 3a, b). Estimates of bank-full flow depths and widths indicate that the rivers that deposited these sand-bodies were relatively shallow and narrow, and that the bedforms within channel-fills were dominated by trough cross-bedding (Fig. 3c–e). Levee complexes are commonly associated with these sand-bodies, but crevasse splay deposits are rare (Supplementary Figs 2 and 3). In contrast, fluvial sand-bodies are thick, laterally continuous, and sheet-like within the Molina member (Fig. 3a, b). Bank-full flow depths are deeper, channels wider, and both display a greater range than in the other members (Fig. 3c, d). Upper-plane bed laminations are the dominant bedform observed, with palaeosols typically purple in colour, levee complexes absent, and crevasse splay deposits ubiquitous (Fig. 3e; Supplementary Figs 2–4).

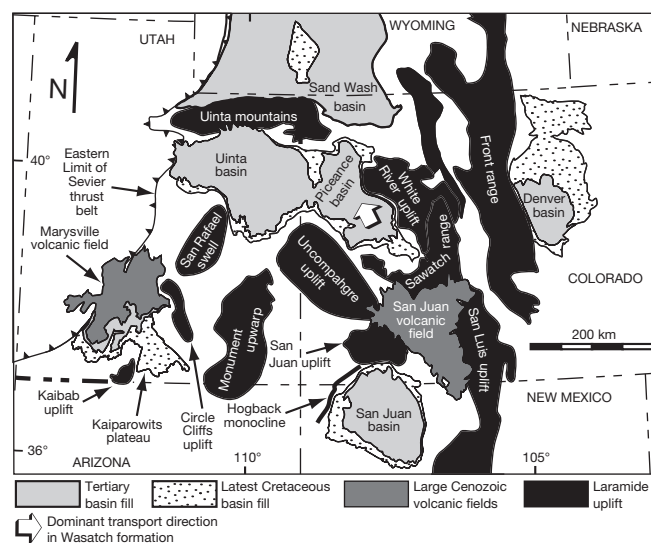


**Figure 1 | Generalized geologic map showing major Laramide structures and associated basins.** The Uinta and Piceance Creek basins were separate during the Palaeocene and the earliest Eocene epochs, and Cenozoic volcanic fields substantially post-date the deposition of the Wasatch formation.

<sup>1</sup>University of Wyoming, Department of Geology and Geophysics, 1000 East University Avenue, Laramie, Wyoming 82071, USA.

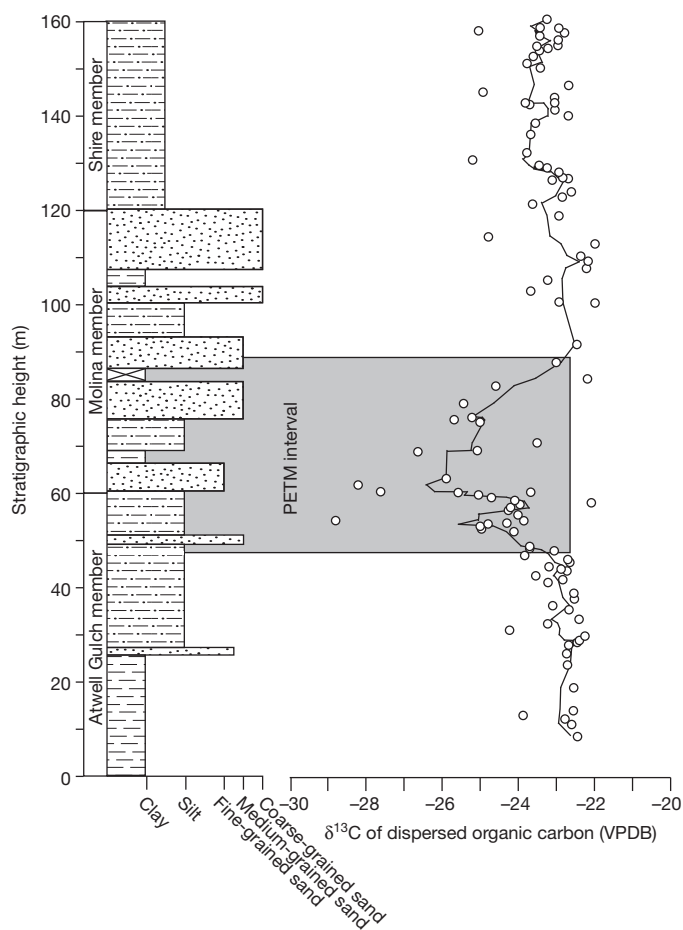


**Figure 2 | Stratigraphic section through the middle portion of the Wasatch formation east of the town of DeBeque in Colorado, and the  $\delta^{13}\text{C}$  record from dispersed organic carbon.** The black line shows the five-point running average, and the width of individual data points represents analytical precision (about 0.1‰). Replicate analyses are  $\pm 0.3\text{‰}$  of average values at a given stratigraphic height.

The strata of the overlying Shire member are similar to the Atwell Gulch member, except that the palaeosols are dominantly red and pink, and sand-bodies tend to be slightly thicker (Fig. 3; Supplementary Figs 2 and 3).

The sand-body and channel measurements are non-normally distributed based on Lilliefors statistical tests at the  $\alpha = 0.05$  level.

Non-parametric Kruskal–Wallis tests reject the null hypothesis that Molina member sand-body thickness (degrees of freedom, d.f. = 2;  $\chi^2 = 46.1982$ ;  $P \ll 0.001$ ), sand-body width (d.f. = 2;  $\chi^2 = 35.1015$ ;  $P \ll 0.001$ ), bank-full flow depth (d.f. = 2;  $\chi^2 = 6.0541$ ;  $P = 0.0485$ ), and flow width (d.f. = 2;  $\chi^2 = 9.5330$ ;  $P = 0.0085$ ) have the same median values as other members (Supplementary Data).

Previous authors ascribed the abrupt sedimentologic transition of the Molina member to either unroofing of Permian/Jurassic-aged aeolianites in the hinterland<sup>18</sup> or to a tectonically induced increase in sediment supply generated from surrounding Laramide uplifts<sup>16</sup> (Fig. 1). Sea level influences were probably unimportant given that western Colorado was separated from the palaeo-shoreline by around 1,000 km and several mountain ranges<sup>14,19</sup>.

The unroofing hypothesis argues for a coarsening of the grain-size probability density function of flux from eroding mountain catchments<sup>18</sup>. We tested the hypothesis by assessing provenance changes within the Wasatch formation using U–Pb detrital zircon age spectra and their similarity to age spectra of the Glen Canyon group aeolianites<sup>20</sup>, the proposed source for the Molina member<sup>18</sup>. All the major peaks and cumulative curves of the age spectra are nearly identical among the three members, indicating no major changes in sediment source during deposition (Fig. 4a; Supplementary Discussion). None show peak ages characteristic of older aeolianite sources from the Colorado plateau and the Uncompahgre uplift<sup>20</sup> (Fig. 4a). Furthermore, sandstone compositions are lithic arenites in all three members, unlike the quartz arenite composition of the aeolianites<sup>21</sup>.

The tectonic hypothesis invokes simultaneous uplift events and corresponding increases in flux from the Uncompahgre and White River Laramide structures flanking the southwest and east of the study area, respectively<sup>16</sup> (Fig. 1). Constant subsidence rates (though limited in resolution) in the basin<sup>22</sup> and uniform palaeocurrent dispersal patterns (Fig. 4b) suggest that there were no periods of new or renewed rapid surface uplift and attendant flexural loading of the basin<sup>23</sup>, nor deflection of rivers as a result of increased sediment flux from these margins. Moreover, the Molina member thins towards the proposed source areas<sup>16</sup>, the opposite geometry of syntectonic deposits, which thicken towards the sediment source<sup>23</sup>. Alternatively, the Molina member could record a period of slowed subsidence with constant sediment flux, in which reduced accommodation causes progradation and denser amalgamation of coarse facies<sup>23</sup>. Existing subsidence histories<sup>22</sup> do not support this scenario either, but owing to age uncertainties neither tectonic scenario can be definitively disproved. However, we find them less parsimonious given the Molina member's correlation with the PETM and its sedimentologic coherency with proposed climatic changes.

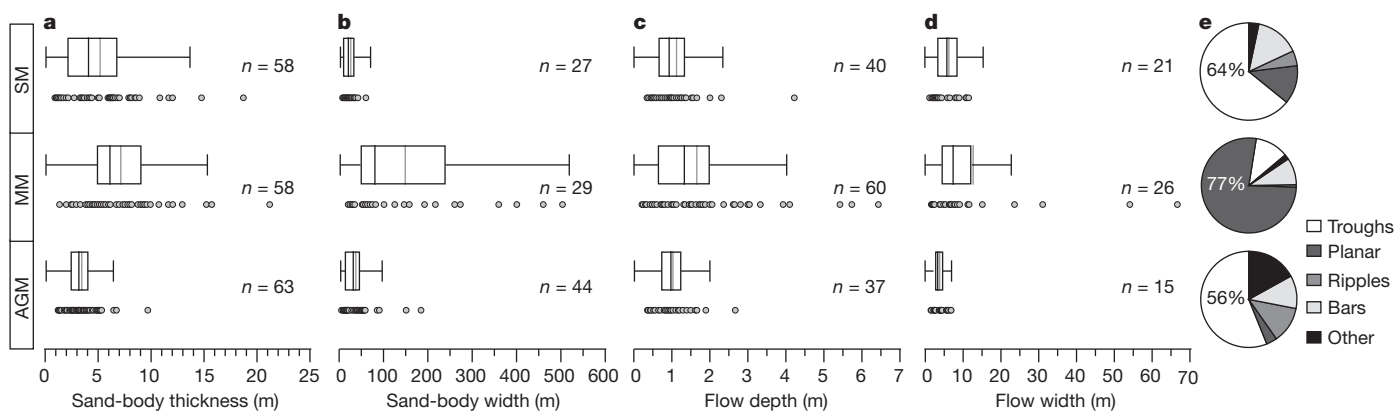


**Figure 3 | Box and whisker plots of fluvial data from the Atwell Gulch, Molina and Shire members.** AGM, Atwell Gulch member; MM, Molina member; SM, Shire member. Edges of boxes denote bounding quartiles, the black vertical lines represent median values, the grey vertical lines represent mean values, and whiskers denote the lower fence and upper fence (that is, 1.5

times the interquartile range). Grey circles denote individual data points. **a**, Sand-body thickness. **b**, Sand-body width perpendicular to local flow direction. **c**, Bank-full flow depth. **d**, Channel flow width perpendicular to mean local flow direction. **e**, Relative abundance of different bedform structures and bar clinoforms within sand-bodies.

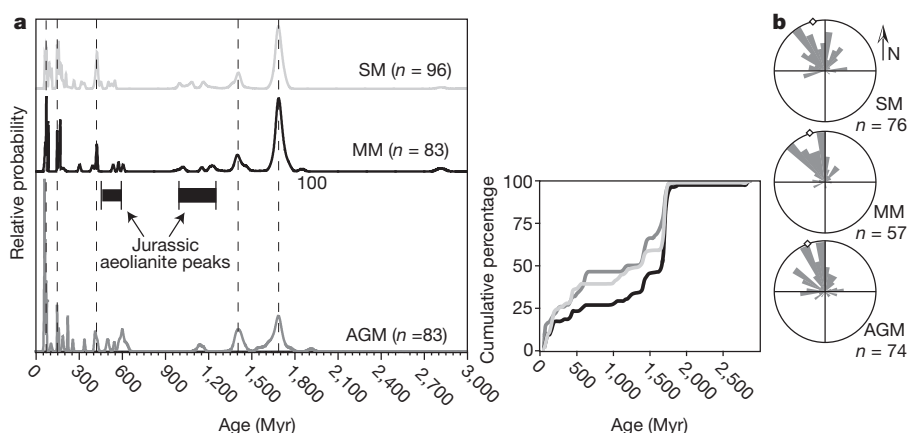


**Figure 4 | Comparison of provenance and palaeodrainage patterns in the Atwell Gulch, Molina and Shire members.** **a**, Normalized U–Pb age-distribution curves for detrital zircon populations ( $n$  is the number of grain ages determined). Key age peaks shared amongst the members are marked with dashed vertical lines. Age range of Jurassic aeolianite peaks are from ref. 20.

Deeper and wider channels in the Molina member, assuming similar slopes, imply greater discharges and potentially higher mean annual precipitation. The greater range of values displayed in bank-full flow depths within the Molina member suggests larger variability in the channel-forming discharges, which may correlate with greater variability in the severity and intensity of rainfall events. Preservation of upper-flow-regime sedimentary structures, such as upper-plane bed laminations and climbing dunes (Supplementary Fig. 4), within channel deposits require either a peaked hydrograph or high in-channel sedimentation rates, or else they would have been reworked by waning flow stages<sup>18,24</sup>. Alternatively, such upper-flow-regime structures can occur in unusually shallow flows; however, this is difficult to reconcile with deeper flows indicated by bar clinoforms and would require sustained steepened river gradients to transport coarser sediment. The abundance of crevasse splay deposits and lack of well-developed levee complexes suggests that channel-breaching and flooding were common occurrences. Finally, a shift to purple palaeosols suggests less well drained conditions<sup>25</sup>.

The high  $p_{\text{CO}_2}$  conditions of the PETM potentially instigated increased atmospheric humidity and intensified the hydrologic cycle<sup>26</sup>. Within the western interior of the USA, circulation models suggest the increased importance of convective atmospheric circulation off the palaeo-Gulf of Mexico, leading to enhanced monsoons<sup>7,8</sup>. Larger channels and preservation of upper-flow-regime structures are broadly consistent with the hypothesis, possibly with periods of higher runoff and greater channel-forming discharges associated with summer monsoonal rains. Yet increases in mean annual precipitation are more uncertain because channel-forming discharge will not necessarily reflect mean flow conditions. Overall, the monsoon hypothesis needs further testing at sites in other Laramide basins, especially since proxies in the Bighorn basin of Wyoming, around 500 km north, suggest drying trends during the PETM<sup>6,25</sup>.

Numerical models predict extensive progradation of coarse-grained lithofacies due to increased discharge and sediment flux, reducing the rate of down-stream fining via selective deposition of coarser grains<sup>1,3,4</sup>. Greater rainfall leads to increased discharge (seasonal or otherwise), causing higher diffusivity and the capacity to transport coarse sediment in rivers<sup>1,3</sup>. Additional sediment flux to rivers will also cause progradation<sup>1</sup>. Continental-scale overturn of vegetation regimes during the PETM<sup>5,6</sup> undoubtedly remobilized sediment from basin hillslopes and floodplains. Similarly, greater hinterland catchment efflux is predicted during periods of vegetation overturn, precipitation

increases and heightened storm intensity that together act to cleanse catchments of colluvium, enhance bedrock erosion by expanding drainage channel networks, increase bedrock channel incision rates, and accelerate sediment provision via landslides and other threshold-dependent hillslope processes<sup>2,4</sup>.

Assuming these geomorphic processes led to increased sediment flux during the PETM, coupled with constant basin subsidence<sup>22</sup>, the observed stratigraphic pattern implies the preferential bypass of fine-grained sediment through the basin towards the north (Fig. 1). The shift to sand-rich deposits is a consequence of selective deposition by alluvial rivers filling the basin<sup>1,3</sup>. Analogously, during the PETM in the Tremp-Graus basin of Spain, a vast conglomeratic braid-plain prograded owing to enhanced seasonal precipitation<sup>27</sup> with correlative shelf and bathyal marine sediments recording greater terrestrially derived clay accumulation<sup>28</sup>. Indeed, many marginal marine settings around the world record an increase in terrestrial clay deposition during the PETM<sup>5,11,12</sup>. The well-studied Bighorn basin may record the reverse scenario, in which basin-wide, enhanced palaeosol formation during the PETM<sup>25</sup> reflects reduced sediment supply due to lower diffusivity of basin rivers and catchment efflux brought on by decreases in precipitation by up to 40% (refs 6 and 25).

While increases in dissolved loads<sup>10</sup> and clay export<sup>5,11,12</sup> to oceans are restricted to the PETM interval, which implies fast response times in step with the climate change, the fluvial response in western Colorado persists 30 m beyond the isotope excursion (Fig. 2). Hysteresis effects such as this result from the dynamic coupling of hinterland erosional and basin depositional regimes and relate to how the perturbation is propagated (for example, a kinematic wave versus diffusion, respectively), the length scales they are transmitted over, and relaxation times for the reattainment of 'equilibrium' slope conditions<sup>1–4</sup>. Even in simplified two-dimensional models these effects may combine to maintain perturbed states for around 500 kyr (ref. 3). The likelihood of nonlinear sedimentation rates and imprecise age control precludes an accurate estimate for the relaxation time in western Colorado, though conservatively we suggest it was on the timescale of  $10^5$  years. More importantly, we emphasize the overall coherency in western Colorado with simplified and scaled-down model and experimental predictions, and that we expect future studies to find similar responses in other terrestrial sequences. If the pattern bears out, the high  $p_{\text{CO}_2}$  concentrations of the PETM did not only have far-reaching consequences for the evolution and ecology of biotic systems<sup>5</sup>, but may also represent a global-scale 'clearing event' for geomorphic systems<sup>13</sup>.

## METHODS SUMMARY

**U–Pb detrital zircon ages.** Medium-grained sandstone samples were obtained near the base of fluvial sand-bodies (see Supplementary Discussion for stratigraphic positions). Samples were disaggregated, and zircons removed using standard water table, magnetic and heavy-liquid separation techniques. U–Pb determinations (about 100 unknown and about 35 standards per sample) were performed at the University of Arizona's LaserChron facility using a laser-ablation multicollector inductively coupled plasma mass spectrometer, measurement error is around 1–2% (2-sigma level). A 10% discordance filter was applied to the generated ages. See ref. 29 for detailed description of analytical methods.

**Carbon isotope analyses.** Samples for isotopic analysis were obtained by trenching until fresh rock was exposed. Approximately 40 mg of powdered sample were loaded into glass vials and loaded into a dry bath held at 50 °C. Then, 100 µl of 6 N HCl was added incrementally each day to the samples over the course of three days. Dried samples were weighed into tin capsules before introduction to the Thermal Finnigan Delta Plus XP elemental-analyser isotopic-ratio mass spectrometer housed at the University of Wyoming Stable Isotope Facility. Results are reported in  $\delta$  notation with reference standard VPDB. Analytical error is around 0.1‰, and replicate analyses are  $\pm 0.3\%$  of average values at a given stratigraphic height.

**Stratigraphic data.** Over 175 sand-bodies were examined during the course of this study across about 1,200 km<sup>2</sup>. Fluvial data were obtained using a Jacob's staff and laser range finder. The accuracy of the laser range finder is  $\pm 0.1$  m, and its precision is better than  $\pm 0.2$  m. Flow depths were determined from relief on bar clinoforms and mud plugs. Flow widths were estimated from 1.5 times the toe-to-crest horizontal distance of bar clinoforms and mud-plug widths<sup>30</sup>, corrected for local palaeocurrent direction relative to outcrop orientation. These estimates should be viewed as minimums because bar clinoform deposition may be oblique to the flow direction.

Received 7 February; accepted 14 August 2012.

Published online 24 October 2012.

- Paola, C., Heller, P. L. & Angevine, C. L. The large-scale dynamics of grain-size variation in alluvial basins. 1: Theory. *Basin Res.* **4**, 73–90 (1992).
- Tucker, G. E. & Slingerland, R. Drainage basin responses to climate change. *Wat. Resour. Res.* **33**, 2031–2047 (1997).
- Armitage, J. J., Duller, R. A., Whittaker, A. C. & Allen, P. A. Transformation of tectonic and climatic signals from source to sedimentary archive. *Nature Geosci.* **4**, 231–235 (2011).
- Allen, P. A. in *Landscape Evolution: Denudation, Climate and Tectonics Over Different Time and Space Scales* Vol. 269 (eds Gallacher, K., Jones, K. S. J. & Wainwright, J.) 7–28 (Geological Society Special Publications, 2008).
- McInerney, F. A. & Wing, S. L. The Paleocene-Eocene Thermal Maximum: a perturbation of carbon cycle, climate, and biosphere with implications for the future. *Annu. Rev. Earth Planet. Sci.* **39**, 489–516 (2011).
- Wing, S. L. *et al.* Transient floral change and rapid global warming at the Paleocene-Eocene boundary. *Science* **310**, 993–996 (2005).
- Shellito, C. J., Sloan, L. C. & Huber, M. Climate model sensitivity to atmospheric CO<sub>2</sub> levels in the early-middle Paleogene. *Palaeogeogr. Palaeoclimatol. Palaeoecol.* **193**, 113–123 (2003).
- Winguth, A., Shellito, C., Shields, C. & Winguth, C. Climate response at the Paleocene Eocene Thermal Maximum to greenhouse gas forcing—a model study with CCSM3. *J. Clim.* **23**, 2562–2584 (2010).
- Murphy, B. H., Farley, K. A. & Zachos, J. C. An extraterrestrial <sup>3</sup>He-based timescale for the Paleocene-Eocene Thermal Maximum (PETM) from Walvis Ridge, IODP Site 1266. *Geochim. Cosmochim. Acta* **74**, 5098–5108 (2010).
- Ravizza, G., Norris, R. N., Blusztajn, J. & Aubry, M.-P. An osmium isotope excursion associated with the late Paleocene thermal maximum: evidence of intensified chemical weathering. *Palaeogeography* **16**, 155–163 (2001).
- Robert, C. & Kennett, J. P. Antarctic subtropical humid episode at the Paleocene-Eocene boundary—clay mineral evidence. *Geology* **22**, 211–214 (1994).
- Gibson, T. G., Bybell, L. M. & Mason, D. B. Stratigraphic and climatic implications of clay mineral changes around the Paleocene/Eocene boundary of the northeastern US margin. *Sedim. Geol.* **134**, 65–92 (2000).
- Jerolmack, D. J. & Paola, C. Shredding of environmental signals by sediment transport. *Geophys. Res. Lett.* **37**, L19401 (2010).
- Dickinson, W. R. *et al.* Paleogeographic and paleotectonic setting of Laramide sedimentary basins in the central Rocky Mountain region. *Geol. Soc. Am. Bull.* **100**, 1023–1039 (1988).
- Johnson, R. C. & May, F. Preliminary stratigraphic studies of the upper part of the Mesaverde Group, the Wasatch Formation, and the lower part of the Green River Formation, DeBeque area, Colorado, including environments of deposition and investigation of palynomorph assemblages. *USGS Misc. Field Investig. Map MF-1050* (1978).
- Johnson, R. C. & Flores, R. M. in *Piceance Basin 2003 Guidebook* (eds Peterson, K. M., Olson, T. M. & Anderson, D. A.) 21–61 (RMAG, 2003).
- Burger, B. J. & Honey, J. G. Plesiadapidae (Mammalia, Primates) from the late Paleocene Fort Union Formation of the Piceance Creek Basin, Colorado. *J. Vert. Paleo.* **28**, 816–825 (2008).
- Lorenz, J. C. & Nadon, G. C. Braided-river deposits in a muddy depositional setting: the Molina Member of the Wasatch Formation (Paleogene) west-central Colorado, U.S.A. *J. Sedim. Res.* **72**, 376–385 (2002).
- Lillegraven, J. A. & Ostresh, L. M., Jr. in *Dawn of the Age of Mammals in the northern part of the Rocky Mountain Interior, North America* Vol. 243 (eds Bown, T. M. & Rose, K. D.) 1–30 (Geological Society of America, GSA Special Paper, 1990).
- Dickinson, W. R. & Gehrels, G. E. U-Pb ages of detrital zircons from Permian and Jurassic eolian sandstones of the Colorado Plateau, USA: paleogeographic implications. *Sedim. Geol.* **163**, 29–66 (2003).
- Blecha, A. M. & Gardner, M. H. Quantifying tectonic and climatic controls on alluvial architecture: Wasatch Formation of western Colorado. *GSA Abstr. Progr.* **36**, 307 (2004).
- Johnson, S. Y. Phanerozoic evolution of sedimentary basins in the Uinta-Piceance Basin region, northwestern Colorado and northeastern Utah. *USGS Bull.* **1787-FF**, FF1–FF38 (1992).
- Heller, P. L., Angevine, C. L., Winslow, N. S. & Paola, C. Two-phase stratigraphic model of foreland-basin sequences. *Geology* **16**, 501–504 (1988).
- Fielding, C. R. Upper flow regimes sheets, lenses and scour fills: extending the range of architectural elements for fluvial sediment bodies. *Sedim. Geol.* **190**, 227–240 (2006).
- Kraus, M. J. & Riggins, S. Transient drying during the Paleocene-Eocene Thermal Maximum (PETM): analysis of paleosols in the Bighorn Basin, Wyoming. *Palaeogeogr. Palaeoclimatol. Palaeoecol.* **245**, 444–461 (2007).
- Bowen, G. J., Beerling, D. J., Koch, P. L., Zachos, J. C. & Quattlebaum, T. A humid climate state during the Paleocene/Eocene thermal maximum. *Nature* **432**, 495–499 (2004).
- Schmitz, B. & Pujalte, V. Abrupt increase in seasonal extreme precipitation at the Paleocene-Eocene boundary. *Geology* **35**, 215–218 (2007).
- Schmitz, B. & Pujalte, V. Sea-level, humidity, and land-erosion records across the initial Eocene thermal maximum from a continental-marine transect in northern Spain. *Geology* **31**, 689–692 (2003).
- Gehrels, G. E., Valencia, V. A. & Ruiz, J. Enhanced precision, accuracy, efficiency and spatial resolution of U-Th-Pb ages by LA-MC-ICPMS. *Geochim. Geophys. Geosyst.* **9** (2008).
- Ethridge, F. G. & Schumm, S. A. in *Fluvial Sedimentology* (ed. Miall, A. D.) 703–721 (Canadian Society of Petroleum Geologists, 1978).

Supplementary Information is available in the online version of the paper.

**Acknowledgements** We thank personnel at the University of Arizona LaserChron Facility and University of Wyoming Stable Isotope Facility for assistance in analysing detrital zircon and carbon isotope samples. The International Association of Sedimentologists, the Tobacco Root Geological Society, the Colorado Scientific Society, and the Chevron Energy Technology Company provided funding for analyses and fieldwork. The research was completed while on a NSF Graduate Research Fellowship and Wyoming NASA Space Grant Consortium Fellowship to B.Z.F.

**Author Contributions** B.Z.F. and P.L.H. designed the study. B.Z.F. collected field data sets. B.Z.F. and M.T.C. carried out isotopic analyses. B.Z.F. wrote the manuscript. All authors contributed to the interpretations and conclusions presented.

**Author Information** Reprints and permissions information is available at [www.nature.com/reprints](http://www.nature.com/reprints). The authors declare no competing financial interests. Readers are welcome to comment on the online version of the paper. Correspondence and requests for materials should be addressed to B.Z.F. ([bforema1@uwyo.edu](mailto:bforema1@uwyo.edu)).

# The elusive Hadean enriched reservoir revealed by $^{142}\text{Nd}$ deficits in Isua Archaean rocks

Hanika Rizo<sup>1</sup>, Maud Boyet<sup>1</sup>, Janne Blichert-Toft<sup>2</sup>, Jonathan O'Neil<sup>1</sup>, Minik T. Rosing<sup>3</sup> & Jean-Louis Paquette<sup>1</sup>

The first indisputable evidence for very early differentiation of the silicate Earth came from the extinct  $^{146}\text{Sm}$ – $^{142}\text{Nd}$  chronometer.  $^{142}\text{Nd}$  excesses measured in 3.7-billion-year (Gyr)-old rocks from Isua<sup>1,2</sup> (southwest Greenland) relative to modern terrestrial samples imply their derivation from a depleted mantle formed in the Hadean eon (about 4,570–4,000 Gyr ago). As dictated by mass balance, the differentiation event responsible for the formation of the Isua early-depleted reservoir must also have formed a complementary enriched component. However, considerable efforts to find early-enriched mantle components in Isua have so far been unsuccessful<sup>3–7</sup>. Here we show that the signature of the Hadean enriched reservoir, complementary to the depleted reservoir in Isua, is recorded in 3.4-Gyr-old mafic dykes intruding into the Early Archaean rocks. Five out of seven dykes carry  $^{142}\text{Nd}$  deficits compared to the terrestrial Nd standard, with three samples yielding resolvable deficits down to  $-10.6$  parts per million. The enriched component that we report here could have been a mantle reservoir that differentiated owing to the crystallization of a magma ocean, or could represent a mafic proto-crust that separated from the mantle more than 4.47 Gyr ago. Our results testify to the existence of an enriched component in the Hadean, and may suggest that the southwest Greenland mantle preserved early-formed heterogeneities until at least 3.4 Gyr ago.

$^{142}\text{Nd}$  is produced by decay of short-lived  $^{146}\text{Sm}$  (half-life 68 million years, Myr; ref. 8). Because the  $^{146}\text{Sm}$ – $^{142}\text{Nd}$  chronometer was present only during the first  $\sim 500$  Myr of Solar System history, it is a powerful tool for understanding the evolution of the silicate Earth during the Hadean. Archaean rocks from the Amitsoq Complex (southwest Greenland) show small positive deviations in  $^{142}\text{Nd}/^{144}\text{Nd}$  ratio relative to other terrestrial samples<sup>1,2,9–13</sup>. This isotopic signature implies their derivation from a depleted mantle formed in the Hadean, and therefore documents that the silicate Earth experienced a differentiation event during the first hundreds of Myr of Solar System history. The early differentiation event resulting in the formation of the depleted reservoir must also have formed a complementary enriched reservoir. Indirect evidence for the existence of this component comes from the independent observations that both the magnitude of  $^{142}\text{Nd}$  excesses in Archaean rocks (Fig. 1) and the Lu/Hf and Sm/Nd ratios of komatiite sources decrease over time<sup>14</sup>. This may reflect the partial remixing of Hadean enriched and depleted reservoirs. Moreover, the presence of an enriched mafic crust is required to explain the Hf isotope compositions of the detrital Hadean Jack Hills zircons<sup>15,16</sup>. Additionally, an enriched basaltic crust may have been identified in the Nuvvuagittuq greenstone belt (Québec, Canada). Mafic samples from this belt have  $^{142}\text{Nd}/^{144}\text{Nd}$  values lower than the terrestrial standard<sup>17</sup>, and the positive correlation between  $^{142}\text{Nd}/^{144}\text{Nd}$  and  $^{147}\text{Sm}/^{144}\text{Nd}$

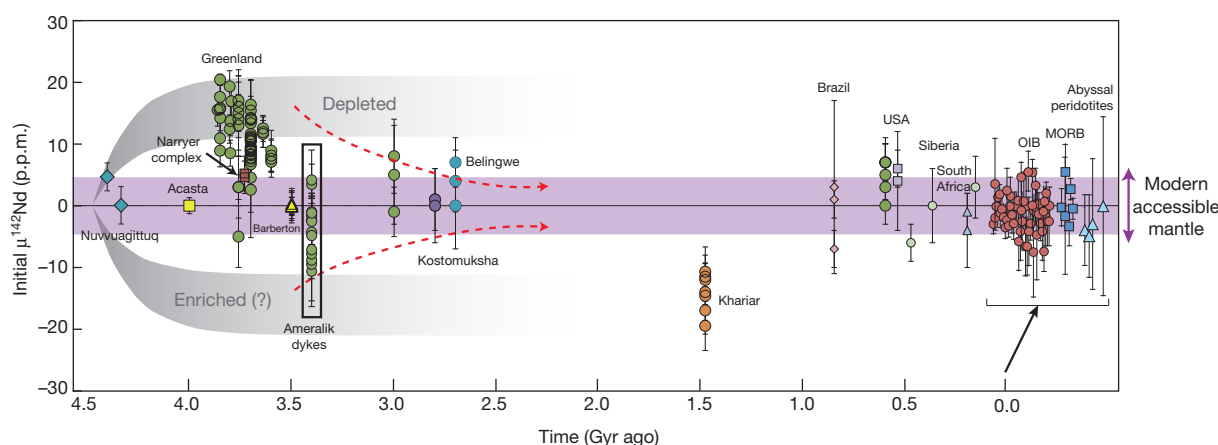


**Figure 1 | Compilation of all published initial  $^{142}\text{Nd}/^{144}\text{Nd}$  ratios for terrestrial samples.** Data are taken from refs 2–7, 9, 12, 13 and 17, except for the data for the Amealik dykes, which are from the present work (green symbols in black rectangle). Data are plotted as  $\mu^{142}\text{Nd}$ , that is, deviations in p.p.m. relative to the terrestrial Nd standard  $J\text{Nd}-1$ . The purple shaded area represents the external analytical error of  $\pm 5$  p.p.m. as a function of the time of emplacement of each sample. The 3.7–3.8-Gyr-old Greenland samples have well-resolved positive  $^{142}\text{Nd}$  anomalies, which suggests that their source was depleted in incompatible elements and formed in the Hadean ( $\sim 4.47$  Gyr ago<sup>9</sup>). The fractionation event responsible for the formation of the Greenland

early-depleted mantle (grey shaded area labelled 'Depleted') must have created a complementary enriched reservoir (grey shaded area labelled 'Enriched(?)). The only samples that seem to derive from a low- $^{142}\text{Nd}/^{144}\text{Nd}$  source are the Khariar samples<sup>4</sup>, but this data set still needs to be duplicated. Note that  $^{142}\text{Nd}$  anomalies seem to decrease with time, which may reflect the remixing of both early-depleted and enriched reservoirs (red dashed curves). OIB (ocean island basalt), MORB (mid-ocean-ridge basalt) and abyssal peridotites are all modern samples (that is, 0 Gyr ago, as indicated by the bracket). Samples derived from the modern accessible mantle are indicated by the purple double-headed arrow.

<sup>1</sup>Clermont Université, Université Blaise Pascal, Laboratoire Magmas et Volcans, CNRS UMR 6524, IRRD R 163, BP 10448, 63000 Clermont-Ferrand, France. <sup>2</sup>Laboratoire de Géologie de Lyon, Ecole Normale Supérieure de Lyon and Université Claude Bernard Lyon 1, CNRS UMR 5276, 69007 Lyon, France. <sup>3</sup>Natural History Museum of Denmark and Nordic Center for Earth Evolution, University of Copenhagen, DK-1350 København, Denmark.

ratios suggests that these rocks crystallized  $\sim 4.4$  Gyr ago (calculated with the new  $^{146}\text{Sm}$  decay constant<sup>8</sup>). All other efforts to identify early-enriched mantle components using the  $^{146}\text{Sm}$ – $^{142}\text{Nd}$  system have so far been either unsuccessful or yielded controversial results<sup>3–7</sup>.

In a new quest for the elusive enriched Hadean reservoir, we analysed the mafic Amlalik dykes from the Amitsoq Complex for major- and trace-element abundances and  $^{146,147}\text{Sm}$ – $^{142,143}\text{Nd}$ ,  $^{176}\text{Lu}$ – $^{176}\text{Hf}$  and U–Pb systematics. The Amitsoq Complex is located in the Nuuk region and includes the Isua Supracrustal Belt (ISB). Mafic dykes known as the ‘Amlalik dykes’ intrude into both the ISB and its enveloping gneisses. We analysed 12 metadoleritic dykes intruding into the ISB, as well as five samples that included margins and central cumulative parts of noritic dykes intruding into the Amitsoq gneisses (Supplementary Information).

The trace-element and isotopic compositions of the centres of the cumulate noritic dykes differ significantly from those of their margins, which have compositions identical to the metadolerite dykes. The cumulate noritic dykes have light rare-earth element (LREE)-enriched chondrite-normalized (CN) profiles ( $\text{La}/\text{Sm}_{\text{CN}} = 3.3$ – $3.6$ ) and low  $^{147}\text{Sm}/^{144}\text{Nd}$  (0.1241–0.1247) and  $^{176}\text{Lu}/^{176}\text{Hf}$  (0.0156–0.0175) ratios (Supplementary Information). These dykes therefore seem to have

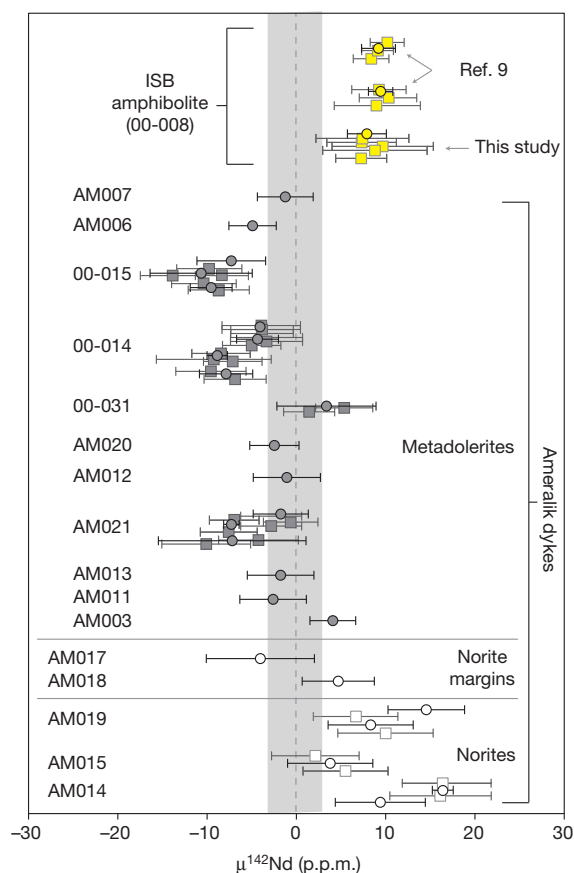


**Figure 2** |  $\mu^{142}\text{Nd}$  values measured for the Amlalik dykes. The  $^{142}\text{Nd}/^{144}\text{Nd}$  data are expressed in p.p.m. deviations ( $\mu^{142}\text{Nd}$ ) relative to the JNd-1 terrestrial standard. The shaded area represents the external analytical error of  $\pm 3$  p.p.m. ( $2\sigma$ ,  $n = 50$ ). The same sample dissolution was analysed one to five times and the different runs are shown by squares. Circles represent separate sample dissolutions and the averages of the different runs of the same dissolution. Errors are  $2\sigma$ . Sample 00-008 (3.7 Gyr-old ISB amphibolite) was analysed during the same analytical session and yielded a well-resolved  $^{142}\text{Nd}$  excess of  $+8.0 \pm 2.2$  p.p.m. ( $2\sigma$ ), identical within error to the data obtained previously on the same sample<sup>9</sup>. Samples AM021, 00-014 and 00-015 all have well resolved negative anomalies down to  $-10.6$  p.p.m., suggesting they have preserved the signature from an enriched Hadean source. All the  $^{142}\text{Nd}$  results are reported in Supplementary Table 5.

been contaminated during or after emplacement into their host gneisses. The best explanation for the contamination of the cumulate norites is via LREE-enriched fluid phases expelled from the surrounding gneisses (see Supplementary Information for more details). Furthermore, these contaminated samples (the noritic dykes) have resolvable  $^{142}\text{Nd}$  excesses (Fig. 2) and  $^{142}\text{Nd}/^{144}\text{Nd}$  ratios similar to the country rock (the host gneisses<sup>12</sup>). This suggests that the assimilation of fluids from the country rock has also modified the  $^{142}\text{Nd}/^{144}\text{Nd}$  ratio of the noritic samples. These results demonstrate that great care must be exercised in the use of the  $^{146}\text{Sm}$ – $^{142}\text{Nd}$  system, as  $^{142}\text{Nd}$  signatures can be inherited by contamination.

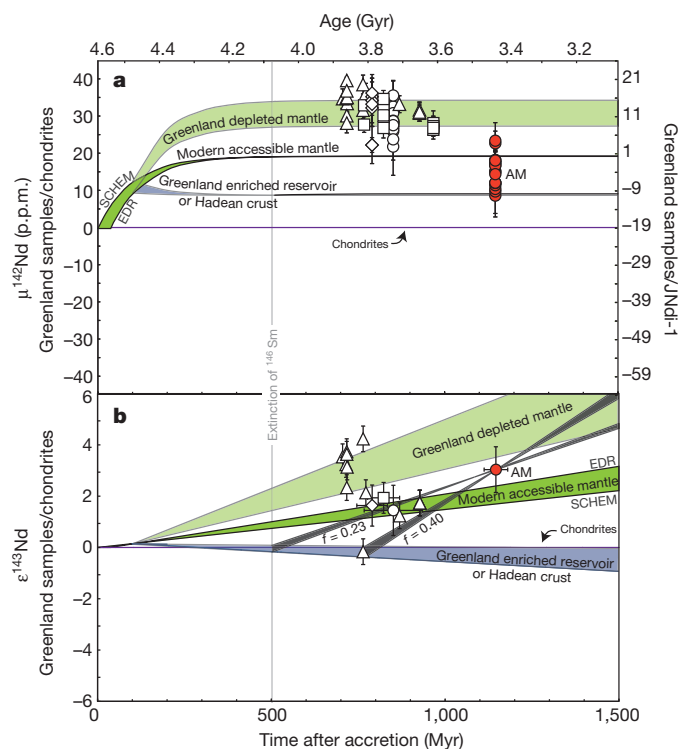


**Figure 3** | Evolution model of the Amlalik dyke reservoir. **a**, **b**, The  $\mu^{142}\text{Nd}$  (**a**) and  $\epsilon^{143}\text{Nd}$  (**b**) values of southwest Greenland samples versus time after accretion (Myr, bottom scale) and versus age (Gyr, top scale).  $\mu^{142}\text{Nd}$  and  $\epsilon^{143}\text{Nd}$  errors are  $2\sigma$ . **a**, The  $^{142}\text{Nd}/^{144}\text{Nd}$  data for the Amlalik dykes (this study, filled symbols labelled ‘AM’) and for all other southwest Greenland samples (open symbols: circles<sup>9</sup>, squares<sup>11</sup>, triangles<sup>12</sup> and diamonds<sup>13</sup>), expressed in p.p.m. deviations relative to the chondritic value (Supplementary Information) and to the JNd-1 terrestrial standard on the left and right scales, respectively. **b**, Initial  $^{143}\text{Nd}/^{144}\text{Nd}$  calculated from isochrons for data from refs 9, 11 and 13, and for each sample for data from ref. 12, using  $\lambda^{147}\text{Sm} = 0.654 \times 10^{-11}$  and CHUR values from ref. 30. Initial values of  $^{143}\text{Nd}/^{144}\text{Nd}$  are given in the  $\epsilon^{143}\text{Nd}$  notation relative to chondrites<sup>30</sup>. The chemical fractionation between Sm and Nd is expressed as the fractionation factor  $f_{\text{Sm}/\text{Nd}}$  (with  $f_{\text{Sm}/\text{Nd}} = \text{Sm}/\text{Nd}_{\text{reservoir}}/\text{Sm}/\text{Nd}_{\text{source}} - 1$ ; ref. 23). The Amlalik dykes show  $^{142}\text{Nd}$  deficits compared to the terrestrial Nd standard and modern terrestrial rocks. These samples, therefore, have preserved the signature of an enriched Hadean reservoir, which differentiated at  $\sim 4.47$  Gyr ago from the modern accessible mantle (both models SCHEM<sup>21</sup> or EDR<sup>22</sup> are represented, see Supplementary Information). The minimum enrichment value for the Hadean reservoir is  $\mu^{142}\text{Nd} = -10$  p.p.m. compared to JNd-1 in order to explain the most enriched Amlalik samples. This early-enriched component satisfies the characteristics for the complementary early-depleted Isua reservoir. To explain simultaneously the positive  $\epsilon^{143}\text{Nd}$  initial values of the Amlalik dykes, this component re-differentiated at  $\sim 770$  Myr ago at the latest, for a maximum  $f_{\text{Sm}/\text{Nd}}$  of  $+0.4$ . Shaded light green area represents the Greenland depleted mantle evolution. The dark green area represents the modern accessible mantle. The purple line represents the chondrites and the blue area represents the Greenland enriched reservoir or Hadean crust evolution.

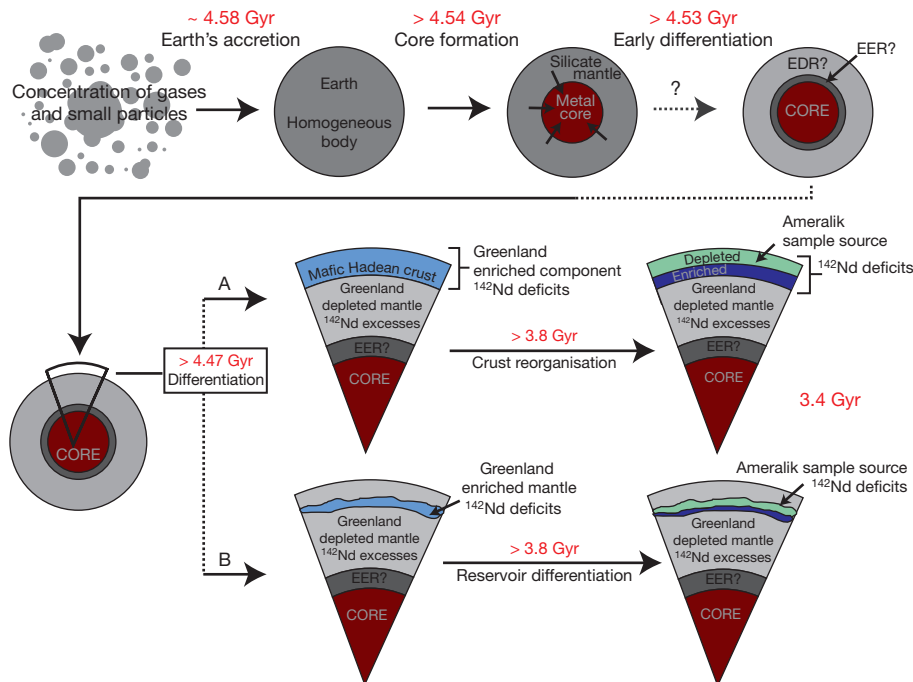


**Figure 4 | From the accretion of the Earth to the differentiation of the Amealik dyke source.** The Earth accreted from gases and particles  $\sim 4.58$  Gyr ago. The metallic core formed rapidly ( $>4.54$  Gyr ago) and separated from the silicates. Comparison with chondrites suggests that the Earth evolved since the beginning of the Solar System history (or a few tens of million years after) with a high Sm/Nd ratio. Therefore, Earth's primitive mantle could have undergone Sm/Nd differentiation  $>4.53$  Gyr ago leading to the formation of an early depleted reservoir (EDR) and a complementary early enriched reservoir (EER). The primitive mantle then underwent differentiation  $>4.47$  Gyr ago,

The  $^{147}\text{Sm}$ – $^{143}\text{Nd}$  whole-rock isochron age obtained for the metadolerites and the margins of the noritic dykes ( $3,403 \pm 250$  Myr ago) is indistinguishable from the mean  $^{207}\text{Pb}/^{206}\text{Pb}$  age recorded by zircons from the norites ( $3,421 \pm 34$  Myr ago; Supplementary Information). This age is also consistent with other noritic dyke age determinations<sup>18–20</sup> and confirms that the Amealik dyke swarm was emplaced at  $\sim 3.4$  Gyr ago. The initial  $\epsilon^{143}\text{Nd}$  of  $+3.0 \pm 0.9$  ( $2\sigma$ ,  $n = 14$ ) from the  $^{147}\text{Sm}$ – $^{143}\text{Nd}$  regression (mean squared weighted deviation MSWD = 2.4) indicates that the source of these dykes was suprachondritic. (Here  $\epsilon^{143}\text{Nd}(t) = \{[(^{143}\text{Nd}/^{144}\text{Nd})_{\text{sample}}(t)/(^{143}\text{Nd}/^{144}\text{Nd})_{\text{CHUR}}(t)] - 1\} \times 10^4$ , where  $t$  is the time of dyke emplacement.) The dyke swarm thus derived from a source depleted in incompatible elements and characterized by a high Sm/Nd ratio. Similar constraints could not be acquired with the Lu–Hf isotope system because the samples scatter significantly in  $^{176}\text{Lu}/^{177}\text{Hf}$ – $^{176}\text{Hf}/^{177}\text{Hf}$  space (MSWD = 21; Supplementary Information). This scatter, observed in Lu–Hf but not in Sm–Nd isotope space, could be due to  $\text{Lu}^{3+}$  being a rare earth element (REE), whereas  $\text{Hf}^{4+}$  is a high-field strength element, making it possible to fractionate Lu from Hf. In contrast,  $\text{Sm}^{3+}$  and  $\text{Nd}^{3+}$  are neighbouring REEs, making it particularly difficult to disturb these two elements independently of each other. Importantly, except for two samples, all the metadolerite dykes have  $^{142}\text{Nd}$  deficits compared to the terrestrial JNdi-1 Nd standard, with three samples showing resolvable  $^{142}\text{Nd}$  deficits down to  $-10.6$  p.p.m. (Fig. 2). These results were duplicated up to four times using different sample dissolution and digestion techniques (see Methods for more details).

The negative  $\mu^{142}\text{Nd}$  values ( $\mu^{142}\text{Nd} = \{[(^{142}\text{Nd}/^{144}\text{Nd})_{\text{sample}}/(^{142}\text{Nd}/^{144}\text{Nd})_{\text{chondrites or JNdi-1}}] - 1\} \times 10^6$ ) of the Amealik dykes are consistent with their derivation from an early-enriched component; however, their positive  $\epsilon^{143}\text{Nd}_{3.4\text{Gyr}}$  value ( $+3.0$ ) indicates that the source of these samples has experienced a multi-stage history. Any Sm/Nd fractionation event occurring after the complete decay of  $^{146}\text{Sm}$

producing the Greenland depleted mantle. The same differentiation event led to a complementary enriched reservoir. The Amealik dykes (southwest Greenland) recorded this enriched component, which must have differentiated before the extinction of  $^{146}\text{Sm}$  (which produced  $^{142}\text{Nd}$ ) and, hence, before  $\sim 500$  Myr ago. The most likely scenario is that this enriched component differentiated at  $>4.47$  Gyr ago and that it constitutes the complementary part to Greenland's depleted reservoir. The enriched component could have been either: a Hadean mafic protocrust (path A on the figure) or a mantle reservoir (path B). This component re-differentiated at the latest 3.8 Gyr ago.

will affect the  $^{147}\text{Sm}$ – $^{143}\text{Nd}$  system exclusively, hence resulting in the decoupling of the long-lived and short-lived Sm–Nd chronometers. Several models were tested, and the most likely scenario is presented in Fig. 3. This model is based on two assumptions. First, the enriched component identified in the source of the Amealik dykes was formed contemporaneously with the depleted Isua reservoir ( $>4.47$  Gyr ago<sup>9,11</sup>) and thus most probably is related to the crystallization of an early terrestrial magma ocean. This assumption is further consistent with the close geographic association of the Amealik dykes and the ISB rocks. Second, since the beginning of Solar System history (or a few tens of million years after) the terrestrial mantle evolved with a Sm/Nd ratio higher than that of chondrites. Such an evolution has been proposed to explain the difference in  $^{142}\text{Nd}$  composition between chondrites and terrestrial samples<sup>21,22</sup>.

The lowest  $^{142}\text{Nd}$  values in the Amealik dykes are consistent with the formation of an enriched component with an  $^{147}\text{Sm}/^{144}\text{Nd}$  ratio of 0.19. The formation of a reservoir with a higher  $^{147}\text{Sm}/^{144}\text{Nd}$  ratio would produce  $^{142}\text{Nd}$  deficits too small for what is observed in the Amealik dykes. The positive initial  $\epsilon^{143}\text{Nd}_{3.4\text{Gyr}}$  of the dykes indicates that their source underwent a second Sm/Nd differentiation event to produce a depleted reservoir. This later event occurred after the extinction of  $^{146}\text{Sm}$ , thus preserving the  $^{142}\text{Nd}$  deficits while the  $^{143}\text{Nd}$  isotopic compositions evolved with time to a positive  $\epsilon^{143}\text{Nd}$  value. This differentiation event therefore could not have taken place earlier than  $\sim 500$  Myr after Earth's accretion. However, the later this differentiation event occurred, the more depleted the newly formed reservoir must have been to evolve to  $\epsilon^{143}\text{Nd}$  of  $+3.0$  by 3.4 Gyr ago. The latest plausible time of re-differentiation is thus controlled by the maximum  $f_{\text{Sm/Nd}}$  possible,  $<0.40$  (ref. 25) ( $f_{\text{Sm/Nd}}$  is defined<sup>23</sup> as  $(\text{Sm}/\text{Nd}_{\text{reservoir}}/\text{Sm}/\text{Nd}_{\text{source}}) - 1$ ; Fig. 3). Using this maximum  $f_{\text{Sm/Nd}}$  value, the latest age of re-differentiation is constrained to  $\sim 670$  Myr after the formation of the early-enriched component (Fig. 3). Depletion of an earlier enriched

component by secondary processes has been previously proposed<sup>24</sup> in a scenario where a thick basaltic Hadean proto-crust (the enriched reservoir) would be thermally unstable, leading to partial melting at its base and leaving a depleted residue.

Partial melting after crystallization of a magma ocean could have formed the first mafic Hadean crust. However, our data cannot be accounted for if the crust formed after 4.3 Gyr ago. In such a scenario, the  $f_{\text{Sm}/\text{Nd}}$  needed to explain the lowest  $^{142}\text{Nd}/^{144}\text{Nd}$  ratios measured in the Ameralik dykes is  $-0.46$ , which is even more enriched than typical granitoids ( $f_{\text{Sm}/\text{Nd}} = -0.40$ ; ref. 23) (Supplementary Information). Alternatively, the Earth's primitive mantle could have undergone Sm/Nd differentiation  $>4.53$  Gyr ago leading to the formation of an early depleted reservoir (EDR) and a complementary early enriched reservoir (EER)<sup>21</sup> (Fig. 4). If the Earth started out with a chondritic  $^{142}\text{Nd}$  composition, mass balance constraints would require the EER to have  $\mu^{142}\text{Nd}$  in the range of  $-38$  to  $-54$  p.p.m. (ref. 26). The lack of samples with such characteristics indicates that the EER has never participated in crustal magmatism. Could the Ameralik sample source have differentiated from the EER? A depleted reservoir separating from an EER-like source before the extinction of  $^{146}\text{Sm}$  would evolve towards less negative  $\mu^{142}\text{Nd}$  values than the EER and positive initial  $\epsilon^{143}\text{Nd}$  values. This could fit the source for the Ameralik dykes. In order to produce a  $\sim 10$  p.p.m.  $^{142}\text{Nd}$  deficit at 3.4 Gyr ago, the latest possible time for the differentiation is  $\sim 100$  Myr after the first solids formed in the early Solar System (see Supplementary Information for more details). Although this scenario adequately explains the present data, it is highly unlikely that the Ameralik dykes sampled the EER. The  $^{142}\text{Nd}$  excess measured in all modern terrestrial samples relative to chondrites requires that the EER has not been remixed in the mantle. Moreover, the EER is probably located in the deep mantle, because mass balance calculations predict a reservoir larger than the size of the continental crust<sup>26</sup>.

The early-enriched component identified in this study satisfies the characteristics of the complementary early-depleted Isua reservoir. This early-enriched component has been missing since the first  $^{142}\text{Nd}$  results<sup>10</sup>. Our findings attest to the existence of either an enriched mantle reservoir or a proto-crust in the Hadean (Fig. 4). It is difficult to argue which of these two protoliths is the best candidate for the source of the Ameralik dykes. However, if the Ameralik source was an enriched mantle reservoir, it demonstrates that the southwest Greenland mantle preserved early-formed heterogeneities until at least 3.4 Gyr ago. This would imply re-mixing of heterogeneities at rates of the order of 1 Gyr, which are 10 times longer than previously estimated<sup>27,28</sup>, but in agreement with recent  $^{182}\text{W}$  findings<sup>29</sup>. Conversely, if the Ameralik source represents proto-crust isolated from mantle convection, it no longer places constraints on the secular survival of mantle heterogeneities, but instead suggests that the Early Archaean crust could preserve relicts formed in Hadean times.

## METHODS SUMMARY

The whole-rock samples were powdered and dissolved in high-pressure, steel-jacketed Parr Teflon bombs. REE and Hf fractions were separated from the bulk samples using ion-exchange columns. For the  $^{142}\text{Nd}$  analyses, Ce and most of the Sm, which together produce isobaric interferences on  $^{142}\text{Nd}$ ,  $^{144}\text{Nd}$ ,  $^{148}\text{Nd}$  and  $^{150}\text{Nd}$ , were eliminated through two consecutive passes on cation-exchange columns using 2-methylacetic acid (0.2 M and pH 4.7) as medium. The rest of the Sm was removed on an Ln-Spec column. Total Nd blanks were  $<60$  pg. The five samples showing resolvable  $^{142}\text{Nd}$  anomalies were dissolved up to four times using different digestion techniques (Savillex vials and high-pressure, steel-jacketed Parr Teflon bombs) and gave identical  $^{142}\text{Nd}$  results within the quoted errors.  $^{142}\text{Nd}$  isotope measurements were done as  $\text{Nd}^+$  using zone-refined double Re filaments. Isotopic analyses were performed using a dynamic routine where Faraday cups are centred successively on masses 145 and 143. The terrestrial Nd standard JNd-I was measured often, and the average long-term value for five analytical sessions gave  $1.141840 \pm 0.000003$  ( $2\sigma$ ,  $n = 50$ ) for  $^{142}\text{Nd}/^{144}\text{Nd}$ . The same dissolution of each Ameralik sample was analysed one to five times depending on the Nd concentrations. The external reproducibility on the  $^{142}\text{Nd}/^{144}\text{Nd}$  ratio was,

on average, better than 5 p.p.m., which is similar to the reproducibility obtained on repeated measurements of the terrestrial standard.  $^{142}\text{Ce}$  and  $^{144}\text{Sm}$  were never high enough to produce corrections higher than the precision obtained on the  $^{142}\text{Nd}/^{144}\text{Nd}$  ratio. Moreover, the measured  $^{142}\text{Nd}/^{144}\text{Nd}$  ratios are not correlated with the amounts of Ce or Sm. The Ameralik samples with  $^{142}\text{Nd}$  deficits do not exhibit negative  $^{148}\text{Nd}$  and  $^{150}\text{Nd}$  anomalies, which corroborate that their anomalous Nd isotopic compositions are not a consequence of mixing of variably depleted domains on the filament.

**Full Methods** and any associated references are available in the online version of the paper.

**Received 27 May; accepted 30 August 2012.**

- Boyett, M. *et al.*  $^{142}\text{Nd}$  evidence for early Earth differentiation. *Earth Planet. Sci. Lett.* **214**, 427–442 (2003).
- Caro, G., Bourdon, B., Birk, J. L. & Moorbath, S. High precision  $^{142}\text{Nd}/^{144}\text{Nd}$  measurements in terrestrial rocks: constraints on the early differentiation of the Earth's mantle. *Geochim. Cosmochim. Acta* **70**, 164–191 (2006).
- Andreasen, R., Sharma, M., Subbarao, K. V. & Viladkar, S. G. Where on Earth is the enriched Hadean reservoir? *Earth Planet. Sci. Lett.* **266**, 14–28 (2008).
- Upadhyay, D., Scherer, E. & Mezger, K.  $^{142}\text{Nd}$  evidence for an enriched Hadean reservoir in cratonic roots. *Nature* **459**, 1118–1121 (2009).
- Murphy, D. T. *et al.* In search of a hidden long-term isolated sub-chondritic  $^{142}\text{Nd}/^{144}\text{Nd}$  reservoir in the deep mantle: implications for the Nd isotope systematics of the Earth. *Geochim. Cosmochim. Acta* **74**, 738–750 (2010).
- Cipriani, A., Bonatti, E. & Carlson, R. W. Non-chondritic  $^{142}\text{Nd}$  in sub-oceanic mantle peridotites. *Geochim. Geophys. Res.* **12**, 1–8 (2011).
- Jackson, M. G. & Carlson, R. W. Homogeneous superchondritic  $^{142}\text{Nd}/^{144}\text{Nd}$  in the mid-ocean ridge basalt and ocean island basalt mantle. *Geochim. Geophys. Res.* **13**, 1–10 (2012).
- Kinoshita, N. *et al.* A shorter  $^{146}\text{Sm}$  half-life measured and implications for  $^{146}\text{Sm}$ – $^{142}\text{Nd}$  chronology in the Solar System. *Science* **335**, 1614–1617 (2012).
- Rizo, H., Boyett, M., Blichert-Toft, J. & Rosing, M. Combined Nd and Hf isotope evidence for deep-seated source of Isua lavas. *Earth Planet. Sci. Lett.* **312**, 267–279 (2011).
- Harper, C. L. & Jacobsen, S. B. Evidence from coupled  $^{147}\text{Sm}$ – $^{143}\text{Nd}$  and  $^{146}\text{Sm}$ – $^{142}\text{Nd}$  systematics for very early (4.5-Gyr) differentiation of the Earth's mantle. *Nature* **360**, 728–732 (1992).
- Caro, G., Bourdon, B., Birk, J.-L. & Moorbath, S.  $^{146}\text{Sm}$ – $^{142}\text{Nd}$  evidence from Isua metamorphosed sediments for early differentiation of the Earth's mantle. *Nature* **423**, 428–432 (2003).
- Bennett, V. C., Brandon, A. D. & Nutman, A. P. Coupled  $^{142}\text{Nd}$ – $^{143}\text{Nd}$  isotopic evidence for Hadean mantle dynamics. *Science* **318**, 1907–1910 (2007).
- Boyett, M. & Carlson, R. W. A new geochemical model for the Earth's mantle inferred from  $^{146}\text{Sm}$ – $^{142}\text{Nd}$  systematics. *Earth Planet. Sci. Lett.* **250**, 254–268 (2006).
- Blichert-Toft, J. & Puchtel, I. S. Depleted mantle sources through time: evidence from Lu–Hf and Sm–Nd isotope systematics of Archean komatiites. *Earth Planet. Sci. Lett.* **297**, 598–606 (2010).
- Blichert-Toft, J. & Albarède, F. Hafnium isotopes in Jack Hills zircons and the formation of the Hadean crust. *Earth Planet. Sci. Lett.* **265**, 686–702 (2008).
- Kemp, A. I. S. *et al.* Hadean crustal evolution revisited: new constraints for Pb–Hf isotope systematics of the Jack Hills zircons. *Earth Planet. Sci. Lett.* **296**, 45–56 (2010).
- O'Neill, J., Carlson, R. W., Francis, D. & Stevenson, R. K. Neodymium-142 evidence for Hadean mafic crust. *Science* **321**, 1828–1831 (2008).
- Gill, C. O. & Bridgwater, D. The Ameralik dykes of west Greenland, the earliest known basaltic rocks intruding stable continental crust. *Earth Planet. Sci. Lett.* **29**, 276–282 (1976).
- Nielsen, S. G., Baker, A. J. & Krogstad, E. J. Petrogenesis of an early Archean (3.4 Ga) norite dyke, Isua, West Greenland: evidence for early Archean crustal recycling? *Precamb. Res.* **118**, 133–148 (2002).
- Nutman, A. P., Friend, C. R. L., Bennett, V. C. & McGregor, V. R. Dating of Ameralik dike swarms of the Nuuk district, southern West Greenland: mafic intrusion events starting from 3510 Ma. *J. Geol. Soc. Lond.* **161**, 421–430 (2004).
- Boyett, M. & Carlson, R. W.  $^{142}\text{Nd}$  evidence for early ( $>4.53$  Ga) global differentiation of the silicate Earth. *Science* **309**, 576–581 (2005).
- Caro, G. & Bourdon, B. Non-chondritic Sm/Nd ratio in the terrestrial planets: consequences for the geochemical evolution for the mantle-crust system. *Geochim. Cosmochim. Acta* **74**, 3333–3349 (2010).
- DePaolo, D. J. In *Neodymium Isotope Geochemistry. An Introduction* 36 (Minerals and Rocks Series no. 20, Springer, 1988).
- Kamber, B. S., Collerson, K. D., Moorbath, S. & Whitehouse, M. J. Inheritance of early Archean Pb-isotope variability from long-lived Hadean protocrust. *Contrib. Mineral. Petrol.* **145**, 25–46 (2003).
- Bennett, V. C., Nutman, A. P. & McCulloch, M. T. Nd isotopic evidence for transient, highly depleted mantle reservoirs in the early history of the Earth. *Earth Planet. Sci. Lett.* **119**, 299–317 (1993).
- Carlson, R. W. & Boyett, M. Composition of the Earth's interior: the importance of early events. *Phil. Trans. R. Soc. A* **366**, 4077–4103 (2008).
- Blichert-Toft, J. & Albarède, F. Short-lived chemical heterogeneities in the Archean mantle with implications for mantle convection. *Science* **263**, 1593–1596 (1994).
- Coltice, C. & Schmaltz, J. Mixing time in the mantle of the early Earth derived from 2-D and 3-D numerical simulations of convection. *Geophys. Res. Lett.* **33**, L23304 (2006).

29. Touboul, M., Puchtel, I. S. & Walker, R. J.  $^{182}\text{W}$  Evidence for long-term preservation of Early mantle differentiation products. *Science* **335**, 1065–1069 (2012).
30. Bouvier, A., Vervoort, J. D. & Patchett, P. J. The Lu–Hf and Sm–Nd isotopic composition of CHUR: constraints from unequilibrated chondrites and implications for the bulk composition of terrestrial planets. *Earth Planet. Sci. Lett.* **273**, 48–57 (2008).

**Supplementary Information** is available in the online version of the paper.

**Acknowledgements** We thank C. Bosq for providing clean-laboratory facilities, D. Auclair for assistance with the TIMS, P. Télouk for assistance with the MC-ICP-MS, and J. L. Devidal for assistance with the Microprobe and the LA-ICP-MS. M. Benbakkar carried out the major element analyses. We thank A. Brandon and M. Jackson for comments that helped clarify the manuscript. We thank the Geological Survey of Japan for providing the isotopic standard JNdi-1. The research leading to these results has received funding from the European Research Council under the European Community's Seventh Framework Programme (to M.B.), the French Programme

National de Planétologie of the Institut National des Sciences de l'Univers and Centre National d'Etudes Spatiales, and the French Agence Nationale de la Recherche (grants BEGDy and M&Ms) (to J.B.T.), and the French embassy in Denmark (to M.R.). This is Laboratory of Excellence ClerVolc contribution no. 30.

**Author Contributions** Samples from the Ameralik dykes were collected by H.R., M.B., J.O'N. and M.T.R. U–Pb analyses were carried out by J.-L.P. Preparation of samples, dissolution, spike calculations, chemical separation of Sm, Nd, Lu, and Hf and isotopic analyses and modelling of data were carried out by J.B.-T., H.R. and M.B. Manuscript preparation was carried out by H.R., M.B., J.O'N. and J.B.-T., and all the authors contributed to discussing the results and their implications.

**Author Information** Reprints and permissions information is available at [www.nature.com/reprints](http://www.nature.com/reprints). The authors declare no competing financial interests. Readers are welcome to comment on the online version of the paper. Correspondence and requests for materials should be addressed to H.R. ([h.rizo@opgc.univ-bpclermont.fr](mailto:h.rizo@opgc.univ-bpclermont.fr)).

## METHODS

**Major and trace elements.** Major and trace elements were determined by ICP-AES (Jobin-Yvon ULTIMA C) and ICP-MS (Agilent 7500), respectively, at the Laboratoire Magmas et Volcans (LMV) in Clermont-Ferrand. Totals of major element oxides were  $99.6 \pm 0.5$  wt%. The rock standards BHVO-2 and BIR were measured frequently and used to estimate the accuracy, which were  $\sim 1\%$  for major elements,  $< 8\%$  for minor elements ( $\text{TiO}_2$ ,  $\text{MnO}$  and  $\text{P}_2\text{O}_5$ ), and 1–10% for trace elements. Analytical precisions were better than 1% for major and minor elements, and better than 15% for trace elements.

**U–Pb systematics.** U–Pb dating was done on polished petrographic thin sections on zircon, baddeleyite and monazite micro-crystals. The minerals were located and referenced using electron microprobe (EMPA). U–Pb isotopic data for the zircons were obtained by laser ablation inductively coupled plasma spectrometry (LA-ICPMS). The analyses involved the ablation of minerals with a Resonetics Resolution M-50 powered by an ultra-short-pulse ( $< 4$  ns) ATL Atlas Excimer laser system operating at a wavelength of 193 nm (for a detailed description, see ref. 31). Spot diameters of 10  $\mu\text{m}$ , associated with repetition rates of 3 Hz and laser energy of 4 mJ producing a fluence of  $9.5 \text{ J cm}^{-2}$ , were used for dating. The ablated material was carried into helium and then mixed with nitrogen and argon before injection into the plasma source of an Agilent 7500 cs ICP-MS equipped with a dual pumping system to enhance sensitivity. Alignment of the instrument and mass calibration were carried out before each analytical session using the NIST SRM 612 reference glass and inspecting the signal of  $^{238}\text{U}$  and minimizing the  $\text{ThO}^+/\text{Th}^+$  ratio ( $< 1\%$ ). The mean sensitivity on  $^{238}\text{U}$  using a spot size of 44  $\mu\text{m}$  was about 30,000 counts per second per p.p.m. The analytical method for isotope dating of zircon with laser ablation ICPMS is similar to that developed for zircon and monazite<sup>32,33</sup>. The signals of the  $^{204}(\text{Pb} + \text{Hg})$ ,  $^{206}\text{Pb}$ ,  $^{207}\text{Pb}$ ,  $^{208}\text{Pb}$ ,  $^{232}\text{Th}$  and  $^{238}\text{U}$  masses were all acquired. The potential occurrence of common Pb in the samples is monitored by the evolution of the  $^{204}(\text{Pb} + \text{Hg})$  signal intensity, but no common Pb correction was applied owing to the large isobaric interference from Hg. The  $^{235}\text{U}$  signal was calculated from  $^{238}\text{U}$  on the basis of the ratio  $^{238}\text{U}/^{235}\text{U} = 137.88$ . Single analyses consisted of 30 s of background integration with the laser off followed by one-minute integration with the laser firing and a 30 s delay to wash out the previous sample and prepare for the next analysis.

The data were corrected for U–Pb fractionation during laser sampling and for instrumental mass discrimination (mass bias) by standard bracketing with repeated measurements of the GJ-1 zircon standard<sup>34</sup>. Repeated analyses of the 91500 zircon standard<sup>35</sup>, treated as an unknown, independently controlled the reproducibility and accuracy of the corrections. Data reduction was carried out with the software package GLITTER from Macquarie Research<sup>36,37</sup>. For each analysis, the time-resolved signal of single isotopes and isotope ratios was monitored and carefully inspected to verify the presence of perturbations related to inclusions, fractures, mixing of different age domains, or common Pb. Calculated ratios were exported and Concordia ages and diagrams were generated using the Isoplot/Ex v. 2.49 software package<sup>37</sup>. The concentrations of U, Th and Pb were calibrated relative to the certified contents of the GJ-1 zircon standard<sup>35</sup>.

The reverse discordant behaviour of baddeleyite is commonly observed in *in situ* analyses using nanosecond laser ablation. It may be attributed partly to U and/or Pb heterogeneities at a small scale and principally to an incomplete instrumental correction of elemental fractionation based on zircon standards<sup>38,39</sup>. For nanosecond lasers, this matrix matching correction of the elemental fractionation is strongly dependant of the different behaviour of baddeleyite ( $\text{ZrO}_2$ ) versus zircon ( $\text{ZrSiO}_4$ ) mineral lattices under a laser beam. This produces an analytical artefact, which fortunately does not compromise the intercept age observed<sup>38</sup>. This is confirmed by U–Pb replicates of the Phalaborwa baddeleyite producing sub-concordant points with an intercept age of  $2,059 \pm 3$  Myr and reverse discordant points with an upper intercept age of  $2,076 \pm 18$  Myr in using 33- $\mu\text{m}$  and 15- $\mu\text{m}$ -wide laser spots, respectively (Supplementary Fig. 9). Both results agree well with published ID-TIMS data at  $2,059.8 \pm 0.8$  Myr (ref. 40).

**Combined  $^{147}\text{Sm}$ – $^{143}\text{Nd}$  and  $^{176}\text{Lu}$ – $^{176}\text{Hf}$ .** Sm–Nd and Lu–Hf isotope measurements were carried out on the same sample dissolutions to minimize potential uncertainties arising from sample powder heterogeneity. Mixed  $^{176}\text{Lu}$ – $^{180}\text{Hf}$  tracer was added to the sample powders ( $\sim 400$  mg) at the outset of the digestion procedure. The sample dissolution and sample-spike equilibration were achieved in high-pressure, steel-jacketed Teflon Parr bombs with a 10:1 mixture of concentrated distilled  $\text{HF}:\text{HNO}_3$ . The Teflon bombs and metal jacket assemblies were placed in an oven at  $160^\circ\text{C}$  for one week. The Teflon vessels were then opened and their contents evaporated to dryness. The dried samples were fumed with  $\text{HClO}_4$  to expel fluorides after which 6 M  $\text{HCl}$  was added and the bombs replaced in the oven for another three days at  $160^\circ\text{C}$ . After this step, the solutions were perfectly clear indicating complete dissolution of the samples and, hence, complete sample-spike homogenization.

To measure the  $^{147}\text{Sm}$ – $^{143}\text{Nd}$  compositions, aliquots equivalent to 10% of each sample solution were taken and spiked with  $^{149}\text{Sm}$ – $^{150}\text{Nd}$  tracer. After evaporation to dryness, equilibration between the sample aliquots and the  $^{149}\text{Sm}$ – $^{150}\text{Nd}$  spike was achieved by adding concentrated distilled  $\text{HNO}_3$  to the mixtures and leaving them in closed Savillex vials on a hotplate for 12 h. From these spiked aliquots the Sm and Nd fractions were separated using the method of ref. 41, which consists of a cation-exchange column, followed by a TRU-Spec column and then an Ln-Spec column. Hafnium and REE fractions were separated from the 90% left after removal of the  $^{147}\text{Sm}$ – $^{143}\text{Nd}$  aliquot using cation-exchange columns. The Hf was subsequently purified first through an anion-exchange column to remove any remaining matrix elements, then through a cation-exchange column to remove Ti. From the REE fraction, Nd (for  $^{142}\text{Nd}$  analyses) and Lu were separated on Ln-Spec columns. Cerium and most of the Sm, which together produce isobaric interferences on  $^{142}\text{Nd}$ ,  $^{144}\text{Nd}$ ,  $^{148}\text{Nd}$  and  $^{150}\text{Nd}$ , were eliminated through two consecutive passes on cation-exchange columns using 2-methylactic acid (0.2 M and  $\text{pH} = 4.7$ ) as medium. The rest of the Sm was removed on an Ln-Spec column. Total Lu, Hf, Sm and Nd blanks were  $< 20$ ,  $< 20$ ,  $< 20$  and  $< 60$  pg, respectively.

The  $^{176}\text{Lu}$ – $^{176}\text{Hf}$  analyses were carried out on the Nu Plasma multi-collector inductively-coupled plasma mass spectrometer (MC-ICPMS) at the Ecole Normale Supérieure de Lyon following the procedures of ref. 42. Instrumental mass bias effects on Hf were corrected using an exponential law and a value for  $^{179}\text{Hf}/^{177}\text{Hf}$  of 0.7325. In order to monitor machine performance, the JMC-475 Hf standard was run systematically every two or three samples and gave  $0.282157 \pm 0.000009$  for  $^{176}\text{Hf}/^{177}\text{Hf}$  during the present analytical session. Since this value is in agreement, within error, with the value of  $0.282163 \pm 0.000009$  of ref. 42, no correction has been applied to the measured sample isotopic compositions. Initial  $\epsilon^{176}\text{Hf}$  values ( $\epsilon^{176}\text{Hf} = (^{176}\text{Hf}/^{177}\text{Hf})_{\text{sample}} / (^{176}\text{Hf}/^{177}\text{Hf})_{\text{CHUR}} - 1$ )  $\times 10^4$ ) were calculated with the CHUR values of ref. 43. The  $^{176}\text{Lu}/^{176}\text{Hf}$  ratio was determined by isotope dilution and Lu was measured following the procedure described in ref. 44.

The  $^{147}\text{Sm}$ – $^{143}\text{Nd}$  and  $^{142}\text{Nd}$  measurements were carried out on the LMV on a Thermo Fisher Triton thermal-ionization mass spectrometer (TIMS). Neodymium isotope ratios were corrected for mass fractionation using an exponential law and  $^{146}\text{Nd}/^{144}\text{Nd} = 0.7219$ . The  $^{147}\text{Sm}/^{144}\text{Nd}$  ratio was determined by isotope dilution. The JNdi-1 Nd standard gave, during this study,  $0.512107 \pm 0.000007$  for  $^{143}\text{Nd}/^{144}\text{Nd}$ . Since this value is in agreement, within error, with the value of  $0.512115 \pm 0.000007$  published in ref. 45, no correction has been applied to the measured sample isotopic compositions. Initial  $\epsilon^{143}\text{Nd}$  values ( $\epsilon^{143}\text{Nd} = (^{143}\text{Nd}/^{144}\text{Nd})_{\text{sample}} / (^{143}\text{Nd}/^{144}\text{Nd})_{\text{CHUR}} - 1$ )  $\times 10^4$ ) were calculated with the CHUR values of ref. 43.

$^{142}\text{Nd}$  isotope measurements were done as  $\text{Nd}^+$  using zone-refined double Re filaments. Each measurement corresponds to 27 blocks of 20 ratios each (8 s integration time) using amplifier rotation. Measurements were performed in two lines, using a dynamic routine where Faraday cups are centred successively on masses 145 and 143 (axial cups). On the second line, zoom optics were applied to centre the isotope mass peaks in the cups ( $-0.5$  V for focus quad and  $8.5$  V for dispersion quad). The terrestrial Nd standard JNdi-1 was measured often and the average long-term value for the five analytical sessions gave  $1.141840 \pm 0.000003$  ( $2\sigma$ ,  $n = 50$ ) for  $^{142}\text{Nd}/^{144}\text{Nd}$ . This error is equivalent to the reproducibility obtained for JNdi-1 measured in each analytical session, which was better than 5 p.p.m. ( $2\sigma$ ,  $n = 6$ –16) (see Supplementary Table 5).

For the  $^{142}\text{Nd}$  measurements, five samples (AM014, AM019, AM021, 00-014 and 00-015) were dissolved up to four times using different digestion techniques (Savillex vials and high-pressure, steel-jacketed Teflon Parr bombs). The measured  $^{142}\text{Nd}/^{144}\text{Nd}$  ratios for these different experiments were identical within error bars (see Fig. 2 in the main text and Supplementary Table 5). The same dissolution of each Ameralik sample was analysed one to five times depending on the Nd concentrations. The external reproducibility on the  $^{142}\text{Nd}/^{144}\text{Nd}$  ratio was, on average, better than 5 p.p.m., which is similar to the reproducibility obtained on repeated measurements of the terrestrial standard. Disregarding samples AM017 and 00-014a,  $^{142}\text{Ce}$  and  $^{144}\text{Sm}$  were never abundant enough to produce corrections higher than the precision obtained on the  $^{142}\text{Nd}/^{144}\text{Nd}$  ratio. Moreover, the measured  $^{142}\text{Nd}/^{144}\text{Nd}$  ratios do not correlate with the amount of Ce and Sm (Supplementary Information, Supplementary Fig. 10).

The ISB amphibolite sample 00-008 previously measured with a  $^{142}\text{Nd}$  excess<sup>46</sup> has been re-analysed in this study and yielded a  $^{142}\text{Nd}$  excess of  $+8.0 \pm 2.2$  p.p.m. ( $2\sigma$ ,  $n = 5$ ). This is identical, within error, to the values of  $+9.4 \pm 1.4$  ( $2\sigma$ ,  $n = 3$ ) and  $+9.2 \pm 1.4$  ( $2\sigma$ ,  $n = 3$ ) obtained by Ref.<sup>46</sup>.

Ameralik samples having  $^{142}\text{Nd}$  deficits do not exhibit negative  $^{148}\text{Nd}$  and  $^{150}\text{Nd}$  anomalies (Supplementary Information, Supplementary Figs 11 and 12),

which confirm that their anomalous Nd isotopic compositions are not a consequence of mixing of variably depleted domains on the filament<sup>47</sup>.

31. Müller, W., Shelley, M., Miller, P. & Broude, S. Initial performance metrics of a new custom-designed ArF excimer LA-ICPMS system coupled to a two-volume laser-ablation cell. *J. Anal. At. Spectrom.* **24**, 209–214 (2009).
32. Tiepolo, M. In situ Pb geochronology of zircon with laser ablation-inductively coupled plasma-sector field mass spectrometry. *Chem. Geol.* **141**, 1–19 (2003).
33. Paquette, J. L. & Tiepolo, M. High-resolution (5 µm) U-Th-Pb isotopes dating of monazite with excimer laser ablation (ELA)-ICPMS. *Chem. Geol.* **240**, 222–237 (2007).
34. Jackson, S. E., Pearson, N. J., Griffin, W. L. & Belousova, E. A. The application of laser ablation-inductively coupled plasma-mass spectrometry to in situ U–Pb zircon geochronology. *Chem. Geol.* **211**, 47–69 (2004).
35. Wiedenbeck, M. *et al.* Three natural zircon standards for U-Th-Pb, Lu-Hf, trace element and REE analyses. *Geostand. Newsl.* **19**, 1–23 (1995).
36. van Achtenberg, E., Ryan, C. G., Jackson, S. E. & Griffin, W. L. Laser ablation-ICPMS in the earth science. *Mineral. Assoc. Can.* **29**, 239–243 (2001).
37. Ludwig, K. R. *User's Manual for Isoplot/Ex Version 2.49, a Geochronological Toolkit for Microsoft Excel* (Berkeley Geochronological Center, 2001).
38. Horn, I., Rudnick, R. L. & McDonough, W. F. Precise elemental and isotope ratio determination by simultaneous solution nebulization and laser ablation-ICP-MS: application to U-Pb geochronology. *Chem. Geol.* **164**, 281–301 (2000).
39. Horn, I. & von Blanckenburg, F. Investigation of elemental and isotopic fractionation during 196 nm femtosecond laser ablation multiple collector inductively coupled plasma mass spectrometry. *Spectrochim. Acta B* **62**, 410–422 (2007).
40. Heaman, L. M. & LeCheminant, A. M. Paragenesis and U-Pb systematics of baddeleyite (ZrO<sub>2</sub>). *Chem. Geol.* **110**, 95–126 (1993).
41. Pin, C. & Santos Zalduegui, J. F. Sequential separation of light rare-earth elements, thorium and uranium by miniaturized extraction chromatography: application to isotopic analyses of silicate rocks. *Anal. Chim. Acta* **339**, 79–89 (1997).
42. Blichert-Toft, J., Chauvel, C. & Albarède, F. Separation of Hf and Lu for high-precision isotope analysis of rock samples by magnetic sector-multiple collector ICP-MS. *Contrib. Mineral. Petrol.* **127**, 248–260 (1997).
43. Bouvier, A., Vervoort, J. D. & Patchett, P. J. The Lu-Hf and Sm-Nd isotopic composition of CHUR: constraints from unequilibrated chondrites and implications for the bulk composition of terrestrial planets. *Earth Planet. Sci. Lett.* **273**, 48–57 (2008).
44. Blichert-Toft, J., Boyet, M., Télouk, P. & Albarède, F. <sup>147</sup>Sm/<sup>143</sup>Nd and <sup>176</sup>Lu/<sup>176</sup>Hf in eucrites and the differentiation of the HED parent body. *Earth Planet. Sci. Lett.* **204**, 167–181 (2002).
45. Tanaka, T. *et al.* JNdi-1: a neodymium isotopic reference in consistency with La Jolla neodymium. *Chem. Geol.* **168**, 279–281 (2000).
46. Rizo, H., Boyet, M., Blichert-Toft, J. & Rosing, M. Combined Nd and Hf isotope evidence for deep-seated source of Isua lavas. *Earth Planet. Sci. Lett.* **312**, 267–279 (2011).
47. Andreasen, R. & Sharma, M. Fractionation and mixing in a thermal ionization mass spectrometer source: implications and limitations for high-precision Nd isotope analyses. *Int. J. Mass Spectrom.* **285**, 49–57 (2009).

# Fault healing promotes high-frequency earthquakes in laboratory experiments and on natural faults

Gregory C. McLaskey<sup>1†</sup>, Amanda M. Thomas<sup>2</sup>, Steven D. Glaser<sup>1</sup> & Robert M. Nadeau<sup>2</sup>

**Faults strengthen or heal with time in stationary contact<sup>1,2</sup>, and this healing may be an essential ingredient for the generation of earthquakes<sup>1–3</sup>. In the laboratory, healing is thought to be the result of thermally activated mechanisms that weld together micrometre-sized asperity contacts on the fault surface, but the relationship between laboratory measures of fault healing and the seismically observable properties of earthquakes is at present not well defined. Here we report on laboratory experiments and seismological observations that show how the spectral properties of earthquakes vary as a function of fault healing time. In the laboratory, we find that increased healing causes a disproportionately large amount of high-frequency seismic radiation to be produced during fault rupture. We observe a similar connection between earthquake spectra and recurrence time for repeating earthquake sequences on natural faults. Healing rates depend on pressure, temperature<sup>4</sup> and mineralogy<sup>1</sup>, so the connection between seismicity and healing may help to explain recent observations of large megathrust earthquakes which indicate that energetic, high-frequency seismic radiation originates from locations that are distinct from the geodetically inferred locations of large-amplitude fault slip<sup>5–7</sup>.**

In laboratory measurements, static-fault frictional strength,  $\mu_s$ , is generally observed to increase linearly with the logarithm of time in stationary contact,  $t_{\text{hold}}$ , according to

$$\mu_s(t_{\text{hold}}) = \alpha_s + \beta_s \log_{10}(t_{\text{hold}}) \quad (1)$$

where  $\beta_s$  is the healing rate and  $\alpha_s$  is the fault strength at time  $t_{\text{hold}} = 1$  s (refs 1–4, 8). These measurements are used to derive rate- and state-dependent friction laws<sup>2,3</sup> that have provided insight into fault behaviour ranging from slow slip to dynamic rupture<sup>2,8–10</sup>. Healing rates have also been inferred from repeating earthquake sequences<sup>10–12</sup> (REs). These are sets of events with nearly identical waveforms, locations and magnitudes, and are thought to represent the repeated rupture of a patch of fault that is slowly loaded by aseismic slip of the surrounding material. Here we consider the stick-slip behaviour of a laboratory fault as a proxy for such a fault patch and compare our results with observations of REs on the San Andreas fault. In addition to measuring static friction, slip and stress drop, we record the stress waves emitted during the rupture of the laboratory fault, which we call laboratory earthquakes (LabEQs). This facilitates a link between friction properties observed in the laboratory and earthquakes produced on natural faults.

Fault healing is typically attributed to an increase in either the area or the strength of asperity contacts due to ‘creep’<sup>2,3</sup>. Mechanisms may include stress-induced diffusion, dislocation motion, chemically aided slow crack growth, dissolution–precipitation processes and other thermally activated processes<sup>2,3,13–15</sup>. Although specific mechanisms may differ, the overall effects of healing are remarkably similar. Equation (1) is applicable to rocks<sup>1</sup>, metals<sup>16</sup>, plastics<sup>4</sup> and paper<sup>17</sup>, which suggests that the mechanics of healing are not greatly dependent on specific chemical or physical properties, but rely on universally observed

surface properties such as multiscale roughness. A better understanding of the relationship between fault healing and earthquake generation may be the key to understanding the physics of earthquakes<sup>18</sup>.

We use test blocks composed of the glassy polymer poly(methyl methacrylate) (PMMA). This and similar glassy polymers are commonly used as model materials for fault rupture and friction studies<sup>2,4,19,20</sup>. Friction on PMMA–PMMA interfaces obeys equation (1) and is well modelled by the rate- and state-dependent friction laws<sup>2,4</sup>. Because of PMMA’s low hardness and melting temperature ( $\sim 160^\circ\text{C}$ ), the behaviour of PMMA–PMMA interfaces at room temperature and modest stress levels (100 kPa) may be somewhat representative of the behaviour of rocks at depth<sup>20</sup>. The similarities and differences between plastic and rock may serve as important points of comparison when studying the range of friction properties expected in the brittle–ductile spectrum of crustal deformation behaviour.

Stick-slip experiments are conducted at room temperature ( $20^\circ\text{C}$ ) and humidity (30% relative humidity) on a direct-shear apparatus consisting of a PMMA slider block (181 mm long, 60 mm wide, 17 mm high) and a larger PMMA base plate (450 mm long, 300 mm wide, 36 mm high) (Fig. 1a, inset). With the normal force,  $F_N$ , held constant, the shear force,  $F_s$ , is increased until the sample undergoes a series of stick-slip instabilities, denoted events. The recurrence time,  $t_r$ , defined as the time since the previous event, is computed for each pair of consecutive events in the sequence. (Despite subtle differences between them<sup>21</sup>, we assume that  $t_r = t_{\text{hold}}$ .) Each event produces a LabEQ, which is recorded with piezoelectric sensors attached to the PMMA base plate. The slider block slips 50–200  $\mu\text{m}$  during each event. Some slow premonitory slip ( $\sim 2 \mu\text{m}$ ) is often detected 1–2 ms before rapid slip commences. We detect no slip between events (to the  $\sim 1 \mu\text{m}$  noise level). The duration of slip for each event is approximately constant (8 ms) and is probably controlled by the combined stiffness of the apparatus and samples rather than fault rupture properties.

Load point displacement,  $x_{\text{LP}}$ , is controlled by turning a fine-threaded screw that presses against the trailing edge of the slider block. When the load point velocity,  $v_{\text{LP}} = dx_{\text{LP}}/dt$ , is systematically increased or decreased, large variations in  $t_r$  can be achieved in a single experimental run, while other experimental variables ( $F_N$ , surface conditions and so on) are kept constant. Typical results are shown in Fig. 1. To isolate cumulative wear and loading-rate effects, experimental runs were conducted in pairs: one with increasing  $v_{\text{LP}}$  (Fig. 1a) and one with decreasing  $v_{\text{LP}}$  (Fig. 1b). For every event in each stick-slip sequence, we measure  $F_{\text{max}}$  and  $F_{\text{min}}$  (Fig. 1) and calculate the stress drop  $\Delta\tau = (F_{\text{max}} - F_{\text{min}})/A$ , where  $A$  is the nominal fault area ( $0.0109 \text{ m}^2$ ). These parameters are plotted against  $\log_{10}(t_r)$  (Fig. 1b, inset, and Supplementary Figs 2–4). Slopes,  $\beta$ , and intercepts,  $\alpha$ , of the best-fit lines are reported in Supplementary Table 1. All tests show results consistent with equation (1) and previous work<sup>1,3,4,8</sup>. The increase in  $\Delta\tau$  with increasing  $t_r$  is due to both an increase in  $F_{\text{max}}$  and a decrease in  $F_{\text{min}}$  with  $\log_{10}(t_r)$  (refs 8, 21). In all cases, healing rates,  $\beta$ , are slightly larger for runs with decreasing  $v_{\text{LP}}$  than for runs with increasing  $v_{\text{LP}}$ , indicating a dependence on loading rate or stress time history.

<sup>1</sup>Department of Civil and Environmental Engineering, University of California, Berkeley, California 94720, USA. <sup>2</sup>Department of Earth and Planetary Science, Berkeley Seismological Laboratory, University of California, Berkeley, California 94720, USA. <sup>†</sup>Present address: United States Geological Survey, 345 Middlefield Road, MS 977, Menlo Park, California 94025, USA.

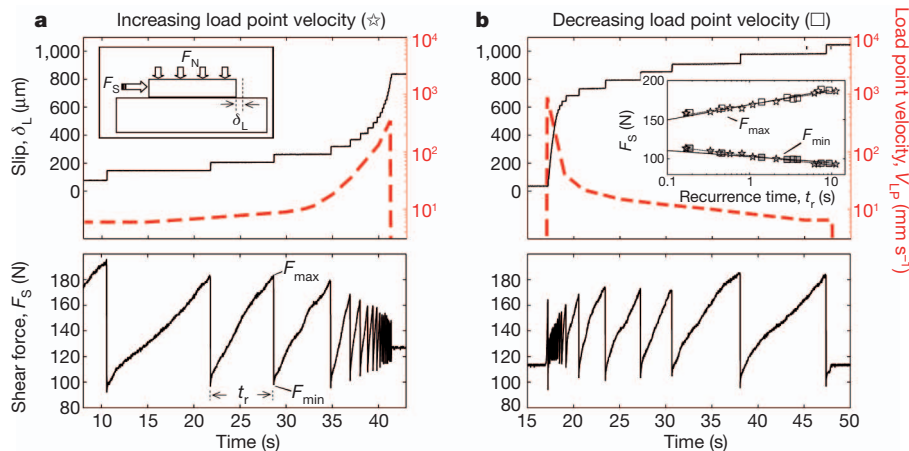


**Figure 1 | Experimental data from a pair of healing tests.** Shear force,  $F_S$ , load point velocity,  $v_{LP}$  (dashed line), and slip  $\delta_L$ , measured from stick-slip experiments at  $\sigma_n = 36$  kPa. All experiments were conducted in pairs, one with increasing  $v_{LP}$  (a) and one with decreasing  $v_{LP}$  (b). Insets: schematic of the

apparatus (a) and the maximum ( $F_{\max}$ ) and minimum ( $F_{\min}$ ) shear forces measured for each event in the stick-slip sequence and plotted against the logarithm of  $t_r$  (b). Stars and squares are from runs with increasing and decreasing  $v_{LP}$ , respectively.

An example sequence of LabEQ seismograms is shown in Fig. 2. The interface properties, apparatus and specimen stiffness, sensor response and wave propagation characteristics do not change between successive events, so differences between LabEQs are attributed to variations in  $t_r$ . When each seismogram is scaled with respect to the total measured slip,  $\delta_\beta$ , the low-frequency components (Fig. 2a) are nearly identical but the high-frequency components (Fig. 2b) depend strongly on

$t_r$ . Absolute source spectra were estimated for each LabEQ by removing the instrument and apparatus response functions from recorded signals by means of a ball-drop calibration source (Methods). Examples of absolute source displacement spectra are shown in Fig. 3a for three LabEQs from Fig. 2. Each source spectrum is roughly linear in  $\log(\omega)$ , where  $\omega$  is the angular frequency, so spectra were fitted with best-fit lines (not shown). Variations in the spectral slopes

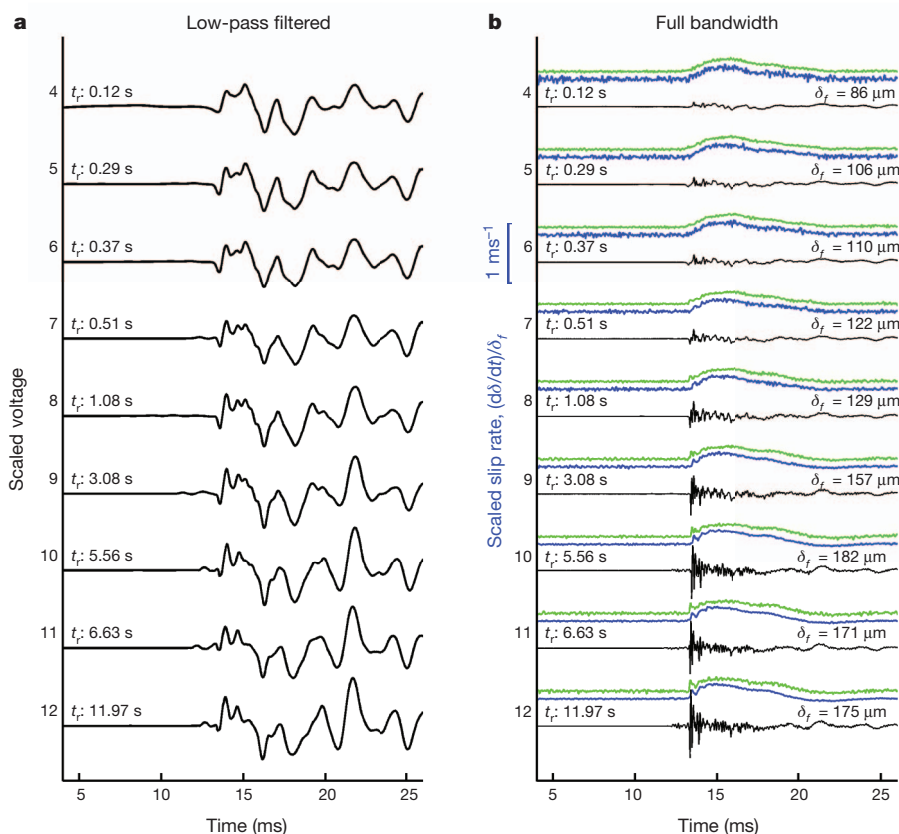


**Figure 2 | Sequence of successive LabEQs.** Events from an experimental run with decreasing  $v_{LP}$  (increasing time between successive events) at  $\sigma_n = 130$  kPa and using a rough sample (run 45-R-Dec; see Supplementary Table 1). Each trace is scaled by the total measured slip,  $\delta_\beta$ , indicated for each trace. **a**, Low-pass-filtered signals (1-kHz cut-off) illustrating the similarity of

low-frequency waveforms. **b**, Full-bandwidth recorded LabEQ data (raw sensor output) plotted alongside scaled slip rates  $(d\delta/dt)/\delta_\beta$  which are derived from slip measured at the leading (blue) and trailing (green) edges of the slider block and low-pass filtered at 5 kHz to reduce high-frequency noise. The green curves have the same scale as the blue curves, and are offset for clarity.

of LabEQ source spectra are shown in Fig. 3b for all 46 events from four tests conducted at normal stress,  $\sigma_n = 130$  kPa. These laboratory results show a disproportionate increase in high-frequency ground motions for greater  $t_r$ . Similar spectral changes were observed for all experiments, but are most pronounced for those conducted at higher  $\sigma_n$ . Peak high-frequency ground motions coincide with the initiation of slip, not maximum slip rate.

To complement the laboratory results, we analysed RESs on the San Andreas fault<sup>22,23</sup> that were perturbed by the 2004, moment-magnitude  $M_w = 6$  Parkfield, California earthquake. As shown in Fig. 4, an increase in high frequencies with increasing  $t_r$  was observed for most RESs. Similar trends were found for the CA1 RES on the Calaveras fault<sup>11</sup>. If spectral changes were due to a propagation effect, such as damage from the Parkfield earthquake, we would expect the effects to be more pronounced in recordings from source–station ray paths that traverse long distances through zones of expected damage<sup>24</sup> (that is, near or within the fault zone and at shallower depths) (Supplementary Fig. 6 and Supplementary Table 2). Instead, many stations see similar spectral variations between the same events and spectral changes vary among RESs (Supplementary Fig. 1), so we suspect that spectral variations are dominantly controlled by changes in earthquake source characteristics and not path effects.

Fault healing seems to cause spectral changes over a broad range of frequencies (Fig. 3a), so we propose that our observations are applicable

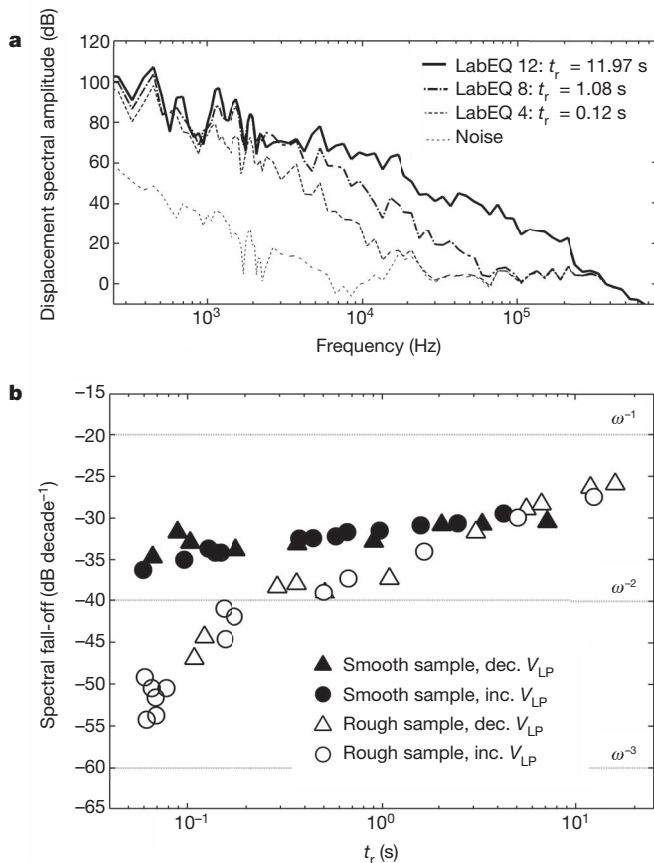


**Figure 3 | LabEQ spectral changes with recurrence time.** **a**, Source displacement spectra and the noise spectrum from three of the LabEQs shown in Fig. 2, which span two orders of magnitude in  $t_r$ . **b**, Slope of source spectrum as a function of recurrence time for all LabEQs from four experimental runs conducted at  $\sigma_n = 130$  kPa. Only the frequency band with a signal-to-noise ratio greater than 6 dB was used for the calculation of these spectral slopes. For the rough sample, spectral slopes increase from  $\omega^{-2.5}$  to  $\omega^{-1.5}$  with increasing  $t_r$ . LabEQs generated from the smooth sample show subtle but systematic spectral changes.

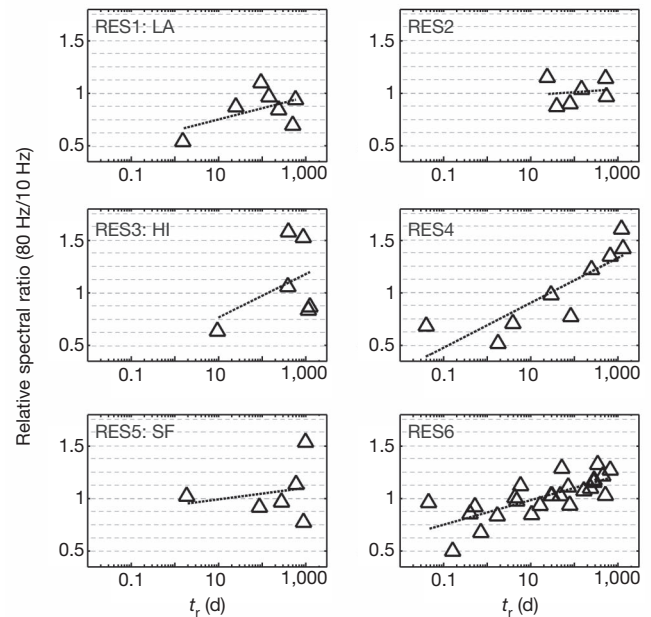


**Figure 4 | Spectral changes of RESs near Parkfield.** The SF, LA and HI RESs were targeted for penetration by the SAFOD deep-drilling experiment (sequences NW, SE and S1 in ref. 23). Relative spectral ratios are calculated from the ratio of relative spectral amplitudes at 75–85 Hz to those at 5–15 Hz (Supplementary Fig. 5 and Supplementary Table 3). Data points indicate the averages of the relative spectral ratios obtained from ground motions recorded at at least three stations for each event in each RES. Dotted lines show a linear best fit to the data, and a positive slope indicates increasing high-frequency ground motions (relative to low-frequency ground motion) with increasing  $\log_{10}(t_r)$ .

not just to the small length scales and high frequencies of LabEQs, but to natural faults and great earthquakes as well. To discuss the underlying mechanisms of these spectral changes, we present a conceptual fault model in which both natural faults and those in the laboratory are composed of a large number of asperity contacts<sup>2,25,26</sup> with a distribution of strengths, which collectively sum to produce the static fault strength,  $\mu_s$ . If the thermally activated healing mechanisms described above cause asperity contacts to strengthen at a rate proportional to the forces they support, then healing would promote a more heterogeneous spatial distribution of fault strength on the asperity scale. When this healed fault ruptures, its heterogeneous fault strength could cause perturbations in slip velocity that would generate high-frequency seismic waves<sup>27</sup>. Alternatively, if healing promotes a larger stress drop<sup>8,21</sup> or a more abrupt slip weakening behaviour, this would promote faster rupture propagation, which could also account for the enhanced high frequencies. This interpretation is consistent with a previous proposal that spectral changes observed for the CA1 RES signify shorter source duration, which could be explained by faster rupture propagation<sup>11</sup>.

The spectral changes shown in Fig. 3b are somewhat analogous to those in Fig. 4, but when comparing the spectra of LabEQs with those from RESs, differences in rise time (the time during which a single point on the fault slips seismically) and rupture duration relative to the recorded frequency band should be taken into account. The LabEQ spectra shown in Fig. 3 are probably controlled by details of rupture propagation. Although the sample geometry and the resolution of the slip sensors do not permit a detailed analysis of dynamic rupture, Fig. 2b does show that slip accelerated more rapidly for events that healed longer. In the case of RESs, even the highest frequencies available for analysis (75–85 Hz) may be too low to contain much information about rupture propagation. Additionally, complicated interaction between rapid, unstable failure of the fault patch and stable slip imposed by slow slip of the surrounding region<sup>9,10</sup> may contribute to

added differences between RESs at Parkfield and current laboratory analogues.

Dense seismic arrays have facilitated back-projection studies of recent megathrust earthquakes that highlight the temporal and spatial complexity of high-frequency seismic radiation and show that sources of high-frequency seismic waves are not spatially correlated with locations of maximum inferred fault slip<sup>5–7</sup>. A mechanism related to fault healing may be responsible for these puzzling observations, particularly for the March 2011 Tohoku earthquake, where high frequencies originated from deeper sections of the fault and contributed to strong ground accelerations felt in eastern Japan. Laboratory experiments on glassy polymers show that healing rate,  $\beta_s$ , increases by an order of magnitude when temperature is increased to close to the glass transition<sup>4</sup>, so it seems possible that variations in healing rate—due to high pressures and temperatures or fault chemistry—could affect fault properties more profoundly than variations in recurrence time. If deeper sections of the fault are more healed than shallower fault sections, this might cause those parts to radiate more high-frequency energy when ruptured in a large earthquake.

The healing-related spectral changes observed in this study demonstrate how earthquake spectra are determined not simply by static fault strength or total fault slip, but by the manner in which slip occurs. Fault sections that heal rapidly or faults that heal for a long time, such as those associated with intraplate earthquakes in low-strain-rate environments, will produce higher-frequency earthquakes. In contrast, fault sections composed of materials that do not heal, such as smectite, a clay mineral found in the creeping section of the San Andreas fault<sup>28</sup> and in subduction zones<sup>29</sup>, will slip slowly and smoothly.

## METHODS SUMMARY

Sliding surfaces of laboratory specimens were milled flat and then roughened by hand lapping with either #60 grit or #600 grit abrasive, producing surface roughnesses referred to as rough and smooth, respectively. Shear force,  $F_s$ , was measured with a load cell located between the loading screw and the slider block. Fault slip,  $\delta$ , was measured at both the leading edge ( $\delta_L$ ) and the trailing edge ( $\delta_T$ ) of the slider using eddy current sensors mounted on the samples. The loading screw was turned by hand; consequently,  $v_{LP}$  was not precisely controlled but was calculated from  $\delta_T$ ,  $F_s$  and the apparatus and specimen stiffness, which was constant for each run. Power spectral estimates were obtained by Fourier-transforming a 65.5-ms (laboratory) or 3.5–4-s (field) signal centred on the first arrival and tapered with a Blackman–Harris window. Noise spectra were obtained similarly. Only data with signal-to-noise ratio of at least 6 dB was used. LabEQs were recorded with a Panametrics V103 sensor located 80 mm from the laboratory fault. RESs near Parkfield were recorded as 250-Hz velocity seismograms by the borehole High-Resolution Seismic Network. Only vertical-component records were used for this study. RES detections and locations follow ref. 22. For each station and each RES, station averages were calculated by linearly averaging spectra from events cleanly recorded by all stations. We computed relative spectral amplitudes by dividing spectra of individual recordings by the station average. Relative spectral ratios were obtained from the ratio of relative spectral amplitudes at high frequencies (75–85 Hz) to those at lower frequencies (5–15 Hz). A different choice of high-frequency band (for example 65–75 Hz) does not affect the results.

**Full Methods** and any associated references are available in the online version of the paper.

**Received 25 April; accepted 14 August 2012.**

1. Dieterich, J. H. Time-dependent friction in rocks. *J. Geophys. Res.* **77**, 3690–3697 (1972).
2. Dieterich, J. H. & Kilgore, B. D. Direct observations of frictional contacts—new insights for state-dependent properties. *Pure Appl. Geophys.* **143**, 283–302 (1994).
3. Scholz, C. *The Mechanics of Earthquakes and Faulting* 81–100 (Cambridge Univ. Press, 2002).

4. Berthoud, P. & Baumberger, T. G'Sell, C. & Hiver, J.-M. Physical analysis of the state- and rate-dependent friction law: static friction. *Phys. Rev. B* **59**, 14313–14327 (1999).
5. Kiser, E. & Ishii, M. The 2010 Mw 8.8 Chile earthquake: Triggering on multiple segments and frequency-dependent rupture behavior. *Geophys. Res. Lett.* **38**, L07301 (2011).
6. Lay, T. *et al.* Depth-varying rupture properties of subduction zone megathrust faults. *J. Geophys. Res.* **117**, B04311 (2012).
7. Meng, L., Inbal, A. & Ampuero, J.-P. A window into the complexity of the dynamic rupture of the 2011 Mw 9 Tohoku-Oki earthquake. *Geophys. Res. Lett.* **38**, L00G07 (2011).
8. Karner, S. L. & Marone, C. in *Geocomplexity and the Physics of Earthquakes* (eds Rundle, J. B., Turcotte, D. & Klein, W.) 187–198 (Geophys. Monogr. Ser. 120, AGU, 2000).
9. Chen, T. & Lapusta, N. Scaling of small repeating earthquakes explained by interaction of seismic and aseismic slip in a rate and state fault model. *J. Geophys. Res.* **114**, B01311 (2009).
10. Chen, K. H., Bürgmann, R., Nadeau, R. M., Chen, T. & Lapusta, N. Postseismic variations in seismic moment and recurrence interval of repeating earthquakes. *Earth Planet. Sci. Lett.* **299**, 118–125 (2010).
11. Vidale, J. E., Ellsworth, W. L., Cole, A. & Marone, C. Variations in rupture process with recurrence interval in a repeated small earthquake. *Nature* **368**, 624–626 (1994).
12. Peng, Z. & Vidale, J. E. Marone, C. & Rubin, A. Systematic variations in recurrence interval and moment of repeating aftershocks. *Geophys. Res. Lett.* **32**, L15301 (2005).
13. Dieterich, J. H. & Conrad, G. Effect of humidity on time and velocity-dependent friction in rocks. *J. Geophys. Res.* **89**, 4196–4202 (1984).
14. Cox, S. F. & Paterson, M. S. Experimental dissolution precipitation creep in quartz aggregates at high temperatures. *Geophys. Res. Lett.* **18**, 1401–1404 (1991).
15. Li, Q., Tullis, T. E., Goldsby, D. & Carpick, R. W. Frictional ageing from interfacial bonding and the origins of rate and state friction. *Nature* **480**, 233–236 (2011).
16. Rabinowitz, E. *Friction and Wear of Materials* (Wiley, 1965).
17. Beeler, N. M., Baumberger, T., Perrin, B., Caroli, B. & Caroli, C. Creep, stick-slip, and dry friction dynamics: experiments and a heuristic model. *Phys. Rev. E* **49**, 4973–4988 (1994).
18. Rice, J. R. & Cocco, M. in *Tectonic Faults: Agents of Change on a Dynamic Earth* (eds Handy, M. R., Hirth, G. & Hovius, N.) 99–137 (MIT Press, 2007).
19. Wu, F. T., Thomson, K. C. & Kuenzler, H. Stick-slip propagation velocity and seismic source mechanism. *Bull. Seismol. Soc. Am.* **62**, 1621–1628 (1972).
20. McLaskey, G. C. & Glaser, S. D. Micromechanics of asperity rupture during laboratory stick slip experiments. *Geophys. Res. Lett.* **38**, L12302 (2011).
21. Beeler, N. M., Hickman, S. H. & Wong, T.-f. Earthquake stress drop and laboratory-inferred interseismic strength recovery. *J. Geophys. Res.* **106**, 30,701–30,713 (2001).
22. Nadeau, R. M. & McEvilly, T. V. Fault slip rates at depth from recurrence intervals of repeating microearthquakes. *Science* **285**, 718–721 (1999).
23. Nadeau, R. M., Michalini, A., Uhrhammer, R. A., Dolenc, D. & McEvilly, T. V. Detailed kinematics, structure and recurrence of micro-seismicity in the SAFOD target region. *Geophys. Res. Lett.* **31**, L12S08 (2004).
24. Rubinstein, J. L. & Beroza, G. C. Depth constraints on nonlinear strong ground motion. *Geophys. Res. Lett.* **32**, L14313 (2005).
25. Johnson, L. An earthquake model with interacting asperities. *Geophys. J. Int.* **182**, 1339–1373 (2010).
26. Dreger, D., Nadeau, R. M. & Chung, A. Repeating earthquake finite source models: strong asperities revealed on the San Andreas fault. *Geophys. Res. Lett.* **34**, L23302 (2007).
27. Page, M., Dunham, E. & Carlson, J. M. Distinguishing barriers and asperities in near-source ground motion. *J. Geophys. Res.* **110**, B11302 (2005).
28. Carpenter, B. M., Marone, C. & Saffer, D. M. Weakness of the San Andreas fault revealed by samples from the active fault zone. *Nature Geosci.* **4**, 251–254 (2011).
29. Saffer, D. M. & Marone, C. Comparison of smectite- and illite rich gouge frictional properties: application to the updip limit of the seismogenic zone along subduction megathrusts. *Earth Planet. Sci. Lett.* **215**, 219–235 (2003).

**Supplementary Information** is available in the online version of the paper.

**Acknowledgements** This paper was improved by suggestions from R. Bürgmann and constructive reviews by T. Tullis, C. Marone, W. Ellsworth and N. Beeler. High-Resolution Seismic Network data was provided by the Berkeley Seismological Laboratory and NCEDC. Research was supported by the US NSF GRF and NSF grants CMMI-1131582, EAR-0738342 and EAR-0910322. This is BSL contribution #11-12.

**Author Contributions** G.C.M. and S.D.G. developed the laboratory experiments. R.M.N. developed and maintained repeating-earthquake catalogues. A.M.T. and G.C.M. performed analysis of the RESs at Parkfield. G.C.M. performed analysis of LabEQs and wrote the manuscript, with contributions from all authors.

**Author Information** Reprints and permissions information is available at [www.nature.com/reprints](http://www.nature.com/reprints). The authors declare no competing financial interests. Readers are welcome to comment on the online version of the paper. Correspondence and requests for materials should be addressed to G.C.M. ([gmclaskey@usgs.gov](mailto:gmclaskey@usgs.gov)).

## METHODS

**Laboratory.** Fault slip,  $\delta$ , is measured at both the leading edge ( $\delta_L$ ) and the trailing edge ( $\delta_T$ ) of the slider block using eddy current sensors mounted on the samples. The shear force,  $F_S$ , is measured with a load cell located between the loading screw and the slider block. The loading screw is turned by hand. Consequently,  $v_{LP}$  is not precisely controlled but is calculated from  $\delta_T$ ,  $F_S$  and the apparatus and specimen stiffness, which was constant for each run. Hydraulic cylinders apply  $F_N$ . Sliding surfaces were milled flat and then roughened by hand lapping with either #60 grit or #600 grit abrasive, producing surface roughnesses referred to as rough and smooth, respectively.  $F_S$ ,  $\delta_L$  and  $\delta_T$  are recorded at 2 kHz throughout the experiment. A second system records LabEQs,  $F_S$ ,  $\delta_L$  and  $\delta_T$  at 2 MHz for 262 ms around each event or set of events.

**Spectral analysis.** Power spectral estimates (PSEs) were obtained by Fourier-transforming a 65.5-ms (laboratory) or 3.5–4-s (field) signal centred on the first arrival and tapered with a Blackman–Harris window. Noise spectra were obtained similarly from signals recorded before the first arrival (field) or before the first event in each sequence (laboratory). Only data with a signal-to-noise ratio of at least 6 dB was used. LabEQs were recorded with a Panametrics V103 sensor

located 80 mm from the laboratory fault, and absolute source spectra were obtained by dividing PSEs by the PSE of a ball-drop calibration source (the stress waves due to a tiny ball impacting the base plate), which has a known source spectrum<sup>30</sup>. Variations in spectra from ball-drop sources at different locations on the specimen indicate that absolute source spectra of LabEQs are accurate to  $\pm 8$  dB, and the precision is better than  $\pm 2$  dB. RESs near Parkfield were recorded as 250-Hz velocity seismograms by the borehole High-Resolution Seismic Network. Only vertical-component records were used for this study. RES detections and locations follow ref. 22. For each station and each RES, station averages were calculated by linearly averaging spectra from events cleanly recorded by all stations. We computed relative spectral amplitudes by dividing spectra of individual recordings by the station average. Relative spectral ratios were obtained from the ratio of relative spectral amplitudes at high frequencies (75–85 Hz) to those at lower frequencies (5–15 Hz). A different choice of high-frequency band (for example 65–75 Hz) does not affect the results.

30. McLaskey, G. C. & Glaser, S. D. Hertzian impact: experimental study of the force pulse and resulting stress waves. *J. Acoust. Soc. Am.* **128**, 1087–1096 (2010).

# Combined pesticide exposure severely affects individual- and colony-level traits in bees

Richard J. Gill<sup>1</sup>, Oscar Ramos-Rodriguez<sup>1</sup> & Nigel E. Raine<sup>1</sup>

**Reported widespread declines of wild and managed insect pollinators have serious consequences for global ecosystem services and agricultural production<sup>1–3</sup>. Bees contribute approximately 80% of insect pollination, so it is important to understand and mitigate the causes of current declines in bee populations<sup>4–6</sup>. Recent studies have implicated the role of pesticides in these declines, as exposure to these chemicals has been associated with changes in bee behaviour<sup>7–11</sup> and reductions in colony queen production<sup>12</sup>. However, the key link between changes in individual behaviour and the consequent impact at the colony level has not been shown. Social bee colonies depend on the collective performance of many individual workers. Thus, although field-level pesticide concentrations can have subtle or sublethal effects at the individual level<sup>8</sup>, it is not known whether bee societies can buffer such effects or whether it results in a severe cumulative effect at the colony level. Furthermore, widespread agricultural intensification means that bees are exposed to numerous pesticides when foraging<sup>13–15</sup>, yet the possible combinatorial effects of pesticide exposure have rarely been investigated<sup>16,17</sup>. Here we show that chronic exposure of bumblebees to two pesticides (neonicotinoid and pyrethroid) at concentrations that could approximate field-level exposure impairs natural foraging behaviour and increases worker mortality leading to significant reductions in brood development and colony success. We found that worker foraging performance, particularly pollen collecting efficiency, was significantly reduced with observed knock-on effects for forager recruitment, worker losses and overall worker productivity. Moreover, we provide evidence that combinatorial exposure to pesticides increases the propensity of colonies to fail.**

The majority of studies to date have focused on pesticide exposure in honeybees, but bumblebees are also crucial pollinators and have smaller colonies, making them ideally suited to investigate effects at both the individual (worker) and colony level. This study mimicked a realistic scenario in which 40 early-stage bumblebee (*Bombus terrestris*) colonies received long-term (4-week) exposure to two widely used pesticides frequently encountered when foraging on flowering crops, the neonicotinoid imidacloprid and the pyrethroid  $\lambda$ -cyhalothrin. Imidacloprid is a systemic pesticide found in all plant tissues, including the pollen and nectar consumed by bees (oral exposure<sup>18–20</sup>).  $\lambda$ -cyhalothrin is sprayed directly on to crops, including their flowers, to which bees will be topically exposed (details in Supplementary Information). Foraging bees are thus simultaneously exposed to both chemicals in the field, making them excellent candidates to investigate the potential for combinatorial effects of pesticide exposure. Using a split block design (see Methods), we monitored colonies exposed to each pesticide independently and in combination (ten control colonies, ten exposed to imidacloprid (I), ten exposed to  $\lambda$ -cyhalothrin (LC) and ten exposed to I and LC (mix = M)). Imidacloprid (dissolved in 40% sucrose solution) was provided at a concentration (10 p.p.b. (parts per billion (10<sup>9</sup>))) within the range found in crop nectar and pollen in the field<sup>9,21</sup>.  $\lambda$ -cyhalothrin was administered following label guidance for field-spray application (see Supplementary Information). Bees were able to forage in the field, providing a

realistic and demanding behavioural setting, and the foraging behaviour of individual workers was recorded using radio frequency identification (RFID) tagging technology<sup>10,11,22</sup> (Supplementary Figs 1 and 2). Colonies were motivated to forage because we provided them with no pollen and limited amounts of sucrose solution.

During colony development, the production of workers (and their survival) is vital to colony success because workers provide the labour (for example, brood care and foraging) for the colony. Total worker production at the end of the experiment was significantly lower in imidacloprid-treated colonies (reduced by 27% in I and 9% in M colonies) compared to control colonies (mean ( $\pm$  s.e.m.) workers per colony, I = 19.7  $\pm$  3.0, M = 24.4  $\pm$  3.2 versus control = 27.0  $\pm$  4.0; linear mixed effects model (LMER), I,  $Z$  = -3.71,  $P$  < 0.001; M,  $Z$  = -2.62,  $P$  = 0.009; Fig. 1a). Two of the forty colonies, both M colonies, did not survive the experiment (they ‘failed’ after 3 and 8 days; see Supplementary Information), a colony failure rate significantly higher than other treatments (Fisher’s Exact test: mid- $P$  correction = 0.029). These two colonies were excluded from statistical analyses to provide a conservative assessment of worker production in M colonies (when included in analysis = 20.0  $\pm$  3.9 workers). During the experiment, 223 (21% of total) workers were found dead inside nest boxes. On average, 36  $\pm$  7.3% and 39  $\pm$  7.5% of workers from LC and M colonies, respectively, died in the nest box; a figure four times higher than control (9  $\pm$  3.4%) colonies (LMER, LC,  $t$  = 4.31,  $P$  < 0.001; M,  $t$  = 4.23,  $P$  < 0.001; Fig. 1b). Moreover, 43% of the workers found dead in LC and M colonies lived fewer than 4 days after eclosion—an apparent waste of resources required for future colony growth given that such young members are unlikely to have contributed any work (for example, foraging) to offset the resources invested to produce them. Queen loss occurred in 14 colonies, although loss rate did not differ significantly among treatments (control = 4; I = 5; LC = 2; M = 3; Fisher’s exact test: mid- $P$ -correction = 0.40) and we accounted for queen loss in our analyses (see Supplementary Information).

Daily counts of newly eclosed bees showed that worker production in I colonies did not become significantly lower than control colonies until the end of week 2, and for M colonies until the end of week 4 (Fig. 1c; see Supplementary Information and Supplementary Table 1). Daily counts of dead bees also revealed that worker mortality in LC colonies did not become significantly higher than that in control colonies until the end of week 3, but worker mortality in M colonies became significantly higher than that in control colonies as early as the end of week 1. The delayed effect of imidacloprid exposure on worker productivity in I and M colonies coincides with the time taken by workers to develop from egg to adult (approximately 22 days), suggesting that the observed effect is a result of imidacloprid on brood development. Indeed, the total number of larvae and pupae combined that were found in colonies at the end of the experiment (‘brood number’) was significantly lower in I and M colonies compared to control colonies (LMER, I,  $Z$  = -6.23,  $P$  < 0.001; M,  $Z$  = -5.60,  $P$  < 0.001). Overall, this represented a 22% reduction in brood production in I colonies and a 7% reduction in M colonies (mean ( $\pm$  s.e.m.) brood number, I = 36  $\pm$  8.0, M = 43  $\pm$  11.7 (including failed colonies:

<sup>1</sup>School of Biological Sciences, Royal Holloway, University of London, Egham, Surrey, TW20 0EX, UK.

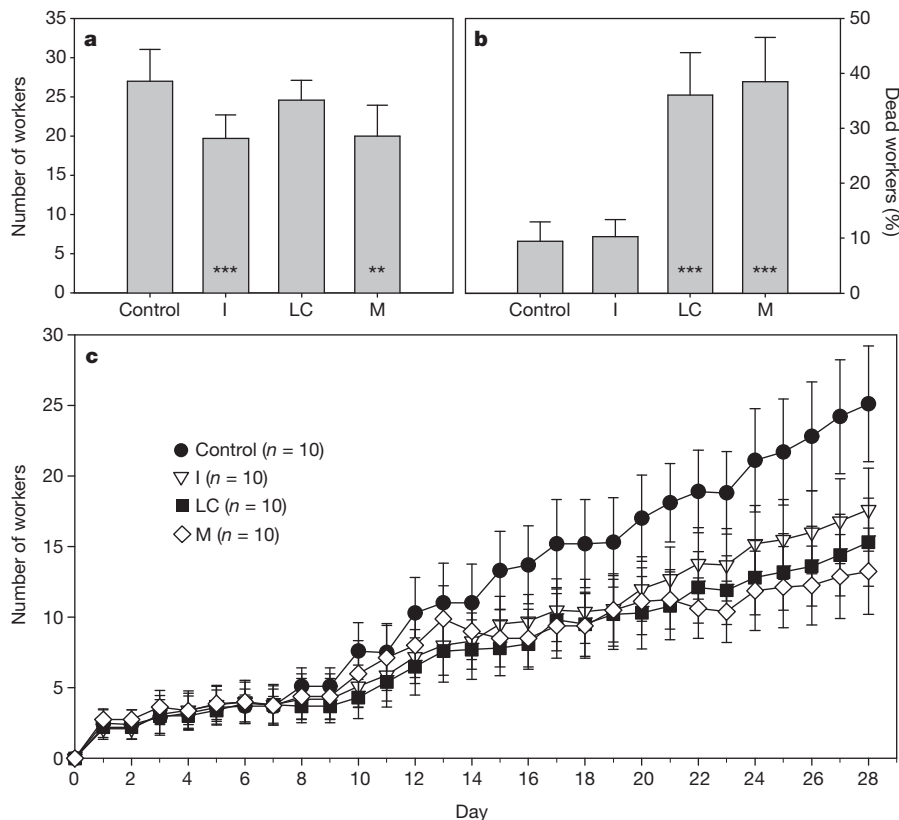


**Figure 1 | Worker production and mortality.** **a**, Mean ( $\pm$  s.e.m.) number of workers per colony that eclosed by the end of the experiment. **b**, Mean percentage of workers per colony found dead inside the nest box by the end of the experiment. **c**, Colony growth shown by daily counts of the cumulative number of workers eclosed minus the cumulative number of workers found

dead (mean ( $\pm$  s.e.m.) per colony). Data shown on the x axis indicate the number of days since the start of the experiment (day 1 = 24 h after the start of experimentation). M treatment includes the two collapsed colonies. \* $P \leq 0.05$ , \*\* $P \leq 0.01$ , \*\*\* $P \leq 0.001$  (comparison with control).

M =  $39 \pm 9.6$ ) versus control =  $46 \pm 9.7$ ). Despite this, there was no significant difference in the mass of the wax nest structure (see Supplementary Information for details) across treatments at the end of the experiment (LMER, I,  $t = -1.12$ ,  $P = 0.27$ ; M,  $t = -1.22$ ,  $P = 0.23$ ; Supplementary Fig. 3) indicating that I and M colonies attempted to raise similar brood numbers but that a lower proportion of larvae and pupae survived to eclosion.

Although imidacloprid could be directly affecting brood (physiological) development, it could also indirectly affect the brood by causing changes to colony behaviour and/or structure: for example, changes to foraging behaviour leading to food limitation<sup>23,24</sup>. We tested this hypothesis by studying worker foraging performance using RFID technology to automatically record the exact time workers left or entered each colony (Supplementary Figs 1 and 2). Overall, we collected data from 259 recognized foragers from 32 colonies ( $n$  colonies: control = 7; I = 10; LC = 8; M = 7) making 8,751 foraging bouts (median (interquartile range) per worker = 23 (10–44); for criteria used to classify foragers and foraging bouts see Methods). We examined whether pesticide treatment affected foraging activity and forager recruitment. We found that foragers from M colonies performed fewer foraging bouts compared to control colonies (LMER,  $t = -2.55$ ,  $P = 0.011$ ; Fig. 2a), and that there were significantly more foragers in both I and M colonies compared to control colonies over the 4 weeks (LMER, I,  $Z = 4.20$ ,  $P < 0.001$ ; M,  $Z = 3.49$ ,  $P < 0.001$ ; Fig. 2a). The higher number of foragers in I and M colonies (compared to control) is unlikely to be due to either pesticide causing a significant repellent or anti-feedant effect (this corroborates the lack of published evidence for pyrethroid repellency in bumblebees despite reports of pyrethroids being repellent to honeybees<sup>25</sup>). This is because workers did not have to visit the feeder, as they could forage for nectar outside, yet we found no difference among

treatments in the amount of sucrose collected from feeders (LMER,  $t \leq 1.63$ ,  $P \geq 0.11$ ; Supplementary Fig. 6).

Given that I and M colonies recruited higher numbers of workers to forage compared to control colonies, we evaluated whether this was a response to reduced individual foraging efficiency by monitoring pollen foraging performance and observing the size of pollen loads (load size scored as: small = 1, medium = 2, large = 3; see Methods) brought back by foragers ( $n = 20$  h of observation per colony). Crucially, imidacloprid-exposed foragers returned with significantly smaller pollen loads per foraging bout compared to control colonies (LMER, I,  $t = -3.31$ ,  $P = 0.0011$ ; M,  $t = -3.38$ ,  $P < 0.001$ ; Fig. 2b). Imidacloprid-exposed foragers collected pollen successfully in a significantly lower percentage of their foraging bouts (mean ( $\pm$  s.e.m.), I =  $59 \pm 7.3\%$ , M =  $55 \pm 8.6\%$  versus control =  $82 \pm 5.8\%$ ; LMER, I,  $t = -3.16$ ,  $P = 0.0018$ ; M,  $t = -3.05$ ,  $P = 0.0026$ ; Supplementary Fig. 4) and we also found that the average duration of successful foraging bouts (during which pollen was collected) was significantly longer for imidacloprid-exposed foragers than for control foragers (LMER, I,  $t = 2.10$ ,  $P = 0.037$ ; M,  $t = 2.87$ ,  $P = 0.005$ ; Fig. 2c). Together, these data show that imidacloprid-exposed workers were significantly less efficient at collecting pollen in the field.

A consequence of recruiting a greater number of workers to forage is that it increases the proportion of colony workforce going outside to undertake a potentially hazardous task<sup>22</sup>. Indeed, our RFID data show the number of foragers per colony was significantly correlated with the number of workers leaving the colony and getting 'lost' outside (that is, workers that did not return: Spearman's Rank,  $\rho = 0.801$ ,  $P < 0.001$ ; Supplementary Fig. 5). Consequently, we found that on average the percentage of workers getting lost in I and M colonies was 50% and 55% higher than control colonies (I =  $30 \pm 3.1\%$ , M =  $31 \pm 5.3\%$  versus control =  $20 \pm 2.9\%$ ; LMER, I,  $t = 2.83$ ,  $P = 0.008$ ; M,  $t = 2.26$ ,

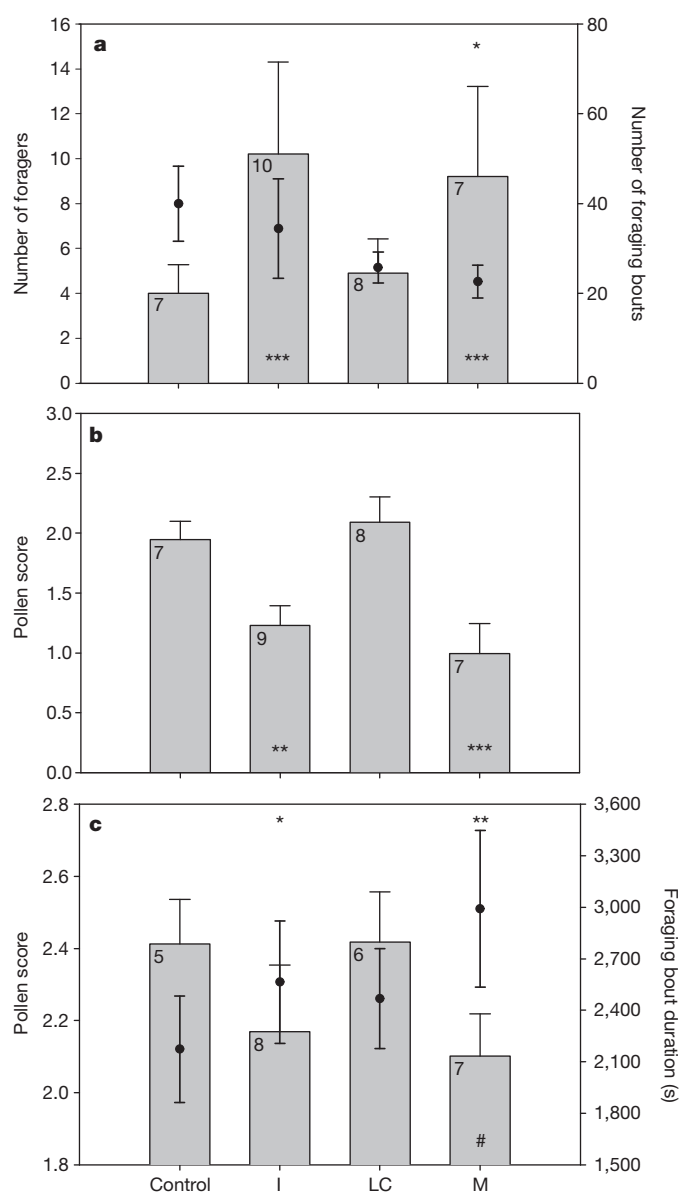


**Figure 2 | Foraging performance.** a, Mean ( $\pm$  s.e.m.) number of foragers per colony (column), and foraging bouts per worker per colony (filled circles;  $n = 259$  foragers). b, Mean pollen score per worker per colony for all observed foraging bouts ( $n = 228$  foragers). c, Mean pollen score per successful (pollen) foraging bout for each worker per colony (column), and mean duration of successful foraging bouts per worker per colony (filled circles) ( $n = 147$  foragers).  $n$  colonies shown in top left corner of columns. Significant differences from control treatment for column data are shown at the bases of columns, and for filled-circle data are shown above columns (a and c). # $P \leq 0.1$ , \* $P \leq 0.05$ , \*\* $P \leq 0.01$ , \*\*\* $P \leq 0.001$  (comparison with control).

$P = 0.03$ ). Furthermore, when considering worker mortality and losses combined over the 4 weeks (mean ( $\pm$  s.e.m.): I =  $41 \pm 4.2\%$ , LC =  $51 \pm 6.8\%$ , M =  $69 \pm 7.1\%$  versus control =  $30 \pm 5.0\%$ , LMER, I,  $t = 1.79$ ,  $P = 0.08$ ; LC,  $t = 3.25$ ,  $P = 0.0026$ ; M,  $t = 5.24$ ,  $P < 0.001$ ; Table 1 and Fig. 3), we found that colonies treated with both pesticides (M) suffered most severely. Moreover, M colonies had significantly higher overall worker losses than either I colonies (LMER,  $t = -3.69$ ,  $P < 0.001$ ) or LC colonies (LMER,  $t = -2.31$ ,  $P = 0.027$ ).

We have shown that imidacloprid exposure at concentrations that can be found in the pollen and nectar of flowering crops causes impairment to pollen foraging efficiency, leading to increased colony demand for food as shown by increased worker recruitment to forage. However, imidacloprid-treated colonies (I and M) were still unable to collect as

**Table 1 | Summary of observed pesticide effects for each treatment group (I, LC or M) in comparison to the control group**

Effect level	Effect type	I	LC	M
<b>Effects on individual behaviour</b>	Number of foragers	+	ND	+
	Foraging bout frequency	ND	ND	–
	Amount of pollen collected	–	ND	–
	Duration of pollen foraging bouts	+	ND	+
<b>Effects at colony level</b>	Worker production	–	ND	–
	Brood number	–	ND	–
	Nest structure mass	ND	ND	ND
	Worker mortality	ND	+	+
	Worker loss	+	–	+
	Worker mortality & loss	ND	+	+
	Colony failure ( $n$ failed/ $n$ survived)	0/10	0/10	2/8

Significant decrease (–), significant increase (+) and no detected effect (ND) at the 5% significance level.

much pollen as control colonies. Such pollen constraints, coupled with a higher number of workers undertaking foraging rather than brood care, seemed to affect brood development, resulting in reduced worker production that can only exacerbate the problem of having an impaired colony workforce. These findings show a mechanistic explanation to link recently reported effects on individual worker behaviour<sup>10,11,26–29</sup> and colony queen production<sup>12</sup> as a result of neonicotinoid exposure. Moreover, exposure to a second pesticide  $\lambda$ -cyhalothrin (pyrethroid) applied at label-guideline concentration for crop use caused additional worker mortality in this study highlighting another potential risk. Bee colonies typically encounter several classes of pesticides when foraging in the field<sup>13–15</sup>, potentially exposing them to a range of combinatorial effects. Indeed, M colonies in our study were consistently negatively affected in all our measures of worker behaviour, suffered the highest overall worker losses (worker mortality and forager losses), which were twice as great as for control colonies, and two colonies did in fact fail (Table 1).

Pesticide-label-guidance concentrations and application rates are approved on the basis of ecotoxicological tests using single pesticides and set at a level for field use deemed ‘sublethal’ (below a dose lethal to 50% of animals tested ( $LD_{50}$ )). However, the risk of exposure to multiple pesticides, or of the same pesticide being applied to different (adjacent) crops, is currently not considered when evaluating the safety of pesticides for bees. Given the serious impacts on M colonies it is concerning that pesticide products containing mixtures of neonicotinoids and pyrethroids are in current use<sup>18</sup>. At present there are also no guidelines for testing chronic or sublethal effects of pesticides on

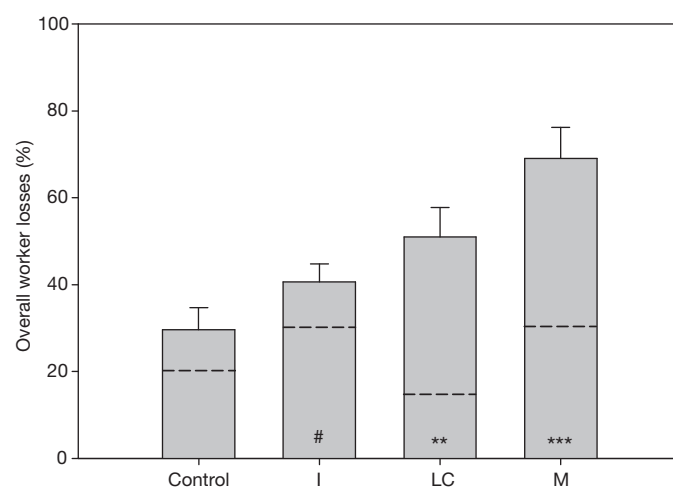


**Figure 3 | Overall worker losses.** Mean ( $\pm$  s.e.m.) overall percentage of workers lost per colony, including workers lost outside (below the dashed line) and worker mortality (dead workers found in nest box; above the dashed line), during the 4-week experiment.  $n = 40$  colonies. # $P \leq 0.1$ , \*\* $P \leq 0.01$ , \*\*\* $P \leq 0.001$  (comparison with control).

bees<sup>30</sup>, and considering that we did not detect significant effects until 2 to 4 weeks into our study, the current European and Mediterranean Plant Protection Organisation (EPPO) and Organization for Economic Co-operation and Development (OECD) guideline of a maximum exposure of 96 h (for testing acute effects of pesticides on honeybees) appears to be insufficient. Our results emphasize the importance of recent recommendations by the European Food Safety Authority (EFSA) Panel on Plant Protection Products and their Residues (<http://www.efsa.europa.eu/en/efsajournal/pub/2668.htm>) proposing the need for longer term toxicity testing on both adult bees and larvae, new protocols to detect cumulative toxicity effects and separate risk assessment schemes for different bee species. Our findings have clear implications for the conservation of insect pollinators in areas of agricultural intensification, particularly social bees with their complex social organization and dependence on a critical threshold of workers performing efficiently to ensure colony success.

## METHODS SUMMARY

Each colony contained a queen and ten or fewer workers at the start of the experiment, with no significant difference among treatments in worker number (Kruskal–Wallis:  $H = 0.26$ ,  $P = 0.97$ ). Colonies were housed in two-chambered nest boxes, with the rear chamber housing the nest and front chamber used for pesticide exposure (Supplementary Figs 1 and 6). Nest boxes were kept in the laboratory but connected via an outlet tube to the outside to allow natural foraging. Foraging activity of tagged workers was automatically recorded by RFID readers placed at the entrance to each nest box (Supplementary Fig. 2). The food chamber housed a feeder containing a specified volume (averaging 13 ml) of control sucrose solution (control and LC) or 10 p.p.b. imidacloprid sucrose solution (I and M) provided every 2 to 3 days (Supplementary Table 2). The feeder was placed in a Petri dish lined with filter paper that was sprayed once at the start of each week with  $0.69 \pm 0.046$  ml of control solution (control and I) or 37.5 p.p.m. (parts per million ( $10^6$ ))  $\lambda$ -cyhalothrin solution (LC and M). Workers walking across the filter paper to the feeder had contact exposure to  $\lambda$ -cyhalothrin (LC and M), and oral exposure to imidacloprid (I and M) when feeding. Colonies were not provided with pollen to motivate foraging behaviour. All workers were RFID tagged, with new workers tagged within 3 days of eclosion (Supplementary Fig. 2). We classified a foraging bout as a period of at least 5 minutes between a worker leaving and returning to a colony, and a forager as a worker that performed at least 4 foraging bouts. Pollen foraging was observed for 1 hour per colony per day (5 days per week) recording the presence and size of pollen loads collected (Supplementary Table 2). Colonies were frozen at the end of the experiment; the number of workers (and tag identifications) and brood was counted, and the mass of the nest structure was recorded.

**Full Methods** and any associated references are available in the online version of the paper.

Received 19 April; accepted 13 September 2012.

Published online 21 October 2012.

1. Biesmeijer, J. C. *et al.* Parallel declines in pollinators and insect-pollinated plants in Britain and the Netherlands. *Science* **313**, 351–354 (2006).
2. Klein, A. M. *et al.* Importance of pollinators in changing landscapes for world crops. *Proc. R. Soc. B* **274**, 303–313 (2007).
3. Kremen, C. *et al.* Pollination and other ecosystem services produced by mobile organisms: a conceptual framework for the effects of land-use change. *Ecol. Lett.* **10**, 299–314 (2007).
4. Potts, S. G. *et al.* Global pollinator declines: trends, impacts and drivers. *Trends Ecol. Evol.* **25**, 345–353 (2010).
5. Oldroyd, B. P. What's killing American honey bees? *PLoS Biol.* **5**, e168 (2007).
6. Brown, M. J. F. & Paxton, R. J. The conservation of bees: a global perspective. *Apidologie* **40**, 410–416 (2009).
7. Thompson, H. M. Behavioural effects of pesticides in bees - their potential for use in risk assessment. *Ecotoxicology* **12**, 317–330 (2003).
8. Desneux, N., Decourtye, A. & Delpuech, J. M. The sublethal effects of pesticides on beneficial arthropods. *Annu. Rev. Entomol.* **52**, 81–106 (2007).

9. Cresswell, J. E. A meta-analysis of experiments testing the effects of a neonicotinoid insecticide (imidacloprid) on honey bees. *Ecotoxicology* **20**, 149–157 (2011).
10. Schneider, C. W., Tautz, J., Grünewald, B. & Fuchs, S. RFID tracking of sublethal effects of two neonicotinoid insecticides on the foraging behavior of *Apis mellifera*. *PLoS ONE* **7**, e30023 (2012).
11. Henry, M. *et al.* A common pesticide decreases foraging success and survival in honey bees. *Science* **336**, 348–350 (2012).
12. Whitehorn, P. R., O'Connor, S., Wackers, F. L. & Goulson, D. Neonicotinoid pesticide reduces bumble bee colony growth and queen production. *Science* **336**, 351–352 (2012).
13. Johnson, R. M., Ellis, M. D., Mullin, C. A. & Frazier, M. Pesticides and honey bee toxicity — USA. *Apidologie* **41**, 312–331 (2010).
14. Mullin, C. A. *et al.* High levels of miticides and agrochemicals in North American apiaries: implications for honey bee health. *PLoS ONE* **5**, e9754 (2010).
15. Krupke, C. H., Hunt, G. J., Eitzer, B. D., Andino, G. & Given, K. Multiple routes of pesticide exposure for honey bees living near agricultural fields. *PLoS ONE* **7**, e29268 (2012).
16. Johnson, R. M., Pollock, H. S. & Berenbaum, M. R. Synergistic interactions between in-hive miticides in *Apis mellifera*. *J. Econ. Entomol.* **102**, 474–479 (2009).
17. Pilling, E. D. & Jepson, P. C. Synergism between EBI fungicides and a pyrethroid insecticide in the honeybee (*Apis mellifera*). *Pestic. Sci.* **39**, 293–297 (1993).
18. Elbert, A., Haas, M., Springer, B., Thielert, W. & Nauen, R. Applied aspects of neonicotinoid uses in crop protection. *Pest Manag. Sci.* **64**, 1099–1105 (2008).
19. Rortais, A., Arnold, G., Halm, M. P. & Touffet-Briens, F. Modes of honeybees exposure to systemic insecticides: estimated amounts of contaminated pollen and nectar consumed by different categories of bees. *Apidologie* **36**, 71–83 (2005).
20. Chauzat, M. P. *et al.* A survey of pesticide residues in pollen loads collected by honey bees in France. *J. Econ. Entomol.* **99**, 253–262 (2006).
21. Blacquière, T., Smagghe, G., van Gestel, C. A. M. & Mommaerts, V. Neonicotinoids in bees: a review on concentrations, side-effects and risk assessment. *Ecotoxicology* **21**, 973–992 (2012).
22. Molet, M., Chittka, L., Stelzer, R. J., Streit, S. & Raine, N. E. Colony nutritional status modulates worker responses to foraging recruitment pheromone in the bumblebee *Bombus terrestris*. *Behav. Ecol. Sociobiol.* **62**, 1919–1926 (2008).
23. Schmid-Hempel, R. & Schmid-Hempel, P. Colony performance and immunocompetence of a social insect, *Bombus terrestris*, in poor and variable environments. *Funct. Ecol.* **12**, 22–30 (1998).
24. Pelletier, L. & McNeil, J. N. The effect of food supplementation on reproductive success in bumblebee field colonies. *Oikos* **103**, 688–694 (2003).
25. Thompson, H. & Wilkins, S. Assessment of the synergy and repellency of pyrethroid/fungicide mixtures. *Bull. Insectol.* **56**, 131–134 (2003).
26. Bortolotti, L. *et al.* Effects of sub-lethal imidacloprid doses on the homing rate and foraging activity of honey bees. *Bull. Insectol.* **56**, 63–67 (2003).
27. Decourtye, A., Devillers, J., Cluzeau, S., Charreton, M. & Pham-Delègue, M. H. Effects of imidacloprid and deltamethrin on associative learning in honeybees under semi-field and laboratory conditions. *Ecotoxicol. Environ. Saf.* **57**, 410–419 (2004).
28. Mommaerts, V. *et al.* Risk assessment for side-effects of neonicotinoids against bumblebees with and without impairing foraging behavior. *Ecotoxicology* **19**, 207–215 (2010).
29. Yang, E. C., Chuang, Y. C., Chen, Y. L. & Chang, L. H. Abnormal foraging behavior induced by sublethal dosage of imidacloprid in the Honey bee (Hymenoptera: Apidae). *J. Econ. Entomol.* **101**, 1743–1748 (2008).
30. Halm, M. P., Rortais, A., Arnold, G., Tasé, J. N. & Rault, S. New risk assessment approach for systemic insecticides: the case of honey bees and imidacloprid (Gaucho). *Environ. Sci. Technol.* **40**, 2448–2454 (2006).

**Supplementary Information** is available in the online version of the paper.

**Acknowledgements** We thank M.J.F. Brown, M. Clook, J. Culverhouse, A. Dixon, M. Fürst, D. Garthwaite, A. Horsell, V. Jansen and I. Pedrosa-Rovira for comments and technical assistance, and Syngenta Bioline Bees for supplying colonies. The study was supported by the Insect Pollinator Initiative (funded under the auspices of the Living with Environmental Change programme, Biotechnology and Biological Sciences Research Council (BBSRC), Wellcome Trust, Scottish Government, Department for Environment, Food and Rural Affairs (DEFRA) and Natural Environment Research Council (NERC): grant BB/I000178/1).

**Author Contributions** R.J.G., O.R.-R. and N.E.R. carried out the experiment; R.J.G. and N.E.R. designed the experiment and wrote the paper; N.E.R. conceived the project.

**Author Information** Reprints and permissions information is available at [www.nature.com/reprints](http://www.nature.com/reprints). The authors declare no competing financial interests. Readers are welcome to comment on the online version of the paper. Correspondence and requests for materials should be addressed to R.J.G. ([richard.gill@rhul.ac.uk](mailto:richard.gill@rhul.ac.uk)) or N.E.R. ([nigel.raine@rhul.ac.uk](mailto:nigel.raine@rhul.ac.uk)).

## METHODS

**Experimental setup.** Each colony contained a queen and an average of four workers (range = 0–10) at the start of the experiment, reflecting the development stage of natural colonies when crops tend to flower in Europe<sup>31,32</sup>, and when most pesticide treatments are applied (March to June)<sup>33,34</sup>. We used a split block design to account for variation in colony size, developmental stage and potential seasonal variation between replicates (20 colonies in July, and 20 colonies in September: see Supplementary Information). For each replicate, colonies were ranked according to the number of workers and pupae, with the 4 highest-ranked (largest) colonies assigned to block 1, the next 4 highest ranked to block 2, and so on. Each replicate consisted of 5 blocks ( $n = 20$  colonies). Within each block the 4 treatments (control, I, LC and M) were randomly assigned among the 4 colonies. There was no significant difference among treatments in either the number of workers or pupae present at the start of the experiment (Supplementary Information). Colonies were provided a two-chambered nest box; the rear chamber housing the nest ('brood chamber') and front chamber used for pesticide exposure ('food chamber'; Supplementary Figs 1 and 6). Nest boxes were kept in the laboratory but connected to the outside environment through an outlet tube leading to an exit hole in the laboratory window, allowing natural foraging (for details see Supplementary Information and Supplementary Fig. 1). Between the outlet tube and nest box were three sections of transparent tubing allowing observation of bees as they left or entered nest boxes (Supplementary Fig. 2). Two RFID readers (Maja IV reader modules with optimized antenna for mic3 transponders: Microsensys GmbH) at the nest entrance allowed automatic monitoring of all tagged workers as they entered and left the colony with minimal disturbance to natural foraging patterns<sup>22</sup>.

**Pesticide treatment.** Bees were exposed to pesticide treatments in the food chamber using a gravity feeder placed on a Petri dish (90 mm diameter) lined with filter paper. The filter paper was sprayed with  $0.69 \pm 0.046$  ml of either control solution (control and I) or 37.5 p.p.m.  $\lambda$ -cyhalothrin solution (LC and M); the maximum label-guidance concentration for spray application to oilseed rape in the United Kingdom. The gravity feeder contained either a control sucrose solution (control and LC) or 10 p.p.b. imidacloprid sucrose solution (I and M). This concentration falls within the range found in the pollen and nectar of flowering crops visited by bees<sup>9,20,21,35–38</sup> (for details on pesticide selection and application see Supplementary Information and Supplementary Box 1). During the experiment the sucrose treatment was applied every 2 days (3 days over weekends) between 13:00 and 14:00 (Supplementary Table 2). Before refilling feeders we measured the volume of any remaining solution to calculate what the bees had collected ( $n = 12$  feeder replenishments per colony during the 28-day period). We provided 10 ml of sucrose treatment per application in week 1, with a 2-ml incremental increase in the volume of sucrose at the start of each subsequent week (week 2 = 12 ml, week 3 = 14 ml, week 4 = 16 ml) to reflect an increase in colony demand as they developed. The amount of sugar provided was less than each colony typically collects by nectar foraging<sup>39</sup>, ensuring that workers were motivated to forage for nectar and pollen outside.

Spray treatments were applied once at the start of each experimental week (Supplementary Table 2) using a new piece of filter paper for each application. This follows label guidance for the maximum application of  $\lambda$ -cyhalothrin to crops that recommends at least 7 days between spraying events and a maximum of 4 applications within the flowering season.

**Observations and measurements.** To monitor colony condition and development, colonies were inspected every day to assess the number of newly eclosed (callow) workers, the number of dead workers (removed and frozen ( $-20^\circ\text{C}$ )), and queen condition. Three days before the start of the experiment faecal samples from each queen were checked for the presence of three parasites: the trypanosome

*Crithidia bombi*, the microsporidian *Nosema bombi* and the neogregarine *Apicystis bombi*. This parasite assessment was repeated on the twenty-eighth experimental day using faecal samples from the queen (if present) and a subset of workers from each nest box (for details of parasite assessment see Supplementary Information).

To monitor foraging performance, all workers present at the start of the experiment (precise age unknown) were individually RFID tagged (for details see Supplementary Information), and during the experiment all newly produced workers were tagged within 3 days of eclosion (age known). Tagging stopped on the twenty-fourth day of the experiment because any workers emerging after this point were unlikely to become foragers<sup>40</sup>. In total, 854 workers were tagged, with each tag providing a unique (16-digit) code for unambiguous identification. We classified a foraging bout as a period of at least 5 minutes elapsing between a worker leaving and entering a colony. We also specified that workers must perform at least four foraging bouts to be considered a forager (for the rationale behind foraging rules see Supplementary Information).

Pollen foraging was observed in each colony for 1 hour per day (5 days a week) to record pollen foraging activity. Observation periods were always 2 h (at approximately 16:00) and 21 h (at approximately 10:00 the following day) after treatment application or renewal (Supplementary Table 2). We recorded the time that each tagged worker entered a colony (observing when it passed through the transparent tubes and under the RFID readers) using a stopwatch synchronised with the RFID (host) data logger. We scored the amount of pollen in the forager's corbiculae (pollen baskets) as small (score of 1), medium (score of 2) or large (score of 3) relative to the size of the worker.

Nest box entrances were closed after dark on the evening of the twenty-eighth experimental day. Each nest box, containing bees and brood, was placed in a freezer ( $-20^\circ\text{C}$ ). Window exits remained open for 18 h with each outlet tube connected to an individual bottle trap to catch any returning foragers. All tagged workers were identified and recently eclosed (untagged) workers were assumed to have developed in the colony they were found in. Worker thorax width was measured using digital callipers. All pupae and larvae were dissected from each nest, counted and weighed to provide final measures of brood development, and the nest structure was also weighed.

31. Thompson, H. M. Assessing the exposure and toxicity of pesticides to bumblebees (*Bombus* sp.). *Apidologie* **32**, 305–321 (2001).
32. Brittain, C. & Potts, S. G. The potential impacts of insecticides on the life-history traits of bees and the consequences for pollination. *Basic Appl. Ecol.* **12**, 321–331 (2011).
33. Garthwaite, D., Thomas, M. R., Parrish, G., Smith, L. & Barker, I. *Pesticide Usage Survey Report 224. Arable Crops in Great Britain 2008 (Including Aerial Applications 07–08)* (Food and Environmental Research Agency, 2008).
34. Garthwaite, D. et al. *Pesticide Usage Survey Report 235. Arable Crops in UK 2010 (Including Aerial Applications 2010)* (Food and Environmental Research Agency, 2010).
35. Bonmatin, J. M. et al. A LC/APCI-MS/MS method for analysis of imidacloprid in soils, in plants, and in pollens. *Anal. Chem.* **75**, 2027–2033 (2003).
36. Bonmatin, J. M. et al. Quantification of imidacloprid uptake in maize crops. *J. Agric. Food Chem.* **53**, 5336–5341 (2005).
37. Chauzat, M. P. et al. Influence of pesticide residues on honey bee (Hymenoptera: Apidae) colony health in France. *Environ. Entomol.* **38**, 514–523 (2009).
38. Krischik, V. A., Landmark, A. L. & Heimpel, G. E. Soil-applied imidacloprid is translocated to nectar and kills nectar-feeding *Anagyrus pseudococci* (Girault) (Hymenoptera: Encyrtidae). *Environ. Entomol.* **36**, 1238–1245 (2007).
39. Raine, N. E. & Chittka, L. The correlation of learning speed and natural foraging success in bumble-bees. *Proc. R. Soc. B* **275**, 803–808 (2008).
40. Goulson, D. *Bumblebees: Behaviour, Ecology and Conservation*. (Oxford Univ. Press, 2010).

# Intrinsically determined cell death of developing cortical interneurons

Derek G. Southwell<sup>1,2,3,†</sup>, Mercedes F. Paredes<sup>2,4</sup>, Rui P. Galvao<sup>2,†</sup>, Daniel L. Jones<sup>1,2</sup>, Robert C. Froemke<sup>5,†</sup>, Joy Y. Sebe<sup>2</sup>, Clara Alfaro-Cervello<sup>6,†</sup>, Yunshuo Tang<sup>2,3,7</sup>, Jose M. Garcia-Verdugo<sup>6</sup>, John L. Rubenstein<sup>8</sup>, Scott C. Baraban<sup>1,2</sup> & Arturo Alvarez-Buylla<sup>1,2</sup>

Cortical inhibitory circuits are formed by  $\gamma$ -aminobutyric acid (GABA)-secreting interneurons, a cell population that originates far from the cerebral cortex in the embryonic ventral forebrain. Given their distant developmental origins, it is intriguing how the number of cortical interneurons is ultimately determined. One possibility, suggested by the neurotrophic hypothesis<sup>1–5</sup>, is that cortical interneurons are overproduced, and then after their migration into cortex the excess interneurons are eliminated through a competition for extrinsically derived trophic signals. Here we characterize the developmental cell death of mouse cortical interneurons *in vivo*, *in vitro* and after transplantation. We found that 40% of developing cortical interneurons were eliminated through Bax (Bcl-2-associated X)-dependent apoptosis during postnatal life. When cultured *in vitro* or transplanted into the cortex, interneuron precursors died at a cellular age similar to that at which endogenous interneurons died during normal development. Over transplant sizes that varied 200-fold, a constant fraction of the transplanted population underwent cell death. The death of transplanted neurons was not affected by the cell-autonomous disruption of TrkB (tropomyosin kinase receptor B), the main neurotrophin receptor expressed by neurons of the central nervous system<sup>6–8</sup>. Transplantation expanded the cortical interneuron population by up to 35%, but the frequency of inhibitory synaptic events did not scale with the number of transplanted interneurons. Taken together, our findings indicate that interneuron cell death is determined intrinsically, either cell-autonomously or through a population-autonomous competition for survival signals derived from other interneurons.

We first characterized the developmental cell death of cortical interneurons by measuring the expression of the apoptotic marker, cleaved caspase-3, in mice in which neurons expressing GAD67 were labelled with green fluorescent protein (GFP; GAD67–GFP mice)<sup>9</sup> (Fig. 1a). The number of cleaved caspase-3-labelled neocortical GAD67–GFP neurons increased from postnatal days 1 to 5 (P1 to P5), reached a maximum at about P7, and declined towards zero by about P15 (Fig. 1b; analysis of variance (ANOVA),  $F = 84.0$  and  $P < 0.0001$ ). Most (75%) cleaved caspase-3-positive cells were observed between P7 and P11 (Fig. 1b), about 11–18 days after the cells were produced in the embryonic ventral forebrain<sup>10</sup>. The temporal profile of expression of cleaved caspase-3 in GAD67–GFP cells was similar to that observed across the total cellular population of the neocortex (Supplementary Fig. 2), which may preserve the relative sizes of different cellular populations<sup>11</sup>. Because the GAD67–GFP knock-in

decreases brain GABA content by about 20–40% (ref. 9), we examined whether this in turn affected cell death in GAD67–GFP mice. Across the entire cellular population of the neocortex, neither the temporal profile nor the extent of apoptosis was significantly different between GAD67–GFP mice and wild-type mice (Supplementary Fig. 3).

We next measured the GAD67–GFP population size during postnatal life and adulthood (Fig. 1c). The number of GAD67–GFP neurons reached a maximum at about P5 (mean  $\pm$  s.e.m.  $(1.65 \pm 0.03) \times 10^6$  cells), and then declined by about 40% during the period of interneuron cell death (Fig. 1b), reaching a stable size of  $(1.01 \pm 0.02) \times 10^6$  cells by P120 (mean; ANOVA,  $F = 32.1$  and  $P < 0.0001$ ). The developmental cell death of cortical interneurons depended on Bax function: at P7, when GAD67–GFP cell death reached a maximum in wild-type mice (Fig. 1b), GAD67–GFP cell death was nearly absent in  $Bax^{-/-}$ ; GAD67–GFP mutants<sup>12</sup> (Fig. 1d; Student's *t*-test,  $P = 0.0034$ ). Between P5 and P120 the cortical GAD67–GFP population did not decline in  $Bax$  mutants (Fig. 1e; ANOVA,  $F = 2.28$ ,  $P = 0.18$ ); at P120 the cortical interneuron population was 33% smaller in wild-type GAD67–GFP mice than in  $Bax^{-/-}$ ; GAD67–GFP littermates  $((1.02 \pm 0.04) \times 10^6$  cells versus  $(1.52 \pm 0.08) \times 10^6$  cells, respectively; Student's *t*-test,  $P = 0.0041$ ). In wild-type and  $Bax$  mutant mice, similar proportions of GAD67–GFP neurons were labelled by parvalbumin, somatostatin, neuropeptide Y and calretinin (Supplementary Fig. 4), indicating that Bax-dependent cell death occurred uniformly across neurochemically defined interneuron subtypes. These findings indicate that Bax-dependent programmed cell death eliminates roughly 40% of neocortical interneurons during postnatal life.

After characterizing neocortical interneuron cell death *in vivo*, we examined whether neocortical interneurons undergo a similar pattern of cell death *in vitro*. We placed interneuron precursors from the embryonic day 13.5 (E13.5) GAD67–GFP medial ganglionic eminence (MGE) onto P0 to P2 neocortical feeder layers<sup>13</sup> (Fig. 2a) and quantified the expression of cleaved caspase-3 at various time points (Fig. 2b). GAD67–GFP neurons underwent cell death *in vitro*, with expression of cleaved caspase-3 reaching a maximum at 13 days (Fig. 2c; ANOVA,  $F = 9.12$  and  $P < 0.0001$ ). Roughly 66% of cell death occurred between 11 and 15 days *in vitro* (DIV), at about which time the GAD67–GFP cell number declined by about 30% (Fig. 2d; ANOVA,  $F = 4.53$  and  $P = 0.0012$ ). As previously mentioned, *in vivo* most interneuron cell death occurred between P7 and P11, when the developing cells were similarly between 11 and 18 days old (Fig. 1b). Interneuron cell death thus manifests *in vitro*, with a temporal pattern resembling that observed *in vivo*.

<sup>1</sup>Neuroscience Graduate Program, University of California, San Francisco, California 94143, USA. <sup>2</sup>Departments of Neuroscience and Neurosurgery, and the Eli and Edythe Broad Center of Regeneration Medicine and Stem Cell Research, University of California, San Francisco, California 94143, USA. <sup>3</sup>Medical Scientist Training Program, University of California, San Francisco, California 94143, USA.

<sup>4</sup>Department of Neurology, University of California, San Francisco, California 94143, USA. <sup>5</sup>Department of Otolaryngology, Coleman Memorial Laboratory and W.M. Keck Foundation Center for Integrative Neuroscience, University of California, San Francisco, California 94143, USA. <sup>6</sup>Instituto Cavanilles, Universidad de Valencia, CIBERNED, Valencia 46071, Spain. <sup>7</sup>Biomedical Sciences Graduate Program, University of California, San Francisco, California 94143, USA. <sup>8</sup>Department of Psychiatry and the Eli and Edythe Broad Center of Regeneration Medicine and Stem Cell Research, University of California, San Francisco, California 94143, USA. <sup>†</sup>Present addresses: Department of Neurosurgery, Stanford University School of Medicine, Stanford, California 94305, USA (D.G.S.); Department of Molecular Biology, University of Oregon, Eugene, Oregon 97403, USA (R.P.G.); Molecular Neurobiology Program, The Helen and Martin Kimmel Center for Biology and Medicine at the Skirball Institute of Biomolecular Medicine, Departments of Otolaryngology, Physiology and Neuroscience, New York University School of Medicine, New York, New York 10016, USA (R.C.F.); Cambridge Centre for Brain Repair, Department of Clinical Neurosciences and Stem Cell Institute, University of Cambridge, Cambridge CB2 0PY, UK (C.A.-C.).

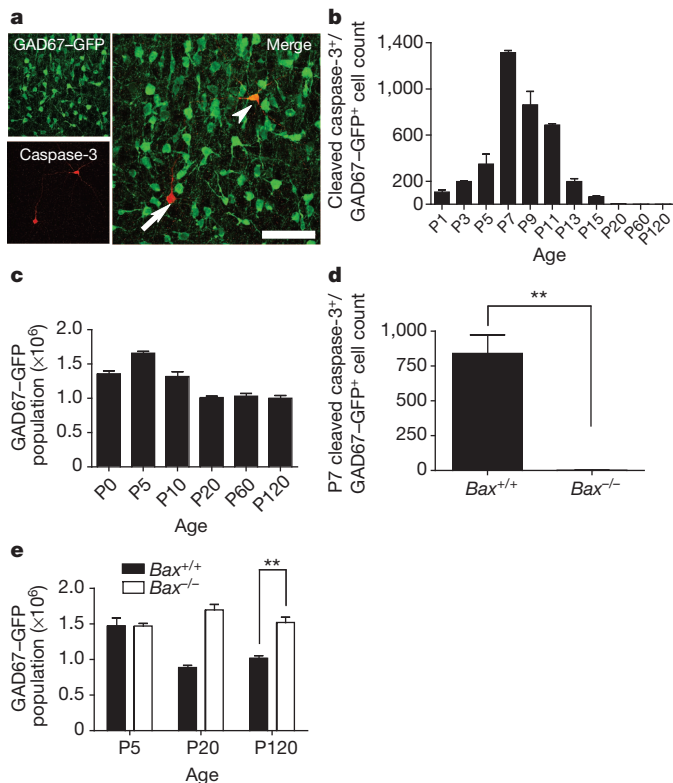


**Figure 1 | Bax-dependent programmed cell death eliminates 40% of developing interneurons from the postnatal mouse neocortex.** **a**, Expression of cleaved caspase-3 (red) observed in GAD67-GFP neurons (green; arrowhead) and other cell types (arrow) of the P7 neocortex. Scale bar, 100  $\mu$ m (left) and 50  $\mu$ m (right). **b**, Temporal profile of expression of cleaved caspase-3 in the neocortex of GAD67-GFP mice. Expression of cleaved caspase-3 is highest at P7, and declines to nearly undetectable levels by P15 (ANOVA,  $F = 84.00$  and  $P < 0.0001$ ;  $n = 3$  per time point). **c**, Temporal profile of the neocortical GAD67-GFP population size. Between P5 and P20, the neocortical GAD67-GFP population decreases by about 40% (ANOVA,  $F = 32.10$  and  $P < 0.0001$ ;  $n = 5$  per time point). **d**, The *Bax* mutation disrupts the developmental cell death of cortical interneurons. *Bax*<sup>-/-</sup> mice show a 99.8% decrease in the number of cells double labelled by cleaved caspase-3 and GAD67-GFP, compared with *Bax*<sup>+/+</sup>; GAD67-GFP littermates (Student's *t*-test;  $**P < 0.01$ ;  $n = 3$  per genotype). **e**, The neocortical GAD67-GFP population does not decrease in *Bax*<sup>-/-</sup> mice (ANOVA,  $F = 2.28$  and  $P = 0.18$ ). At P120, the neocortical GAD67-GFP population is roughly 33% smaller in wild-type mice (Student's *t*-test,  $**P < 0.01$ ;  $n = 3$  per genotype at each time point). All error bars represent s.e.m.

We next transplanted embryonic interneuron precursors into the postnatal neocortex during the period of endogenous interneuron cell death<sup>14,15</sup>. We postulated that, if the timing of interneuron cell death reflected the maturation of interneurons into a trophic signal-dependent state, transplanted interneuron precursors would undergo developmental cell death asynchronously from endogenous interneurons. We transplanted  $5 \times 10^5$  cells from the MGE of E13.5 to E14.5  $\beta$ -actin:GFP mice<sup>16</sup> into P3 wild-type recipients (Supplementary Fig. 5) and then quantified the expression of cleaved caspase-3 at various time points after transplantation. Given that mouse gestation ends at about E19, the transplanted interneuron precursors were roughly 6–10 days younger than their endogenous counterparts<sup>10</sup>. As described previously<sup>14,15,17</sup>, transplanted MGE cells dispersed in the recipient cortex, developed the morphological features of GABA-secreting interneurons (Supplementary Fig. 5) and formed synaptic contacts with recipient neurons (Supplementary Fig. 6). We did not observe labelling of the transplanted interneuron precursors by antigen Ki-67, indicating that the cells did not proliferate in the recipient (Supplementary Fig. 7). Expression of cleaved caspase-3 increased 200% in the transplanted

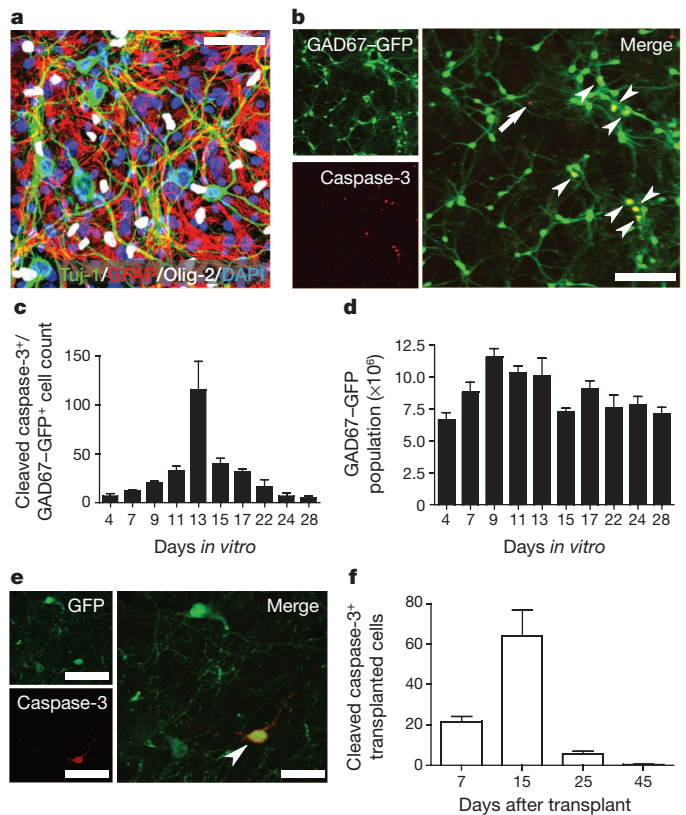


**Figure 2 | In vitro, and after heterochronic transplantation, interneuron precursors undergo programmed cell death during a period defined by their intrinsic cellular age.** **a**, Primary feeder layers prepared from P0 to P2 neocortex. At 14 DIV, the feeder layer contains neurons (Tuj-1, green), astrocytes (glial fibrillary acidic protein (GFAP), red) and oligodendrocytes (Olig-2, white). All cells are labelled by 4',6-diamidino-2-phenylindole (DAPI, blue). Scale bar, 50  $\mu$ m. **b**, At 14 DIV, double-labelled cells expressing cleaved caspase-3 (red) and GAD67-GFP (green; arrowheads) are observed along with cells singly labelled by cleaved caspase-3 (arrow). Scale bar, 200  $\mu$ m. **c**, Temporal profile of expression of cleaved caspase-3 in GAD67-GFP neuronal cultures. Expression of cleaved caspase-3 is highest at 13 DIV (ANOVA,  $F = 9.12$  and  $P < 0.0001$ ). **d**, Temporal profile of the GAD67-GFP population size *in vitro*. The GAD67-GFP population increases in number between 4 and 9 DIV, probably as a result of cell proliferation (see Methods), reaches a maximum size at about 9–11 DIV, and then declines by about 30% before reaching a stable size at about 17–22 DIV (ANOVA,  $F = 4.53$  and  $P < 0.01$ ). **e**, A transplanted interneuron precursor expressing cleaved caspase-3 (red) and  $\beta$ -actin:GFP (green; arrowhead) at 15 DAT. Scale bars, 50  $\mu$ m (left) and 25  $\mu$ m (right). **f**, Temporal profile of expression of cleaved caspase-3 in transplanted interneuron precursors. Cleaved caspase-3 is highest at 15 DAT, when the transplanted population reaches an intrinsic cellular age similar to that of endogenous interneurons during the peak of normal developmental cell death (Fig. 1b; ANOVA,  $F = 17.79$  and  $P < 0.0001$ ;  $n = 5$  per time point). All error bars represent s.e.m.

population between 7 and 15 days after transplantation (DAT), reached a maximum at 15 DAT, then declined to undetectable levels by 45 DAT (Fig. 2e, f; ANOVA,  $F = 17.79$  and  $P < 0.0001$ ). By contrast, in endogenous cells of the recipient neocortex, expression of cleaved caspase-3 reached a relative maximum at 7 DAT, then declined roughly 80% between 7 and 15 DAT (Supplementary Fig. 8; ANOVA,  $F = 401.20$  and  $P < 0.0001$ ). The addition of transplanted cells did not affect endogenous cell death, because expression of cleaved caspase-3 was similar between hemispheres that received transplanted cells and hemispheres that received injections of vehicle medium (Supplementary Fig. 8; Student's *t*-test,  $P = 0.76$  (7 DAT),  $P = 0.83$  (15 DAT),  $P = 0.89$  (25 DAT),  $P = 0.67$  (45 DAT)). Transplanted interneuron cell death thus reached a maximum at about 15 DAT, when the transplanted cells reached a cellular age equivalent to that of endogenous interneurons

during the peak of normal developmental cell death (Figs 1b and 2f). Taken together with the *in vitro* data (Fig. 2a–d), these findings suggest that interneuron cell death is timed by the intrinsic maturational state of the developing cells.

We also used heterochronic transplantation to introduce varying numbers of embryonic interneuron precursors into the neocortex. We expected that, if interneuron cell death were determined by intercellular competition for extrinsically derived signals, the amount of interneuron cell death would increase with larger transplant sizes. However, across initial transplant sizes that varied 200-fold ( $5 \times 10^3$ ,  $5 \times 10^4$ ,  $5 \times 10^5$  and  $10^6$  cells), similar fractions of the transplanted cells survived in the recipient neocortical hemisphere at 60 DAT ( $20.8 \pm 2.4\%$ ,  $22.2 \pm 1.4\%$ ,  $17.8 \pm 0.6\%$  and  $15.3 \pm 0.3\%$ , respectively; Fig. 3a; ANOVA,  $F = 0.34$  and  $P = 0.12$ ). When  $10^6$  or  $2 \times 10^6$  cells were transplanted, similar numbers of cells survived ( $(1.65 \pm 0.18) \times 10^5$  cells versus  $(1.53 \pm 0.01) \times 10^5$  cells, respectively; Student's *t*-test,  $P = 0.58$ ), suggesting that the neocortical hemisphere has a limited capacity for about  $1.6 \times 10^5$  additional interneurons. However, when the initial transplant size was far smaller than this theoretical limit, transplanted cell death still occurred, and it occurred at a constant rate. This finding indicates that interneuron cell death is not governed by competition for limited trophic signals derived from other cell types.

To further examine whether soluble neurotrophic signals regulate interneuron cell death, we studied the survival of mutant interneurons lacking the neurotrophin receptor, tropomyosin kinase receptor B (TrkB). We transplanted interneuron precursors from *TrkB*<sup>−/−</sup> donors<sup>18</sup> into P2 wild-type recipients and examined the survival of the cells at 60 DAT. The survival of transplanted *TrkB*<sup>−/−</sup> interneurons was similar to that of transplanted wild-type cells (Fig. 3b;  $(2.32 \pm 0.32) \times 10^4$  wild-type cells versus  $(2.20 \pm 0.20) \times 10^4$  *TrkB*<sup>−/−</sup> cells; Student's *t*-test,  $P = 0.75$ ), indicating that the cell death of transplanted interneurons is not governed by neurotrophin signalling through TrkB. This finding is consistent with other reports suggesting that the death of neurons in the central nervous system during development is regulated by mechanisms other than neurotrophin signalling<sup>6,19</sup>.

To confirm that transplanted interneuron cell death occurred through Bax-dependent apoptosis, we examined the survival of transplanted *Bax*<sup>−/−</sup> mutant cells<sup>12</sup>, and compared their survival with that of transplanted wild-type and *Bax*<sup>+/-</sup> cells. We pooled counts of wild-type and *Bax*<sup>+/-</sup> interneurons, because endogenous interneuron cell death was not disrupted in P20 *Bax*<sup>+/-</sup> GAD67–GFP mutants ( $(8.88 \pm 0.03) \times 10^5$  wild-type cells versus  $(9.63 \pm 0.04) \times 10^5$  *Bax*<sup>+/-</sup> cells; Student's *t*-test,  $P = 0.20$ ). At 60 DAT into P2 recipients, transplanted *Bax*-null interneurons survived in greater numbers than transplanted *Bax* heterozygous and wild-type interneurons (Fig. 3c;  $(4.31 \pm 0.21) \times 10^4$  *Bax*<sup>+/-</sup> and wild-type cells versus  $(9.11 \pm 1.63) \times 10^4$  wild-type cells; Student's *t*-test,  $P = 0.03$ ), indicating that the death of transplanted interneurons, like that of endogenous interneurons, occurs at least partly through a Bax-dependent mechanism.

While our transplantation experiments strongly suggested that interneuron cell death is not determined through competition for extrinsic survival signals, it was possible that the transplanted cells competed with endogenous cells, and the survival of the transplanted interneurons occurred at the expense of endogenous interneuron survival. To examine this possibility, we transplanted  $10^6$  β-actin:DsRed MGE cells<sup>20</sup> to one neocortical hemisphere of P2 to P3 GAD67–GFP recipients, and then compared the number of endogenous interneurons between the recipient and contralateral control hemispheres (Fig. 3d). As expected (Fig. 3a), we observed an average of roughly  $1.7 \times 10^5$  transplanted interneurons in the recipient cortical hemisphere at 60 DAT (Fig. 3e; mean  $(1.69 \pm 0.41) \times 10^5$  cells). In the recipient and control hemispheres we observed equal numbers of endogenous interneurons (Fig. 3e; mean endogenous cell count, recipient hemisphere =  $(4.81 \pm 0.12) \times 10^5$ ; mean endogenous cell count, control hemisphere =  $(5.04 \pm 0.15) \times 10^5$ ; Student's *t*-test,  $P = 0.28$ ), consistent with the findings presented in Supplementary

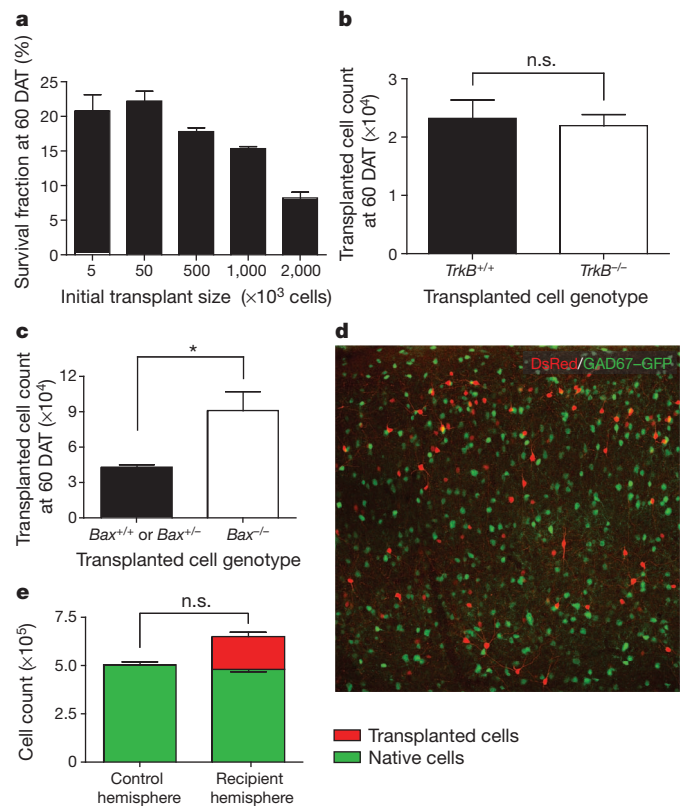


**Figure 3 | Transplanted interneuron cell death is not governed by competition for survival signals derived from other cell types in the recipient neocortex.** **a**, Over a broad range of transplant sizes (from  $5 \times 10^3$  to  $10^6$  cells), nearly constant fractions of the transplanted populations survive at 60 DAT (about 15–22%; ANOVA,  $F = 0.34$  and  $P = 0.12$ ;  $n = 6, 7, 3, 3$  per transplant size, respectively). When the initial transplant size is increased to  $2 \times 10^6$  cells, a smaller fraction of transplanted cells survives in the recipient neocortex (about 8%;  $n = 3$ ). **b**, Equal numbers of transplanted *TrkB*<sup>−/−</sup>;β-actin:GFP interneurons and *TrkB*<sup>+/+</sup>;β-actin:GFP interneurons survive in the recipient neocortex at 60 DAT (Student's *t*-test,  $P = 0.75$ ;  $n = 5$  per genotype). **c**, Transplanted cortical interneuron cell death occurs through a Bax-dependent mechanism. Greater numbers of *Bax*<sup>−/−</sup>;β-actin:GFP cortical interneurons survive in the recipient cortex at 60 DAT, compared with transplanted *Bax*<sup>+/+</sup>;β-actin:GFP and *Bax*<sup>+/-</sup>;β-actin:GFP cortical interneurons (Student's *t*-test;  $*P < 0.05$ ;  $n = 5$  for wild-type and *Bax*<sup>+/-</sup>;  $n = 6$  for *Bax*<sup>−/−</sup>). **d**, Transplanted β-actin:DsRed interneurons (red) and endogenous GAD67–GFP neurons (green) at 60 DAT (initial transplant size  $10^6$  cells; scale bar, 150 μm). **e**, At 60 DAT, transplanted DsRed-labelled interneurons increase the cortical interneuron population size by 34% (red) without affecting the endogenous GAD67–GFP population (green; Student's *t*-test,  $P = 0.28$ ;  $n = 3$ ). n.s., not significant. All error bars represent s.e.m.

Fig. 8, which indicated that transplantation did not affect the expression of cleaved caspase-3 in endogenous cells. The neocortex is thus able to support roughly 35% additional interneurons, with no effect on the endogenous interneuron population size. This suggests that developmental cell death does not tune the number of developing interneurons towards a cellular limit, as would occur if interneuron number were determined by the availability of limited, extrinsically derived survival signals.

Given that transplantation increases the number of interneurons in the neocortex, it offers a strategy for studying the relationship between interneuron number and cortical inhibition. To explore this relationship we transplanted varying numbers of interneuron precursors into P2 to P3 recipients, and then performed *in vitro* patch-clamp recordings on endogenous neocortical pyramidal neurons at 30–40 DAT. We recorded the amplitudes and frequencies of spontaneous inhibitory postsynaptic currents (sIPSCs; Fig. 4a) and then performed post-hoc quantification of transplanted interneuron cell densities.

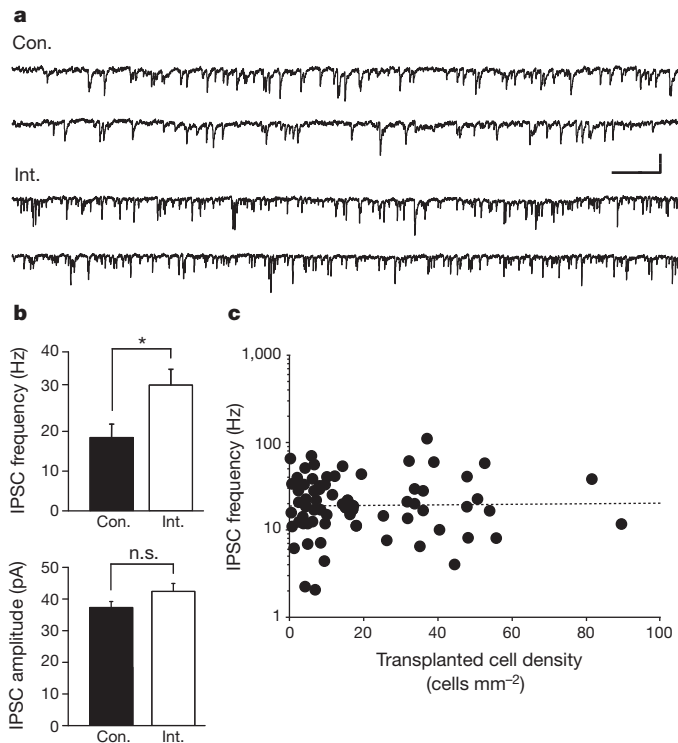


**Figure 4 | Interneuron population size is not a primary determinant of the level of functional cortical inhibition.** **a**, Representative traces of sIPSCs recorded from endogenous neocortical pyramidal neurons *in vitro* (top, control (medium vehicle (Con.); bottom, interneuron transplant recipient (Int)). Vertical scale bar, 40 pA; horizontal scale bar, 200 ms. **b**, Transplanted interneurons increase the frequency (top) but not the amplitude (bottom) of sIPSCs recorded at 30–40 DAT (Wilcoxon rank-sum test;  $*P < 0.05$  and  $P = 0.22$ , respectively;  $n = 23$  recorded cells from control animals,  $n = 37$  recorded cells from interneuron transplant recipients). The mean transplanted cell density for transplant recipient group was  $23.3 \pm 3.8$  cells mm<sup>-2</sup>. Error bars represent s.e.m. **c**, The frequency of sIPSCs onto host pyramidal neurons does not increase with the density of transplanted interneurons (linear regression analysis, slope = 0.0003,  $r^2 = 0.0003$ ).

Consistent with previous findings<sup>15,17</sup>, transplanted interneurons increased the frequency of sIPSCs onto endogenous pyramidal neurons (Fig. 4b; controls,  $18.4 \pm 3.4$  Hz; transplant recipients,  $31.7 \pm 3.9$  Hz; Wilcoxon rank-sum test,  $P = 0.02$ ). However, the amplitudes of inhibitory events were not significantly increased by transplantation (Fig. 4b; controls,  $37.3 \pm 1.9$  pA; transplant recipients,  $42.4 \pm 2.5$  pA; Wilcoxon rank-sum test,  $P = 0.22$ ). Inhibitory event frequencies did not increase with transplanted interneuron density (linear regression analysis, slope = 0.0003 and  $r^2 = 0.0003$ ; Fig. 4c). Thus, the extent of cortical inhibition is more likely to be determined by mechanisms that adjust synaptic strength and number, rather than mechanisms that govern interneuron population size. These findings indicate that transplantation can add a limited amount of new inhibition to the neocortex, and this limit is reached with transplanted cell numbers much smaller than that which the neocortex can support.

Our findings suggest that interneuron cell death is regulated by intrinsically defined mechanisms. When interneuron precursors were cultured *in vitro* or heterochronically transplanted, they died when they reached a cellular age equivalent to that of endogenous interneurons during the peak of endogenous interneuron cell death (Figs 1 and 2). This suggests that interneuron cell death is timed by the expression of a maturational program intrinsic to interneurons, rather than the developmental state of the cortex itself. Similarly, the extent of interneuron cell death seems to be intrinsically defined: across a range of transplant sizes, a constant fraction of the transplanted interneurons died in the recipient cortex, even when the transplant size was significantly below

the number of interneurons that the cortex could support (Fig. 3). Interneuron cell death is therefore unlikely to follow from intercellular competition for limiting survival signals derived from other cell types.

We propose two mechanisms that may govern the developmental cell death of cortical interneurons (Supplementary Fig. 1). In the first, which we refer to as ‘cell-autonomous’, interneuron cell death is intrinsically determined within each embryonic interneuron precursor. In this model, interneuron precursors would be individually destined to die in a manner independent from their interactions with other cell types. For example, the production of interneurons could occur with a certain rate of error<sup>21</sup> such that a fraction of defective interneuron precursors cannot survive past a certain cellular age. Similarly, a fixed fraction of interneuron precursors may be cell-autonomously programmed to die during a specific stage of their development. Alternatively, in a ‘population-autonomous’ mechanism, developing interneurons may require and compete for limiting survival signals produced by other isochronic interneurons. These neurotrophic signals, which may be obtained through cell–cell contact, synaptic transmission or neurotrophin signalling independent of TrkB, would be present in a quantity that scales to the number of isochronic developing interneurons. Either a cell-autonomous or population-autonomous mechanism could explain why cell death occurred at a constant rate across broad range of interneuron transplant sizes, and also why the survival of endogenous interneurons was not affected by the transplantation of additional interneurons.

Interneurons have a critical role in cortical physiology, and their dysfunction has been implicated in neurological disorders such as epilepsy, schizophrenia and Alzheimer’s disease<sup>22–24</sup>. The detailed examination of interneuron cell death is thus expected to yield new insights into cortical development, the pathophysiology of brain disorders and the therapeutic application of neuronal transplantation.

## METHODS SUMMARY

**Cell transplantation.** Interneuron precursor transplantation was performed as described previously<sup>14,15,17</sup>. For the transplantation of *TrkB* and *Bax* mutant cells (Fig. 3b, c), whole MGE explants were transplanted.

**In vitro cell culture, immunostaining and cell counts.** As described previously<sup>13</sup>, E13.5 GAD67–GFP MGE cells were added to feeder layers prepared from P0 to P2 CD1 mice. Immunostaining was then performed against the various markers at the specified time points. Cleaved caspase-3-positive cells and GAD67–GFP cells were counted under a standard fluorescence microscope.

**In vivo immunostaining and cell counts.** Floating sections were immunostained against the specified marker(s). Cell counts were made throughout the entire depth, rostrocaudal extent and mediolateral extent of the neocortex; cell counts were not made in other cortical areas such as the olfactory bulb, piriform cortex or hippocampus. Cleaved caspase-3-positive cells and transplanted GFP interneuron precursors (initial transplant sizes of less than  $10^5$  cells) were directly counted under a standard fluorescence microscope. To quantify larger populations (endogenous GAD67–GFP cells and initial transplant sizes of  $5 \times 10^5$  cells or more), design-based stereology was performed with StereoInvestigator (MicroBrightField).

**Electrophysiology and cell counts.** sIPSCs were recorded from layer 2/3 pyramidal cells in coronal slices prepared from recipient somatosensory cortex. All electrophysiology was performed with the experimenter blinded to the number of transplanted interneurons.

**Statistical analysis.** An analysis of variance was used to test for differences among three or more groups. A Student’s *t*-test was used to compare cell counts between two groups. A Wilcoxon rank-sum test and a linear regression analysis were used to analyse the sIPSC data. Statistical analyses were performed with Prism 4.0 (Graphpad) and Sigma Plot 12 (Systat Software).

**Full Methods** and any associated references are available in the online version of the paper.

Received 25 June 2009; accepted 17 August 2012.

Published online 7 October 2012.

- Buss, R. R., Sun, W. & Oppenheim, R. W. Adaptive roles of programmed cell death during nervous system development. *Annu. Rev. Neurosci.* **29**, 1–36 (2006).
- Oppenheim, R. W. Cell death during development of the nervous system. *Annu. Rev. Neurosci.* **14**, 453–501 (1991).

3. Hamburger, V. & Levi-Montalcini, R. Proliferation, differentiation and degeneration in the spinal ganglia of the chick embryo under normal and experimental conditions. *J. Exp. Zool.* **111**, 457–501 (1949).
4. Levi-Montalcini, R. The development of the acoustico-vestibular centers in the chick embryo in the absence of the afferent root fibers and of descending fiber tracts. *J. Comp. Neurol.* **91**, 209–241 (1949).
5. Boya, P. & De la Rosa, E. J. Cell death in early neural life. *Birth Defects Res.* **75**, 281–293 (2005).
6. Nikolettou, V. *et al.* Neurotrophin receptors TrkA and TrkB cause neuronal death whereas TrkB does not. *Nature* **467**, 59–64 (2010).
7. Polleux, F., Whitford, K. L., Dijkhuizen, P. A., Vitalis, T. & Ghosh, A. Control of cortical interneuron migration by neurotrophins and PI3-kinase signaling. *Development* **129**, 3147–3160 (2002).
8. Gorba, T. & Wahle, P. Expression of TrkB and TrkC but not BDNF mRNA in neurochemically identified interneurons in rat visual cortex *in vivo* and in organotypic cultures. *Eur. J. Neurosci.* **11**, 1179–1190 (1999).
9. Tamamaki, N. *et al.* Green fluorescent protein expression and colocalization with calretinin, parvalbumin, and somatostatin in the GAD67–GFP knock-in mouse. *J. Comp. Neurol.* **467**, 60–79 (2003).
10. Wonders, C. P. & Anderson, S. A. The origin and specification of cortical interneurons. *Nature Rev. Neurosci.* **7**, 687–696 (2006).
11. Sahara, S., Yanagawa, Y., O'Leary, D. D. M. & Stevens, C. F. The fraction of cortical GABAergic neurons is constant from near the start of cortical neurogenesis to adulthood. *J. Neurosci.* **32**, 4755–4761 (2012).
12. Knudson, C. M., Tung, K. S., Tourtellote, W. G., Brown, G. A. & Korsmeyer, S. J. Bax-deficient mice with lymphoid hyperplasia and male germ cell death. *Science* **270**, 96–99 (1995).
13. Xu, Q., Cobos, I., De la Cruz, E., Rubenstein, J. L. & Anderson, S. A. Origins of cortical interneuron subtypes. *J. Neurosci.* **24**, 2612–2622 (2004).
14. Wichterle, H., Garcia-Verdugo, J. M., Herrera, D. G. & Alvarez-Buylla, A. Young neurons from medial ganglionic eminence disperse in adult and embryonic brain. *Nature Neurosci.* **2**, 461–466 (1999).
15. Alvarez-Dolado, M. *et al.* Cortical inhibition modified by embryonic neural precursors grafted into the postnatal brain. *J. Neurosci.* **26**, 7380–7389 (2005).
16. Hadjantonakis, A., Gertenstein, M., Ikawa, M., Okabe, M. & Nagy, A. Generating green fluorescent mice by germline transmission of green fluorescent ES cells. *Mech. Dev.* **76**, 79–90 (1998).
17. Southwell, D. G., Froemke, R. C., Alvarez-Buylla, A., Stryker, M. P. & Gandhi, S. P. Cortical plasticity induced by inhibitory neuron transplantation. *Science* **327**, 1145–1148 (2010).
18. Galvao, R. P., Garcia-Verdugo, J. M. & Alvarez-Buylla, A. Brain-derived neurotrophic factor signaling does not stimulate subventricular zone neurogenesis in adult mice and rats. *J. Neurosci.* **28**, 13368–13383 (2008).
19. Silos-Santiago, I. *et al.* Severe sensory deficits but normal CNS development of newborn mice lacking TrkB and TrkC tyrosine protein kinase receptors. *Eur. J. Neurosci.* **9**, 2045–2056 (1997).
20. Vintersten, K. *et al.* Mouse in red: red fluorescent protein expression in mouse ES cells, embryos, and adult animals. *Genesis* **40**, 241–246 (2004).
21. Saunders, J. Death in embryonic systems. *Science* **154**, 604–612 (1966).
22. Cossart, R., Bernard, C. & Ben-Ari, Y. Multiple facets of GABAergic neurons and synapses: multiple fates of GABA signaling in epilepsies. *Trends Neurosci.* **28**, 108–115 (2005).
23. Marin, O. Interneuron dysfunction in psychiatric disorders. *Nature Rev. Neurosci.* **13**, 107–120 (2012).
24. Verret, L. *et al.* Inhibitory interneuron deficit links altered network activity and cognitive dysfunction in Alzheimer model. *Cell* **149**, 708–721 (2012).

**Supplementary Information** is available in the online version of the paper.

**Acknowledgements** We thank Y. Yanagawa for GAD67–GFP mice, L. Reichardt for *TrkB* mutant mice and R. Romero for technical contributions. D.G.S. and M.F.P. were supported by training grants from the California Institute for Regenerative Medicine. J.Y.S. was supported by a fellowship from the National Institute of Neurologic Disorders and Stroke (F32NS061497). This work was supported by the California Institute for Regenerative Medicine (A.A.-B., TR2-01749), the John G. Bowes Research Fund (A.A.-B.), the Spanish Ministry of Science and Innovation (J.M.G.-V., SAF-2008-01274), and the National Institutes of Health (J.L.R., S.C.B. and A.A.-B., R01 NS071785; A.A.-B., R01 NS048528).

**Author Contributions** D.G.S. and A.A.-B. devised experiments. D.G.S. performed all experiments, with the exception of the following: M.F.P. performed *in vitro* culture experiments and measurements of Ki67 labelling, R.P.G. collected cleaved caspase-3 counts in GAD67–GFP mice, C.A.-C. and J.M.G.-V. produced electron micrographs, Y.T. performed cell transplantations for the examination of Ki67 labelling, and D.L.J., J.Y.S. and R.F. performed electrophysiological recordings. D.G.S. and A.A.-B. wrote the manuscript.

**Author Information** Reprints and permissions information is available at [www.nature.com/reprints](http://www.nature.com/reprints). The authors declare no competing financial interests. Readers are welcome to comment on the online version of the paper. Correspondence and requests for materials should be addressed to D.G.S. ([dereksouthwell@gmail.com](mailto:dereksouthwell@gmail.com)) or A.A.-B. ([abuylla@stemcell.ucsf.edu](mailto:abuylla@stemcell.ucsf.edu)).

## METHODS

**Animals.** All protocols and procedures followed the guidelines of the Laboratory Animal Resource Center at the University of California, San Francisco. Neonatal GAD67–GFP mice were produced by crossing heterozygous GAD67–GFP (Aneo) mice<sup>9</sup> to wild-type C57Bl/6 mice. *Bax*<sup>−/−</sup>;GAD67–GFP mice were produced by crossing *Bax*<sup>+/-</sup> mice<sup>12</sup> to *Bax*<sup>−/−</sup>;GAD67–GFP mice. Embryonic donor tissue was produced by crossing CD-1 wild-type mice to homozygous,  $\beta$ -actin:GFP mice<sup>16</sup> and homozygous  $\beta$ -actin:Discosoma red fluorescent protein-expressing (DsRed) mice<sup>20</sup>. Adult C57Bl/6 and CD-1 breeder mice were obtained from Charles River Laboratories. *TrkB*<sup>−/−</sup>;GFP donor tissue was obtained from embryos produced by crossing *TrkB*<sup>+/-</sup> mice<sup>18</sup> to *TrkB*<sup>−/−</sup>;GFP mice. *Bax*<sup>−/−</sup>;GFP donor tissue was obtained from embryos produced by crossing *Bax*<sup>+/-</sup> mice<sup>12</sup> to *Bax*<sup>−/−</sup>;GFP mice. Adult C57Bl/6 and CD-1 breeder mice were obtained from Charles River Laboratories. *Bax*<sup>+/-</sup> mice were obtained from Jackson Laboratories. GAD67–GFP offspring were genotyped under an epifluorescence dissection microscope (Leica), while *Bax* mice and *TrkB* mice were genotyped by PCR. Unless noted, all cell transplantation experiments were performed with wild-type C57Bl/6 recipient mice. All mice were housed under identical conditions.

**Preparation of primary MGE cultures and feeder cell layers.** Primary cortical cultures were prepared as described previously<sup>13</sup>. The neocortex was dissected from P0 to P2 CD1 mice, macerated using fine forceps, then trypsinized in the presence of Leibovitz L-15 medium (University of California at San Francisco (UCSF) Cell Culture Facility) and DNase (1 U ml<sup>−1</sup>; Promega). The tissue was triturated with a pipette, and then resuspended in DMEM–F12 medium (UCSF Cell Culture Facility) containing 10% FBS (Hyclone). Cells (50 × 10<sup>3</sup>) were added to each well of eight-well chamber slides (70 mm<sup>2</sup>; BD Falcon) coated with polylysine (10 g ml<sup>−1</sup>) and laminin (5 g ml<sup>−1</sup>; UCSF Cell Culture Facility). Cultures were maintained at 37 °C in the presence of 5% carbon dioxide and ambient oxygen.

Medial ganglionic eminences were dissected from E13.5 GAD67–GFP embryos and mechanically dissociated in a solution of Leibovitz L-15 medium and DNase. The resultant cell suspension was then concentrated by brief centrifugation and placed in N5 medium (DMEM–F12 with glutamax, 100 × N2 supplement (Invitrogen)) containing DNase, bovine pituitary extract (35  $\mu$ g ml<sup>−1</sup>; Invitrogen), human epidermal growth factor (20 ng ml<sup>−1</sup>), human fibroblast growth factor-2 (20 ng ml<sup>−1</sup>; Preprotech) and 5% fetal bovine serum (Hyclone). The MGE cells were added to wells containing feeder layers grown for 24 h (5 × 10<sup>3</sup> cells per well). The cultures were thereafter maintained in Neurobasal/B27 medium (Invitrogen). We measured proliferation of the cultured neurons by immunostaining for the proliferative marker, phosphohistone H3 (pH3). At 4 DIV, 1.5 ± 0.9% of GAD67–GFP cells expressed pH3. Proliferation was nearly absent at later time points: 0.2 ± 0.2% of cells were pH3-positive at 14 DIV, and no pH3-positive cells were observed at 21 DIV.

**Cell transplantation.** The ventricular and subventricular layers of the MGE were dissected from E13.5 to E14.5 donor embryos. The time point when the sperm plug was detected was considered E0.5. Embryonic MGE explants were dissected in Leibovitz L-15 medium containing DNase I (100  $\mu$ g ml<sup>−1</sup>). Unless otherwise noted, the explants were mechanically dissociated into a single-cell suspension by repeated pipetting. The dissociated cells were then concentrated by centrifugation (3 min at 1,000g). For the transplantation of *TrkB* and *Bax* mutant interneuron precursors, whole MGE explants were directly transplanted. Concentrated cell suspensions (about 10<sup>3</sup> cells nl<sup>−1</sup>) or whole MGE explants were loaded into bevelled glass micropipettes (about 50  $\mu$ m tip diameter; Wiretrol 5  $\mu$ l; Drummond Scientific Company). Micropipettes were positioned at an angle of 35–45° from the vertical in a stereotactic injection apparatus. Recipient mice were anaesthetized by hypothermia and positioned in a clay head mould that stabilized the skull. The concentrated cell suspensions were injected into the neocortex at a depth of 700  $\mu$ m, as depicted in Supplementary Fig. 5. In the experiments described in Fig. 3d, e, the contralateral hemispheres received a control injection of L-15 containing DNase. After the injections were completed, transplant recipients were placed on a warm surface to recover from hypothermia. The mice were then returned to their mothers until they were perfused or weaned (P20).

**Immunostaining.** Cell cultures were fixed for 10 min in 4% paraformaldehyde, and immunostaining was performed directly in 8-well chamber slides. Mice were perfused transcardially with 4% paraformaldehyde; the brains were then removed, postfixed overnight in 4% paraformaldehyde and cryoprotected in 25% sucrose. Coronal brain sections were cut with a frozen sliding microtome. For immunostaining of cell cultures, tissue blocking and antibody incubations were performed with a solution of 2% BSA, 1% normal goat serum and 0.1% Triton X-100 in PBS. For immunostaining of floating sections, tissue blocking and antibody incubations were performed with a solution of 2% BSA, 8% normal goat serum and 0.5% Triton X-100 in PBS. Samples were blocked for 1 h at room temperature (20–24 °C), incubated overnight in primary antibody solutions at 4 °C, and incubated

for 2 h in secondary antibody solutions at room temperature. Immunostaining was performed with the following primary antibodies: chicken anti-GFP (dilution 1:500; Aves Labs), rabbit anti-cleaved caspase-3 (dilution 1:500; Cell Signaling Technologies), mouse anti-Tuj1 (1:500; Covance), mouse anti-GFAP (dilution 1:1,000; Millipore), rabbit anti-Olig-2 (dilution 1:1,500; Millipore), rabbit anti-phosphohistone H3 (dilution 1:750; Millipore) and rabbit anti-DsRed (dilution 1:500; Clontech). The following secondary antibodies were used for fluorescence labelling: Alexa Fluor 488 goat anti-chicken and Alexa Fluor 594 donkey anti-rabbit (Molecular Probes). For diaminobenzidine labelling, a peroxidase-conjugated goat anti-chicken secondary antibody was used (Sigma). Diaminobenzidine (DAB)-labelled sections were developed in 0.3% diaminobenzidine and 0.01% hydrogen peroxide for about 30 min. After the primary and secondary antibody incubations were finished, sections were washed four times in PBS. Floating sections were mounted on glass slides and covered with a coverslip.

**Cell quantification.** For cell counts *in vitro*, phosphohistone H3-positive cells, cleaved caspase-3-positive cells and GAD67–GFP cells were directly counted with an Olympus AX70 microscope with a ×20 objective. At each time point, cell counts were made in four separate wells. In each well, counts were obtained from five different fields. For cell counts *in vivo*, cells expressing cleaved caspase-3, GAD67–GFP cells and transplanted cells were counted in all layers of the entire neocortex. Cell counts were not performed in other areas of the cortex such as the olfactory bulb, piriform cortex or hippocampus. At all time points, only transplanted cells that expressed neuronal morphologies were counted. As described previously, the vast majority of cells transplanted from the E13.5 to E14.5 MGE exhibited neuronal morphologies in the recipient<sup>14,15,17</sup>. Cleaved caspase-3-positive cells and transplanted interneuron precursors (initial transplant sizes of 10<sup>5</sup> cells or less) were directly counted in every sixth coronal section (except for the counts of cleaved caspase-3 in transplant recipients, which were made in alternate coronal sections) with an Olympus AX70 microscope with a ×20 objective. The raw cell counts were then multiplied by the inverse of the section sampling frequency (6 or 2, respectively) to obtain an estimate of total cell number. To quantify populations of larger sizes (endogenous GAD67–GFP cells and initial transplant sizes of 5 × 10<sup>5</sup> cells or more), design-based stereology was performed on DAB-labelled sections (endogenous GAD67–GFP cells) or fluorescently labelled sections (transplanted cells) using an optical fractionator (StereoInvestigator; MicroBrightField) and a Nikon Eclipse microscope with a ×100 objective.

**Histological imaging.** Images were obtained with a confocal microscope (Leica SP5). Figures 1a, 2a, b, f, g and 3d depict flattened Z-series of confocal slices (Fig. 1a, six slices, 0.8  $\mu$ m per slice; Fig. 2a, b, five slices, 8  $\mu$ m per slice; Fig. 2f, ten slices, 1  $\mu$ m per slice; Fig. 2g, seven slices, 1.1  $\mu$ m per slice; Fig. 3d, nine slices, 1.2  $\mu$ m per slice). Images were adjusted for brightness and contrast with Adobe Photoshop CS3 (Adobe Systems).

**Electron microscopy.** Mice were perfused transcardially with 4% paraformaldehyde and 0.5% glutaraldehyde. The brains were removed, postfixed overnight in 4% paraformaldehyde, and cryoprotected in 25% sucrose. Coronal brain sections (50  $\mu$ m) were cut with a frozen sliding microtome and then freeze-thawed three times in methylbutane and solid CO<sub>2</sub>. Sections were washed in phosphate buffer (PB), blocked for 1 h at room temperature in 0.3% BSA (Aurion) in PB and incubated for 72 h at 4 °C in chicken anti-GFP (dilution 1:200) in PB. Sections were washed in PB and blocked in 0.5% BSA and 0.1% fish gelatin for 1 h at room temperature, and then incubated for 24 h at 4 °C in blocking solution plus 1:50 colloidal gold-conjugated anti-chicken secondary antibody (Aurion). Sections were washed in PB containing 2% sodium acetate at room temperature. Silver enhancement was performed in accordance with the manufacturer's instructions (Aurion), and sections were washed in 2% sodium acetate. To stabilize the silver particles, the sections were immersed in 0.05% gold chloride for 10 min at 4 °C and washed in sodium thiosulphate. Sections were then postfixed for 30 min in 2% glutaraldehyde at room temperature. Sections were contrast-enhanced in 1% osmium and 7% glucose, then embedded in Araldite. Semithin 1.5- $\mu$ m sections were prepared and selected using a light microscope before being re-embedded for ultrathin sectioning (70 nm). Electron micrographs were obtained under a Fei microscope (Tecnaï-Spirit) with a digital camera (Morada, Soft-imaging System).

**Electrophysiology.** Fluorescently labelled (GFP or DsRed) E13.5 MGE cells were transplanted into P2 to P3 wild-type C57Bl/6 recipients. The initial transplant size was varied from about 10<sup>3</sup> cells to 5 × 10<sup>5</sup> cells, to produce a recipient group that ranged with respect to the transplanted population size. Coronal brain slices (300  $\mu$ m thickness) were prepared from recipient mice at 30–40 DAT of either vehicle (L-15 medium) or MGE cells. Slices were perfused with carbogen-bubbled artificial cerebrospinal fluid containing (in mM): 124 NaCl, 3 KCl, 1.25 NaH<sub>2</sub>PO<sub>4</sub>·H<sub>2</sub>O, 2 MgSO<sub>4</sub>·7H<sub>2</sub>O, 26 NaHCO<sub>3</sub>, 10 dextrose and 2 CaCl<sub>2</sub>, and maintained at 33–34 °C. sIPSCs were recorded from layer 2/3 pyramidal cells in the somatosensory cortex with Clampex software (Molecular Devices) at a gain of 5 and a filter at 1 kHz. Patch electrodes (3–5 M $\Omega$ ) were filled with (in mM): 140

CsCl, 1 MgCl<sub>2</sub>, 10 HEPES, 11 EGTA, 2 NaATP, 0.5 Na<sub>2</sub>GTP and 1.25 QX-314. Pyramidal neurons were held at  $-60$  mV and bathed in  $25$   $\mu$ M DL-2-amino-5-phosphonopivalic acid (APV) and  $20$   $\mu$ M 6,7-dinitroquinoxaline-2,3-dione (DNQX) (Sigma) to block glutamate receptors. Gabazine ( $100$   $\mu$ M) was applied to the bath at the end of the experiment to confirm the inhibitory nature of recorded events. The series resistance was measured after each recording, and data were discarded if the resistance changed by more than 20%, or if the series resistance was found to be greater than  $20$  M $\Omega$ . MiniAnalysis software (Synaptosoft) was used to quantify sIPSC frequency and amplitude. All electrophysiology was performed with the experimenter blinded to the number of transplanted interneurons. After the recordings were completed, the slices were placed in 4%

paraformaldehyde overnight, postfixed in 25% sucrose, and then cut into  $50$ - $\mu$ m sections on a vibratome. The number of transplanted interneurons in the neocortex of a  $50$ - $\mu$ m slice was counted for each recipient. To obtain the cell density, the cell count was then divided by the area of neocortex in the coronal section.

**Statistical analysis.** The Student's *t*-test was used to compare cell counts between two groups. An analysis of variance was used to test for differences between three or more groups. With the exception of the electrophysiology experiments, all statistical analyses were performed with Prism 4.0 (Graphpad). The statistical analysis of the electrophysiology data was performed with Sigma Plot 12 (Systat Software). A Wilcoxon rank-sum test and linear regression analysis were used to analyse the sIPSC data.

# In vivo genome editing using a high-efficiency TALEN system

Victoria M. Bedell<sup>1\*</sup>, Ying Wang<sup>2\*</sup>, Jarryd M. Campbell<sup>1\*</sup>, Tanya L. Poshusta<sup>1</sup>, Colby G. Starker<sup>3</sup>, Randall G. Krug II<sup>1</sup>, Wenfang Tan<sup>3</sup>, Sumedha G. Penheiter<sup>1</sup>, Alvin C. Ma<sup>1,4</sup>, Anskar Y. H. Leung<sup>4</sup>, Scott C. Fahrenkrug<sup>3,5</sup>, Daniel F. Carlson<sup>3,5</sup>, Daniel F. Voytas<sup>3</sup>, Karl J. Clark<sup>1</sup>, Jeffrey J. Essner<sup>2</sup> & Stephen C. Ekker<sup>1</sup>

The zebrafish (*Danio rerio*) is increasingly being used to study basic vertebrate biology and human disease with a rich array of *in vivo* genetic and molecular tools. However, the inability to readily modify the genome in a targeted fashion has been a bottleneck in the field. Here we show that improvements in artificial transcription activator-like effector nucleases (TALENs) provide a powerful new approach for targeted zebrafish genome editing and functional genomic applications<sup>1–5</sup>. Using the GoldyTALEN modified scaffold and zebrafish delivery system, we show that this enhanced TALEN toolkit has a high efficiency in inducing locus-specific DNA breaks in somatic and germline tissues. At some loci, this efficacy approaches 100%, including biallelic conversion in somatic tissues that mimics phenotypes seen using morpholino-based targeted gene knockdowns<sup>6</sup>. With this updated TALEN system, we successfully used single-stranded DNA oligonucleotides to precisely modify sequences at predefined locations in the zebrafish genome through homology-directed repair, including the introduction of a custom-designed *EcoRV* site and a modified *loxP* (*mloxP*) sequence into somatic tissue *in vivo*. We further show successful germline transmission of both *EcoRV* and *mloxP* engineered chromosomes. This combined approach offers the potential to model genetic variation as well as to generate targeted conditional alleles.

Custom zinc finger nucleases (ZFNs)<sup>7–9</sup> and TALENs<sup>1–5</sup> have been used to introduce locus-specific double-stranded breaks in the zebrafish genome, generating dozens of mutant alleles<sup>10</sup>. Recent work has been facilitated by the relatively straightforward DNA base recognition cipher underlying TALEN technology<sup>11,12</sup>. However, the efficacy of previously described custom sequence-specific nucleases was limiting in some applications<sup>1–5,7–9</sup>. For example, standard TALENs using the pTAL scaffold<sup>13</sup> (Supplementary Fig. 1) targeting exon 2 of the zebrafish *ponzr1* locus<sup>14</sup> resulted in a measurable level of locus modification in somatic tissue (median value of 5%; Fig. 1b, c). This pTAL-*ponzr1* pair yielded 4 germline-transmitting founder animals carrying a mutation in *ponzr1* out of the 24 tested (Supplementary Fig. 3d). TALENs against a second locus (*crhr1*) using the pTAL scaffold yielded a modest rate of locus modification (<1%; Fig. 1b, c). These results are characteristic of the standard TALEN efficacy range, demonstrating room for improvement.

Multiple TALEN scaffold designs have been described<sup>13,15,16</sup>, including those with different amino- and carboxy-terminal truncations, diverse FokI nuclease linkers, and various nuclear localization sequences. To improve *in vivo* efficacy, we tested the GoldyTALEN scaffold (Supplementary Fig. 1 and Supplementary Fig. 2) in a messenger RNA expression vector backbone (pT3TS<sup>17</sup>) using DNA analysis that measures the loss of a restriction enzyme recognition sequence at the TALEN cut site (Fig. 1a). Using the same recognition domains in the GoldyTALEN scaffold, there is a sixfold increase in

somatic gene modification at the *ponzr1* locus (Fig. 1b, c and Supplementary Fig. 3b) over the pTAL scaffold. The germline modification rate was similarly increased when switching scaffolds, from 17% (4/24; pTAL-*ponzr1*; Supplementary Fig. 3d) to 71% (10/14; GoldyTALEN-*ponzr1*; Supplementary Fig. 3e). We also detected improved efficacy using a cell-free assay system with *in vitro*-translated TALEN protein and purified *ponzr1* PCR DNA (Fig. 1d). The GoldyTALENs against *crhr1* showed an increase in the genome modification rate, improving from <1% to 7% median cutting efficacy (Fig. 1b, c and Supplementary Fig. 3c). Sequence comparisons of pTAL and GoldyTALEN scaffolds in both loci demonstrate similar insertions or deletions (indels) at the cut site, which is diagnostic of non-homologous end joining (NHEJ) repair (Supplementary Fig. 3).

To further test the efficacy of the GoldyTALEN scaffold, we generated TALENs against three additional loci (*moesina*, also known as *msna*, *ppp1cab* and *cdh5*; Supplementary Fig. 4a). We observed efficient gene modification at each locus (5 out of 5 loci in total; Fig. 1 and Fig. 2a). In three instances, the mutagenesis efficiency ranged from 70 to 100% as demonstrated by loss of the restriction enzyme recognition sequence at the TALEN cut sites (Fig. 2a) and DNA sequence analyses (Supplementary Fig. 4b–d) of amplicons from pooled injected embryos. To determine the time course of the GoldyTALEN-induced changes, we examined restriction enzyme nuclease activity at 256-cell, 28 h post-fertilization (hpf) and 50 hpf stages. A majority of the DNA was modified by the 256-cell stage (Supplementary Fig. 5). Together, these results indicate early, efficient gene targeting in somatic tissues, including biallelic conversion in some animals. Somatic targeting efficacy using the GoldyTALEN scaffold compares favourably with previous TALEN scaffolds in zebrafish, with three out of five GoldyTALENs demonstrating as high or higher mutation frequency as any of the previously reported loci using the first generation TALEN systems<sup>1–5</sup>.

In response to the increased efficacy of the GoldyTALENs, we investigated whether injection of TALENs could recapitulate a known morpholino<sup>6</sup> loss of function phenotype. We conducted a dose-response curve of the *moesina*, *ppp1cab* and *cdh5* GoldyTALEN pairs, optimizing GoldyTALEN concentration to the number of embryos with biallelic changes, and per cent dead or malformed embryos (Supplementary Fig. 6). Embryos injected with either *cdh5* GoldyTALENs (Fig. 2d) or morpholinos<sup>18</sup> (Fig. 2c) showed similar vascular phenotypes: pronounced cardiac oedema (Fig. 2b, top panels), loss of patent lumens in the Tg(*flil-egfp*)<sup>19</sup> vasculature<sup>19</sup> (Fig. 2c, d, bottom panels), and loss of circulating Tg(*gata1:dsred*)<sup>sd2</sup> red blood cells<sup>20</sup> (Fig. 2c, d, bottom panels, and Supplementary Movies 1–3). A similar pericardial oedema phenotype was observed in F1 offspring from F0 *cdh5* founder incrosses (data not shown), suggesting specificity of the phenotype described in F0 fish to *cdh5* loss of function. Furthermore, *cdh5* GoldyTALEN-injected embryos have little or no Cdh5 protein

<sup>1</sup>Department of Biochemistry and Molecular Biology, Mayo Clinic, Rochester, Minnesota 55905, USA. <sup>2</sup>Department of Genetics, Development and Cell Biology, Iowa State University, Ames, Iowa 50011, USA. <sup>3</sup>Department of Genetics, Cell Biology and Development, the Center for Genome Engineering, and the Department of Animal Science, University of Minnesota, Minneapolis, Minnesota 55455, USA. <sup>4</sup>Department of Medicine, LKS Faculty of Medicine, the University of Hong Kong, Pok Fu Lam Road, Hong Kong. <sup>5</sup>Recombinetics, Inc., 2575 University Ave. West, Suite 100, Saint Paul, Minnesota 55114, USA.

\*These authors contributed equally to this work.

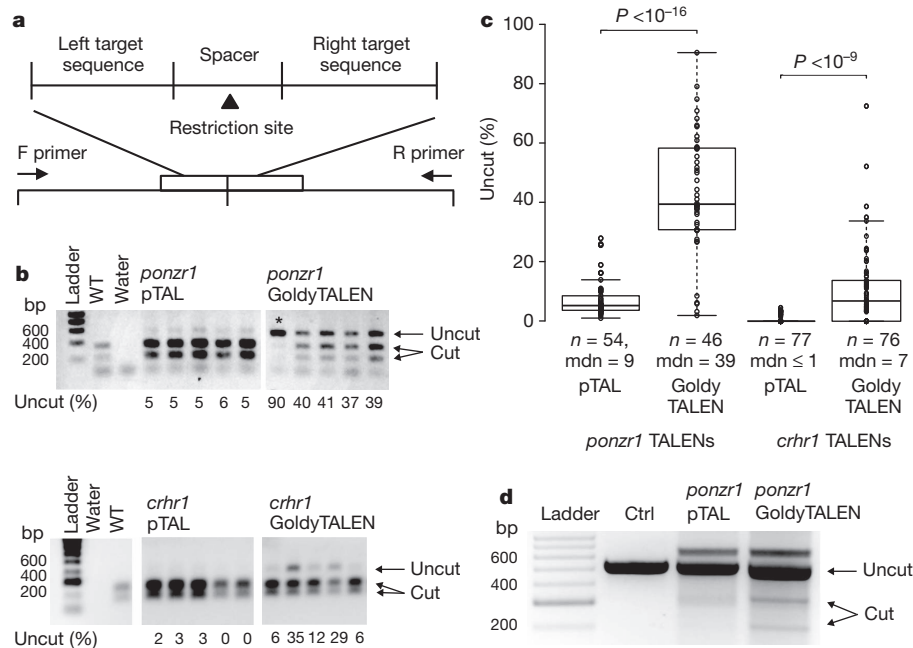


**Figure 1 | Second-generation GoldyTALEN scaffold improves genome-editing efficacy.** **a**, Schematic showing the layout of TALEN target sites. TALENs were targeted to flanking sequences surrounding a restriction enzyme site for easy screening through introduction of a restriction fragment length polymorphism. **b**, Relative activity of the GoldyTALEN and pTAL scaffolds at two loci, *ponzr1* and *crhr1*. Under each lane is the percent uncut DNA of a single larva, illustrating the increased activity of GoldyTALEN. WT, wild type.

**c**, Whisker plots of the percent uncut DNA demonstrates TALEN cutting efficiency at two loci. *ponzr1* TALENs demonstrate a significant ( $P < 10^{-16}$ ), sixfold increase in activity using GoldyTALEN. *crhr1* TALENs also demonstrate a significant ( $P < 10^{-9}$ ), 15-fold increase in activity. *n*, number of embryos screened; mdn, the median percent cut. **d**, The *ponzr1* GoldyTALENs were more active in a cell-free restriction enzyme digestion assay. *ponzr1* DNA is labelled in both uncut and cut forms. Ctrl, negative control.

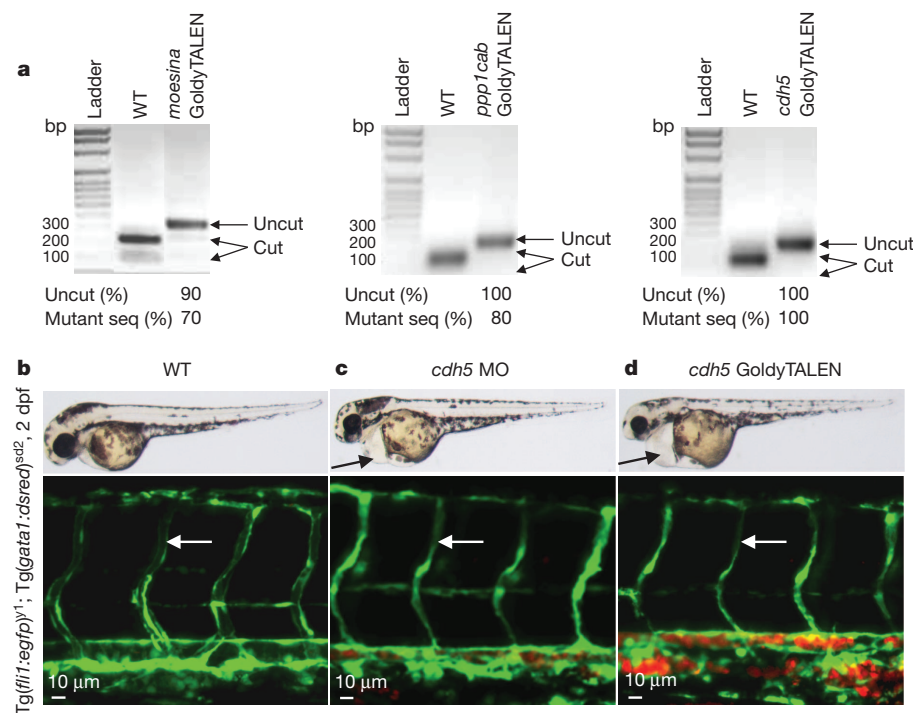


**Figure 2 | Increased TALEN efficiency results in biallelic gene targeting.** **a**, GoldyTALENs were designed against the *moesina*, *ppp1cab* and *cdh5* genes. All three gene targets contained a restriction enzyme site within the spacer region between the TALEN binding sites. Injection of GoldyTALEN mRNAs demonstrated a nearly complete loss of the restriction enzyme site in the amplicons of somatic tissue. Each lane is the amplification product from a group of 10 embryos. Mutant seq (%), percentage of amplicons that carry mutant sequences as determined by sequencing 10 clones (Supplementary Fig. 4). **b–d**, Injection of *cdh5* GoldyTALENs (**d**) phenocopies the morpholino-based

loss-of-function phenotype (**c**). Bright field images (top panels) show pronounced cardiac oedema (arrows) in both GoldyTALEN-injected (**d**) and morpholino-injected (**c**) larvae at 2 days post fertilization (dpf). Using the *Tg(fli1:egfp)<sup>y1</sup>* line, the intersomitic vessels were visualized (bottom panels) and show a loss of lumen formation (white arrow) in both the morpholino-injected (**c**) and GoldyTALEN-injected larvae (**d**). The *Tg(gata1:dsred)<sup>sd2</sup>* line revealed reduced circulation in GoldyTALEN- and morpholino-injected larvae, demonstrated by the increase in red fluorescence in the confocal images (see Supplementary Movies 1–3).

(Supplementary Fig. 7). Together, these results indicate that the GoldyTALEN platform can achieve efficient biallelic targeting recapitulating known loss-of-function phenotypes. Furthermore, these data demonstrate that GoldyTALENs have the potential to be a complementary, but distinct, approach to morpholino-based somatic phenotype assessment.

The biallelic GoldyTALEN-injected fish were raised to assess germline mutation transmission. The *moesina*, *ppp1cab* or *cdh5* F0 founders were outcrossed. Ten pooled F1 embryos were screened and showed a 9 to 55% locus mutation frequency (Supplementary Fig. 8a–c). From two founder F0 outcrosses per locus, 10 individual F1 embryos were sequenced with mutant alleles identified in 20% to 100% of the F1 offspring (Supplementary Fig. 8). Furthermore, in two out of three of these loci we detected germline mosaicism, indicating several independent repair events. These data indicate that the efficient somatic TALEN targeting is effectively passed through the germline.

Recent *in vitro* work demonstrates that single-stranded DNA (ssDNA) can be an effective donor for homology-directed repair (HDR)-based genome editing at a ZFN-induced double-stranded break<sup>21,22</sup>. With the highly efficient genome modification success of GoldyTALENs, we hypothesized that synthetic oligonucleotides designed to span the predicted TALEN cut site could serve as a template for HDR *in vivo* (Fig. 3). Using *ponzr1* as a test locus, we introduced an *EcoRV* restriction site by co-injection of *ponzr1* GoldyTALENs and a ssDNA oligonucleotide (Fig. 3a). In these experiments, 42 out of 74 injected embryos had a detectable level of chromosomes containing the introduced *EcoRV* sequence with an estimated 9% ratio of converted chromosomes in these animals (Supplementary Fig. 9a). Sequence analysis indicated two precisely modified chromosome events from different larvae (Supplementary Fig. 9b) demonstrating successful somatic HDR at the *ponzr1* locus. Other events show precise addition at the 3' end while small indels were noted at the 5' side of the modification site (Supplementary Fig. 9b). Several homology arm lengths were tested for the highest HDR signal. In this experimental approach, an increase in homology arm length that spanned the TALEN binding site decreased the frequency of HDR events (Supplementary Table 1).

To test whether the HDR sequence modification was stably maintained in zebrafish somatic tissue, fin biopsies from 2-month-old fish were assayed for addition of the *EcoRV* sequence at the *ponzr1* locus. Out of 186 fish, 8 showed a visible incorporation of *EcoRV* (Supplementary Fig. 9c). To determine whether a lack of somatic *EcoRV* incorporation also indicated a lack of germline incorporation, 13 randomly selected fish with *EcoRV*-negative fin biopsies were outcrossed. The offspring from all 13 adults were negative for *EcoRV* incorporation at the *ponzr1* locus (clutch sizes ranged from 16 to 96 embryos). Therefore, fin-biopsy-positive fish were prioritized for determining germline transmission. Outcross embryos from three out of four fin-tissue-positive fish yielded clutches with introduction of the *EcoRV* site at the *ponzr1* locus (Fig. 3b). Two out of three of these germline fish demonstrated precise *EcoRV* addition (Fig. 3c).

We next asked whether TALEN/oligonucleotide co-injection could introduce larger sequences such as a *loxP* site, an essential step in making Cre-dependent conditional genetic alleles. We used TALENs against an intron in the *crhr2* gene and a ssDNA oligonucleotide were used to add a modified *loxP*<sup>IT217</sup> (*mloxP*)<sup>23</sup> site at this location (Fig. 4a). PCR analysis demonstrates somatic introduction of the *mloxP* sequence at the *crhr2* TALEN cut site (Supplementary Fig. 10a). Sequence characterization confirmed integration of the *mloxP* site in three assayed somatic chromosomes (Supplementary Fig. 10b). A similar method was used to introduce an *mloxP* sequence at the *ponzr1* locus (Supplementary Fig. 11a). Sequencing confirmed precise somatic addition at this locus (Supplementary Fig. 11b, c).

Maintenance of somatic *mloxP*-modified *crhr2* chromosomes by fin biopsy was used to identify germline transmission of the *mloxP* sequence. Positive chromosomes were detected by quantitative PCR in 20 out of 53 animals (Supplementary Fig. 10a). Embryos were

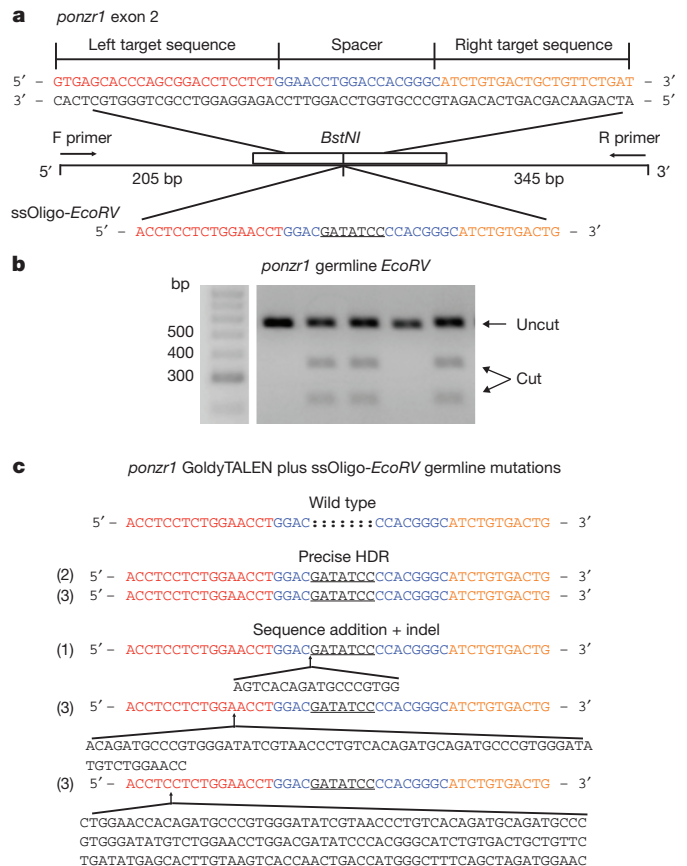


**Figure 3 | Targeted genome editing using GoldyTALENs.** **a**, A schematic of the *ponzr1* locus with the ssDNA sequence used to introduce a targeted exogenous *EcoRV* sequence (underlined, note the extra C added to make the sequence mutagenic) into the genome *in vivo*. The left and right TALEN binding sites are shown in red and orange, respectively, and the spacer region is in blue. **b**, A representative gel from founder fish no. 2 demonstrating germline transmission of the HDR-based *EcoRV* sequence. Three out of four fin-tissue-positive fish demonstrated germline transmission of the *EcoRV* sequence. **c**, Sequence analysis of the three germline-transmitting lines. The first fish transmitting HDR-based genome changes through the germline (1) yielded 7 out of 96 embryos with an incorporated *EcoRV* site. The genomes of all 7 embryos showed the same modified sequence. The second founder fish (2) yielded 7 out of 46 embryos with *EcoRV* incorporation. All 7 embryos showed precise HDR-based addition of the *EcoRV* sequence. The third fish with germline transmission (3) yielded 5 out of 18 embryos with an incorporated *EcoRV* site, and showed a mosaic germline as demonstrated by offspring with three different modified sequences. One embryo included precise HDR-based *EcoRV* addition. The other 4 embryos contained sequence insertions on the 5' end with two embryos each harbouring the specific sequences changes.

obtained from 16 of the somatic-positive fish as well as 42 fish that had not been pre-screened by PCR. Both groups transmitted HDR events through the germline (Fig. 4b). However, no significant enrichment for probable germline transmitting animals was noted, perhaps owing to the less stringent PCR assay than that used for *ponzr1*. In total, 6 out of 58 injected animals transmitted *mloxP*-modified chromosomes through the germline at the *crhr2* locus (Fig. 4b). Sequence confirmation of three of these fish demonstrated a precise HDR event as well as other, non-precise events (Fig. 4c).

Here, we focused on local genome-editing changes induced by TALENs, especially those induced by HDR. However, more complete analyses will be required to assess any off-target effects of TALENs or ssDNA-based HDR. Whole-genome sequencing on germline-transmitting fish from different parental lines would be particularly instructive. Should this analysis demonstrate off-target mutations, TALENs using obligate heterodimer-based nuclease fusions have

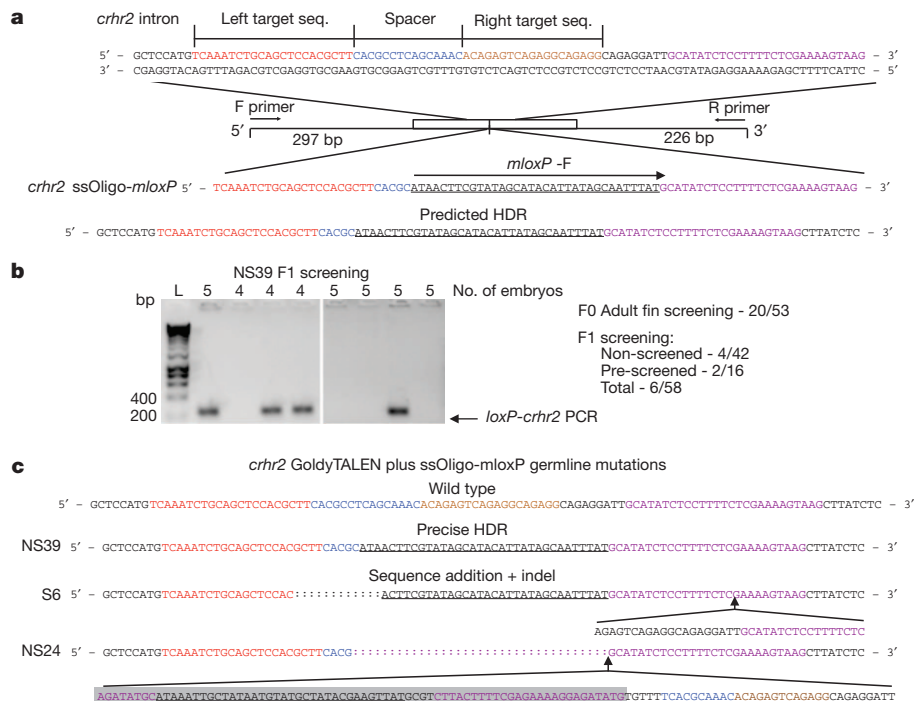


**Figure 4 | Germline *mloxP* integration into the *crhr2* locus.** **a**, A diagram of the TALEN target sites with the *mloxP* ssDNA oligonucleotide. The left and right TALEN target sequences are red and orange, respectively, the spacer region is blue, and the right homology arm of the oligonucleotide is in purple. The *mloxP* sequence is underlined. **b**, Germline screening of the *crhr2* locus. 53 adult fish were pre-screened via fin biopsy. Of those pre-screened, 20

demonstrated *mloxP* maintenance. A total of 16 F0 fish were outcrossed with 2 showing germline transmission. A total of 42 unscreened F0 fish were outcrossed and 4 demonstrated germline transmission. **c**, Sequence confirmation of three *mloxP* germline fish. One fish demonstrated precise germline HDR whereas two showed indels. In NS24, the reverse complement of the *mloxP* was noted (shaded in grey).

recently been reported as an alternative approach<sup>3,5,24</sup>. Using obligate heterodimers in the GoldyTALEN scaffold is one future method for potentially optimizing HDR-directed gene-editing specificity.

To our knowledge, these results represent the first description of successful HDR in zebrafish and the first demonstration of HDR using ssDNA as a donor template *in vivo*. This approach complements the error-prone NHEJ toolkit for model organisms (Fig. 5). The use of ssDNA facilitates an array of genome changes, including the introduction of single-nucleotide polymorphisms for vertebrate genetic applications. The asymmetry in precise editing suggests an additional mechanism for genome editing that incorporates both HDR and NHEJ (Fig. 5). For example, the donor ssDNA may serve as a primer for new strand synthesis at the TALEN break. Extension from the 3' end of the oligonucleotide would create long regions of homology for recombination. However, the 5' end of the oligonucleotide limits the extent of strand invasion and a limited opportunity for HDR. This leads to 5' end resolution by either HDR or NHEJ. For applications

where new sequences are introduced into non-coding genomic regions, such as the introduction of *loxP* sites into intronic sequences, either event will probably be of high utility.

Using the zebrafish, we report an updated TALEN system for use in genome modification and functional genomic applications. The high efficacy enables new approaches, including somatic gene targeting for reverse genetics applications. Furthermore, we show that synthetic ssDNA oligonucleotides can be used with this TALEN system for genome editing, including the precise introduction of exogenous DNA sequence at a specific locus. Although deployed here in zebrafish, this approach has the potential to be effective for *in vivo* applications in a wide array of model organisms.

## METHODS SUMMARY

TALENs were assembled via the GoldenGate method<sup>13</sup>. For ease of analysis, TALEN recognition sequences flanked a unique restriction site within the targeted gene. TALEN repeat variable di-residues (RVDs) were cloned into a pT3TS<sup>17</sup>-driven TALEN scaffold, and mRNA was injected into single-cell zebrafish embryos. The injected larvae were either molecularly tested or raised for germline mutation analysis. Somatic and germline TALEN-induced mutations were evaluated via PCR and restriction fragment length polymorphisms. To induce HDR events, single-stranded DNA oligonucleotides with either an *EcoRV* or *mloxP* site were designed with short homology arms around a TALEN target site and were injected into one-cell zebrafish embryos. PCR analysis of modified loci was used to detect the resulting somatic and germline HDR events.

**Full Methods** and any associated references are available in the online version of the paper.

Received 3 May; accepted 6 September 2012.

Published online 23 September 2012.

- Huang, P. *et al.* Heritable gene targeting in zebrafish using customized TALENs. *Nature Biotechnol.* **29**, 699–700 (2011).
- Sander, J. D. *et al.* Targeted gene disruption in somatic zebrafish cells using engineered TALENs. *Nature Biotechnol.* **29**, 697–698 (2011).

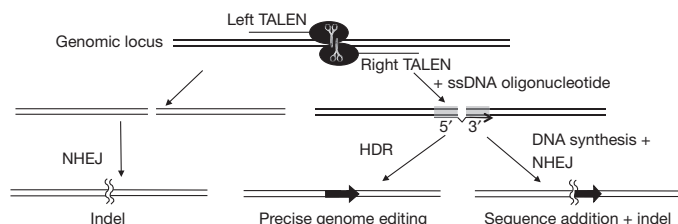


**Figure 5 | In vivo TALEN-induced genome editing outcomes.** TALENs efficiently create double-stranded breaks in chromosomal DNA and catalyse three major outcome classes. First, error-prone NHEJ produces an indel in and near the spacer region of the TALEN binding site. If a complementary ssDNA oligonucleotide is also added, two different outcomes are noted. First, HDR precisely uses the exogenous sequence information in the ssDNA to add sequence at the cut site. Alternatively, ssDNA acts as a primer for 3' integration of the oligonucleotide but the 5' end undergoes error-prone NHEJ<sup>22</sup>.

3. Cade, L. *et al.* Highly efficient generation of heritable zebrafish gene mutations using homo- and heterodimeric TALENs. *Nucleic Acids Res.* **40**, 8001–8010 (2012).
4. Moore, F. E. *et al.* Improved somatic mutagenesis in zebrafish using transcription activator-like effector nucleases (TALENs). *PLoS ONE* **7**, e37877 (2012).
5. Dahlem, T. J. *et al.* Simple methods for generating and detecting locus-specific mutations induced with TALENs in the zebrafish genome. *PLoS Genet.* **8**, e1002861 (2012).
6. Nasevicius, A. & Ekker, S. C. Effective targeted gene 'knockdown' in zebrafish. *Nature Genet.* **26**, 216–220 (2000).
7. Doyon, Y. *et al.* Heritable targeted gene disruption in zebrafish using designed zinc-finger nucleases. *Nature Biotechnol.* **26**, 702–708 (2008).
8. Meng, X., Noyes, M. B., Zhu, L. J., Lawson, N. D. & Wolfe, S. A. Targeted gene inactivation in zebrafish using engineered zinc-finger nucleases. *Nature Biotechnol.* **26**, 695–701 (2008).
9. Foley, J. E. *et al.* Rapid mutation of endogenous zebrafish genes using zinc finger nucleases made by Oligomerized Pool Engineering (OPEN). *PLoS ONE* **4**, e4348 (2009).
10. Lawson, N. D. & Wolfe, S. A. Forward and reverse genetic approaches for the analysis of vertebrate development in the zebrafish. *Dev. Cell* **21**, 48–64 (2011).
11. Moscou, M. J. & Bogdanove, A. J. A simple cipher governs DNA recognition by TAL effectors. *Science* **326**, 1501 (2009).
12. Boch, J. *et al.* Breaking the code of DNA binding specificity of TAL-type III effectors. *Science* **326**, 1509–1512 (2009).
13. Cermak, T. *et al.* Efficient design and assembly of custom TALEN and other TAL effector-based constructs for DNA targeting. *Nucleic Acids Res.* **39**, e82 (2011).
14. Bedell, V. M. *et al.* The lineage-specific gene *ponzr1* is essential for zebrafish pronephric and pharyngeal arch development. *Development* **139**, 793–804 (2012).
15. Miller, J. C. *et al.* A TALE nuclease architecture for efficient genome editing. *Nature Biotechnol.* **29**, 143–148 (2011).
16. Mussolino, C. *et al.* A novel TALE nuclease scaffold enables high genome editing activity in combination with low toxicity. *Nucleic Acids Res.* **39**, 9283–9293 (2011).
17. Hyatt, T. M. & Ekker, S. C. Vectors and techniques for ectopic gene expression in zebrafish. *Methods Cell Biol.* **59**, 117–126 (1998).
18. Wang, Y. *et al.* Moesin1 and Ve-cadherin are required in endothelial cells during *in vivo* tubulogenesis. *Development* **137**, 3119–3128 (2010).
19. Lawson, N. D. & Weinstein, B. M. *In vivo* imaging of embryonic vascular development using transgenic zebrafish. *Dev. Biol.* **248**, 307–318 (2002).
20. Traver, D. *et al.* Transplantation and *in vivo* imaging of multilineage engraftment in zebrafish bloodless mutants. *Nature Immunol.* **4**, 1238–1246 (2003).
21. Chen, F. *et al.* High-frequency genome editing using ssDNA oligonucleotides with zinc-finger nucleases. *Nature Methods* **8**, 753–755 (2011).
22. Radecke, S., Radecke, F., Cathomen, T. & Schwarz, K. Zinc-finger nuclease-induced gene repair with oligodeoxynucleotides: wanted and unwanted target locus modifications. *Mol. Ther.* **18**, 743–753 (2010).
23. Thomson, J. G., Rucker, E. B. III & Piedrahita, J. A. Mutational analysis of *loxP* sites for efficient Cre-mediated insertion into genomic DNA. *Genesis* **36**, 162–167 (2003).
24. Doyon, Y. *et al.* Enhancing zinc-finger-nuclease activity with improved obligate heterodimeric architectures. *Nature Methods* **8**, 74–79 (2011).

**Supplementary Information** is available in the online version of the paper.

**Acknowledgements** State of Minnesota grant H001274506 to S.C.E. and D.F.V.; NIH GM63904 to S.C.E.; NIH grant P30DK084567 to S.C.E. and K.J.C.; NIH grant DK083219 to V.M.B.; Mayo Foundation; NIH DA032194 to K.J.C.; NIH grant R41HL108440 to D.F.C. and S.C.F.; NIH grant GM088424 to J.J.E.; NSF grant DBI0923827 to D.F.V.; General Research Fund (HKU771611, HKU771110, HKU769809M) from the Research Grant Council, The University of Hong Kong and the Tang King Yin Research Fund to A.C.M. and A.Y.H.L. We thank G. Davis for discussion on ssDNA use with custom restriction enzymes, H. J. Fadel for *in vitro* RNA synthesis, and S. Westcot for comments on this manuscript. We thank G. Moulder for help in DNA analyses and members of the Mayo Clinic Zebrafish Core Facility for excellent animal care.

**Author Contributions** W.T. designed and constructed full-length pT3TS-Tal vectors targeting *Danio rerio chr1* and *chr2* against exon sequences provided by K.J.C.; D.F.C. and S.C.F. designed and produced the pT3TS-Tal and GoldyTALEN cloning vectors. D.F.C. synthesized *chr1* and *chr2* TALEN mRNA from the pT3TS-Tal vectors. C.G.S. designed and assembled *ponzr1* TALENs and transferred TAL repeats from original *chr1* and *chr2* TALEN vectors into GoldyTALEN. T.L.P. and K.J.C. did initial *chr1* TALEN microinjections. T.L.P. performed initial characterization of *chr1* mutagenesis efficiency by PCR and restriction fragment length polymorphism analysis. T.L.P. and K.J.C. microinjected *chr2* TALEN and *loxP* oligonucleotides. T.L.P. performed initial characterization by PCR demonstrating *loxP* integration. R.G.K. fully characterized efficiency and sequence of somatic *loxP* insertions in the *chr2* locus. K.J.C. screened adult fin clips for *mloxP* integrations into *chr2*. T.L.P. screened F1 offspring for *mloxP* integrations into *chr2* and together with J.M.C. cloned and sequenced integration events. K.J.C. designed experiments associated for *chr1* and *chr2* modification. K.J.C. selected *loxP* mutant JTZ17 for integration. A.C.M. developed initial zebrafish genetic testing, TALEN cell-free assays, and ssDNA HDR protocols. S.G.P. conducted the cell-free TALEN endonuclease assay. A.Y.H.L. contributed to the design of initial TALEN and ssDNA HDR experiments. Y.W. and J.J.E. conducted biallelic conversion TALEN experiments in somatic and germline tests. D.F.V. and S.C.E. initiated the strategy to use custom restriction enzymes for genome editing in zebrafish. S.C.E. developed the plan for HDR targeting using ssDNAs, conducted overall project design and data analysis, and wrote the initial manuscript text. All authors contributed to manuscript composition. V.M.B. and J.M.C. conducted *ponzr1* and *chr1* TALEN scaffold comparison experiments. V.M.B. and K.J.C. designed ssDNA oligonucleotides for HDR experiments. V.M.B. and J.M.C. injected and screened the *EcoRV* and *mloxP* HDR experiments at the *ponzr1* locus. J.M.C. ran quantitative data assessments and statistical analyses. V.M.B. and J.M.C. made first drafts and legends of Figs 1, 3 and 5. V.M.B. and J.M.C. conducted fin biopsy analyses of the *ponzr1* locus. V.M.B. completed the analysis of *ponzr1* germline transmission with assistance from J.M.C.

**Author Information** Reprints and permissions information is available at [www.nature.com/reprints](http://www.nature.com/reprints). The authors declare competing financial interests: details are available in the online version of the paper. Readers are welcome to comment on the online version of the paper. Correspondence and requests for materials should be addressed to S.C.E. ([ekker.stephen@mayo.edu](mailto:ekker.stephen@mayo.edu)).

## METHODS

**TALEN design.** The software developed by the Bogdanove laboratory (<https://boglab.plp.iastate.edu/node/add/taLEN>) was initially used to find candidate binding sites as described<sup>13</sup>. Three criteria were used for TALEN design. First, TALEN binding sites were selected that ranged from 15–25 bases in length. Second, the spacer length was initially selected to be 14 to 18 base pairs (bp), but subsequent GoldyTALEN designs were restricted to 15–16 bp. Additionally, when possible TALEN cut sequences were selected around a restriction enzyme centrally located within the spacer. To simplify the TALEN design process, a free, open access software (Mojo Hand) was created and made available online (<http://www.talendesign.org>). Mojo Hand downloads sequence from NCBI and uses an exhaustive database of commercially available restriction enzymes to identify TALEN binding sites with a restriction enzyme site in the spacer region to simplify downstream analysis (personal communication, Neff *et al.*). Mojo Hand also features a BLAST interface that will search genomes for potential second site effects.

**TALEN binding sites and spacer regions.** The *ponzr1* TALEN recognition sequences are: left TALEN 5'-GTGAGCAGCCAGCGGACCTCCTCT-3' and right TALEN 5'-ATCAGAACACAGTCAGAGAT-3'. Between the two binding sites is an 18-bp spacer with a *BstNI* sequence (GGAACCTGGACACGGGC, *BstNI* underlined). The *chrh1* TALEN recognition sequences are: left TALEN 5'-TGCAACACTGAGCTCTGTAAACCT-3' and right TALEN 5'-CTGCTGC GACTGGACCTGAGGT-3'. Between the two binding sites is a 15-bp spacer with a *BstUI* site (GTCCGCGTGTGGCGA, *BstUI* underlined). The *moesina* TALEN recognition sequences are: left TALEN 5'-ACCCAGAAGACGTTT-3' and right TALEN 5'-CTTTGAGTGGCCTCT-3'. Between the two binding sites is a 15-bp spacer with an *XmnI* site (CTGAGGAAGTATTC, *XmnI* underlined). The *ppl1cab* TALEN recognition sequences are: left TALEN 5'-CCACCA GAGAGTAAC-3' and right TALEN 5'-GCCTCTGTCAACATAGT-3'. Between the two binding sites is a 15-bp spacer with a *BsII* site (ACCTATTT CTGGGAG, *BsII* underlined). The *cdh5* TALEN recognition sequences are: left TALEN 5'-CTCCTCAACATACATACT-3' and right TALEN 5'-ACAAAT GATTTCATCTT-3'. Between the two binding sites is a 16-bp spacer with a *HincII* site (GGAGGTTAGTTGACA, *HincII* underlined). The *chrh2* binding sites are: left TALEN 5'-GTCAAATCTGCAGCTCCAGCCTT-3' and right TALEN 5'-CCTCTGCCTCTGACTCTGT-3'. Between the two binding sites is a 15-bp spacer (CAGCCTCAGCAAC).

**TALEN constructs.** TALEN assembly of the RVD-containing repeats was conducted using the Golden Gate approach<sup>13</sup>. Once assembled, the RVDs were cloned into a pT3TS destination vector with the appropriate TALEN backbone to generate mRNA expression plasmids—pT3TS-TAL (pTAL) and pT3TS-GoldyTALEN (GoldyTALEN). *In vitro* transcription of TALEN mRNA was conducted by linearizing the expression plasmids with SacI endonuclease at 37 °C for 2–3 h, transcribing the linearized DNA (T3 mMessage Machine kit, Ambion) and purifying the mRNA by phenol/chloroform extraction (T3 mMessage Machine kit user manual protocol) for injection.

**TALEN mutation screening.** One-cell embryos were microinjected with 50–400 pg of TALEN mRNA. The dose of each pair of TALENs injected was empirically determined, with up to a threefold difference noted between different TALEN pairs. In each case, conditions were used where over 50% embryos survived post-injection. Genomic DNA for Figs 1, 3 and 4 were collected at 2–4 days post-fertilization from 24–32 individual larvae by incubating in 50 mM NaOH at 95 °C, followed by cooling to 4 °C and adding 1/10 volume 1 M Tris-HCL pH 8.0 (ref. 25). Genomic DNA for Fig. 2 was isolated from groups of 10 larval zebrafish using DNeasy Blood and Tissue kit (Qiagen). Genotyping was conducted using PCR followed by restriction enzyme digest. For *ponzr1*, the primers were 5'-GTTCACACAAAATGTCTCTCAAGTCTCTAAATC-3' and 5'-AGTGGCC AGTGAGTGTATGTTACCT-3'. For *chrh1* the primers were 5'-CGTGAAG AGACAGCGAAGGGATTG-3' and 5'-AGAACTACCATTTGCACACTGAG CAGAG-3'. The primers for *moesina* were 5'-GTTACGGCTCAAGACCTG-3' and 5'-CAGGATGCCCTCTTTAAC-3'. The primers for *ppl1cab* were 5'-GAT GTTCATGGTCAGTAC-3' and 5'-TGATTGAGGCACATTCATGG-3'. The primers for *cdh5* were 5'-TTGTTGTCTCTGCAAGAGCTG-3' and 5'-TCTAGAG TATTCGCTGAT-3'. The primers for *chrh2* were 5'-CCCTGATGTGGAACT TTTTCAGACGA-3' and 5'-TGGTTTGGAAATTAGTCAGCATGAGTA-3'. Mutations were assessed by loss of restriction enzyme digestion. To sequence-verify mutations, the gel-purified, uncut PCR products were cloned into the TOPO TA Cloning Kit (Invitrogen).

**Analysis of *cdh5*.** A *cdh5* morpholino<sup>18</sup> was injected at the 1–4 cell stage into Tg(*flil:efgp*)<sup>11</sup> embryos<sup>19</sup>. The vascular phenotype of the morpholino and the GoldyTALEN-injected embryos were assessed using a confocal microscope. Antibody staining using the anti-Cdh5 antibody<sup>26</sup> was performed as described<sup>18</sup>.

**Genome editing.** For the *ponzr1* locus, a ssDNA oligonucleotide was designed to target the spacer sequence between the TALEN cut sites. The oligonucleotide

extends to half the length of the TALEN recognition site. An *EcoRV* site (5'-GAT ATC-3') or a modified *loxP* (*mloxP*) site (5'-ATAACTTCGTATAGCATACA TTATAGCAATTTAT-3') was introduced near the centre of the oligonucleotide resulting in a 20-base homology arm on the 5' end and an 18-base homology arm on the 3' end. For the *chrh2* locus, the *chrh2 mloxP* oligonucleotide (5'-TCA AATCTGCAGCTCCACGCTTCACGCATAAATTCGTATAGCATACATTATA GCAATTTATGCATATCTCCTTTCTCGAAAAGTAAG-3') was designed to replace the 3' TALEN binding site with an *mloxP* site while providing 27 bases of homology at both 5' and 3' end. The oligonucleotides were ordered from Integrated DNA Technologies (IDT) and purified using the Nucleotide Removal Kit (Qiagen).

One-cell embryos were microinjected with both the GoldyTALEN mRNA and ssDNA donor. The ssDNA oligonucleotide dose was varied to improve the rate of HDR without increasing toxicity beyond 50% embryonic death post-injection. For the *ponzr1* locus, 50–75 pg of *ponzr1* GoldyTALEN mRNA and 50–75 pg of the ssDNA donor. For the *chrh2* locus, 50 pg of *chrh2* GoldyTALEN mRNA was injected with either 25 pg or 50 pg of *chrh2 mloxP* oligonucleotide. Genomic DNA was isolated as described above. If the embryos were injected with the *EcoRV* oligonucleotide, PCR was conducted using the same primers as listed above and the product was digested using *EcoRV*. The full-length amplicon from *EcoRV*-positive larvae was cloned into a TOPO TA Cloning Kit (Invitrogen). Colony PCR was used to identify plasmids with *EcoRV*-modified inserts. Those plasmids were subsequently sequenced to confirm *EcoRV* integration and determine details of sequence changes due to HDR. If the embryos were injected with the *mloxP* oligonucleotide, the genomic DNA was amplified using the same forward primer as listed above and a *mloxP* reverse primer, 5'-ATAAATTGCTATAATGTA TGCTATACGAAGT-3', or the same reverse primer as listed above and a *mloxP* forward primer, 5'-ACTTCGTATAGCATACATTATAGCAATTTAT-3'. For sequence analysis, the complete amplicon was produced using the gene-specific primers listed above and cloned (TOPO TA Cloning Kit, Invitrogen). Colony PCR was used to find *mloxP*-positive plasmids. The positive plasmids were sequenced for confirmation of *mloxP* integration.

Injected fish from the same batch of somatically screened embryos were raised. When the fish were at least two months old, fin tissue was obtained using standard protocols pre-approved by Institutional Animal Care and Use Committee guidelines. The fish were anesthetized using Tricaine (approximately 200 µg ml<sup>-1</sup>). The tail fins were trimmed with a fresh razor blade for each fish to prevent contamination. The most caudal 2–3 mm of fin was biopsied and placed on ice until all fin biopsies were collected. 150 µl of 50 mM NaOH was added to the fin clips before DNA isolation (above). Those fish that maintained somatic modifications were outcrossed to wild-type fish and the embryos were screened for germline mutations. Somatic mutations were determined by RFLP analysis for *EcoRV* integration into *ponzr1*. Quantitative PCR of *mloxP* integrations into the *chrh2* locus were compared to a reference gene, *RPS6Kb1*. Twenty of 53 fish included >0.2% of their DNA containing *mloxP* integrations into *chrh2* (CT of ≤ 10) and were prioritized for screening. For *mloxP* integration into *chrh2*, 42 fish that were not screened by quantitative PCR were also tested for germline transmission and no appreciable difference in germline transmission between these two methods was noted.

The PCR product for germline HDR events were cloned and sequenced. In one clone that contained a sequence insertion along with integration of the *EcoRV* site, the sequencing was more difficult, presumably because the insertion tended to form a hairpin and disrupted the sequencing reaction. To obtain the full sequence, the PCR product was digested with *EcoRV* and each half sequenced separately. Similar cloning difficulties were observed in some *chrh2* lineages, but not for precise HDR or limited sequence addition.

The sequence addition process using ssDNA oligonucleotides is inherently less efficient than the relatively simpler NHEJ events seen in the GoldyTALEN-alone injected embryos. Therefore, to identify a precise HDR event, more fish will need to be raised and screened. Fin clipping the fish for maintenance of the somatic insertion may be a good indicator of germline transmission. Continued investigation into the mechanism of HDR incorporation in zebrafish will likely increase the efficiency of this technique.

**Zebrafish work.** The zebrafish work was conducted under full animal care and use guidelines with prior approval by the local institutional animal care committee's approval. *Danio rerio* transgenic lines were described previously: Tg(*flil:efgp*)<sup>11</sup> vasculature<sup>19</sup> and Tg(*gata1:dsred*)<sup>sd2</sup> red blood cells<sup>20</sup>.

**Data analysis and statistics.** ImageJ was used to quantify the percent GoldyTALEN-modified chromosomes by measuring the intensity of bands post-digestion. For each gel, the background was subtracted and each lane isolated to generate individual intensity plot profiles. A straight line was drawn across the bottom of each plot to eliminate inconsistencies caused by baseline skew. The intensity measurement for each band was added together to determine total intensity. To calculate percent cutting, the intensity of the top band was divided

by the total intensity. A student's *t*-test was used to compare TALEN scaffold cutting efficiencies. To measure the differences between pTAL and GoldyTALEN at two different loci, several whisker plots were constructed (Fig. 1c). The interquartile range (IQR; Q3–Q1) is shown as a box, with the median value (Q2) being the horizontal line within the box. The upper and lower whiskers are the highest and lowest data point within 1.5 times the IQR added or subtracted from Q3 or Q1, respectively.

A similar approach was used to calculate the percent of HDR-converted chromosomes. The intensity of the digested products were added together and divided by the total intensity. The percent of embryos with an HDR signal was determined by dividing the number of embryos with signal by the total number of screened embryos.

**Cell-free TALEN restriction endonuclease assay.** *In vitro* translation of 2 µg of each TALEN mRNA was conducted using the TNT Quick Coupled Transcription and Translation System (Promega). 5 µg of the *ponzr1* PCR product was included in the assay mix during *in vitro* translation of different TALEN combinations, allowing the translation and *in vitro* nuclease digestion to occur simultaneously.

The highest signal was obtained when translation and digestion steps were conducted simultaneously presumably because the TALEN protein is unstable using these *in vitro* conditions. Translation was conducted for 2 h at 30 °C. To further facilitate TALEN *in vitro* nuclease activity, the assay mix was diluted five fold in *in vitro* digestion buffer (20 mM Tris-HCl pH 7.5, 5 mM MgCl<sub>2</sub>, 50 mM KCl, 5% glycerol and 0.5 mg ml<sup>-1</sup> BSA)<sup>27</sup>. The assay mix was incubated at 30 °C for 4 h. The digested DNA was purified using a PCR Purification kit (Qiagen), concentrated via ethanol precipitation, and separated on a 2% agarose gel. No TALEN mRNA was added to the negative control.

25. Meeker, N. D., Hutchinson, S. A., Ho, L. & Trede, N. S. Method for isolation of PCR-ready genomic DNA from zebrafish tissues. *Biotechniques* **43**, 610–614 (2007).
26. Blum, Y. *et al.* Complex cell rearrangements during intersegmental vessel sprouting and vessel fusion in the zebrafish embryo. *Dev. Biol.* **316**, 312–322 (2008).
27. Mahfouz, M. M. *et al.* De novo-engineered transcription activator-like effector (TALE) hybrid nuclease with novel DNA binding specificity creates double-strand breaks. *Proc. Natl Acad. Sci. USA* **108**, 2623–2628 (2011).

# Host–microbe interactions have shaped the genetic architecture of inflammatory bowel disease

A list of authors and their affiliations appears at the end of the paper.

Crohn's disease and ulcerative colitis, the two common forms of inflammatory bowel disease (IBD), affect over 2.5 million people of European ancestry, with rising prevalence in other populations<sup>1</sup>. Genome-wide association studies and subsequent meta-analyses of these two diseases<sup>2,3</sup> as separate phenotypes have implicated previously unsuspected mechanisms, such as autophagy<sup>4</sup>, in their pathogenesis and showed that some IBD loci are shared with other inflammatory diseases<sup>5</sup>. Here we expand on the knowledge of relevant pathways by undertaking a meta-analysis of Crohn's disease and ulcerative colitis genome-wide association scans, followed by extensive validation of significant findings, with a combined total of more than 75,000 cases and controls. We identify 71 new associations, for a total of 163 IBD loci, that meet genome-wide significance thresholds. Most loci contribute to both phenotypes, and both directional (consistently favouring one allele over the course of human history) and balancing (favouring the retention of both alleles within populations) selection effects are evident. Many IBD loci are also implicated in other immune-mediated disorders, most notably with ankylosing spondylitis and psoriasis. We also observe considerable overlap between susceptibility loci for IBD and mycobacterial infection. Gene co-expression network analysis emphasizes this relationship, with pathways shared between host responses to mycobacteria and those predisposing to IBD.

We conducted an imputation-based association analysis using autosomal genotype-level data from 15 genome-wide association studies (GWAS) of Crohn's disease and/or ulcerative colitis (Supplementary Fig. 1 and Supplementary Table 1). We imputed 1.23 million single-nucleotide polymorphisms (SNPs) from the HapMap3 reference set (Supplementary Methods 1a), resulting in a high-quality data set with reduced genome-wide inflation (Supplementary Figs 2 and 3) compared with previous meta-analyses of subsets of these data<sup>2,3</sup>. The imputed GWAS data identified 25,075 SNPs that were associated ( $P < 0.01$ ) with at least one of the Crohn's disease, ulcerative colitis, or combined IBD analyses. A meta-analysis of GWAS data with Immunochip<sup>6</sup> validation genotypes from an independent, newly genotyped set of 14,763 Crohn's disease cases, 10,920 ulcerative colitis cases and 15,977 controls was performed (Supplementary Fig. 1 and Supplementary Table 1). Principal-components analysis resolved geographic stratification, as well as Jewish and non-Jewish ancestry (Supplementary Fig. 4), and reduced inflation to a level consistent with residual polygenic risk, rather than other confounding effects (from a median test statistic inflation ( $\lambda_{GC}$ ) = 2.00 to  $\lambda_{GC}$  = 1.23 when analysing all IBD samples; Supplementary Fig. 5 and Supplementary Methods 1b).

Our meta-analysis of the GWAS and Immunochip data identified 193 statistically independent signals of association at genome-wide significance ( $P < 5 \times 10^{-8}$ ) in at least one of the three analyses (Crohn's disease, ulcerative colitis, IBD). Because some of these signals (Supplementary Fig. 6) probably represent associations to the same underlying functional unit, we merged these signals (Supplementary Methods 1b) into 163 regions, 71 of which are reported here for the first time (Table 1 and Supplementary Table 2). Fig. 1a shows the relative contributions of each locus to the total variance explained in

ulcerative colitis and Crohn's disease. We have increased the total disease variance explained (variance being subject to fewer assumptions than heritability<sup>7</sup>) from 8.2% to 13.6% in Crohn's disease and from 4.1% to 7.5% in ulcerative colitis (Supplementary Methods 1c). Consistent with previous studies, our IBD risk loci seem to act independently, with no significant evidence of deviation from an additive combination of log odds ratios.

Our combined genome-wide analysis of Crohn's disease and ulcerative colitis enables a more comprehensive analysis of disease specificity than was previously possible. A model-selection analysis (Supplementary Methods 1c) showed that 110 out of 163 loci are associated with both disease phenotypes; 50 of these have an indistinguishable effect size in ulcerative colitis and Crohn's disease, whereas 60 show evidence of heterogeneous effects (Table 1). Of the remaining loci, 30 are classified as Crohn's-disease-specific and 23 as ulcerative-colitis-specific. However, 43 of these 53 loci show the same direction of effect in the non-associated disease (Fig. 1b; overall  $P = 2.8 \times 10^{-6}$ ). Risk alleles at two Crohn's disease loci, *PTPN22* and *NOD2*, show significant ( $P < 0.005$ ) protective effects in ulcerative colitis, exceptions that may reflect biological differences between the two diseases. This degree of sharing of genetic risk suggests that nearly all of the biological mechanisms involved in one disease have some role in the other.

The large number of IBD associations, far more than reported for any other complex disease, increases the power of network-based analyses to prioritize genes within loci. We investigated the IBD loci using functional annotation and empirical gene network tools (Supplementary Table 2). Compared with previous analyses that identified candidate genes in 35% of loci<sup>2,3</sup> our updated GRAIL<sup>8</sup>-connectivity network identifies candidates in 53% of loci, including increased statistical significance for 58 of the 73 candidates from previous analyses. The new candidates come not only from genes within newly identified loci, but also integrate additional genes from previously established loci (Fig. 1c). Only 29 IBD-associated SNPs are in strong linkage disequilibrium ( $r^2 > 0.8$ ) with a missense variant in the 1000 Genomes Project data, which reinforces previous evidence that a large fraction of risk for complex disease is driven by non-coding variation. By contrast, 64 IBD-associated SNPs are in linkage disequilibrium with variants known to regulate gene expression (Supplementary Table 2). Overall, we highlighted a total of 300 candidate genes in 125 loci, of which 39 contained a single gene supported by two or more methods.

Seventy per cent (113 out of 163) of the IBD loci are shared with other complex diseases or traits, including 66 among the 154 loci previously associated with other immune-mediated diseases<sup>9</sup>, which is 8.6-times the number that would be expected by chance ( $P < 10^{-16}$ ; Fig. 2a and Supplementary Fig. 7). Such enrichment cannot be attributed to the immune-mediated focus of the Immunochip (Supplementary Methods 4 and Supplementary Fig. 8), as the analysis is based on our combined GWAS–Immunochip data. Comparing overlaps with specific diseases is confounded by the variable power in studies of different diseases. For instance, although type 1 diabetes shares the largest number of loci (20 out of 39; tenfold enrichment) with IBD, this is partially driven by the large number of known type 1 diabetes associations. Indeed, seven other immune-mediated diseases

**Table 1 | Crohn's disease-specific, ulcerative colitis-specific and IBD general loci**

Crohn's disease				Ulcerative colitis			
Chr.	Position (Mb)	SNP	Key genes (+ no. of additional genes in locus)	Chr.	Position (Mb)	SNP	Key genes (+ no. of additional genes in locus)
1	78.62	rs17391694	(5)	1	2.5	rs10797432	<b>TNFRSF14</b> (10)
1	114.3	<b>rs6679677</b>	<b>PTPN22</b> † (8)	1	20.15†	<b>rs6426833</b>	(9)
1	120.45	rs3897478	ADAM30 (5)	1	200.09	<b>rs2816958</b>	(3)
1	172.85	<b>rs9286879</b>	<b>FASLG, TNFSF18</b> (0)	2	198.65	rs1016883	RFTN2, PLCL1 (7)
2	27.63	<b>rs1728918</b>	UCN (23)	2	199.70*	<b>rs17229285</b>	0
2	62.55	rs10865331	(3)	3	53.05	rs9847710	PRKCD, ITIH4 (8)
2	231.09	<b>rs6716753</b>	SP140 (5)	4	103.51	rs3774959	<b>NFKB1, MANBA</b> (2)
2	234.15	<b>rs12994997</b>	<b>ATG16L1</b> † (8)	5	0.59	rs11739663	SLC9A3 (8)
4	48.36	rs6837335	(6)	5	134.44	rs254560	(6)
4	102.86	rs13126505	(1)	6	32.595	<b>rs6927022</b>	(15)
5	55.43	rs10065637	<b>IL6ST, IL31RA</b> (1)	7	2.78	<b>rs798502</b>	<b>CARD11, GNA12</b> (5)
5	72.54	rs7702331	(4)	7	27.22†	rs4722672	(14)
5	173.34	rs17695092	CPEB4 (2)	7	107.45*	<b>rs4380874</b>	DLD (9)
6	21.42	rs12663356	(3)	7	128.57	<b>rs4728142</b>	<b>IRF5</b> † (13)
6	31.27	<b>rs9264942</b>	(22)	11	96.02	rs483905	JRKL, MAML2 (2)
6	127.45	rs9491697	(3)	11	114.38	<b>rs561722</b>	NXPE1, NXPE4 (5)
6	128.24	<b>rs13204742</b>	(2)	15	41.55	rs28374715	(11)
6	159.49	<b>rs212388</b>	TAGAP (5)	16	30.47	rs11150589	<b>ITGAL</b> (20)
7	26.88†	rs10486483	(2)	16	68.58	rs1728785	ZFP90 (6)
7	28.17	rs864745	CREB5, JAZF1 (1)	17	70.64	rs7210086	(3)
8	90.87	rs7015630	RIPK2 (4)	19	47.12†	rs1126510	CALM3 (14)
8	129.56	<b>rs6651252</b>	0	20	33.8	rs6088765	(11)
13	44.45	<b>rs3764147</b>	LACC1 (3)	20	43.06	<b>rs6017342</b>	ADA, HNF4A (9)
15	38.89	rs16967103	<b>RASGRP1, SPRED1</b> (2)				
16	50.66†	<b>rs2066847</b>	<b>NOD2</b> † (6)				
17	25.84	<b>rs2945412</b>	<b>LGALS9, NOS2</b> (3)				
19	1.12	<b>rs2024092</b>	GPX4, HMHA1 (20)				
19	46.85†	rs4802307	(9)				
19	49.2	<b>rs516246</b>	FUT2, (25)				
21	34.77	<b>rs2284553</b>	<b>IFNGR2, IFNAR1</b> (10)				

IBD				IBD			
Chr.	Position (Mb)	SNP	Key genes (+ no. of additional genes in locus)	Chr.	Position (Mb)	SNP	Key genes (+ no. of additional genes in locus)
1	1.24	<b>rs12103</b>	<b>TNFRSF18, TNFRSF4</b> (30)	10	35.3	<b>rs11010067</b> §	<b>CREM</b> (3)
1	8.02	<b>rs35675666</b>	TNFRSF9 (6)	10	59.99	rs2790216	CISD1, IPMK (2)
1	22.7	<b>rs12568930</b> §	(3)	10	64.51†	<b>rs10761659</b> §	(3)
1	67.68†	<b>rs11209026</b> §	<b>IL23R</b> † (5)	10	75.67	rs2227564§	(13)
1	70.99	rs2651244§	(3)	10	81.03	<b>rs1250546</b> §	(5)
1	151.79	<b>rs4845604</b> §	RORC (14)	10	82.25	<b>rs6586030</b> §	TSPAN14, C10orf58 (4)
1	155.67	rs670523§	(31)	10	94.43	rs7911264	(4)
1	160.85	rs4656958§	<b>CD48</b> (15)	10	101.28	<b>rs4409764</b>	NKX2-3 (6)
1	161.47	<b>rs1801274</b> §	<b>FCGR2A, FCGR2B &amp; FCGR3A</b> (13)	11	1.87	rs907611	<b>TNNI2, LSP1</b> (17)
1	197.6	<b>rs2488389</b>	C1orf53 (2)	11	58.33	rs10896794	CNTF, LPXN (8)
1	200.87	<b>rs7554511</b>	KIF21B (6)	11	60.77	<b>rs11230563</b>	<b>CD6</b> (14)
1	206.93	<b>rs3024505</b> §	IL10 (10)	11	61.56	<b>rs4246215</b> §	(15)
2	25.12	<b>rs6545800</b> §	ADCY3 (6)	11	64.12	rs559928	<b>CCDC88B</b> (23)
2	28.61	<b>rs925255</b> §	FOSL2, BRE (1)	11	65.65	rs2231884§	RELA (25)
2	43.81	rs10495903§	(5)	11	76.29	<b>rs2155219</b> §	(5)
2	61.2	<b>rs7608910</b>	<b>REL</b> (9)	11	87.12	rs6592362	(1)
2	65.67	rs6740462	SPRED2 (1)	11	118.74	rs630923§	CXCR5 (17)
2	102.86*	<b>rs917997</b> §	IL18RAP, IL1R1 (7)	12	12.65	rs11612508§	LOH12CR1 (8)
2	163.1	rs2111485	IFIH1 (5)	12	40.77*	<b>rs11564258</b> §	MUC19 (1)
2	191.92	rs1517352	<b>STAT1, STAT4</b> (2)	12	48.2	rs11168249§	VDR (8)
2	219.14	rs2382817	(15)	12	68.49	<b>rs7134599</b> §	<b>IFNG</b> (3)
2	241.57*	<b>rs3749171</b> §	<b>GPR35</b> (12)	13	27.52	<b>rs17085007</b> §	(2)
3	18.76	<b>rs4256159</b> §	0	13	40.86†	<b>rs941823</b> §	(3)
3	48.96†	<b>rs3197999</b>	<b>MST1, PFKFB4</b> (63)	13	99.95	<b>rs9557195</b>	GPR183, GPR18 (6)
4	74.85	rs2472649§	(11)	14	69.27	rs194749§	ZFP36L1 (4)
4	123.22	<b>rs7657746</b>	<b>IL2, IL21</b> (2)	14	75.7	rs4899554§	<b>FOS, MLH3</b> (6)
5	10.69	rs2930047	DAP (2)	14	88.47	<b>rs8005161</b>	<b>GPR65, GALT</b> (1)
5	40.38†	<b>rs11742570</b> §	PTGER4 (1)	15	67.43	<b>rs17293632</b> §	SMAD3 (2)
5	96.24	<b>rs1363907</b>	ERAP2, ERAP1 (3)	15	91.17	rs7495132	CRTC3 (3)
5	130.01	rs4836519§	(1)	16	11.54*	<b>rs529866</b> §	<b>SOC1, LITAF</b> (11)
5	131.19*	<b>rs2188962</b> §	IBD5 locus (18)	16	23.86	rs7404095	<b>PRKCB</b> (5)
5	141.51	<b>rs6863411</b> §	SPRY4, NDFIP1 (5)	16	28.6	<b>rs26528</b> §	IL27 (14)
5	150.27	<b>rs11741861</b> §	<b>IRGM</b> † (10)	16	86	rs10521318§	IRF8 (4)
5	158.8†	<b>rs6871626</b> §	<b>IL12B</b> (3)	17	32.59	<b>rs3091316</b> §	<b>CCL13, CCL2</b> (5)
5	176.79	rs12654812	<b>DOK3</b> (17)	17	37.91	<b>rs12946510</b>	ORMDL3 (16)
6	14.71	rs17119	0	17	40.53	<b>rs12942547</b> §	<b>STAT3</b> (15)
6	20.77*	<b>rs9358372</b> §	(2)	17	57.96	<b>rs1292053</b> §	TUBD1, RPS6KB1 (9)
6	90.96	rs1847472	(1)	18	12.8	<b>rs1893217</b> §	(6)
6	106.43	<b>rs6568421</b> §	(2)	18	46.39	rs7240004§	SMAD7 (2)
6	111.82	<b>rs3851228</b>	<b>TRAF3IP2</b> (4)	18	67.53	rs727088	<b>CD226</b> (2)
6	138	<b>rs6920220</b> §	TNFAIP3 (1)	19	10.49*	<b>rs11879191</b>	<b>TYK2</b> (27)

Table 1 | Continued

IBD				IBD			
Chr.	Position (Mb)	SNP	Key genes (+ no. of additional genes in locus)	Chr.	Position (Mb)	SNP	Key genes (+ no. of additional genes in locus)
6	143.9	rs12199775	<i>PHACTR2</i> (5)	19	33.73	<b>rs17694108</b>	<i>CEBPG</i> (8)
6	167.37	<b>rs1819333</b> §	<i>CCR6, RPS6KA2</i> (4)	19	55.38	rs11672983	(19)
7	50.245*	<b>rs1456896</b>	<i>ZBPB, IKZF1</i> (4)	20	30.75	rs6142618§	<i>HCK</i> (10)
7	98.75	rs9297145	<i>SMURF1</i> (6)	20	31.37	rs4911259	<i>DNMT3B</i> (8)
7	100.34	<b>rs1734907</b> §	<i>EPO</i> (21)	20	44.74	<b>rs1569723</b> §	<i>CD40</i> (13)
7	116.89	rs38904§	(6)	20	48.95	rs913678	<i>CEBPG</i> (5)
8	126.53	<b>rs921720</b> §	<i>TRIB1</i> (1)	20	57.82	rs259964	<i>ZNF831, CTSZ</i> (5)
8	130.62	rs1991866	(2)	20	62.34	<b>rs6062504</b>	<i>TNFRSF6B</i> (26)
9	4.98	<b>rs10758669</b>	<i>JAK2</i> (4)	21	16.81	<b>rs2823286</b> §	0
9	93.92	rs4743820§	<i>NFIL3</i> (2)	21	40.46	<b>rs2836878</b> §	(3)
9	117.60†	<b>rs4246905</b>	<i>TNFSF15</i> (4)	21	45.62	<b>rs7282490</b>	<i>ICOSLG</i> (9)
9	139.32*	<b>rs10781499</b> §	<i>CARD9</i> (22)	22	21.92	<b>rs2266959</b>	(13)
10	6.08	rs12722515§	<i>IL2RA, IL15RA</i> (6)	22	30.43	<b>rs2412970</b>	<i>LIF, OSM</i> (9)
10	30.72	rs1042058§	<i>MAP3K8</i> (3)	22	39.69*	<b>rs2413583</b> §	<i>TAB1</i> (18)

The position given is the middle of the locus window, with all positions relative to human reference genome GRCh37. Bolded rs numbers indicate SNPs with  $P$  values less than  $1 \times 10^{-13}$ . Grey shading indicates newly discovered loci. Listed are genes implicated by one or more candidate gene approaches. Bolded genes have been implicated by two or more candidate gene approaches. For each locus, the top two candidate genes are listed. A complete listing of gene prioritization is provided in Supplementary Table 2. \*Additional genome-wide significant associated SNP in the region. †Two or more additional genome-wide significant SNPs in the region. ‡These regions have overlapping but distinct ulcerative colitis and Crohn's disease signals. §Heterogeneity of odds ratios. || Crohn's disease risk allele is significantly protective in ulcerative colitis. ¶Gene for which functional studies of associated alleles have been reported. Chr., chromosome; Mb, megabase.

show stronger enrichment of overlap, with the largest being ankylosing spondylitis (8 out of 11; 13-fold) and psoriasis (14 out of 17; 14-fold).

IBD loci are also markedly enriched (4.9-fold;  $P < 10^{-4}$ ) in genes involved in primary immunodeficiencies (PIDs; Fig. 2a), which are characterized by a dysfunctional immune system resulting in severe infections<sup>10</sup>. Genes implicated in this overlap correlate with reduced levels of circulating T cells (*ADA*, *CD40*, *TAP1*, *TAP2*, *NBN*, *BLM*, *DNMT3B*) or of specific subsets, such as T-helper cells producing IL-17 ( $T_H17$  cells) (*STAT3*), memory (*SP110*) or regulatory T cells (*STAT5B*). The subset of PID genes leading to Mendelian susceptibility to mycobacterial disease (MSMD)<sup>10–12</sup> is enriched still further; six of the eight known autosomal genes linked to MSMD are located within IBD loci (*IL12B*, *IFNGR2*, *STAT1*, *IRF8*, *TYK2*, *STAT3*; 46-fold enrichment;  $P = 1.3 \times 10^{-6}$ ), and a seventh, *IFNGR1*, narrowly missed genome-wide significance ( $P = 6 \times 10^{-8}$ ). Overlap with IBD is also seen in complex mycobacterial disease; we find IBD associations in seven out of eight loci identified by leprosy GWAS<sup>13</sup>, including six cases in which the same SNP is implicated. Furthermore, genetic defects in *STAT3* (refs 14, 15) and *CARD9* (ref. 16), also within IBD

loci, lead to PIDs involving skin infections with *Staphylococcus* and candidiasis, respectively. The comparative effects of IBD and infectious-disease-susceptibility-risk alleles on gene function and expression are summarized in Supplementary Table 3, and include both opposite (for example, *NOD2* and *STAT3*; Supplementary Fig. 9) and similar (for example, *IFNGR2*) directional effects.

To extend our understanding of the fundamental biology of IBD pathogenesis we conducted searches across the IBD locus list: (1) for enrichment of specific Gene Ontology terms and canonical pathways; (2) for evidence of selective pressure acting on specific variants and pathways; and (3) for enrichment of differentially expressed genes across immune-cell types. We tested the 300 prioritized genes (see above) for enrichment in Gene Ontology terms (Supplementary Methods 4a) and identified 286 Gene Ontology terms and 56 pathways demonstrating significant enrichment in genes contained within IBD loci (Supplementary Figs 10 and 11 and Supplementary Table 4). Excluding high-level Gene Ontology categories such as 'immune system processes' ( $P = 3.5 \times 10^{-26}$ ), the most significantly enriched term is regulation of cytokine production ( $P = 2.7 \times 10^{-24}$ ), specifically

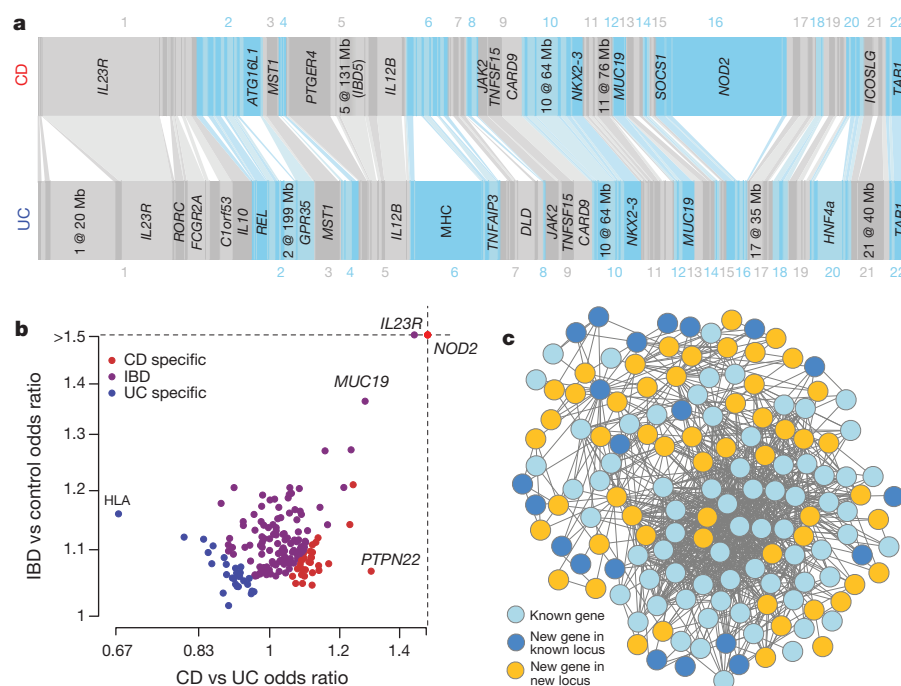


**Figure 1 | The IBD genome.** a, Variance explained by the 163 IBD loci. Each bar, ordered by genomic position, represents an independent locus. The width of the bar is proportional to the variance explained by that locus in Crohn's disease (CD) and ulcerative colitis (UC). Bars are connected together if they are identified as being associated with both phenotypes, and loci are labelled if they explain more than 1% of the total variance explained by all loci for that phenotype. Labels are either the best-supported candidate gene in Table 1, or the chromosome and position of the locus if either no, or multiple, well-supported candidates exist. b, The 193 independent signals, plotted by total IBD odds ratio and phenotype specificity (measured by the odds ratio of Crohn's disease relative to ulcerative colitis), and coloured by their IBD phenotype classification from Table 1. Note that many loci (for example, *IL23R*) show very different effects in Crohn's disease and ulcerative colitis despite being strongly associated to both. c, GRAIL network for all genes with GRAIL  $P < 0.05$ . Genes included in our previous GRAIL networks in both phenotypes are shown in light blue, newly connected genes in previously identified loci in dark blue, and genes from newly associated loci in gold. The gold genes reinforce the previous network (light blue) and expand it to include dark blue genes.

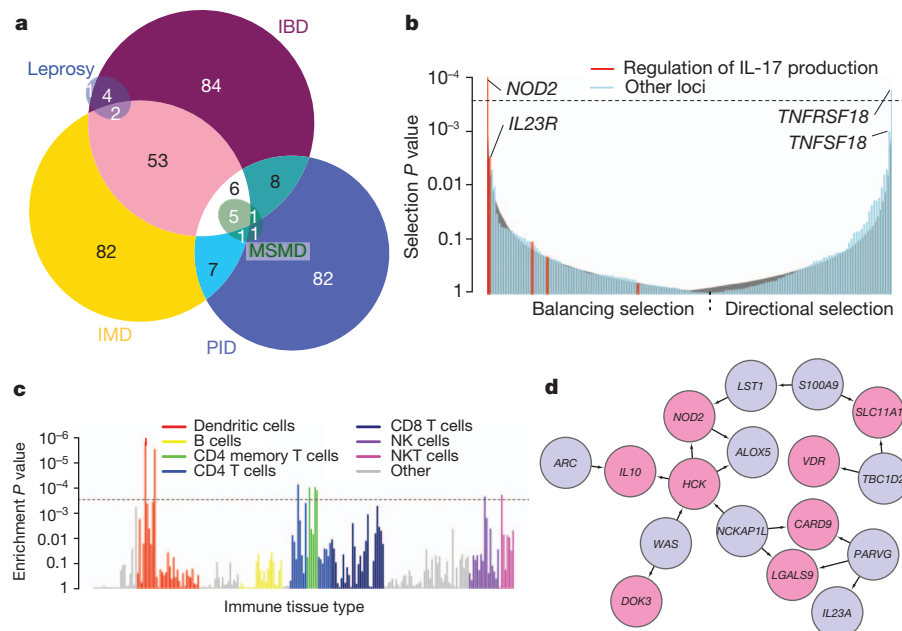


**Figure 2 | Dissecting the biology of IBD.**

**a**, Number of overlapping IBD loci with other immune-mediated diseases (IMD), leprosy and Mendelian PIDs. Within PID, we highlight MSMD. **b**, Signals of selection at IBD SNPs, from strongest balancing on the left to strongest directional on the right. The grey curve shows the 95% confidence interval for randomly chosen frequency-matched SNPs, illustrating our overall enrichment ( $P = 5.5 \times 10^{-6}$ ), and the dashed line represents the Bonferroni significance threshold. SNPs highlighted in red are annotated as being involved in the regulation of IL-17 production, a key IBD functional term related to bacterial defence, and are enriched for balancing selection. **c**, Evidence of enrichment in IBD loci of differentially expressed genes from various immune tissues. Each bar represents the empirical  $P$  value in a single tissue, and the colours represent different cell type groupings. The dashed line is Bonferroni-corrected significance for the number of tissues tested. **d**, *NOD2*-focused cluster of the IBD causal sub-network. Pink genes are in IBD-associated loci, blue are not. Arrows indicate inferred causal direction of regulation of expression.

interferon- $\gamma$ , interleukin (IL)-12, tumour-necrosis factor- $\alpha$  and IL-10 signalling. Lymphocyte activation was the next most significant ( $P = 1.8 \times 10^{-23}$ ), with activation of T cells, B cells and natural killer (NK) cells being the strongest contributors to this signal. Strong enrichment was also seen for response to molecules of bacterial origin ( $P = 2.4 \times 10^{-20}$ ), and for the Kyoto Encyclopedia of Genes and Genomes (KEGG) JAK-STAT signalling pathway ( $P = 4.8 \times 10^{-15}$ ). We note that no enriched terms or pathways showed specific evidence of Crohn's disease or ulcerative colitis specificity.

As infectious organisms are known to be among the strongest agents of natural selection, we investigated whether the IBD-associated variants are subject to selective pressures (Supplementary Table 5 and Supplementary Methods 4c). Directional selection would imply that the balance between these forces shifted in one direction over the course of human history, whereas balancing selection would suggest an allele-frequency-dependent scenario typified by host-microbe co-evolution, as can be observed with parasites. Two SNPs show Bonferroni-significant selection: the most significant signal, in *NOD2*, is under balancing selection ( $P = 5.2 \times 10^{-5}$ ), and the second most significant, in the receptor *TNFRSF18*, showed directional selection ( $P = 8.9 \times 10^{-5}$ ). The next most significant variants were in the ligand of that receptor, *TNFSF18* (directional;  $P = 5.2 \times 10^{-4}$ ), and *IL23R* (balancing;  $P = 1.5 \times 10^{-3}$ ). As a group, the IBD variants show significant enrichment in selection (Fig. 2b) of both types ( $P = 5.5 \times 10^{-6}$ ). We discovered an enrichment of balancing selection (Fig. 2b) in genes annotated with the Gene Ontology term 'regulation of interleukin-17 production' ( $P = 1.4 \times 10^{-4}$ ). The important role of IL-17 in both bacterial defence and autoimmunity suggests a key role for balancing selection in maintaining the genetic relationship between inflammation and infection, and this is reinforced by a nominal enrichment of balancing selection in loci annotated with the broader Gene Ontology term 'defense response to bacterium' ( $P = 0.007$ ).

We tested for enrichment of cell-type expression specificity of genes in IBD loci in 223 distinct sets of sorted, mouse-derived immune cells from the Immunological Genome Consortium<sup>17</sup>. Dendritic cells showed the strongest enrichment, followed by weaker signals that support the Gene Ontology analysis, including CD4<sup>+</sup> T cells, NK cells and NKT cells (Fig. 2c). Notably, several of these cell types express genes near our IBD associations much more specifically when stimulated; our strongest signal, a lung-derived dendritic cell, had

$P_{\text{stimulated}} < 1 \times 10^{-6}$  compared with  $P_{\text{unstimulated}} = 0.0015$ , consistent with an important role for cell activation.

To further our goal of identifying likely causal genes within our susceptibility loci and to elucidate networks underlying IBD pathogenesis, we screened the associated genes against 211 co-expression modules identified from weighted gene co-expression network analyses<sup>18</sup>, conducted with large gene-expression data sets from multiple tissues<sup>19–21</sup>. The most significantly enriched module comprised 523 genes from omental adipose tissue collected from morbidly obese patients<sup>19</sup>, which was found to be 2.9-fold enriched for genes in the IBD-associated loci ( $P = 1.1 \times 10^{-13}$ ; Supplementary Fig. 12 and Supplementary Table 6). We constructed a probabilistic causal gene network using an integrative Bayesian network-reconstruction algorithm<sup>22–24</sup>, which combines expression and genotype data to infer the direction of causality between genes with correlated expression. The intersection of this network and the genes in the IBD-enriched module defined a sub-network of genes enriched in bone marrow-derived macrophages ( $P < 10^{-16}$ ) and is suggestive of dynamic interactions relevant to IBD pathogenesis. In particular, this sub-network featured close proximity among genes connected to host interaction with bacteria, notably *NOD2*, *IL10* and *CARD9*.

A *NOD2*-focused inspection of the sub-network prioritizes multiple additional candidate genes within IBD-associated regions. For example, a cluster near *NOD2* (Fig. 2d) contains multiple IBD genes implicated in the *Mycobacterium tuberculosis* response, including *SLC11A1*, *VDR* and *LGALS9*. Furthermore, both *SLC11A1* (also known as *NRAMP1*) and *VDR* have been associated with *M. tuberculosis* infection by candidate gene studies<sup>25,26</sup>, and *LGALS9* modulates mycobacteriosis<sup>27</sup>. Of interest, *HCK* (located in our new locus on chromosome 20 at 30.75 megabases) is predicted to upregulate expression of both *NOD2* and *IL10*, an anti-inflammatory cytokine associated with Mendelian<sup>28</sup> and non-Mendelian<sup>29</sup> IBD. *HCK* has been linked to alternative, anti-inflammatory activation of monocytes (M2-group macrophages)<sup>30</sup>; although not identified in our aforementioned analyses, these data implicate *HCK* as the causal gene in this new IBD locus.

We report one of the largest genetic experiments involving a complex disease undertaken to date. This has increased the number of confirmed IBD susceptibility loci to 163, most of which are associated with both Crohn's disease and ulcerative colitis, and is substantially

more than reported for any other complex disease. Even this large number of loci explains only a minority of the variance in disease risk, which suggests that other factors—such as rarer genetic variation not captured by GWAS or environmental exposures—make substantial contributions to pathogenesis. Most of the evidence relating to possible causal genes points to an essential role for host defence against infection in IBD. In this regard, the current results focus ever-closer attention on the interaction between the host mucosal immune system and microbes, both at the epithelial cell surface and within the gut lumen. In particular, they raise the question, in the context of this burden of IBD-susceptibility genes, of what triggers components of the commensal microbiota to switch from a symbiotic to a pathogenic relationship with the host. Collectively, our findings begin to shed light on these questions and provide a rich source of clues to the pathogenic mechanisms underlying this archetypal complex disease.

## METHODS SUMMARY

We conducted a meta-analysis of GWAS data sets after imputation to the HapMap3 reference set, and aimed to replicate in the Immunochip data any SNPs with  $P < 0.01$ . We compared likelihoods of different disease models to assess whether each locus was associated with Crohn's disease, ulcerative colitis, or both. We used databases of expression quantitative trait loci SNPs and coding SNPs in linkage disequilibrium with our hit SNPs, as well as the network tools GRAIL and DAPPLE, and a co-expression network analysis to prioritize candidate genes in our loci. Gene Ontology, the Immunological Genome Project (ImmGen) mouse immune-cell-expression resource, the TreeMix selection software and a Bayesian causal network analysis were used to functionally annotate these genes.

Received 17 May; accepted 12 September 2012.

- Molodecky, N. A. *et al.* Increasing incidence and prevalence of the inflammatory bowel diseases with time, based on systematic review. *Gastroenterology* **142**, 46–54 (2012).
- Anderson, C. A. *et al.* Meta-analysis identifies 29 additional ulcerative colitis risk loci, increasing the number of confirmed associations to 47. *Nature Genet.* **43**, 246–252 (2011).
- Franke, A. *et al.* Genome-wide meta-analysis increases to 71 the number of confirmed Crohn's disease susceptibility loci. *Nature Genet.* **42**, 1118–1125 (2010).
- Khor, B., Gardet, A. & Xavier, R. J. Genetics and pathogenesis of inflammatory bowel disease. *Nature* **474**, 307–317 (2011).
- Cho, J. H. & Gregersen, P. K. Genomics and the multifactorial nature of human autoimmune disease. *N. Engl. J. Med.* **365**, 1612–1623 (2011).
- Cortes, A. & Brown, M. A. Promise and pitfalls of the Immunochip. *Arthritis Res. Ther.* **13**, 101 (2011).
- Zuk, O., Hechter, E., Sunyaev, S. R. & Lander, E. S. The mystery of missing heritability: genetic interactions create phantom heritability. *Proc. Natl Acad. Sci. USA* **109**, 1193–1198 (2012).
- Raychaudhuri, S. *et al.* Identifying relationships among genomic disease regions: predicting genes at pathogenic SNP associations and rare deletions. *PLoS Genet.* **5**, e1000534 (2009).
- Hindorf, L. A. *et al.* Potential etiologic and functional implications of genome-wide association loci for human diseases and traits. *Proc. Natl Acad. Sci. USA* **106**, 9362–9367 (2009).
- Notarangelo, L. D. *et al.* Primary immunodeficiencies: 2009 update. *J. Allergy Clin. Immunol.* **124**, 1161–1178 (2009).
- Bustamante, J., Picard, C., Boisson-Dupuis, S., Abel, L. & Casanova, J. L. Genetic lessons learned from X-linked Mendelian susceptibility to mycobacterial diseases. *Ann. NY Acad. Sci.* **1246**, 92–101 (2011).
- Patel, S. Y., Doffinger, R., Barcenas-Morales, G. & Kumararatne, D. S. Genetically determined susceptibility to mycobacterial infection. *J. Clin. Pathol.* **61**, 1006–1012 (2008).
- Zhang, F. *et al.* Identification of two new loci at *IL23R* and *RAB32* that influence susceptibility to leprosy. *Nature Genet.* **43**, 1247–1251 (2011).
- Holland, S. M. *et al.* *STAT3* mutations in the hyper-IgE syndrome. *N. Engl. J. Med.* **357**, 1608–1619 (2007).
- Minegishi, Y. *et al.* Dominant-negative mutations in the DNA-binding domain of *STAT3* cause hyper-IgE syndrome. *Nature* **448**, 1058–1062 (2007).
- Glocker, E. O. *et al.* A homozygous *CARD9* mutation in a family with susceptibility to fungal infections. *N. Engl. J. Med.* **361**, 1727–1735 (2009).
- Hu, X. *et al.* Integrating autoimmune risk loci with gene-expression data identifies specific pathogenic immune cell subsets. *Am. J. Hum. Genet.* **89**, 496–506 (2011).
- Zhang, B. & Horvath, S. A general framework for weighted gene co-expression network analysis. *Stat. Appl. Genet. Mol. Biol.* **4**, Article 17 (2005).
- Greenawald, D. M. *et al.* A survey of the genetics of stomach, liver, and adipose gene expression from a morbidly obese cohort. *Genome Res.* **21**, 1008–1016 (2011).
- Emilsson, V. *et al.* Genetics of gene expression and its effect on disease. *Nature* **452**, 423–428 (2008).
- Schadt, E. E. *et al.* Mapping the genetic architecture of gene expression in human liver. *PLoS Biol.* **6**, e107 (2008).
- Chen, Y. *et al.* Variations in DNA elucidate molecular networks that cause disease. *Nature* **452**, 429–435 (2008).
- Zhong, H. *et al.* Liver and adipose expression associated SNPs are enriched for association to type 2 diabetes. *PLoS Genet.* **6**, e1000932 (2010).
- Zhu, J. *et al.* Increasing the power to detect causal associations by combining genotypic and expression data in segregating populations. *PLoS Comput. Biol.* **3**, e69 (2007).
- Lewis, S. J., Baker, I. & Davey Smith, G. Meta-analysis of vitamin D receptor polymorphisms and pulmonary tuberculosis risk. *Int. J. Tuberc. Lung Dis.* **9**, 1174–1177 (2005).
- Li, X. *et al.* *SLC11A1* (NRAMP1) polymorphisms and tuberculosis susceptibility: updated systematic review and meta-analysis. *PLoS ONE* **6**, e15831 (2011).
- Kumar, D. *et al.* Genome-wide analysis of the host intracellular network that regulates survival of *Mycobacterium tuberculosis*. *Cell* **140**, 731–743 (2010).
- Glocker, E. O. *et al.* Infant colitis—it's in the genes. *Lancet* **376**, 1272 (2010).
- Franke, A. *et al.* Sequence variants in *IL10*, *ARPC2* and multiple other loci contribute to ulcerative colitis susceptibility. *Nature Genet.* **40**, 1319–1323 (2008).
- Bhattacharjee, A., Pal, S., Feldman, G. M. & Cathcart, M. K. Hck is a key regulator of gene expression in alternatively activated human monocytes. *J. Biol. Chem.* **286**, 36709–36723 (2011).

Supplementary Information is available in the online version of the paper.

**Acknowledgements** We thank all the subjects who contributed samples and the physicians and nursing staff who helped with recruitment globally. UK case collections were supported by the National Association for Crohn's and Crohn's disease; Wellcome Trust grant 098051 (L.J., C.A.A., J.C.B.); Medical Research Council UK; the Catherine McEwan Foundation; an NHS Research Scotland career fellowship (R.K.R.); Peninsula College of Medicine and Dentistry, Exeter; the National Institute for Health Research, through the Comprehensive Local Research Network, and through Biomedical Research Centre awards to Guy's & Saint Thomas' National Health Service Trust, King's College London, Addenbrooke's Hospital, University of Cambridge School of Clinical Medicine and to the University of Manchester and Central Manchester Foundation Trust. The British 1958 Birth Cohort DNA collection was funded by Medical Research Council grant G0000934 and Wellcome Trust grant 068545/Z/02, and the UK National Blood Service controls by the Wellcome Trust. The Wellcome Trust Case Control Consortium projects were supported by Wellcome Trust grants 083948/Z/07/Z, 085475/B/08/Z and 085475/Z/08/Z. North American collections and data processing were supported by funds to the National Institute of Diabetes, Digestive and Kidney diseases (NIDDK) IBD Genetics Consortium, which is funded by the following grants: DK062431 (S.R.B.), DK062422 (J.H.C.), DK062420 (R.H.D.), DK062432 (J.D.R.), DK062423 (M.S.S.), DK062413 (D.P.M.), DK076984 (M.J.D.), DK084554 (M.J.D. and D.P.M.) and DK062429 (J.H.C.). Additional funds were provided by funding to J.H.C. (DK062429-S1 and Crohn's & Colitis Foundation of America, Senior Investigator Award (5-2229)) and R.H.D. (CA141743). K.Y.H. is supported by the National Institutes of Health (NIH) MSTP TG T32GM07205 training award. Cedars-Sinai is supported by USPHS grant P01DK046763 and the Cedars-Sinai F. Widjaja Inflammatory Bowel and Immunobiology Research Institute Research Funds, National Center for Research Resources (NCRR) grant M01-RR00425, UCLA/Cedars-Sinai/Harbor/Drew Clinical and Translational Science Institute (CTSI) Grant (UL1 TR000124-01), the Southern California Diabetes and Endocrinology Research Grant (DERC) (DK063491), The Helmsley Foundation (D.P.M.) and the Crohn's and Colitis Foundation of America (D.P.M.). R.J.X. and A.N.A. are funded by DK83756, AI062773, DK043351 and the Helmsley Foundation. The Netherlands Organization for Scientific Research supported R.K.W. with a clinical fellowship grant (90.700.281) and C.W. (VICI grant 918.66.620). C.W. is also supported by the Celiac Disease Consortium (BSIK03009). This study was also supported by the German Ministry of Education and Research through the National Genome Research Network, the Popgen biobank, through the Deutsche Forschungsgemeinschaft (DFG) cluster of excellence 'Inflammation at Interfaces' and DFG grant no. FR 2821/2-1. S.B. was supported by DFG BR 1912/6-1 and the Else Kröner-Fresenius-Stiftung (Else Kröner-Exzellenzstipendium 2010\_EKES.32). Italian case collections were supported by the Italian Group for IBD and the Italian Society for Paediatric Gastroenterology, Hepatology and Nutrition and funded by the Italian Ministry of Health GR-2008-1144485. Activities in Sweden were supported by the Swedish Society of Medicine, Ihre Foundation, Örebro University Hospital Research Foundation, Karolinska Institutet, the Swedish National Program for IBD Genetics, the Swedish Organization for IBD, and the Swedish Medical Research Council. D.F. and S.V. are senior clinical investigators for the Funds for Scientific Research (FWO/FNRS) Belgium. We acknowledge a grant from Viborg Regional Hospital, Denmark. V. Andersen was supported by SHS Aabenraa, Denmark. We acknowledge funding provided by the Royal Brisbane and Women's Hospital Foundation, National Health and Medical Research Council, Australia and by the European Community (5th PCRD). We acknowledge the following groups that provided biological samples or data for this study: the Inflammatory Bowel in South Eastern Norway (IBSEN) study group, the Norwegian Bone Marrow Donor Registry (NMBDR), the Avon Longitudinal Study of Parents and Children, the Human Biological Data Interchange and Diabetes UK, and Banco Nacional de ADN, Salamanca. This research also uses resources provided by the Type 1 Diabetes Genetics Consortium, a collaborative clinical study sponsored by the NIDDK, National Institute of Allergy and Infectious Diseases (NIAID), National Human Genome Research Institute (NHGRI), National Institute of Child Health and Human Development (NICHD), and Juvenile Diabetes Research Foundation (JDRF) and supported by U01 DK062418. The KORA study was initiated and financed by the Helmholtz Zentrum München – German Research Center for Environmental Health, which is funded by the German Federal Ministry of Education and Research (BMBF) and by the State of Bavaria. KORA research was supported within the Munich Center of

Health Sciences (MC Health), Ludwig-Maximilians-Universität, as part of LMUinnovativ.

**Author Contributions** R.K.W., R.H.D., D.P.M., C.G.M., J.D.R., E.E.S., M.J.D., A.F., M.P. and S.V. contributed equally to the manuscript. J.H.C., J.C.B., R.K.W., R.H.D., D.P.M., A.F., M.P., C.G.M., J.D.R., S.V., M.D.A. and V. Annesse conceived, designed and managed the study and managed the funding. J.H.C., J.C.B., L.J., S. Ripke, R.K.W., R.H.D., D.P.M., M.J.D., M.P. and C.G.M. were involved in manuscript preparation. J.H.C., J.C.B., L.J., S. Ripke, R.K.W., K.Y.H., C.A.A., J.E., K.N., S.L.S., S. Raychaudhuri, Z.W., C.A., A.C., G.B., M.H., X.H., B.Z., C.K.Z., H.Z., J.D.R., E.E.S. and M.J.D. performed or supervised statistical and computational analyses. R.K.W., R.H.D., D.P.M., J.C.L., L.P.S., Y.S., P.G., J.-P.A., T.A., L.A., A.N.A., V. Andersen, J.M.A., L.B., P.A.B., A.B., S.B., C.B., S.C., M.D.A., D.D.J., K.L.D., M.D., C.E., L.R.F., D.F., M.G., C.G., R.G., J.G., A.H., C.H., T.H.K., L.K., S.K., A.L., D.L., E.L., I.C.L., C.W.L., A.R.M., C.M., G.M., J.M., W.N., O.P., C.Y.P., U.P., N.J.P., M.R., J.I.R., R.K.R., J.D.S., M.S., J. Satsangi, S.S., L.A.S., J. Sventoraityte, S.R.T., M.T., H.W.V., M.D.V., C.W., D.C.W., J.W., R.J.X., S.Z., M.S.S., V. Annesse, H.H., IBDGC, S.R.B., J.D.R., G.R.S., C.G.M., A.F., M.P., S.V. and J.H.C. were involved in study subject recruitment and assembling phenotypic data. R.K.W., R.H.D., D.P.M., L.P.S., Y.S., M.M., I.C., E.T., T.B., D.E., K.F., T.H., K.D.T., C.G.M., A.F., M.P. and J.H.C. established DNA collections, genotyping and data management. All authors read and approved the final manuscript before submission.

**Author Information** Data have been deposited in the NCBI database of Genotypes and Phenotypes under accession numbers phs000130.v1.p1 and phs000345.v1.p1. Summary statistics for imputed GWAS are available at <http://www.broadinstitute.org/mpg/ricopili/>. Summary statistics for the meta-analysis markers are available at <http://www.ibdgenetics.org/>. The 523 causal gene network cytoscape file is available on request. Reprints and permissions information is available at [www.nature.com/reprints](http://www.nature.com/reprints). The authors declare no competing financial interests. Readers are welcome to comment on the online version of the paper. Correspondence and requests for materials should be addressed to J.H.C. ([judy.cho@yale.edu](mailto:judy.cho@yale.edu)).

Luke Jostins<sup>1\*</sup>, Stephan Ripke<sup>2,3\*</sup>, Rinse K. Weersma<sup>4</sup>, Richard H. Duerr<sup>5,6</sup>, Dermot P. McGovern<sup>7,8</sup>, Ken Y. Hui<sup>9</sup>, James C. Lee<sup>10</sup>, L. Philip Schumm<sup>11</sup>, Yashoda Sharma<sup>12</sup>, Carl A. Anderson<sup>1</sup>, Jonah Essers<sup>13</sup>, Mitja Mitrovic<sup>14,15</sup>, Kaida Ning<sup>12</sup>, Isabelle Cleyne<sup>16</sup>, Emilie Theatre<sup>17,18</sup>, Sarah L. Spin<sup>19</sup>, Soumya Raychaudhuri<sup>20,21,22</sup>, Philippe Goyette<sup>23</sup>, Zhi Wei<sup>24</sup>, Clara Abraham<sup>12</sup>, Jean-Paul Achkar<sup>25,26</sup>, Tariq Ahmad<sup>27</sup>, Leila Amininejad<sup>28</sup>, Ashwin N. Ananthakrishnan<sup>29</sup>, Vibeke Andersen<sup>30</sup>, Jane M. Andrews<sup>31</sup>, Leonard Baidoo<sup>3</sup>, Tobias Balschun<sup>32</sup>, Peter A. Bampton<sup>33</sup>, Alain Bitton<sup>34</sup>, Gabrielle Boucher<sup>23</sup>, Stephan Brand<sup>35</sup>, Carsten Büning<sup>36</sup>, Ariella Cohain<sup>37</sup>, Sven Cichon<sup>38</sup>, Mauro D'Amato<sup>39</sup>, Dirk De Jong<sup>4</sup>, Kathy L. Devaney<sup>29</sup>, Marla Dubinsky<sup>40</sup>, Cathryn Edwards<sup>41</sup>, David Ellinghaus<sup>32</sup>, Lynnette R. Ferguson<sup>42</sup>, Denis Franchimont<sup>28</sup>, Karin Fransen<sup>5,43</sup>, Richard Geary<sup>44,45</sup>, Michel Georges<sup>17</sup>, Christian Gieger<sup>46</sup>, Jürgen Glas<sup>34</sup>, Talin Haritunians<sup>8</sup>, Ailsa Hart<sup>47</sup>, Chris Hawkey<sup>48</sup>, Matija Hedi<sup>12</sup>, Xinli Hu<sup>20</sup>, Tom H. Karlsen<sup>49</sup>, Limas Kupcinskas<sup>50</sup>, Subra Kugathasan<sup>51</sup>, Anna Latiano<sup>52</sup>, Debby Laukens<sup>53</sup>, Ian C. Lawrence<sup>54</sup>, Charlie W. Lees<sup>55</sup>, Edouard Louis<sup>18</sup>, Gillian Mahy<sup>56</sup>, John Mansfield<sup>57</sup>, Angharad R. Morgan<sup>42</sup>, Craig Mowat<sup>58</sup>, William Newman<sup>59</sup>, Orazio Palmieri<sup>52</sup>, Cyriel Y. Posse<sup>60</sup>, Uros Potocnik<sup>14,61</sup>, Natalie J. Prescott<sup>19</sup>, Miguel Regueiro<sup>5</sup>, Jerome I. Rottier<sup>62</sup>, Richard K. Russell<sup>62</sup>, Jeremy D. Sanderson<sup>63</sup>, Miquel Sans<sup>64,65</sup>, Jack Satsangi<sup>55</sup>, Stefan Schreiber<sup>32,66</sup>, Lisa A. Simms<sup>57</sup>, Jurgita Sventoraityte<sup>60</sup>, Stephan R. Targan<sup>7</sup>, Kent D. Taylor<sup>7,8</sup>, Mark Tremelling<sup>68</sup>, Hein W. Verspaget<sup>69</sup>, Martine De Vos<sup>53</sup>, Cisca Wijmenga<sup>43</sup>, David C. Wilson<sup>62,70</sup>, Juliane Winkelmann<sup>71</sup>, Ramnik J. Xavier<sup>29,72</sup>, Sebastian Zeissig<sup>66</sup>, Bin Zhang<sup>37</sup>, Clarence K. Zhang<sup>73</sup>, Hongyu Zhao<sup>73</sup>, The International IBD Genetics Consortium (IBDGC)<sup>74</sup>, Mark S. Silverberg<sup>74</sup>, Vito Annesse<sup>52,75</sup>, Hakon Hakonarson<sup>76,77</sup>, Steven R. Brant<sup>78</sup>, Graham Radford-Smith<sup>67,79</sup>, Christopher G. Mathew<sup>19</sup>, John D. Rioux<sup>23</sup>, Eric E. Schadt<sup>37</sup>, Mark J. Daly<sup>2,3</sup>, Andre Franke<sup>32</sup>, Miles Parkes<sup>10</sup>, Severine Vermeire<sup>16,80</sup>, Jeffrey C. Barrett<sup>1\*</sup> & Judy H. Cho<sup>9,12\*</sup>

<sup>1</sup>Wellcome Trust Sanger Institute, Wellcome Trust Genome Campus, Hinxton, Cambridge CB10 1HH, UK. <sup>2</sup>Analytic and Translational Genetics Unit, Massachusetts General Hospital, Harvard Medical School, Boston, Massachusetts 02114, USA. <sup>3</sup>Broad Institute of MIT and Harvard, Cambridge, Massachusetts 02142, USA. <sup>4</sup>Department of Gastroenterology and Hepatology, University of Groningen and University Medical Center Groningen, Groningen 9700 RB, The Netherlands. <sup>5</sup>Division of Gastroenterology, Hepatology and Nutrition, Department of Medicine, University of Pittsburgh School of Medicine, Pittsburgh, Pennsylvania 15261, USA. <sup>6</sup>Department of Human Genetics, University of Pittsburgh Graduate School of Public Health, Pittsburgh, Pennsylvania 15261, USA. <sup>7</sup>F. Widjaja Foundation Inflammatory Bowel and Immunobiology Research Institute, Los Angeles, California 90048, USA. <sup>8</sup>Medical Genetics Institute, Cedars-Sinai Medical Center, Los Angeles, California 90048, USA. <sup>9</sup>Department of Genetics, Yale School of Medicine, New Haven, Connecticut 06520, USA. <sup>10</sup>Inflammatory Bowel Disease Research Group, Addenbrooke's Hospital, University of Cambridge, Cambridge CB2 0QQ, UK. <sup>11</sup>Department of Health Studies, University of Chicago, Chicago, Illinois 60637, USA. <sup>12</sup>Department of Internal Medicine, Section of Digestive Diseases, Yale School of Medicine, New Haven, Connecticut 06520, USA. <sup>13</sup>Center for Human Genetic Research, Massachusetts General Hospital, Harvard Medical School, Boston, Massachusetts 02114, USA. <sup>14</sup>University of Maribor, Faculty of Medicine, Center for Human Molecular Genetics and Pharmacogenomics, Maribor 2000, Slovenia. <sup>15</sup>University Medical Center Groningen, Department of Genetics, Groningen 9700 RB, The Netherlands. <sup>16</sup>Department of Clinical and Experimental Medicine, Gastroenterology section, KU Leuven, Leuven 3000, Belgium. <sup>17</sup>Unit of Animal Genomics, Groupe Interdisciplinaire de Génoprotéomique Appliquée (GIGA-R) and Faculty of Veterinary Medicine, University of Liège, Liège 4000, Belgium. <sup>18</sup>Division of Gastroenterology, Centre Hospitalier Universitaire, Université de Liège, Liège 4000, Belgium. <sup>19</sup>Department of Medical and

Molecular Genetics, Division of Genetics and Molecular Medicine, King's College London School of Medicine, Guy's Hospital, London SE1 9RT, UK. <sup>20</sup>Division of Rheumatology Immunology and Allergy, Brigham and Women's Hospital, Boston, Massachusetts 02115, USA. <sup>21</sup>Program in Medical and Population Genetics, Broad Institute, Cambridge, Massachusetts 02142, USA. <sup>22</sup>Division of Genetics, Brigham and Women's Hospital, Boston, Massachusetts 02115, USA. <sup>23</sup>Université de Montréal and the Montreal Heart Institute, Research Center, Montréal, Québec H1T 1C8, Canada. <sup>24</sup>Department of Computer Science, New Jersey Institute of Technology, Newark, New Jersey 07102, USA. <sup>25</sup>Department of Gastroenterology & Hepatology, Digestive Disease Institute, Cleveland Clinic, Cleveland, Ohio 44195, USA. <sup>26</sup>Department of Pathobiology, Lerner Research Institute, Cleveland Clinic, Cleveland, Ohio 44195, USA. <sup>27</sup>Peninsula College of Medicine and Dentistry, Exeter EX1 2LU, UK. <sup>28</sup>Erasmus Hospital, Free University of Brussels, Department of Gastroenterology, Brussels, 1070 Belgium. <sup>29</sup>Massachusetts General Hospital, Harvard Medical School, Gastroenterology Unit, Boston, Massachusetts 02114, USA. <sup>30</sup>Viborg Regional Hospital, Medical Department, Viborg 8800, Denmark. <sup>31</sup>Inflammatory Bowel Disease Service, Department of Gastroenterology and Hepatology, Royal Adelaide Hospital, and School of Medicine, University of Adelaide, Adelaide 5000, Australia. <sup>32</sup>Institute of Clinical Chemistry, Christian-Albrechts-University, Kiel 24105, Germany. <sup>33</sup>Department of Gastroenterology and Hepatology, Flinders Medical Centre and School of Medicine, Flinders University, Adelaide 5000, Australia. <sup>34</sup>Division of Gastroenterology, McGill University Health Centre, Royal Victoria Hospital, Montréal, Québec H3A 1A1, Canada. <sup>35</sup>Department of Medicine II, University Hospital Munich-Grosshadern, Ludwig-Maximilians-University, Munich 80336, Germany. <sup>36</sup>Department of Gastroenterology, Charité, Campus Mitte, Universitätsmedizin Berlin, Berlin 10117, Germany. <sup>37</sup>Department of Genetics and Genomic Sciences, Mount Sinai School of Medicine, New York City, New York 10029, USA. <sup>38</sup>Department of Genomics, Life & Brain Center, University Hospital Bonn, Bonn 53012, Germany. <sup>39</sup>Department of Biosciences and Nutrition, Karolinska Institutet, Stockholm 14 183, Sweden. <sup>40</sup>Department of Pediatrics, Cedars Sinai Medical Center, Los Angeles, California 90048, USA. <sup>41</sup>Torbay Hospital, Department of Gastroenterology, Torbay, Devon TQ2 7AA, UK. <sup>42</sup>School of Medical Sciences, Faculty of Medical & Health Sciences, The University of Auckland, Auckland 1142, New Zealand. <sup>43</sup>University of Groningen, University Medical Center Groningen, Department of Genetics, Groningen T9700 RB, The Netherlands. <sup>44</sup>Department of Medicine, University of Otago, Christchurch 8140, New Zealand. <sup>45</sup>Department of Gastroenterology, Christchurch Hospital, Christchurch 8011, New Zealand. <sup>46</sup>Institute of Genetic Epidemiology, Helmholtz Zentrum München - German Research Center for Environmental Health, Neuherberg 85764, Germany. <sup>47</sup>St Mark's Hospital, Watford Road, Harrow, Middlesex HA1 3UJ, UK. <sup>48</sup>Nottingham Digestive Diseases Center, Queens Medical Centre, Nottingham NG7 1AW, UK. <sup>49</sup>Research Institute of Internal Medicine, Oslo University Hospital Rikshospitalet, Oslo 0424, Norway. <sup>50</sup>Kaunas University of Medicine, Department of Gastroenterology, Kaunas 44307, Lithuania. <sup>51</sup>Department of Pediatrics, Emory University School of Medicine, Atlanta, Georgia 30322, USA. <sup>52</sup>Unit of Gastroenterology, Istituto di Ricovero e Cura a Carattere Scientifico-Casa Sollievo della Sofferenza (IRCCS-CSS) Hospital, San Giovanni Rotondo 71013, Italy. <sup>53</sup>Ghent University Hospital, Department of Gastroenterology and Hepatology, Ghent 9000, Belgium. <sup>54</sup>School of Medicine and Pharmacology, The University of Western Australia, Fremantle, Western Australia 6009, Australia. <sup>55</sup>Gastrointestinal Unit, Molecular Medicine Centre, University of Edinburgh, Western General Hospital, Edinburgh EH4 2XU, UK. <sup>56</sup>Department of Gastroenterology, The Townsville Hospital, Townsville, Queensland 4810, Australia. <sup>57</sup>Institute of Human Genetics, Newcastle University, Newcastle upon Tyne NE1 7RU, UK. <sup>58</sup>Department of Medicine, Ninewells Hospital and Medical School, Dundee DD1 9SY, UK. <sup>59</sup>Genetic Medicine, MAHSC, University of Manchester, Manchester M13 9PL, UK. <sup>60</sup>Academic Medical Center, Department of Gastroenterology, Amsterdam 1105 AZ, The Netherlands. <sup>61</sup>University of Maribor, Faculty for Chemistry and Chemical Engineering, Maribor 2000, Slovenia. <sup>62</sup>Royal Hospital for Sick Children, Paediatric Gastroenterology and Nutrition, Glasgow G3 8SJ, UK. <sup>63</sup>Guy's & St Thomas' NHS Foundation Trust, St Thomas' Hospital, Department of Gastroenterology, London SE1 7EH, UK. <sup>64</sup>Department of Gastroenterology, Hospital Clinic/Institut d'Investigacions Biomèdiques August Pi i Sunyer (IDIBAPS), Barcelona, Spain. <sup>65</sup>Centro de Investigación Biomédica en Red de Enfermedades Hepáticas y Digestivas (CIBER-EHD), Barcelona 08036, Spain. <sup>66</sup>Department for General Internal Medicine, Christian-Albrechts-University, Kiel, Kiel 24118, Germany. <sup>67</sup>Inflammatory Bowel Diseases, Genetics and Computational Biology, Queensland Institute of Medical Research, Brisbane 4029, Australia. <sup>68</sup>Norfolk and Norwich University Hospital, Norwich NR4 7UY, UK. <sup>69</sup>Department of Gastroenterology, Leiden University Medical Center, Leiden 2333 ZA, The Netherlands. <sup>70</sup>Child Life and Health, University of Edinburgh, Edinburgh, Scotland EH9 1UW, UK. <sup>71</sup>Institute of Human Genetics and Department of Neurology, Technische Universität München, Munich 80336, Germany. <sup>72</sup>Center for Computational and Integrative Biology, Massachusetts General Hospital, Boston, Massachusetts 02114, USA. <sup>73</sup>Department of Biostatistics, School of Public Health, Yale University, New Haven, Connecticut 06520, USA. <sup>74</sup>Mount Sinai Hospital Inflammatory Bowel Disease Centre, University of Toronto, Toronto, Ontario M5G 1X5, Canada. <sup>75</sup>Azienda Ospedaliero Universitaria (AOU) Careggi, Unit of Gastroenterology SOD2, Florence 50134, Italy. <sup>76</sup>Center for Applied Genomics, The Children's Hospital of Philadelphia, Philadelphia, Pennsylvania 19104, USA. <sup>77</sup>Department of Pediatrics, Center for Pediatric Inflammatory Bowel Disease, The Children's Hospital of Philadelphia, Philadelphia, Pennsylvania 19104, USA. <sup>78</sup>Meyerhoff Inflammatory Bowel Disease Center, Department of Medicine, School of Medicine, and Department of Epidemiology, Bloomberg School of Public Health, Johns Hopkins University, Baltimore, Maryland 21205, USA. <sup>79</sup>Department of Gastroenterology, Royal Brisbane and Women's Hospital, and School of Medicine, University of Queensland, Brisbane 4029, Australia. <sup>80</sup>Department of Gastroenterology, University Hospital Leuven, Leuven 3000, Belgium.

\*These authors contributed equally to this work.

†Lists of participants and their affiliations appear in the Supplementary Information.

# Codon-usage-based inhibition of HIV protein synthesis by human schlafen 11

Manqing Li<sup>1</sup>, Elaine Kao<sup>1</sup>, Xia Gao<sup>1</sup>, Hilary Sandig<sup>1</sup>, Kirsten Limmer<sup>1</sup>, Mariana Pavon-Eternod<sup>2</sup>, Thomas E. Jones<sup>2</sup>, Sebastien Landry<sup>3</sup>, Tao Pan<sup>2</sup>, Matthew D. Weitzman<sup>3</sup> & Michael David<sup>1,4</sup>

**In mammals, one of the most pronounced consequences of viral infection is the induction of type I interferons, cytokines with potent antiviral activity. Schlafen (*Sfn*) genes are a subset of interferon-stimulated early response genes (ISGs) that are also induced directly by pathogens via the interferon regulatory factor 3 (IRF3) pathway<sup>1</sup>. However, many ISGs are of unknown or incompletely understood function. Here we show that human SLFN11 potently and specifically abrogates the production of retroviruses such as human immunodeficiency virus 1 (HIV-1). Our study revealed that SLFN11 has no effect on the early steps of the retroviral infection cycle, including reverse transcription, integration and transcription. Rather, SLFN11 acts at the late stage of virus production by selectively inhibiting the expression of viral proteins in a codon-usage-dependent manner. We further find that SLFN11 binds transfer RNA, and counteracts changes in the tRNA pool elicited by the presence of HIV. Our studies identified a novel antiviral mechanism within the innate immune response, in which SLFN11 selectively inhibits viral protein synthesis in HIV-infected cells by means of codon-bias discrimination.**

*SLFN* genes encode a family of proteins limited to mammalian organisms. Nine murine and six human *SLFN* genes share a conserved NH2-terminus containing a putative AAA-domain, and long *SLFN* genes possess motifs resembling DNA/RNA helicase domains, a trait they share with the nucleic acid sensors RIG-I and MDA-5<sup>2</sup>. Beyond that, *SLFN* proteins harbour no sequence similarity to other proteins. *In vivo*, short and long murine *SLFN* proteins inhibit T-cell development<sup>3–5</sup>, and levels of murine *SLFN* proteins are elevated after infection with *Brucella* or *Listeria*<sup>4</sup>. Lipopolysaccharide, poly-inosine-cytosine (poly-IC) or interferon (IFN)- $\alpha/\beta$  treatment of macrophages results in induction of several murine *Sfn* genes (our unpublished results). Treatment of human foreskin fibroblasts with IFN- $\beta$ , poly-IC or poly-dAdT revealed similar induction of *SLFN* genes (Supplementary Fig. 1a), and human SLFN5 and SLFN11 were consistently the most prominent family members (Supplementary Fig. 1b). Notably, we observed a striking difference in *SLFN* levels between HEK293 (293) and HEK293T (293T) cells (Supplementary Fig. 1b), and exploited this differential expression to focus on SLFN11 for further studies. We further used *SLFN11*-targeted short hairpin RNA to generate stable 293 cells that specifically lack SLFN11 expression (293shRNA<sup>SLFN</sup>) (Supplementary Fig. 1c, d).

To test whether lack of SLFN11 in 293shRNA<sup>SLFN</sup> or 293T cells alters their ability to subdue viral infections, we infected these cells with vesicular stomatitis virus (VSV)-G pseudotyped HIV (HIV<sup>VSV-G</sup>), or amphotropic murine stem cell virus (MSCV), adeno-associated virus (AAV), or herpes simplex virus (HSV). HIV<sup>VSV-G</sup>-infected cells expressed luciferase after integration of the viral complementary DNAs into the host genome. Regardless of SLFN11 expression, all cell lines had comparable luciferase levels after HIV<sup>VSV-G</sup> infection (Supplementary Fig. 2). A similar lack of influence of SLFN11 was observed when cells were infected with MSCV, AAV or HSV (not shown).

HEK293T cells are used as packaging cells for production of retroviruses, and we therefore considered the possibility that virus production rather than the response towards them is afflicted by SLFN11. Indeed, 293T cells produced markedly higher HIV<sup>VSV-G</sup> (Fig. 1b) or MSCV (Supplementary Fig. 3a) titres than 293 cells from the viral vectors pNL4-3.Luc.R<sup>+</sup>E<sup>-</sup> or MSCV-IRES-GFP, respectively. Most importantly, this increase in viral titre was also clearly evident in 293shRNA<sup>SLFN</sup> cells, whereas 293 and 293shRNA<sup>Ctrl</sup> cells produced the same low levels of virus (Fig. 1b and Supplementary Fig. 3a). Notably, the modulation of virus production is limited to particular viruses, as fabrication of retroviruses (Fig. 1b and Supplementary Fig. 3a), but not of AAV (Supplementary Fig. 3c), was affected by SLFN11. We also did not observe any modulation of ISGs such as ISG15, ISG54 or APOBEC3G (not shown) as a consequence of SLFN11 expression, supporting the notion that SLFN11 does not create a general virus-resistant phenotype.

To corroborate that the observed differences are attributable to dissimilar SLFN11 expression, we expressed full-length SLFN11 (amino acids 1–901) in 293T cells and analysed their ability to produce HIV<sup>VSV-G</sup>. Indeed, SLFN11 strongly inhibited HIV<sup>VSV-G</sup> (Fig. 1a) or MSCV (Supplementary Fig. 3b) production from 293T cells, with the inhibitory activity residing in the AAA-domain-containing, amino-terminal region (SLFN11-N; amino acids 1–579). No effect of the isolated carboxy-terminal region (SLFN11-C; amino acids 523–901) harbouring the putative helicase sequence was observed (Fig. 1a and Supplementary Fig. 3b). Intriguingly, SLFN5 failed to inhibit retrovirus production but yielded slightly elevated viral titres, illustrating specificity among *SLFN* proteins in their antiviral activity.

To discern whether SLFN11 reduced the number or the viability of released virus, we measured p24 capsid and viral RNA (vRNA) levels in supernatants of pNL4-3.Luc.R<sup>+</sup>E<sup>-</sup>-transfected, HIV<sup>VSV-G</sup>-producing cells. Extracellular p24 (Fig. 1c and d) or vRNA (Fig. 1e and f) concentration patterns closely matched the titre results from infection assays, demonstrating that SLFN11 diminishes the number of viral particles released from the cells.

To assess a possible reduction of intracellular vRNA, we determined its levels in 293T cells expressing chloramphenicol acetyl transferase (CAT), SLFN5, SLFN11, SLFN11-N or SLFN11-C (Fig. 1g), as well as in 293, 293shRNA<sup>Ctrl</sup> and 293shRNA<sup>SLFN</sup> cells (Fig. 1h). In contrast to the pronounced variations in extracellular vRNA, only insignificant differences in intracellular vRNA were evident among those cells. We also analysed vRNA in the cytoplasmic fraction specifically, as nuclear export of unspliced vRNA is a hallmark of retroviral RNA processing<sup>6–8</sup>, but again found no significant alterations attributable to SLFN11 (Supplementary Fig. 4a).

Unlike in BST2-expressing cells<sup>9,10</sup>, electron-microscopic analysis failed to document accumulation of virions inside or on the surface of virus-producing cells in the presence of SLFN11 (Supplementary Fig. 4b). As such, SLFN11 greatly diminishes the formation of viral particles inside the cell, despite the fact that vRNA is equally available.

<sup>1</sup>Section of Molecular Biology, Division of Biological Sciences, University of California San Diego, La Jolla, California 92093, USA. <sup>2</sup>Department of Biochemistry and Molecular Biology, University of Chicago, Chicago, Illinois 60637, USA. <sup>3</sup>Laboratory of Genetics, The Salk Institute for Biological Studies, La Jolla, California 92037, USA. <sup>4</sup>Moores Cancer Center, University of California San Diego, La Jolla, California 92093, USA.

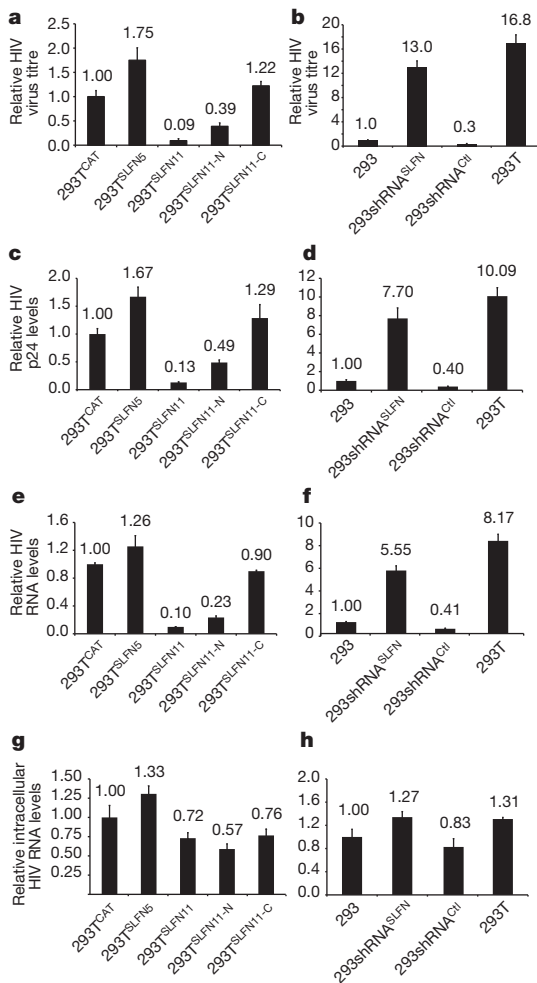


**Figure 1 | SLFN11 inhibits retrovirus production without affecting intracellular vRNA levels.** **a–h**, 293T cells were transfected with pNL4-3.Luc.R<sup>+</sup>E<sup>-</sup>/pCMV-VSV-G together with SLFN5, SLFN11, SLFN11-N, SLFN11-C or CAT (**a**, **c**, **e**, **g**), or 293, 293shRNA<sup>Ctl</sup>, 293shRNA<sup>SLFN</sup> and 293T cells were transfected with pNL4-3.Luc.R<sup>+</sup>E<sup>-</sup> and pCMV-VSV-G (**b**, **d**, **f**, **h**). **a**, **b**, VSV-G-pseudotyped HIV production was assayed by titrated infection and luciferase assay. **c**, **d**, Viral particle content in supernatants was analysed by p24 ELISA. **e**, **f**, extracellular vRNA concentration was analysed by qPCR of p24. **g**, **h**, intracellular vRNA was determined by qPCR of p24. (average  $\pm$  s.d.;  $n = 3$ ).

When the two cell sets were analysed for the expression of viral proteins encoded by pNL4-3.Luc.R<sup>+</sup>E<sup>-</sup>, we noted a marked effect of SLFN11 on p55 Gag and p24 capsid proteins<sup>11</sup> (Fig. 2a, b). To create a clearer picture of the effect of SLFN11 on p55, we abolished expression of the viral protease by introducing a stop codon into *pro* in pNL4-3.Luc.R<sup>+</sup>E<sup>-</sup>. As anticipated, p24 could no longer be detected; however, modulation of p55 expression by SLFN11 was clearly present (Supplementary Fig. 5a). As with *gag*-derived proteins, SLFN11 had a notable effect on the protein levels of RT, Vif, Vpu and Vpr (Fig. 2a, b). Intriguingly, we did not observe any reduction of enhanced green fluorescent protein (EGFP) derived from a co-transfected vector, or of GAPDH (Fig. 2a, b, bottom), indicating that the limited viral protein production is not due to a global shutdown of protein synthesis.

Even more surprising was that luciferase expression, coded in pNL4-3.Luc.R<sup>+</sup>E<sup>-</sup> in place of *nef*, was mostly impervious to SLFN11 (Fig. 2c, top), contrasting the SLFN11-mediated diminishment of other proteins encoded on this vector. Notably, Nef expression was inhibited by SLFN11 in the context of pNL4-3- $\Delta$ Env-EGFP, which has part of *env* replaced by EGFP, but retains *nef* in its original position. (Fig. 2c, bottom). We thus conclude that SLFN11 selectively suppresses viral protein expression via transcript-intrinsic properties

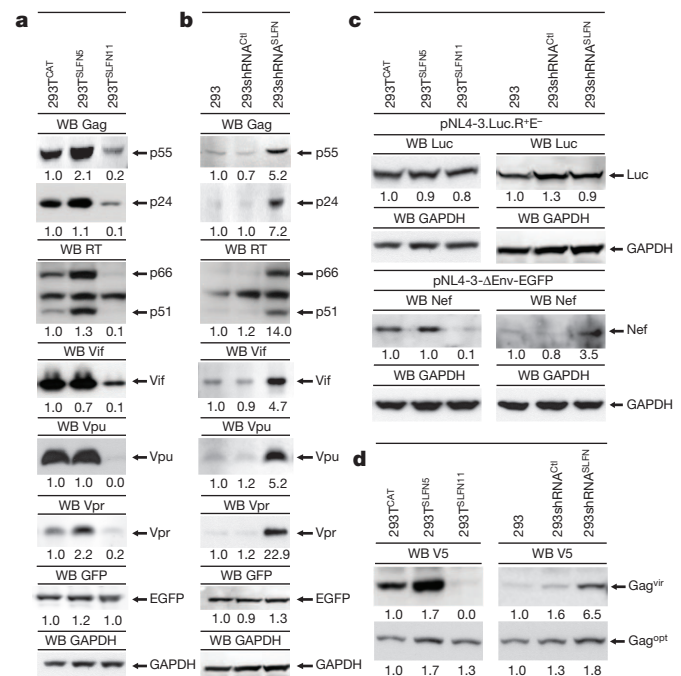


**Figure 2 | SLFN11 selectively inhibits viral protein expression on the basis of codon usage.** **a**, 293T cells were transfected with pNL4-3.Luc.R<sup>+</sup>E<sup>-</sup> and pcDNA5-EGFP together with SLFN5, SLFN11 or CAT, and cell lysates immunoblotted for HIV proteins, EGFP and GAPDH. **b**, 293, 293shRNA<sup>Ctl</sup> and 293shRNA<sup>SLFN</sup> cells were transfected with pNL4-3.Luc.R<sup>+</sup>E<sup>-</sup> and pcDNA5-EGFP, and lysates analysed as in **a**. **c**, Top: 293T cells were co-transfected with pNL4-3.Luc.R<sup>+</sup>E<sup>-</sup> and SLFN5, SLFN11 or CAT (left), or 293, 293shRNA<sup>Ctl</sup> and 293shRNA<sup>SLFN</sup> cells were transfected with pNL4-3.Luc.R<sup>+</sup>E<sup>-</sup> (right). Lysates were probed for luciferase and GAPDH. Bottom: as above, except pNL4-3- $\Delta$ Env-EGFP was used instead of pNL4-3.Luc.R<sup>+</sup>E<sup>-</sup>, and lysates were immunoblotted for Nef and GAPDH; **d**, Cells were transfected with viral codon-usage-based *gag* (Gag<sup>vir</sup>, top) or synonymous human codon usage-optimized *gag* (Gag<sup>opt</sup>, bottom). Expression of Gag in cell lysates was determined by anti-V5 immunoblotting.

rather than external factors or positional elements. This notion is further corroborated by the fact that SLFN11 had no effect on Rev response element (RRE)-mediated events such as nuclear export of unspliced vRNA (Supplementary Fig. 5b).

Viral genomes have biased nucleotide compositions different from human genes<sup>12–18</sup>. Extremely high frequencies of A nucleotides are found in the RNA genomes of lentiviruses and influenza virus<sup>13,17,19,20</sup>. Wild isolates of HIV-1, particularly *gag* and *pol* sequences, are characterized by low GC content and suboptimal codon usage compared to the host cell preference<sup>14,21–24</sup>. The unusual rare codon bias favours A/U in the third position, which induces ribosome pausing and inefficient translation. As the inhibitory effect of SLFN11 on viral protein expression is intrinsic to the transcripts, we proposed that SLFN11 exploits viral codon preferences to specifically attenuate viral protein synthesis. We therefore generated vectors containing only the open reading frame of HIV-1 *gag* with either viral codon-bias (Gag<sup>vir</sup>), or synonymous substitutions optimizing for human cell expression (Gag<sup>opt</sup>). As shown in Fig. 2d, SLFN11 strongly affected expression of Gag<sup>vir</sup>, but was without consequence for Gag<sup>opt</sup> expression. Differences in translation initiation are not likely, as both Gag<sup>vir</sup> and Gag<sup>opt</sup> contain the same translation start sequences. This finding strongly indicates that SLFN11 is exploiting the distinct viral codon bias to selectively attenuate the expression of viral proteins.

Previous reports indicated changes in cellular tRNA levels after HIV infection<sup>20</sup>, prompting us to investigate whether SLFN11 alters the tRNA composition in the absence or presence of HIV. Using tRNA arrays<sup>25,26</sup>, we observed little to no changes in tRNA levels as a

consequence of SLFN11 expression (Fig. 3a, left column). However, whereas HIV triggered substantial changes in tRNA concentrations in SLFN11-knockdown cells, no changes were observed in the presence of SLFN11 (Fig. 3a, middle and right). Thus, SLFN11 counteracts HIV-induced changes in tRNA composition, presumably initiated to promote viral protein synthesis. To test whether SLFN11 interacts directly with tRNA, we used human tRNA as electrophoretic mobility shift assay (EMSA) probe with fast protein liquid chromatography (FPLC)-purified His-conjugated SLFN11-N. As shown in Fig. 3b, SLFN11-N

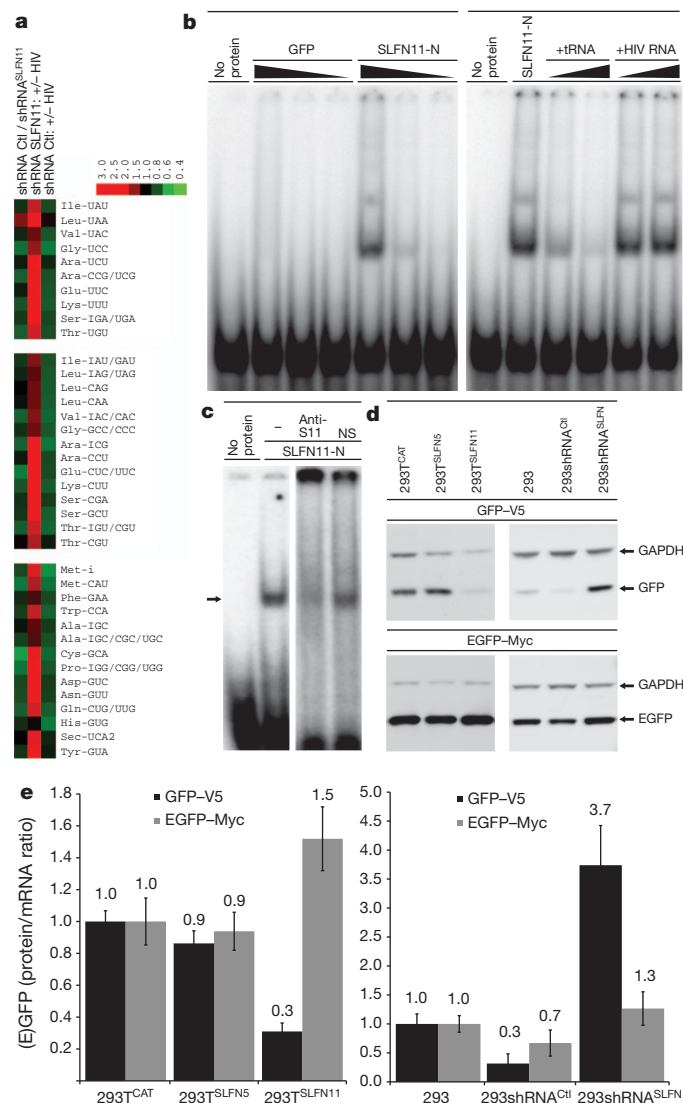


**Figure 3 | SLFN11 binds tRNAs and selectively inhibits protein expression based on codon usage.** **a**, 293T cells transfected with SLFN11 shRNA or control vector (indicated as +/- HIV). Relative abundances of mature tRNA species were analysed by microarray as described<sup>25,26</sup>. **b**, Left: increasing amounts of SLFN11-N or GFP were incubated with <sup>32</sup>P-labelled tRNA and subjected to EMSA. Right: 2 × or 10 × unlabelled tRNA or *in-vitro*-transcribed vRNA corresponding to the *gag-pol* frame-shifting sequence (120 bases) were added to the binding reaction. **c**, As in **b**, except non-specific (NS) or anti-SLFN11 (Anti-S11) monoclonal antibody was added to the binding reaction. **d**, 293T cells were transfected with V5-tagged GFP, Myc-tagged EGFP and pNL4-3.Luc.R<sup>+</sup>E<sup>-</sup> together with either CAT, SLFN5 or SLFN11 (left). Lysates were probed for V5-GFP, Myc-EGFP and GAPDH. Similarly, V5-tagged GFP, Myc-tagged EGFP and pNL4-3.Luc.R<sup>+</sup>E<sup>-</sup> were co-transfected into 293, 293shRNA<sup>Ctrl</sup> and 293shRNA<sup>SLFN</sup> cells (right), and V5-GFP, Myc-EGFP and GAPDH expression determined by immunoblotting. **e**, V5-GFP and Myc-EGFP protein levels determined from **d** were quantified and normalized to V5-GFP and Myc-EGFP mRNA levels, respectively (average ± s.d.; n = 4).

produced a clear shift of the tRNA in a dose-dependent manner. The shifted band was competed with unlabelled tRNA, but not *in-vitro*-transcribed vRNA (Fig. 3b), and was disrupted by an antibody against SLFN11 (Fig. 3c). To determine whether SLFN11 has binding preference for particular tRNAs, we performed EMSAs with increasing amounts of SLFN11-N to obtain approximately 50% shifting efficiency (Supplementary Fig. 6). When the shifted (S), unshifted (U) and total tRNA (T) bands were isolated and recovered tRNAs hybridized to tRNA arrays, no enrichment of particular tRNAs in the shifted band was noticeable (Supplementary Fig. 6), indicating a lack of discerning binding preference of SLFN11-N.

The results shown lead to the premise that any protein that uses similar codon usage as HIV would be modulated by HIV and/or SLFN11. To demonstrate unequivocally that codon-bias rather than cryptic regulatory elements in *gag* accounted for the influence of SLFN11, we tested this hypothesis using non-viral proteins. Natural green fluorescent protein (GFP) harbours a similar codon-bias as that of HIV, whereas EGFP has been optimized for mammalian expression by substituting synonymous codons of highly expressed human genes throughout the GFP open reading frame<sup>22</sup>. As anticipated, co-transfection of pNL4-3.Luc.R<sup>+</sup>E<sup>-</sup> with V5-tagged GFP and Myc-tagged EGFP in the absence of SLFN11 resulted in increased GFP, but not EGFP, expression (not shown). Most importantly, SLFN11 inhibited the expression of GFP in a manner identical to viral proteins, whereas EGFP was largely refractory to suppression by SLFN11 (Fig. 3d, e). As (E)GFP protein levels have been normalized to their respective messenger RNA levels (Fig. 3e), we conclude that any differences in GFP expression are the consequence of altered protein synthesis rather than variations in transcription or mRNA stability.

Finally, to demonstrate that the anti-retroviral effects of SLFN11 are not limited to a system using HIV<sup>VSU-G</sup> and 293 cells, we used CEM cells, a T-cell line widely used to assess HIV replication kinetics. Human peripheral blood mono-nuclear cells (PBMCs) display similar levels of SLFN11 after IFN-β stimulation as CEM cells (Fig. 4a). Control or SLFN11-directed shRNAs were used to generate stable CEM variants (Fig. 4b), and the resulting CEMshRNA<sup>Ctrl</sup> and CEMshRNA<sup>SLFN</sup> cells and parental CEM cells were infected with wild-type X4-HIV-1<sub>LAI</sub>, and viral replication was assessed via p24 enzyme-linked immunosorbent assays (ELISA) of the supernatants.

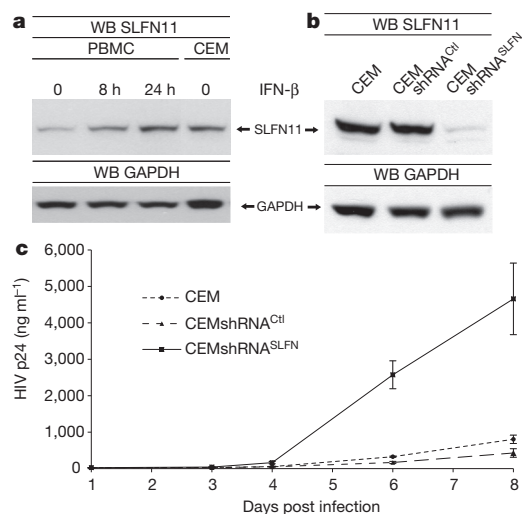


**Figure 4 | SLFN11 inhibits replication of wild-type HIV-1<sub>LAI</sub> in CEM cells.** **a**, Human PBMCs were stimulated with 6,000 U ml<sup>-1</sup> IFN-β. SLFN11 expression in the derived lysates and in CEM cell lysates was analysed by immunoblotting. **b**, SLFN11 expression in CEM, CEMshRNA<sup>Ctrl</sup> and CEMshRNA<sup>SLFN</sup> cells as analysed by immunoblotting. **c**, CEM, CEMshRNA<sup>Ctrl</sup> and CEMshRNA<sup>SLFN</sup> cells were infected with HIV-1<sub>LAI</sub> at a multiplicity of infection (m.o.i.) of 0.01, and viral replication was assayed by p24 ELISA of culture supernatants (average ± s.d.; n = 4).

As anticipated, CEM and CEMshRNA<sup>chl</sup> cells produced comparable viral titres at all time points. In contrast, CEMshRNA<sup>SLFN</sup> cells facilitated significantly enhanced HIV-1 replication, yielding an exponentially increasing difference in viral titres (Fig. 4c). A second CEMshRNA<sup>SLFN</sup> cell line established by means of a distinct *SLFN11* shRNA further corroborated these results (Supplementary Fig. 7).

In summary, systematic analysis of the HIV replication cycle revealed that *SLFN11* does not inhibit reverse transcription, integration or production and nuclear export of viral RNA, nor did we observe a block in budding or release of viral particles. However, we discovered a selective inhibition in the synthesis of virally encoded proteins. Intriguingly, a specific inhibition of viral protein synthesis in HIV-infected cells in response to interferon was previously observed, but the factors responsible for the effect were not identified<sup>27</sup>. We postulate that *SLFN11* acts at the point of virus protein synthesis by exploiting the unique viral codon bias towards A/T nucleotides. This model supports the notion that the antiviral activity of *SLFN11* extends to other viruses with rare codon bias such as influenza, but apparently not to AAV or HSV. The exact mechanism by which HIV alters tRNA function in its favour and how *SLFN11* counteracts this process will require considerable further analysis. Evidently, *SLFN11* interacts with all tRNAs *in vitro*. Direct binding of *SLFN11* to tRNA offers the possibility that *SLFN11* either sequesters tRNAs, prevents their maturation via post-transcriptional processing or accelerates their deacylation. In either case, if already rare tRNAs are further reduced, tRNA availability might manifest as the rate-limiting step in the synthesis of proteins involving those tRNAs. In contrast, a lesser or no impact would be expected on proteins synthesized via plentiful tRNAs, as even if a fraction of those tRNAs is 'eliminated', translation initiation will likely remain the rate-limiting event. In conclusion, our results establish *SLFN11* as a potent, interferon-inducible restriction factor against retroviruses such as HIV, mediating its antiviral effects on the basis of codon usage discrimination.

## METHODS SUMMARY

**Plasmids and antibodies.** *SLFN5* and *SLFN11* were cloned into pcDNA6/V5-His. PCR fragments of *SLFN11* were cloned into pcDNA6/V5-His to generate *SLFN11-N* (amino acids 1–579) and *SLFN11-C* (amino acids 523–901). The pNL4-3.Luc.R<sup>+</sup>E<sup>-</sup> HIV-1 vector has been described previously<sup>28</sup>. *SLFN11* antibodies were from Sigma and Abmart. pNL4-3-ΔEnv-EGFP, pNL-GFP-RRE(SA) and antibodies against HIV-1 proteins were obtained through the NIH AIDS Research and Reference Reagent Program. Generation of Gag<sup>vir</sup>, Gag<sup>opt</sup> and (E)GFP vectors is in Methods. pLKO.1 shRNA lentivirus constructs were from Open Biosystems.

**Virus production and titre assays.** HIV production was determined by transfection of pNL4-3.Luc.R<sup>+</sup>E<sup>-</sup> and pCMV-VSV-G into cells of interest. Supernatants were used to spin-infect HEK293T cells, and luciferase was measured by Bright-Glo Luciferase Assay (Promega). p24 ELISAs were performed at the Center for AIDS Research, UCSD using Alliance p24 ELISA kits (Perkin Elmer).

**HIV replication kinetics.** Wild type X4 strain of HIV-1<sub>LAI</sub> was used to inoculate CEM, CEMshRNA<sup>chl</sup> and CEMshRNA<sup>SLFN</sup> cells at a multiplicity of infection of 0.01, and viral titres were measured by p24 ELISA.

**Data analysis and presentation.** Unless indicated otherwise, results presented in graphs are average ± s.d. of at least three independent transfections or infections. For immunoblots, a representative of at least three independent transfections or infections is shown.

**Full Methods** and any associated references are available in the online version of the paper.

Received 22 November 2011; accepted 23 July 2012.

Published online 23 September 2012.

1. Sohn, W. J. *et al.* Novel transcriptional regulation of the schlafen-2 gene in macrophages in response to TLR-triggered stimulation. *Mol. Immunol.* **44**, 3273–3282 (2007).
2. Yoneyama, M. *et al.* Shared and unique functions of the DExD/H-box helicases RIG-I, MDA5, and LGP2 in antiviral innate immunity. *J. Immunol.* **175**, 2851–2858 (2005).

3. Schwarz, D. A., Katayama, C. D. & Hedrick, S. M. *Schlafen*, a new family of growth regulatory genes that affect thymocyte development. *Immunity* **9**, 657–668 (1998).
4. Geserick, P., Kaiser, F., Klemm, U., Kaufmann, S. H. & Zerrahn, J. Modulation of T cell development and activation by novel members of the Schlafen (slfn) gene family harbouring an RNA helicase-like motif. *Int. Immunol.* **16**, 1535–1548 (2004).
5. Berger, M. *et al.* An *Slfn2* mutation causes lymphoid and myeloid immunodeficiency due to loss of immune cell quiescence. *Nature Immunol.* **11**, 335–343 (2010).
6. Fritz, C. C. & Green, M. R. HIV Rev uses a conserved cellular protein export pathway for the nucleocytoplasmic transport of viral RNAs. *Curr. Biol.* **6**, 848–854 (1996).
7. Fischer, U., Huber, J., Boelens, W. C., Mattaj, J. W. & Luehrmann, R. The HIV-1 Rev activation domain is a nuclear export signal that accesses an export pathway used by specific cellular RNAs. *Cell* **82**, 475–483 (1995).
8. Malim, M. H., Hauber, J., Le, S. Y., Maizel, J. V. & Cullen, B. R. The HIV-1 rev trans-activator acts through a structured target sequence to activate nuclear export of unspliced viral mRNA. *Nature* **338**, 254–257 (1989).
9. Van Damme, N. *et al.* The interferon-induced protein BST-2 restricts HIV-1 release and is downregulated from the cell surface by the viral Vpu protein. *Cell Host Microbe* **3**, 245–252 (2008).
10. Neil, S. J., Zang, T. & Bieniasz, P. D. Tetherin inhibits retrovirus release and is antagonized by HIV-1 Vpu. *Nature* **451**, 425–430 (2008).
11. Ganser-Pornillos, B. K., Yeager, M. & Sundquist, W. I. The structural biology of HIV assembly. *Curr. Opin. Struct. Biol.* **18**, 203–217 (2008).
12. Coleman, J. R. *et al.* Virus attenuation by genome-scale changes in codon pair bias. *Science* **320**, 1784–1787 (2008).
13. Zhou, T., Gu, W., Ma, J., Sun, X. & Lu, Z. Analysis of synonymous codon usage in H5N1 virus and other influenza A viruses. *Biosystems* **81**, 77–86 (2005).
14. Meintjes, P. L. & Rodrigo, A. G. Evolution of relative synonymous codon usage in human immunodeficiency virus type-1. *J. Bioinform. Comput. Biol.* **3**, 157–168 (2005).
15. Frelin, L. *et al.* Codon optimization and mRNA amplification effectively enhances the immunogenicity of the hepatitis C virus nonstructural 3/4A gene. *Gene Ther.* **11**, 522–533 (2004).
16. Forsberg, R. & Christiansen, F. B. A codon-based model of host-specific selection in parasites, with an application to the influenza A virus. *Mol. Biol. Evol.* **20**, 1252–1259 (2003).
17. Plotkin, J. B. & Dushoff, J. Codon bias and frequency-dependent selection on the hemagglutinin epitopes of influenza A virus. *Proc. Natl Acad. Sci. USA* **100**, 7152–7157 (2003).
18. Grantham, P. & Perrin, P. AIDS virus and HTLV-I differ in codon choices. *Nature* **319**, 727–728 (1986).
19. Wong, E. H. M., Smith, D. K., Rabadan, R., Peiris, M. & Poon, L. L. M. Codon usage bias and the evolution of influenza A viruses. Codon usage biases of influenza virus. *BMC Evol. Biol.* **10**, 253 (2010).
20. van Wieringh, A. *et al.* HIV-1 modulates the tRNA pool to improve translation efficiency. *Mol. Biol. Evol.* **28**, 1827–1834 (2011).
21. Kofman, A. *et al.* HIV-1 gag expression is quantitatively dependent on the ratio of native and optimized codons. *Tsitologia* **45**, 86–93 (2003).
22. Haas, J., Park, E. C. & Seed, B. Codon usage limitation in the expression of HIV-1 envelope glycoprotein. *Curr. Biol.* **6**, 315–324 (1996).
23. Berkhout, B. & van Hemert, F. J. The unusual nucleotide content of the HIV RNA genome results in a biased amino acid composition of HIV proteins. *Nucleic Acids Res.* **22**, 1705–1711 (1994).
24. Kypr, J. & Mrazek, J. Unusual codon usage of HIV. *Nature* **327**, 20 (1987).
25. Pavon-Eternod, M. *et al.* tRNA over-expression in breast cancer and functional consequences. *Nucleic Acids Res.* **37**, 7268–7280 (2009).
26. Dittmar, K. A., Mobley, E. M., Radek, A. J. & Pan, T. Exploring the regulation of tRNA distribution on the genomic scale. *J. Mol. Biol.* **337**, 31–47 (2004).
27. Coccia, E. M., Krust, B. & Hovanessian, A. G. Specific inhibition of viral protein synthesis in HIV-infected cells in response to interferon treatment. *J. Biol. Chem.* **269**, 23087–23094 (1994).
28. Connor, R. I., Chen, B. K., Choe, S. & Landau, N. R. Vpr is required for efficient replication of human immunodeficiency virus type-1 in mononuclear phagocytes. *Virology* **206**, 935–944 (1995).

**Supplementary Information** is available in the online version of the paper.

**Acknowledgements** We thank D. Smith for help with the HIV replication studies; M. Wood for performing the electron microscope analysis; D. Xu and D.-Y. Song for technical assistance; and J. Young, J. Guatelli, D. Smith, M. Kaul and S. Chanda for discussion. This work was supported in part by NIH AI81019 and AI074967 to M.D.W., NIH P01AI090935, R01GM101982 and R21AI088490 to M.D., and by resources from the UCSD Center for AIDS Research, NIH P30AI36214, and the HINT Program, NIH P01AI090935. The authors declare no competing financial interests.

**Author Contributions** M.L., M.D.W., T.P. and M.D. planned the experiments; M.L., E.K., X.G., M.P.-E., K.L., H.S., T.E.J. and S.L. conducted the experiments; M.L., T.P., M.D.W. and M.D. analysed the data; and M.L. and M.D. wrote the manuscript.

**Author Information** Reprints and permissions information is available at [www.nature.com/reprints](http://www.nature.com/reprints). The authors declare no competing financial interests. Readers are welcome to comment on the online version of the paper. Correspondence and requests for materials should be addressed to M.D. ([midavid@ucsd.edu](mailto:midavid@ucsd.edu)).

## METHODS

**Cell culture.** HEK293, HEK293T, NIH3T3, HeLa, HFFs (human foreskin fibroblasts) and their derivative cells were maintained in high glucose DMEM. CEM and their derivative cells were maintained in RPMI 1640 medium. Both media were supplemented with 10% heat-inactivated fetal bovine serum, 100 U ml<sup>-1</sup> penicillin, 100 µg ml<sup>-1</sup> streptomycin, 2 mM L-glutamine, MEM non-essential amino acids, 1 mM sodium pyruvate and 55 µM 2-mercaptoethanol. The Phoenix amphotropic retrovirus packaging cell line (293T) originates from the laboratory of G. Nolan. Human PBMCs were obtained from the San Diego Blood Bank.

**Plasmids.** The template vectors encoding SLFN5 and SLFN11 sequences were acquired from Open Biosystems (Human MGC Verified FL cDNA (IRAU), clone ID 40123369 and 6258140). The coding sequences were amplified by PCR with PfuUltra (Stratagene) and subcloned into the pcDNA6/V5-His vector (Invitrogen) for mammalian cell expression. Portions of the human SLFN11 coding sequence (GenBank accession no. NM\_001104587) were amplified by PCR and subcloned into the pcDNA6/V5-His vector to generate the SLFN11-N (amino acids 1–579) and SLFN11-C (amino acids 523–901) truncation mutants. The pcDNA6/V5-His CAT (chloramphenicol acetyl transferase) vector was generated the same way using pcDNA5/FRT/TO CAT (Invitrogen) as the PCR template for the CAT sequence. The following plasmids were obtained from the Addgene plasmid repository: MSCV-IRES-GFP (Addgene plasmid 20672, source D. Baltimore); pCL-Eco retrovirus packaging vector (Addgene plasmid 12371, source I. Verma); psPAX2 lentivirus packaging vector (Addgene plasmid 12260, source D. Trono); pMD2.G helper vector (Addgene plasmid 12259, source D. Trono) and pCMV-VSV-G vector (Addgene plasmid 8454, source R. M. Weinberg). The following plasmids were obtained through the NIH AIDS Research and Reference Reagent Program, Division of AIDS, NIAID, NIH: pNL-GFP-RRE(SA) (catalogue no. 11466) from J. Marsh and Y. Wu, pNL4-3-deltaE-EGFP (catalogue no. 11100) from H. Zhang, Y. Zhou and R. Siliciano. The pNL4-3.Luc.R<sup>+</sup>E<sup>-</sup> HIV-1 vector has been described previously<sup>28</sup>. The pNL4-3.Luc.R<sup>+</sup>E<sup>-</sup>PRstop construct was created by deletion of thymidine 2478 in pNL4-3.Luc.R<sup>+</sup>E<sup>-</sup> HIV-1 to put the following 'TAGTAG' into frame such that no *pol*-encoded viral enzyme proteins would be expressed. Gag<sup>vir</sup> and Gag<sup>opt</sup> constructs: *gag* sequences were cloned into pcDNA6/V5/His between AflIII and XhoI sites. Nine base pairs of the wild-type viral sequence preceding the initiation codon were present in both final constructs to assure identical translation initiation sites. Gag<sup>vir</sup> was generated through PCR amplification of the *gag* sequence from pGag-EGFP (NIH AIDS Research & Reference Reagent Program, no. 11468) in which only the inhibitory RNA sequence (INS) was eliminated through introduction of silent mutations while otherwise retaining the original viral codon usage. Gag<sup>opt</sup> was generated through PCR amplification of the *gag* sequence from p6ZM651gag-opt (NIH AIDS Research & Reference Reagent Program, no. 8675) in which the entire *gag* sequence was converted to use codon usage in line with highly expressed human genes. GFP and EGFP sequences were cloned into pcDNA6.2/V5 using the pcDNA6.2/GW/D-TOPO kit (Invitrogen). The GFP sequence was tagged with a V5 epitope whereas the EGFP sequence was tagged with a Myc tag (5'-GAGCAGAAGCTGATCA GCGAGGAGGACCTG-3'). The GFP sequence used retains most of the original wild-type protein sequence. The EGFP sequence contains more than 190 silent base changes following human genes codon-usage preferences. Sequences flanking both GFP and EGFP translation initiation site have been converted to a Kozak consensus translation initiation site (5'-CACCATGGTGAGC...) to ensure identical translation initiation efficiency in eukaryotic cells.

**shRNA constructs.** The pLKO.1 shRNA lentivirus constructs (TRCN0000148990, TRCN0000152230, TRCN0000155578, TRCN0000157747, TRCN0000152057, TRCN0000155564) against SLFN11 were obtained from The RNAi Consortium via Open Biosystems. Construct TRCN0000148990 (5'-CCGGGCTCAGAA TTTCCTGACTGAACTCGAGTTCAGTACGGAAATCTGAGCTTTTGTG-3') produced maximum SLFN11 knockdown at the protein level and was thus designated as SLFN11 shRNA in this study. pLKO.1-Blasticidin construct was created by replacing puromycin resistance gene of the original pLKO.1 construct with blasticidin resistance gene using BamHI and KpnI sites. The control shRNA construct in the same pLKO.1 vector system (5'-CCGGTGAAGAACTAA CCGGGACTTCTCGAGAAGTCCCGGGTTAGTTCTTCATTTTGTG-3') was also obtained from The RNAi Consortium via Open Biosystems and does not match any human genes.

**Antibodies.** Anti-SLFN11 antibody for immunoblotting was purchased from Sigma Life Sciences (Atlas Antibodies). Monoclonal anti-SLFN11 antibody for supershift experiments was custom-generated by Abmart. Murine anti-V5 antibody (E10) antibodies were from eBiosciences and Santa Cruz Biotechnology, respectively. Goat polyclonal anti-luciferase antibody was obtained from Promega, rabbit anti-GFP (D5.1) and rabbit anti-GAPDH monoclonal antibodies (14C10) were

acquired from Cell Signaling Technology. The following antibodies were obtained through the AIDS Research and Reference Reagent Program, Division of AIDS, NIAID, NIH: monoclonal antibody against HIV-1 Gag/p24 (AG3.0) from J. Allan; anti-HIV-1 RT monoclonal antibody (8C4) from D. E. Helland; anti-HIV-1 Vif monoclonal antibody (no. 319) from M. H. Malim; anti-HIV-1 Vpr (1–50) antibody from J. Kopp; rabbit anti-HIV-1<sub>NL4-3</sub> Vpu antiserum from K. Strebel, and anti-HIV-1 Nef (Ag11) monoclonal antibody from J. Hoxie.

**Quantitative PCR and primers.** Total cellular RNA was extracted with QIAGEN RNeasy Mini kits, and virion RNA in culture supernatants was extracted with QIAGEN QIAamp Viral RNA Mini kits. Cytoplasmic RNA was prepared with QIAGEN RNeasy Mini kits following the manufacturer's protocol. Briefly, freshly harvested cells were gently lysed on ice for 5 min in buffer RLN (50 mM Tris-Cl, pH 8.0, 140 mM NaCl, 1.5 mM MgCl<sub>2</sub>, 0.5% (v/v) IGEAL CA-630, 1,000 U ml<sup>-1</sup> RNasin Plus RNase Inhibitor (Promega) and 1 mM DTT). Intact cell nuclei were removed by centrifugation at 4 °C for 2 min at 300g, and cytoplasmic RNA was extracted from the remaining supernatant. RNA was cleaned using Ambion DNA-free kits and reverse transcribed with Applied Biosystems' High Capacity cDNA Reverse Transcription kit. qPCR was performed on Applied Biosystems 7000 Sequence Detection System or Applied Biosystems StepOnePlus Real-Time PCR System using Power SYBR Green PCR Master Mix. Relative RNA level were calculated after normalization to 18S rRNA unless specified otherwise. The following primer sequences were used in these assays: *SLFN5* forward 5'-CAAGCCTGTGTGCATTCATAA-3', reverse 5'-TCTGGAGTATATACCA CTCTGTCTGAA-3'; *SLFN11* forward 5'-AAGGCCTGGAACATAAAAAAGG-3', reverse 5'-GGAGTATATCGCAAATATCCTGGT-3'; *SLFN12* forward 5'-CTT TGTTCACACGCCAAGA-3', reverse 5'-ATGCAGTGTCCAAGCAGAAA-3'; *SLFN13* forward 5'-GAGAAAATGATGGACGCAGAT-3', reverse 5'-AGACTC AAAGGCCTCAGCAA-3'; *SLFN12L* forward 5'-GAAAGTCAGTTTCTGAGG AATTTCA-3', reverse 5'-CCAGCTCAGCATAGTTTGTGTC-3'; *SLFN14* forward 5'-GGTGGTCATGATGCTGGATA-3', reverse 5'-TGATGAAATCA GGCAAGAGTTG-3'; *ISG54* forward 5'-TGGTGGCAGAAGAGGAAGAT-3', reverse 5'-CCAAGGAATCTTATTGTTCTCACT-3'; *TBP* forward 5'-GCTGG CCCATAGTGATCTTT-3', reverse 5'-CTTCACACGCCAAGAACAGT-3'; *18S rRNA* forward 5'-GGATGCGTGCATTTATCAGA-3', reverse 5'-GTTGATA GGGCAGACGTTTCG-3'; *GFP* forward 5'-CTGGAGTTGTCCCAATTCTTG-3', reverse 5'-TCACCCCTCTCCACTGACAGA-3'; *EGFP* forward 5'-CAGCAGAA CACCCCATCT-3', reverse 5'-TGGGTGCTCAGGTAGTGGTT-3'; *luciferase* forward 5'-AGGCTTCCCGACGATGA-3', reverse 5'-GTCTTCCGTGCTCC AAAAC-3'; *HIV p24* forward 5'-TGCATGGGTAAAAGTAGTAGAAGAGA-3', reverse 5'-TGATAATGCTGAAAACATGGGTA-3'.

**Generation of stable SLFN11 knockdown HEK293 and CEM cell lines.** HEK293T cells were transfected with the SLFN11 shRNA or control lentivirus vector and the lentivirus packaging vectors psPAX2 and pMD2.G using Lipofectamine 2000 (Invitrogen) according to the manufacturer's protocol. The cell culture medium was collected and replaced with fresh medium 48, 72 and 96 h after the transfection. The combined supernatants were cleared by centrifugation at 1,000g at 4 °C for 15 min. To generate stable SLFN11 knockdown HEK293 cell lines, cleared supernatants were added to pre-plated HEK293 cells in the presence of 8 µg ml<sup>-1</sup> polybrene and centrifuged at 600g for 90 min at room temperature. After 48 h, infected cells were subject to resistance selection with 2 µg ml<sup>-1</sup> puromycin. The efficiency of SLFN11 knockdown in the selected cells was assayed by qPCR and immunoblotting. To generate stable SLFN11 knockdown CEM cell lines, cells were first infected and selected as outlined above. Although the same shRNA construct was used, knockdown in CEM cells was less efficient when compared to HEK293 cells. To improve the SLFN11 knockdown in CEM cells, puromycin-selected CEM cells were re-infected with the pLKO.1-Blasticidin construct carrying the same shRNA and subject to resistance selection with 15 µg ml<sup>-1</sup> blasticidin and 2 µg ml<sup>-1</sup> puromycin. Such double-selected cells displayed a > 90% knockdown of SLFN11 (see Fig. 4b).

**Assay for MSCV, HIV and AAV production.** To analyse MSCV retrovirus production, MSCV-IRES-GFP (MIG) plasmid and pCL Eco packaging vector were transfected into the cells of interest using Lipofectamine 2000 (Invitrogen) according to the manufacturer's instructions. After 24 h the cells were moved to 32 °C, and supernatants were collected after 24 h and cleared by centrifugation. Transfection efficiency was determined by analysis of GFP expression in the cells and was subsequently incorporated into the virus titre calculations. The amount of (infectious) virus particles in the supernatants was determined by both infection assays and qPCR analysis of viral RNA. For infection assays, pre-plated NIH3T3 cells were spin-infected with tenfold serially diluted supernatants in the presence of 8 µg ml<sup>-1</sup> polybrene at 600g for 90 min at room temperature. 48 h after the spin infection, the NIH3T3 cells were examined for GFP expression by flow cytometry, and the number of GFP<sup>+</sup> cells was used to calculate relative viral titres. For viral RNA qPCR assays, viral RNA was extracted from the virus supernatant and

quantified as described above with EGFP-specific primers. The production of HIV was tested similarly after pNL4-3.Luc.R<sup>+</sup>E<sup>-</sup> HIV vector, pCMV-VSV-G vector and pcDNA5 GFP vector were transfected into cells of interest using Lipofectamine 2000. The transfection efficiency was established by flow cytometric determination of the number of GFP<sup>+</sup> cells and used to adjust relative viral titres. Viral titres were determined via infection assays, qPCR of viral RNA and HIV p24 ELISA. The infection assay was similar to the MSCV virus infection assay except HEK293T cells were used for analysis. Expression of luciferase was measured by using the Bright-Glo Luciferase Assay System (Promega) and a microplate luminometer (LUMistar, BMG-LABTECH) 24 h after the spin infection. HIV viral RNA was quantified by qPCR using luciferase- or HIV-p24-specific primers. The HIV p24 ELISA was performed by the Viral Pathogenesis Core at the UCSD Center for AIDS Research using Alliance HIV1 p24 ELISA kits (Perkin Elmer). For recombinant AAV production assays, cells were transfected with pXX6 (0.6 µg), pXX2 (0.2 µg) and pACLALuc (0.2 µg) using lipofectamine 2000 (Invitrogen), and collected 72 h after transfection. rAAVLuc-containing lysates were generated by freeze/thaw cycles followed by centrifugation and were used to infect HEK293T cells. Luciferase activity was quantified 48 h post-transduction using Steady-Glo luciferase substrate reagent (Promega) in 96-well Lumiplates (Greiner Bio-One) in a TopCount NXT scintillation and luminescence counter (PerkinElmer).

**Assays for MSCV and HIV infection.** Amphotropic MSCV-IRES-GFP (MIG) retrovirus was prepared by transfecting Phoenix amphotropic retrovirus packaging cells with MSCV-IRES-GFP (MIG) vector using Lipofectamine 2000. The cell culture medium was collected and replaced with fresh medium 48, 72 and 96 h after the transfection. The combined supernatants were cleared by centrifugation at 1,000g at 4 °C for 15 min. Cells to be tested were spin-infected with the indicated dilutions in the presence of 8 µg ml<sup>-1</sup> polybrene at 600g for 90 min at room temperature. 48 h after the spin infection, cells were analysed for GFP expression by flow cytometry. Infection efficiency was established by both the number of GFP<sup>+</sup> cells and the level of GFP expression. VSV-G pseudotyped HIV was prepared by transfecting HEK293T cells with pNL4-3.Luc.R<sup>+</sup>E<sup>-</sup> HIV and pCMV-VSV-G vectors using Lipofectamine 2000. The cell culture medium was collected and cleared as described above. Cells to be tested were spin-infected with the indicated dilutions in the presence of 8 µg ml<sup>-1</sup> polybrene at 600g for 90 min at room temperature. 24 h after the spin infection, luciferase expression was measured to determine the relative infection efficiencies.

**Transmission electron microscopy.** HEK293T cells were transfected with pNL4-3.Luc.R<sup>+</sup>E<sup>-</sup> HIV vector together with either pcDNA6/V5-His CAT or pcDNA6/V5-His SLFN11 vectors using Lipofectamine 2000. 48 h after the transfection, cells were fixed and processed by the Microscopy Core at the Scripps Research Institute. Images were acquired with a Philips CM100 transmission electron microscope.

**Whole-cell lysis and western blotting.** Cells were lysed directly in 1 × NuPAGE LDS Sample Buffer (Invitrogen) containing 2.5% 2-mercaptoethanol and heated at 90 °C for 5 min. Samples were homogenized by QIAshredder (Qiagen), total protein resolved by NuPAGE (Invitrogen) and transferred to PVDF (polyvinylidene difluoride) membranes followed by western blotting with the

specified antibodies. Corresponding horseradish peroxidase (HRP)-conjugated secondary antibodies and Amersham ECL Plus Western Blotting Detection Reagent (GE Healthcare) were used to visualize the signals followed by quantification using densitometer and NIH ImageJ64 software. Alternatively, fluorochrome-conjugated secondary antibodies were used and signals were acquired and quantified using Typhoon Trio Variable Mode Imager and ImageQuant software. **Wild-type HIV virus replication assay in CEM cells.** HIV-1<sub>LAI</sub> was used to infect the CEM stable cell lines (CEM, CEMshRNA<sup>CL</sup> and CEMshRNA<sup>SLFN</sup>) at a m.o.i. of 0.01 in 5 ml of culture at 0.5 × 10<sup>6</sup> cells per ml using RPMI/poly medium containing 3 µg ml<sup>-1</sup> polybrene, 1% glutamine, 100 U ml<sup>-1</sup> penicillin, 100 µg ml<sup>-1</sup> streptomycin and 10% FBS. The cultures were sampled at the indicated time points and the viral titres were measured by HIV p24 ELISA.

**tRNA arrays.** mirVana miRNA Isolation kit (Ambion) was used to prepare total RNA from freshly collected cells following the total RNA isolation protocol. RNA samples were labelled and the relative abundances of individual tRNAs were measured using microarrays as previously described<sup>25,26</sup>.

**tRNA electrophoretic mobility shift assay (EMSA).** The partial coding sequence of human SLFN11 (amino acids 1–579; SLFN11-N) and the coding sequence of GFP were cloned into the bacterial expression vector pET101/D-TOPO (Invitrogen) with a 6×His epitope tag. 6×His-tagged SLFN11-N and GFP proteins were expressed in Origami B *Escherichia coli* cells and purified over Ni-NTA and FPLC columns. The purity of the proteins was >95% as estimated by Coomassie blue staining. Total human tRNA was extracted with the mirVana miRNA Isolation kit (Ambion) following the small RNA isolation protocol, and further purified on a 15% denaturing polyacrylamide TBE-urea gel (Invitrogen). To generate EMSA probes, purified human tRNA was deacylated to remove charging amino acid, dephosphorylated and 5'-labelled using [<sup>32</sup>P]γ-ATP. Total yeast tRNA was purchased from Invitrogen. To prepare the HIV viral RNA, the sequence corresponding to the *gag-pol* frame-shifting region (2041–2161, pNL4-3.Luc.R<sup>+</sup>E<sup>-</sup> vector) was amplified by PCR with T7 promoter-containing primers and *in vitro* transcribed using MEGAscript T7 kit (Ambion). Purified proteins, unlabelled competitor RNA or anti-SLFN11 antibody (Abmart), and probe were combined as specified and incubated on ice for 30 min in EMSA buffer (5% glycerol, 10 mM pH 7.4 Tris-HCl, 5 mM MgCl<sub>2</sub>, 100 mM KCl, 1% Triton X-100, 1 mM DTT and 1 U µl<sup>-1</sup> RNasin Plus RNase Inhibitor). After samples were resolved on a 6% DNA retardation gel (Invitrogen), the gel was dried and visualized with Typhoon Trio Variable Mode Imager (storage phosphor mode).

**Data analysis and presentation.** Unless indicated otherwise, results are presented in graphs as average ± s.d. of at least three independent transfections or infections. For western blots, a representative of at least three independent transfections or infections is shown. For the experiments shown in Fig. 3d, e, GFP and EGFP protein and mRNA levels were quantified and adjusted to the corresponding GAPDH protein or mRNA concentrations, respectively. Expression levels of the proteins were then normalized to their corresponding standardized mRNA concentrations to compensate for minor variations in mRNA concentrations between the samples.

# Vaccine-induced CD8<sup>+</sup> T cells control AIDS virus replication

Philip A. Mudd<sup>1,2</sup>, Mauricio A. Martins<sup>3</sup>, Adam J. Ericson<sup>1</sup>, Damien C. Tully<sup>4</sup>, Karen A. Power<sup>4</sup>, Alex T. Bean<sup>1</sup>, Shari M. Piaskowski<sup>1</sup>, Lijie Duan<sup>5</sup>, Aaron Seese<sup>4</sup>, Adrienne D. Gladden<sup>4</sup>, Kim L. Weisgrau<sup>1</sup>, Jessica R. Furlott<sup>1</sup>, Young-il Kim<sup>6</sup>, Marlon G. Veloso de Santana<sup>7</sup>, Eva Rakasz<sup>8</sup>, Saverio Capuano III<sup>8</sup>, Nancy A. Wilson<sup>1,8</sup>, Myrna C. Bonaldo<sup>7</sup>, Ricardo Galler<sup>9</sup>, David B. Allison<sup>10</sup>, Michael Piatak Jr<sup>11</sup>, Ashley T. Haase<sup>5</sup>, Jeffrey D. Lifson<sup>11</sup>, Todd M. Allen<sup>4</sup> & David I. Watkins<sup>3</sup>

Developing a vaccine for human immunodeficiency virus (HIV) may be aided by a complete understanding of those rare cases in which some HIV-infected individuals control replication of the virus<sup>1–3</sup>. Most of these elite controllers express the histocompatibility alleles *HLA-B\*57* or *HLA-B\*27* (ref. 3). These alleles remain by far the most robust associations with low concentrations of plasma virus<sup>4,5</sup>, yet the mechanism of control in these individuals is not entirely clear. Here we vaccinate Indian rhesus macaques that express *Mamu-B\*08*, an animal model for *HLA-B\*27*-mediated elite control<sup>6</sup>, with three *Mamu-B\*08*-restricted CD8<sup>+</sup> T-cell epitopes, and demonstrate that these vaccinated animals control replication of the highly pathogenic clonal simian immunodeficiency virus (SIV) mac239 virus. High frequencies of CD8<sup>+</sup> T cells against these Vif and Nef epitopes in the blood, lymph nodes and colon were associated with viral control. Moreover, the frequency of the CD8<sup>+</sup> T-cell response against the Nef RL10 epitope (Nef amino acids 137–146) correlated significantly with reduced acute phase viraemia. Finally, two of the eight vaccinees lost control of viral replication in the chronic phase, concomitant with escape in all three targeted epitopes, further implicating these three CD8<sup>+</sup> T-cell responses in the control of viral replication. Our findings indicate that narrowly targeted vaccine-induced virus-specific CD8<sup>+</sup> T-cell responses can control replication of the AIDS virus.

A vaccine is desperately needed to curb the global HIV pandemic. Estimates project that for every HIV-infected individual initiating antiretroviral treatment, more than two individuals are newly infected<sup>7</sup>. Vaccines have historically been chosen based on their ability to induce responses that mimic successful immune responses to human pathogens, yet correlates of successful immune responses against HIV remain an enigma. Elite control of chronic phase viral replication is the best example of an effective immune response against the virus<sup>1</sup>. Understanding why elite controllers control viral replication may enable the design of an effective vaccine for HIV.

Recently, we have discovered similarities between an animal model of elite control and the same phenomenon in humans<sup>8</sup>. The Indian rhesus macaque major histocompatibility complex (MHC) class I molecule *Mamu-B\*08* and the human leukocyte antigen (HLA) class I molecule *HLA-B\*27* bind many of the same peptides<sup>9</sup>. Despite being divergent at 28 amino acid positions, these molecules share similar peptide-binding motifs, including an identical position 2 arginine primary anchor<sup>6</sup>. Both MHC class I molecules also exhibit considerable overlap in preferred binding residues at the other dominant position 1 and position 9 residues<sup>6</sup>. Remarkably, 50% of *Mamu-B\*08*<sup>+</sup> animals show some measure of control of the highly pathogenic SIVmac239 virus<sup>6,9</sup>. It is important to note, however, that several key

differences exist between *HLA-B\*27*-mediated elite control and the *Mamu-B\*08*<sup>+</sup> animal model. Humans are infected with a variety of different viruses and it is widely thought that CD8<sup>+</sup> T cells directed against conserved epitopes in Gag have an important role in viral control<sup>1</sup>. By contrast, the animal model of elite control has been developed using macaques infected only with the SIVmac239 clone. Furthermore, *Mamu-B\*08*<sup>+</sup> macaques do not usually recognize Gag-derived epitopes<sup>10</sup>. Finally, Indian rhesus macaques infected with SIVmac239 have average chronic phase viral loads of more than 10<sup>6</sup> viral RNA (vRNA) copies per millilitre, whereas humans normally have mean plasma viral concentrations of 30,000 vRNA per millilitre in the chronic phase. Owing to the high replicative capacity of SIVmac239, most drug- or vaccine-naïve SIVmac239-infected monkeys die from AIDS-defining illnesses by 2 years after infection<sup>11</sup>.

Three *Mamu-B\*08*-restricted CD8<sup>+</sup> T-cell responses make up more than half of the T-cell response against the virus in *Mamu-B\*08*<sup>+</sup> elite controllers<sup>10,12</sup>; these CD8<sup>+</sup> T cells recognize Vif RL8 (Vif amino acids 172–179), Vif RL9 (Vif amino acids 123–131) and Nef RL10 (Nef amino acids 137–146). CD8<sup>+</sup> T cells directed against these three epitopes select for escape mutations preferentially in *Mamu-B\*08*<sup>+</sup> macaques that do not become elite controllers<sup>13</sup>, suggesting that these three immunodominant T-cell responses are important for the development of elite control.

To test the hypothesis that antigen-specific CD8<sup>+</sup> T cells are responsible for the development of elite control, we vaccinated eight *Mamu-B\*08*<sup>+</sup> macaques (Fig. 1a, group 1) with two small regions of the SIV proteome that include the three immunodominant T-cell epitopes bound by *Mamu-B\*08*: Vif RL8, Vif RL9 and Nef RL10. We used a recombinant yellow fever 17D (rYF17D) prime and boosted with recombinant adenovirus serotype 5 (rAd5). As controls, we vaccinated another eight *Mamu-B\*08*<sup>+</sup> macaques (Fig. 1a, group 2) with two small regions of the SIV proteome that do not encode any known *Mamu-B\*08* epitopes<sup>10</sup>. The group 1 vaccinees mounted high frequency CD8<sup>+</sup> T-cell responses against the three *Mamu-B\*08*-bound epitopes after vaccination, whereas the group 2 animals did not make CD8<sup>+</sup> T-cell responses against these three epitopes (Fig. 1b). Group 1 and 2 animals exhibited similar SIV-specific total T-cell and CD4<sup>+</sup> T-cell response frequencies against the vaccine inserts after vaccination, as demonstrated by interferon (IFN)- $\gamma$  enzyme-linked immunospot (ELISPOT) assay (Supplementary Fig. 1a, b).

Fifteen weeks after the final vaccine boost, we challenged all 16 animals intrarectally with a high dose of SIVmac239 (10,000 half-maximal tissue-culture infectious dose (TCID<sub>50</sub>)). Four out of eight group 1 animals and six out of eight group 2 animals were infected after this first challenge. The remaining uninfected macaques were

<sup>1</sup>Department of Pathology and Laboratory Medicine, University of Wisconsin-Madison, Madison, Wisconsin 53711, USA. <sup>2</sup>Medical Scientist Training Program, University of Wisconsin-Madison, Madison, Wisconsin 53705, USA. <sup>3</sup>Department of Pathology, University of Miami Miller School of Medicine, Miami, Florida 33136, USA. <sup>4</sup>Ragon Institute of MGH, MIT and Harvard, Boston, Massachusetts 02129, USA. <sup>5</sup>Department of Microbiology, University of Minnesota, Minneapolis, Minnesota 55455, USA. <sup>6</sup>Department of Medicine, Division of Preventive Medicine, University of Alabama at Birmingham, Birmingham, Alabama 35294, USA. <sup>7</sup>Laboratório de Biologia Molecular de Flavivírus, Instituto Oswaldo Cruz—FIOCRUZ, Rio de Janeiro, Brazil. <sup>8</sup>Wisconsin National Primate Research Center, University of Wisconsin-Madison, Madison, Wisconsin 53711, USA. <sup>9</sup>Instituto de Tecnologia em Imunobiológicos, Fundação Oswaldo Cruz, Rio de Janeiro, Brazil. <sup>10</sup>Department of Biostatistics, Section on Statistical Genetics, University of Alabama at Birmingham, Birmingham, Alabama 35294, USA. <sup>11</sup>AIDS and Cancer Virus Program, SAIC Frederick, Inc., National Cancer Institute, Frederick, Maryland 21702, USA.

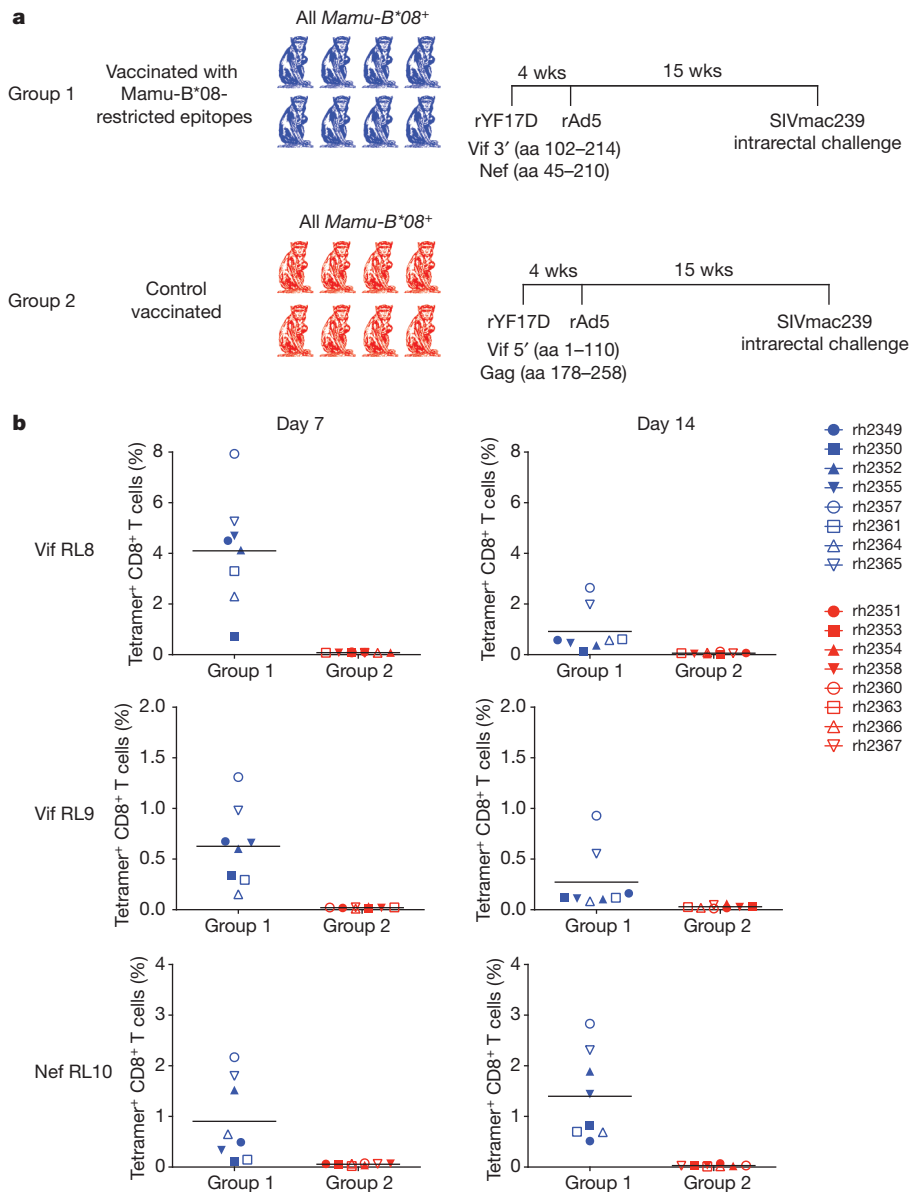


**Figure 1 | Experimental design.** **a**, *Mamu-B\*08*<sup>+</sup> macaques were vaccinated with an identical rYF17D/rAd5 regimen. Group 1 animals received two SIVmac239 constructs: Vif 3' (amino acids (aa) 102–214; includes the Mamu-B\*08-restricted Vif<sub>123–131</sub>RL9 and Vif<sub>172–179</sub>RL8 epitopes) and Nef (amino acids 45–210; includes the Mamu-B\*08-restricted Nef<sub>137–146</sub>RL10 epitope). Group 2 received two SIVmac239 constructs: Gag (amino acids

178–258) and Vif 5' (amino acids 1–110), which do not contain any known Mamu-B\*08-restricted CD8<sup>+</sup> T-cell epitopes<sup>10</sup>. Animals were challenged with SIVmac239 intrarectally 15 weeks after the rAd5 boost. **b**, Frequencies of tetramer<sup>+</sup> CD8<sup>+</sup> T cells in PBMCs at days 7 and 14 after the rAd5 boost. Lines represent mean frequency.

rechallenged with a second high dose of SIVmac239 (10,000 TCID<sub>50</sub>) three weeks after the initial challenge. All of the group 2 control-vaccinated animals were infected after this second challenge. A single group 1 vaccinee, rh2355, resisted four high-dose SIVmac239 challenges and was only infected after the fifth challenge.

Surprisingly, all eight infected group 1 animals, vaccinated with the three immunodominant Mamu-B\*08-restricted T-cell epitopes, controlled viral replication during acute infection when compared with the group 2 animals (Fig. 2a–d). Remarkably, six of the seven group 1 vaccinated *Mamu-B\*08*<sup>+</sup> animals that were infected after one or two challenges became elite controllers with post-acute phase viral loads of less than 1,000 vRNA copies per ml (Fig. 2a). The seventh animal (rh2349) controlled viral replication to less than 10,000 vRNA copies per ml by 8 weeks after infection. The group 1 animal (rh2355)

that required five high-dose challenges for infection controlled viral replication to less than 10,000 vRNA copies per ml by 10 weeks after infection. By contrast, viral replication in the group 2 animals was indistinguishable from viral replication in four concurrently challenged unvaccinated *Mamu-B\*08*<sup>+</sup> controls (Fig. 2c). We also measured viral replication during acute infection in lymph node biopsies using *in situ* hybridization<sup>14,15</sup>. Group 1 animals demonstrated significantly less viral replication in lymph node tissue at time points near peak plasma viral load than group 2 animals (Fig. 2e).

To evaluate potential correlates of viral protection in the group 1 vaccinees, we characterized the kinetics of T-cell responses after SIV infection using peptides and Mamu-B\*08 tetramers. We first measured SIV-specific T-cell responses after infection in both group 1 and 2 vaccinated animals with a panel of synthetic peptides spanning

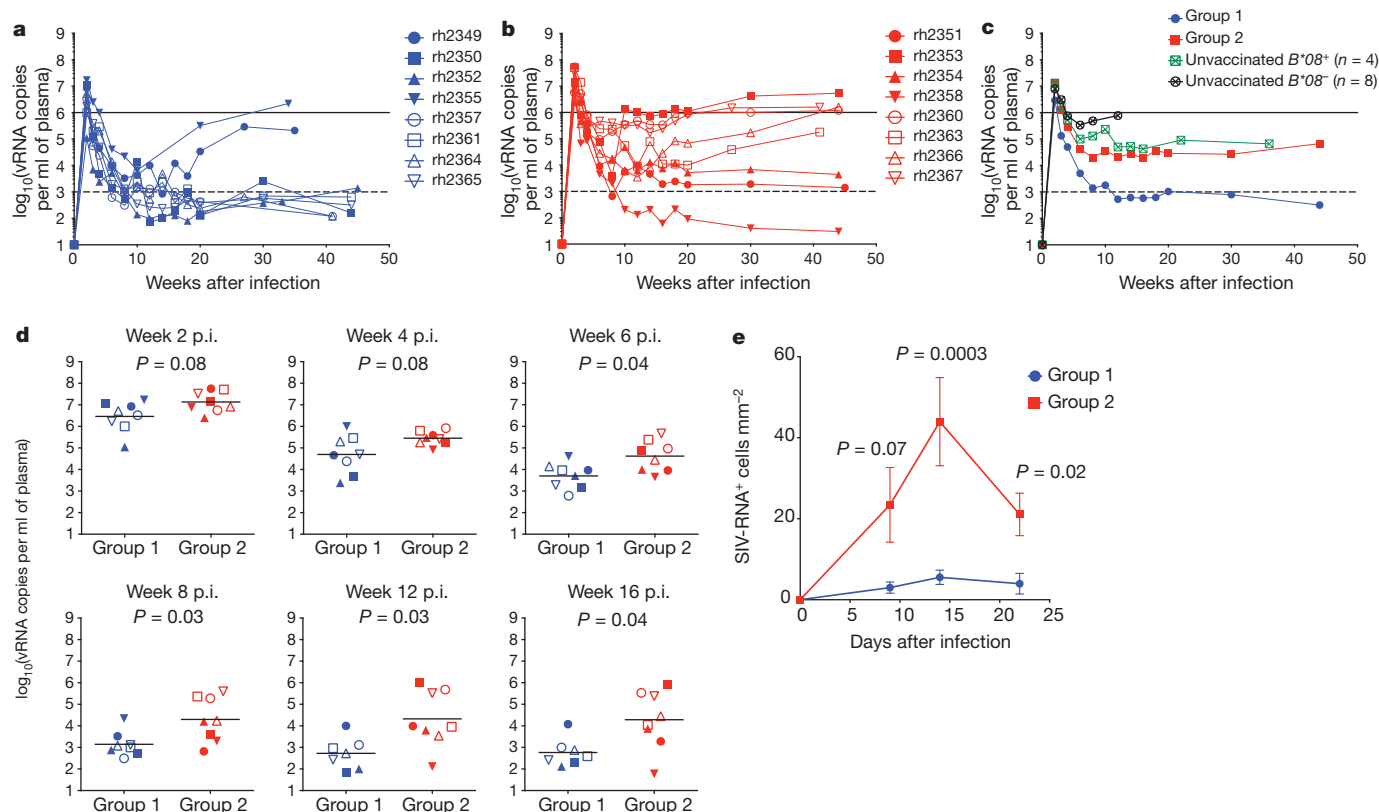


**Figure 2 | In vivo viral replication.** **a**, Plasma viral loads (VL) for group 1 animals. The dashed line ( $10^3$  vRNA copies per ml) represents the threshold that defines elite control in Indian rhesus macaques<sup>9</sup>. **b**, Plasma viral loads for group 2 control animals. **c**, Geometric mean plasma viral loads for groups 1, 2 and unvaccinated *Mamu-B\*08*<sup>+</sup> ( $n = 4$ ) or *Mamu-B\*08*<sup>-</sup> ( $n = 8$ ) control

macaques. **d**, Plasma viral load comparisons between groups 1 and 2. Lines represent geometric means. p.i., post-infection. **e**, Viral replication measured using *in situ* hybridization<sup>14,15</sup> in lymph node biopsy specimens. Data are mean  $\pm$  s.e.m.

both the vaccine inserts and the entire SIV proteome using IFN- $\gamma$  ELISPOT (Supplementary Fig. 1a, b). Interestingly, peripheral blood mononuclear cell (PBMC) responses against the entire proteome were equivalent in the two groups after infection. At days 14 and 17 after infection, however, higher frequency insert-specific (total T cell and CD4<sup>+</sup> T-cell) and proteome-specific (CD4<sup>+</sup> T-cell) responses were observed in the group 1 animals, perhaps reflecting preservation of the CD4<sup>+</sup> T-cell responses owing to reduced peak viral replication in this group. These preserved antigen-specific CD4<sup>+</sup> T-cell responses may have facilitated the control of chronic phase viral replication in the group 1 animals. We also found that group 1 vaccinated macaques exhibited earlier and higher magnitude Vif RL9- and Nef RL10-specific responses in the peripheral blood than the group 2 macaques (Fig. 3a). This pattern was also detected in lymph node biopsy specimens (Fig. 3b) and colon biopsy tissue (Fig. 3c). Notably, T-cell responses directed against the Vif RL8 epitope were similar between the group 1 and 2 macaques (Fig. 3a–c). Taken together, these results suggest that early, high frequency Vif RL9- and Nef RL10-specific responses in the blood and in key immunological tissues were directly responsible for viral control in the group 1 *Mamu-B\*08*<sup>+</sup> macaques.

Remarkably, we found a significant correlation between high frequency Nef RL10-specific responses and decreased day 14 peak viral loads (Fig. 3d) in our cohort of infected macaques. Furthermore, these vaccine-induced Nef RL10-specific CD8<sup>+</sup> T cells expressed both granzyme B and perforin at day 17 after infection, at a time when Nef RL10-specific CD8<sup>+</sup> T cells showed little or no expression of these important markers of cytotoxicity in the group 2 animals (Fig. 3e, f and Supplementary Fig. 2). Furthermore, the frequency of Nef RL10- (but not Vif RL8- or Vif RL9-) specific CD8<sup>+</sup> T-cell responses has recently

been shown to correlate with the control of chronic phase viral replication in SIVmac239-infected, unvaccinated *Mamu-B\*08*<sup>+</sup> macaques (D. Douek, personal communication). These results suggest that early, high frequency cytotoxic Nef RL10-specific responses in the blood and in key immunological tissues were directly responsible for viral control in group 1 *Mamu-B\*08*<sup>+</sup> macaques. This is the first described correlate of viral control in the *Mamu-B\*08* model of elite control.

After controlling viral replication during the acute phase, increased plasma viraemia was observed in two of the group 1 vaccinees during the chronic phase (rh2349 and rh2355). Viral sequencing showed that despite the presence of wild-type virus in one of these two animals at 6 weeks after infection, all three targeted epitopes had escaped by the time viral replication started to increase in the chronic phase (Table 1 and Supplementary Fig. 3a, b). By contrast, most of the three epitopes were intact in virus from two of the elite controllers in group 1 at 48 weeks after infection (Table 1 and Supplementary Fig. 3b). This finding further implicates CD8<sup>+</sup> T cells against these three epitopes in control of viral replication, and suggests that the virus cannot replicate in the face of these CD8<sup>+</sup> T-cell responses. The canonical escape mutants that arose in these animals did not seem to affect viral fitness because the virus replicated to high levels in these two 'break-through' animals. Furthermore, we have previously engineered mutant viruses bearing several of the escape mutants observed in these animals and these mutations caused abrogation of CD8<sup>+</sup> T-cell recognition and did not seem to cause significant fitness loss *in vitro* and *in vivo*<sup>10</sup>.

With this report, we demonstrate that vaccine-induced Vif- and Nef-specific CD8<sup>+</sup> T cells can control replication of a highly pathogenic

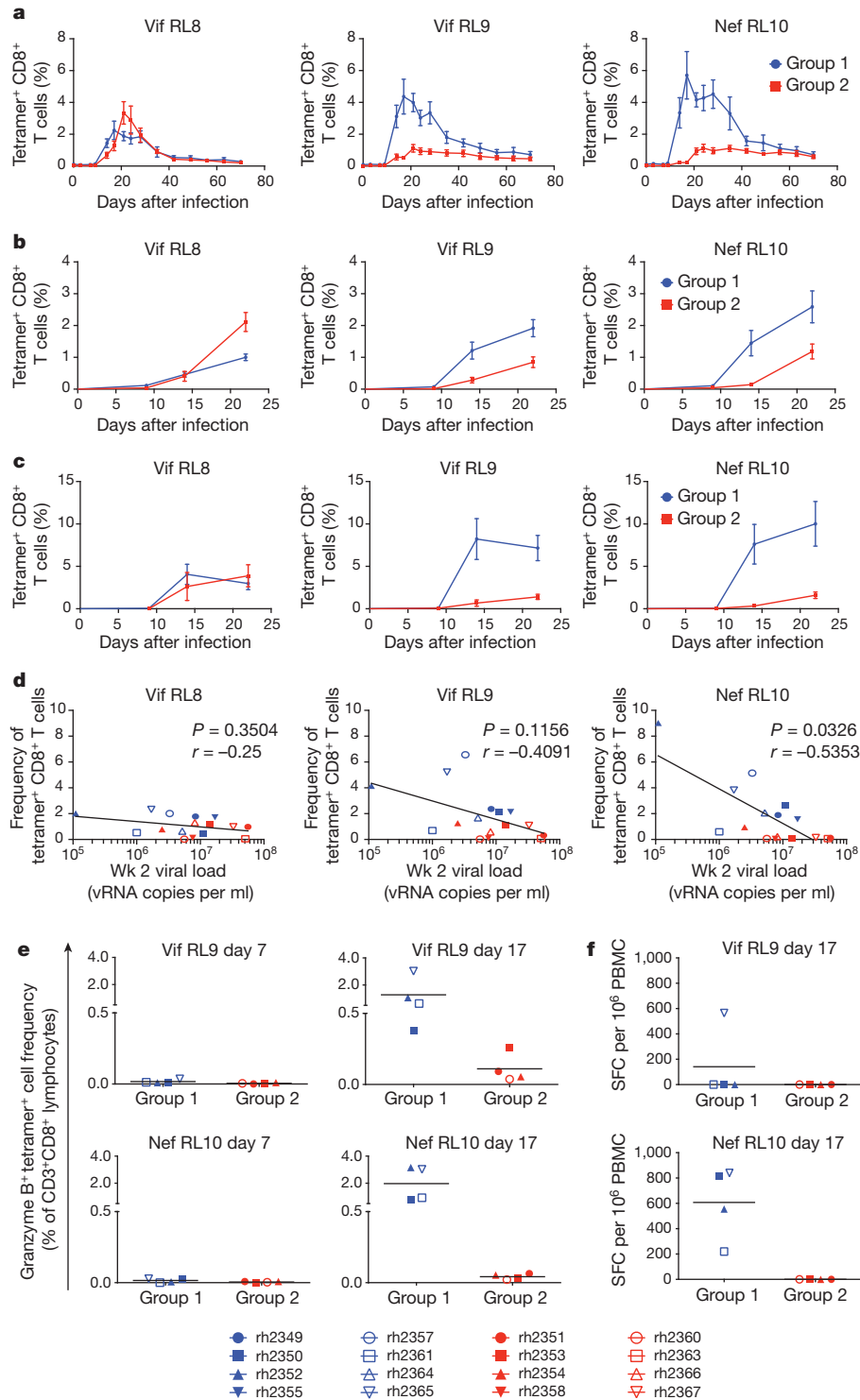


**Figure 3 | CD8<sup>+</sup> T-cell responses in vaccinated animals after SIVmac239 infection.** **a–c**, Peptide/Mamu-B\*08 tetramer staining in PBMCs (**a**), lymph node biopsies (**b**) and colon biopsies (**c**). Error bars represent s.e.m. **d**, Correlations between the frequency of tetramer<sup>+</sup> cells and the viral load at week 2 after infection. **e**, Granzyme B production by SIV-specific CD8<sup>+</sup> T cells

in group 1 and 2 vaccinees at days 7 and 17 after SIV infection. **f**, Perforin production by SIV-specific CD8<sup>+</sup> T cells in group 1 and 2 vaccinees at day 17 after infection. Assay results are shown as spot forming cells (SFC) per 10<sup>6</sup> PBMCs.

AIDS virus in an animal model of MHC class I-associated elite control. Further analysis of the Vif RL9- and Nef RL10-specific CD8<sup>+</sup> T-cell responses in Mamu-B\*08<sup>+</sup> macaques could shed light on the general principles of effective AIDS virus-specific CD8<sup>+</sup> T-cell responses. It is possible that vaccines that generate high frequency efficacious effector CD8<sup>+</sup> T cells against only a few epitopes in the mucosae might intercept

the virus during this crucial acute phase and result in long-term virological control. These types of effective immune response might be inducible in the setting of an appropriate vaccination regimen<sup>16–19</sup>. Therefore, understanding why these particular T-cell responses control viral replication when most other T-cell responses do not may enable the design of an effective approach to HIV vaccination.

**Table 1 | Viral sequence analysis**

	Vif RL8	Vif RL9	Nef RL10
Acute phase, group 1 animals			
<b>rh2349 (wk 6)</b>	<b>ND</b>	<b>ND</b>	<b>ND</b>
<b>rh2355 (wk 6)</b>	<b>100%</b>	<b>100%</b>	<b>100%</b>
rh2350 (wk 6)	99%	27%	ND
rh2352 (wk 6)	97%	47%	ND
rh2357 (wk 6)	87%	75%	97%
rh2361 (wk 6)	100%	100%	100%
rh2364 (wk 6)	59%	37%	92%
rh2365 (wk 6)	ND	ND	ND
Acute phase, group 2 animals			
rh2351 (wk 6)	22%	33%	97%
rh2353 (wk 6)	38%	40%	95%
rh2354 (wk 6)	92%	92%	100%
rh2358 (wk 6)	100%	100%	99%
rh2360 (wk 6)	50%	64%	99%
rh2363 (wk 6)	94%	99%	95%
rh2366 (wk 6)	100%	69%	99%
rh2367 (wk 6)	97%	78%	100%
Chronic phase, group 1 animals			
<b>rh2349 (wk 35)</b>	<b>4%</b>	<b>4%</b>	<b>7%</b>
<b>rh2355 (wk 37)</b>	<b>0%</b>	<b>0%</b>	<b>0%</b>
rh2350 (wk 48)	ND	ND	91%
rh2352 (wk 48)	97%	17%	69%
rh2357 (wk 45)	ND	ND	99%
rh2361 (wk 48)	99%	68%	99%
rh2364 (wk 45)	ND	ND	ND
rh2365 (wk 48)	ND	ND	ND

454 sequencing of the three Mamu-B\*08-restricted Vif RL8, Vif RL9 and Nef RL10 CD8<sup>+</sup> T-cell epitopes. Vif and Nef were amplified independently and PCR amplicons were sequenced by 454. Sequence analysis was carried out using RC454 and V-phaser as previously described<sup>21,22</sup>. Percentages indicate the frequencies of wild-type epitope sequence reads for both the acute and chronic phases of infection. Breakthrough animals in group 1 are in bold. ND, not determined.

## METHODS SUMMARY

**Animals.** Animals were cared for according to Animal Welfare Assurance no. A3368-01 (protocol no. G00639).

**Vaccination.** Animals were vaccinated subcutaneously with two separate rYF17D constructs ( $2.0 \times 10^5$  plaque-forming units of each) and were then boosted intramuscularly with two separate rAd5 vectors ( $10^{11}$  particles of each) containing the same SIVmac239 inserts.

**SIV infection, *in situ* hybridization and viral load measurement.** Animals were challenged intrarectally with 10,000 TCID<sub>50</sub> of SIVmac239. Viral loads were measured from EDTA anti-coagulated plasma using a previously described protocol<sup>20</sup>. *In situ* hybridization of lymph node biopsy tissues was performed as previously described<sup>14,15</sup>.

**Tetramer staining and flow cytometry.** For tetramer staining, we followed previously published staining protocols<sup>10</sup>.

**Amplicon-based 454 sequencing of Vif and Nef epitopes in plasma virus.** We used an amplicon-based 454 sequencing approach to analyse the Vif and Nef epitopes as previously described<sup>13</sup>. A single-step reverse transcription PCR (RT-PCR) was carried out for each of the unique amplicon/animal/multiplex-identifier-tag sequence combinations using SuperScript III one-step RT-PCR system. Sequencing and run processing were performed on a GS Junior 454 sequencing instrument. We used the ReadClean 454 (RC454) and V-Phaser algorithms as previously described<sup>21,22</sup> to call variants from the 454 data sets.

**Statistics.** We compared the geometric mean of viral loads and the mean of SIV-RNA<sup>+</sup> cells per mm<sup>2</sup> for each time point and then performed Mann-Whitney tests. We also used the Mann-Whitney test to compare the magnitude of SIV-specific T-cell responses in groups 1 and 2. We determined correlation coefficients (*r*) and *P* values using the Spearman rank correlation test. All significance tests were two-tailed.

**Full Methods** and any associated references are available in the online version of the paper.

Received 3 April; accepted 26 July 2012.

Published online 30 September 2012.

- Deeks, S. G. & Walker, B. D. Human immunodeficiency virus controllers: mechanisms of durable virus control in the absence of antiretroviral therapy. *Immunity* **27**, 406–416 (2007).

- Goulder, P. J. & Watkins, D. I. HIV and SIV CTL escape: implications for vaccine design. *Nature Rev. Immunol.* **4**, 630–640 (2004).
- Migueles, S. A. & Connors, M. Long-term nonprogressive disease among untreated HIV-infected individuals: clinical implications of understanding immune control of HIV. *J. Am. Med. Assoc.* **304**, 194–201 (2010).
- Fellay, J. *et al.* A whole-genome association study of major determinants for host control of HIV-1. *Science* **317**, 944–947 (2007).
- The International HIV Controllers Study. The major genetic determinants of HIV-1 control affect HLA class I peptide presentation. *Science* **330**, 1551–1557 (2010).
- Loffredo, J. T. *et al.* Two MHC class I molecules associated with elite control of immunodeficiency virus replication, Mamu-B\*08 and HLA-B\*2705, bind peptides with sequence similarity. *J. Immunol.* **182**, 7763–7775 (2009).
- Johnston, M. I. & Fauci, A. S. An HIV vaccine—challenges and prospects. *N. Engl. J. Med.* **359**, 888–890 (2008).
- Mudd, P. A. & Watkins, D. I. Understanding animal models of elite control: windows on effective immune responses against immunodeficiency viruses. *Curr. Opin. HIV AIDS* **6**, 197–201 (2011).
- Loffredo, J. T. *et al.* Mamu-B\*08-positive macaques control simian immunodeficiency virus replication. *J. Virol.* **81**, 8827–8832 (2007).
- Valentine, L. E. *et al.* Infection with “escaped” virus variants impairs control of simian immunodeficiency virus SIVmac239 replication in Mamu-B\*08-positive macaques. *J. Virol.* **83**, 11514–11527 (2009).
- Dang, Q. & Hirsch, V. M. Rapid disease progression to AIDS due to Simian immunodeficiency virus infection of macaques: host and viral factors. *Adv. Pharmacol.* **56**, 369–398 (2008).
- Loffredo, J. T. *et al.* Patterns of CD8<sup>+</sup> immunodominance may influence the ability of Mamu-B\*08-positive macaques to naturally control simian immunodeficiency virus SIVmac239 replication. *J. Virol.* **82**, 1723–1738 (2008).
- Mudd, P. A. *et al.* Escape from CD8<sup>+</sup> T cell responses in Mamu-B\*0801<sup>+</sup> macaques differentiates progressors from elite controllers. *J. Immunol.* **188**, 3364–3370 (2012).
- Li, Q. *et al.* Peak SIV replication in resting memory CD4<sup>+</sup> T cells depletes gut lamina propria CD4<sup>+</sup> T cells. *Nature* **434**, 1148–1152 (2005).
- Li, Q. *et al.* Glycerol monolaurate prevents mucosal SIV transmission. *Nature* **458**, 1034–1038 (2009).
- Hansen, S. G. *et al.* Effector memory T cell responses are associated with protection of rhesus monkeys from mucosal simian immunodeficiency virus challenge. *Nature Med.* **15**, 293–299 (2009).
- Hansen, S. G. *et al.* Profound early control of highly pathogenic SIV by an effector memory T-cell vaccine. *Nature* **473**, 523–527 (2011).
- Kawada, M. *et al.* Gag-specific cytotoxic T-lymphocyte-based control of primary simian immunodeficiency virus replication in a vaccine trial. *J. Virol.* **82**, 10199–10206 (2008).
- Tsukamoto, T. *et al.* Impact of cytotoxic-T-lymphocyte memory induction without virus-specific CD4<sup>+</sup> T-cell help on control of a simian immunodeficiency virus challenge in rhesus macaques. *J. Virol.* **83**, 9339–9346 (2009).
- Cline, A. N., Bess, J. W., Piatak, M. J. & Lifson, J. D. Highly sensitive SIV plasma viral load assay: practical considerations, realistic performance expectations, and application to reverse engineering of vaccines for AIDS. *J. Med. Primatol.* **34**, 303–312 (2005).
- Henn, M. R. *et al.* Whole genome deep sequencing of HIV-1 reveals the impact of early minor variants upon immune recognition during acute infection. *PLoS Pathog.* **8**, e1002529 (2012).
- Macalalad, A. R. *et al.* Highly sensitive and specific detection of rare variants in mixed viral populations from massively parallel sequence data. *PLoS Comput. Biol.* **8**, e1002417 (2012).

**Supplementary Information** is available in the online version of the paper.

**Acknowledgements** We would like to thank M. Stevenson, M. Reynolds, N. Maness and J. Sacha for discussions and suggestions. We also thank D. Evans, L. Heyer and Z. R. Bergman for facilitating the experiments. This work was funded in part by National Institutes of Health (NIH) grants R37 AI052056, R01 AI076114, RR015371, contract number HHSN261200800001E and FAPERJ, INCTV, CNPq, MCT and FIOCRUZ.

**Author Contributions** D.I.W., T.M.A. and P.A.M. conceived of and designed the experiments. P.A.M., A.J.E., M.A.M., K.A.P., A.S., A.D.G., A.T.B., S.M.P., L.D., K.L.W., J.R.F., S.C., M.P., A.T.H. and J.D.L. performed the experiments. P.A.M., M.A.M., N.A.W., E.R., M.P., A.T.H., J.D.L., D.C.T., T.M.A. and D.I.W. compiled and analysed the data. Y.K. and D.B.A. oversaw statistical analysis of the data and aided in interpretation. M.G.V., M.C.B. and R.G. designed and manufactured the rYF17D vectors used in these studies. P.A.M., A.T.H., J.D.L., T.M.A. and D.I.W. wrote the manuscript.

**Author Information** The sequence data for this study are available at the NCBI Sequence Read Archive (<http://www.ncbi.nlm.nih.gov/Traces/sra>) under accession number SRA055739. Reprints and permissions information is available at [www.nature.com/reprints](http://www.nature.com/reprints). The authors declare competing financial interests: details are available in the online version of the paper. Readers are welcome to comment on the online version of the paper. Correspondence and requests for materials should be addressed to D.I.W. ([dwatkins@med.miami.edu](mailto:dwatkins@med.miami.edu)).

## METHODS

**Animals.** The sixteen *Mamu-B\*08*<sup>+</sup> Indian rhesus macaques in groups 1 and 2 were from the Oregon National Primate Research Center. Among the four unvaccinated *Mamu-B\*08*<sup>+</sup> macaques shown in Fig. 2c, one animal came from Pfizer, one came from the Harlow Primate laboratory at the University of Wisconsin-Madison, and the two remaining animals were raised in-house at the Wisconsin National Primate Research Center (WNPRC). All eight unvaccinated, *Mamu-B\*08*<sup>+</sup> animals shown in Fig. 2c were also raised in-house at the WNPRC. All animals were housed and studies were conducted at the WNPRC. Animals were cared for according to the regulations and guidelines of the University of Wisconsin Institutional Animal Care and Use Committee, Animal Welfare Assurance no. A3368-01. Full details of the study were approved (University of Wisconsin-Madison Animal Care and Use Protocol no. G00639) by the University of Wisconsin Institutional Animal Care and Use Committee in accordance with the recommendations of the Weatherall report. Macaques in groups 1 and 2 ( $n = 16$ ) were males, with a mean age of 7.95 years (range 7.1–9.2). The four unvaccinated, *Mamu-B\*08*<sup>+</sup> control animals were also males and their mean age was 12.4 years (range 7.5–18.3). Among the eight unvaccinated, *Mamu-B\*08*<sup>−</sup> control animals, six were males and two were females; their mean age was 8.3 years (range 7.7–9.2). Once infected, animals were singly housed to prevent cross contamination of SIV infection and spread of opportunistic infections. Animals were closely monitored daily for pain or discomfort and treated accordingly by a veterinarian to ameliorate any suffering. After progression to AIDS or at the end of the study, animals with high viral loads were humanely euthanized. Animals that controlled viral replication during this study have been maintained for continuing study as a part of the elite controller resource at the Wisconsin National Primate Research Center. Group 1 vaccinee rh2349 was euthanized at 35 weeks after infection after a 20% loss of its body weight. At necropsy, this animal had right-sided dilated cardiomyopathy and cardiomyocyte necrosis, with minimal inflammation. This may be related to SIV infection but it is not a typical lesion. All animals were MHC class I-typed to verify the presence of the *Mamu-B\*08* allele according to a previously reported protocol<sup>9</sup>.

**Vaccination.** Vaccinated animals received constructs as shown in Fig. 1a. Animals receiving the three immunodominant *Mamu-B\*08*-restricted epitopes were vaccinated with two separate rYF17D constructs. rYF17D viruses were created with a single insert between the viral proteins E and NS1, as previously described<sup>23,24</sup>. The first was engineered to contain SIVmac239 Vif amino acids 102–214 (including the Vif<sub>123–131</sub>RL9 and Vif<sub>172–179</sub>RL8 epitopes), and the second contained SIVmac239 Nef amino acids 45–210 (including the Nef<sub>137–146</sub>RL10 epitope). Animals were vaccinated subcutaneously with  $2.0 \times 10^5$  plaque-forming units of each of these constructs in separate locations on each forearm. The animals were then boosted intramuscularly in each thigh 4 weeks later with two separate doses of  $10^{11}$  particles of rAd5 vectors (Viraquest) each containing SIVmac239 Vif and Nef inserts identical to those in the rYF17D. Control vaccinated animals underwent the same vaccination regimen, except rYF17D and recombinant adenoviral vectors included portions of SIVmac239 without known *Mamu-B\*08* epitopes<sup>10</sup>—SIVmac239 Vif amino acids 1–110 and SIVmac239 Gag amino acids 178–258.

**SIV infection and viral load measurement.** Animals in groups 1, 2 and the unvaccinated *Mamu-B\*08*<sup>+</sup> controls were challenged intrarectally with 10,000 TCID<sub>50</sub> ( $8.15 \times 10^7$  vRNA copies) of SIVmac239 15 weeks after vaccination with rAd5. Animals that remained uninfected after the initial inoculation were challenged a second time 3 weeks later. The group 1 vaccinee rh2355 resisted a total of four challenges. Each of these intrarectal inoculations occurred approximately 3 weeks after the previous challenge. The eight unvaccinated, *Mamu-B\*08*<sup>−</sup> animals described in Fig. 2c were used as experimental controls as part of a separate SIV vaccine trial conducted in our laboratory (M.A.M. *et al.*, manuscript in preparation). They were challenged intrarectally every week with the same stock of SIVmac239 described above, albeit at doses ranging from 800 to 50,000 TCID<sub>50</sub> ( $6.52 \times 10^6$  to  $4.07 \times 10^8$  vRNA copies, respectively).

Clonal SIVmac239 was generated by transfection of Vero cells with plasmid DNA encoding proviral sequences. Activated PBMCs from four SIV-naïve rhesus macaques were then added to the culture 1 day later and removed from the Vero cells into flasks 3 days after the initial transfection. Virus was amplified in the activated PBMCs and cell-free supernatant was collected 2 days after peak syncytium formation. Viral loads were measured from EDTA anti-coagulated plasma following a previously described protocol<sup>20</sup>. Viral RNA was dissolved in 30 µl 10 mM TrisCl, pH 8.0. Samples were run in duplicate. Each reaction contained 10 µl RNA and 20 µl of a reverse transcriptase master mix so that the final reactions contained 50 mM Tris-HCl, pH 8.3, 50 mM KCl (1× PCR II Buffer; Applied Biosystems), 0.05% gelatin (Sigma), 0.02% Tween 20 (Sigma), 5 mM MgCl<sub>2</sub>, 0.5 mM of each dNTP, 150 ng random hexamer primers (Promega), 20 U RNaseOUT and 20 U Superscript II reverse transcriptase (Life Technologies). Viral RNA was converted to complementary DNA using the following conditions: 25 °C

for 15 min, 42 °C for 40 min, 90 °C for 10 min, 25 °C for 30 min, and 5 °C until the reaction was removed from the thermocycler. At the second 25 °C stage, or later, the reactions were unsealed and 20 µl of a cocktail containing primers, probe and thermostable polymerase were added so that the final reactions contained 1× PCR II buffer, 0.03% gelatin, 0.012% Tween 20, 4.5 mM MgCl<sub>2</sub>, 600 nM of each primer (forward primer (SGAG21), 5′-GTCTGCGTCATPTGGTGCATTC-3′, reverse primer (SGAG22), 5′-CACTAGKTGTCTGCACTATPTGTTT-3′), 100 nM probe (pSGAG23, 5′-(FAM)CTTCPTCAGTGTGTTTCACTTTCTCTCTGCG-(BHQ)-3′), 45 nM SuperROX passive reference dye (Biosearch Technologies), and 1.25 U Taq-gold polymerase (Life Technologies). P and K are non-standard bases (Glen Research) that minimize the effect of potential sequence mismatches at positions of described heterogeneity in SIV isolates (Los Alamos Sequence Database); FAM is the reporter fluorochrome 6-carboxyfluorescein; BHQ is black hole quencher (Biosearch Technologies); and ROX is 5-carboxyrhodamine. The final reactions were then run on an ABI 7500 Sequence Detection System (Life Technologies). The run conditions were 95 °C for 10 min, followed by 45 cycles of 95 °C for 15 s and 60 °C for 1 min. Copy numbers for test samples were determined using an RNA standard curve run at the same time. Thirty viral copy equivalents per millilitre of plasma is the limit of reliable quantification for this assay.

**Colon and lymph node biopsies.** Lymph node and colon biopsies were obtained from all animals with positive viral loads on days 9, 14 and 21 after SIVmac239 infection. Animals were anaesthetized and a single inguinal or axillary lymph node was obtained from a separate biopsy site each day by a veterinarian using aseptic technique. Lymph node biopsy specimens were sieved through a 100-µm screen to obtain a single-cell suspension and any remaining red blood cells were removed by hypotonic lysis. During the same anaesthetic event, colon biopsy samples (approximately ten separate  $2 \times 2 \times 2$  mm pieces of tissue) were collected by the veterinarian using a pinch biopsy device and a fibre optic endoscope. Colon biopsy samples were washed with R10 (RPMI 1640 media supplemented with 10% FBS, 1% antibiotic/antimycotic and 1% L-glutamine) and then resuspended in pre-digestion buffer (HBSS supplemented with 5% FBS, 1% antibiotic/antimycotic, 5 mM EDTA and 1 mM DTT), and incubated in an orbital shaker at 50 r.p.m., 37 °C for 30 min. Samples were then washed once with R10 media and resuspended in collagenase medium (R10 with 15 µg ml<sup>−1</sup> type II collagenase from *Clostridium histolyticum* (Sigma-Aldrich)) and incubated at 50 r.p.m., 37 °C for 30 min. The supernatant was collected and lamina propria lymphocytes (LPL) contained within the supernatant were washed three times with R10 media. The collagenase digestion was repeated twice more and the collected, washed LPL were pooled in R10 media and layered over a 40–90% Percoll gradient before being centrifuged for 30 min at 450g. Purified LPL were collected from the interface between the 40% and 90% Percoll layers and washed once with R10 media before being counted and stained for flow cytometry.

**In situ hybridization.** *In situ* hybridization was performed as previously described<sup>14,15</sup>. In brief, 5-mm sections were cut from 4% paraformaldehyde-fixed lymph node tissues. After deparaffinization, pretreatment to permeabilize the tissues and blocking of non-specific binding, the sections were hybridized to <sup>35</sup>S-labelled SIV RNA antisense or sense (as a negative control) riboprobes covering SIV sequences at the 5′, middle and 3′ end of the genome. After overnight hybridization at 45 °C, the sections were washed, digested with RNases, coated with nuclear track emulsion, exposed, developed and counterstained with haematoxylin and eosin. Viral load was quantified as SIV RNA<sup>+</sup> cells per mm<sup>2</sup> of tissue.

**Tetramer staining and flow cytometry.** For tetramer staining, we used MHC class I tetramers produced by the Wisconsin National Primate Research Center Tetramer Core conjugated to either phycoerythrin or allophycocyanin. Prepared PBMCs, lymph node cells or colon biopsy cells suspended in R10 were centrifuged for 5 min at 530g in 1.2-ml cluster tubes and excess media was aspirated leaving all samples in 100–200 µl of R10. Approximately 50,000–100,000 colon biopsy cells or 500,000–1,000,000 PBMC/lymph node cells were stained with tetramer for 90 min at 37 °C. After the incubation, surface staining antibodies were added and samples were incubated at room temperature for 30 min. Cells were then washed twice with FACS buffer (PBS with 10% FBS) and fixed with 1% paraformaldehyde in PBS. Cells were run on a BD-LSRII instrument (BD Biosciences) and analysis was performed using FlowJo software (version 9.3.1, Tree Star). We used the following antibodies from BD Biosciences during this study: anti-CD3 Alexa Fluor 700 (clone SP34-2) and anti-CD8 Pacific blue (RPA-T8).

For the MHC class I tetramer/granzyme B combined staining, cryopreserved PBMCs were thawed at 37 °C and washed twice in R10 media before staining. Approximately  $2.0 \times 10^5$ – $2.0 \times 10^6$  PBMCs were stained with 5 µl of phycoerythrin-conjugated tetramer in a volume of 100–200 µl of R10 media for 90 min at 37 °C. Cells were then stained with 2 µl anti-CD3 Alexa Fluor 700 (clone SP34-2; BD Biosciences) and 1 µl anti-CD8 Pacific Blue (clone RPA-T8; BD Biosciences) for 30 min at room temperature. Subsequent washes and fixation

with 1% paraformaldehyde were performed as described above. Fixed cells were washed twice with FACS buffer, and excess liquid was aspirated to leave samples in approximately 75  $\mu$ l of FACS buffer. Cells were then permeabilized by adding 100  $\mu$ l medium B (Life Technologies), and simultaneously stained for granzyme B with 1  $\mu$ l anti-GzmB allophycocyanin (clone GB12; Life Technologies) for 30 min at room temperature. Cells were then washed twice with FACS buffer, and fixed in 1% paraformaldehyde. Cells were run on a SORP BD-LSRII (BD Biosciences) and analysis was performed using FlowJo software (version 9.4.2, Tree Star). Owing to sample limitations, only rh2350, rh2352, rh2361 and rh2365 from group 1 and rh2351, rh2353, rh2354 and rh2360 from group 2 were included in this analysis.

**IFN- $\gamma$  and perforin ELISPOT.** ELISPOT assays were performed on PBMCs or PBMCs depleted of CD8<sup>+</sup> cells at the indicated time points. CD8 depletion was performed on PBMCs before ELISPOT in some assays using the Miltenyi Biotec non-human primate CD8 MicroBead kit and LS columns according to the manufacturer's protocols (Miltenyi Biotec). CD8 depletion was determined to be >99% in every assay performed. All IFN- $\gamma$  and perforin ELISPOT assays (ELISPOT<sup>PLUS</sup>-ALP) were performed with 100,000 cells per well, in duplicate, according to the manufacturer's instructions (MABTECH). For all IFN- $\gamma$  assays, we used pools of peptides (ten peptides of 15 residues each, each overlapping by 11 amino acids) covering the SIVmac239 antigens, and these pools were tested at a final concentration of 1  $\mu$ M. For the perforin assays, only the minimal peptides were tested, each at a final concentration of 10  $\mu$ M. Each individual animal on each separate plate included at least two separate positive control wells (5  $\mu$ g ml<sup>-1</sup> concanavalin A) and two or more negative control wells. Wells were imaged and spots were enumerated with an AID ELISPOT reader (AID). Positive responses were determined as follows: test wells were run with two replicates whereas positive and negative control wells were run in replicates of 2, 4 or 6 depending on the assay. Responses containing <50 spot-forming cells (SFC) per 10<sup>6</sup> cells were considered negative and not tested statistically. Positive responses were determined using a one-tailed *t*-test and  $\alpha = 0.05$ , in which the null hypothesis ( $H_0$ ): background level = treatment level. If determined to be positive statistically, the reported values equal the average of the test wells minus the average of all negative control wells. For the perforin ELISPOT in Fig. 3f, we only included rh2350, rh2352, rh2361 and rh2365 from group 1 and rh2351, rh2353, rh2354 and rh2360 from group 2 in the analysis owing to sample limitations.

**Amplicon-based 454 sequencing of Vif and Nef epitopes.** One to three millilitres of plasma was thawed on ice and centrifuged at 20,817g for 1.5 h at 4 °C, after which the pellet was resuspended in 140  $\mu$ l of the supernatant. The QIAamp viral RNA mini kit (Qiagen) was used to isolate viral RNA per manufacturer protocol. Viral RNA was eluted in 60  $\mu$ l of buffer AVE, aliquoted and stored at -80 °C for future RT-PCR.

An amplicon-based 454 sequencing approach was used to analyse the Vif and Nef epitopes as previously described<sup>13</sup>. In brief, primers were synthesized with Roche 454 amplicon (Lib-A) adaptor sequences, multiplex identifier tags (MID) 1 to 18, and sequence-specific regions (Vif: forward, 5'-GAAAAAGGGTGGCTCA GT-3', reverse, 5'-AGGTGGTTTACCGCTCTCT-3'; Nef: forward, 5'-ACT GGAAGGGATTATTAC-3', reverse, 5'-GAGTTTCCTTCTTGTCAGCC-3'), which allowed multiplexing of up to 16 animal/amplicon combinations per sequencing run.

A single-step RT-PCR was carried out for each of the unique amplicon/animal/MID sequence combinations using SuperScript III one-step RT-PCR system with platinum Taq high fidelity (Invitrogen). Each 25- $\mu$ l reaction contained 12.5  $\mu$ l of 2 $\times$  reaction mix, a further 0.3 mM MgSO<sub>4</sub>, 1  $\mu$ l of enzyme mix, 0.2  $\mu$ M each of the sequence specific, adaptor/MID-tagged forward and reverse primers, and up to 10  $\mu$ l of template RNA. Cycling parameters for the Vif RT-PCR were as follows: 50 °C for 30 min, 94 °C for 2 min followed by 40 cycles of 94 °C for 15 s, 50 °C for 30 s and 68 °C for 30 s, 68 °C for 5 min, hold at 10 °C. The Nef RT-PCR parameters were identical with the exception of an annealing temperature of 54 °C. Amplicons were visualized on a 1% agarose gel and purified using the Purelink quick gel extraction kit (Invitrogen). RT-PCR products were quantified using a Promega quantiflor-ST fluorometer (Promega) and analysed for quality using an Agilent 2100 bioanalyzer with high sensitivity DNA chips.

For each sequencing run, up to 16 animal/amplicon samples were pooled in equimolar ratios and 20 million molecules of pooled sample were added to 10 million DNA capture beads for a final ratio of 2.0 DNA molecules per bead. Emulsion PCR, enrichment, breaking and DNA sequencing were all performed according to the GS Junior FLX titanium series manuals for Lib-A (Roche). Sequencing and run processing were performed on a GS Junior 454 sequencing instrument (Roche).

We used the ReadClean 454 (RC454) and V-Phaser algorithms as previously described<sup>21</sup> to call variants from the 454 data sets. In brief, RC454 was used to align reads to SIVmac239 and reads were corrected for sequencing related artefacts such as indels resulting from overcalls and undercalls in homopolymeric regions and carry forward and incomplete extension (CAFIE) errors. Furthermore, RC454 optimizes read alignments using coding-frame information. The V-Phaser algorithm was then used to distinguish an observed variant as a true variant from an amplification or sequencing artefact<sup>22</sup>.

23. Bonaldo, M. C. *et al.* Recombinant yellow fever vaccine virus 17D expressing simian immunodeficiency virus SIVmac239 gag induces SIV-specific CD8<sup>+</sup> T-cell responses in rhesus macaques. *J. Virol.* **84**, 3699–3706 (2010).
24. Bonaldo, M. C. *et al.* Construction and characterization of recombinant flaviviruses bearing insertions between E and NS1 genes. *Virol. J.* **4**, 115 (2007).

# The molecular basis of phosphate discrimination in arsenate-rich environments

Mikael Elias<sup>1\*</sup>, Alon Wellner<sup>1\*</sup>, Korina Goldin-Azulay<sup>1</sup>, Eric Chabriere<sup>2</sup>, Julia A. Vorholt<sup>3</sup>, Tobias J. Erb<sup>3</sup> & Dan S. Tawfik<sup>1</sup>

**Arsenate and phosphate are abundant on Earth and have striking similarities: nearly identical  $pK_a$  values<sup>1,2</sup>, similarly charged oxygen atoms, and thermochemical radii that differ by only 4% (ref. 3). Phosphate is indispensable and arsenate is toxic, but this extensive similarity raises the question whether arsenate may substitute for phosphate in certain niches<sup>4,5</sup>. However, whether it is used or excluded, discriminating phosphate from arsenate is a paramount challenge. Enzymes that utilize phosphate, for example, have the same binding mode and kinetic parameters as arsenate, and the latter's presence therefore decouples metabolism<sup>6,7</sup>. Can proteins discriminate between these two anions, and how would they do so? In particular, cellular phosphate uptake systems face a challenge in arsenate-rich environments. Here we describe a molecular mechanism for this process. We examined the periplasmic phosphate-binding proteins (PBPs) of the ABC-type transport system that mediates phosphate uptake into bacterial cells, including two PBPs from the arsenate-rich Mono Lake *Halomonas* strain GFAJ-1. All PBPs tested are capable of discriminating phosphate over arsenate at least 500-fold. The exception is one of the PBPs of GFAJ-1 that shows roughly 4,500-fold discrimination and its gene is highly expressed under phosphate-limiting conditions. Sub-ångström-resolution structures of *Pseudomonas fluorescens* PBP with both arsenate and phosphate show a unique mode of binding that mediates discrimination. An extensive network of dipole-anion interactions<sup>8,9</sup>, and of repulsive interactions, results in the 4% larger arsenate distorting a unique low-barrier hydrogen bond. These features enable the phosphate transport system to bind phosphate selectively over arsenate (at least  $10^3$  excess) even in highly arsenate-rich environments.**

Phosphate transport is mediated by two distinct systems in bacteria and archaea: the phosphate inorganic transport (Pit), a low-affinity and low-selectivity system operating at high phosphate concentrations<sup>10</sup>, and the phosphate-specific transport (Pst)<sup>10</sup>. The latter is a high-affinity and high-selectivity ATP-fuelled transporter operating at low phosphate concentration<sup>11</sup> and in high arsenate conditions<sup>10,12</sup>. It comprises a periplasmic high-affinity PBP (or pstS) whose  $K_d$  for phosphate is in the submicromolar range<sup>13</sup>. The PBP-captured phosphate anion is subsequently transported across the membrane by an ABC transporter that is energized by ATP to transfer phosphate against the concentration gradient<sup>11</sup>. We examined five bacterial PBPs for their discrimination of phosphate from arsenate. Two PBPs came from arsenate-sensitive species (*Escherichia coli* and *P. fluorescens*), and the other three came from arsenate-resistant bacteria: *Klebsiella variicola* from Lake Albano (Italy)<sup>14</sup> and the highly arsenate-resistant bacterium *Halomonas* sp. GFAJ-1 (Mono Lake, USA), for which controversy exists over whether it incorporates arsenate into its DNA<sup>5</sup> or not<sup>15,16</sup>. The genome of the latter contains two pstS paralogues from two distinct *pst* operons belonging to so-called 'arsenic islands'<sup>17</sup>. To what degree do these five PBPs distinguish between phosphate and arsenate? What is the molecular basis of their discrimination? Do PBPs adapt to arsenate-rich environments by

evolving higher selectivity for phosphate, or perhaps by divergence to import arsenate under certain circumstances?

The five PBPs studied share little sequence identity (Supplementary Fig. 1 and Supplementary Table 1). However, the two *Halomonas* GFAJ-1 PBPs are closely related (Supplementary Fig. 2), and one of them, PBP-2, resides in a phylogenetic clade that comprises extremophiles, and in particular high-salt-resistant and arsenate-resistant organisms (Supplementary Fig. 3 and Supplementary Table 2). We cloned, purified and characterized these five PBPs (Supplementary Information). Despite being isolated from very different sources, four PBPs discriminated phosphate from arsenate 500–850-fold. The exception was the *Halomonas* GFAJ-1 PBP-2 paralogue, which showed much higher discrimination (at least 4,500-fold; Fig. 1a and Supplementary Table 3). Both PBPs of *Halomonas* GFAJ-1 showed specificity for phosphate, which ruled out the possibility that one of them had diverged to serve in arsenate transport. However, the presence of two PBPs raised the question of which of them might be active under phosphate-limiting (and in particular arsenate-rich) environments. Analysis of messenger RNA levels showed that PBP-2 is upregulated more than 40-fold and highly expressed at limiting phosphate concentrations (10  $\mu$ M), whereas PBP-1 shows barely detectable expression that is only moderately affected by the phosphate level independent of the presence or absence of arsenate (Supplementary Tables 4a, b and 5).

All PBPs have a similar fold that consists of two structurally similar domains linked by a flexible hinge<sup>9</sup> (Supplementary Fig. 4a, b). In the closed form, the binding pocket is buried between the domains and the bound ion is totally dehydrated and completely sequestered. The structure opens to release its cargo anion on binding the transporter. Dipole-ion hydrogen bonds underline the high selectivity of PBPs<sup>18–21</sup> as manifested in the reported  $10^5$ -fold discrimination of phosphate over sulphate<sup>8,9,22</sup>. In both *E. coli* and *P. fluorescens* PBP (the latter dubbed PfluDING), phosphate is bound through 12 hydrogen bonds, of which 9 are ion-dipole interactions: 5 backbone NH groups and 4 hydroxyl groups of serine and threonine (Supplementary Fig. 5).

Phosphate and sulphate differ significantly, not only in having three and two ionizable oxygens, respectively (the structure of sulphate is  $(O=)_2S-O_2^{2-}$ ), and in having different  $pK_a$  values, but also in size<sup>3</sup>. Indeed, sulphate and similar anions such as iodate are readily distinguished by phosphate-using enzymes<sup>23</sup>. It is less clear, however, how the far more similar phosphate and arsenate are discriminated. In fact, the differences between their binding interactions are so subtle that they could only be unravelled in sub-ångström-resolution structures obtained for the arsenate-bound PfluDING at pH 4.5 and 8.5 (Supplementary Tables 7 and 9; PDB 4F19 and 4F18; 0.95 and 0.96 Å resolution, respectively). The arsenate structures were compared with the equivalent structures with phosphate (Supplementary Tables 8 and 9; PDB 4F1U and 4F1V; 0.98 and 0.88 Å resolution, respectively). Besides the observable difference in the electronic content of phosphorus and arsenic atoms (15 versus 33 electrons), the substitution of phosphate by arsenate was verified by anomalous scattering X-ray

<sup>1</sup>Department of Biological Chemistry, Weizmann Institute of Science, Rehovot 76100, Israel. <sup>2</sup>Unité de recherche sur les maladies infectieuses et tropicales émergentes, Faculté de Médecine et de Pharmacie, CNRS-Université de la Méditerranée, 13385 Marseille, France. <sup>3</sup>Institute of Microbiology, Eidgenössische Technische Hochschule Zurich, Wolfgang Pauli Strasse 10, 8093 Zurich, Switzerland. \*These authors contributed equally to this work.

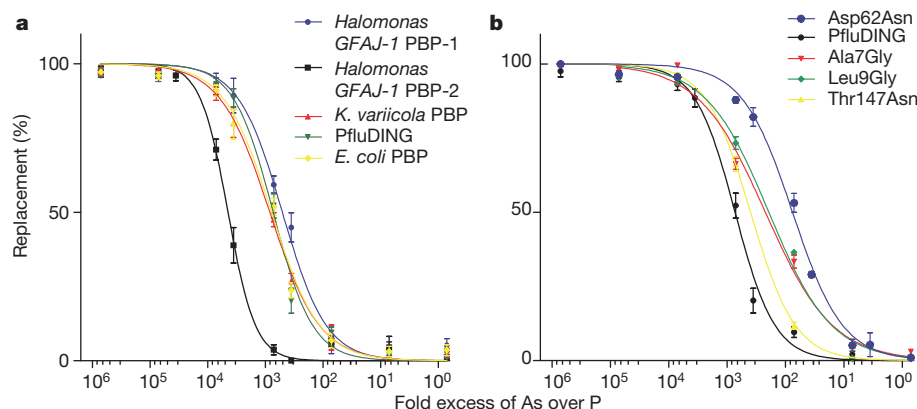


**Figure 1 | The phosphate-arsenate selectivity of PBPs.** **a**, PBPs were equilibrated with radiolabelled phosphate and varying arsenate concentrations (0.1  $\mu$ M to 100 mM). The level of radioactivity (that is, of protein-bound phosphate) with no arsenate corresponded to 0% replacement. *Halomonas* PBP-2 was also found to have higher selectivity for vanadate and sulphate (Supplementary Fig. 12). **b**, The phosphate-arsenate selectivity of PfluDING mutants. The mutation Thr147Asn decreased phosphate binding<sup>18</sup> but hardly

affected selectivity. In contrast, mutations in the residues mediating unfavourable interactions (Ala7Gly and Leu9Gly), and mutation Asp62Asn altering the short hydrogen bond, decreased selectivity between fourfold and tenfold (see also Supplementary Figs 9 and 10). Details of the curve fitting and the inferred discrimination factors are provided in Supplementary Tables 3 and 14. Error bars show s.e.m. calculated with two to four independent repeats.

diffraction (Supplementary Table 10 and Supplementary Fig. 6). As observed in arsenate-bound enzyme structures<sup>23,24</sup>, the arsenate binds in exactly the same mode as phosphate, and the side chains of the protein within the binding cleft superimpose perfectly (Fig. 2a). Further, the hydrogen locations as determined from the high-quality electronic density maps (Fig. 2b and Supplementary Fig. 7) reveal that, as expected from their identical  $pK_a$  values, arsenate and phosphate are both bound in their dibasic forms ( $H(As/P)O_4^{2-}$ ) at both pH 4.5 and pH 8.5 (also confirmed by As–O bond lengths; Supplementary Table 11). This feature—the binding of dibasic phosphate at pH 4.5—was attributed to the unusually high number of hydrogen bonds that solvate the bound anion<sup>22</sup> and to a specific charge network in *Mycobacterium tuberculosis* PBP<sup>21</sup>. Finally, the differences in P–O and As–O bond lengths (0.08–0.14 Å) barely perturb the donor-acceptor hydrogen bond distances (D–H) and angles (Supplementary Tables 11–13). How, then, is arsenate discriminated against?

The only significant difference that we could observe between the arsenate-bound and phosphate-bound structures resided in the remarkably short interaction distance (about 2.50 Å) from the carboxylate of Asp 62 to O2 of the anions, a proposed key interaction for specificity<sup>8,21,25</sup>. This distance is typical of low-barrier hydrogen bonds (LBHBs)<sup>26</sup>, and is specifically categorized as a heteromolecular negative-charge-assisted hydrogen bond ((–)CAHB). The shared hydrogen atoms involved in these bonds are rarely observable by diffraction techniques because of their diffuse character<sup>27</sup>. Nonetheless, the high resolution and quality of our structures allowed the shared proton to be located, although at relatively low signal-to-noise ratios (Fig. 3). In the phosphate complex, the hydrogen atom occupies a nearly central position at pH 8.5 (D–H 1.19 Å; Fig. 3a and Supplementary Table 13) but not at pH 4.5 (Supplementary Table 12), as expected for optimal CAHBs. In the arsenate-bound structure, this short donor-acceptor distance is maintained (2.50 Å). However, the

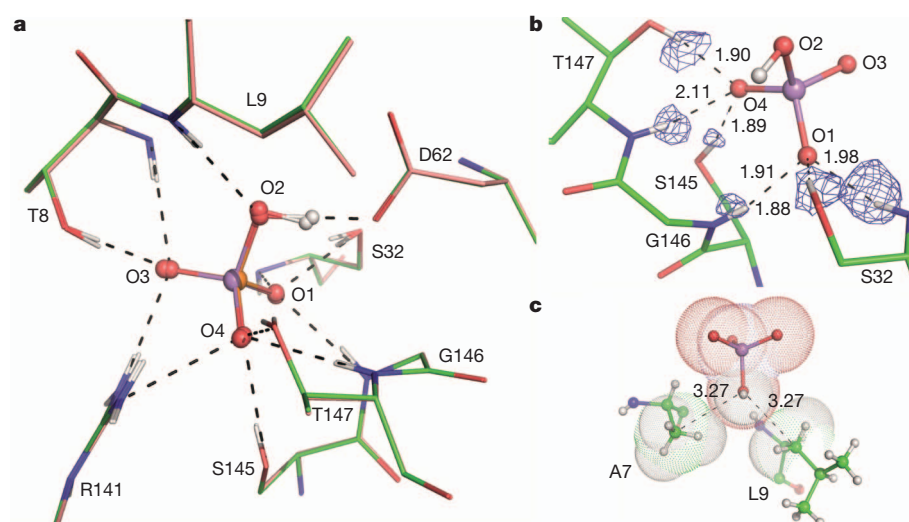


**Figure 2 | Binding of arsenate and phosphate to PfluDING.**

**a**, Superimposition of the arsenate-bound (green sticks; PDB 4F18; pH 8.5) and phosphate-bound (pink sticks; PDB 4F1V; pH 8.5) PfluDING structures. The arsenate (red and violet spheres) and phosphate (orange and red spheres) superimpose perfectly, as do all protein residues. Hydrogen bonds underlining the bound anion are shown as black dashes. **b**, Key ion-dipole interactions in the arsenate structure. Residues involved in the binding (green sticks) donate

hydrogen atoms (white sticks, revealed by the omit-H Fourier difference map (blue mesh) contoured at  $2\sigma$ ) to the bound arsenate ion. **c**, Unfavourable contacts between the arsenate ion (red and violet) and the C $\beta$  atoms of Ala 7 and Leu 9 (see also Supplementary Fig. 13). The van der Waals radii are shown as dashes. Distances are indicated in ångströms (standard deviations are available in Supplementary Tables 13 and 11).

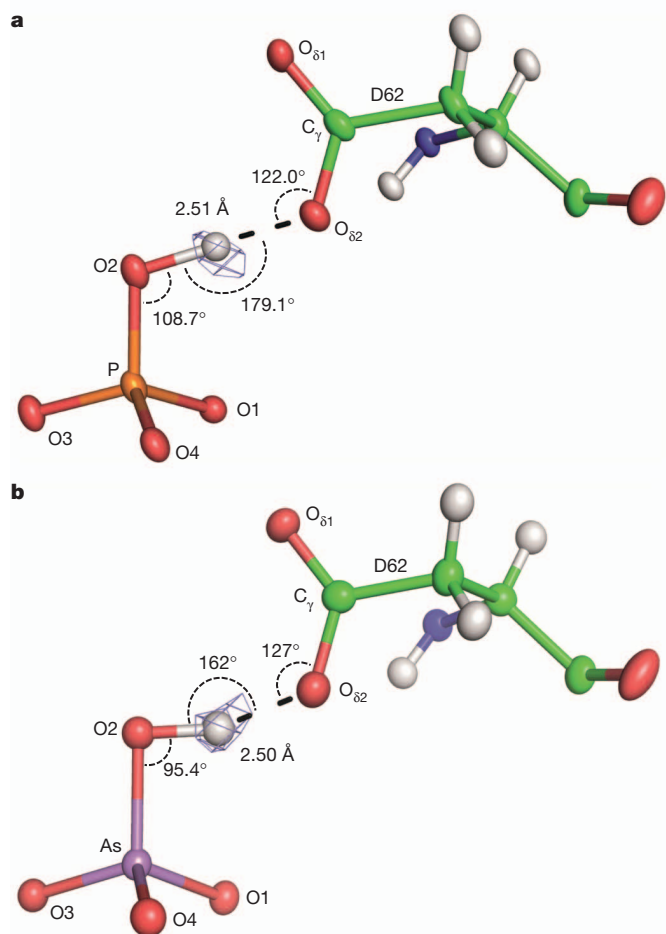


**Figure 3 | The (–)CAHB angles are optimal in the phosphate-bound structure but distorted with arsenate.** **a**, A close-up view of the short hydrogen bond ((–)CAHB, or LBHB) between O2 of the bound phosphate and the carboxylate of Asp 62 (pH 8.5; PDB 4F1V). The shared hydrogen atom is revealed by the omit-H Fourier difference map (blue mesh) contoured at  $2.5\sigma$  (peak height  $3.3\sigma$ ). **b**, The same bond in the arsenate-bound structure, with the omit-H Fourier difference map (blue mesh) contoured at  $1.4\sigma$  (peak height  $1.9\sigma$ ; the pH 4.5 structure is presented for clarity). Noted are the bond lengths and the angles of the short hydrogen bonds. Atoms are represented as their anisotropic thermal ellipsoids. Measurements made in structures at both pH values (4.5 and 8.5) and corresponding standard deviation values are available in Supplementary Tables 11–13. Alternative models are presented in Supplementary Fig. 8.

proton is asymmetrically located at both pH values ( $D-H \approx 1.08 \text{ \AA}$ ), suggesting a weaker interaction (Supplementary Tables 12 and 13).

The three angles that define the CAHB are nearly canonical in the phosphate structure ( $P-O_2-H = 108.7^\circ$ ;  $O_2-H \cdots O_{\delta 2} = 179.1^\circ$ ;  $C_\gamma-O_{\delta 2} \cdots H = 122^\circ$ ; which are all  $\pm 2^\circ$  from the canonical angles). However, these angles are all suboptimal for the bound arsenate ( $As-O_2-H = 95.4^\circ$ ;  $O_2-H \cdots O_{\delta 2} = 162^\circ$ ;  $C_\gamma-O_{\delta 2} \cdots H = 127^\circ$ ; Fig. 3 and Supplementary Tables 11–13). This distortion is the consequence of the longer As–O2 bond than the P–O2 bond (Supplementary Fig. 8b), and may readily account for the difference of about 500-fold in favour of phosphate binding. We note that even when the shared hydrogen was modelled with the canonical As–O2–H angle, and not according to the observed residual density, the remaining two angles were severely distorted (Supplementary Fig. 8a).

The distorted bonding angles with Asp 62 suggest that the primary contribution of Asp 62 is not in anion binding itself. Indeed, the mutation Asp81Asn in *E. coli* PBP (equivalent to Asp62Asn) showed no effect on phosphate binding<sup>25</sup>. However, we found that this mutation,

in PfluDING, significantly disturbed the discrimination against arsenate (about tenfold; Fig. 1b and Supplementary Table 14). The equivalent mutation in *E. coli* PBP gave a similar decrease in arsenate discrimination (Supplementary Fig. 9) and an even greater effect with sulphate (about 100-fold; Supplementary Fig. 10). Conversely, a mutation that affected the phosphate-binding ability (Thr147Asn)<sup>18</sup> had little effect on the discrimination (Fig. 1b and Supplementary Table 14). The energy of this short bond may therefore be channelled not towards anion-binding affinity but rather towards anion selectivity.

In that conformational flexibility mediates promiscuity<sup>28</sup>, the high selectivity of PBPs relies on structural rigidity. This rigidity relates to the protein's conformation as well as extremely precise positioning and tight packing of the phosphate<sup>21</sup>. The former is illustrated by an analysis of *B*-factors of the region of the binding site (Supplementary Table 15). Moreover, most H-donor groups are backbone NH groups coming from the first turns of  $\alpha$ -helices, or from residues with a short side chain (serine or threonine) whose rotameric states are fixed by a network of hydrogen bonds. In addition to the extensive constellation of anion–dipole interactions, the bound anions are also immobilized by tight van der Waals interactions. The O2 of the phosphate is equidistant (3.35 Å) from the C $\beta$  atoms of Ala 7 and Leu 9, thus resulting in two short, unfavourable interactions (Fig. 2c). These distances are smaller than the sum of the van der Waals radii (1.92 Å (radius of CH<sub>2</sub> and CH<sub>3</sub>) plus 1.54 Å (radius of OH)<sup>29</sup> = 3.46 Å) and become even shorter (and thus more unfavourable) with arsenate (3.27 Å; values for pH 8.5 structures are given in Supplementary Table 11). Although not previously noted, these interactions seem to be conserved in PBPs (Supplementary Fig. 11). Accordingly, the mutations of either Ala 7 or Leu 9 into glycine that may eliminate these repulsive interactions resulted in a marked decrease in arsenate discrimination (about fourfold; Fig. 1b and Supplementary Table 14).

Taken together, our data indicate that PBPs show exquisite selectivity with respect to arsenate, whereas phosphate-binding proteins tested so far, enzymes and transporters alike, show no or low selectivity<sup>7</sup>. PBPs therefore seem to have evolved a unique mode of binding that is capable of distinguishing between the highly similar phosphate and arsenate. Anion binding is mediated by a dense and rigid network of ion–dipole interactions<sup>9,30</sup>. This network is sensitive to geometric changes. However, the perturbation imposed by the slightly larger arsenate is not equally distributed between all bonds but rather it is channelled almost solely to the short, high-energy hydrogen bond which is most sensitive to both angle and distance perturbations (Fig. 3). The channelling of this unique interaction is the outcome of the extremely tight positioning of the anion, mediated also by unfavourable interactions of the bound anions with two juxtaposed C $\beta$  atoms (Fig. 2c) within a rigid, highly connected binding site (Fig. 2a). Weakening of these interactions (for example by site-directed mutagenesis) significantly decreases the discrimination against arsenate (Fig. 1b); however, at least in the case of the short hydrogen bond, this seems to have little effect on phosphate binding. These structural features therefore support the notion that anion binding and anion selectivity are two independently evolved features.

The notion that PBPs evolved to meet arsenate challenges is also consistent with the observation that the *pst* system seems to be essential for the survival of *E. coli* in arsenate medium<sup>12</sup>. It also seems that the selectivity of bacterial PBPs can be further increased in arsenate-rich environments. The PBP-2 paralogue of *Halomonas* GFAJ-1 showed roughly tenfold higher selectivity than any other bacterial PBP we tested (Fig. 1). PBP-2 also belongs to a phylogenetic clade of high-salt-resistant and arsenate-resistant bacterial species (Supplementary Fig. 3 and Supplementary Table 2). The structural features of this clade and the origin of the high selectivity of PBP-2 remain unknown (Supplementary Fig. 4c, d). However, we note that PBP-2 seems to be functional *in vivo* and is selectively expressed at very low phosphate concentrations (10  $\mu\text{M}$ ; Supplementary Tables 4a, b, 5 and 16–18). Finally, the observed discrimination factor for PBP-2, *in vitro* as isolated protein (4,500-fold) is strikingly close to the discrimination levels

*in vivo*, by which a 4,000-fold excess of arsenate in the medium yielded only a 2.5-fold excess of intracellular arsenate (Supplementary Table 6). Thus, *Halomonas* GFAJ-1 seems to have evolved to extract phosphate<sup>16</sup> and, owing to the unique discrimination mode of its PBP, can do so at arsenate-to-phosphate ratios that are more than 3,000-fold higher than those observed in Mono Lake.

## METHODS SUMMARY

**Discrimination assays.** The five PBPs in this study were cloned, overexpressed in *E. coli* and purified. PBPs were tested for discrimination of phosphate from different anions (arsenate, vanadate and sulphate) by dialyzing them against 50 mM Tris-HCl buffer pH 8.0 containing a total of 140 nM phosphate (with 1  $\mu$ Ci of radiolabelled phosphate, <sup>32</sup>P) and increasing concentrations of the competing anion at tenfold serial dilutions (0.1  $\mu$ M to 100 mM). All experiments were performed with two to four independent repeats and included a control assay without PBP in the dialysis tube. The background absorption rate by 0.1% BSA was over 1,000-fold less than the PBP signal.

**Crystallization and diffraction data collection.** PfluDING was extensively dialysed against 50 mM Tris-HCl buffer pH 8 containing 10 mM arsenate and 1 mM CaCl<sub>2</sub> (to chelate phosphate). Crystals of the arsenate-bound form were subsequently obtained using hanging-drop vapour diffusion as described previously<sup>22</sup>, but using 100 mM arsenate solution as buffer at pH 4.5 or 8.5. Diffraction data collections on PfluDING crystals, including anomalous data at the arsenate edge, were performed at the European Synchrotron Radiation Facility (Grenoble, France) at beamlines ID-29 and ID-23-1. For both data collections in Supplementary Table 7, only 180° out of the 360° collected were used for refinement, to minimize the effect of radiation damage.

A complete description of materials and methods is provided in Supplementary Methods.

Received 6 May; accepted 15 August 2012.

Published online 3 October 2012.

- Kohn, R. A. & Dunlap, T. F. Calculation of the buffering capacity of bicarbonate in the rumen and *in vitro*. *J. Anim. Sci.* **76**, 1702–1709 (1998).
- Larsen, E. H. & Hansen, S. H. Separation of arsenic species by ion-pair and ion exchange high performance liquid chromatography. *Microchim. Acta* **109**, 47–51 (1992).
- Kish, M. M. & Viola, R. E. Oxyanion specificity of aspartate- $\beta$ -semialdehyde dehydrogenase. *Inorg. Chem.* **38**, 818–820 (1999).
- Westheimer, F. H. Why nature chose phosphates. *Science* **235**, 1173–1178 (1987).
- Wolfe-Simon, F. *et al.* A bacterium that can grow by using arsenic instead of phosphorus. *Science* **332**, 1163–1166 (2011).
- Dixon, H. B. F. The biochemical action of arsenic acids especially as phosphate analogues. *Adv. Inorg. Chem.* **44**, 191–227 (1997).
- Tawfik, D. S. & Viola, R. E. Arsenate replacing phosphate: alternative life chemistries and ion promiscuity. *Biochemistry* **50**, 1128–1134 (2011).
- Luecke, H. & Quijcho, F. A. High specificity of a phosphate transport protein determined by hydrogen bonds. *Nature* **347**, 402–406 (1990).
- Quijcho, F. A. & Ledvina, P. S. Atomic structure and specificity of bacterial periplasmic receptors for active transport and chemotaxis: variation of common themes. *Mol. Microbiol.* **20**, 17–25 (1996).
- Willsky, G. R. & Malamy, M. H. Characterization of two genetically separable inorganic phosphate transport systems in *Escherichia coli*. *J. Bacteriol.* **144**, 356–365 (1980).
- Rao, N. N. & Torriani, A. Molecular aspects of phosphate transport in *Escherichia coli*. *Mol. Microbiol.* **4**, 1083–1090 (1990).
- Willsky, G. R. & Malamy, M. H. Effect of arsenate on inorganic phosphate transport in *Escherichia coli*. *J. Bacteriol.* **144**, 366–374 (1980).
- Quijcho, F. A. Atomic structures of periplasmic binding proteins and the high-affinity active transport systems in bacteria. *Phil. Trans. R. Soc. Lond. B* **326**, 341–351 (1990).
- Butt, A. & Rehman, A. Isolation of arsenite-oxidizing bacteria from industrial effluents and their potential use in wastewater treatment. *World J. Microbiol. Biotechnol.* **27**, 2435–2441 (2011).
- Reaves, M. L., Sinha, S., Rabinowitz, J. D., Kruglyak, L. & Redfield, R. J. Absence of detectable arsenate in DNA from arsenate-grown GFAJ-1 cells. *Science* **337**, 470–473 (2012).
- Erb, T. J., Kiefer, P., Hattendorf, B., Gunther, D. & Vorholt, J. A. GFAJ-1 is an arsenate-resistant, phosphate-dependent organism. *Science* **337**, 467–470 (2012).
- Kim, E.-H. & Rensing, C. Genome of *Halomonas* strain GFAJ-1, a blueprint for fame or business as usual. *J. Bacteriol.* **194**, 1643–1645 (2012).
- Ahn, S. *et al.* Structure–function relationships in a bacterial DING protein. *FEBS Lett.* **581**, 3455–3460 (2007).
- Ledvina, P. S., Yao, N., Choudhary, A. & Quijcho, F. A. Negative electrostatic surface potential of protein sites specific for anionic ligands. *Proc. Natl Acad. Sci. USA* **93**, 6786–6791 (1996).
- Tanabe, M. *et al.* Structures of OppA and PstS from *Yersinia pestis* indicate variability of interactions with transmembrane domains. *Acta Crystallogr. D* **63**, 1185–1193 (2007).
- Vyas, N. K., Vyas, M. N. & Quijcho, F. A. Crystal structure of *M. tuberculosis* ABC phosphate transport receptor: specificity and charge compensation dominated by ion–dipole interactions. *Structure* **11**, 765–774 (2003).
- Liebschner, D. *et al.* Elucidation of the phosphate binding mode of DING proteins revealed by subangstrom X-ray crystallography. *J. Am. Chem. Soc.* **131**, 7879–7886 (2009).
- Faehnl, C. R., Blanco, J. & Viola, R. E. Structural basis for discrimination between oxyanion substrates or inhibitors in aspartate- $\beta$ -semialdehyde dehydrogenase. *Acta Crystallogr. D* **60**, 2320–2324 (2004).
- Kline, P. C. & Schramm, V. L. Purine nucleoside phosphorylase. Catalytic mechanism and transition-state analysis of the arsenolysis reaction. *Biochemistry* **32**, 13212–13219 (1993).
- Wang, Z., Luecke, H., Yao, N. & Quijcho, F. A. A low energy short hydrogen bond in very high resolution structures of protein receptor–phosphate complexes. *Nature Struct. Biol.* **4**, 519–522 (1997).
- Cleland, W. W. Low-barrier hydrogen bonds and enzymatic catalysis. *Arch. Biochem. Biophys.* **382**, 1–5 (2000).
- Steiner, T. & Saenger, W. Lengthening of the covalent O–H bond in O–H...O hydrogen bonds re-examined from low-temperature neutron diffraction data of organic compounds. *Acta Crystallogr. B* **50**, 348–357 (1994).
- Khersonsky, O. & Tawfik, D. S. Enzyme promiscuity: a mechanistic and evolutionary perspective. *Annu. Rev. Biochem.* **79**, 471–505 (2010).
- Li, A. J. & Nussinov, R. A set of van der Waals and coulombic radii of protein atoms for molecular and solvent-accessible surface calculation, packing evaluation, and docking. *Proteins* **32**, 111–127 (1998).
- Pflugrath, J. W. & Quijcho, F. A. Sulphate sequestered in the sulphate-binding protein of *Salmonella typhimurium* is bound solely by hydrogen bonds. *Nature* **314**, 257–260 (1985).

Supplementary Information is available in the online version of the paper.

**Acknowledgements** We thank G. Gotthard for valuable inputs, C. Jelsch for help with the software Mopro, and A. Toth-Petroczy for help with the phylogenetic analysis. Financial support by the Israel Science Foundation is gratefully acknowledged. M.E. is a fellow supported by the Intra-European Fellowships Marie Curie program (grant No. 252836). D.S.T. is the Nella and Leon Benozziyo Professor of Biochemistry. T.J.E. was supported by an Eidgenössische Technische Hochschule fellowship.

**Author Contributions** M.E. initiated the project, designed experiments, crystallized the proteins, collected and processed crystallographic data, performed discrimination assays, analysed the data and wrote the manuscript. A.W. cloned, purified and crystallized proteins, performed discrimination assays and analysed data. K.G.A. cloned and constructed the mutants, purified proteins and performed discrimination assays. T.J.E. and J.A.V. designed, performed and analysed reverse transcription PCR, as well as cellular experiments, and provided physiological data. E.C. purified proteins and collected diffraction data. D.S.T. initiated the project, designed experiments, analysed data and wrote the manuscript.

**Author Information** Coordinates and structure factors for the arsenate-bound PfluDING structures at pH 4.5 and 8.5 are deposited in the Protein Data Bank (accession codes 4F18 and 4F19); the phosphate-bound PfluDING coordinates and structures at pH 4.5 and 8.5 (re-refinement) are deposited in the Protein Data Bank (accession codes 4F1U and 4F1V). Reprints and permissions information is available at [www.nature.com/reprints](http://www.nature.com/reprints). The authors declare no competing financial interests. Readers are welcome to comment on the online version of the paper. Correspondence and requests for materials should be addressed to D.S.T. (tawfik@weizmann.ac.il) or M.E. (mikael.elias@weizmann.ac.il).

# The spatial architecture of protein function and adaptation

Richard N. McLaughlin Jr<sup>1,2†</sup>, Frank J. Poelwijk<sup>1,2</sup>, Arjun Raman<sup>1,2</sup>, Walraj S. Gosal<sup>1,2</sup> & Rama Ranganathan<sup>1,2</sup>

Statistical analysis of protein evolution suggests a design for natural proteins in which sparse networks of coevolving amino acids (termed sectors) comprise the essence of three-dimensional structure and function<sup>1–5</sup>. However, proteins are also subject to pressures deriving from the dynamics of the evolutionary process itself—the ability to tolerate mutation and to be adaptive to changing selection pressures<sup>6–10</sup>. To understand the relationship of the sector architecture to these properties, we developed a high-throughput quantitative method for a comprehensive single-mutation study in which every position is substituted individually to every other amino acid. Using a PDZ domain (PSD95<sup>pdz3</sup>) model system, we show that sector positions are functionally sensitive to mutation, whereas non-sector positions are more tolerant to substitution. In addition, we find that adaptation to a new binding specificity initiates exclusively through variation within sector residues. A combination of just two sector mutations located near and away from the ligand-binding site suffices to switch the binding specificity of PSD95<sup>pdz3</sup> quantitatively towards a class-switching ligand. The localization of functional constraint and adaptive variation within the sector has important implications for understanding and engineering proteins.

A basic tenet of biology is that the amino acid sequence of proteins specifies their three-dimensional structure and biochemical function, at least in a physiological setting<sup>11</sup>. Statistical coupling analysis (SCA)<sup>1,2,5</sup> is a quantitative approach for understanding the information content of protein sequences through a generalization of the principle of evolutionary conservation. The underlying premise is that the pattern of energetic couplings between residues in a protein—the functional constraints between amino acids—might be exposed through a statistical analysis of coevolution of those residue positions in a family of homologous sequences. A main conclusion of SCA is that most residues in proteins evolve nearly independently, without much influence from even their immediate structural environment, whereas about 20% of amino acids (Fig. 1a and Supplementary Fig. 1) are organized into physically contiguous networks of coevolving amino acids, termed protein sectors<sup>1,2</sup>. Sectors are typically built around protein active sites, but connect to distant functional surfaces through pathways of residue interactions in the protein core<sup>12</sup>. For example, in the PDZ family of protein interaction modules, the sector connects the ligand-binding pocket with an allosteric site (Fig. 1b, asterisk) on the opposite surface<sup>2,13</sup>. Sectors are found in every protein family studied so far and are related to conserved functional activities, suggesting that this structural feature is a general property of natural proteins<sup>1,3,5,14–16</sup>.

An important next step is to understand why the design of natural proteins should look like the sector architecture, with distributed sparse networks of cooperatively acting residues embedded within an environment of weakly coupled amino acids. One reason might be necessity for native folding and function, but this seems unlikely. The marked recent advances in physics-based protein design are largely based on homogeneous optimization of local interactions in protein structures<sup>17,18</sup>, and alternative explanations for long-range communication within proteins have been suggested<sup>19</sup>. Our proposal is that the

sector is the natural consequence of evolutionary constraints not typically considered in protein engineering or biophysical models, primarily of the need for adaptive variation in response to fluctuating conditions of fitness. By placing the constraints on native folding and function on sector positions, this architecture might provide the capacity for rapid adaptive variation through mutation of a few cooperatively acting residues. If so, the plurality of non-sector positions, regardless of structural location, should display much more mutation tolerance and less adaptive potential.

Previous studies have tested the role of sectors in protein function using targeted mutagenesis of a few amino acid positions<sup>1–3,13–16,20</sup>. Although useful, these studies cannot convincingly test the sector hypothesis posed here, mainly due to the limited scale of experimentation. To address this, we developed a quantitative high-throughput method based on next-generation sequencing suitable for a large-scale mutational analysis of proteins in a cellular context (Fig. 2 and Supplementary Fig. 2). The method is implemented here for comprehensive single mutagenesis in one representative member of the PDZ family of protein interaction modules (PSD95<sup>pdz3</sup>) as a model system, but could be used for the study of many other proteins and for higher-order mutational studies (F.J.P. and R.R., unpublished observations).

The method involves three components: (1) a bacterial two-hybrid (B2H) system modified from a previous study<sup>21</sup> in which the ability of PSD95<sup>pdz3</sup> to bind its cognate ligand (–TKNYKQTSV–COOH, derived from the cysteine-rich interactor of PDZ (CRIPT)<sup>22</sup>) is quantitatively linked to the expression of enhanced green fluorescent protein (eGFP) (Supplementary Fig. 2a); (2) a fluorescence-activated cell sorting (FACS) step, in which bacterial populations carrying large libraries of mutations in the protein are selected for those cells displaying

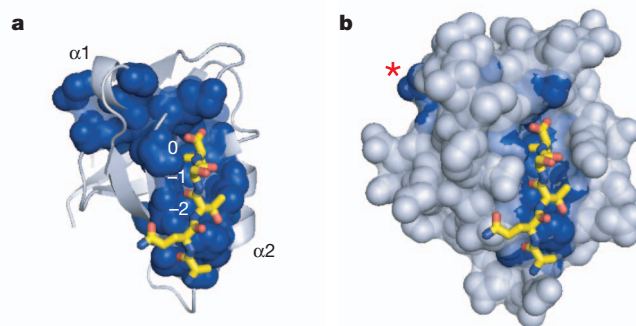


**Figure 1 | Sector architecture in the PDZ domain family.** **a, b**, The PDZ sector (blue spheres) shown in a cartoon (**a**) or space filling (**b**) representation of the structure of rat PSD95<sup>pdz3</sup> (Protein Data Bank (PDB) accession 1BE9). Yellow stick bonds represent the co-crystallized peptide ligand, with ligand positions numbered (0, –1, –2). The sector comprises a sparse network of residues built around the ligand-binding pocket and connecting to a distant surface site (marked with asterisk) through a subset of amino acid interactions within the protein core.

<sup>1</sup>Green Center for Systems Biology, University of Texas Southwestern Medical Center, Dallas, Texas 75390-9050, USA. <sup>2</sup>Department of Pharmacology, University of Texas Southwestern Medical Center, Dallas, Texas 75390-9050, USA. <sup>†</sup>Present address: Division of Basic Sciences, Fred Hutchinson Cancer Research Center, 1100 Fairview Avenue North, Seattle, Washington 98109-1024, USA.

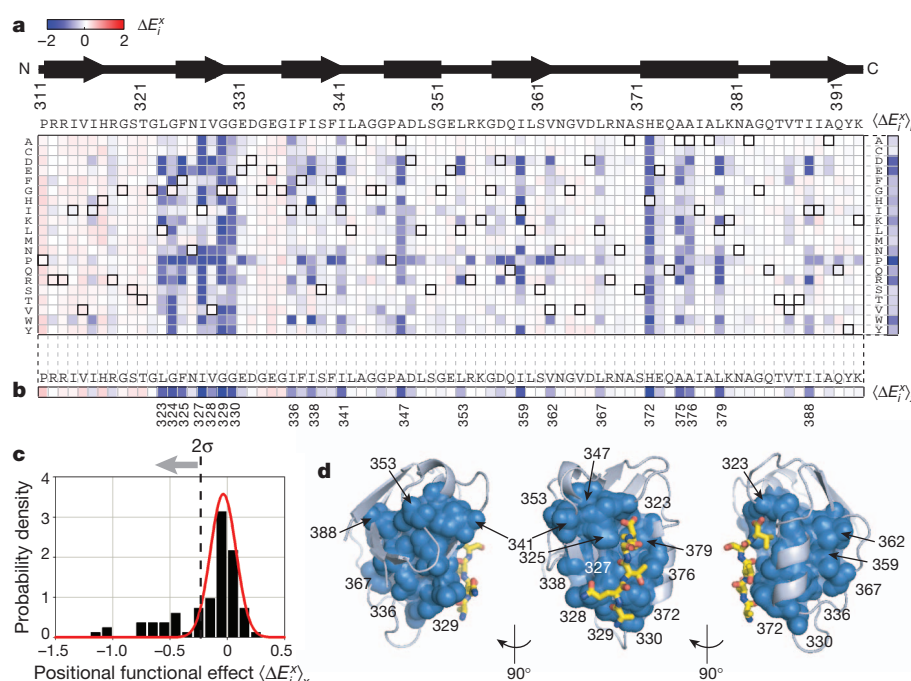


**Figure 2 | Complete single mutagenesis in PSD95<sup>Pdz3</sup>.** **a**, The data matrix showing  $\Delta E_i^x$ —the functional cost of every mutation  $x$  at each position  $i$  relative to wild-type PSD95<sup>Pdz3</sup>—colorimetrically, with blue representing loss-of-function and red representing gain-of-function mutations. The wild-type amino acid at each position is indicated by bold squares in the grid. The average functional cost of each amino acid substitution over all positions ( $\langle \Delta E_i^x \rangle_x$ ) is shown at the right. **b**, The functional cost of all amino acid substitutions at each

position shown as the average taken over each column ( $\langle \Delta E_i^x \rangle_x$ ). **c**, A histogram of the data in panel **b** indicates positions with a significant effect ( $>2\sigma$ , 20 out of 83). **d**, Mapping of the 20 functionally significant positions on the PSD95<sup>Pdz3</sup> structure, the peptide ligand shown as yellow stick bonds. These positions comprise a distributed, physically contiguous network built around the binding pocket and extending through the protein structure.

eGFP levels above a specified threshold (Supplementary Fig. 2b, c); and (3) Solexa high-throughput sequencing to determine the frequency of each allele in the unselected and selected populations<sup>23–26</sup> (Supplementary Fig. 2c). The effect of each mutation is then expressed as the log frequency of observing each amino acid  $x$  at each position  $i$  in the selected (sel) versus the unselected (unsel) population, relative to wild type (WT):

$$\Delta E_i^x = \log \left[ \frac{f_i^{x,\text{sel}}}{f_i^{x,\text{unsel}}} \right] - \log \left[ \frac{f_i^{\text{WT},\text{sel}}}{f_i^{\text{WT},\text{unsel}}} \right]$$

In this assay, mutations that show no functional effect should show a relative frequency in the selected population that is identical to wild type ( $\Delta E_i^x \approx 0$ ), and deviations from this expectation should provide a quantitative measure of the functional effect of each mutation. Tuning of growth and induction parameters and introduction of a point mutation in the bacteriophage  $\lambda$ -cI at Glu 34 (ref. 27) (Supplementary Fig. 3) led to experimental conditions that showed a near-linear relationship between the binding free energy of the PSD95<sup>Pdz3</sup> ligand interaction ( $\Delta G_{\text{bind}}$ ) and  $\Delta E_i^x$  over the range of binding affinities reported for natural PDZ domains ( $\sim 0.1$ – $200 \mu\text{M}$ ; Supplementary Figs 2d and 4).

We used the B2H-sequencing assay to carry out a complete single-mutation scan for the PSD95<sup>Pdz3</sup> domain in which every position shared with the overall PDZ family (83 total) is individually mutated to every other amino acid (Fig. 2a, 83 positions  $\times$  19 mutations + wild type = 1,578 variants). The data reveal several aspects of the global pattern of mutational sensitivity in the protein. First, the effect of each amino acid substitution averaged over all positions (across rows in the data matrix) is what might be predicted from the chemical properties of the side chains ( $\langle \Delta E_i^x \rangle_x$ , Fig. 2a, right). Proline is the most unfavourable substitution, followed by amino acids that are formally charged at neutral pH (Asp, Glu, Lys and Arg), and by tryptophan, the volumetrically largest side chain. Substitutions to alanine or cysteine

introduce the least perturbation on average, consistent with their use for scanning mutation or solvent accessibility studies, respectively.

To examine the position-specific effects of mutation in PSD95<sup>Pdz3</sup>, we considered both the full data matrix (Fig. 2a) and the average effect of all mutations per position ( $\langle \Delta E_i^x \rangle_x$ , Fig. 2b, c). This analysis indicates a heterogeneous, distributed and physically contiguous network of functional residues in PSD95<sup>Pdz3</sup> (Fig. 2b–d). Most positions show little effect on mutation, tolerating nearly every substitution even if radically different in chemical character (Fig. 2a–c and Supplementary Fig. 5). This includes some that are in direct contact with peptide ligand (for example, 326 and 380), and some that are buried in the protein core and largely conserved (for example, 314, 316, 356, 357 and 390). By contrast, a subset of positions (20 out of 83, Fig. 2c) shows significant sensitivity to mutation ( $>2\sigma$  from mean). Within the binding pocket, His 372 tolerates essentially no other substitution and Leu 323, Phe 325, Ile 327, and Leu 379 show tolerance to only the most chemically conservative mutations. However, outside the direct spatial environment of the ligand, Gly 329, Gly 330, Ile 336, Ala 347, Leu 353, Val 362 and Ala 375 comprise a subset of buried residues that also show significant sensitivity to mutation—the largest average mutational effect in the whole protein comes from position 329.

Analysis of the relationship between this global mutational analysis and the protein sector in the PDZ domain (Fig. 3a, top) shows that sector positions selectively comprise the tail region of the distribution of mutational sensitivity. Of 81 positions tested and statistically well-represented in the PDZ multiple sequence alignment (MSA), 20 positions show a significant functional effect (Fig. 2b, c), and 15 of these are sector positions (out of 20 sector positions in total) (Fig. 1 and Supplementary Fig. 1), indicating very strong statistical correlation between sector positions and functional effect on mutation ( $P < 10^{-8}$ , Fisher's exact test, Supplementary Fig. 6a). This correlation is robust to cut-offs used for both categories (Supplementary Fig. 6b).

Furthermore, the analysis shows that more standard measures for predicting functional importance of amino acids—such as burial in the

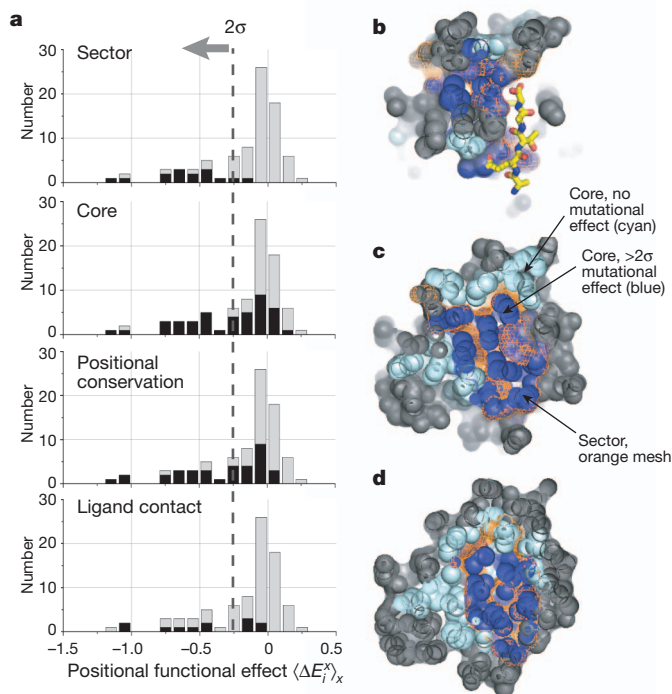


**Figure 3 | The relationship of mutational sensitivity of positions to the protein sector.** **a**, The distribution of mutational effect in PSD95<sup>pdz3</sup> (grey), overlaid with distributions (in black) of sector, core (solvent accessibility  $< 0.15$ ), positionally conserved (relative entropy  $> 1$ , the mean value over all positions in the MSA) and ligand contacting positions (within 4 Å shell of ligand atoms). **b–d**, Slices through the core of PSD95<sup>pdz3</sup>, showing mutationally significant core positions (dark blue), mutationally non-significant core positions (cyan), and the sector (orange mesh). All non-core positions are in grey, with the peptide ligand shown in yellow stick bonds.

protein core, positional conservation and contact with ligand—can also identify functional sites, but these criteria are not good overall descriptors of the data. Indeed, there are more conserved and buried positions that show no significant effect on mutation than otherwise (Fig. 3a, middle panels). Spatial proximity to ligand is the least likely hypothesis for explaining functional importance (Fig. 3a, bottom), consistent with the observations that not every direct interaction with ligand contributes to binding energy<sup>28</sup> and that non-local sites can influence active site function indirectly<sup>2</sup>. Serial slices through the core of the PSD95<sup>pdz3</sup> domain are also consistent with these observations; the sector (Fig. 3b–d, orange mesh) largely captures the functional subset of core positions (dark blue spheres) embedded among many other non-functional core positions (cyan spheres). We conclude that the main functional constraints on the PDZ domain are localized within the distributed network of amino acid positions that define the sector.

To determine whether the sector specifically encodes the ability to adapt to altered selection pressures, we repeated the global single-mutation study in PSD95<sup>pdz3</sup>, challenging the domain to bind a non-native peptide ligand (T<sub>-2</sub>F, TKNYKQFSV-COOH, indicating a Thr to Phe mutation at the minus two position (Fig. 1a); ligand positions are numbered in reverse order from the carboxy terminus (position 0)) (Supplementary Fig. 7). T<sub>-2</sub>F switches the CRIPT PDZ ligand from class I (-S/T-X-Ψ-COOH, where X is any amino acid, Ψ is hydrophobic) to class II (-X-Ψ-X-Ψ-COOH) specificity, and represents a substantial but physiologically relevant variation in PDZ function<sup>29</sup>. Accordingly, PSD95<sup>pdz3</sup> binds to the T<sub>-2</sub>F peptide with an approximately 45-fold decrease in binding affinity compared with the wild-type class I ligand (Fig. 4f).

We measured the difference in the functional effect of mutations when binding either the wild-type or T<sub>-2</sub>F ligands, a global analysis of the context dependence (or epistasis) between every mutation of every position in PSD95<sup>pdz3</sup> and the T<sub>-2</sub>F mutation on the peptide ligand (Fig. 4a, b). The data show that nearly all mutations at positions in PSD95<sup>pdz3</sup>—even if they have an absolute effect on ligand binding—show the same effect on binding the T<sub>-2</sub>F ligand as for the wild-type ligand, resulting in no significant epistasis with the T<sub>-2</sub>F mutation (Fig. 4c). These positions are insensitive to the switch in peptide identity and would therefore be non-adaptive with regard to this perturbation. However, mutations at nine positions in PSD95<sup>pdz3</sup> show statistically significant epistasis with the T<sub>-2</sub>F mutation (Fig. 4b, c); these positions show a mutational response that depends on the identity of the target ligand. These positions uniformly show an effect on mutation that is less deleterious for the T<sub>-2</sub>F ligand than for the wild-type ligand (Fig. 4b, red pixels). All of these positions are within the sector (Fig. 4d, see overlap between sector (blue mesh) and epistatic positions (red)), and map out a pattern of epistasis for the T<sub>-2</sub>F mutation that involves a spatially distributed network in the PDZ protein structure comprising residues both near and far from the minus two ligand position (Figs. 1a and 4d).

A subset of the sector positions (322, 330, 336 and 372) shows such extreme epistasis that the positions flip in the direction of mutational effect between the wild-type and T<sub>-2</sub>F ligands (Fig. 4a, b, d). Mutations at these positions destabilize or are neutral for binding to the wild-type ligand, but are favourable for binding the T<sub>-2</sub>F ligand and would therefore be selected when challenged to bind this class-switching variant. Notably, only one of the selectable sites (372) directly contacts the T<sub>-2</sub> ligand position. The other sites are located either one shell (329, 330) or two shells (336) of residues away from the binding pocket, or act at a distance from a loop contacting the terminal carboxylate of the ligand (322; Fig. 4d). We also find that for these few sites of selection for T<sub>-2</sub>F, it is not merely one or two mutations, but nearly every substitution that shows the effect of stabilizing binding to the T<sub>-2</sub>F ligand (Fig. 4b and Supplementary Fig. 7).

These data describe many potential mutational routes for switching the binding specificity PSD95<sup>pdz3</sup> towards the class II T<sub>-2</sub>F ligand. For example, mutation of position 330, which does not contact ligand (Fig. 4d), to threonine is expected to moderately destabilize binding to wild-type CRIPT ligand, but is the most favourable of all single mutants for the T<sub>-2</sub>F ligand (Fig. 4e). Also, His372Ala, a mutation at a position directly linking the -2 position of the ligand and position 330 (Fig. 4d), is expected to decrease binding for CRIPT more strongly than the Gly330Thr mutation, but to increase binding for T<sub>-2</sub>F to a similar degree (Fig. 4e). Binding affinities for Gly330Thr, His372Ala and the double mutant combination were measured using a fluorescence polarization assay and show excellent consistency with the B2H data (Fig. 4f). His372Ala converts PSD95<sup>pdz3</sup> from a protein with an approximately 45-fold preference for the CRIPT ligand to one with about a 14-fold preference for the T<sub>-2</sub>F ligand, a partial specificity switch from a single mutation. By contrast, Gly330Thr converts PSD95<sup>pdz3</sup> to a domain with an unexpected phenotype: high-affinity but non-specific recognition of both CRIPT and T<sub>-2</sub>F ligands. Such a phenotype could be evolutionarily important when a mutational path characterized by a promiscuous but biologically functional intermediate is advantageous. Finally, the combination of both mutations (Gly330Thr and His372Ala) completes the specificity switch; this double mutant displays an approximately 45-fold preference for the T<sub>-2</sub>F ligand. These data demonstrate that short, cooperative paths of mutation within the sector can suffice to change functional specificity quantitatively.

In summary, the data presented here indicate that protein robustness and adaptability can be explained through a model in which the main functional constraints are loaded in the sector—a sparse, collectively evolving network within the protein structure. By saturation point mutagenesis, we find that sector positions selectively resist variation when challenged with wild-type ligand, but can flip to promote

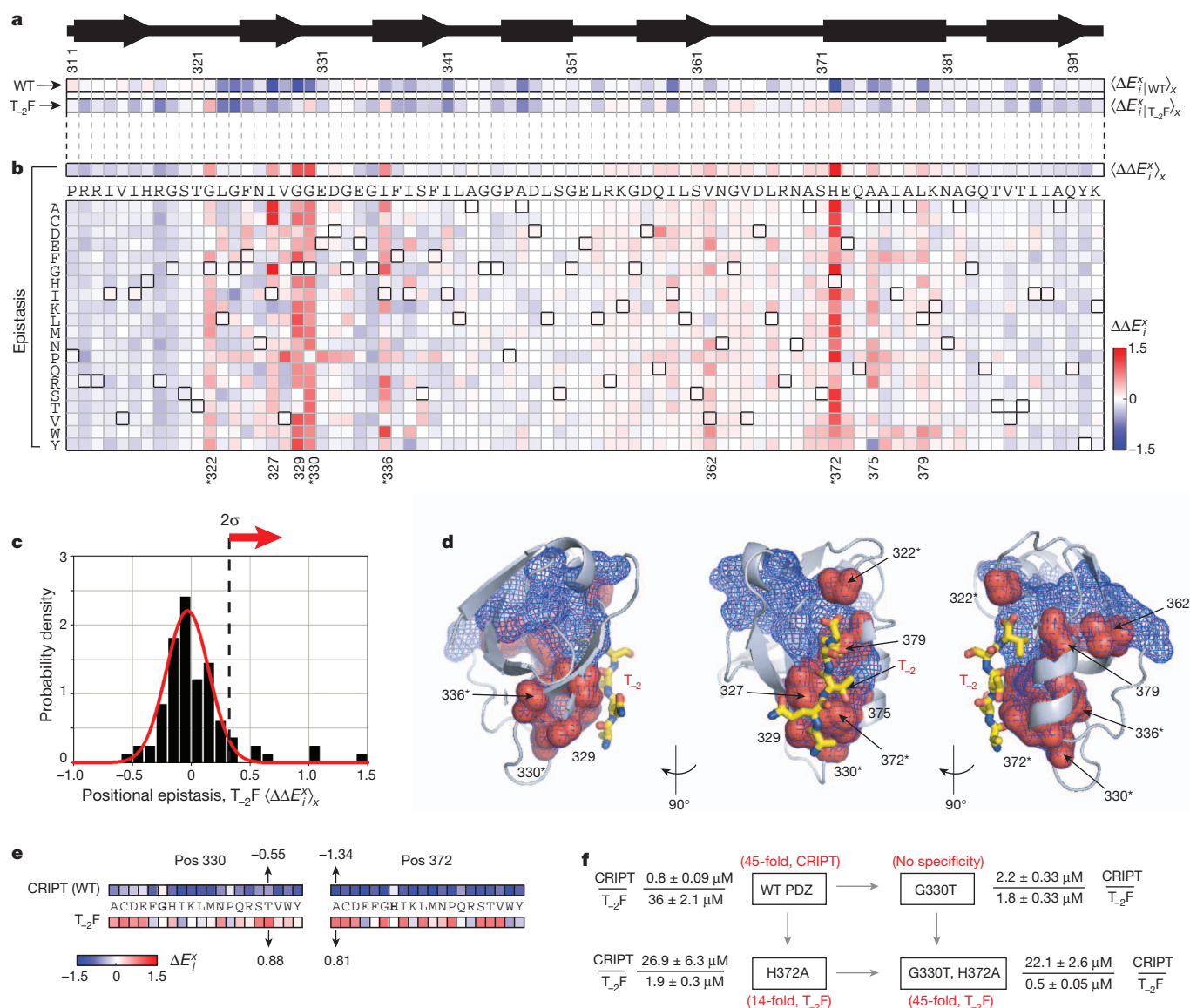


**Figure 4 | Adaptation through sector variation.** **a**, Average mutational effect in PSD95<sup>pdz3</sup> when binding the wild-type ligand CRIP1 ( $\langle \Delta E_{ij}^{WT} \rangle_x$ , top) or a class-switching T<sub>-2</sub>F variant ( $\langle \Delta E_{ij}^{T_{-2}F} \rangle_x$ , bottom). T<sub>-2</sub>F contains a Thr to Phe mutation at position minus two of the peptide ligand (Fig. 1a). **b**, The difference, or epistasis, between mutational effects for binding wild-type or T<sub>-2</sub>F ligands, shown either averaged over amino acids at each position (top,  $\langle \Delta \Delta E_{ij}^x \rangle_x$ ) or broken down by amino acid (bottom,  $\Delta \Delta E_{ij}^x = \Delta E_{ij}^{T_{-2}F} - \Delta E_{ij}^{WT}$ ). The nine positions showing statistically significant epistasis (c) are numbered, and the asterisks mark positions where mutations on average can be positively selected for the T<sub>-2</sub>F ligand. **c**, A histogram of epistasis between mutations at each position in PSD95<sup>pdz3</sup> and the T<sub>-2</sub>F ligand variation. **d**, A mapping of epistatic positions (red) on the structure of PSD95<sup>pdz3</sup>; the wild-type peptide

variation when challenged with a functionally distinct ligand. This epistatic coupling between ligand and sector underlies efficient functional adaptation, permitting considerable changes in specificity through very few mutations. Turned around, these data provide support for the hypothesis that the sector architecture might be the natural solution to design by evolution under conditions of constantly fluctuating environments. Such environments impose the need for maintaining robustness to mutation and adaptability to varying selection pressures and have been shown theoretically to influence the design of evolving systems<sup>30</sup>. It will be important to now experimentally test the notion that the statistical history of fluctuations in conditions of selection fundamentally defines the physical design of natural proteins.

ligand is shown in yellow stick bonds, the T<sub>-2</sub> position is indicated in red and sector positions are in blue mesh. The positions showing mutational epistasis with T<sub>-2</sub>F comprise a physically distributed network propagating from the T<sub>-2</sub> position, and are entirely composed of sector positions. The asterisks are as in **b**, **e**. The B2H-sequencing data for sector positions 330 and 372 when binding CRIP1 (Fig. 2c) or T<sub>-2</sub>F (Supplementary Fig. 7) ligands suggest mutations for altering the specificity of PSD95<sup>pdz3</sup> towards T<sub>-2</sub>F; the wild-type amino acid is shown in bold. **f**, Binding affinities for purified PSD95<sup>pdz3</sup> carrying the Gly330Thr and His372Ala mutations both singly and together. Gly330Thr displays high affinity but non-specific binding for CRIP1 and T<sub>-2</sub>F ligands, His372Ala shows a partial specificity switch towards T<sub>-2</sub>F and the double mutant represents a complete specificity switch for these two ligands.

## METHODS SUMMARY

SCA and sector identification were carried out using version 5.0 of the SCA MATLAB toolbox. The software and a script for carrying out the calculations is available for download from our laboratory website ([http://systems.swmed.edu/rr\\_lab](http://systems.swmed.edu/rr_lab)).

Comprehensive single-mutation libraries in PSD95<sup>pdz3</sup> were constructed by oligonucleotide-directed mutagenesis, randomizing each codon to NNS, in which N represents a mixture of all four bases, and S represents a mixture of G and C. NNS libraries for each codon were separately amplified by PCR, mixed in an equimolar ratio, and cloned into pZS22-PDZ3 (see later) to make the library.

The B2H system consists of three plasmids: (1) pZS22-PDZ3 (kanamycin resistant), providing IPTG-inducible expression of PSD95<sup>pdz3</sup> variants fused to the DNA-binding domain of bacteriophage  $\lambda$ -cI; (2) pZA31-RNA $\alpha$ -CRIP1 (or T<sub>-2</sub>F) (chloramphenicol resistant), providing anhydrotetracycline-inducible

expression of the amino-terminal domain of *Escherichia coli* RNA polymerase  $\alpha$ -subunit fused to the target peptide ligand; and (3) pZE1RM-eGFP (ampicillin resistant), containing the target promoter driving the enhanced green fluorescent protein (eGFP). MC4100-Z1 *E. coli* cells transformed with these three plasmids were grown in ZYM-505 media, diluted with inducers to attenuance at 600 nm ( $D_{600\text{ nm}}$ ) of 0.4, grown for 2 h, and subjected to FACS sorting (BD FACSAria, gates set at top 10% and 25% of eGFP distribution for wild-type PSD95<sup>pdz3</sup>). Sorted cells were grown in ZYM-505 for 12 h, miniprep and amplified by PCR to prepare samples for Solexa paired-end sequencing completed using Solexa v4 PE-flowcell (University of Texas Southwestern genomics core) and analysed through CLC Genomics Workbench and self-coded software.

For biophysical measurements, PSD95<sup>pdz3</sup> variants were expressed in BL21(DE3) *E. coli* cells as glutathione S-transferase (GST) fusions and purified using affinity chromatography and cleavage of the GST tag. Binding affinities were determined using tetramethylrhodamine (TMR)-labelled target peptides, monitoring fluorescence polarization of TMR on a Victor<sup>3</sup>V plate reader as a function of PSD95<sup>pdz3</sup> concentration.

**Full Methods** and any associated references are available in the online version of the paper.

**Received 18 July 2011; accepted 10 August 2012.**

**Published online 7 October 2012.**

- Halabi, N., Rivoire, O., Leibler, S. & Ranganathan, R. Protein sectors: evolutionary units of three-dimensional structure. *Cell* **138**, 774–786 (2009).
- Lockless, S. W. & Ranganathan, R. Evolutionarily conserved pathways of energetic connectivity in protein families. *Science* **286**, 295–299 (1999).
- Russ, W. P., Lowery, D. M., Mishra, P., Yaffe, M. B. & Ranganathan, R. Natural-like function in artificial WW domains. *Nature* **437**, 579–583 (2005).
- Socolich, M. *et al.* Evolutionary information for specifying a protein fold. *Nature* **437**, 512–518 (2005).
- Süel, G. M., Lockless, S. W., Wall, M. A. & Ranganathan, R. Evolutionarily conserved networks of residues mediate allosteric communication in proteins. *Nature Struct. Mol. Biol.* **10**, 59–69 (2003).
- Bershtein, S., Segal, M., Bekerman, R., Tokuriki, N. & Tawfik, D. S. Robustness-epistasis link shapes the fitness landscape of a randomly drifting protein. *Nature* **444**, 929–932 (2006).
- Bloom, J. D., Labthavikul, S. T., Otey, C. R. & Arnold, F. H. Protein stability promotes evolvability. *Proc. Natl Acad. Sci. USA* **103**, 5869–5874 (2006).
- Draghi, J. A., Parsons, T. L., Wagner, G. P. & Plotkin, J. B. Mutational robustness can facilitate adaptation. *Nature* **463**, 353–355 (2010).
- Tiana, G., Shakhnovich, B. E., Dokholyan, N. V. & Shakhnovich, E. I. Imprint of evolution on protein structures. *Proc. Natl Acad. Sci. USA* **101**, 2846–2851 (2004).
- Voigt, C. A., Kauffman, S. & Wang, Z. G. Rational evolutionary design: the theory of *in vitro* protein evolution. *Adv. Protein Chem.* **55**, 79–160 (2000).
- Anfinsen, C. B. Principles that govern the folding of protein chains. *Science* **181**, 223–230 (1973).
- Reynolds, K. A., McLaughlin, R. N. & Ranganathan, R. Hot spots for allosteric regulation on protein surfaces. *Cell* **147**, 1564–1575 (2011).
- Peterson, F. C., Penkert, R. R., Volkman, B. F. & Prehoda, K. E. Cdc42 regulates the Par-6 PDZ domain through an allosteric CRIB-PDZ transition. *Mol. Cell* **13**, 665–676 (2004).
- Hatley, M. E., Lockless, S. W., Gibson, S. K., Gilman, A. G. & Ranganathan, R. Allosteric determinants in guanine nucleotide-binding proteins. *Proc. Natl Acad. Sci. USA* **100**, 14445–14450 (2003).
- Shulman, A. I., Larson, C., Mangelsdorf, D. J. & Ranganathan, R. Structural determinants of allosteric ligand activation in RXR heterodimers. *Cell* **116**, 417–429 (2004).
- Smock, R. R. O., Russ, W. P., Swain, J. F., Leibler, S., Ranganathan, R. & Gierasch, L. M. An interdomain sector mediating allostery in Hsp70 molecular chaperones. *Mol. Syst. Biol.* **6**, 414 (2010).
- Bradley, P., Misura, K. M. S. & Baker, D. Toward high-resolution *de novo* structure prediction for small proteins. *Science* **309**, 1868–1871 (2005).
- Kuhlman, B. *et al.* Design of a novel globular protein fold with atomic-level accuracy. *Science* **302**, 1364–1368 (2003).
- Hilser, V. J. & Thompson, E. B. Intrinsic disorder as a mechanism to optimize allosteric coupling in proteins. *Proc. Natl Acad. Sci. USA* **104**, 8311–8315 (2007).
- Chi, C. N. *et al.* Reassessing a sparse energetic network within a single protein domain. *Proc. Natl Acad. Sci. USA* **105**, 4679–4684 (2008).
- Dove, S. L., Joung, J. K. & Hochschild, A. Activation of prokaryotic transcription through arbitrary protein-protein contacts. *Nature* **386**, 627–630 (1997).
- Niethammer, M. *et al.* CRIP, a novel postsynaptic protein that binds to the third PDZ domain of PSD-95/SAP90. *Neuron* **20**, 693–707 (1998).
- Adkar, B. V. *et al.* Protein model discrimination using mutational sensitivity derived from deep sequencing. *Structure* **20**, 371–381 (2012).
- Fowler, D. M. *et al.* High-resolution mapping of protein sequence-function relationships. *Nature Methods* **7**, 741–746 (2010).
- Kinney, J. B., Murugan, A., Callan, C. G. & Cox, E. C. Using deep sequencing to characterize the biophysical mechanism of a transcriptional regulatory sequence. *Proc. Natl Acad. Sci. USA* **107**, 9158–9163 (2010).
- van Opijnen, T., Bodi, K. L. & Camilli, A. Tn-seq: high-throughput parallel sequencing for fitness and genetic interaction studies in microorganisms. *Nature Methods* **6**, 767–772 (2009).
- Whipple, F. W., Ptashne, M. & Hochschild, A. The activation defect of a  $\lambda$ -cl positive control mutant. *J. Mol. Biol.* **265**, 261–265 (1997).
- Clackson, T. & Wells, J. A. A hot spot of binding energy in a hormone-receptor interface. *Science* **267**, 383–386 (1995).
- Songyang, Z. *et al.* Recognition of unique carboxyl-terminal motifs by distinct PDZ domains. *Science* **275**, 73–77 (1997).
- Kussell, E. & Leibler, S. Phenotypic diversity, population growth, and information in fluctuating environments. *Science* **309**, 2075–2078 (2005).

**Supplementary Information** is available in the online version of the paper.

**Acknowledgements** We thank W. Russ, P. Mishra and other members of the Ranganathan laboratory for contributions to this work, W. Wakeland and C. Liang for assistance with Solexa sequencing, E. Curry and A. Mobley for assistance with flow cytometry, and M. Elowitz for providing the pZ plasmids. We acknowledge support from the University of Texas Southwestern Graduate School and Pharmacology Training Grant (R. N. M.), the Helen Hay Whitney Fellowship program (F.J.P.) and support from the National Institutes of Health (R01EY018720-05, R.R.), The Robert A. Welch Foundation (I-1366, R.R.) and the Green Center for Systems Biology (R.R.).

**Author Contributions** R.N.M. and R.R. developed the research plan and experimental strategy. R.N.M. built the B2H assay, collected the data and wrote and executed the code for analysis of the B2H and sequencing data. F.J.P. and W.S.G. improved the dynamic range of the B2H assay. A.R. carried out the mutational analysis in Fig. 4 e, f. R.N.M. and R.R. analysed the data and wrote the paper.

**Author Information** Reprints and permissions information is available at [www.nature.com/reprints](http://www.nature.com/reprints). The authors declare no competing financial interests. Readers are welcome to comment on the online version of the paper. Correspondence and requests for materials should be addressed to R.R. ([rama.ranganathan@utsouthwestern.edu](mailto:rama.ranganathan@utsouthwestern.edu)).

## METHODS

**SCA.** SCA was carried out on a multiple sequence alignment comprising 240 diverse eukaryotic PDZ domains based on previously reported methods<sup>1</sup> but using an updated version (v5.0) of the SCA MATLAB toolbox (O. Rivoire, S. Leibler and R. R. manuscript in preparation). A multiple sequence alignment can be represented mathematically as a three-dimensional binary tensor  $x_{s,i}^a$  ( $M$  sequences by  $L$  positions by 20 amino acids) whose elements are 1 if sequence  $s$  has amino acid  $a$  at position  $i$ , and 0 otherwise. The frequency of each amino acid  $a$  at each position  $i$  is simply the number of sequences with amino acid  $a$  at  $i$  divided by the total number of sequences; this can be written as  $f_i^a = \langle x_{s,i}^a \rangle_s$ , in which the angle brackets indicate mean value. The usual definition of a correlation tensor describing the statistical coupling of each pair of amino acids  $a$  and  $b$  at each pair of positions  $i$  and  $j$  would be  $C_{ij}^{ab} = f_{ij}^{ab} - f_i^a f_j^b$ , the joint frequency of observing the two amino acids at the pair of positions minus the expected frequency if the two were statistically independent. However, as described previously<sup>1</sup>, a basic principle of SCA is to weight the raw correlations by a position specific function of the conservation of the amino acids in question; thus the SCA correlation tensor is  $\tilde{C}_{ij}^{ab} = \phi_i^a \phi_j^b C_{ij}^{ab}$ , with  $\phi_i^a = \ln[f_i^a(1 - q^a)/(1 - f_i^a q^a)]$ , and in which  $q^a$  is the background frequency of amino acid  $a$  in the overall non-redundant database of protein sequences. Properties of  $\tilde{C}_{ij}^{ab}$  suggest an approach for reducing this tensor to a matrix of positional correlations  $\tilde{C}_{ij}$  in which the overall correlation of all pairs of amino acids at positions  $i$  and  $j$  is captured in a scalar value<sup>1</sup> (O. Rivoire, S. Leibler and R. R., manuscript in preparation). The PDZ sector is defined by positions showing statistically significant weights in the top eigenmode of the  $\tilde{C}_{ij}$  matrix (Supplementary Fig. 1). The PDZ sequence alignment, the SCA 5.0 toolbox and a script for carrying out the SCA calculations are available for download from the Ranganathan laboratory website ([http://systems.swmed.edu/rr\\_lab](http://systems.swmed.edu/rr_lab)).

**Expression and purification of PDZ3 mutants.** pGEX-4T-1 plasmids containing Glutathione S-transferase (GST)-fusions of wild-type or mutant PSD95<sup>pdz3</sup> cloned into the BsmBI/XbaI sites were used to transform BL21(DE3) bacterial cells and grown overnight on LB plus 100  $\mu\text{g ml}^{-1}$  ampicillin plates. MDG minimal media cultures were inoculated with streaks of fresh-transformants and grown overnight. Expression was carried out using an auto-induction protocol<sup>31</sup>: 11 cultures in ZYM-5052 plus 50  $\mu\text{g ml}^{-1}$  ampicillin were inoculated with 1 ml starter culture, grown at 37 °C until attenuation ( $D_{600\text{ nm}}$ ) of around 0.5, cooled on ice, and induced at 20 °C until growth plateaued (usually at 16–18 h). Cells were collected at 500g for 15 min and resuspended in 35 ml with NMR buffer (25 mM KHPO<sub>4</sub>, 50 mM NaCl, 1 mM EDTA, pH 7.0) plus 1 mM phenylmethylsulphonyl fluoride (PMSF), 10  $\mu\text{g ml}^{-1}$  leupeptin, 2  $\mu\text{g ml}^{-1}$  pepstatin and frozen in liquid N<sub>2</sub> for storage at –80 °C.

Frozen pellets were slow-thawed in an ice and water bath and cells were lysed by sonication with a 1.9-cm dual tip (10 s on, 5 s off cycles, 5 min total). Lysate was cleared by centrifugation at 50,000g for 1 h, and incubated for 1 h at 4 °C with 2 ml glutathione sepharose (GE-Amersham) pre-equilibrated in NMR buffer. The resin was washed three times with 25 bed volumes of PBS (10 mM Na<sub>2</sub>HPO<sub>4</sub>, 1.8 mM KH<sub>2</sub>PO<sub>4</sub>, 140 mM NaCl, 2.7 mM KCl, pH 7.4) and three times with 25 bed volumes of NMR buffer. To cleave the GST tag the resin was resuspended in 1.8 ml NMR buffer, incubated with 20 U thrombin for 12 h at room temperature or until cleavage reached ~75%. PDZ domains were recovered from the supernatant by collecting 200  $\mu\text{l}$  elutions until  $D_{280\text{ nm}} < 0.4$ . Elutions were combined and incubated with 20  $\mu\text{l}$  benzamidine sepharose for 30 min at 4 °C to clear the protease. A disposable column was used to elute the cleaved, thrombin-free PDZ protein. Proteins were checked for purity on SDS-PAGE and concentration was determined using bicinchoninic acid (BCA) (Pierce) assay and normalized to a wild-type PSD95<sup>pdz3</sup> preparation that had been analysed using amino acid analysis (University of California Davis, Proteomics Core).

**Fluorescence polarization-based assay for peptide binding.** Fluorescence polarization measurements were carried out using a tetramethyl rhodamine (TMR)-labelled CRIPT peptide (TMR-TKNYKQTSV-COOH), synthesized by the University of Texas Southwestern Protein Chemistry Core and reconstituted to 100 nM peptide in NMR Buffer with 0.5 % BSA plus 5 mM dithiothreitol (DTT) at pH 7.0. Each purified PDZ protein preparation was diluted to 100  $\mu\text{M}$ . In triplicate, serial dilutions of each PDZ domain were made in an untreated 96-well plate (50  $\mu\text{l}$  volume of 8 concentrations spanning 100  $\mu\text{M}$  to 781 nM). Forty microlitres of each PDZ dilution is mixed with 10  $\mu\text{l}$  TMR-labelled peptide solution in a black, clear bottom untreated 384-well, incubated at room temperature for 1 h, and fluorescence polarization (531 nm excitation, 590 nm emission, 1 s integration) was measured using a Perkin Elmer Victor<sup>3</sup> plate reader. The data for the three triplicate assays were fit using the saturation binding model in GraphPad prism software and used to extract the equilibrium dissociation constant.

**NNS library construction.** Comprehensive single mutant libraries were constructed using oligonucleotide-directed mutagenesis of PSD95<sup>pdz3</sup>. To mutate each position in PSD95<sup>pdz3</sup> (positions 311–393), two mutagenic oligonucleotides (one sense, one antisense) were synthesized (IDT) that contain sequence complementary to 15 base pairs (bp) on either side of the targeted position. For the targeted position, the oligonucleotides contain NNS codons, in which N is a mixture of A, T, C and G, and S is a mixture of G and C. This biased randomization results in 32 possible codons with all 20 amino acids sampled—a significant decrease in library complexity without loss of amino acid complexity. One round of PCR was carried out with either the sense or antisense oligonucleotide and a flanking antisense or sense oligonucleotide. A second PCR round using a combination of the first round products and both flanking primers produced the full-length double stranded product. For the 83 positions randomized here, this constituted 83  $\times$  2 first round PCR reactions and 83 second round reactions, for a total of 249 PCR reactions. All reactions yielded a single intense band on an agarose gel. PCR product concentrations were measured using Picogreen (Invitrogen), pooled in equimolar ratios, purified, digested and ligated into the B2H  $\lambda$ -cI fusion expression vector. Each ligation was purified, eluted into 7  $\mu\text{l}$  dH<sub>2</sub>O, and measured in the B2H assay as described earlier. Each transformation yielded greater than 10<sup>6</sup> variants.

To permit coverage of the full PSD95<sup>pdz3</sup> gene (~300 bp) with 75-base paired-end reads by Solexa sequencing, we split the PSD95<sup>pdz3</sup> sequence into three subgroups (positions 311–338, 339–365 and 366–393, respectively). The NNS-mutagenesis products for the positions of each subgroup were mixed and ligated as a single library. Each subgroup was independently subject to the B2H assay, FACS, amplification and sample preparation for Solexa sequencing (see later).

**The B2H assay.** Electrocompetent MC4100-Z1 cells<sup>32</sup> containing pZE1RM-eGFP (ampicillin resistant) and pZA31-RNA $\alpha$ -CRIPT (chloramphenicol resistant)<sup>33</sup> plasmids were transformed with 1  $\mu\text{l}$  of 20 ng  $\mu\text{l}^{-1}$  pZS22-PDZ3-WT (kanamycin resistant) plasmid and recovered for 1 h in ZYM-505 media. To quantify library complexity, 1  $\mu\text{l}$  recovered transformation mixture was plated on LB plus kanamycin. The entire 1 ml transformation was then added to 10 ml ZYM-505 (ref. 31) plus kanamycin (30  $\mu\text{g ml}^{-1}$ ) and ampicillin (50  $\mu\text{g ml}^{-1}$ ) and chloramphenicol (25  $\mu\text{g ml}^{-1}$ ) in a 50 ml baffled flask, grown 6 h at 37 °C at 225 r.p.m., then diluted 10  $\mu\text{l}$  culture into 10 ml ZYM-505 plus antibiotics, and grown 12 h at 37 °C at 225 r.p.m., and finally measured for attenuation (D) at 600 nm. A 35  $\mu\text{l}$  aliquot of each culture was added to one well of a 48-well plate containing 500  $\mu\text{l}$  LB with antibiotics plus anhydrotetracycline (100 ng  $\text{ml}^{-1}$ ) plus isopropylthiogalactoside (IPTG) (100  $\mu\text{M}$ ) for a final  $D_{600} = 0.4$ , and incubated at 18 °C, 150 r.p.m. for 2 h for induction. Induced cells were diluted to 30  $\mu\text{l}$  cells in 1 ml filter-sterilized M9 plus 0.4% glucose for flow cytometry. Before analysis or sorting, cells were passed through a 30-gauge needle for disaggregation to single cells.

All flow cytometry was performed with standardized settings on a BD FACScan, setup to measure GFP fluorescence (FL1). Cell sorting was performed on the BD FACSAria by technicians in the UT Southwestern Medical Center cytometry core. For library selections, flow-cytometry gates were placed relative to the fluorescence distribution of WT-PDZ3 to control for systematic assay-to-assay variability. For each NNS library, two populations were collected at gates set at the top 10% and 25% of the WT-PDZ3 distribution. When sorting a complex library of PDZ3 mutants, a positive cell population numbering greater than 1,000 times the complexity of the library was collected. Cells were sorted into chilled rich medium (ZYM-505 without antibiotics, 4 °C), and the collection tube was kept chilled in the cytometer during sorting to maximize cell viability. Typical viability of sorted cell populations were >70 % when plated on selective medium.

**Identification of  $\lambda$ -cI Glu34Pro to increase B2H dynamic range.** An initial problem with dynamic range in the B2H assay was high basal activity, such that eGFP was expressed to some degree even without PDZ domain function. A mechanistic explanation for this high basal activity was suggested by the observation that one of the  $\lambda$ -cI-binding sites on the eGFP promoter is sufficiently close to the RNA polymerase  $\sigma$  subunit as to activate transcription through direct (PDZ-independent) contact. Previous studies showed one  $\lambda$ -cI position (Glu 34) underlies this non-specific mode of transactivation<sup>27,34,35</sup>. To identify  $\lambda$ -cI variants with reduced basal activity, a library of all possible amino acid substitutions at position 34 (Glu34X) was cloned and expressed in the B2H assay as described earlier. Induced B2H Glu34X libraries containing wild-type PSD95<sup>pdz3</sup> and CRIPT peptide (high-affinity interaction) were plated on selective medium, and the GFP intensity of hundreds of colonies was visually assessed using a wide-field fluorescence microscope. Twenty colonies with high intensity were picked, pooled, grown in liquid culture and minipreped to isolate plasmid DNA. This library of high intensity clones was then induced in the B2H assay containing a peptide that should not bind wild-type PSD95<sup>pdz3</sup> (TKNYKQGGG) for negative selection. This library was plated on selective medium and four colonies with low intensity were picked and sequenced. All four colonies contained the Glu34Pro  $\lambda$ -cI variant,

suggesting that this variant should provide an increased dynamic range for the B2H assay. This prediction was confirmed in the standard B2H assay using a set of PSD95<sup>bdz3</sup> mutants as described in Supplementary Fig. 2.

**Solexa sequencing.** Sorted cell populations were diluted into ZYM-505 plus kanamycin and grown 12 h at 37 °C with shaking (250 r.p.m.). Overnight cultures were centrifuged and miniprep (Promega Wizard Plus SV miniprep kit). Purified DNA was quantified (Nanodrop ND-1000 Spectrophotometer), and 200 ng of plasmid DNA per 50 µl PCR reaction was used as template for the first round of adaptor addition. To preserve the ratio of template alleles, we used a large template concentration and few amplification cycles (16 cycles). This first PCR reaction added the Solexa paired-end sequencing oligonucleotide annealing site as well as a 3-bp barcode that indicates the origin of the sample (input or selected library, selection gate). The second PCR reaction added the remainder of the sequencing oligonucleotide annealing site and the annealing site for the flow cell oligonucleotide. All oligonucleotides were purchased from IDT as 100 nM syntheses with standard purification. Each PCR reaction included 5% dimethylsulphoxide (DMSO) and produced a single intense band on an agarose gel.

The second round PCR products were purified (ZYMO DNA clean and concentrator-5 Kit) and eluted in 20 µl dH<sub>2</sub>O. Purified PCR products were quantified (Invitrogen quant-IT picogreen dsDNA quantification kit) in triplicate using lambda-DNA as a standard. PCR products were diluted to 10 nM and 8 pmol was loaded onto a Solexa v4 PE-flow cell in the University of Texas South-western Genome Sequencing Core that yielded 250,000–300,000 clusters per lane.

Owing to the unbalanced nature of the first bases of each PCR product, a PhiX control lane was used for matrix and phasing calculations as per manufacturer recommendation.

Sequences from the Illumina RTA base-caller were imported into CLC Genomics Workbench as '.qseq' files and trimmed for quality using a cut-off of 0.05 for the modified Mott algorithm. Bases that did not pass the trim filter were deleted from each read, and reads shorter than 49 bp were discarded. Reads were sorted into groups according to the 3-bp barcode contained in each PCR product, and barcode groups were exported as FASTQ files for further analysis. Custom software written in MATLAB was used to count the number of occurrences of each allele in each population. The functional effect of each allele was calculated as the average of the value from the two FACS gates (Supplementary Fig. 4).

31. Studier, F. W. Protein production by auto-induction in high density shaking cultures. *Protein Expr. Purif.* **41**, 207–234 (2005).
32. Lutz, R. & Bujard, H. Independent and tight regulation of transcriptional units in *Escherichia coli* via the LacR/O, the TetR/O and AraC/I<sub>1</sub>-I<sub>2</sub> regulatory elements. *Nucleic Acids Res.* **25**, 1203–1210 (1997).
33. Elowitz, M. B. & Leibler, S. A synthetic oscillatory network of transcriptional regulators. *Nature* **403**, 335–338 (2000).
34. Bushman, F. D., Shang, C. & Ptashne, M. A single glutamic acid residue plays a key role in the transcriptional activation function of lambda repressor. *Cell* **58**, 1163–1171 (1989).
35. Jain, D., Nickels, B. E., Sun, L., Hochschild, A. & Darst, S. A. Structure of a ternary transcription activation complex. *Mol. Cell* **13**, 45–53 (2004).